

KSA-10

N71-30756

NASA SP-270

NASA AIRCRAFT SAFETY AND OPERATING PROBLEMS

VOL I JULY 29, 1971
VOL II JUN 30, 1971
VOLUME I

NASA FILE COPY

Return to

NASA HQ. LIBRARY (KSA-10)

WASHINGTON, D. C. 20546 STOP 85

HQ. LIBRARY (KSA-10)

A conference held at
LANGLEY RESEARCH CENTER
Hampton, Virginia
May 4-6, 1971



NATIONAL AERONAUTICS AND SPACE ADMINISTRATION

NASA AIRCRAFT SAFETY AND OPERATING PROBLEMS VOLUME I

Proceedings of a conference
held at
Langley Research Center
Hampton, Virginia
May 4-6, 1971

Prepared by Langley Research Center



Scientific and Technical Information Office

NATIONAL AERONAUTICS AND SPACE ADMINISTRATION
Washington, D.C.

1971

PREFACE

The proceedings of the Conference on NASA Aircraft Safety and Operating Problems held at Langley Research Center, Hampton, Virginia, on May 4-6, 1971, are reported in this NASA Special Publication.

The purpose of this conference was to discuss the results of research of the National Aeronautics and Space Administration in the field of aircraft safety and operating problems. The unclassified program components include the following:

- (1) Flight Safety
- (2) Airway and Runway Environment
- (3) Operational Experience With Subsonic Cruise Aircraft
- (4) Cockpit Environment
- (5) Terminal Area Operations
- (6) Flight Environment
- (7) Induced Environmental Effects

Contributions to this compilation were made by representatives from Ames, Flight, Langley, and Lewis Research Centers, Manned Spacecraft Center, George C. Marshall Space Flight Center, the University of Virginia, the Research Triangle Institute, and the Federal Aviation Administration.

The confidential material is presented in NASA SP-271.

Page intentionally left blank

CONTENTS

PREFACE	iii
-------------------	-----

General Chairman: Philip Donely, Langley Research Center

FLIGHT SAFETY

Session Chairman: I. Irving Pinkel, Lewis Research Center

Co-Chairman: Solomon Weiss, Lewis Research Center

1. FACTORS AFFECTING DITCHING OF NEW TRANSPORT AIRPLANES	1
Lloyd J. Fisher	
2. STUDY OF PROTECTION OF PASSENGERS IN AIRCRAFT CRASH FIRES	11
Carr B. Neel and Richard H. Fish	
3. IMPROVEMENT OF FIRE SAFETY IN AIRCRAFT	33
Matthew I. Radnofsky	
4. A CONTINUOUS-WAVE DOPPLER SYSTEM FOR AIRCRAFT COLLISION HAZARD WARNING	49
Richard H. Couch and Charles L. Britt	
5. LIGHTNING-INDUCED VOLTAGES IN AIRCRAFT ELECTRICAL CIRCUITS	61
Paul T. Hacker	
6. STATUS OF ENGINE ROTOR BURST PROTECTION PROGRAM FOR AIRCRAFT	75
Patrick T. Chiarito	

AIRWAY AND RUNWAY ENVIRONMENT

Session Chairman: Homer G. Morgan, Langley Research Center

7. CLEAR-AIR-TURBULENCE DETECTION USING LASERS	89
Edwin A. Weaver	
8. PROGRESS REPORT ON WING-TRAILING-VORTEX STUDIES	101
R. Earl Dunham, Jr., Harry A. Verstynen, Jr., and Margaret S. Benner	
9. AIRCRAFT RESPONSE TO THE WING TRAILING VORTICES GENERATED BY LARGE JET TRANSPORTS	115
William H. Andrews, Glenn H. Robinson, and Richard R. Larson	
10. STATUS OF RESEARCH ON RUNWAY ROUGHNESS	127
Albert W. Hall, Paul A. Hunter, and Garland J. Morris	

11. RUNWAY SLIPPERINESS 143
Walter B. Horne
12. EFFECT OF AIRPLANE OPERATIONS ON TIRE WEAR 153
John L. McCarty and Upshur T. Joyner

OPERATIONAL EXPERIENCE WITH SUBSONIC CRUISE AIRCRAFT

Session Chairman: Gene J. Matranga

13. APPLICATION OF ADVANCED AERODYNAMICS TO FUTURE TRANSPORT
AIRCRAFT 165
Albert L. Braslow and Theodore G. Ayers

COCKPIT ENVIRONMENT

Session Chairman: Maurice D. White, Ames Research Center

14. FLIGHT EVALUATION OF A DISPLAY FOR STEEP APPROACH 177
R. Earl Dunham, Jr., Jack J. Hatfield, Henry C. Elkins,
and Richard H. Sawyer
15. HANDLING QUALITIES OF LIGHT AIRCRAFT WITH ADVANCED CONTROL
SYSTEMS AND DISPLAYS 189
Paul C. Loschke, Marvin R. Barber, Calvin R. Jarvis,
and Einar K. Enevoldson
16. THE INFLUENCE OF MOTION ON THE EFFECTIVENESS OF FLIGHT
SIMULATORS IN TRAINING MANEUVERS 207
Richard S. Bray, Fred J. Drinkwater III, and Emmett B. Fry

TERMINAL AREA OPERATIONS

Session Chairman: George E. Cooper, Ames Research Center

17. SAFETY CONSIDERATIONS FOR POWERED-LIFT STOL AIRCRAFT 221
Curt A. Holzhauser and Robert C. Innis
18. OPERATIONAL ASPECTS OF V/STOL INSTRUMENT APPROACHES 233
Lee H. Person, Jr., Samuel A. Morello, Curt A. Holzhauser,
and Ronald M. Gerdes
19. ANALYSIS OF SOME HELICOPTER OPERATING PROBLEMS 249
Charles E. K. Morris, Jr., John F. Ward, Julian L. Jenkins, Jr.,
and William J. Snyder

20. SOME ASPECTS OF THE AERODYNAMICS OF STOL PORTS	263
Hermon M. Parker, Jeffry N. Blanton, and Kalman J. Grunwald	
21. SIMULATION STUDIES FOR DEVELOPMENT OF CERTIFICATION CRITERIA APPLICABLE TO SST TAKE-OFF	277
C. Thomas Snyder, Richard S. Bray, Fred J. Drinkwater III, and Raymond D. Forrest	

FLIGHT ENVIRONMENT

Session Chairman: James B. Whitten, Langley Research Center

22. DEVELOPMENT OF TURBULENCE AND WIND SHEAR MODELS FOR SIMULATOR APPLICATION	291
Richard L. Kurkowski, George H. Fichtl, and Joseph Gera	
23. RADIATION SAFETY IN HIGH-ALTITUDE AIRPLANE TRAFFIC	307
Trutz Foelsche	
24. PRELIMINARY STUDY OF AIRPLANE-AUTOPILOT RESPONSE TO ATMOSPHERIC TURBULENCE	323
Waldo I. Oehman	
25. PRELIMINARY STUDY OF EFFECT OF VIBRATION ON AIRCRAFT RIDE QUALITY	335
Sherman A. Clevenson, William J. Snyder, and John J. Catherines	
26. PROGRESS REPORT ON THE NASA V-G/VGH GENERAL AVIATION PROGRAM	347
Joseph W. Jewel, Jr.	
27. SOME FACTORS THAT AFFECT THE INSPECTION OF AIRCRAFT FOR FATIGUE DAMAGE	391
C. C. Poe, Jr., and Herbert A. Leybold	

INDUCED ENVIRONMENTAL EFFECTS

Session Chairman: John A. Zalovecik, Langley Research Center

28. PROGRESS IN REDUCING EXHAUST POLLUTANTS FROM JET AIRCRAFT . .	403
Helmut F. Butze and Jack Grobman	
29. TRENDS IN NOISE CONTROL FOR AIRCRAFT GAS-TURBINE POWER PLANTS	417
David Chestnutt, Harvey H. Hubbard, and Charles E. Feiler	

30. EVALUATION OF MEASURES OF AIRCRAFT NOISE	429
Philip M. Edge, Jr., Randall M. Chambers, and Harvey H. Hubbard	
31. STATUS OF STUDIES ON SONIC BOOM	439
Domenic J. Maglieri, Harry L. Carlson, and Norman J. McLeod	

FACTORS AFFECTING DITCHING OF NEW TRANSPORT AIRPLANES

By Lloyd J. Fisher
Langley Research Center

SUMMARY

Full-scale ditching experience and small-scale dynamic-model investigations have shown that airplanes are never designed to have fuselages that are undamaged in a ditching, and, as a matter of fact, the undamaged shape of an airplane is not very good for a water landing.

Ditching technique can be determined with dynamic models. The selection of the safest landing attitude and an indication of the probable behavior and damage are important contributions of investigations since the ditching problem currently has not warranted a design specification that alleviates the ditching hazard. Ditching safety can be increased if certain design features are used, such as suitable floor structure and wing location.

INTRODUCTION

No ditching investigations were conducted by the NASA for a number of years because of the similarity of most of the modern transport airplanes with respect to ditching features. A renewed activity in investigating ditching is now underway, however, because of the new family of large airplanes, such as the C-5 and the jumbo jets. The NASA has been cognizant of the ditching problem since the early part of World War II. About 60 different airplanes have been investigated with small-scale models, and the results have been reported; some full-scale ditching investigations have been conducted in cooperation with the U.S. Air Force.

The scope of this paper includes, first, some results from full-scale ditchings; then, results and techniques from small-scale dynamic-model tests; and finally, a discussion of the factors affecting ditching behavior and a discussion of how these factors might be used to improve ditching safety.

DISCUSSION

As an introduction to the ditching problem, a B-24 ditching in the James River is described. This planned, experimental ditching was performed with a structurally reenforced airplane. It was conducted about 27 years ago during World War II, when ditching was a major problem. The airplane was landed by an expert pilot under ideal conditions in smooth water. The sink speed was 0.61 m/sec (2 ft/sec) and the forward speed was

43.7 m/sec (85 knots). The landing attitude was 8° . After running smoothly for a short time in the water, the airplane pitched up to about 15° , then down. A maximum normal acceleration of $1g$ (9.8 m/sec^2) and a maximum longitudinal acceleration of $2\frac{1}{2}g$ occurred. The airplane sank to wing level and floated. It was then lifted from the water and brought ashore. The landing was fairly smooth and the crew was unharmed, but severe damage occurred to the airplane. A photograph showing some of the damage is given in figure 1. The damage included a large hole in the nose section, severely damaged nacelles, a big dent in the bomb-bay area, and holes in the aft fuselage. The actual strength of the reenforced bottom was not determined, but it had heavy ribs installed from nose to tail and the very weak bomb-bay doors were replaced with a 0.32-cm-thick ($\frac{1}{8}$ -inch) boiler plate so that the bottom was very much stronger than that of a normal B-24 airplane. Water pressures as high as 414 kN/m^2 (60 psi) were recorded. Although severe damage is common in many ditchings, occasionally an airplane will have surprisingly little damage.

In recent years, there have been two dramatic water-impact accidents of DC-8 airliners on the west coast with extraordinarily different results. The upper sketch of figure 2 illustrates the one in San Francisco Bay which occurred in November 1968. The lower sketch of figure 2 illustrates the one near Los Angeles in January 1969. The important factors affecting the San Francisco Bay ditching were a low sink speed and calm, shallow water (about 2.1 meters (7 feet) deep). The airliner came to rest with the wheels sitting on the bottom of the bay and the wing only partially in the water. Very little damage occurred and none of the occupants were injured. The airliner has been refurbished and flown again. The Los Angeles ditching occurred at a high sink speed, in deep water, in a rough sea of 2.4- to 3-meter (8- to 10-foot) swells. The fuselage broke into three parts. The wing and forward fuselage floated, the other parts, including wheels and nacelles, sank. Several lives were lost. The difference in results in these accidents is due to a high sink speed and rough water in one while in the other the airliner apparently flared to a low sink speed and actually got its wheels on the ground. Neither of these is a typical ditching. Damage somewhere between these two extremes would generally be expected. In the last 10 years, there have been 20 accidents in which commercial jet airplanes have crashed into the water. Not all were true ditchings, but nevertheless they are frequently discussed when ditching is considered. The latest ditching was in May 1970 near the Virgin Islands. A DC-9 ditched because of fuel depletion. The behavior was fairly smooth but there was bottom damage and the airliner sank in about 10 minutes.

With these actual ditchings as background, recent dynamic-model investigations will be discussed. Figure 3 shows a $\frac{1}{30}$ -scale dynamic model of the C-5 airplane ready for launch from the catapult. In tests such as these, the models are launched as free-bodies at various landing attitudes and speeds. They are greatly overstrength so special

techniques are used to simulate the scale strength of significant parts. The landing flaps and engine nacelles are attached at approximately scale strength and since bottom damage has a major influence on behavior, portions of the fuselage are removed and replaced with approximately scale-strength sections. For the C-5 model, the portion below the cargo floor was replaced between the aft ramp and the nose ramp. (See fig. 4.) Very simplified approximations of the full-scale structures were used. In tests at a 12° nose-up attitude (near stall warning condition), the model pitched down rapidly immediately after contact with the water. This pitch-down was due to a tripping force resulting when the bottom fuselage skin was damaged allowing strong bulkheads to be subjected to heavy water pressure. The pitch-down motion was greatly reduced in landings at a 7° nose-up attitude. The physical magnitude of an airplane appears to affect the degree of violence of ditching. As the size of the airplane increases, the ditching behavior becomes less violent; this trend was apparent in the rough-water test of the C-5 since the C-5 is a big airplane relative to the 2.4-m (8-foot) wave simulated in the investigation.

Since both of the west coast ditchings mentioned previously occurred with wheels down, the advisability of having the landing gear down has been questioned. The NASA investigations have shown only two instances of improvement in behavior due to the landing gear being down. (One was a result of a very high sink speed and the other was our current C-5 investigation.) Figure 5 shows the C-5 model with landing gear extended. The C-5 has a very unusual landing-gear configuration. There are 24 wheels on the main gear, and when viewed from the front, there is a continuous footprint for the full width of the fuselage. When the model was landed at the 7° nose-up attitude, the behavior was relatively smooth and the fuselage bottom was protected some from heavy-water impact because the wheels hit first. The dynamic models float high in the water at the end of a run, but the actual airplane would sink to wing level.

The typical behavior in the dynamic-model ditching investigation of the C-5 with wheels up or wheels down was a fairly smooth run in which most of the landing flaps failed and one or more of the engine nacelles were torn away. Flap failure and engine loss on a high-wing configuration, such as the C-5, are of little consequence in a ditching runout. On the other hand, fuselage-bottom failure could be a serious problem in a full-scale ditching. Figures 6 and 7 show scale-strength bottom sections after ditching tests. The scale-strength sections were constructed so that a load equivalent to about 103 kN/m^2 (15 psi), the average strength for the C-5, would cause a section to fail. A new scale-strength section was required for each test run. Damage with wheels retracted is shown in figure 6 and with wheels extended in figure 7. Fuselage damage was somewhat less with wheels extended. The scale-strength bottom sections are simplified approximations of the full-scale structure, and their main usefulness is in showing approximate amounts of damage and the areas of the fuselage bottom where damage is likely to occur. This damage looks bad, but there is a rugged cargo floor (about 1.5 meters (5 feet) full scale)

above the fuselage bottom that should afford appreciable protection from water flow through holes in the bottom.

Typical time-history plots of the center-of-gravity acceleration for the C-5 are shown in figure 8. These data were obtained with a relatively rigid model. Tests were made at landing attitudes of 12° , $9\frac{1}{2}^{\circ}$, 7° , and 4° , but data for only the 7° attitude are shown here since acceleration peaks were minimum at this attitude. Normal and longitudinal accelerations are given for the wheels-up (solid line) and wheels-down (dashed line) conditions. Longitudinal accelerations were about 3g for each condition. Normal accelerations were about 6g. Since the maximum acceleration at the 7° landing attitude was appreciably less than that at the other attitudes investigated, it was concluded that the 7° landing attitude would be favorable for a ditching. Fortunately, 7° is approximately the normal landing attitude for the C-5, so the pilot can probably make his most precise landing at this attitude.

Possibly the most important question revived by the recent airliner ditchings is that of the feasibility of designing airplanes to survive a ditching. A listing of major factors affecting ditching is as follows:

- (1) Bottom damage
- (2) Landing attitude
- (3) Flap setting
- (4) Gear position
- (5) Wave heading
- (6) Floor strength
- (7) Wing location

The damage that is expected in a ditching, the magnitude of the water pressures, and the differences in results that occur because of fuselage damage have been discussed. All these things indicate the difficulties of accomplishing actual design for ditchings. But there are some data that can be of real use in a practical facing of the ditching problem. One bit of practical information is the selection of the preferred landing attitude, as shown in the C-5 tests. In general a nose-up attitude, not too close to the stall condition, is preferred. Flaps should be down to get as low a forward speed as possible. There seems to be a trend developing for the large airplane favoring an extended landing gear for ditching. Ditchings should be made parallel to wave crests if the wind is light but into the wind if it is strong enough to appreciably decrease ground speed in landing. Other factors affecting ditching are airplane design features such as floor strength and wing location, which will be discussed in the next paragraphs.

One of the best features of present-day airplane designs as far as ditching safety is concerned, if there is an interest in designing and building airplanes for ditching, is the rugged cargo floor. An illustration of the support structure of the lower floor of the C-5 airplane is given in figure 9. Even though the bottom skin of an airplane will likely be damaged, a floor structure such as this will afford a great deal of protection to occupants. The backbone or keel shown in figure 9 is also a safety feature that helps prevent the fuselage from breaking apart. This is a cargo floor, and passenger airplanes do not need such a floor to support the weight of passengers. But, this type of floor will give great protection in a ditching and is a much more practical safety feature than an upgraded fuselage skin. Actually, the undamaged shape of an airplane is not very good for a water landing. If the undamaged shape could be maintained, it would cause pitching and skipping, behavior that would be unacceptable in an actual ditching because it would create excessive loads and damage.

Another design feature of appreciable importance is wing location. Figure 10 shows the characteristic low-wing and flap arrangement for the current transport airplane, the high wing of the military cargo airplane, and possible wing-flap arrangements for future vehicles such as the SST and the STOL. The vertical location of the wing with respect to the fuselage is a compromise between having the wing low enough to provide buoyancy to help keep the airplane afloat after ditching and having the wing high enough so that landing flaps and engine installations do not seriously impair ditching behavior. Generally the most favorable position of the wing is slightly above the bottom of the fuselage or in a low midwing position.

CONCLUDING REMARKS

Full-scale ditching experience and small-scale dynamic-model investigations have shown that airplanes are never designed to have fuselages that are undamaged in a ditching, and, as a matter of fact, the undamaged shape of an airplane is not very good for a water landing.

Ditching technique can be determined with dynamic models. The selection of the safest landing attitude and an indication of the probable behavior and damage are important contributions of investigations since the ditching problem currently has not warranted a design specification that alleviates the ditching hazard. Ditching safety can be increased if certain design features are used, such as suitable floor structure and wing location.

There is also a need for a realistic look at ditching water pressures in order to have a basis for judging specification on bottom strength. The NASA is now conducting such an investigation (an investigation of initial-contact pressures) using a model of a current airplane.

B-24 DAMAGE

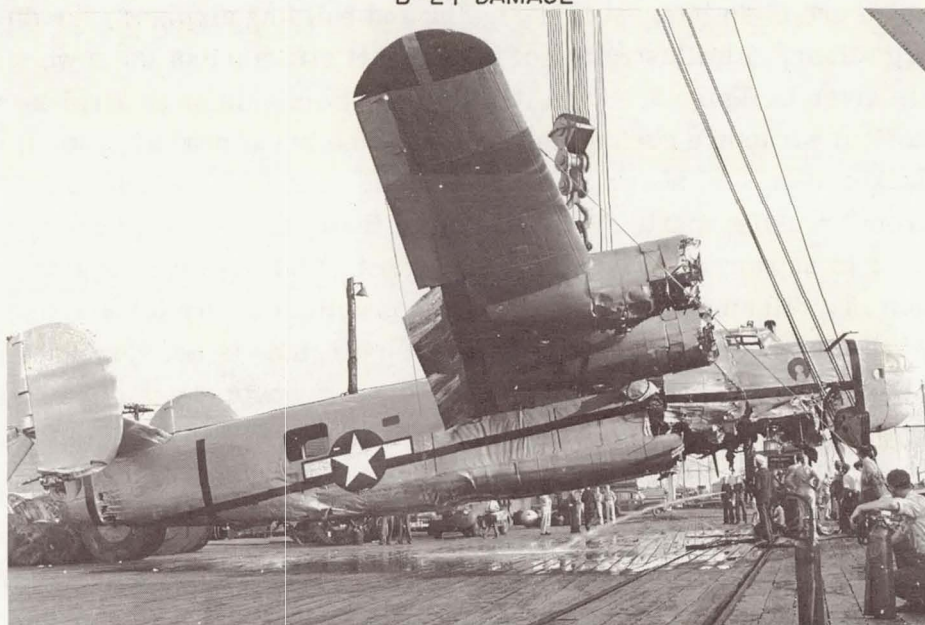


Figure 1

WEST COAST DITCHINGS SAN FRANCISCO BAY; NOVEMBER 1968



NEAR LOS ANGELES; JANUARY 1969

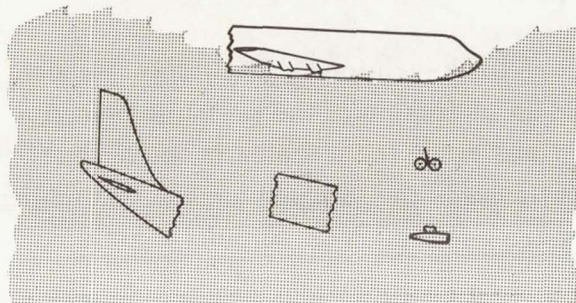


Figure 2



Figure 3

REMOVABLE SCALE - STRENGTH SECTION

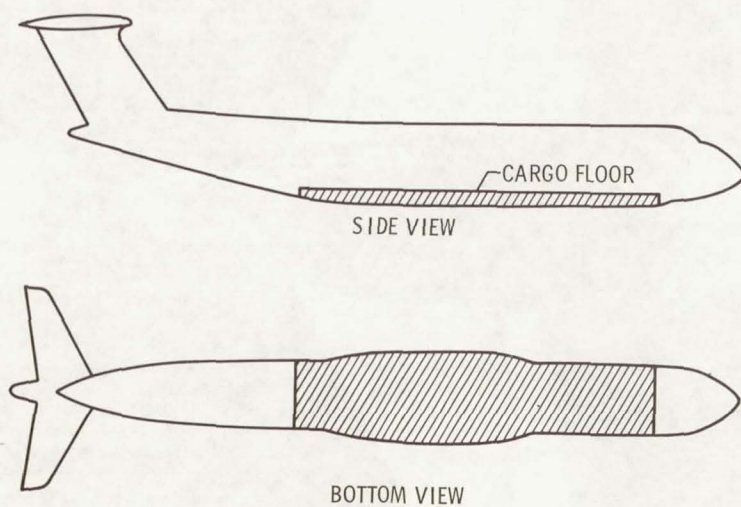


Figure 4

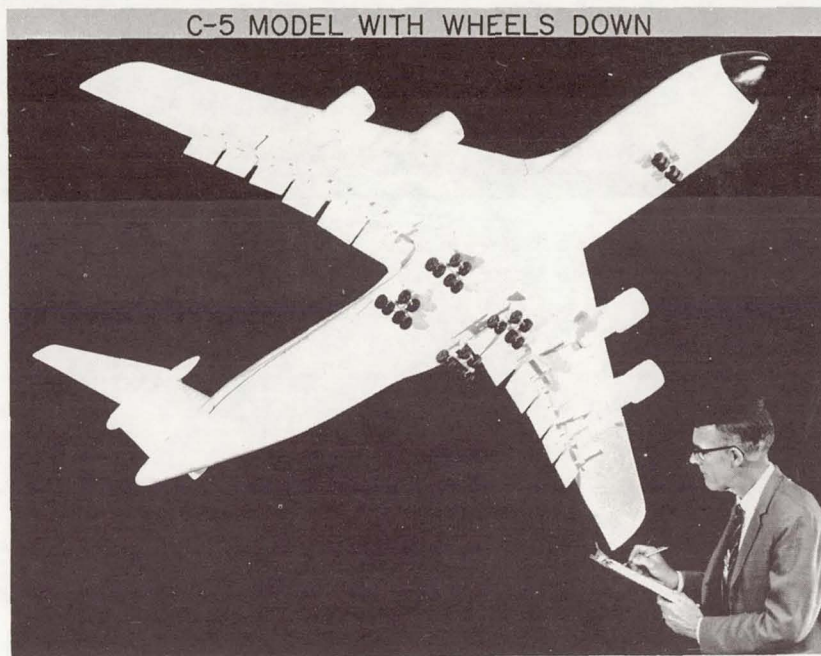


Figure 5



Figure 6

C-5 BOTTOM DAMAGE WHEELS DOWN

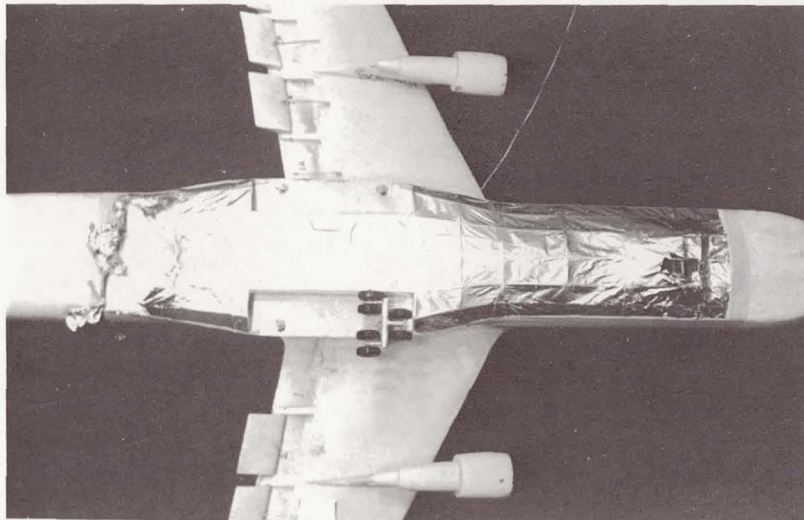


Figure 7

C-5 ACCELERATIONS LANDING ATTITUDE, 7°

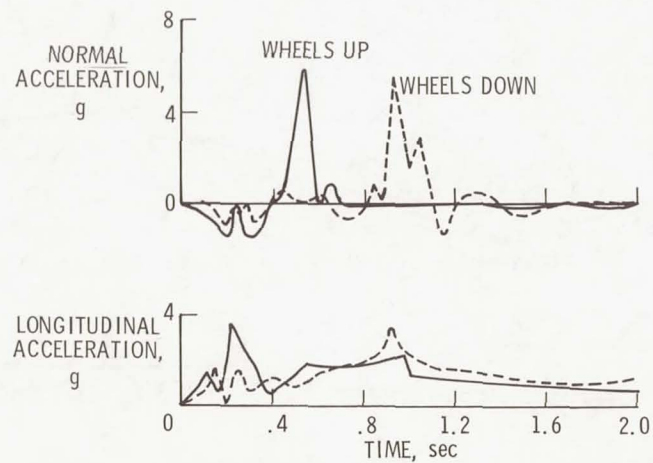


Figure 8

CARGO FLOOR

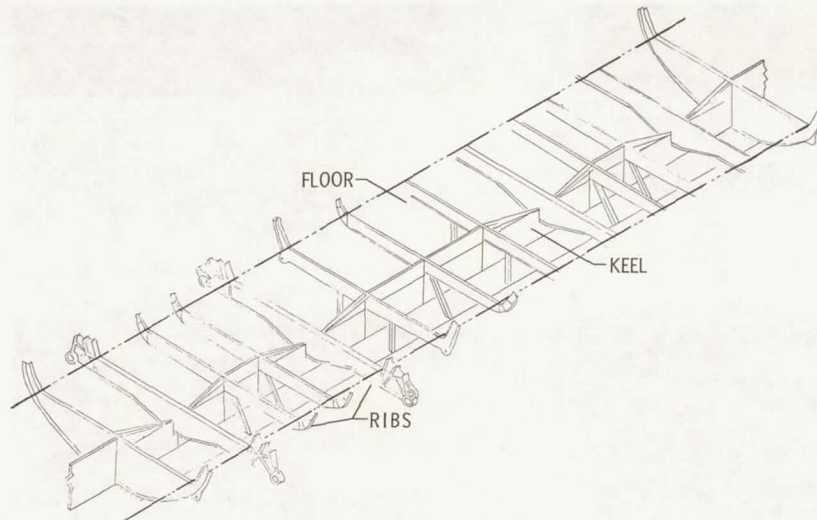


Figure 9

CONFIGURATIONS

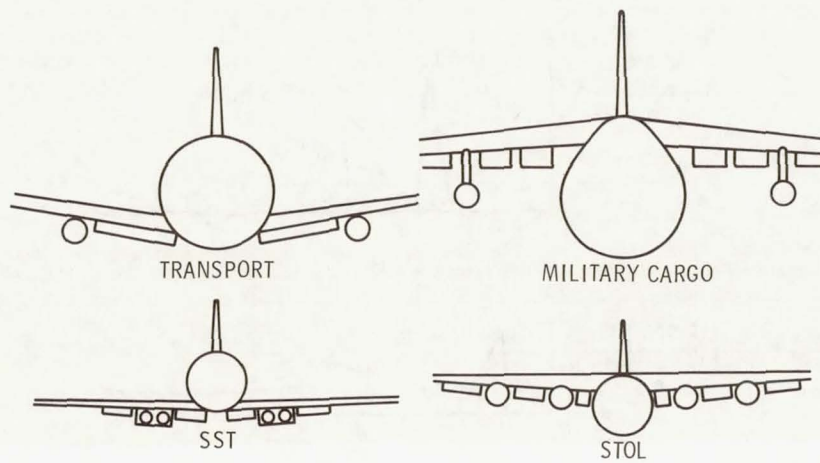


Figure 10

STUDY OF PROTECTION OF PASSENGERS IN AIRCRAFT CRASH FIRES

By Carr B. Neel and Richard H. Fish
Ames Research Center

INTRODUCTION

Passengers caught in an aircraft ground accident that has resulted in fire have only a very short time to escape. Those failing to exit quickly probably will die from exposure to heat and fumes. (See ref. 1.)

As part of a program of development of fire-retardant materials at Ames Research Center, a concept for passenger survival has been studied which differs from those that have been considered in the past. Previous studies generally have stressed quick-evacuation techniques; some have dealt with possible ways to prevent or control the fire. (See refs. 2 to 5.) In contrast, the study at Ames was directed toward the approach of surrounding the passenger compartment with a fire-retardant shell that would protect the occupants long enough for the fire to burn out or for fire-fighting equipment to reach the airplane and extinguish the fire.

This approach has been made possible by the recent development of two new fire-retardant materials: a lightweight foam plastic, called polyisocyanurate foam, and an intumescent paint. The intumescent paint is a material that expands to many times its original thickness when exposed to heat; thus, it insulates the surface on which it is applied. The thermal-protection mechanisms of these materials operate on the same ablative principles as those used to protect the astronauts during reentry. To demonstrate their use in a full-scale application, an airplane fuselage was fitted with the materials and tested in a jet-fuel fire.

This paper describes the fire-protection system and the fire test and presents an analysis of some of the results. It should be emphasized that this constitutes a progress report and that a number of problems remain to be solved before such a system can be used for passenger protection.

FIRE-RETARDANT MATERIALS

Thermal-Protection Mechanisms

In developing fire-retardant materials, it was recognized that the same ablation mechanisms used to protect the Apollo astronauts from the searing heat of reentry could also be used for protection from a fire. The thermal-protection mechanisms of ablative

materials are shown in figure 1. At all times, the material acts as an insulator. When exposed to heat, the material converts to a stable char and at the same time absorbs some heat. As the char heats, it radiates a large amount of heat. During decomposition in the char-forming process, gases are generated that blow outward, cooling the char by transpiration. At the surface of the char, the gases block convective heating by forming an outflowing front of gas. In the case of protection against fire, the gases also chemically interfere with the flames. These mechanisms were built into both the polyisocyanurate foam and the intumescent paint. In the demonstration test, the paint was used only in a secondary, but very important, capacity. The paint was applied to the primary structure of the test fuselage to expand and to fill any cracks developing from shrinkage of the foam away from the structure in order to prevent intrusion of flames.

Development of Materials

In developing these materials, the approach taken was to use readily available chemical components but to modify and chemically manipulate them to create the desired characteristics. The active pigment for the intumescent paint was the one exception to this approach. This pigment was specially developed and represents a new discovery. Development and tests of the foam are described in references 6 and 7. Development and full-scale evaluation of the intumescent paint are described in references 8 and 9.

PREPARATION OF TEST FUSELAGE

Considerations for Passenger Protection

In the design of a test to demonstrate how these materials could be used to protect passengers, two factors influencing survival in a crash fire must be considered. First, the penetration of heat must be minimized. At the same time, a way must be devised to prevent the intrusion of smoke and toxic gases, which can be lethal even though the temperature is controlled.

A factor that influences both of these threats in the case of a survivable crash is the effect of structural damage that results in rupture of the fuselage. Crash damage was not considered in the present test nor was the presence of windows, which also could be a point of heat and gas penetration. These factors have been purposely omitted because it was believed that the basic concept of passenger protection should be explored first. The effect of crash damage and the protection of windows will be included in future studies.

Installation of Fire-Protection System

Installation of the fire-protection system and conduct of the test were done by the Avco Systems Division of Lowell, Massachusetts, under contract to NASA. For the test vehicle, Avco procured a surplus McDonnell Douglas C-47 airplane. From the airplane fuselage, a test section 7.9 meters (26 feet) long was removed, as illustrated in figure 2. This section was divided and capped on either end by steel bulkheads, resulting in two equal sections typical of traditional airplane construction. One half was left essentially unchanged; whereas, the other half was fitted with the thermal-protective materials to form a shell around the passenger compartment. Thus, the test would validate the feasibility of a retrofit system for existing aircraft.

The details of installation of the fire-protection system are shown in figure 3. The circular frames were first painted with intumescent paint 0.13 centimeter (0.05 inch) thick. Next, a layer of loosely woven fiber-glass matting was bonded to the skin. The polyisocyanurate foam was sprayed over the matting and was built up to the full 6.4-centimeter (2.5 inch) depth of the frames and 5 to 8 centimeters (2 to 3 inches) over the floor structure. Excess foam was trimmed off. To finish the installation, a liner of fiber-glass-epoxy laminate 0.08 centimeter (1/32 inch) thick was cemented to the foam and then riveted to the frames. This laminate is similar to airliner decorative interior paneling. The floor foam was also covered with the laminate, and all joints were sealed to exclude smoke and gases. The properties of the foam used in the test are given in table I.

In the unprotected section, the space between the aluminum skin and the interior paneling was filled with 5 centimeters (2 inches) of fiber-glass batting, a material typical of conventional aircraft insulation.

The steel bulkheads that divided the protected and unprotected sections and capped the two ends were insulated with a 2.5-centimeter-thick (1 inch) commercial firewall insulation covered with 8 centimeters (3 inches) of fiber-glass batting.

Instrumentation and Test Arrangement

The fuselage was instrumented to measure both the exterior and interior thermal environments. Thermocouples were used to measure temperatures both inside and outside the cabin. The exterior heat flux was measured by slug-type calorimeters.

The fire-test arrangement is illustrated in figure 4. The test was conducted at Otis Air Force Base, Massachusetts. The fuselage was placed directly on the ground and was flanked by two shallow pits about 9 by 15 meters (30 by 50 feet) in size. Water was placed in the bottom of the pits, and 9.5 meters³ (2500 gallons) of JP-4 fuel was floated on top of the water in each pit, forming two large fuel ponds. Water-cooled probes

containing motion-picture cameras and gas-sampling equipment were positioned at either end of the test fuselage so that they could observe the interior of each section. The probes were arranged so that they could be withdrawn when temperatures became excessive. Several cameras were placed around the vehicle to record the test.

The exterior of the test fuselage before the test is shown in figure 5. The interior of the protected section before the test is shown in figure 6. Simulated exit signs and an optical target were installed to permit evaluation of possible smoke effects. The interior of the unprotected section appeared much the same as the protected section, except that no exit signs or optical target was installed.

Test Plan

The plan was to ignite both ponds of fuel simultaneously at several points to obtain a uniform buildup of flames over the surface of each pond. The quantity of fuel and configuration of the ponds were calculated to envelop the fuselage completely with flames and to expose the vehicle to maximum heat flux for 10 minutes. It was believed that the unprotected section would be destroyed within 1 to 2 minutes. The protected section hopefully would survive the fire, but fire trucks were stationed nearby in the event that certain monitored thermocouples indicated flame intrusion.

FIRE TEST

The test was made on August 13, 1970. Within 1/2 minute after ignition, the fire was fully developed. By this time, smoke had already started to penetrate the unprotected section. Occupants of this part of the cabin would have had to have evacuated the vehicle by this time to have survived. Two views of the fire during the test are shown in figure 7.

Throughout most of the test, the entire test section was completely engulfed in flames. Because of the volume of flames and smoke, visual observation of the test section was difficult. About 5 minutes after ignition, a light wind arose from the southeast and directed the flames so that occasionally the end of the protected section was visible. Accompanying this flame shift was a tremendous vortex action of flames around the entire fuselage. This swirling action continued for about 30 meters (100 feet) upward. Peaks of the flames reached a height of approximately 60 meters (200 feet).

Motion pictures of the interior of the unprotected section, although obscured by dense smoke, show flame penetration within 1 minute after ignition. After 2 minutes, the unprotected section apparently collapsed and was completely destroyed.

Meanwhile, in the protected section, the motion pictures showed no smoke, the gas-sampling probe showed no toxic gas, and the thermocouples showed no temperature

change. A power failure prevented further motion pictures of the interior and necessitated removal of the probe containing the motion-picture cameras and the gas-sampling equipment after $5\frac{1}{2}$ minutes. The last gas sample was taken 5 minutes after ignition and still showed no toxic gases.

The fire lasted for 12 minutes, at which time the fire in the ponds burned out, and only residual flames remained around the edges where fuel had soaked into the dirt mounds surrounding the ponds.

Following the test, the visual comparison between the protected and unprotected sections was dramatic. Figure 8 shows virtually no trace of the unprotected section, whereas the foam-protected fuselage is intact. The interior appears habitable, as shown by figure 9. Some time during tailoff of the fire, flames reached a relatively unprotected floor seam along the top of the dirt mound supporting the test section. Heat penetrated at this point, and eventually resulted in a slight burn-through, which caused considerable blackening of the walls. This occurred after the main fire burned out and is attributed to the design of the test and not to a failure of the thermal-protective system.

Soon after the fire died down, fire hoses were played on the test section, to preserve it for study, and on the remaining flames around the edges of the ponds.

RESULTS AND DISCUSSION

Cabin Air Temperatures

The cabin air temperature histories were used to analyze the results. These histories are plotted in figure 10. In the unprotected section, the air temperature rose to 300°C (600°F) in less than 2 minutes after the start of the fire and was climbing rapidly. By this time, the unprotected section was destroyed. In contrast, the temperature in the protected section changed very little for the first 6 minutes; then, as the heat finally penetrated, the temperature rose faster, reaching 150°C (300°F) as the fire burned out in 12 minutes.

To give an idea of the chance that passengers might have had of surviving inside the cabin, a curve labeled "Human tolerance limit" has been plotted. This curve is a composite of two studies of exposure of humans to extreme heat (refs. 10 and 11) and represents more severe conditions than existed in our test. Also shown for comparison is the exposure envelope for the sauna-bath ritual, which calls for repeated exposures of 10 to 15 minutes at temperatures ranging from 80°C to 100°C (175°F to 210°F). This is done for the health. The fact that the temperature in the protected section just reached the human tolerance limit (for more severe conditions) in 12 minutes, as the fire burned out, indicates that, if temperature were the only consideration, passengers could have survived for this time.

Generation of toxic gases is as important a consideration as temperature. Up to 5 minutes into the test, no toxic gases were generated. At this point, the gas-sampling probe was withdrawn; therefore, no measurements were made late in the test. During the last few minutes before burnout of the fire, segments of the fiber-glass-epoxy liner reached temperatures at which partial decomposition of the resin might have occurred. Gases might have been generated that could have been somewhat toxic. Although such gas generation was a possibility, the amount of toxic fumes was not believed to have been sufficiently high to have influenced survivability, even at 12 minutes.

If this test represented an actual airliner crash fire at an airport, fire-fighting equipment generally could have reached the airplane and extinguished the fire in less than 8 minutes. At this point in the test, conditions were much more favorable for survival than at 12 minutes, and there would be no question of either heat or toxic gases endangering life in the cabin. Thus, the concept of passenger protection was adequately demonstrated by this test.

Consider again briefly the analysis of the cabin air temperature. After the fire burned out in the ponds, small flames remained along the sides of the test section from residual fuel that had soaked into the dirt mounds surrounding the ponds. At $12\frac{1}{2}$ minutes after the start of the fire, the air temperature suddenly increased, indicating flame intrusion into the cabin. The cracks at the floor-wall intersection are believed to have occurred at this time. The cause of the cracks, which resulted from melting structure, is discussed later. The flame intrusion was probably rather small, being limited to the low flames remaining at the edges of the ponds. At 14 minutes, water hoses were played on the protected section and on the remaining flames, causing the cabin air temperature to drop rapidly.

Sources of Cabin Heating

Although the system of foam, paint, and fiber-glass liner gave satisfactory protection, ways were explored to improve the system, with the objective of indicating how the weight might be reduced. The most useful information from this standpoint is the thermal data. Accordingly, these data were analyzed to identify and evaluate the sources of heating. To aid in the analysis, temperature histories at various locations in the cabin for the last 5 minutes of the test were plotted. A typical history for several locations in the cabin is given in figure 11. Shown in this figure is the temperature of the air measured in the middle of the cabin, on the fiber-glass liner at a location alongside the air thermocouple, and in the foam 0.6 centimeter ($\frac{1}{4}$ inch) away from the fiber glass. Note that the temperature of the air was higher than that of the fiber-glass liner, and the liner temperature was higher than that of the foam. This means that the air was

heating the sidewall of the cabin. This reversal in heat-flow direction was unexpected, and it indicates that most of the cabin heating came from heat leaks rather than through the main area of the sidewalls.

Two sources of heat leaks are identified by the temperature histories shown in figure 12. The temperatures were measured over a frame and on the fiber-glass liner opposite a region of the foam that had fissured. At both of these points, the temperatures were well above the air temperature. These temperature histories typify the two primary sources of heat leaks. The frames formed highly conductive heat-flow paths through the foam. Calculations indicate that about one-third of the total heat input to the cabin for the last 5 minutes of the test came through the frames. Fissuring of the foam caused the second source of heat leaks. The sudden increase in fiber-glass-liner temperature indicates the appearance of a fissure in the foam. These fissures apparently were the primary source of heat leaks into the cabin, and, according to calculation, contributed over half of the heating of the cabin. A photograph of these fissures after the test is shown as figure 13. The deep cracks, some of which penetrated clear to the fiber-glass liner, were obvious heat-flow paths to the liner.

To minimize heating from the frames, the obvious solution would be to insulate the fiber-glass liner from the frame flanges. Because of its low thermal conductivity, isocyanurate foam would be a good material for this application. Calculations indicate that, if 1.3 centimeters (1/2 inch) of foam were placed between the frame flanges and the fiber-glass liner, the heat input from the frames could be decreased to one-fifth of the value with no insulation.

The problem of fissuring of the foam is one that needs further study. Tests have shown that isocyanurate foam in the lower-density range (30 to 40 kg/m³ (2 to 2.5 lb/ft³)) does not fissure. Laboratory studies made since the fire test show that the lower-density foam, because of its greater integrity, provides thermal protection equivalent to that of the higher-density foam (65 kg/m³ (4 lb/ft³)) used in the fire test. This means, of course, that the lower-density foam should give as good protection in a fire as was provided in the test by the higher-density foam. Use of the lower-density foam would have the advantage of providing a much lighter installation.

There are several possible explanations for the fissuring. The most obvious one is that the higher density creates greater stresses upon heating of the foam than the lower density. Spraying the foam, which undergoes an exothermic reaction upon curing, against cold aluminum structure might create built-in stresses that are relieved when the foam is heated. Other processing problems could also have led to the conditions that caused fissuring. These various possibilities must be studied to eliminate fissuring.

Floor-Line Failure

Another area for improvement is the design of the floor-line protection. In order to understand how to improve the design, the cause of failure during the fire test should be examined. Figure 14 illustrates how the failure developed. Dirt had been banked part way up the fuselage wall to create a mound that formed one side of the fuel pond. The mound stopped just below the floor line. This protected the bottom part of the fuselage from the fire, but left exposed a portion of the structure just below the floor line. Heat from the fire finally melted the exposed frames to which the floor beams were fastened. Thus, the support for the floor was removed and this caused the floor to sag just as the fire was burning out. This opened the floor-line cracks and allowed the flames to enter the cabin.

In the foam installation, the floor foam was placed on top of the floor structure, where it did not protect the primary structure. This installation proved satisfactory for the test of the protective concept, but an improvement in design of the protective system would be required for an operational installation. To protect the floor structure properly, the foam should be placed under the structure, as shown in figure 15. The foam should surround the primary structure to protect it from melting.

Weight Penalty

Because of its ablative character, the fire-retardant foam generally provides increased fire protection with increase in density. Accordingly, the foam in the test fuselage was made heavier than usual, with the intent of providing protection equal to the protection that would have been obtained from a thicker application of lower-density foam in a larger airplane. Analysis of the data from the fire test indicates that the foam installation was heavier than needed for adequate fire protection.

Now consider the various factors that would permit a reduction in weight. First of all, as was mentioned previously, by minimizing the heat leaks, one could expect improved thermal performance, which would permit a reduction in weight. In fact, the indication was that the foam density could be reduced from 65 kg/m^3 (4 lb/ft^3) to about 40 kg/m^3 (2.5 lb/ft^3) with no reduction in performance. Also, by designing for a shorter protection time, such as 8 minutes instead of 12 minutes, the required protection and the corresponding weight could be further reduced.

Based on these considerations, an estimate was made of the weight penalty for installation of a fire-protective system in a typical modern-day airplane — an airliner with a gross weight of 180 000 kg (400 000 pounds). The increase in weight is estimated to be 1.5 kg/m^2 (0.3 lb/ft^2) of protected surface area. This would increase the gross weight 770 kg (1700 pounds). The corresponding increase in structural-weight fraction would be from 30.0 percent to 30.4 percent.

It should be pointed out that the protective system discussed in this paper would be essentially a retrofit installation for airplanes currently in service or in production. The foam would be added for the single purpose of fire protection. None of its other useful characteristics, such as high compressive strength and compressive modulus or acoustical damping properties, would be taken full advantage of. To utilize the foam most effectively, the foam and structure should be integrated at the beginning of the structural design phase for a new airplane. With this approach, it is conceivable that the structural gain would permit the addition of foam with no weight penalty.

CONCLUDING REMARKS

A test that constitutes a first step in developing a system to protect passengers in a crash fire has been described. Many problems, such as protecting against fuselage rupture and providing protection for windows, must be solved before such a system can be used. Nevertheless, results of the test give promise of providing protection for passengers caught in a crash fire.

REFERENCES

1. Sarkos, Constantine, P.: Titanium Fuselage Environmental Conditions in Post-Crash Fires. Rep. No. RD-71-3, FAA, Mar. 1971.
2. Caldara, Joseph D.; and Pollard, Frank B.: Emergency Egress Systems for Commercial and Military Aircraft. Teledyne McCormick Selph paper presented at the 8th Annual SAFE Symposium (Las Vegas, Nev.), Sept. 1970.
3. Conley, Don W.: Post-Crash Fire-Fighting Studies on Transport Category Aircraft. Rep. No. RD-65-50, FAA, May 1965.
4. Pinkel, I. Irving; Preston, George Merritt; and Pesman, Gerard J.: Mechanism of Start and Development of Aircraft Crash Fires. NACA Rep. 1133, 1953. (Supersedes NACA RM E52F06.)
5. Pinkel, I. Irving: Crash-Fire Research With Jet Aircraft. Aeronaut. Eng. Rev., vol. 15, no. 1, Jan. 1956, pp. 53-57.
6. Riccitiello, S. R.; Fish, R. H.; Parker, J. A.; and Gustafson, E. J.: Development and Evaluation of Modified Polyisocyanurate Foams for Low-Heating-Rate Thermal Protection. J. Cell. Plast., vol. 7, no. 2, Mar./Apr. 1971, pp. 91-96.
7. Fish, Richard H.: The Performance of Lightweight Plastic Foams Developed for Firesafety. Proceedings of the NASA Conference on Materials for Improved Fire Safety, May 1970, pp. 11-1 - 11-20.
8. Fohlen, G. M.; Parker J. A.; Riccitiello, S. R.; and Sawko, P. M.: Intumescence: An In Situ Approach to Thermal Protection. Proceedings of the NASA Conference on Materials for Improved Fire Safety, May 1970, pp. 12-1 - 12-20.
9. Sawko, P. M.; and Riccitiello, S. R.: Intumescent Coatings for Improved Fuel-Fire Protection of Sensitive Articles. Paper presented at 161st National Meeting of American Chemical Society (Los Angeles, Calif.), Mar.-Apr. 1971.
10. Blockley, W. V.; and Taylor, Craig L.: Studies in Human Tolerance for Extreme Heat. Tech. Rep. No. 5831, U.S. Air Force, Feb. 1950. (Available from DDC as AD 73 854).
11. Webb, Paul: Pain Limited Heat Exposures. Temperature - Its Measurement and Control in Science and Industry, Vol. 3, Pt. 3, Reinhold Pub. Corp., c.1962, pp. 245-250.

TABLE I.- PHYSICAL PROPERTIES OF POLYISOCYANURATE
FOAM USED IN FIRE TEST

Property	Value	
Density	60 to 70 kg/m ³	(3.8 to 4.3 lb/ft ³)
Open-cell porosity	1% to 2%	(1% to 2%)
Thermal conductivity	0.29 to 0.43 $\frac{\text{mW}}{\text{cm } ^\circ\text{K}}$	$\left(0.2 \text{ to } 0.3 \frac{\text{Btu in.}}{\text{hr ft}^2 ^\circ\text{F}}\right)$
Shear strength	0.10 to 0.14 MN/m ²	(15 to 20 psi)
Compressive strength:		
Parallel to rise direction	0.21 to 0.28 MN/m ²	(30 to 40 psi)
Perpendicular to rise direction	0.24 to 0.31 MN/m ²	(35 to 45 psi)
Compressive modulus:		
Parallel to rise direction	12 to 20 MN/m ²	(1800 to 3000 psi)
Perpendicular to rise direction	7 to 10 MN/m ²	(1000 to 1500 psi)
Tensile strength	0.25 to 0.29 MN/m ²	(36 to 42 psi)

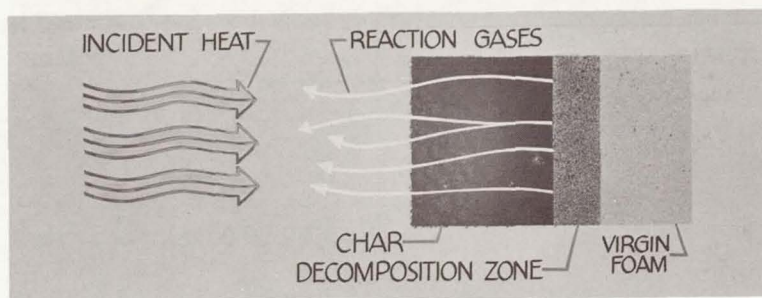


Figure 1.- Thermal-protection mechanisms of ablative materials.

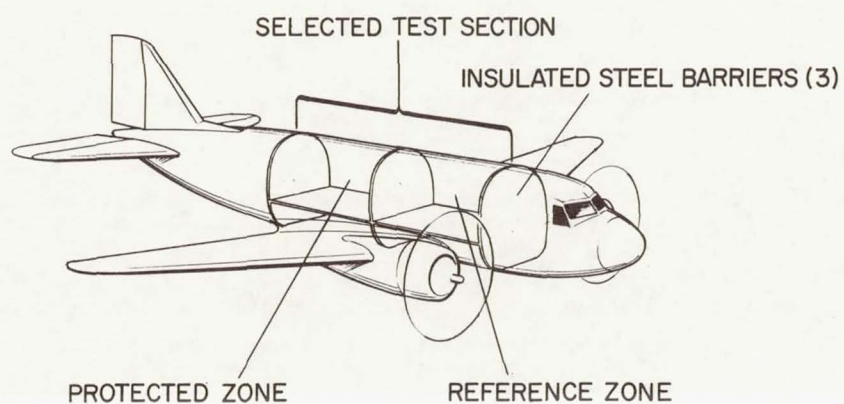


Figure 2.- Portion of McDonnell Douglas C-47 airplane fuselage used for test section.

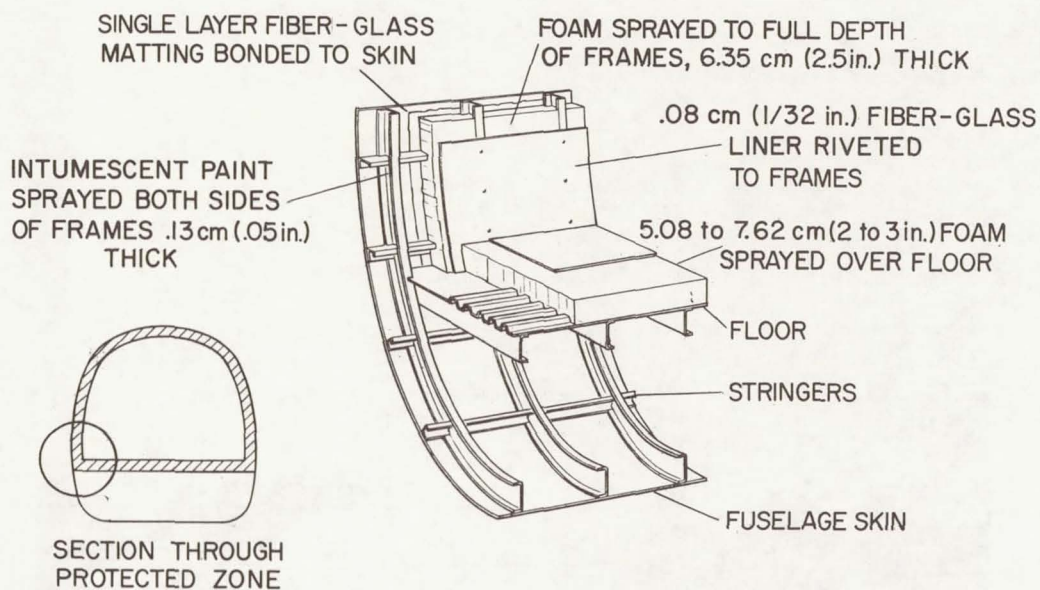


Figure 3.- Installation details of fire-protective materials.

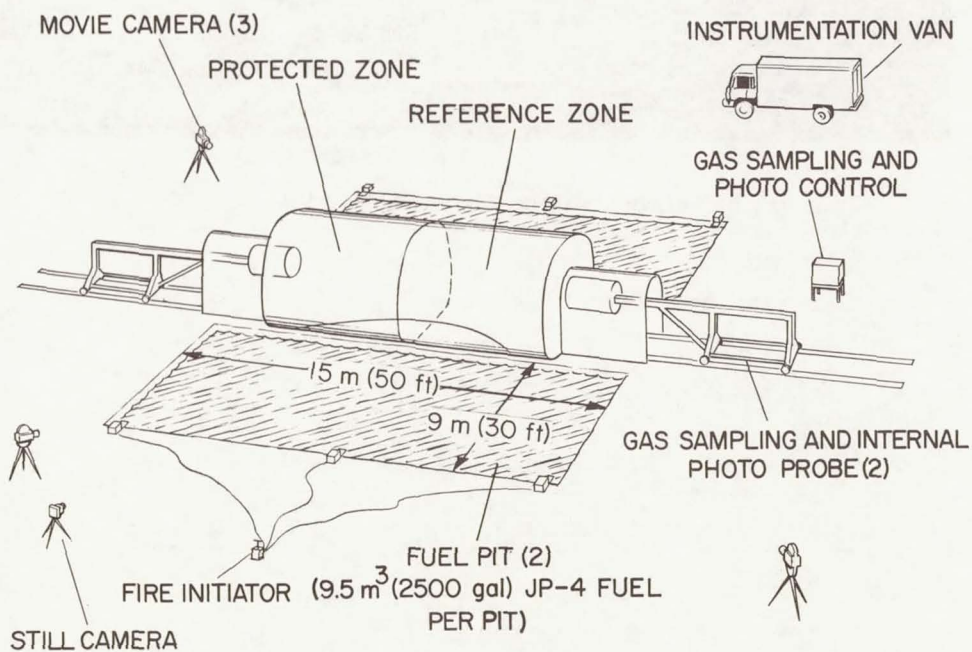


Figure 4.- Fire-test arrangement.

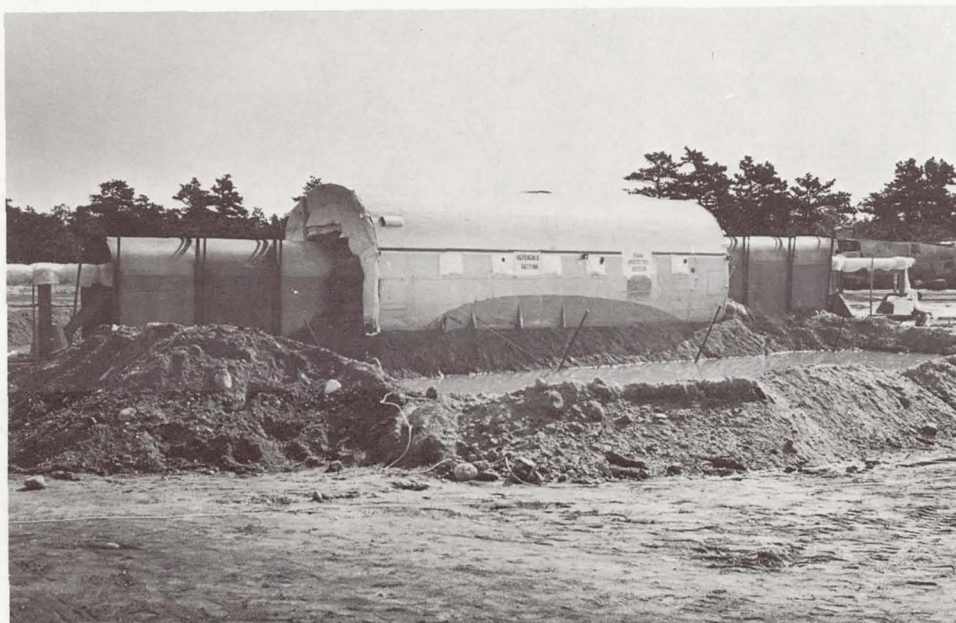
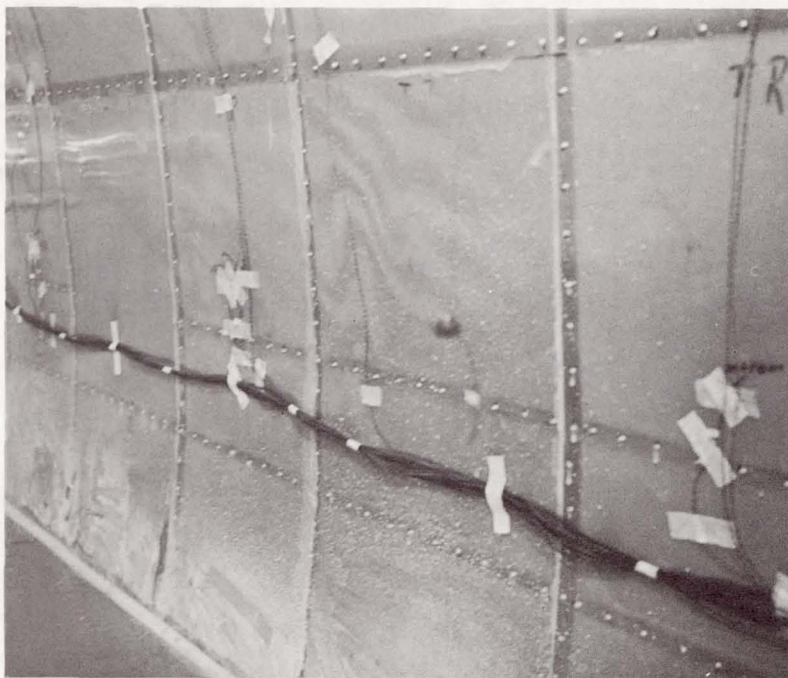


Figure 5.- Exterior of test section before test.



(a) South side.



(b) North side.

Figure 6.- Interior of protected section before test.



(a) View from north side of test section.



(b) View from east end of test section, showing protected section.

Figure 7.- Fire during test.

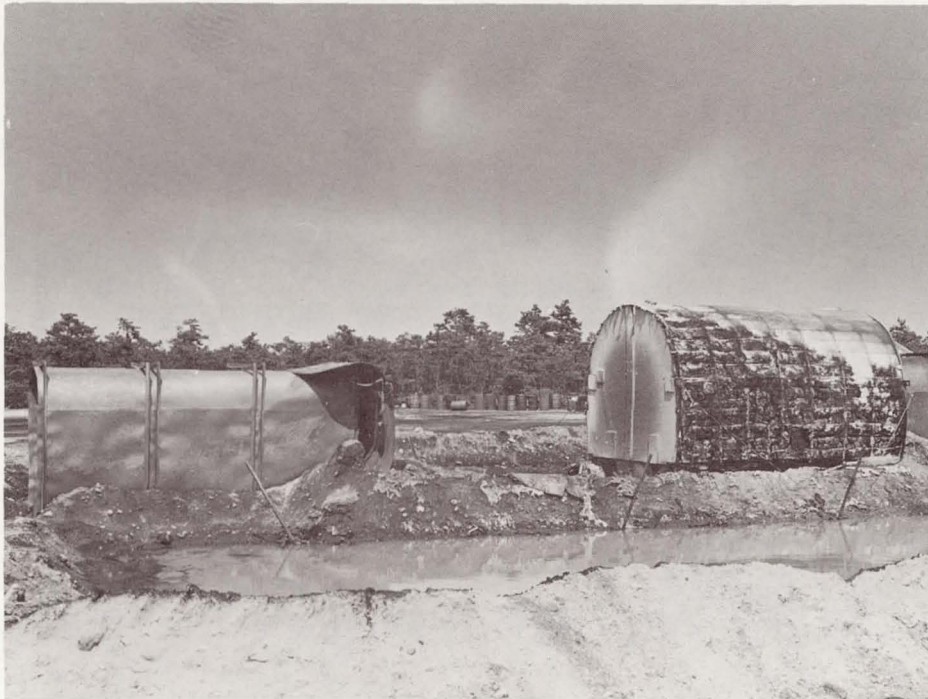
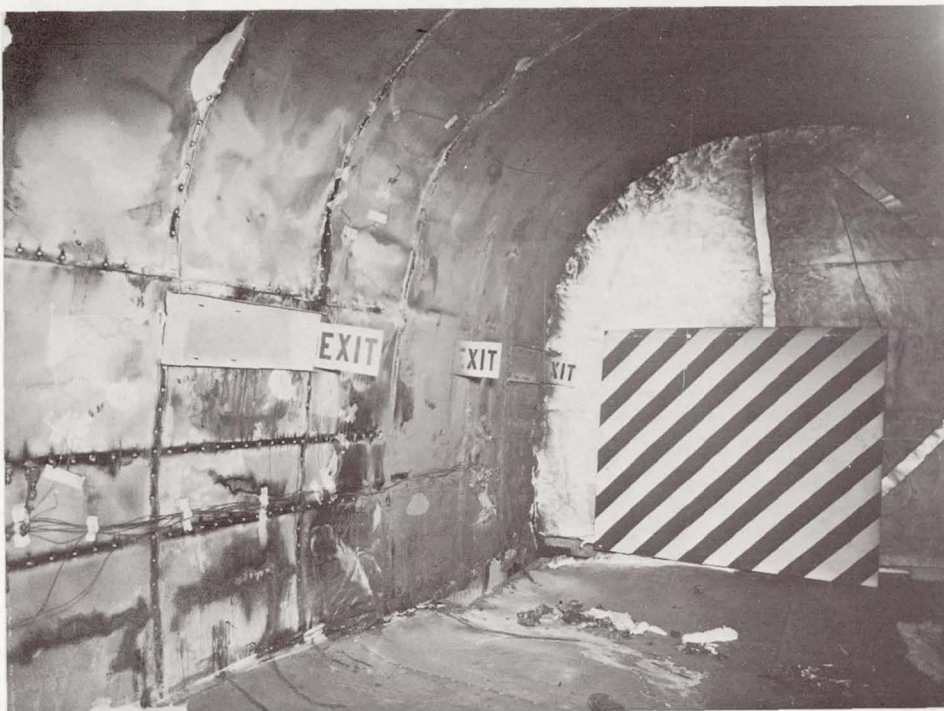


Figure 8.- Exterior of test section after test.



(a) South side.



(b) North side.

Figure 9.- Interior of protected section after test.

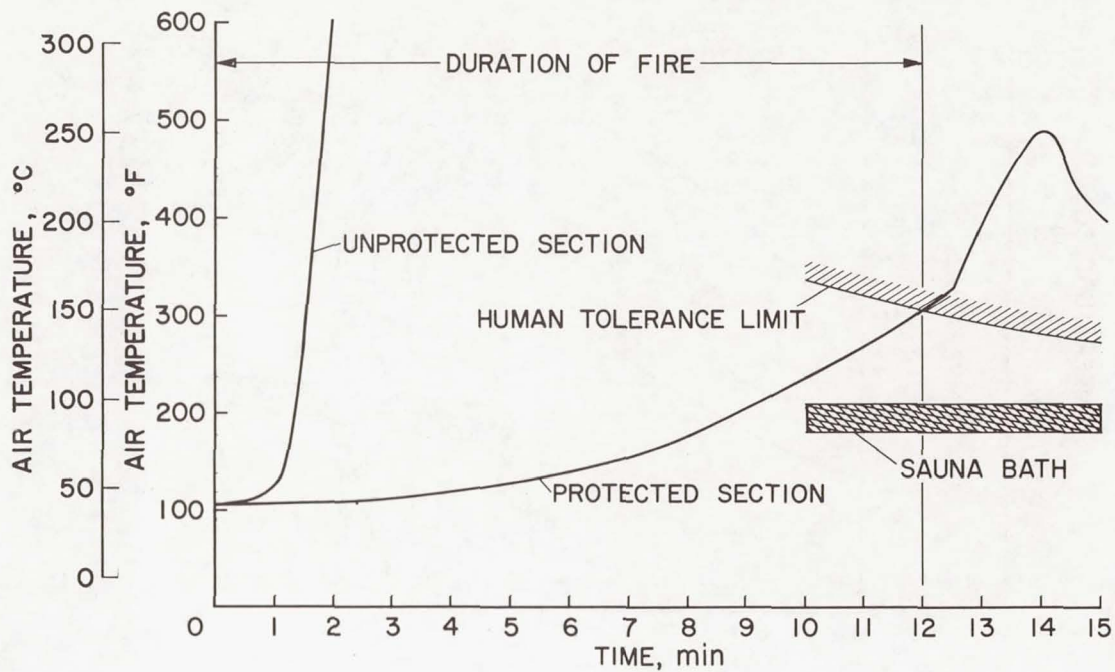


Figure 10.- Cabin air temperature during fire.

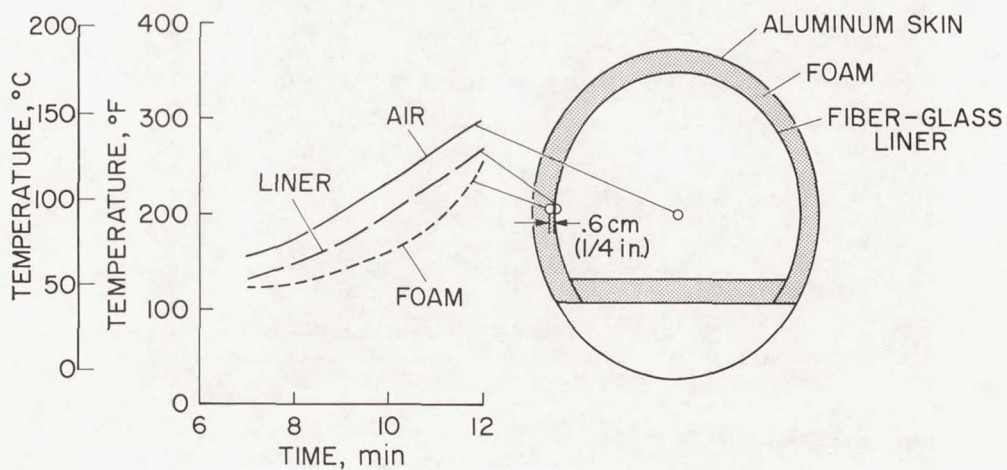


Figure 11.- Temperatures inside cabin during fire.

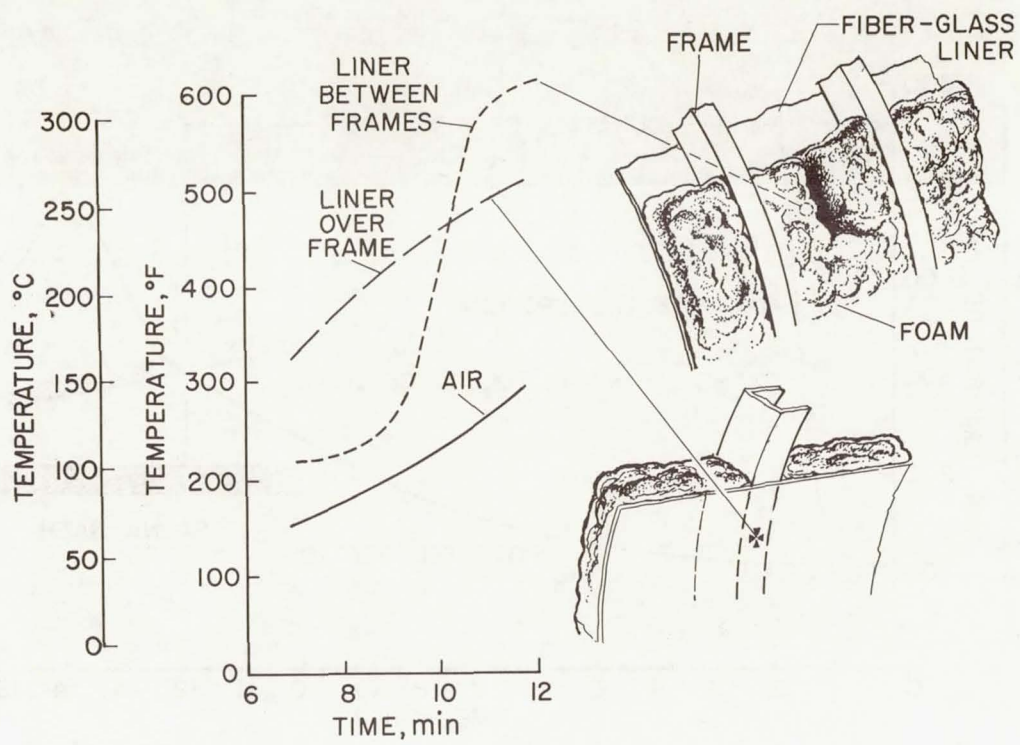


Figure 12.- Sources of heat leaks into cabin during fire.



Figure 13.- Fissures in fire-retardant foam after test.

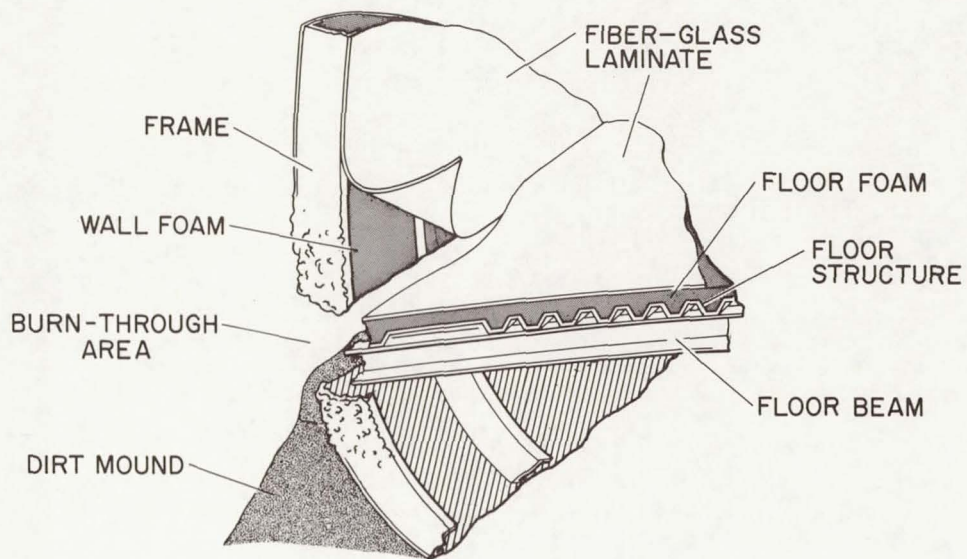


Figure 14.- Burn-through failure at floor seam.

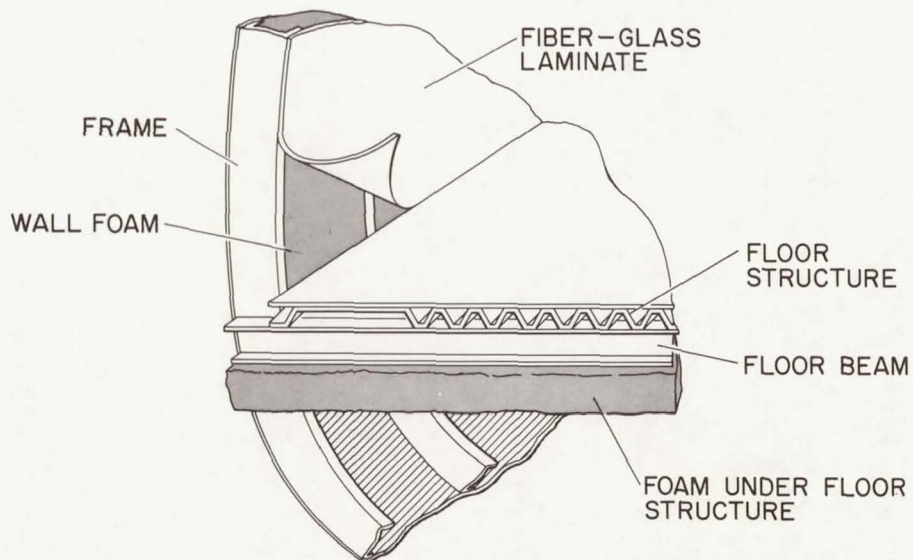


Figure 15.- Recommended location of foam to protect floor structure.

Page intentionally left blank

IMPROVEMENT OF FIRE SAFETY IN AIRCRAFT

By Mathew I. Radnofsky
Manned Spacecraft Center

INTRODUCTION

Since the inception of manned space flights, NASA has been actively engaged in a search for nonflammable materials to be used within spacecraft. This NASA search, conducted with the assistance of industry, has progressed from the relatively unsophisticated materials available 10 years ago to the great variety of fibers, cellulose, elastomers, and composites which can now be fabricated into nonflammable end-items. Many of these nonflammable and fire-resistant materials and much of the supporting technology developed for spacecraft application can significantly contribute toward the achievement of a fireproof aircraft interior. This effort is a part of the overall NASA commitment of making space technology available and practical for commercial uses.

Certain physical considerations that may be of secondary importance for some spacecraft applications are of primary importance when materials for aircraft interiors are selected. Foremost among these considerations is durability, requiring flameproof materials that will withstand the rigors of repetitive usage in various functional applications.

Esthetic qualities also are of major importance for airline applications. Since many of the fibrous materials currently being used in spacecraft cannot be dyed and are available only in white or in varying shades of brown, additional development is required. Advancements have been and are being made in techniques for pigmenting, spraying, laminating, embossing, and printing to achieve decorative results by using nonflammable and flameproof materials.

Such commercial aircraft items as curtains, upholstery, carpets, decorative panels, cabinets, paper products, oxygen lines (and associated equipment such as masks), and straps have been fabricated or replaced with nonflammable substitutes.

DISCUSSION

Materials Evaluated for the Space Program

Applicable to Aircraft Refurbishment

Fibrous materials.- Undoubtedly, the highest degree of nonflammability can be obtained with inorganic fibers such as asbestos and fiber glass. Containers using asbestos as insulation are used in spacecraft to stow flammable materials.

Beta fiberglass, characterized by an extremely fine diameter, is used extensively within spacecraft. Textile structures can be fabricated from Beta fiberglass to provide the maximum in flexibility and performance within the limits of the inherently low abrasion resistance of fiber glass. Various techniques have been used successfully to improve the abrasion resistance of Beta fiberglass. These techniques generally have centered around the use of coatings, applied either to the woven fabric itself or to the individual yarns before weaving.

Several modified aromatic polyamide fibers that are nonflammable in air and in moderately enriched-oxygen atmospheres have recently been developed. Two of these fibers are Durette and Fypro. Fabrics made from these fibers exhibit excellent physical and fabrication characteristics. Clothing made from one of these fabrics is currently under consideration for use in the NASA Skylab program. Natural colors of the fibers are gold, dark brown, and black; however, developmental efforts to dye the fibers are underway.

Another more recent candidate material is a fire-retardant wool (treated with a chemical process called Proban) which meets many of the characteristics desirable for aircraft and other vehicle interiors. This material does not burn in air, is available in a wide range of colors, and can be considered for any application in which wool is a potential candidate.

Cellulosics.- A cellulosic material, developed by the Scheufelen Paper Company of Germany and processed primarily as a paper, carbonizes in the presence of a flame but does not propagate the flame. This nonflammable characteristic is evident in both air and oxygen-enriched atmospheres. This paper prints well and, with some minor exceptions, has physical properties that are comparable with conventional paper.

This paper can be processed into a continuous roll of 1.27-cm-thick (0.5-in.) foam, similar to papier-mache. When placed on a ceiling, for example, the foam has both the appearance and function of conventional acoustic tile and offers the additional advantage of nonflammability.

In addition to the paper, a process called Laminite, which treats cellulose-base fiberboard with ammonium aluminum sulfate, has been developed. The resultant material is minimally flammable in oxygen and nonflammable in air. It can be formed wet, coated, cemented, and joined like a composite; yet it is lightweight and inexpensive.

Elastomers.- Fluorocarbon elastomers which have been developed for the space program are basically copolymers of hexafluoropropene and vinylidene fluoride. Although these elastomers are themselves slightly flammable, nonflammability concomitant with a wide range of physical properties has been achieved through the judicious use of compounding ingredients and plasticizers. Notable among these elastomers are Fluorel (developed by the 3M Company and available from the Mosites Rubber

Company and Raybestos-Manhattan, Inc.) and Viton, which was developed by E. I. du Pont de Nemours & Co. (Du Pont). The compounded elastomers can be foamed, cast, molded, or extruded. The materials can also be applied as a paste, a coating, or a spray solution.

Mineral pigments in a wide variety of colors can be formulated into fluorocarbon-based paints. Aircraft panel skins fashioned of elastomer-backed nonflammable materials to which decorative patterns have been applied have been manufactured. The inclusion of asbestos in the back skin provides insulating properties. These skins when laminated to a honeycomb interior afford fireproofing plus flexibility in decorative panel design.

Elastomeric coatings can be applied to polyurethane foams and to cellulosic materials such as paper, wood, and sponge, thereby effectively fireproofing the materials for structural and insulative applications.

Materials Available for Aircraft Refurbishment

As NASA has become more and more involved in fireproofing and refurbishment, a wide variety of applications of nonflammable, fire-retardant materials have been investigated.

Several European airlines (such as Swissair and KLM) have switched to Proban-treated woolens to serve their upholstery needs. The Proban process imparts fire-retardant qualities based on the use of tetrakis-(hydroxymethyl) phosphonium chloride (THPC), a chemical which does not adversely affect the wool but enables the treated woolens to meet Federal Aviation Agency (FAA) flammability regulations. This material is available in decorator colors and weaves.

NASA has developed a 0.5-mm-thick (20-mil) Fluorel sheet, backed with Durette knit, to simulate a leatherlike finish. This material can be made porous by a special process called "poralating" to impart "breathe" qualities to the material. This material is completely nonflammable, durable, and available in almost any desired color. It is intended for use in fabricating armrests, headers, magazine covers, or in areas where leather or leatherlike materials are used.

Seat cushions can be made fireproof by using polyurethane foam sprayed with Fluorel. This process is relatively inexpensive, about \$3 per seat. An airline seat with this cushion and further protected with nonflammable upholstery, armrests, and headers will provide a significant measure of fire protection until rescue can be accomplished.

Because approximately 85 percent of aircraft fires are externally caused, methods for flameproofing the aircraft metal skin have been examined. During flame-impingement testing in an 1870° C (3400° F) environment, the following increases in burn-through

times have been achieved by spraying Fluorel on an aluminum surface. Although uncoated 0.5-mm-thick (20-mil) aluminum burns through in 30 seconds, a threefold increase to 90 seconds is obtained when the aluminum is coated on one side with a 0.25-mm-thick (10-mil) coating of Fluorel. A 0.18-mm-thick (7-mil) coating of Fluorel on both sides of the aluminum increases the burn-through time to 180 seconds.

Time-to-flame-breakthrough into the aircraft cabin can, of course, be increased dramatically by the use of nonflammable insulation between the skin and the aircraft interior. There has been much activity directed toward nonflammable insulating foams, of which three notable examples are an asbestos foam, Pyrelle foam, and a polyimide foam. The asbestos foam was developed by the Rex Asbestos Works of Germany. This material is marketed in batting and sheets, is inexpensive, and should be useful for general insulation applications. The Scott Paper Company developed Pyrelle foam, a polyurethane, with good weight-to-thickness ratio. This material is also inexpensive and commercially available. The Monsanto Corporation developed the polyimide foam; however, it is considerably more expensive than asbestos.

A definite need exists for an insulative material which can be foamed in place. The Avco Corporation has developed (under NASA contract) an isocyanurate foam which is nonflammable in air environments. Although easy to apply, the material is at the present time expensive. The Ventron Corporation has developed a glucose-based polymer which can also be foamed in place, is self-extinguishing in air, and is extremely low in cost.

The Du Pont Company is developing a high-resiliency polyurethane foam which can be foamed in place and which is nonflammable in air. Potential for use of this foam is good. Du Pont has also developed a paperlike material of polyimide and mica which foams and forms a hard char when heated. This material may have application as a sealant for aircraft skins, with the ability to seal a skin rupture in the event of an externally caused fire.

The capability for coating or replacing electrical components and accessories with Fluorel has been developed and has been used to some extent in the space program. The material can be molded to form wire ties, conduits, circuit breakers, and electrical connectors. When mixed with asbestos for increased nonflammability in oxygen atmospheres, the Fluorel can be applied as a conformal coating over electrical parts, presenting a firebreak in case of ignition from electrical sources.

Numerous other areas within an aircraft can be effectively fireproofed. Developmental efforts to perfect a nonflammable emergency escape slide are progressing. Problems to date have centered around the selection of a supporting fabric which retains its fiber integrity under intense heat. It is hoped that flame- and heat-resistant fabrics coated with Fluorel will solve these problems and make available slides which are

reasonable in cost, which meet FAA specifications, and which are nonflammable when tested under deployment conditions.

Floor matting used within an aircraft can present a hazard during a fire situation. Fluorel has been calendered into mats of varying thicknesses and supplied in a variety of colors. When fiber glass is used as a substrate, thereby decreasing the amount of Fluorel required, the cost is decreased and tear resistance and durability are increased. Such mats are not only nonflammable but protect the aircraft floor against flame propagation.

Paper is used aboard an aircraft in many more places than are apparent. Non-flammable paper, developed by the Scheufelen Paper Company of Germany, can substitute for a large number of these applications. This paper is available in a wide variety of thicknesses and colors and can replace flammable writing materials, maps, tray covers, doilies, headrests, napkins, and (because it is receptive to printing) even booklets, brochures, and magazines.

Nonflammable blankets can be made from Kynol, Fypro, or Durette batting, quilted to covers of Fypro or Durette. Pillows can also be fabricated of Kynol, Durette, or Fypro battings, or from treated polyurethane foam. Pillow cases can be made from cotton treated with THPC.

For replacements in areas where molded plastics are used, NASA (in conjunction with industrial sources) has developed a number of nonflammable substitutes. The Whittaker Corporation has developed a nonflammable polyquinoxalate, and North American Rockwell has developed a polyimide in cooperation with Du Pont. Both these materials can be molded into nonflammable trays, panels, seats, light fixtures, and overhead racks, as well as into cabinets and counter tops.

Another major development in nonflammable composites can be cited as a definite advance toward fireproofing the aircraft cabin interior. A nonflammable fabric layup which, when used as a curtain, provides a firebreak against flame propagation from one interior area to another has been fabricated. This curtain material is composed of three layers, Durette batting sandwiched between two layers of Fluorel-coated Durette. These fabrics are either quilted together or sewn at the edges. The composite weighs approximately 0.5 kg/m^2 (1 lb/yd^2) and drapes beautifully. This layup can be used as galley and compartment curtains or as a firebreak between the pilot's cabin and passenger compartments.

Materials Developed for Aircraft Refurbishment

One of the more vulnerable areas in an aircraft fire is the ceiling area. For this reason, a good deal of effort has been directed toward fireproofing ceiling panels.

As a first step, Manned Spacecraft Center (MSC) personnel, working at United Airlines' facility, fireproofed four existing panels for reinstallation into the 727 aircraft (fig. 1). Existing panels were of resin-impregnated board, coated with vinyl. Two fireproof coating techniques were used, Fluorel spray and Fluorel-impregnated fiber glass laminated onto the panel surface. These coatings were applied both to vinyl-coated panels and to panels with the vinyl stripped away. A protective coating of transparent Kel-F was applied to all panels for soil and stain resistance. The backs of all panels were coated with a 75 to 25 percent mixture of Fluorel and asbestos to provide added fire protection. The panels still remain in place after almost 1 year of continuous service, and the interior airline decor was matched well enough that the panels are not discernible from the rest of the ceiling.

The same technique is applicable to ceiling panels of all types since the combination of Fluorel, fiber glass, and Kel-F can be supplied for direct adhesive application to the panels. This nonflammable skin can be furnished in decorator designs, textures, and colors and is an inexpensive method of fireproofing aircraft ceilings. (See fig. 2.)

Another approach is the replacement of existing ceiling panels with new panels, fabricated completely from nonflammable materials. Two types of new panels are being developed: corrugated board and a honeycombed composite structure.

The Laminite Corporation is involved in the development of a nonflammable corrugated board. Two curved panels of Laminite board have been supplied to American Airlines to demonstrate the feasibility of this approach. These panels were a preliminary effort, and Laminite is presently working toward improving the physical characteristics, including weight reduction. They are also experimenting with a number of different techniques for applying a decorative finish to the panel surface.

The Hexcel Corporation is primarily concerned with the development of a nonflammable honeycomb structure. This honeycomb will be sandwiched between two nonflammable "skins," with the exterior skin surface decorated and protected against soil and staining. A number of candidate materials, such as fiber glass, Nomex, aluminum, and X-P film, variously compounded or impregnated, are being considered for honeycombing to achieve optimum physical properties. The ultimate in panel construction, that is, lightweight, insulative, nonflammable, and with good strength, durability, and acoustical properties, is being sought. It is fairly well established that the skin material will be an impregnated fiber glass. Both American and United Airlines will evaluate these panels.

In another forward step in the development and application of nonflammable technology, the Monsanto Company has refurbished an Aero Commander aircraft with gold-colored Durette fabric (fig. 3). This material developed and marketed by Monsanto is completely nonflammable in air environments and was used to replace upholstery,

curtains, and baggage-compartment liners. Durette is available in plushes, brocades, and sculptured patterns as well as in conventional knits and weaves.

CURRENT NASA REFURBISHMENT PROGRAMS

In order to apply these technological advances, two Air Force T-39 and one NASA Gulfstream aircraft are being refurbished.

Two MSC personnel, working onsite in Winnipeg, Canada, accomplished a large part of the T-39 effort and trained personnel there to complete the refurbishment.

To fireproof the T-39 ceiling panels, a skin of Fluorel, fiber glass, and Kel-F was laminated to the existing wooden panels (fig. 4). Kick panels were completely replaced by a composite of Pyrelle foam, fiber glass, decorative Fluorel, and Kel-F.

All seat cushions were fireproofed with ammonium dihydrogen phosphate (ADP) and Fluorel spray. The entire seats were then upholstered with Durette fabrics. Armrests were covered with the Fluorel-coated Durette, simulating leather, and seat side panels were protected with Fluorel-based paint. New fiber glass curtains were installed, and wool carpets were installed in the passenger compartment. Fluorel-coated fiber glass matting was used as a nonflammable floor covering in the vestibule area and on the outside stairs leading into the aircraft (fig. 5). Deep treads were molded into the Fluorel surface to assure good traction.

Refurbishment of the Gulfstream follows the same general philosophy but utilizes several different materials in a more extensive refurbishment and takes advantage of more advanced fabrication techniques (fig. 6).

The Gulfstream walls and ceilings presently are covered with a vinyl fabric. All of this covering will be stripped and new nonflammable fabrics developed especially for this program will be substituted. The new headliner fabric will be a Fluorel-coated fiber glass, off-white and textured. The walls will be covered with Fluorel-coated Durette fabric, backed with a thin Pyrelle foam padding. (See figs. 7 and 8.)

All seats within the aircraft (figs. 9 and 10) will be completely redone; flotation cushions will be fabricated and fireproofed; new upholstery will be installed, armrests and footrests will be recovered; nonflammable headrests will be fabricated; and seat bottom shrouds will be painted with Fluorel paint.

All curtains will be replaced with curtains fabricated from nonflammable fabrics. The firebreak curtain discussed earlier will be used at the entryway to the aircraft (fig. 11). The leatherlike Fluorel-coated Durette will be used to fabricate a curtain protecting the area where the hydraulics are stored. The other curtains are standard, with the exception of the nonflammable fabrics used in their construction (figs. 12 and 13).

All existing floor coverings will be replaced, including the padding. Wool carpeting over fireproofed padding will be used in the passenger area (fig. 14), and a Fluorel-coated fiber glass with treads will be used to replace the present vinyl floor covering in the vestibule area, as shown in figure 5.

All these materials have been developed, evaluated for feasibility of installation and fabrication, color keyed to the aircraft decor, procured, and delivered ready for installation.

In addition to these programs, MSC has available onsite a United Airlines 737 fuselage which will be used to conduct an aircraft flammability test program. Regions within compartments will be furnished according to a predetermined test plan so that instrumented comparisons may be made between the variety of these new fire-resistant materials. Flammability test sequences will involve the use of realistic, electrically initiated ignitors, located in predetermined areas, with full television and motion-picture coverage. Results of this testing will be made available to the aircraft industry as a part of the overall NASA effort to apply space technology toward increased survivability in the event of aircraft fires.

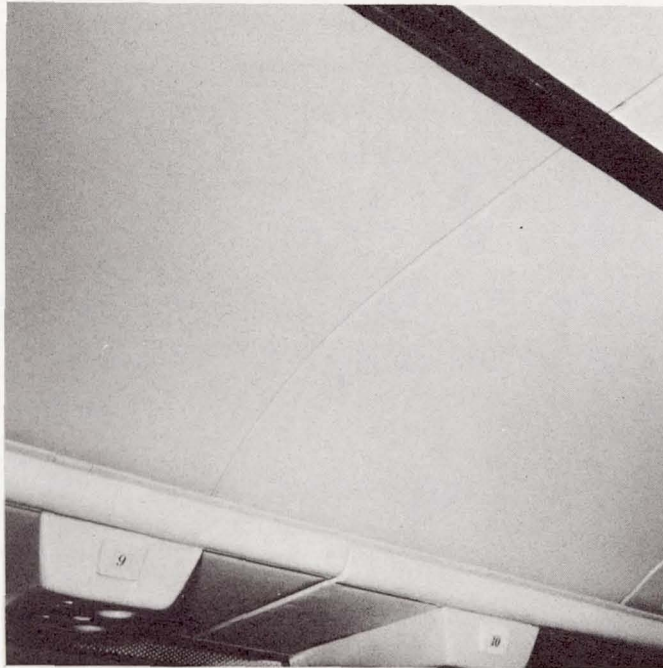


Figure 1.- 727 ceiling panel.

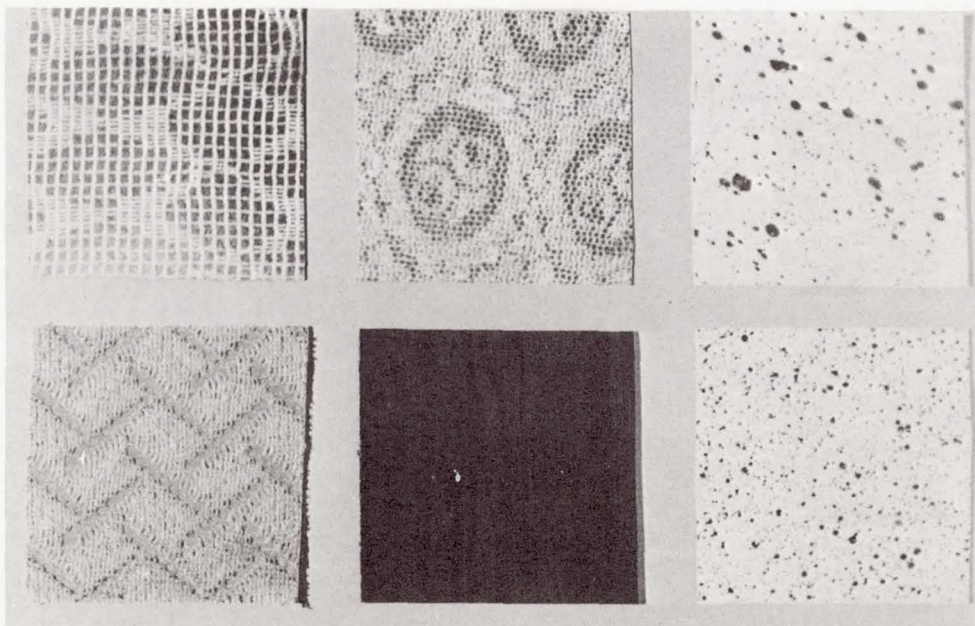


Figure 2.- Nonflammable paneling.



Figure 3.- Aero Commander crew compartment.

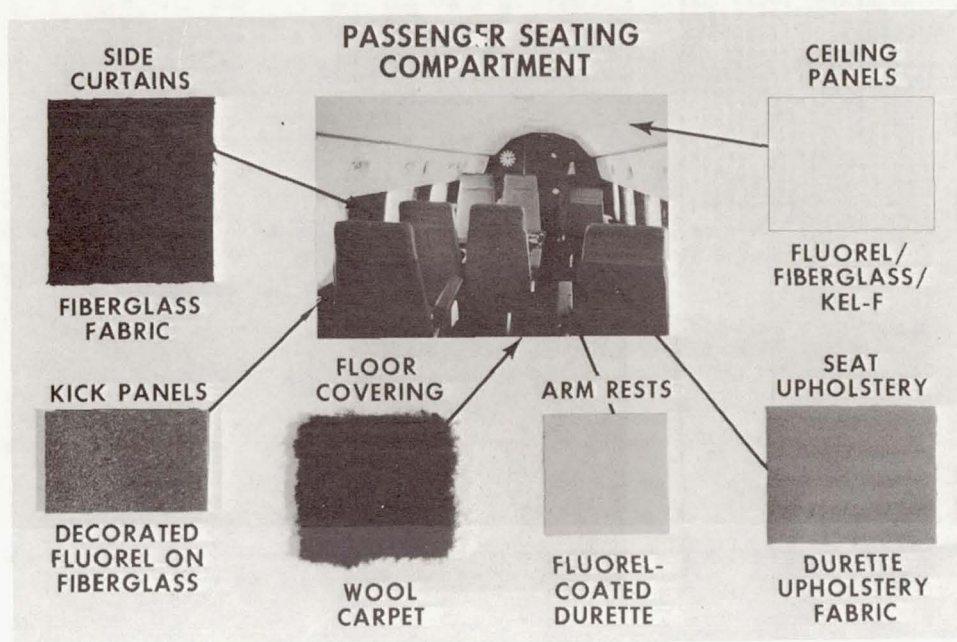


Figure 4.- T-39 passenger seating compartment.

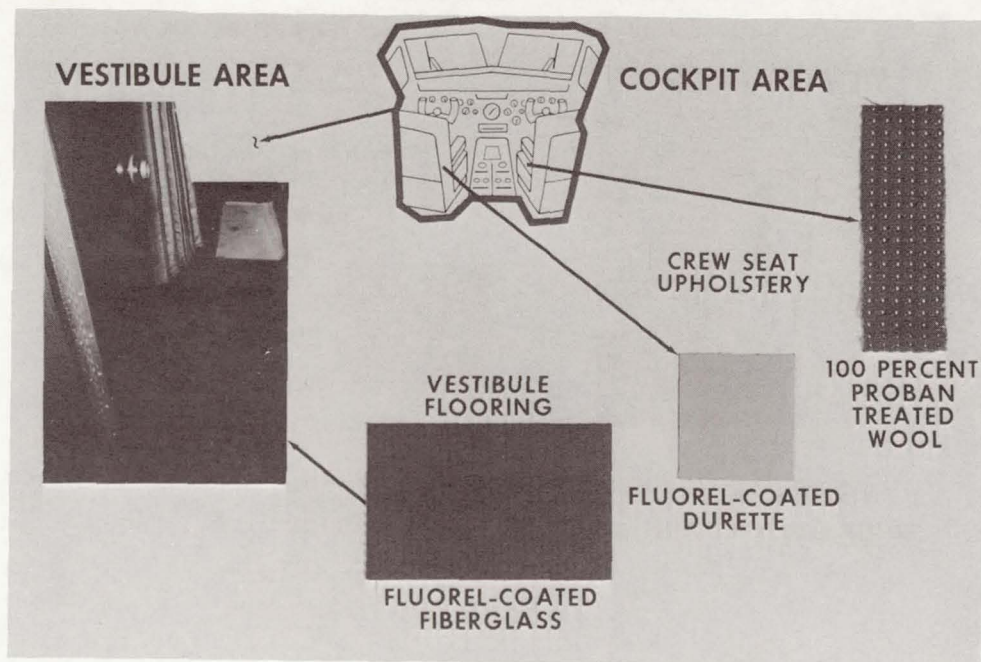


Figure 5.- T-39 vestibule and cockpit area.

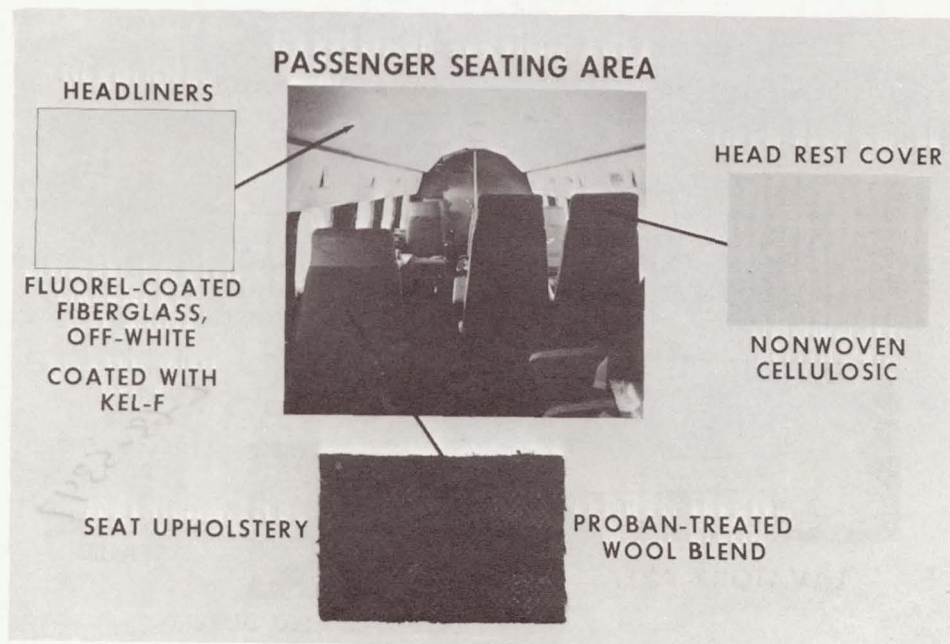


Figure 6.- Gulfstream - passenger seating area.

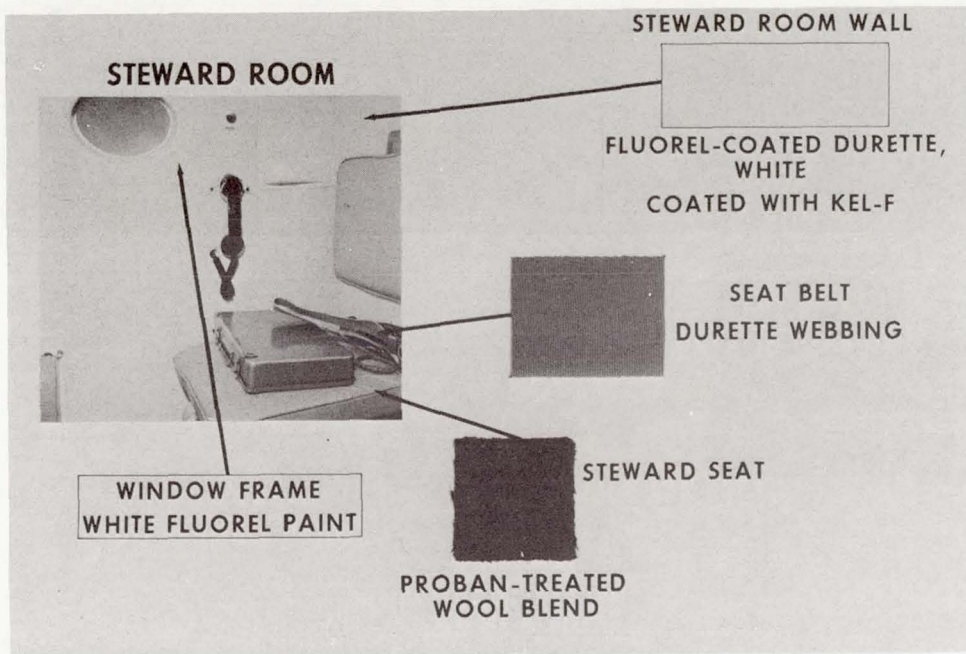


Figure 7.- Gulfstream - steward room.

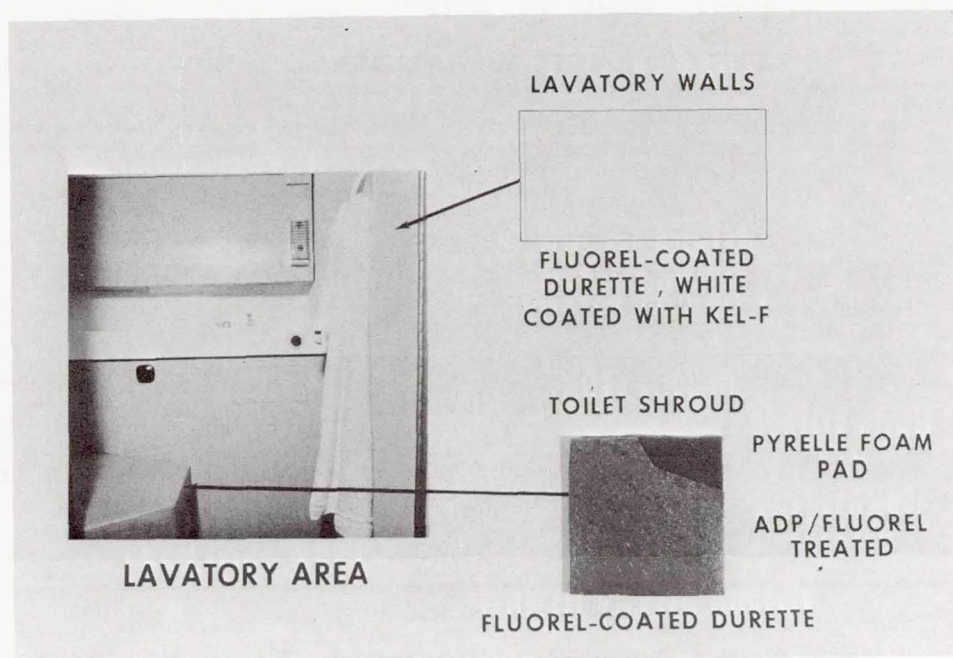


Figure 8.- Gulfstream - lavatory area.

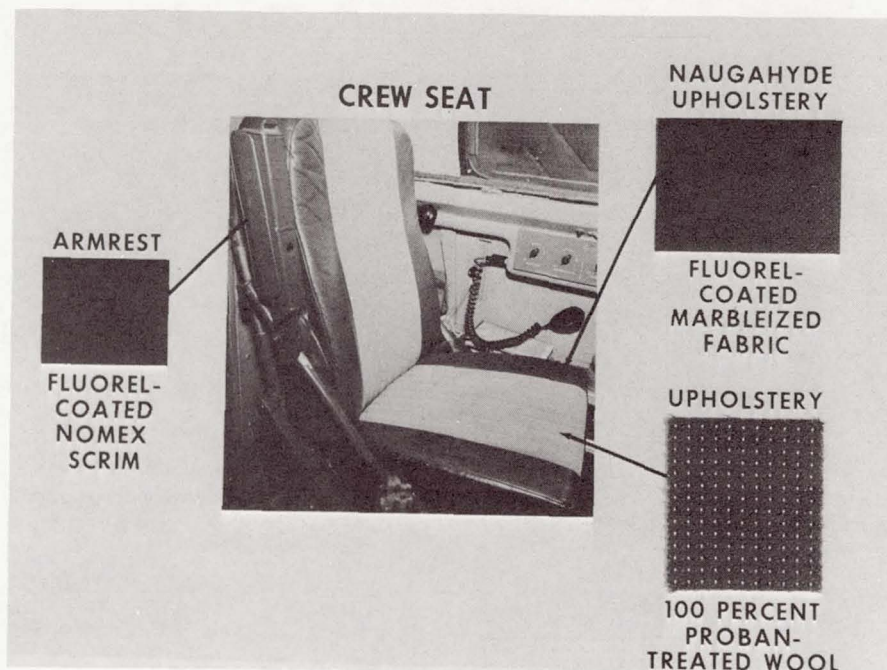


Figure 9.- Gulfstream - crew seat.

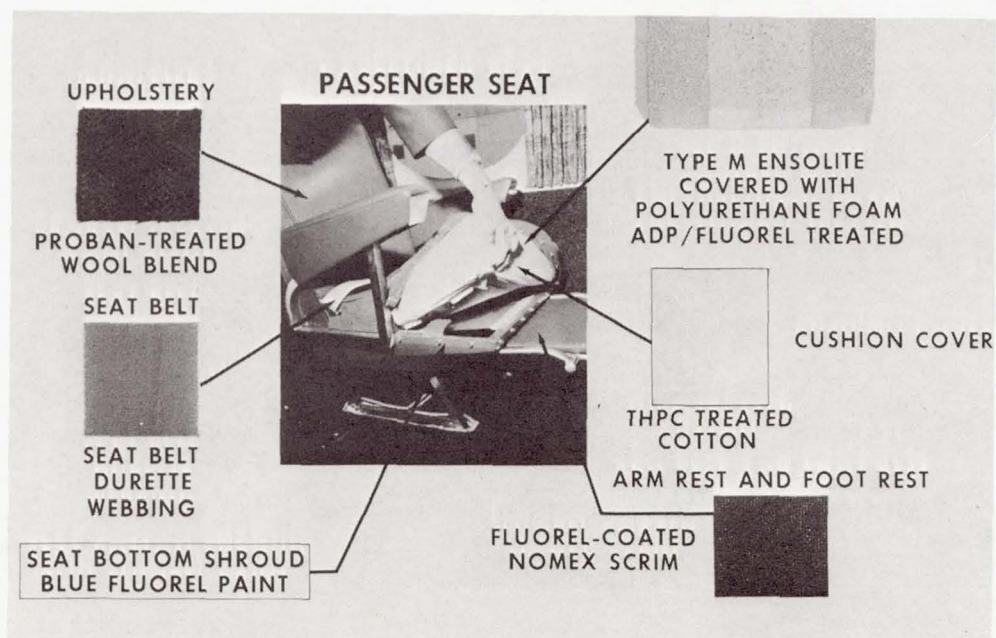


Figure 10.- Gulfstream - passenger seat.

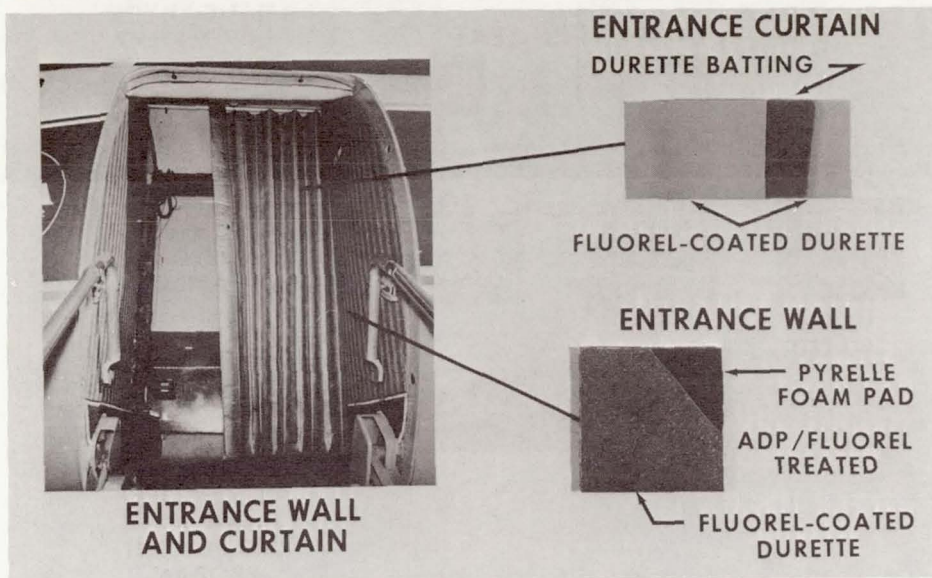


Figure 11.- Gulfstream - entrance wall and curtain.

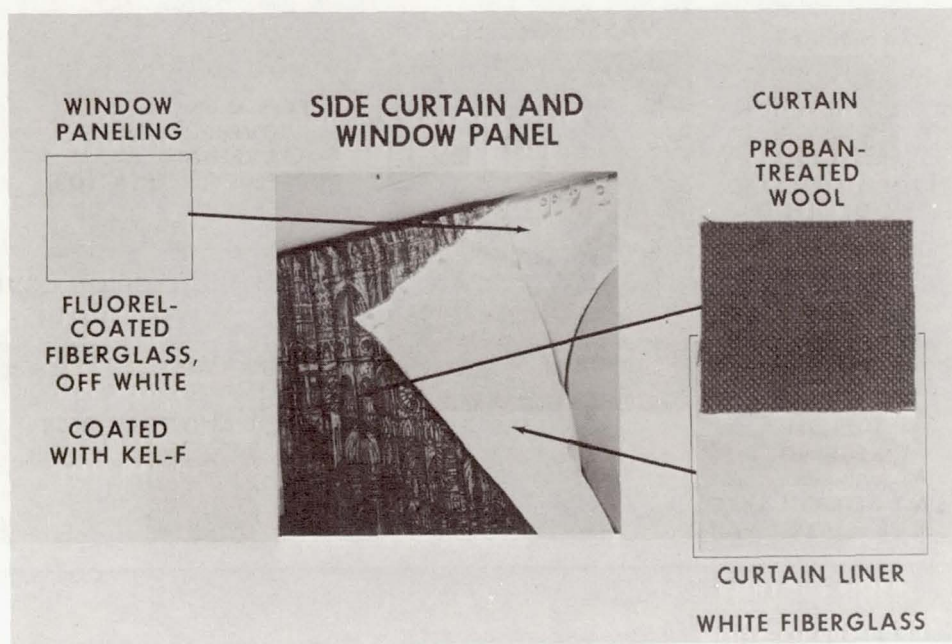


Figure 12.- Gulfstream - side curtain and window panel.

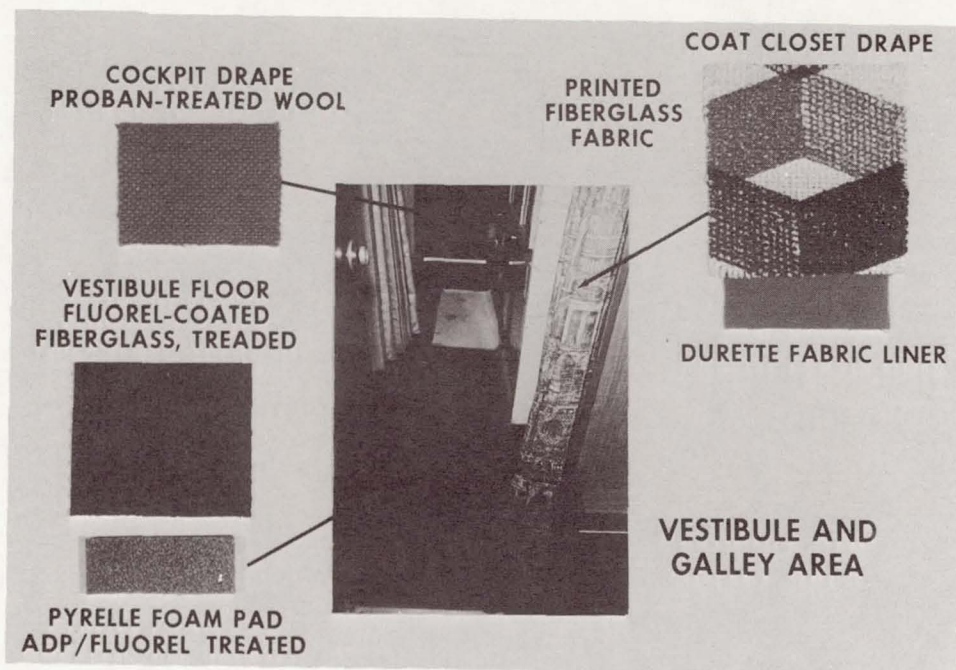


Figure 13.- Gulfstream - vestibule and galley-area curtains.

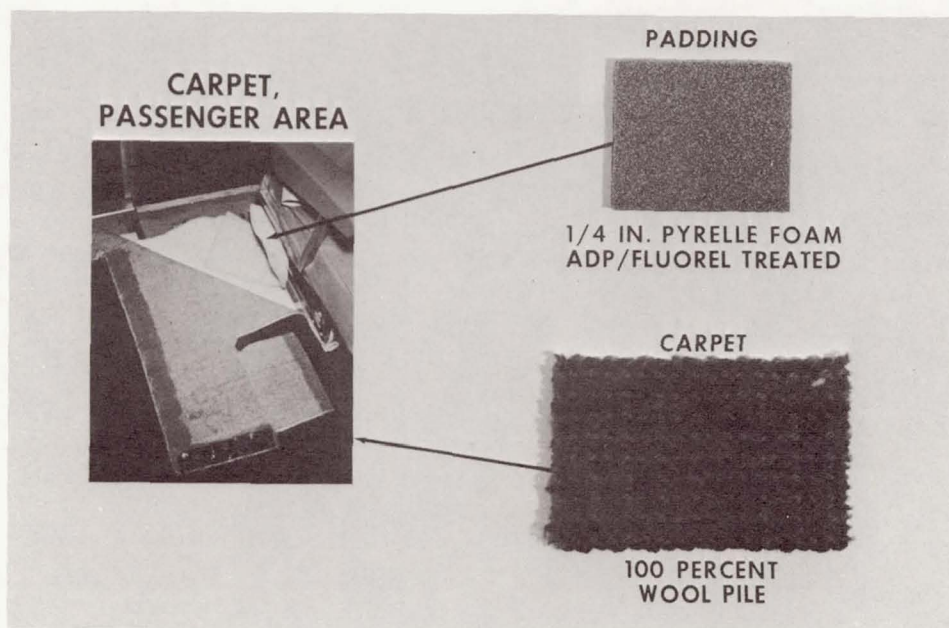


Figure 14.- Gulfstream - carpet in passenger area.

Page intentionally left blank

A CONTINUOUS-WAVE DOPPLER SYSTEM FOR AIRCRAFT COLLISION HAZARD WARNING

By Richard H. Couch
Langley Research Center
and
Charles L. Britt
Research Triangle Institute
Durham, North Carolina

INTRODUCTION

For the past 4 years, research has been conducted at NASA Langley Research Center on the problem of providing a low-cost instrument to warn the pilot of an impending midair collision hazard. The development of a warning device suitable for both commercial and general aviation presents the dual problem of defining minimum acceptable instrument performance requirements and then formulating a system design within stringent economic constraints.

In order to provide a feasible pilot warning indicator (PWI), a program of system studies, equipment simulations, and hardware development has been conducted. Figure 1 indicates some of the major features of this program. Statistical studies using realistic traffic data were performed to determine the system requirements. Also, a continuous-wave Doppler radar system has been defined and two engineering models have been successfully flight-tested. Based on the system studies and flight tests, a second-generation system which provides more accurate measurements and has a potentially lower cost has been developed. At present, the development and construction of this second-generation system is near completion.

The simulation studies used actual aircraft traffic data obtained by the Federal Aviation Administration from the radar system at the Atlanta airport. These data consisted of the three-dimensional position coordinates of each aircraft under radar track in the terminal area taken at 4-second intervals. Twelve 1-hour samples of data were taken over a 5-day period. By using these data, it was possible to determine the performance of the system as if each aircraft had been equipped with the PWI system during the period covered by the data base. Particular attention was given to determining the alarm statistics and the probabilities of system saturation under multiple-aircraft conditions.

MAJOR PROBLEM AREAS IN PWI DEVELOPMENT

The major problem areas in PWI development are (1) excessive alarms, (2) system saturation, and (3) cost. It is necessary to select a warning criterion that indicates a future hazardous condition and that has the ability to differentiate between a hazardous and nonhazardous situation. Also, the equipment must have the capability of making the required measurements without saturation or the generation of false alarms while observing a large number of aircraft simultaneously. The technical problems in themselves are relatively easy to overcome if the economic constraint is removed; however, considerable ingenuity is required to perform the required functions at a low cost.

With the use of the Atlanta data base, general studies were conducted to compare the alarm performance of various ideal systems having different warning criteria. Figure 2 shows the type of results obtained from the most dense hour of the data period (61 operations per hour). The vertical scale represents the average percent of flying time that an aircraft observed another aircraft within the warning time plotted on the horizontal scale. The upper curve represents a system measuring range only, the middle curve represents a system using range and closing-velocity measurements, and the lower curve represents a system using range, closing-velocity, and altitude measurements. These curves were derived for terminal-area conditions, with the assumption of a maximum differential velocity of 400 knots and maximum total acceleration of 0.5g. For a system with range, closing-velocity, and altitude criteria, the indicated coverage is not provided against aircraft with significant vertical velocity. Inspection of the curves indicates that under the conditions existing during the data period, a pure proximity system with a threshold set to provide a 25-second warning would indicate an alarm approximately 50 percent of the time. For the system using both range and closing velocity, a 25-second warning can be provided while reducing the percentage of time in an alarm status to less than 1 percent. The addition of altitude information to the range and closing-velocity system reduces the alarms to less than 0.3 percent for a 25-second warning and 152-meter (500-foot) altitude-difference threshold. Thus, from the Atlanta data studies, it was concluded that, as a minimum, the required measurements were relative range, closing velocity, and altitude difference.

The probability of observing more than one aircraft using a system based on range, closing velocity, and altitude is shown in figure 3. No cases were observed in which two hazards occurred simultaneously for warning times on the order of 25 seconds. Thus, the data indicate that such a system would not require a capability of providing for multiple-aircraft alarms if means are provided for selecting the most hazardous aircraft. By equipment design that effectively filters out aircraft that are less hazardous, considerable equipment simplification can and has been achieved.

SYSTEM DESCRIPTION

The PWI hardware that is currently being developed is shown pictorially in figure 4. It consists of a transceiver and display unit onboard the protected aircraft and a linear transponder onboard the intruding aircraft. The protected aircraft should also carry the transponder. The display might consist of an alarm indication coupled variously with indications of relative intruder position, altitude separation, and time-to-collision.

A simplified block diagram of the system is shown in figure 5. It is basically a continuous-wave Doppler radar. It operates at a transmitter power of approximately 1 watt to ensure a low probability of system saturation. This low probability is due to range limiting on a signal-strength basis via a low-power transmitter. The carrier frequency of 5.20 GHz is frequency modulated by a recognition code generated on each aircraft by a pseudorandom process. The purpose of this recognition code is to allow all aircraft to operate simultaneously in the same frequency allocation without significant interference.

The transponder onboard the intruding aircraft is simply a linear repeater which receives interrogations from other aircraft transmitters, amplifies them, shifts their frequency, and retransmits them. The recognition code on each received signal is preserved at the transponder output. In addition, a coded message that conveys the intruding-aircraft altitude is applied to all transponder reply signals. The maximum transponder output power is 1 watt, and the nominal output frequency is 5.1 GHz.

At the receiver, the signal strength varies inversely as the fourth power of the range between aircraft. The received frequency differs from the transmitted frequency by an amount equal to the offset introduced in the transponder plus the Doppler shift associated with the closing velocity between the two aircraft. There are modulation components in the received frequency which are the result of the recognition code and the altitude coded message.

In practice, there will be many reply signals present at the receiver input simultaneously. Some of these replies will be the result of interrogations of a number of transponders by the protected-aircraft transmitter (desired replies). Others will be replies to transmitters other than the protected-aircraft transmitter (interfering replies). It is the job of the receiver to distinguish between the desired replies and the interfering replies. This function is accomplished in the receiver front end by a correlation process which suppresses interfering replies and amplifies desired replies.

The overall receiver gain-versus-frequency characteristic is chosen such that the signal from the intruding aircraft which has the most hazardous combination of range and closing velocity produces the largest magnitude signal at the receiver output. Thus, the

signal with the smallest modified tau (shortest possible time-to-collision) appears largest at the receiver output. This statement implies that degree of hazard is measured in the receiver by observing a combination of signal strength and Doppler shift.

Once the signal from the most hazardous aircraft has been selected, it is further acted upon by the data processor to obtain differential measurements of velocity, range, and altitude. The closing velocity is measured by observing the average Doppler shift with a discriminator. The range is measured by observing the time delay between the time of transmission and the time of arrival back at the receiver of the recognition code, and altitude difference is measured by comparing the decoded altitude message from the intruding aircraft with the protected-aircraft altitude. Approximate time to closest approach is determined by calculating the ratio of measured range to measured closing velocity. The addition of a second receiver channel allows the determination of intruder bearing.

SYSTEM PERFORMANCE

Alarm Performance

It is possible for the following two types of erroneous indications to occur in the system: (1) an alarm occurs when a collision hazard does not exist, and (2) an alarm is missed when a collision hazard does exist. The first type of alarm has been discussed previously and occurs even in ideal systems because the alarm criteria selected fail to provide sufficient discrimination between hazards and nonhazards. The probability of this type of alarm can be reduced to any degree desired by reducing the warning time, as shown in figure 6. Thus, a tradeoff is involved between warning time and pilot workload allocated to responding to alarms. It is believed desirable to provide an adjustable threshold such that the pilot sets the warning time on the basis of the existing flight conditions. For example, it may be desirable to accept a shorter warning time in the terminal area than in en route sectors.

The second type of false indication occurs because of the particular techniques used in generating and decoding the recognition code for the radar. It is possible for codes from different transmitters to be in synchronism and if this situation occurs, a loss of communications will exist and result in a failure in the indication of an alarm in either aircraft. The probability of total communication loss during a period when an alarm should be given is called the probability of a missed alarm.

The probability of a missed alarm has been calculated for various recognition codes and other system parameters. For the coding technique and parameters selected, a calculation indicates that the probability of a missed alarm (defined as a communications loss of 10 seconds or greater) is less than 1×10^{-6} . This probability could be reduced

to an even smaller value by using different recognition codes for different transmitters or by increasing system bandwidths.

Another factor which can result in a failure in the indication of an alarm in one of the two aircraft involved in an encounter is the intentionally restricted antenna coverage. The transceiver antenna pattern is shaped to provide uniform coverage in the forward half plane over an angle of $\pm 100^\circ$ horizontally and $\pm 15^\circ$ vertically. The transponder antenna pattern is uniform over 360° horizontally and $\pm 15^\circ$ vertically. Thus, alarms due to aircraft approaching from behind the protected aircraft or from above or below with a large vertical velocity would not be indicated until the range between the aircraft became very small.

Saturation Performance

In order to determine the severity of the saturation and interference problems for the PWI system, a simulated system has been "flown" on all aircraft represented in the radar traffic data from the Atlanta airport. Statistics have been derived which indicate the probabilities of system saturation and interference.

Figure 7 shows the saturation performance of the transponder. The vertical scale indicates the average percent of time that the power level from the transponder was greater than the level given along the horizontal axis. Two curves are plotted; one represents the saturation performance obtained when using the Atlanta radar data, while the other represents results obtained from a simulation with a traffic density approximately three times as great as the Atlanta radar traffic density. Note that for either case, the power output of the transponder did not exceed 1 watt (or 30 dBm), and for a large percent of the time the transponder is operating at power levels considerably less than this value. Thus, the transponder is not prone to saturation under traffic densities considerably in excess of the Atlanta density. The total transponder output power exceeded 0.3 watt only 0.7 percent of the time for the Atlanta density.

At the receiver, the most important saturation-indicating parameter is the signal-to-interference ratio during periods in which a hazard should be indicated. Figure 8 indicates the percent of alarm time that the signal-to-interference ratio is greater than a value given along the horizontal axis, with a warning time of 25 seconds used. Again, curves are shown for results taken from the Atlanta traffic data and also from the simulation using a traffic density approximately three times that of the Atlanta data. As may be seen, the signal-to-interference ratio during alarm situations exceeded 160 (that is, 22 dB) in the case of the Atlanta traffic density and exceeded 20 (that is, 13 dB) for the simulated-density case during at least 90 percent of the alarm time.

CONCLUDING REMARKS

Considerable progress has been made at Langley Research Center towards the development of a PWI system suitable for all classes of aircraft including general aviation. Figure 9 summarizes the major features of the system and its expected performance. The system requirements and technical approach are now well defined and the major problem areas, such as differentiation between hazards and nonhazards and development of the capability for handling a large number of aircraft without saturation, have been solved with relatively simple equipment. The studies indicate that the operation of the system will be satisfactory in a multiple-aircraft environment. Finally, the system concept has the potential of being made available at a moderate to low user cost.

INTRODUCTION

1. STATISTICAL STUDY OF PERFORMANCE OF VARIOUS SYSTEMS IN REALISTIC TRAFFIC

(a) SYSTEM REQUIREMENTS

2. CONTINUOUS-WAVE DOPPLER SYSTEM DEFINITION

(a) FEASIBILITY TESTS

(b) SYSTEM DESIGN

COST

SIZE

WEIGHT

3. SIMULATION OF SYSTEM PERFORMANCE

(a) ALARMS

(b) MISSED ALARMS

(c) SATURATION

Figure 1

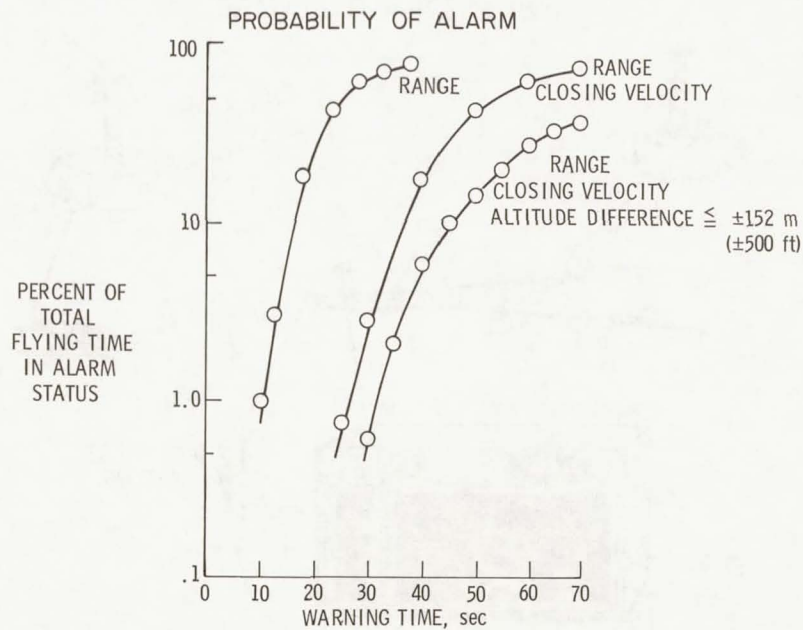


Figure 2

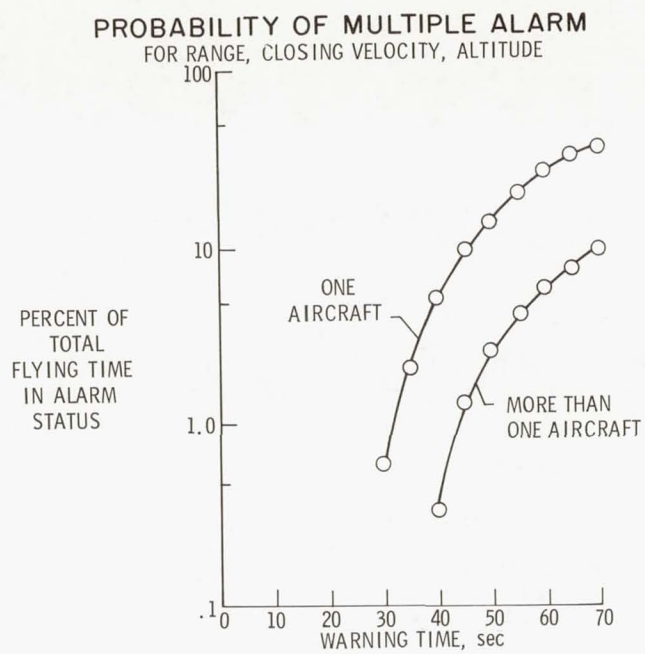


Figure 3

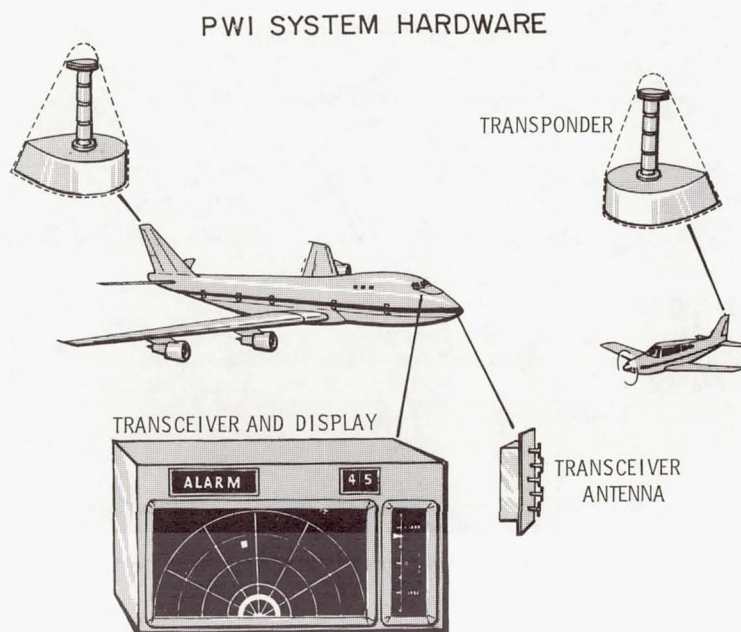


Figure 4

PILOT-WARNING-INDICATOR SYSTEM FUNCTIONAL BLOCK DIAGRAM

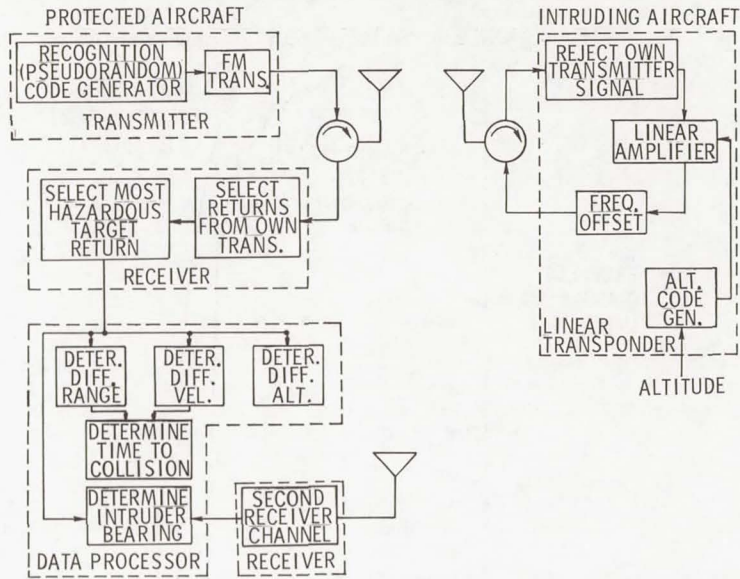


Figure 5

ALARM PROBABILITY

WARNING TIME, sec	ALARM PROBABILITY
15	< .001
25	.0055
35	.041

MISSED-ALARM PROBABILITY

≈ 1 IN 1 000 000

Figure 6

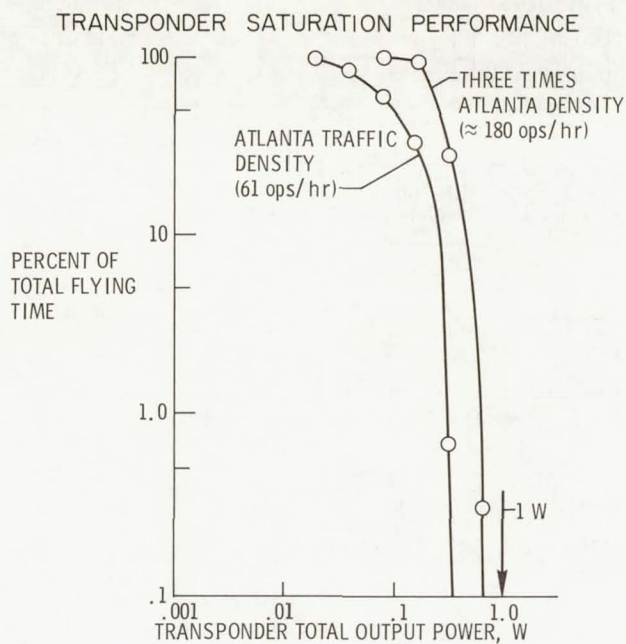


Figure 7

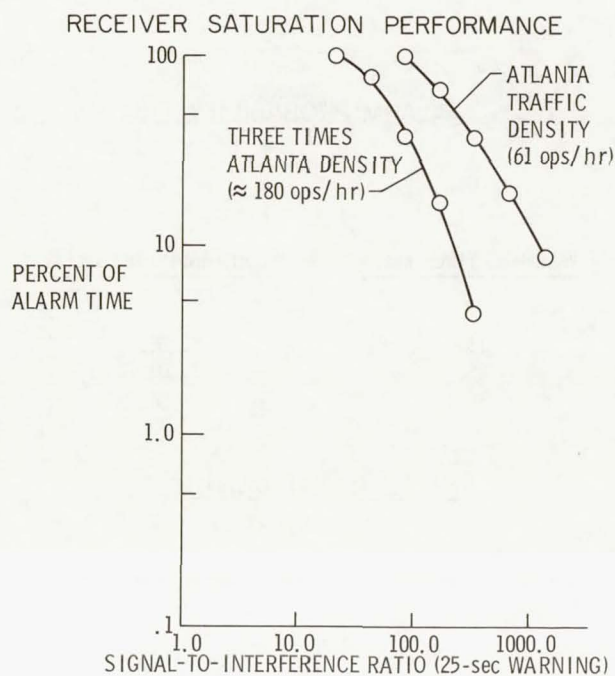


Figure 8

STATUS SUMMARY

1. SYSTEM DESIGN STUDY
 - (a) LOW-COST IMPLEMENTATION
 - (b) VARIABLE WARNING TIME (15 TO 35 sec)
 - (c) EXPANDABLE MODULAR HARDWARE
2. PERFORMANCE ANALYSIS
 - (a) HIGH PROBABILITY OF HAZARD DETECTION
 - (b) LOW ALARM RATE
 - (c) LOW PROBABILITY OF SATURATION AND MISSED ALARMS

Figure 9

Page intentionally left blank

LIGHTNING-INDUCED VOLTAGES IN AIRCRAFT ELECTRICAL CIRCUITS

By Paul T. Hacker
Lewis Research Center

SUMMARY

Experience has shown that aircraft avionics and electrical systems have been damaged or caused to malfunction when an aircraft is struck by lightning. It has been suspected in many cases that these failures are due to voltages being induced in the electrical systems by lightning currents flowing through the aircraft structure. A study was conducted to determine the magnitude of induced voltages and their relation to the characteristics of the lightning discharge and to the physical and electrical characteristic of the aircraft and its electrical systems. The investigation was performed with a wing of an F-89 airplane and a simulated lightning facility. The induced voltages measured for some circuits and simulated lightning characteristics were of sufficient magnitude to adversely affect sensitive avionics.

INTRODUCTION

An aircraft in commercial service will, on the average, be struck by lightning once a year. Lightning presents several hazards to an aircraft. It can produce

- (1) Mechanical and thermal damage to the structural material
- (2) Ignition of vapor in fuel tanks
- (3) Damage to and malfunction of electrical and avionic systems

Most of these hazards have been the subject of many investigations. The studies conducted to date on the adverse effect of lightning on electrical systems have been primarily concerned with direct strikes to external electrical components. This paper deals with voltages induced in electrical circuits by lightning current flowing through the aircraft structure.

Induced voltages are a concern because the avionic equipment used on modern aircraft for navigation, communication, and automatic flight control makes extensive use of semiconductors and microcircuitry, which are much more susceptible to damage from transient overvoltages than the vacuum tubes and large electronic components formerly used. In addition to permanent physical damage, transient voltages may introduce spurious signals in critical avionic equipment, such as computers, to cause them to temporarily malfunction or to produce false information. Although experience has shown that

avionics are affected during lightning strikes and that the probable causes are induced voltages, very little work has been done to evaluate the magnitude of the problem. Thus, a program was initiated by the Aerospace Safety Research and Data Institute at the Lewis Research Center to determine the magnitude of induced voltages and their relationship to the characteristics of the lightning discharge and to the physical and electrical characteristics of an aircraft and its electrical systems. The study was conducted by the High Voltage Laboratory of the General Electric Company. The experimental portion of the investigation was performed with the right wing, complete with electrical circuits, of an F-89 fighter aircraft and a simulated lightning facility.

The primary objective of this study was to measure the induced voltages and currents resulting from simulated lightning strikes. This paper presents some of the results of these measurements. A detailed description of the program and results are published in reference 1.

INDUCED-VOLTAGE MECHANISM

Figure 1 illustrates how voltages are induced in circuits inside an aircraft. Shown is a schematic representation of an airplane-wing—electrical-circuit combination. The structure is used as the return path for the circuit. When lightning strikes an airplane, the lightning current usually enters at one extremity of the airplane, flows through the skin and structure, and exits at another extremity. Thus, the lightning-current flow path may be fairly long and may flow past many electrical circuits inside the airplane. The lightning current i_L flowing in the wing structure creates a magnetic field. Most of the magnetic flux generated will be outside the wing ϕ_o , but a significant amount will be inside the wing ϕ_i because the wing structure is not a perfect shield or "Faraday cage." The imperfect shielding is a result of the noncylindrical geometry of the wing, the nonuniform distribution of the current flow through the structure, and openings in the structure. The magnetic field generated inside the wing couples the electrical circuit. In actuality, the magnetic coupling between the structure and circuit is distributed along their lengths, but it is represented here by the lumped inductances L_w and L for the structure and circuit, respectively. These two inductances possess a mutual inductance M . The magnetically induced voltage V_M is equal to the product of the mutual inductance M and the rate of change of the lightning current di_L/dt .

In addition to the magnetically induced voltage, there is another source of voltage, namely, a resistive voltage rise V_R . As the lightning current flows through the wing skin, it produces a voltage rise along the wing due to the resistance R_w of the wing material. This voltage rise also appears across circuit terminals a and b. This resistive voltage rise is equal to the product of the lightning current i_L and the resistance

R_w of the structure along the current flow path. The total open-circuit voltage e_{oc} at terminals a and b is the sum of the magnetically induced voltage and the resistive voltage rise. Whether the induced voltage is positive or negative with respect to the airframe depends upon the polarity of the lightning discharge and the current flow path with respect to the circuit. When a load impedance is connected across terminals a and b, the voltage drop across the load will generally be less than the open-circuit voltage and will depend upon the effective value of the circuit impedances, that is, the circuit inductance L and resistance R .

The circuit shown in figure 1 utilizes the airplane structure as a return path. For circuits that are open ended, such as antennas and circuits that use a separate ground return, the resistive portion of the induced voltage will not be present. There may, however, be a relatively small induced voltage due to capacitive coupling between the current-carrying structure and the circuit.

LIGHTNING DISCHARGE PHENOMENA

The current flow in a typical lightning discharge as a function of time is illustrated in figure 2. A lightning discharge usually consists of a series of high-amperage short-duration spikes separated by nearly constant-value low-amperage continuing currents. These continuing currents range up to a few hundred amperes with durations up to several hundred ms. The duration of the current spikes range up to a few hundred μs . Measurements of natural lightning show that 20 percent of the lightning discharges exceed a peak current amplitude of 70 kA and have initial rates of change of current in the spikes of 30 kA/ μs . The maximum possible peak current in natural lightning is not known, but it is in excess of 100 kA. To cover the probable maximum of natural lightning, Military Specification MIL-B-5087B(ASG) (ref. 2) for electrical-bonding and lightning-protection testing of aerospace electrical systems requires a peak amplitude of 200 kA and an initial rate of change of current of 100 kA/ μs . Since the induced voltage depends on the time rate of change of the lightning current and the amplitude of the current, only the current spikes are of importance as far as induced voltages are concerned.

As just discussed, the currents and rate of change of currents in the lightning-discharge spikes are large, this will result in large induced voltages if the effective mutual inductance M and effective wing resistance R_w (fig. 1) are significant. With the present state of knowledge, neither the mutual inductance nor the effective structural resistance can be directly determined by either calculations or measurements. However, effective values for these parameters can be calculated indirectly from experimental measurement (fig. 1) of the open-circuit voltage between terminals a and b and the current that flows in the circuit when terminals a and b are shorted. The results of such

calculations made during the study indicate that both the mutual inductance and effective resistance were significant in many cases.

APPARATUS AND PROCEDURE

A photograph of the F-89 airplane wing installed in the simulated lightning test facility is presented in figure 3. The wing is 6.7 meters (22 feet) long, which is short compared with today's jet transports. The wing skin is aluminum and is also considerably thicker than the skins on modern transports. A nonjettisonable fuel tank was attached to the wing tip. The flap on the inboard trailing edge was removed to get the wing into the test area. However, removal of the flap did not create any more openings into the interior of the wing, through which magnetic flux might enter, than would be present with the flap fully extended.

The wing contained a wide variety of circuits with respect to the number of conductors, the type of return path, the type of shielding employed, the routing within the wing and the function performed. Induced-voltage measurements were made on eight of the existing circuits. In addition, two special multiconductor circuits were installed in the wing so as to acquire some controlled comparison data.

The simulated lightning-current generator consisted of a bank of condensers which can be seen below the tip tank (fig. 3). The simulated lightning strike was delivered to the wing by means of a movable electrode. To study the effect of stroke location on induced voltages, strokes were delivered to five different points on the wing. These stroke locations were as follows:

- (1) At the forward end of the tip tank
- (2) Outboard on the wing leading edge
- (3) Outboard at the trailing edge of the aileron
- (4) At the center of the wing surface
- (5) Inboard on the wing leading edge

The exit point for the lightning current was the wing root.

The lightning-current generator produced a critically damped unidirectional current pulse to simulate the natural-lightning-current spike. Two current wave shapes were used for most of the tests. Sketches of these are shown in figure 4. The wave-shape designations, "slow" and "fast," are based on the time to crest, that is, the time required to reach maximum current. For the "slow" wave the time to crest is $36 \mu s$ and the time to 50 percent of the maximum value on the current decay is $82 \mu s$. Thus the notation is $36 \times 82 \mu s$. The corresponding times for the "fast" wave are $8.2 \times 14 \mu s$. The maximum

current for both pulses shown is 40 kA. At this maximum amplitude, the initial rate of change of current is 2 kA/ μ s for the "slow" wave and 8 kA/ μ s for the "fast" wave. Thus, these current pulses simulate only moderate lightning discharges and the induced voltages produced may be small compared with those generated by the severe natural-lightning discharges described previously.

The open-circuit voltage and the short-circuit current were measured at the wing-root end of each circuit for the different simulated lightning-stroke conditions. Sketches of typical oscillograms of open-circuit voltage and short-circuit current are shown in figure 5. Both signal traces are transient in nature with shape and duration similar to the applied lightning stroke. For many circuits and test conditions, there was a very high-frequency damped oscillation at the beginning of the voltage trace. The amplitude of the first cycle of this high-frequency component was usually much larger than the amplitude of the lower frequency component. In the data to be presented later, the open-circuit voltages and short-circuit currents will correspond to the peak values measured.

RESULTS AND DISCUSSION

The range of induced voltages and currents obtained in this study can be illustrated by the results from three circuits, the position-light circuit and the two specially installed multiconductor circuits. The location of the position-light circuit is shown in figure 6. In this case, the circuit is routed along the trailing edge of the main wing section, is partially exposed in the region of the flap, and passes through a conduit in the tip tank to a position light. The circuit is unshielded and uses the structure as a return path. The variation of the induced current and voltage with lightning-current amplitude for the position-light circuit is presented in figure 7. The data points represent the peak values measured at each lightning-current level. Both the open-circuit voltage and short-circuit current show an almost linear variation with lightning-current amplitude. At a lightning current of 70 kA, the induced voltage is 45 volts and the corresponding current is 14 amperes. If these trends are extrapolated to the 200 kA called for in the Military Specification (ref. 2) mentioned earlier, the induced voltage would be about 130 volts and the current would be about 40 amperes. Figure 8 summarizes the peak values of induced effects for various test conditions for the position-light circuit. Shown are the open-circuit voltages and the short-circuit currents for both the "slow" and "fast" lightning wave shapes and for the five stroke locations. Two values of open-circuit voltage are given. The first number listed is the peak value of the high-frequency component discussed previously, and the second number is the peak value for the lower frequency component. For the "slow" lightning discharge, the induced voltages for the high-frequency component ranged from 6 to 40 volts and for the lower frequency component the range was 1.8 to 20 volts, while the induced currents ranged from 0.7 to 9.0 amperes. For the

"fast" lightning discharge, the induced voltage for the high-frequency component ranged from 15 to 96 volts. For the lower frequency component, the range was from 2 to 48 volts and the currents ranged from 1.1 to 15 amperes. The voltages induced by the "fast" discharge are about twice those induced by the "slow" discharge. Since the peak current for both discharges is 40 kA, this difference in induced voltages must be due to the rate of change of lightning current. The initial rate of change of current was 2 kA/ μ s for the "slow" discharge and 8 kA/ μ s for the "fast" discharge. These are relatively small compared with the rate of change of current of 100 kA/ μ s called for in the Military Specification (ref. 2). If the trend indicated by these data can be extrapolated, then the induced voltage for a lightning strike with a rate of change of current of 100 kA/ μ s would be hundreds of volts. These data show that fairly large voltages can be induced in electrical circuits. Whether they are of sufficient magnitude and duration to cause avionics to malfunction has yet to be determined. A point of interest in this regard is the voltage limits established by Aeronautical Radio, Inc., to protect sensitive avionics from transient overvoltages due to either surges in power supplies or surges generated internally in equipment during operation. (See ref. 3.) These limits are -24 and +80 volts for any transient overvoltage duration from 1 μ s to 10 ms. Since the polarity of the voltage induced in a circuit depends upon the polarity of the lightning discharge, the induced voltages for the position-light circuit tabulated in figure 8 may be either positive or negative and thus some of these voltages exceed both of the established limits. Another observation made during the study was that, with energized and operating circuits, the induced voltages and currents are superimposed on the normal operating voltages and currents.

Two special multiconductor circuits were installed in the wing for the purpose of making some comparative measurements which could not be made with existing circuits. The information desired was

- (1) A comparison of voltages induced in circuits that terminate at the same point but have different lengths and routings
- (2) A comparison of voltages induced in a parallel pair and a twisted pair of conductors
- (3) A comparison of voltages induced in a single conductor and a coaxial cable
- (4) A comparison of voltages induced between two conductors and between a conductor and ground

To obtain these comparisons, each circuit bundle contained a single wire, a coaxial cable, a twisted pair of conductors, and a parallel pair of conductors. The location of these circuits is shown in figure 9. The common terminus for both circuits is at a point between the aileron and the flap. At this point all conductors in both circuits are grounded

to the airframe. One circuit was routed directly to the wing root along the trailing-edge spar. This circuit is 3.7 meters (12 feet) long. The other circuit was routed outboard along the trailing edge to the wing tip, across the wing, and inboard through the deicing heat duct to the wing root. This circuit was 11.6 meters (38 feet) long. All the conductors in each circuit were covered with a copper-braid shielding, except for that portion of the long circuit which was inside the heat duct. All tests on these circuits were made with a 40 kA "fast" simulated lightning stroke to the forward end of the tip tank.

The peak values of open-circuit voltages measured between a conductor and airframe and between conductors for both the long circuit and the short circuit are summarized in figure 10. The largest voltage measured was 6 volts between one of the conductors in the long parallel pair and the airframe. This voltage is relatively small compared with the voltages measured in the unshielded position-light circuit and indicates that the copper braid and heat duct are effective shields. As was expected, the induced voltages measured in the long conductors were larger than those measured in the corresponding short conductors. Also, the voltages were larger when the measurements were made between a conductor and the airframe than between conductors. The voltage induced in the parallel pair of conductors was up to 10 times larger than that induced in the twisted pair of conductors. Finally, the voltages induced in the single wire and the coaxial cable were almost identical, indicating that the coaxial cable shield does not provide any additional protection over that provided by the copper braid and the heating duct.

CONCLUDING REMARKS

This investigation has shown that lightning strikes to aircraft can induce voltages in electrical circuits inside the metal structure. Further, the data showed that there was considerable variation in the amount of voltage induced in the different circuits. An identical stroke could induce up to 96 volts in some circuits but less than 1 volt in others. The lowest voltages were induced in circuits with the following characteristics:

- (1) Used a separate conductor as return path
- (2) Used a twisted pair of conductors
- (3) Employed shielding
- (4) Were entirely within the wing enclosure
- (5) Extended only a short distance into the wing

The installation or modification of aircraft electrical circuits to take advantage of these characteristics may be an effective means of minimizing the effects of lightning on aircraft avionics.

The modern large jet transports may be susceptible to much higher induced voltages than were found in this investigation for several reasons. First, the simulated lightning discharge used in the investigation was only equivalent to a moderate natural lightning discharge. In addition, the F-89 wing is short and has thick wing skins compared with that of the modern transport. Thus both the resistive voltage rise and the magnetically produced portions of the induced voltage may be greater for the large modern jets. Also, the use of materials with a higher electrical resistance than aluminum, like titanium and nonmetallics, may accentuate the induced-voltage problem.

The main concern of the investigation reported herein was the measurement of lightning-induced voltages and not the effect of induced voltages on avionic equipment. However, a follow-on effort to this investigation has been initiated to

(1) Determine the effects of induced voltages on typical avionic equipment

(2) Develop and evaluate a convenient technique for the in-the-field determination of the susceptibility of electrical circuits in operational aircraft to lightning-induced voltages

REFERENCES

1. Lloyd, K. J.; Plumer, J. A.; and Walko, L. C.: Measurements and Analysis of Lightning-Induced Voltages in Aircraft Electrical Circuits. NASA CR-1744, Feb. 1971.
2. Anon.: Military Specifications - Bonding, Electrical, and Lightning Protection, for Aerospace Systems. MIL-B-5087B(ASG), Oct. 15, 1964.
3. Anon.: Guidance for Aircraft Electrical Power Utilization and Transient Protection. ARINC Specif. No. 413, Aeronautical Radio, Inc., May 1, 1967.

INDUCED-VOLTAGE MECHANISM

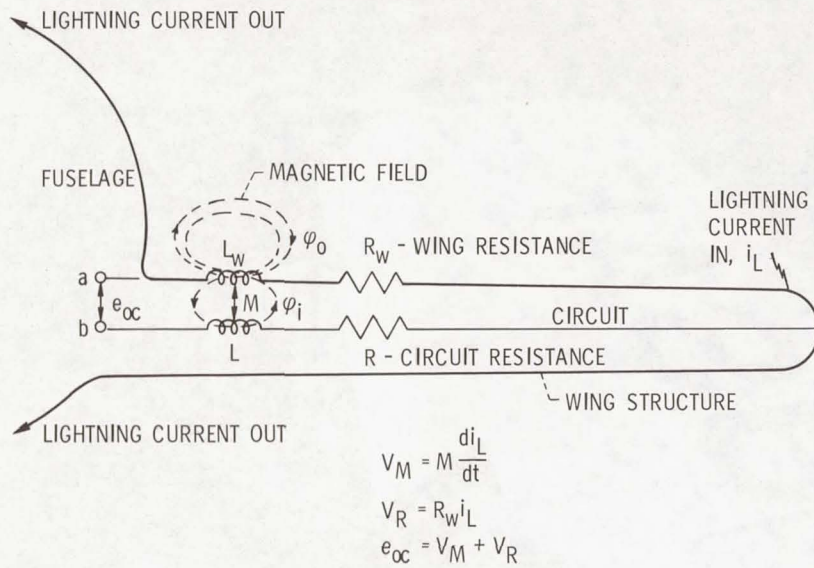


Figure 1

TYPICAL LIGHTNING DISCHARGE

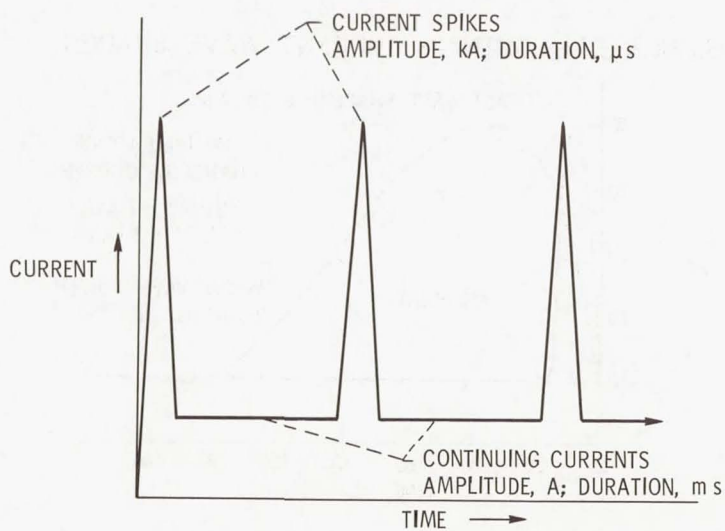


Figure 2



Figure 3

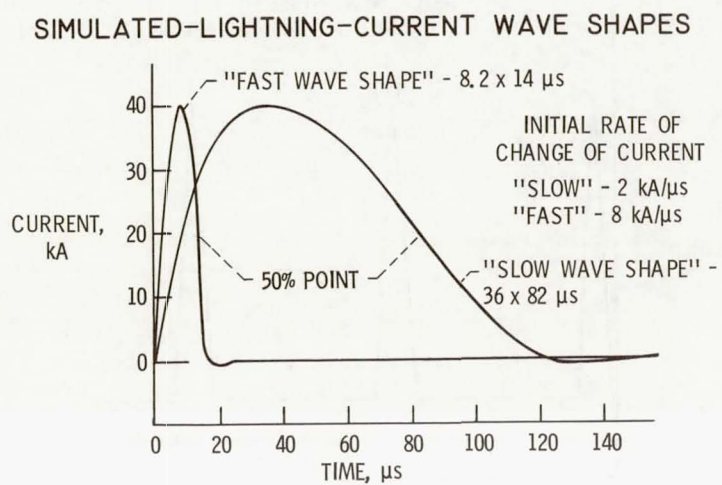


Figure 4

TYPICAL INDUCED-VOLTAGE AND CURRENT TRACES

40 kA - "SLOW" (36 x 82 μ s) LIGHTNING DISCHARGE

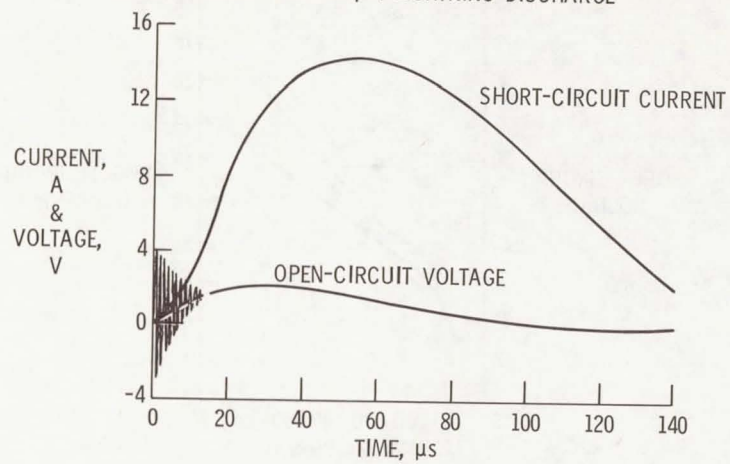


Figure 5

WIRING LOCATION

POSITION-LIGHT CIRCUIT

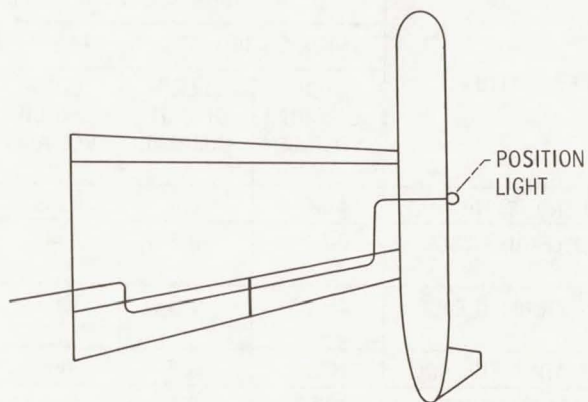


Figure 6

AMPLITUDE OF INDUCED EFFECTS

LIGHTNING-CURRENT WAVE SHAPE - $12 \times 24 \mu s$

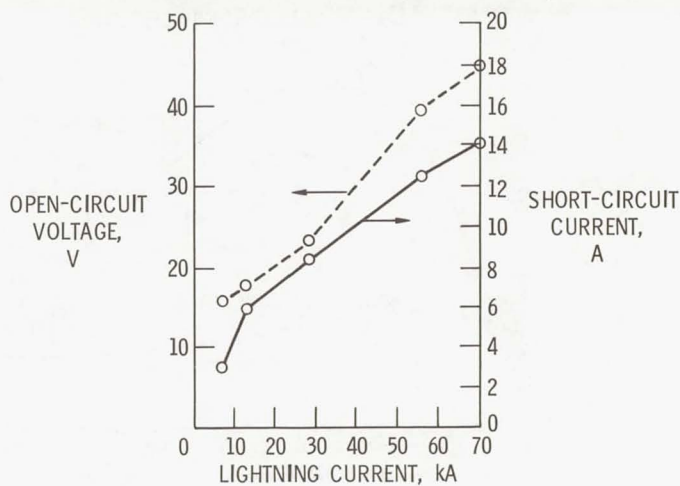


Figure 7

INDUCED VOLTAGES AND CURRENTS

POSITION-LIGHT CIRCUIT; LIGHTNING-STROKE AMPLITUDE, 40 kA

STROKE LOCATION	LIGHTNING WAVE SHAPE			
	"SLOW" - $36 \times 82 \mu s$		"FAST" - $8.2 \times 14 \mu s$	
	OPEN-CIRCUIT VOLTAGE, V	SHORT-CIRCUIT CURRENT, A	OPEN-CIRCUIT VOLTAGE, V	SHORT-CIRCUIT CURRENT, A
FORWARD END OF TIP TANK	40/20	9.0	96/48	15.0
OUTBOARD LEADING EDGE OF WING	6/2.2	0.8	15/4	1.1
OUTBOARD TRAILING EDGE OF AILERON	15/3.8	1.3	30/12	4.0
CENTER OF WING SURFACE	10/2.4	0.8	20/2	1.5
INBOARD LEADING EDGE OF WING	10/1.8	0.7	17/2.8	1.7

Figure 8

SPECIAL MULTICONDUCTOR CIRCUITS

LOCATION OF CIRCUITS

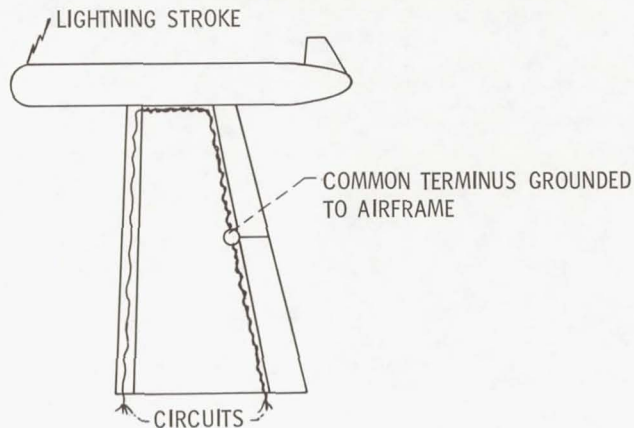


Figure 9

SPECIAL MULTICONDUCTOR CIRCUITS

OPEN-CIRCUIT VOLTAGES, V
40 kA - "FAST" (8.2 x 14 μ s) DISCHARGE

TYPE OF CONDUCTORS	TYPE OF MEASUREMENT			
	CONDUCTOR TO AIRFRAME		CONDUCTOR TO CONDUCTOR	
	LENGTH OF CIRCUIT			
	11.6 M (38')	3.7 M (12')	11.6 M (38')	3.7 M (12')
SINGLE WIRE	2.0 V	0.4 V	----	----
COAXIAL CABLE	2.1 V	0.4 V	----	----
TWISTED PAIR	1.0 V	0.5 V	0.22 V	0.04 V
PARALLEL PAIR	6.0 V	1.0 V	2.30 V	0.10 V

Figure 10

Page intentionally left blank

STATUS OF ENGINE ROTOR BURST PROTECTION PROGRAM FOR AIRCRAFT

By Patrick T. Chiarito
Lewis Research Center

SUMMARY

The extensive use of turbomachinery in aircraft has been accompanied by the danger that occasionally a high-speed rotor will fail and the uncontrolled fragments will damage equipment and threaten passenger safety. Accordingly, NASA is sponsoring a coordinated theoretical and experimental research program to develop criteria for the design of practical devices to protect the aircraft from serious damage. Means to contain rotor fragments as well as to deflect them away from critical aircraft components are being studied. This paper presents the status of this program and some of its highlights.

Test rotors are intentionally failed and generate fragments which impact the containment/deflection devices in a unique facility. High-speed photographs record the complex interaction for subsequent analysis.

Test results indicate that the capability of a ring to contain rotor fragments depends upon the number of fragments as well as the mechanical properties of the structural material. Both metals and nonmetals show good potential. It was demonstrated that partial rings can deflect fragments away from areas to be protected, and more related tests are planned.

A computer program has been developed which predicts the ring deformation if the forces applied by the fragments are known. Another program uses measured ring deflections to calculate the applied forces. These forces are subsequently used to calculate ring deflections. Predicted and measured ring profiles are in reasonable agreement for single-rotor-blade impacts of freely supported rings. The calculation methods are being improved to apply to more complex fragments and protective devices.

INTRODUCTION

Accompanying today's increased use of turbomachinery in aircraft is the associated danger that occasionally a high-speed rotor will fail and the uncontrolled fragments will damage equipment and threaten passenger safety. During the 9 years shown in figure 1, 170 uncontained failures of gas-turbine engine components were reported by U.S. commercial airlines to the Federal Aviation Administration and the National Transportation Safety Board.

For these data, an uncontained failure is defined as a rotor failure which generates fragments that penetrate the engine casing and might cause additional damage. For example, these fragments might damage fuel lines, fuel tanks, and control lines or depressurize the aircraft cabin. It is apparent, therefore, that the consequences of a rotor burst could be even more critical than the initial loss of the turbomachine. Note that the number of failures has increased during the last 2 years shown in figure 1 and that the data are incomplete for 1970. This figure indicates that it is unrealistic to assume that a rotor will never burst. The failure initiated most frequently in the compressor rotor (39 percent), and the turbine rotor was next at 19 percent.

Because the next generation of commercial aircraft will operate at higher gas temperatures and use large fan rotors, the probability of rotor failure will remain.

The adverse effects of turbomachinery failure on the airplane can be reduced either by the prevention of rotor burst or protection against damage should rotor burst occur. A significant effort is being expended to improve the operational utilization of turbomachinery; for example, there is an increased awareness of the need to improve methods for detecting defects during fabrication, operation, and maintenance. Also, attempts are made to relate cracks and other defects to tolerable levels in order to measure the remaining life of a structure. Despite such efforts, however, statistics continue to reflect the persistence of rotor failures. Accordingly, NASA has been sponsoring a research program with a view toward providing protection to the aircraft without imposing large weight penalties.

ROTOR BURST PROTECTION PROGRAM

Objective

This program is directed toward the development of criteria for the design of practical devices to protect the aircraft from serious damage resulting from rotor bursts. Means to contain rotor fragments as well as to deflect them away from the critical aircraft components are being studied. Because the interaction between rotor fragments and protective devices is complex, the immediate aim is to develop meaningful tests and analytical methods to evaluate possible solutions.

Approach

In order to generalize the results, experiments are closely coordinated with the analytical methods. Experiments are conducted in the Containment Evaluation Facility financed by NASA and located at the Naval Air Propulsion Test Center (NAPTC), Philadelphia Naval Base. (See refs. 1 to 4.) The test data are compared with results of calculation methods developed by the Aeroelastic and Structures Research Laboratory,

Massachusetts Institute of Technology. (See refs. 5 and 6.) The test facility is essentially a spin chamber and is shown in figure 2. Test rotors, modified to fail with predetermined sizes and shapes of fragments, are caused to impact containment/deflection devices. In order to study the complex interaction between the fragments and the protective device, it is necessary to use high-speed photographs. Accordingly, a unique photographic system, which uses a camera with a capability of 35 000 frames per second, was developed. This camera is mounted at the observation port and records the fragment-ring interaction for subsequent analysis. The deformations of the containment/deflection device are measured on the photographs and, by relating them to the time reference, the dynamics of the system are studied. This paper presents some highlights of accomplishments to date as well as plans for the future.

ANALYSIS OF SINGLE-BLADE EXPERIMENT

Simple tests were first run to support the analytical procedures being developed, and some results of one test appear in figure 3. As shown in the pre-test photograph, a single blade was mounted in a rotor disk which rotated counterclockwise. The blade was modified to fail at a specified speed and it impacted the aluminum alloy (2024-T4) containment ring, which was freely supported, i.e., there were no restraints to motion in the plane of the ring. The response is shown at the three elapsed times (t) indicated. Measurements of the ring deflections around the circumference (at the alternate black and white marks) were recorded at approximately 30-microsecond intervals.

An example of the comparison between the measured and predicted ring profiles at 570 microseconds after impact is presented in figure 4. The original circular ring shape is represented by the solid line. The measured deflections are shown by the circles and the calculated deflections by the squares. These preliminary results indicate that the measurements and predictions are in useful agreement for analysis. However, improvements in the calculation methods are being pursued in order to increase the accuracy of the predictions and to be able to handle the interaction between more complex fragments and containment rings. The method of analysis also calculates the stresses that result from the ring deformation.

EXPERIMENTAL RESULTS

Investigations have been conducted to study the influence of several parameters on the interaction between the fragment and the protective device which it impacts. Some early results will be presented regarding (1) the deformation of the containment ring, (2) the number of fragments that impact the containment ring, (3) candidate ring materials, and (4) deflection devices.

Three-Fragment Attack

Figure 5 shows the response of a ring to the impact of three fragments generated by the test rotor shown in the pre-test photograph. Three blades were removed and the disk was cut radially at these locations. Rotation is clockwise and the motion of the fragments can be determined by observing the positions of the fragment marked with a cross at the various elapsed times. Note that the fragment rotates about its center of mass as well as translates tangentially. The ring was freely supported because of the complex interactions that would be introduced by restraints and because to specify which restraints should be considered was premature. It can be seen that the steel ring experiences large deformations and a lobe develops for each fragment.

Containment Ring Plastic Deformation

Post-test measurements indicate that the rings that contained the fragment attacks deform plastically only in localized areas. It was therefore concluded that any criteria for containment that are based on large failure strains throughout the ring are not well founded. One such questionable theory, which is accepted by some investigators, states that containment will be provided by a ring only if the fragment attack energy does not exceed the potential strain energy (defined as the area under the stress-strain curve multiplied by the volume of material in the ring). Results of the present investigation indicate that such a theory is not valid. Under similar attack by three fragments, rings of the same weight (3.2 kg, or 7.0 lb) provided containment at average values of attack energy equal to three times the potential strain energy for a high-strength steel (4130A) and only one-half the potential strain energy for an aluminum alloy (2024-T3). In other words, the energy ratios were 3.0 and 0.5, respectively – and not 1.0 as this theory predicts.

Containment Ring Restraints

The extent to which a containment ring can absorb the energy of an impacting fragment depends on the restraints imposed on the ring. Figure 6 shows the results of an exploratory test with a ring which was restrained at three equally spaced points as indicated in the pre-test photograph. Rotation of the rotor is counterclockwise. One fragment has been marked with a cross to facilitate observing it in the successive photographs. Although this ring deforms like the similar freely mounted containment ring (fig. 5), failure occurred near all three restraints; whereas, the other ring did not fail under the same attack energy.

The majority of the tests have been conducted with freely supported containment rings. Although this may not simulate the mounting of protective devices for engines,

it does approximate possible installations for protecting smaller turbomachinery (e.g., starters and auxiliary power units).

Number of Fragments

Tests were performed to determine how the response of a containment ring is influenced by the number of fragments that impact it. Similar high-strength-steel (4130A) freely supported rings (weight, 3.2 kg (7.0 lb); inside diameter, 38.1 cm (15.0 in.); radial thickness T , 0.86 cm (0.34 in.); and axial length L , 3.8 cm (1.5 in.)) were attacked by rotors modified to generate two, three, four, and six equal fragments. The results shown in figure 7 indicate that such a ring is least effective when attacked by the four-fragment burst. This conclusion suggests that the proposed federal requirement, that containment by a three-fragment burst be demonstrated for certification, might not be the most severe case. Because these data are based on a limited number of tests, additional tests are being performed to check this preliminary conclusion.

Containment Ring Materials

In order to get an indication of the influence of the mechanical properties of candidate structural materials on their capability to protect against attack by rotor fragments, containment rings of several materials were evaluated (fig. 8). All containment rings were freely supported, of the same axial length (3.8 cm, or 1.5 in.), and were attacked by three-fragment bursts of 35.6-centimeter (14-in.) rotors. The ability of the ring material to absorb the fragment attack energy is expressed in terms of the ratio of attack energy contained to ring weight. The length of each bar represents the value of this ratio for the maximum attack energy contained. The materials were selected to provide a variation in strength and ductility and a range of potential strain energy of about one decade (i.e., 0.28×10^5 to 2.03×10^5 meter-newtons or 0.25×10^6 to 1.80×10^6 in-lb).

The steels are possible candidates for protective devices in the turbine region, and the aluminum and nonmetallics might be used in the lower temperature compressor region or other auxiliary equipment. The top bar in figure 8 is for a high-strength steel (4130A). The next bar is for a TRIP steel, one of a relatively new class of steels that exhibit outstanding combinations of strength and ductility. In fact, it is claimed that TRIP steels have higher toughness values than any other known metal. An increase in the initial toughness is achieved by the austenite-to-martensite phase transformation, which can be strain induced and would result from fragment impact. Its potential for defeating fragment attack appears promising. The aluminum alloy (2024-T3) is the least effective of the metals tested.

Composite rings of ballistic nylon cloth wrapped around an 0.81-millimeter-thick (0.032-in.) stainless-steel ring appear to have good potential. The filament-wound rings

were fabricated using E-glass rovings (at a wrap angle of 1.3 radians, or 75°) and epoxy resin matrix. For these tests, it was hoped that the ring would be stiff enough to remain nearly circular and that considerable energy would be dissipated by sliding of the fragments around the inner circumference. These rings, however, did deform appreciably and failed in the areas of maximum bending.

It was learned from these tests that the techniques for evaluating ring materials must be improved before absolute values of their effectiveness can be determined. The study will continue after the techniques are further developed.

Deflection Devices

Another way to protect the aircraft from the impact of rotor fragments is to use a shield in the form of a partial ring to deflect the fragments away from the critical areas of the airplane. In this way, a "window" is provided through which fragments may escape in order to minimize the consequent effects of a rotor burst. Exploratory tests have been conducted to study the response of partial rings to fragment attack. The pre-test photograph in figure 9 shows a mild-steel (1025) half ring supported at two points, similar to the rear engine mount of a pod-mounted engine. The area to be protected is the shaded area shown at the top of the photograph. The rotor is simulated by a flat disk which turns counterclockwise and generates three fragments. By observing the consecutive positions of the fragment marked with a cross, it is seen that the partial ring did deflect it downward and to the left. Similarly, the other two fragments were also deflected away from the protected area by this "static" shield.

In another approach to deflection devices, two mild-steel (1025) half rings free at one end and hinged at the other were investigated. The concept was to control the fragment trajectories as the "dynamic" shield deforms and pivots about its hinge under fragment attack. As illustrated in the pre-test photograph in figure 10, this approach represents simultaneous tests of two partial rings of different thicknesses. The 8.4-millimeter (0.33-in.) half ring on the left is free at the lower end and hinged at the top and is intended to protect the shaded area in the upper left corner. The 6.4-millimeter (0.25-in.) half ring on the right is free at the top and hinged at the bottom and protects the shaded area in the lower right corner. The rotor is simulated by a flat disk which rotates counterclockwise and bursts into two fragments. The successive positions of the fragment marked with a cross indicate that it was indeed deflected away from the protected area. Although it appears that this fragment impacted the lower support, this was not the case; the fragment and support are actually in different planes. Similarly, the other fragment was also deflected away from the other protected area. Because of the good potential for such devices, additional tests are being performed.

STATUS OF PROGRAM

Experiments

The tests performed to date were directed at the study of the interaction between the fragments and the containment/deflection device which they impacted. This study included the effect of the number of fragments, the relative merit of some ring materials, and simple tests to support the analysis. An experimental program is now being pursued to determine the weight of ring required to contain the fragments of a rotor that bursts at its maximum operating speed. Such information will provide a guideline to the designer who is charged with protecting an aircraft from fragments that could be generated by a rotor of a given size and mass. Two sizes of rotor will be used as fragment generators: 78.7-centimeter (31-in.) diameter to represent turbine rotors of current airplane engines (J65) and 35.6-centimeter (14-in.) diameter to represent turbine rotors of current helicopter engines (T58).

More realistic tests will also be performed to support the analytical procedures.

Based on the early work that has been done, four nondimensional parameters are recognized to be of importance:

- (1) The ratio of the axial length of the ring to the radius of the ring (L/R)
- (2) The ratio of the radial thickness of the ring to the radius of the ring (T/R)
- (3) The ratio of the mass of the ring to the mass of the rotor (M_R/M_F)
- (4) The number of rotor fragments (N_F)

For tests of a rotor of fixed size, the radius of the containment ring will be constant and the parameters of significance are the thickness-length ratio T/L and the number of fragments N_F , and these are being investigated. The effectiveness of the ring to contain the fragments, expressed as the ratio of the total energy contained to the weight of the ring, will be determined as a function of T/L and N_F , that is,

$$\frac{E_A}{W_R} = f\left(\frac{T}{L}, N_F\right)$$

where

E_A fragment attack energy contained

W_R containment ring weight

T radial thickness of containment ring

L axial length of containment ring

N_F number of fragments

The axial length of the ring will be set at $\frac{1}{2}$, 1, and $1\frac{1}{2}$ times the axial length of the rotor, and the ring thickness will be varied until fragment containment is achieved.

Analysis

A computer program (JET 2) has been developed which calculates the response of a freely supported ring to the impact forces exerted by the fragments. This program is valid for predicting the ring deformation and the accompanying stresses if the applied forces are known. Another program (TEJ 2) uses the measured ring deflections to calculate the forces. These forces are then introduced into the first program (JET 2) to calculate the ring response, which is compared with the measured deformation. These programs have been published (refs. 5 and 6) and they are being used by engine manufacturers. Work will be continued to improve the accuracy of the results.

Another computer program (JET 3) is under development and accounts for the effect of mode of support of complete or partial rings.

Related Work

As a companion effort to the rotor burst protection program, NASA has initiated a study of a detection system which will provide in-flight indications of incipient structural failure. Methods for detecting cracks in rotating disks are in progress and experimental hardware is currently being fabricated. The successful development of such a system will permit on-demand maintenance, in contrast to the usual maintenance at specified time intervals, and should reduce the number of occurrences of rotor bursts during airplane operation.

REFERENCES

1. Martino, Albert A.: Turbine Disk Burst Protection Study. Phase I - Final Report on Problem Assignment NASA DPR R-105. NAEC-AEL-1793, U.S. Navy, Mar. 1965. (Available as NASA CR-80962.)
2. Martino, A. A.; and Mangano, G. J.: Turbine Disk Burst Protection Study. Phases II-III - Final Report on Problem Assignment NASA DPR R-105. NAEC-AEL-1848, U.S. Navy, Feb. 1967. (Available as NASA CR-84967.)
3. Martino, A. A.; and Mangano, G. J.: Rotor Burst Protection Program Initial Test Results. Phase IV - Final Report [on Problem Assignment] NASA DPR R-105. NAPTC-AED-1869, U.S. Navy, Apr. 1968. (Available as NASA CR-95967.)
4. Martino, A. A.; and Mangano, G. J.: Rotor Burst Protection Program. Phase V - Final Report [on] Problem Assignment NASA DPR R-105. NAPTC-AED-1901, U.S. Navy, May 1969. (Available as NASA CR-106801.)
5. McCallum, R. Bruce; Leech, John W.; and Witmer, Emmett A.: Progress in the Analysis of Jet Engine Burst-Rotor Containment Devices. ASRL TR 154-1, Aeroelastic Struct. Res. Lab., Massachusetts Inst. Technol., Aug. 1969. (Available as NASA CR-107900.)
6. McCallum, R. Bruce; Leech, John W.; and Witmer, Emmett A.: On the Interaction Forces and Responses of Structural Rings Subjected to Fragment Impact. ASRL TR 154-2, Aeroelastic Struct. Res. Lab., Massachusetts Inst. Technol., Sept. 1970. (Available as NASA CR-72801.)

UNCONTAINED ENGINE FAILURES REPORTED BY COMMERCIAL AIRLINES

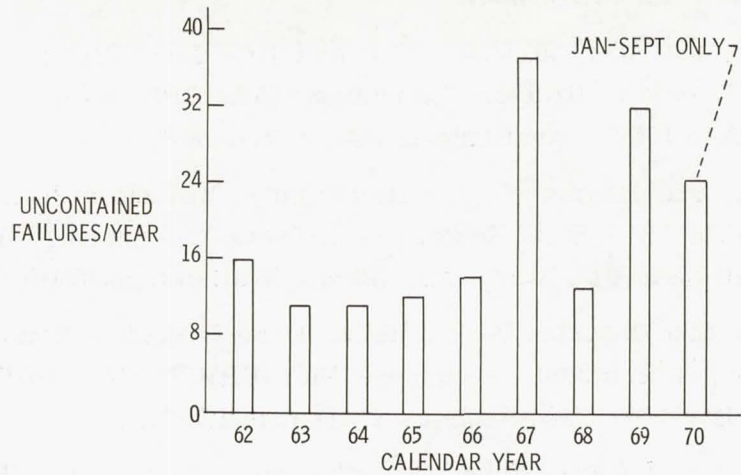


Figure 1

NAPTC CONTAINMENT EVALUATION FACILITY

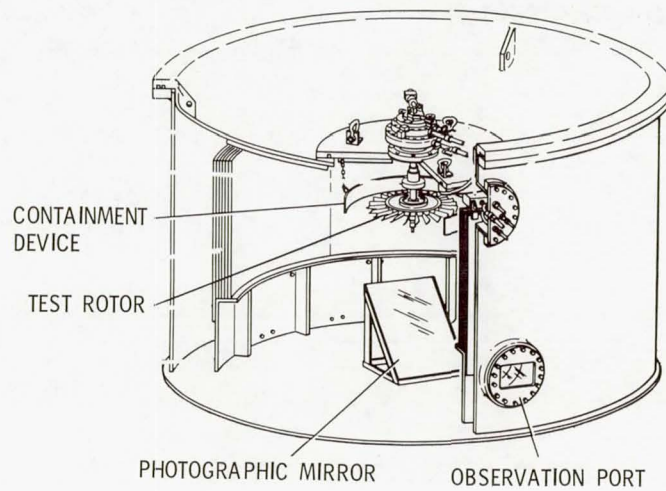


Figure 2

RESPONSE OF FREE RING TO SINGLE-BLADE IMPACT

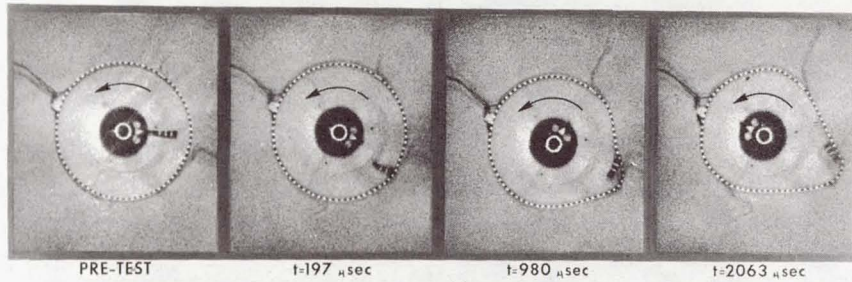


Figure 3

COMPARISON OF PREDICTED AND MEASURED RING PROFILES AT 570 μSEC AFTER IMPACT

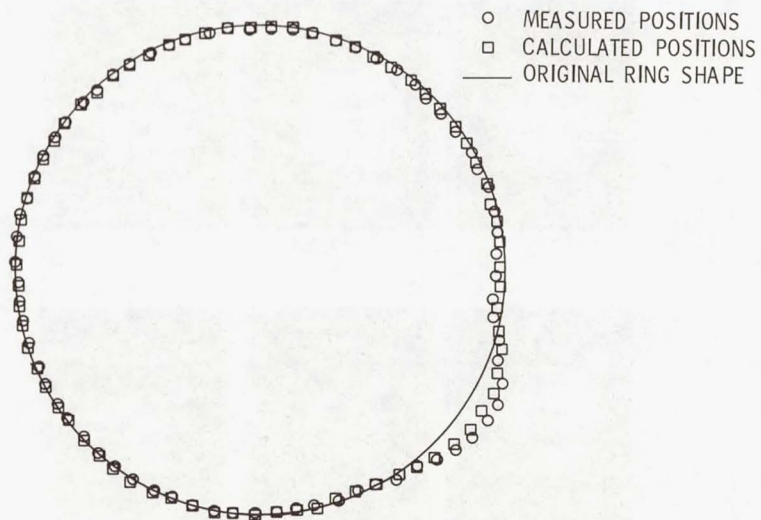


Figure 4

RESPONSE OF FREE RING TO ATTACK BY ROTOR FRAGMENTS

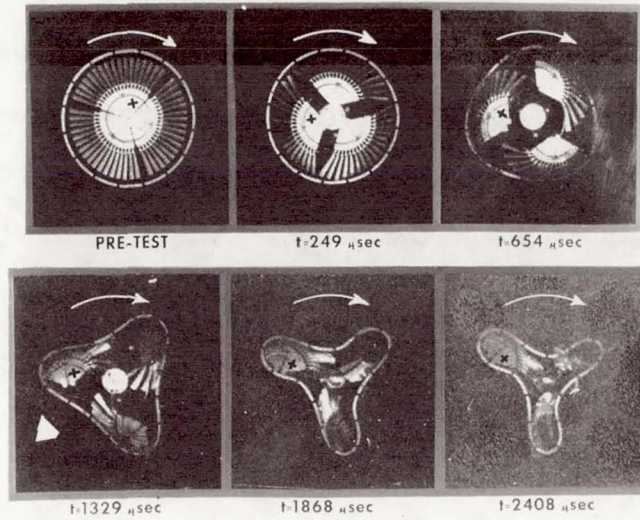


Figure 5

RESPONSE OF RESTRAINED RING TO ATTACK BY ROTOR FRAGMENTS

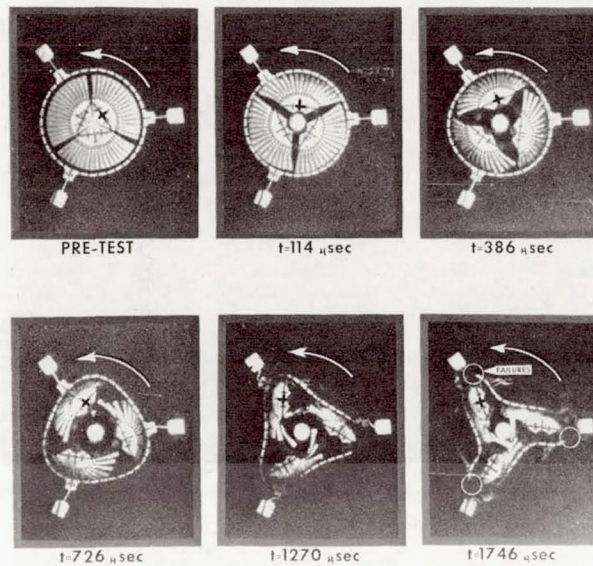


Figure 6

EFFECT OF NUMBER OF FRAGMENTS ON CONTAINMENT BY RING

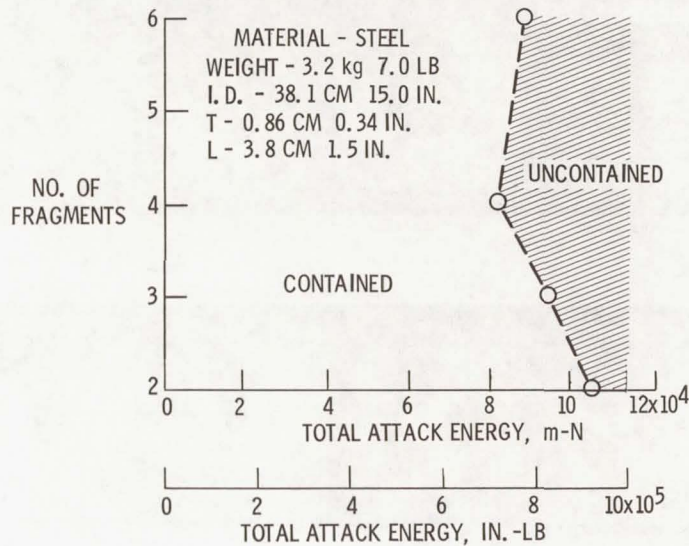


Figure 7

RELATIVE MERIT OF MATERIALS FOR CONTAINMENT RINGS

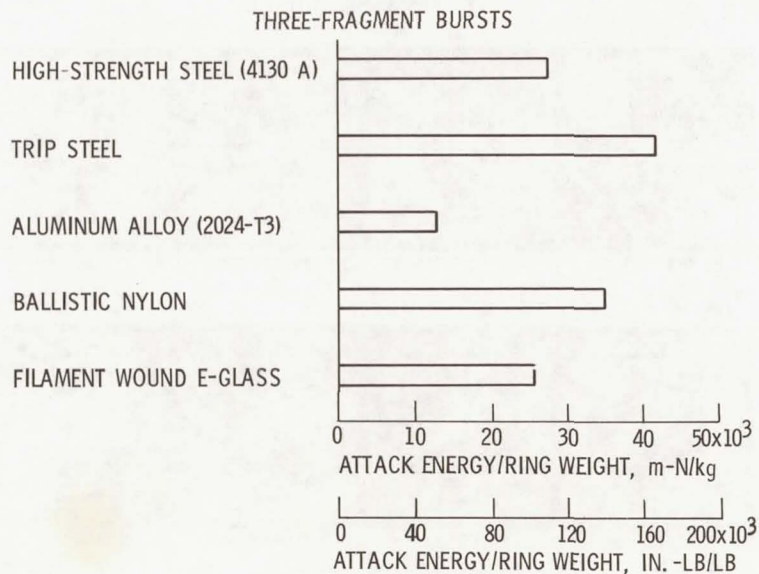


Figure 8

DEFLECTION OF THREE FLAT-DISK FRAGMENTS BY STATIC SHIELD

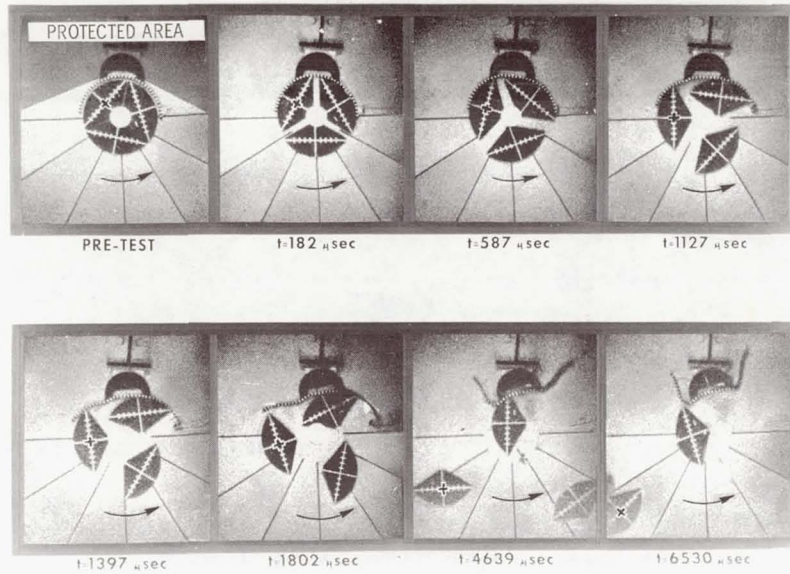


Figure 9

DEFLECTION OF TWO FLAT-DISK FRAGMENTS BY DYNAMIC SHIELD

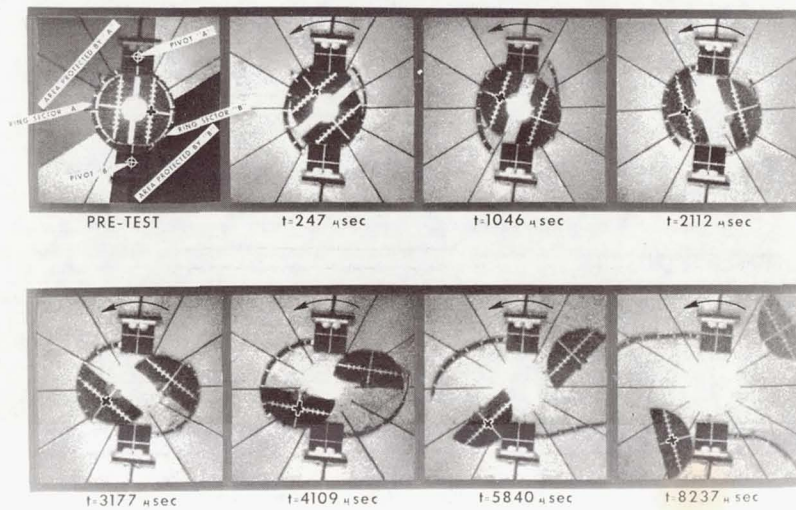


Figure 10

CLEAR-AIR-TURBULENCE DETECTION USING LASERS

By Edwin A. Weaver
George C. Marshall Space Flight Center

SUMMARY

Clear-air-turbulence (CAT) detection and measuring aboard aircraft appear to be feasible using a CO₂ laser Doppler system. It is planned to use an airborne ruby laser as a tool for investigating particulate matter or aerosols in the atmosphere to supplement the CO₂ laser instrumentation tests. These developments are based on test results from a ground-based ruby laser that detected an aerosol density gradient in the region of clear-air turbulence and an airborne ruby laser that confirmed atmospheric molecular scattering predictions in the lower atmosphere. This paper discusses the instruments, test results, status, and plans. Langley Research Center conducted the ruby laser developments and tests. The development of the CO₂ laser Doppler system is being directed by Marshall Space Flight Center.

INTRODUCTION

Clear-air turbulence (CAT) has been defying detection since it was first considered to be a major problem to aircraft operations. It is a special problem because it is unexpectedly encountered. In 1964 a major national effort was initiated to develop sensors for detecting CAT and determining its physical characteristics. The causes of this hidden sky hazard were also a part of this intensive effort by the Federal Government.

Many concepts to detect CAT have been tried, but because positive information about the causes of CAT are not available, these efforts have been based on speculation about the causes and have not resulted in the types of reliable instrumentation systems needed in the military and commercial aircraft operations. The approaches to airborne CAT detection include sonic techniques, microwave and infrared radiometry, microwave radar, low-frequency radar, scintillation techniques, electric-field discharge techniques, optical laser radar, and pulsed laser Doppler techniques. (See ref. 1.) Some techniques have been attractive because of simplicity and low cost, but the high false-alarm rate problem must be solved before any of the techniques will be feasible. Of these, the laser Doppler technique appears to be the most promising.

NASA is doing CAT research with programs to measure the physical characteristics and to develop instrumentation that will warn the pilot in advance of CAT along the flight path. These programs primarily involve the use of lasers and can be divided into three major areas: ground-based systems (ruby laser and carbon dioxide laser),

airborne systems (ruby laser and carbon dioxide laser), and satellites. Satellites will be discussed briefly at this time. They are part of the long-range program and will eventually be feasible when the characteristics of CAT are known. Then it may be appropriate to observe these characteristics continuously. There are conceptual studies in the very early planning phases for a satellite that will remotely sense CAT characteristics. These data would be used to develop maps showing locations and intensities of clear-air turbulence for a specific time. This very appealing approach, however, is still many years in the future as an operational activity. The ground-based and airborne systems will be discussed in greater depth in this survey.

GROUND-BASED RUBY LASER

A ruby laser was used by the Langley Research Center in a series of tests for CAT detection. These experiments identified a concentration of minute particles called aerosols in regions of the atmosphere where clear-air turbulence was encountered by a jet aircraft. They were conducted during 1967 and 1968 over Williamsburg and Wallops Island, Virginia.

These experiments involved a ground-based system and an instrumented T-33 jet aircraft. The system on the ground shown in figure 1 consisted of a pulsed ruby laser, a 1.52-meter (60-inch) parabolic searchlight mirror, a photomultiplier signal detector, and associated signal processing and display equipment. The coherent light from the laser was scattered by aerosols. Part of the scattered light was collected by the searchlight mirror and reflected to the detector through a filter to limit the signal return to that signal near the laser frequency.

The tests were conducted at night to gain the benefit of the lower background radiance of the sky. This condition permitted strong signal returns of backscattered laser light from an altitude of 25.9 kilometers (85 000 feet). The T-33 aircraft, equipped with recording accelerometers probed altitudes up to 12.2 kilometers (40 000 feet) downwind from the laser represented schematically in figure 2.

Concentration of aerosols or aerosol density gradients were located from the back-scattered laser light by the ground-based system. CAT was encountered by the aircraft only in regions identified as having aerosol concentrations. The results from the tests on the night of June 5, 1967, are shown in figure 3. These results are representative of the 33 cases of correlation between turbulence encountered by the aircraft and the prominent scattering found by the ruby laser system. A more detailed report on these experiments is contained in reference 2.

These data have encouraged the researcher to continue development of this experimental equipment. It is expected that these experiments will be resumed during the next

year with an improved ground-based system. A more powerful ruby laser and a more sophisticated receiver system containing very high quality optics will permit greater operational flexibility. The information from the improved system will be combined with known meteorological data and is expected to increase the understanding of the association of aerosol concentrations and clear-air turbulence.

AIRBORNE RUBY LASERS

A ruby laser system was flown in 1966 and 1967 to study CAT. The purpose of these experiments conducted by the Langley Research Center was to investigate the relationship between clear-air turbulence and the concentration of aerosols that were to be identified from the backscattered laser light. A T-33 aircraft, shown in figure 4, was instrumented with accelerometers and carried a small ruby laser system in a pod mounted beneath the aircraft. The laser system controls and displays were located in the cockpit. No correlation between aerosol concentrations and CAT was possible because the laser power was too low and the system signal-to-noise ratio was low. The data that were received showed good agreement with existing theoretical models for aerosol distribution in the lower atmosphere. These results are encouraging to experimenters in this field for they have some, although small in quantity, data to support scattering theories that they must use in designing their experiments. Further information that may be of interest to designers of airborne visible laser systems and that was developed from the experimental data can be found in reference 3.

These experiments did not preclude the use of laser backscattering systems in the study of CAT. The program, however, was not continued by NASA because of the potential shown by the high-powered carbon dioxide laser, especially from the safety viewpoint. This laser will be discussed in more detail.

The Air Force Cambridge Research Laboratories in collaboration with NASA continued the development of the airborne ruby laser system. They recognized the importance of having sufficient aerosols in the atmosphere to permit the detection of CAT by laser Doppler systems. The development was completed in 1970 on a research system containing a more powerful ruby laser and an improved receiver and associated electronics. It will be used to study the presence of aerosols at aircraft altitudes and to determine whether their amount is sufficient to be used as air-motion tracers. The initial airborne tests of the system were made in January 1971 on the NASA Convair 990 aircraft which is based at and operated by the Ames Research Center. The system detected fog, smog, thin cirrus clouds, and the aircraft wake. This system may be used to check aerosol data during the flights of the laser Doppler CAT system on this same airplane. Further information on this system will be given later in this report.

THE LASER DOPPLER PRINCIPLE

The laser Doppler principle was first applied by the Marshall Space Flight Center to measure gas flows and now many successful experiments are recorded in scientific literature. This principle is basically the same as Doppler radar except for the medium that undergoes the frequency change, laser light, and the reflection source, aerosols. Figure 5 shows this principle. The aerosols in the atmosphere are in motion at the velocities of the steady wind or turbulence. In this case a laser beam undergoes a frequency change when it is reflected or scattered from an aerosol. This change in frequency is directly proportional to the velocity of the aerosol. Part of the scattered light beam at its new frequency is gathered by the receiving optics and reflected to a detector. The change in frequency is defined by comparing or photomixing the frequency of the laser beam with the frequency of the scattered laser beam at the detector. This procedure results in the measurement of the velocity component between the axis of the laser and the axis of the receiver. (See ref. 4.) When the receiver and the laser are on the same axis, the velocity component along this axis is measured. The coaxial arrangement is used for the Marshall Space Flight Center laser Doppler systems.

GROUND-BASED CARBON DIOXIDE LASER DOPPLER SYSTEM

The ground-based system that applies the laser Doppler principle uses a 20-watt carbon dioxide gas (CO_2) laser and is currently being used to measure ground winds. This system is used as a testbed for components development of other laser Doppler systems. In 1969 a very early version of this system was used in a cooperative effort between the Langley Research Center and the Marshall Space Flight Center. It detected the velocity spectrum of aircraft trailing vortices in tests that are discussed in the paper by Dunham, Verstynen, and Benner. In addition to the laser, this system has a 0.3-meter (12-inch) transmitter-receiver telescope and optics that focus the beam near the cup anemometer, a standard ground-wind measuring instrument. The velocity component of aerosols at the focus is measured by the Doppler technique. In addition, the cup anemometer data are also collected. Data taken from tests in November 1970 at Huntsville, Alabama, are shown in figure 6. The top set of curves show measurements of a steady wind. The velocity changes sensed by the laser Doppler system generally lead the cup anemometer velocities. In the lower set of curves, a variable-wind condition is shown. Again, the laser Doppler data lead the cup anemometer data in showing velocity changes. This difference is attributed to the relatively slow response of the anemometer to wind-speed changes. In both cases, there is good agreement on the wind speed. These curves are representative of several hundred hours of test data. During these tests wind gusts of 56 kilometers (35 miles) per hour were recorded at Huntsville. This system

has been in operation at Fort Collins, Colorado, since February 1971. Wind speeds of 160 kilometers (100 miles) per hour were measured.

THE AIRBORNE CARBON DIOXIDE LASER DOPPLER SYSTEM

A program to develop an airborne pulsed CO₂ laser system based on the Doppler principle was initiated in 1969. A 1-year research study resulted in a preliminary design of the research instrumentation for flight tests. This study recommended a high-powered pulsed CO₂ laser because it has a narrow spectral bandwidth at its 10.6-micrometer wavelength and a twenty times better signal to noise ratio over visible lasers. Safety is also an important feature; ordinary glass and plastics will reflect the CO₂ laser beam and prevent eye damage.

Development of a research unit of a laser Doppler CAT detection system started in 1970 and is a cooperative effort between the U.S. Air Force through the Cambridge Research Laboratories and NASA through the Marshall Space Flight Center. The system has been designed and is now being assembled.

This airborne laser Doppler system has a power of 5 kilowatts and a transmitting-receiving 0.3-meter (12-inch) telescope. The backscattered signal, heterodyned at the detector, is fed to a filter bank where velocities and ranges are determined. These signals will be displayed in a manner close to the concept shown in figure 7. The shaded lines represent homogeneous CAT velocities at several ranges. The length of each line represents the magnitude of the disturbance found by the laser Doppler system. (See ref. 5.)

Present development schedules call for flight tests on the Ames Convair 990 in 1972. Figure 8 is an artist's concept of the flight test of this instrumentation. A special forward-looking port shown over the wing is being designed for the aircraft and will house in the forward end, a 35.6-centimeter-diameter (14-inch) germanium window; germanium is the only available material that is transparent to the CO₂ laser frequency of 10.6 micrometers. Figure 9 represents the laser Doppler CAT detection instrument and the three rows of electrical support equipment. This equipment houses power suppliers, instrumentation controls and displays, and the signal-processing equipment. Figure 10 is a closeup view of the CAT detection instrumentation. It is a research system. Care has been taken not to compromise those components of the system that would reduce the chances of detecting turbulence ahead of the aircraft.

Key hurdles to overcome before the flight tests can begin are systems integration, ground checkout tests, and the development of a 35.6-centimeter-diameter (14-inch) germanium window with state-of-the-art optical properties and coatings.

If the tests in 1972 prove the feasibility of this instrumentation system for detecting CAT, major changes must appear before the next unit is built. The system must be miniaturized and technology advances are needed for the detector, the power amplifier, and the modulator or pulsing mechanism. When these advances are available, an operational prototype might be built to be flown aboard weather aircraft. In any event, more work is required even for this promising technique for detecting CAT.

CONCLUDING REMARKS

This survey has shown that lasers may be the secret key that will unlock the door to clear-air-turbulence detection. Ruby lasers can detect and measure aerosol concentrations. In the regions of these concentrations, CAT has been encountered. CAT detection and measuring appear to be feasible if a CO₂ pulsed laser Doppler system is used. Feasibility tests of a research unit aboard the NASA Convair 990 aircraft are planned in 1972. This development has been supported by a ground-wind-measuring program with a CO₂ laser Doppler system. There is good agreement with cup anemometer data. Winds of 160 kilometers (100 miles) per hour have been measured.

Ground tests have established that high-velocity wind measurements are possible with the CO₂ laser Doppler system. It seems that aerosols appear to concentrate in turbulent regions where CAT has been located; thus, a system that requires backscattering from aerosols should be feasible. Aerosol scattering theories in the lower atmosphere have been supported by a very small amount of data, which is encouraging, for it again supports the design of a CAT detection system using aerosols as air-motion tracers. In all cases examined, lasers, the ruby and the CO₂, have been the key elements in systems providing the data to support proceeding the design of a "breadboard" airborne CAT detection system. Now that data are available to support the use of the Doppler principle in turbulence research, a practical way must be found to apply this principle and, most of all, the laser to the problem of clear air turbulence.

REFERENCES

1. Paulsen, Wilbur H.: Airborne Clear Air Turbulence (CAT) Systems. Paper presented at FAA Symposium on Turbulence (Washington, D.C.), Mar. 1971.
2. Lawrence, J. D., Jr.; McCormick, M. P.; Melfi, S. H.; and Woodman, D. P.: Laser Backscatter Correlation With Turbulent Regions of the Atmosphere. Clear Air Turbulence and Its Detection, Yih-Ho Pao and Arnold Goldberg, eds., Plenum Press, 1969, pp. 481-497.
3. Melfi, Samuel H.; and Stickle, Joseph W.: Airborne Laser-Radar Studies of the Lower Atmosphere. NASA TN D-5558, 1969.
4. Huffaker, R. M.: Laser Doppler Detection Systems for Gas Velocity Measurement. Appl. Opt., vol. 9, no. 5, May 1970, pp. 1026-1039.
5. Sonnenschein, C.; Jelalian, A.; and Keene, W.: Development of CO₂ Laser Doppler Instrumentation Detection of Clear Air Turbulence. Final Report. ER70-4203 (Contract NAS-8-24742), Raytheon Co., June 5, 1970.

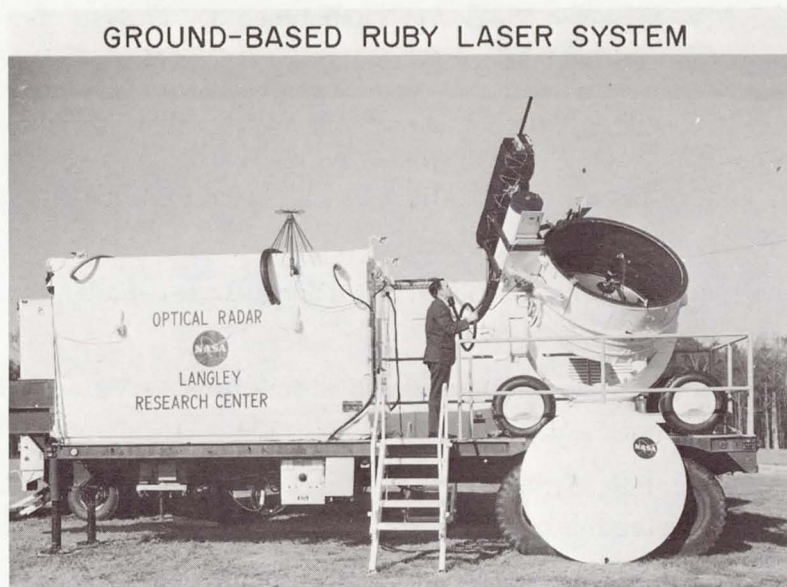


Figure 1

THE GEOMETRY OF THE RUBY LASER CAT EXPERIMENT

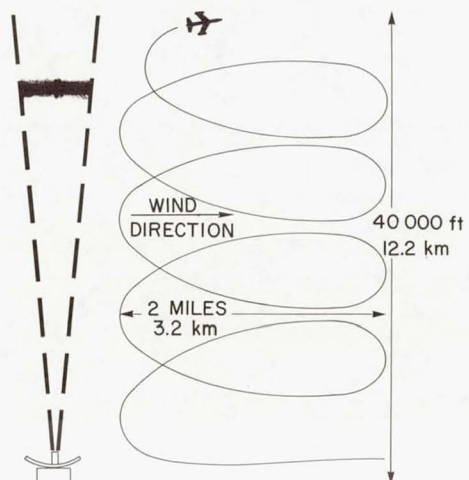


Figure 2

DATA FROM RUBY LASER CAT EXPERIMENT

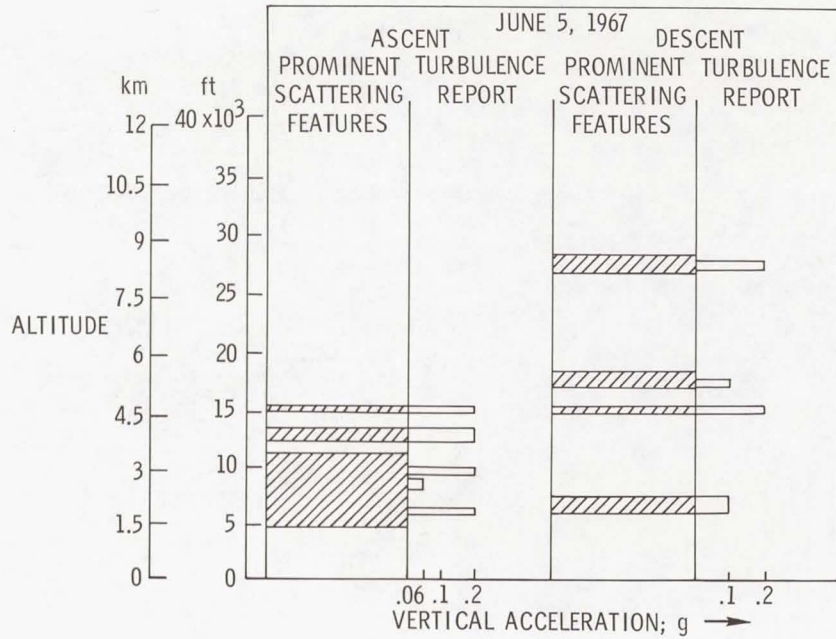


Figure 3

T-33 AIRCRAFT WITH RUBY LASER SYSTEM



Figure 4

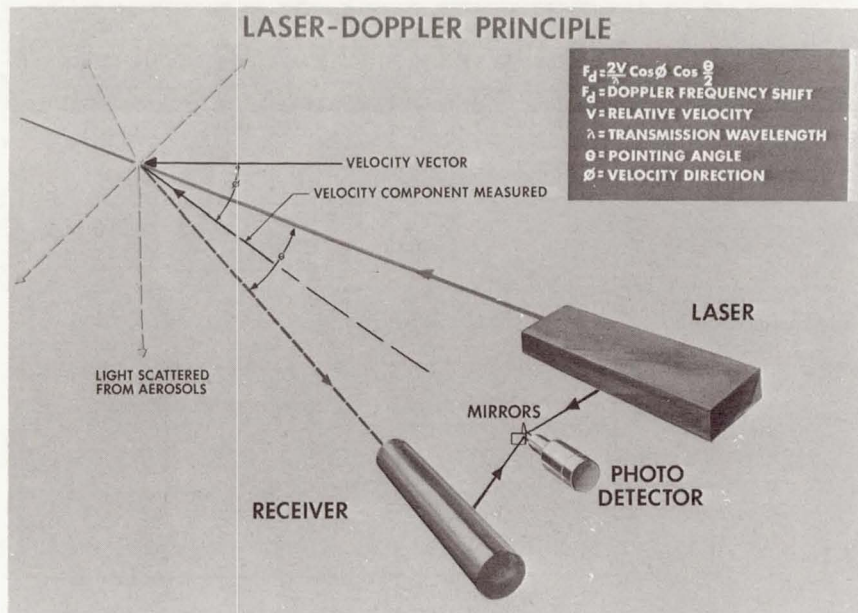


Figure 5

GROUND-WIND DATA FROM CO₂ LASER DOPPLER SYSTEM

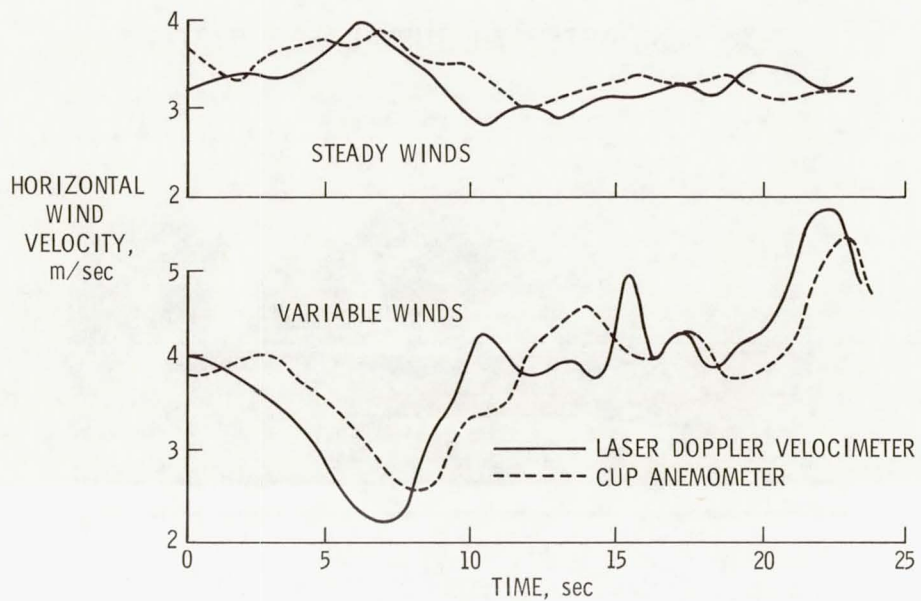


Figure 6

CONCEPT OF RANGE INDICATOR FOR HOMOGENEOUS CAT

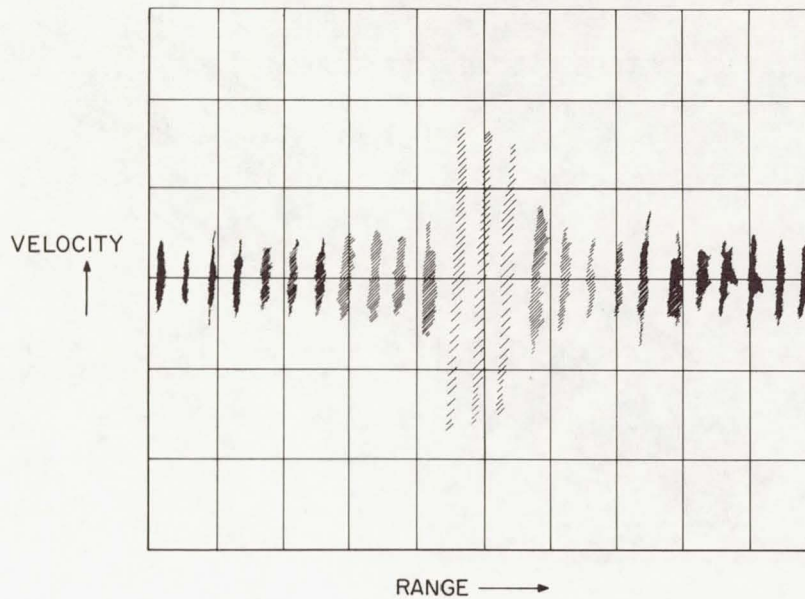


Figure 7

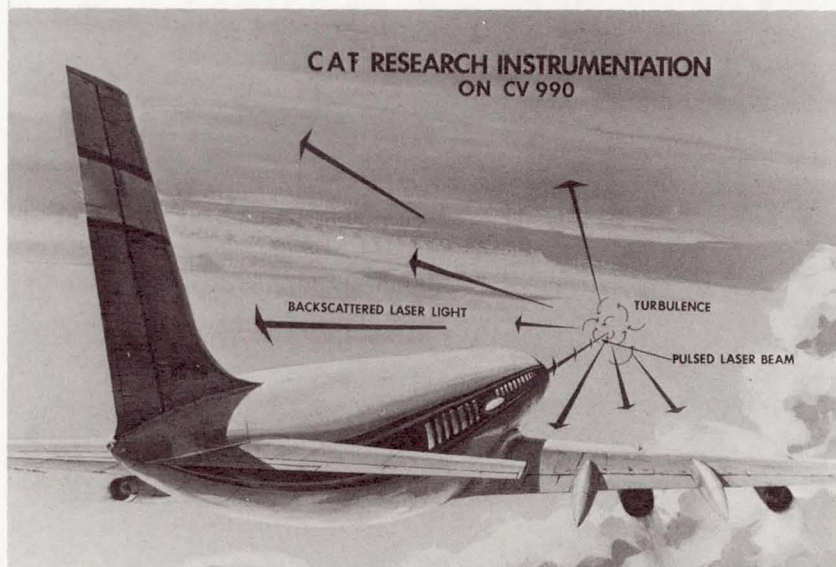


Figure 8

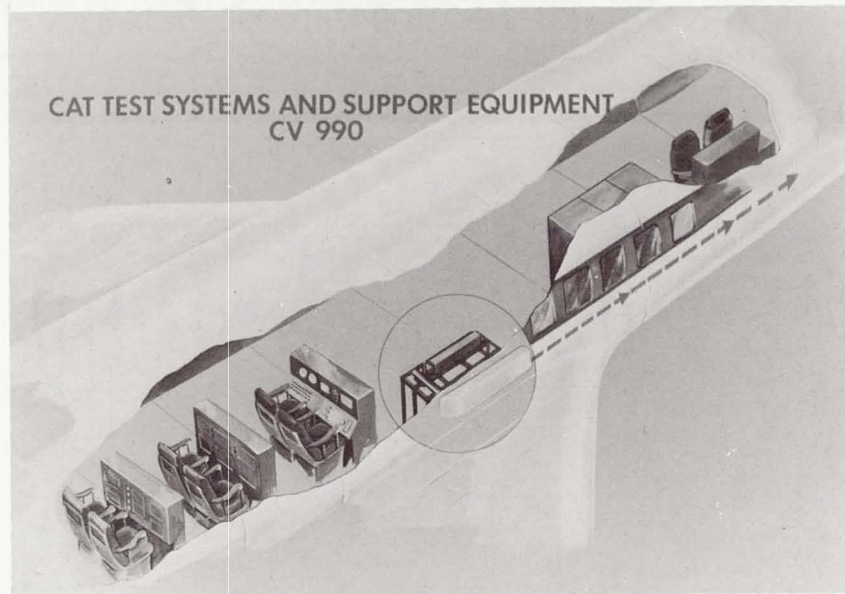


Figure 9

CAT TRANSMITTER ON CV990

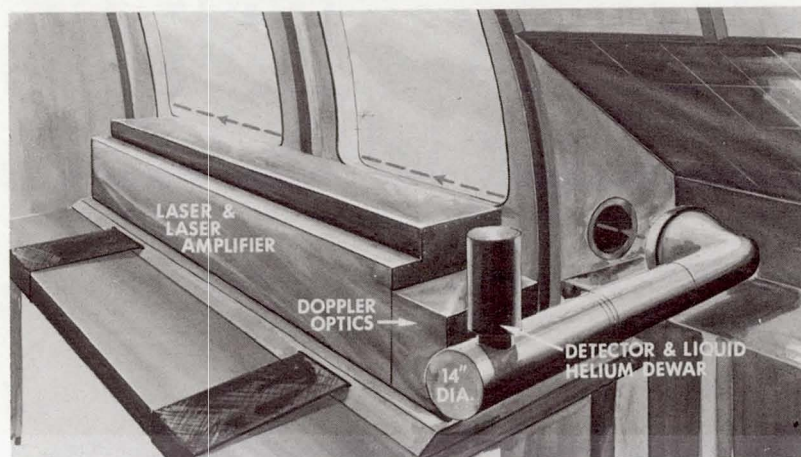


Figure 10

PROGRESS REPORT ON WING-TRAILING-VORTEX STUDIES

By R. Earl Dunham, Jr., Harry A. Verstynen, Jr.,
and Margaret S. Benner
Langley Research Center

INTRODUCTION

Wing trailing vortices shed by large aircraft, particularly jumbo jet transports, have become a serious safety problem in the terminal area and have imposed economic penalties on air carriers because of limitations on landing and departure rates. In an attempt to find a solution to this problem, the National Aeronautics and Space Administration is conducting research on aircraft trailing vortices at several of its Centers. This paper presents the activities to date in three major areas of vortex research.

The first area of research is concerned with the measurement of the characteristics of full-scale aircraft vortices. This work is aimed at obtaining an understanding of the behavior of wing trailing vortices generated both at altitude in the cruise/holding configuration and near the ground during landing and departure. Of particular interest are the velocities and their distributions within the vortex and the vortex persistence as affected by atmospheric conditions and aircraft configurations.

The second area of research involves investigations of possible techniques to effect a more rapid breakdown or decay of the wing trailing vortices. As has been noted in paper 9 by William H. Andrews, Glenn H. Robinson, and Richard R. Larson and in reference 1 by John H. Olsen, the deployment of wing flaps on aircraft create a trailing-vortex system which is less intense and decays more rapidly than vortices created in a flaps-up condition.

The third area of research concerns an investigation of the feasibility of remotely detecting the presence of wing trailing vortices in the terminal area.

SYMBOLS

b	wing span, m (ft)
c	wing chord, m (ft)
s	wing semispan, m (ft)
t	vortex age, sec

V	measured vortex velocity, m/sec (fps)
V_0	aircraft velocity, m/sec (fps)
V_∞	free-stream velocity, m/sec (fps)
W	aircraft weight, N (lb)
x	distance downstream from wing trailing edge, m (ft)
y	lateral distance from wing center line, m (ft)
Γ_0	vortex circulation based on elliptical lift loading, $\frac{4W}{\pi\rho V_0 b}$, m ² /sec (ft ² /sec)
ρ	air density, kg/m ³ (lb/ft ³)

MEASUREMENT OF WING-TRAILING-VORTEX CHARACTERISTICS

The Langley Research Center is using the two experimental methods shown in figure 1 to obtain measurements of wing trailing vortices generated by full-scale aircraft both at altitude and near the ground. At altitudes out of ground effect, a Lockheed T-33 airplane is used to probe the vortices of a generating airplane. The T-33 is instrumented to record in analog form the altitude, angle of attack, angle of sideslip, total temperature, accelerations of the center of gravity along the three aircraft body axes, rotational rates about the three body axes, and attitude about the three body axes. The T-33 is flown through the wake of a generating aircraft both normal to the flight path and in a parallel-type traverse. During the penetration, the distance between the T-33 and generating aircraft is determined by ground-based radars. This distance is used to determine the age of the segment of the vortex penetrated. The data recorded onboard the airplane are analyzed to determine the distribution of the three velocity components of the vortex.

Measurements of vortices at lower altitudes in ground effect are obtained by flying an airplane down a crosswind runway and allowing the action of the wind and natural vortex-induced motion to cause the vortices to drift past a measurement station. The measurement station consists of (1) a tower which is 60.96 m (200 ft) from the runway edge and from which smoke is released in order to make the vortices visible and (2) a second tower which is 15.24 m (50 ft) downwind of the smoke tower and which has eight vertically spaced sensors capable of making three-component velocity measurements.

These sensors are aerodynamically actuated bivane anemometers built by Meteorology Research, Inc. (ref. 2).

Exploratory tests which were conducted primarily to check out the instrumentation and operating techniques have thus far been made with a Lockheed C-5A airplane at altitude and a Lockheed C-130 airplane and a McDonnell Douglas C-47 airplane near the ground. The results obtained from these flight tests are preliminary in nature and limited in extent; however, some interesting observations can be made.

Shown in figure 2 are two typical velocity profiles obtained behind the C-5A airplane at altitude for the right-wing trailing vortex at two different ages, one 45 sec old and the other 105 sec old. Both were generated in a flaps-up configuration with a span loading W/b of 25 685 N/m (1760 lb/ft) at a lift coefficient of about 0.8. Analyses of the data obtained during these two penetrations indicated that the measurements were made nearly through the center of the vortex; thus, the vertical-velocity distribution is nearly the same as that of the tangential velocity. For the 45-sec old vortex, the core diameter as indicated by the distance between the peak velocities is about 2.13 m (7 ft) and the maximum velocity is about 19.81 m/s (65 fps). Sixty seconds later the core diameter, which increases with time, has enlarged to 7.32 m (24 ft) in diameter and the maximum velocities have decreased to about 4.57 m/s (15 fps). The predicted core diameter for the initially rolled-up vortex as given in reference 3 is 10.36 m (34 ft). The measurements therefore show that at long distances downstream, there is an appreciably smaller core diameter and higher velocities than would be predicted even for an initially rolled-up vortex (one to two wing spans behind the aircraft according to ref. 3).

Shown in figure 3 is the vertical-velocity distribution through the center of the right-wing trailing vortex of a C-130. This vortex was generated in ground effect in a flaps-up condition and is approximately 45 sec old. Again, the measured core diameter of 1.22 m (4 ft) was considerably smaller than that of 6.1 m (20 ft) predicted by reference 3.

The variation of maximum tangential velocity with separation distance or vortex age is plotted in figure 4 for vortices behind the C-5A airplane. The open symbols represent penetrations which passed near but not through the core of the vortex; thus, the maximum velocity present may not have been measured. The solid symbols represent penetrations through the core of the vortex and these data are the maximum tangential velocities recorded. For comparative purposes, two semiempirical methods for predicting the variation of maximum velocity with time are included. One is based on the method of Dr. Barnes W. McCormick as given in reference 4, and the other method is that given in reference 5. The data tend to fall between these two formulations and appear to indicate a higher rate of decay than that predicted by either of the methods. However, as

previously mentioned, the data are meager and, since the decay rate is strongly dependent on the atmospheric conditions, this result is somewhat inconclusive.

The data shown in figure 4 were obtained in apparently smooth air as was indicated by the accelerometers and flow vanes on the T-33 airplane; however, in the test area there was some evidence of general convective activity of sufficiently long wavelength to be undetected by the T-33 instrumentation. This convective activity causes a snaky motion of the vortices which has been observed from the T-33. This snaky motion caused considerable scatter in the vertical position of the C-5A vortices behind the airplane as shown in figure 5. This thermal activity tended to counteract the induced downward drift of the vortices, and on one occasion a segment of the vortex was found slightly above the C-5A flight path.

Figure 6 shows the measured variation of vortex velocities with time behind a C-130 airplane at low altitude in ground effect. The vortices were generated at a span loading of about 14 593.9 N/m (1000 lb/ft) in a flaps-up condition under steady winds with a velocity of 2.13 m/s (7 fps). These data fall between the two prediction methods of references 4 and 5 and indicate a higher rate of decay than that predicted by either of these methods; however, neither method takes into account the effect of the ground, winds, or local turbulence.

Exploratory tests were also conducted with a C-47 airplane to determine the effects of flaps on vortex persistence. Results of these tests are presented in figure 7. All the data shown in this figure were obtained on the same day under the same wind conditions. The data indicate that vortices generated in a flaps-up condition persist longer than those generated in a flaps-down condition.

Thus, on the basis of results from some exploratory flight tests with a C-5A at altitude (out-of-ground effect) and with a C-130 and a C-47 near the ground (in-ground effect), the wing trailing vortices were found to contain higher velocities and smaller cores than would be predicted by Spreiter and Sacks (ref. 3). For the conditions encountered in the flight tests, the vortex intensity apparently diminished more rapidly than would be predicted by some empirical methods. The decay of the vortices and the vertical drift rate were affected by apparent convective activity in the atmosphere. Vortices generated with flaps down diminished more rapidly than those generated with flaps up.

ACCELERATED BREAKUP OR DECAY OF VORTICES

Various methods have been proposed to accelerate the decay rate or breakup of vortices. Some of these methods are blowing or sucking air at the wing tip to interact with the axial flow, spoilers to introduce turbulence and/or modify the axial flow,

counterrotating flow jets, and actuation of an aerodynamic surface or inducing aircraft motions of a characteristic wavelength to create an instability in the vortices. Preliminary research in this area with a wing-tip spoiler has been done by the Ames Research Center in wind-tunnel and flight tests. The spoiler tested in a wind tunnel is shown on the wing model in figure 8. The spoiler was deflected 90° to the wing surface and mounted on the quarter-chord at the wing tip. Its height was 12 percent of the wing chord and its span was 4 percent of the wing semispan. Both smoke and tuft-grid studies showed that with the device installed, major changes in the vortex structure were achieved as far as 60 chord lengths downstream of the wing. Measurements made with a hot-wire anemometer in the wake of this device confirmed the qualitative results and gave the velocity profile shown in figure 9. The lower trace shows that the maximum circumferential velocity was reduced by the spoiler by approximately one-half, while the core diameter was approximately doubled. In addition, the direction of the axial flow was reversed by the device. These results were interpreted as significantly altering the vortex structure in a manner which would contribute to a more rapid dissipation of the vortex and an accompanying reduction of vortex intensity. More detailed measurements obtained during these tests can be found in reference 6.

For the flight tests, a spoiler similar to that used in the wind-tunnel tests was installed on the left wing tip of a Convair 990 airplane (fig. 10). In the flight program, a Lear Jet-23 airplane was used to probe the vortices from both the right and left wing tips of the Convair 990. The rolling response of the Lear Jet was used as an index of the intensities of the vortices. Analysis of the response of the Lear Jet indicated that both aileron activity and peak rolling moment had been reduced about 50 percent in the right-wing-tip vortex. This change in rolling moment is of the same order of magnitude as would be estimated on the basis of the flow measurements made in the wind tunnel. The magnitude of the peak rolling acceleration experienced with the spoiler was still greater than the roll control of the airplane, and it was therefore not surprising that the pilots considered this spoiler ineffective. Calculations based on linear aerodynamic theory and a simplified vortex model indicate that, for the Lear Jet in the wake of the Convair 990, the vortex-core diameter would have to be increased to be about $1\frac{1}{4}$ times the span of the Lear Jet in order to reduce the induced rolling moment to less than the roll control of the airplane. The corresponding increase in core diameter from the unmodified state would be about fivefold.

The results of this work have indicated that very large reductions in tangential velocities with associated core size increases will have to be made far downstream in order to reduce the hazard. It would appear to be more desirable to create an instability within the vortex to cause it to break up rapidly. The wing tip spoiler apparently did not trigger such an instability within the vortex. Work is continuing at Ames in both the wind

tunnel and in flight in order to provide information on basic vortex characteristics and to develop more successful methods of dissipating the vortex.

REMOTE DETECTION OF VORTICES

The George C. Marshall Space Flight Center has been investigating the feasibility of using a CO₂ Doppler laser to detect the presence of vortices in the atmosphere. A detailed description of the laser and its associated equipment can be found in reference 7. A sketch of the test equipment is shown in figure 11. This vortex detection technique was intended to show a correlation between the visual sighting of the vortex by smoke entrainment and a prior detection by the laser. The laser beam was focused at a point about 24.38 m (80 ft) out along the beam and about 10.67 m (35 ft) above the ground. The Doppler laser measured the velocity component along the beam at the focal point. The tests were conducted by flying a C-47 airplane over the laser van and allowing vortex drift and the wind to carry the vortex into the laser sensing region.

Figure 12 is a typical velocity time history as measured by the laser. Initially, the laser measured the component of the free wind along the beam. As the vortex passed the focal point, its presence was indicated by a sharp rise in the velocity indication. For all measurements where the vortex was detected by the laser, its presence was visually observed by smoke entrainment. These tests therefore demonstrated the feasibility of using a CO₂ Doppler laser to detect the presence of aircraft vortices in the atmosphere.

In the future, such a detection device operating in the terminal area, in combination with an effective means of rapidly dissipating the vortices, should allow a reduction in the present aircraft separation with regard to the vortex hazard. NASA is continuing the development of laser Doppler technology through both contractual and in-house efforts.

REFERENCES

1. Olsen, John H.: Configuration Effects on Wake Structure and Aircraft Interactions. Paper presented at FAA Symposium on Turbulence (Washington, D.C.), Mar. 1971.
2. MacCready, Paul B., Jr.; and Jex, Henry R.: Response Characteristics and Meteorological Utilization of Propeller and Vane Wind Sensors. *J. Appl. Meteorol.*, vol. 3, no. 2, Apr. 1964, pp. 182-193.
3. Spreiter, John R.; and Sacks, Alvin H.: The Rolling Up of the Trailing Vortex Sheet and Its Effect on the Downwash Behind Wings. *J. Aeronaut. Sci.*, vol. 18, no. 1, Jan. 1951, pp. 21-32, 72.
4. McCormick, Barnes W.; Tangler, James L.; and Sherrieb, Harold E.: Structure of Trailing Vortices. *J. Aircraft*, vol. 5, no. 3, May-June 1968, pp. 260-267.
5. Wetmore, Joseph W.; and Reeder, John P.: Aircraft Vortex Wakes in Relation to Terminal Operations. NASA TN D-1777, 1963.
6. Corsiglia, Victor R.; Jacobsen, Robert A.; and Chigier, Norman: An Experimental Investigation of Trailing Vortices Behind a Wing With a Vortex Dissipator. NASA paper presented at Symposium on Aircraft Wake Turbulence (Seattle, Wash.), Sept. 1970.
7. Huffaker, R. M.; Jelalian, A. V.; and Thomson, J. A. L.: Laser-Doppler System for Detection of Aircraft Trailing Vortices. *Proc. IEEE*, vol. 58, no. 3, Mar. 1970, pp. 322-326.

MEASUREMENT METHODS

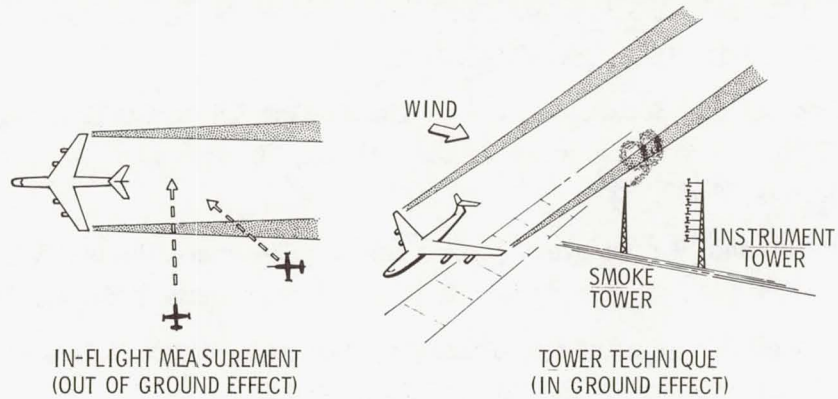


Figure 1

TYPICAL C-5A VELOCITY PROFILES OUT OF GROUND EFFECT

$W/b = 25\ 685\ \text{N/m}\ (1760\ \text{lb/ft})$
 $\Gamma_0 = 350.71\ \text{m}^2/\text{sec}\ (3775\ \text{ft}^2/\text{sec})$

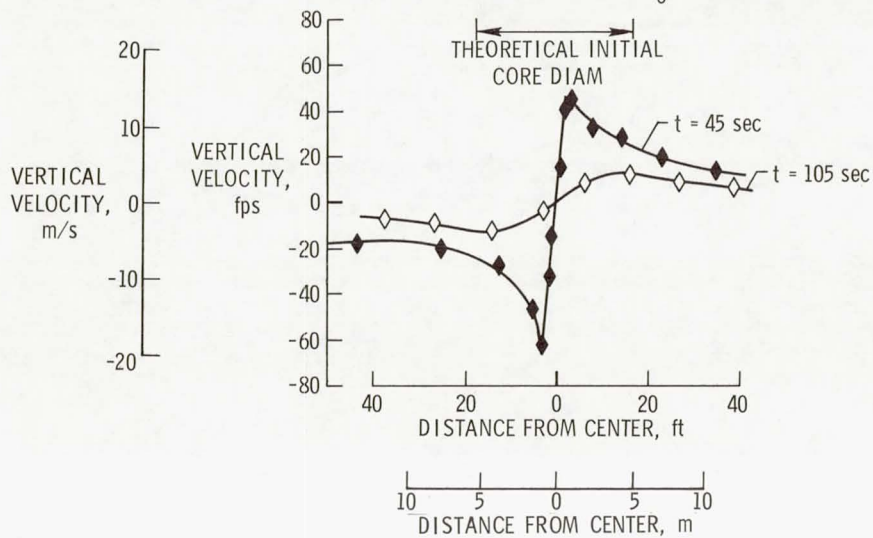


Figure 2

TYPICAL C-130 VELOCITY PROFILE IN GROUND EFFECT

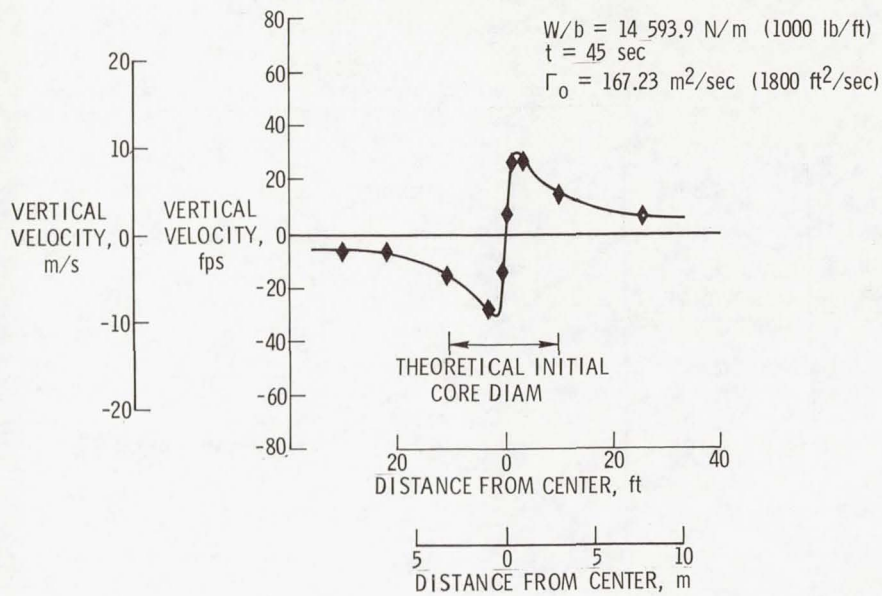


Figure 3

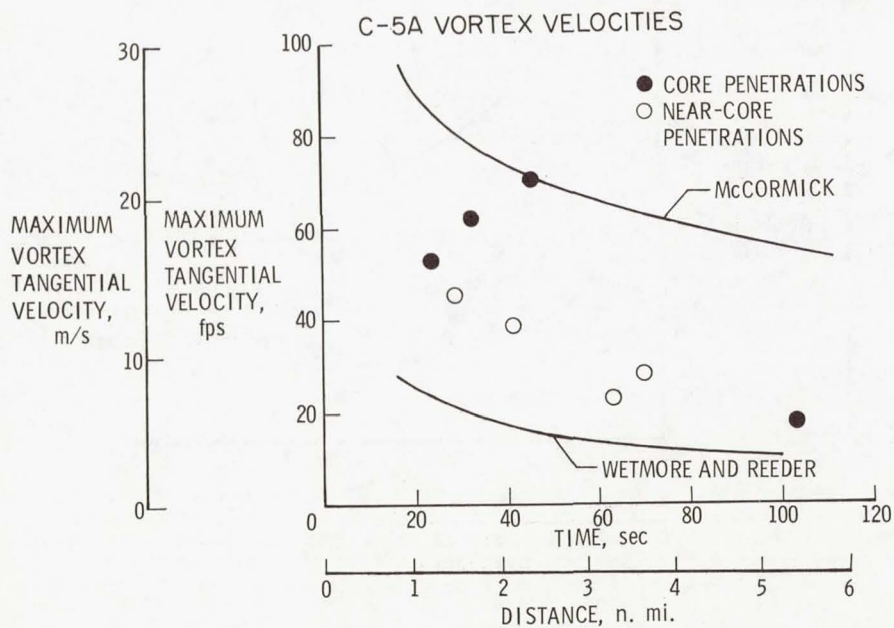


Figure 4

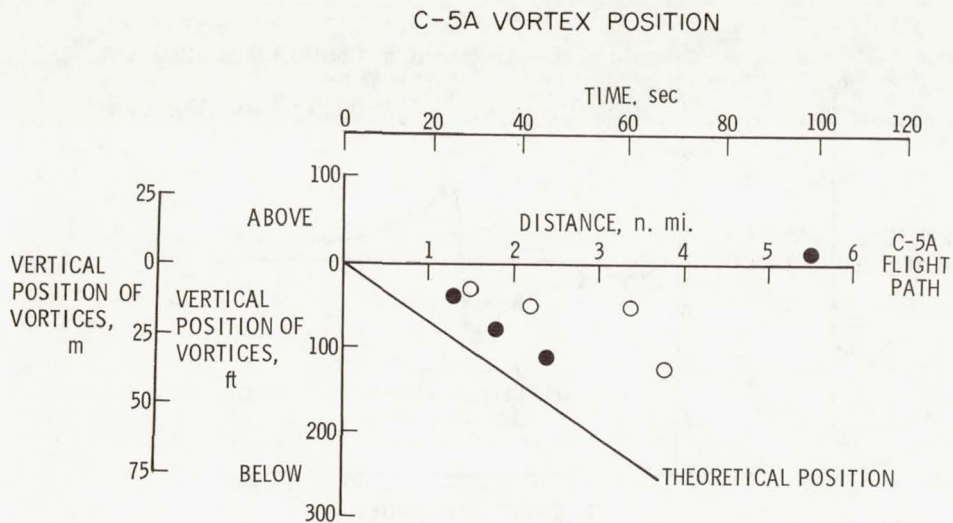


Figure 5

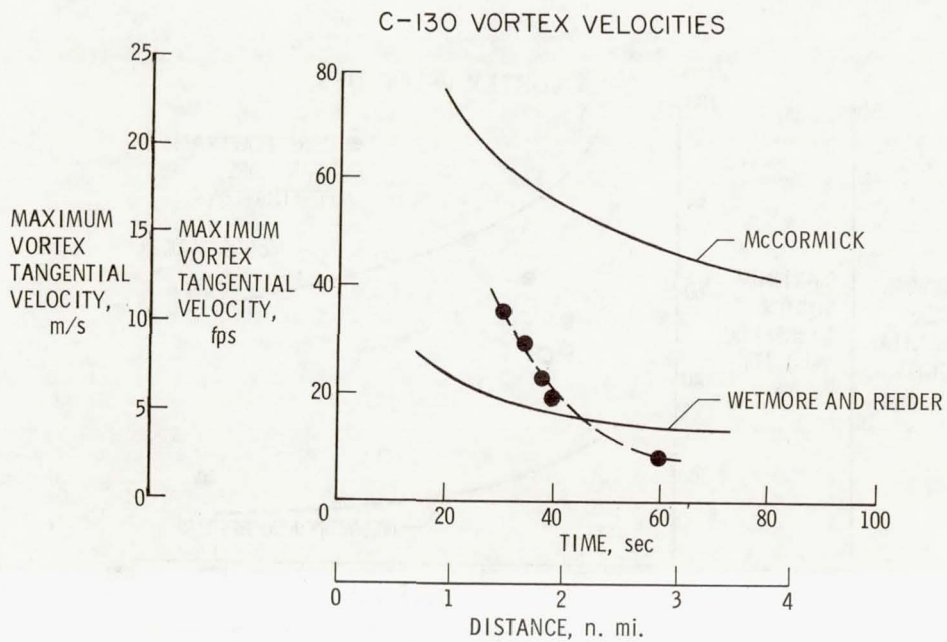


Figure 6

C-47 VORTEX VELOCITIES

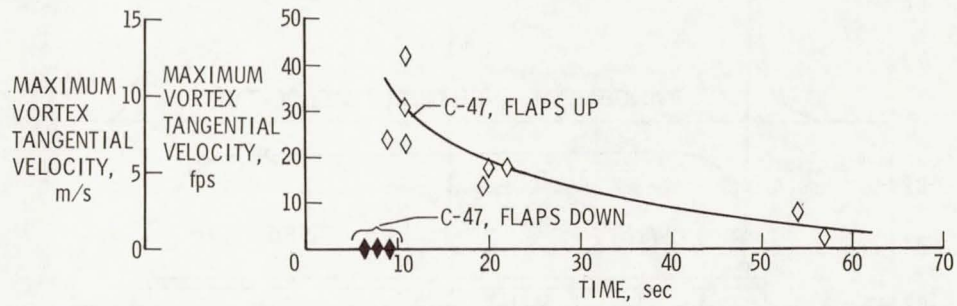


Figure 7



Figure 8

TANGENTIAL AND STREAMWISE VELOCITY COMPONENTS FOR
TRAILING VORTEX (left tip) AND DISSIPATED VORTEX (right tip)

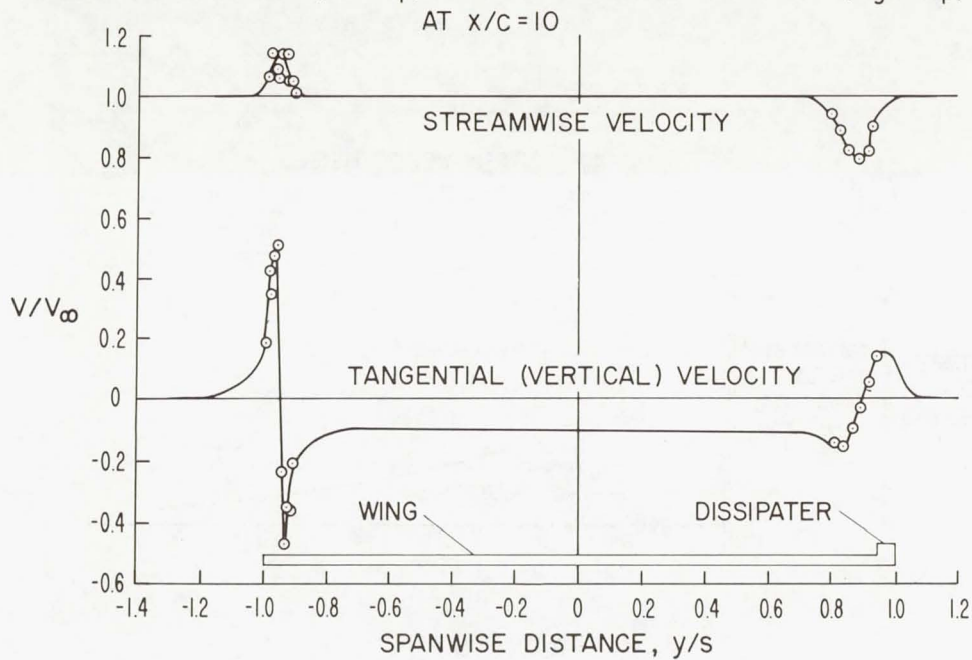


Figure 9

CONVAIR 990 WITH SPOILER MOUNTED ON LEFT WING TIP

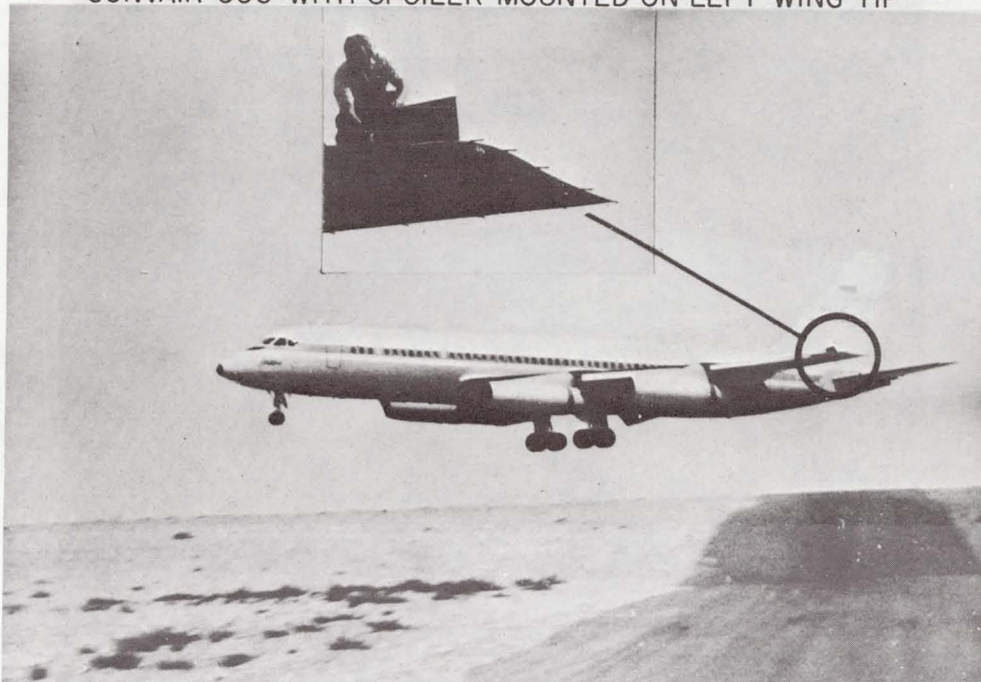


Figure 10

DOPPLER LASER VORTEX DETECTION

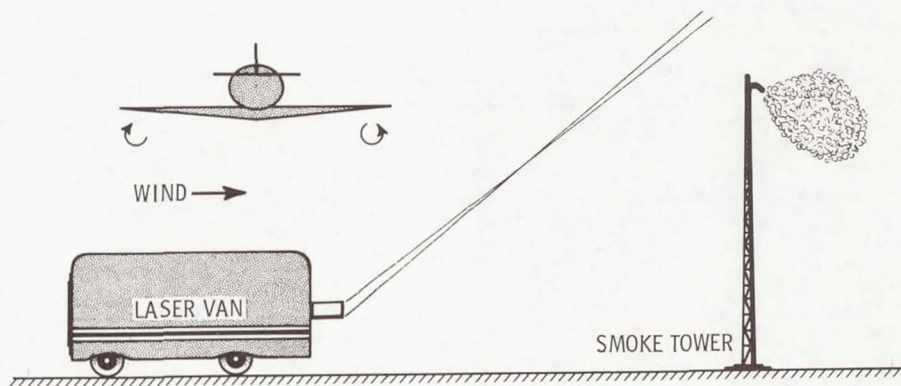


Figure 11

TYPICAL DOPPLER LASER MEASUREMENT

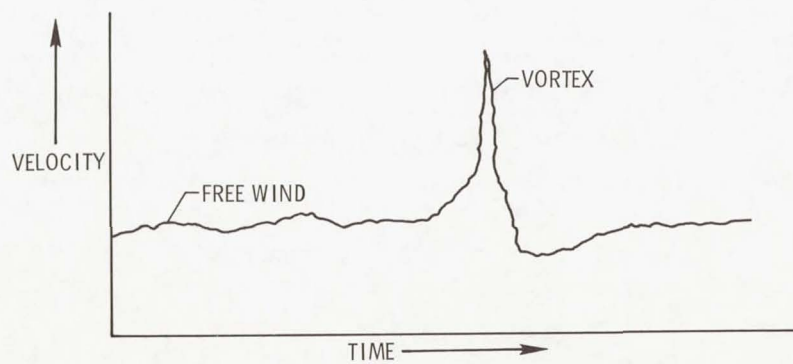


Figure 12

Page intentionally left blank

AIRCRAFT RESPONSE TO THE WING TRAILING VORTICES GENERATED BY LARGE JET TRANSPORTS

By William H. Andrews, Glenn H. Robinson,
and Richard R. Larson
Flight Research Center

INTRODUCTION

The potential hazard to an airplane penetrating the region of turbulence created by the vortices from another airplane has been emphasized by numerous incidents, accidents, and investigations reported previously. From these reports it is evident that the wing vortex emanating from the region near the tip contains a major portion of the total energy in the overall vortex system and that the strength and dissipation of this element of the system theoretically depend upon the span loading of the generating airplane and vary inversely with the airspeed and atmospheric density. The severity of the hazard to the penetrating airplane depends on the structural load limit, control recovery capability, the separation distance between the two airplanes, and the altitude at which the encounter occurred.

The influence of the trailing vortices on aircraft scheduling in the air-traffic system, specifically in the airport terminal area, has been considered at various periods throughout aviation history, particularly with the introduction of jet transports in 1959. However, the impact has become even more acute with the increase of mixed traffic conditions and the inauguration of the jumbo jets in 1970. As a consequence, NASA and the U.S. Air Force were requested by the Federal Aviation Administration to initiate a flight-test program to evaluate the effect of the wing-tip vortex wake generated by large jet transport airplanes on a variety of smaller airplanes. The resulting flight investigation was designed to obtain data essential to the determination of the wing-wake location relative to the generating aircraft and the apparent strength and dissipation of the vortex at a specified point along the wake trail. An additional objective of the investigation was to evaluate the upset potential and subsequent recovery capability of a variety of airplanes penetrating the vortex system.

The program was conducted in two phases beginning in December 1969 and ending in April of 1970. Operations were performed at Edwards Air Force Base in California under the supervision of the Flight Research Center in cooperation with Ames Research Center and the U.S. Air Force.

SYMBOLS

$ \dot{p} _{\text{MEASURED}}$	maximum roll acceleration induced to the probe airplane from generating-airplane wing trailing vortex, deg/sec ²
$ \dot{p} _{\delta a_{\text{MAX}}}$	maximum aileron control power of the probe aircraft, deg/sec ²
V_i	indicated velocity, knots

TEST AIRCRAFT

Figure 1 summarizes the test aircraft combinations used in the program. The generating aircraft were a Boeing B-52, a Lockheed C-5A, a McDonnell Douglas DC-9, and a Convair 990 (designated herein as CV-990). The gross-weight range covered by these airplanes varied from approximately 35 380 kg (78 000 lb) to a maximum gross weight of about 272 154 kg (600 000 lb). The airplanes were flown in either the clean configuration or the landing-approach configuration common to operations in the terminal areas.

The test airplanes used to probe the wake of the generating airplanes are shown on the right-hand side of figure 1 in conjunction with the respective aircraft separation distances that were evaluated. Only a representative portion of the data acquired during the program will be presented. The airplanes were instrumented with handling-qualities-type instrumentation to record the airplane response and pilot control input. The configuration of the CV-990 and the DC-9 during the testing was similar to that of the generating aircraft. However, in the case of the smaller airplanes the configurations were dictated by gear and flap placard speeds and the associated load limits.

TEST PROCEDURES

The test procedures used to probe the vortex of the generating aircraft are illustrated in figure 2. The penetrations were made from directly aft of the generating airplane to minimize the induced structural loads. Two types of penetration were performed. The initial test procedure was to position the probe airplane at the maximum separation distance for which the vortex trail was visible and proceed to fly in the trail to a specified safe minimum distance. The second method was to position the probe aircraft at a pre-arranged separation distance and evaluate the response characteristics for a period of approximately 2 minutes. In both cases the pilot task was to maintain wings level and to return to the wake path as soon as possible following an upset.

To expedite the program and provide a margin of safety for potential upset recovery, the tests were conducted at altitudes of 2591 and 3810 m (8500 and 12 500 ft). The generating airplanes were flown between 130 and 170 knots, which is considered normal for terminal-area operations. The speed of the probe aircraft was generally comparable with that of the generator; however, during the early stages of testing the CV-990 and an F-104 were flown at speeds of 250 and 300 knots, respectively. This procedure was followed so that a continuous probe could be made over the detectable vortex range to identify the location of the wake path.

Separation distances were established through the use of AN/FPS-16 and Nike Ajax precision radars operated by the Air Force at Edwards. Consequently, a major portion of the testing was observed and recorded on a video-tape system and the relative space location of the test aircraft was recorded on a digital system.

Throughout the testing the vortex path of the generating airplane was identified by the engine exhaust smoke entrapped in the vortex system. During the tests involving the DC-9 and CV-990 as generating airplanes, it was necessary to use JP-5 fuel to intensify the definition of the vortex trail.

DISCUSSION OF RESULTS

Airplane Roll Response

In the early test phase a continuous wake penetration was made with the CV-990 in the vortex wake of the C-5A. Figure 3 presents the relative altitude separation of the two airplanes experienced during the test. The C-5A was in a clean configuration, flying at an altitude of approximately 3810 m (12 500 ft) and an airspeed of 170 knots. The CV-990 was also in a clean configuration and flying at an airspeed of 250 knots. The vortex path of the C-5A was detected at approximately 21.3 km (11.5 n. mi.), and the CV-990 proceeded to fly that path to a point approximately 5.6 km (3.0 n. mi.) aft of the C-5A. The random and abrupt displacements indicated may be attributed to intermittent radar losses during the slight upsets resulting from the C-5A vortex. However, the significance of the data is the fact that at a separation distance of 20.4 km (11 n. mi.) the vortex path extends to approximately 305 m (1000 ft) below the cruise altitude of the C-5A. The ± 61 -m (± 200 -ft) oscillations of the vortex trail throughout the separation distances are considered to be primarily the result of atmospheric disturbances experienced during the test run.

The lateral control and roll response experienced by the CV-990 at a separation distance of approximately 5.6 km (3 n. mi.) during this probe is presented in figure 4. The data are presented in terms of roll rate and lateral wheel deflection as a function of

time. The right-hand vortex trail was probed. This is evident from the amount of right aileron being applied to keep the airplane in a wings-level condition. Normally the rolling moments from the vortex would roll the plane to the left. By observing the wheel deflections it may be seen that even with two-thirds to full wheel being applied to oppose the vortex-induced roll during a major portion of the time, the roll rates in several instances reached approximately 10 to 12 deg/sec. Under conditions where the airplane is not being disturbed, this amount of aileron is capable of producing roll rates in the order of 15 to 20 deg/sec. Consequently, the vortex wake at this separation distance appears to be of sufficient magnitude to require a major portion of the available lateral control to maintain the airplane within the prescribed wings-level attitude. The airplane is not considered to be uncontrollable under these conditions however, because as soon as it is rolled out of the wake path, recovery control is immediately effective.

During the various vortex penetrations, the crew of the probe airplane noted the influence of the configuration of the generating airplane on the apparent vortex strength and dissipation. To illustrate this effect, figure 5 summarizes the lateral control input used during the test run just described. These data are presented in terms of the control activity recorded for a 30-second period at discrete separation ranges. The data points are the percentages of the 30-second sample period that one-third, two-thirds, and full lateral wheel deflection were used to maintain the airplane within the vortex wake.

It is evident from the clean-configuration data that the predominate control input is to the right to counteract the vortex influence producing left-roll accelerations. Up to a separation distance of 16.7 km (9 n. mi.), at least one-third wheel deflection was required more than 50 percent of the time. Also, within this separation range approximately 10 percent of the time full wheel deflection was required to prevent ejection from the wake path. Beyond a separation distance of 16.7 km (9 n. mi.), there is a considerable reduction in the control manipulation required, either as a result of a reduced vortex-core definition or reduced vortex strength.

For the conditions with the C-5A in the landing configuration there is an obvious decrease in the lateral control required over the entire range of test conditions. The previously discussed attenuation of the vortex influence due to landing-flap deployment is verified by these data. In this case the separation distance where one-third wheel deflection exceeds 50 percent of the sample time is 7.4 km (4 n. mi.) or less.

As indicated previously, similar tests to those just described were performed with a variety of probe airplanes. Figure 6 presents a typical time history of a lateral-control roll response of the Lear Jet-23 flying in the C-5A vortex wake. Based on observations just discussed, it was determined that the safest conditions at which to evaluate the Lear response was with the C-5A in the landing configuration. This particular time history was taken from data at a separation range of 6.9 km (3.7 n. mi.). The

data are presented in terms of bank angle, roll rate, aileron-control input, and sideslip angle. It may be observed that as the Lear Jet-23 entered the vortex, it rolled abruptly to the left 360° . The pilot indicated that the influence of the vortex rotated the airplane approximately 270° . However, the pilot allowed the airplane to continue the roll 360° rather than return to his original wings-level flight condition. From the sideslip data it appears that the airplane passed through the wake core at approximately 2.5 seconds of the time history. Initially, full right aileron was applied to counteract the roll. However, in spite of the fact that full aileron is sufficient to produce roll rates in the order of 120 deg/sec in smooth-air conditions, it was ineffective in counteracting the vortex-induced roll.

Figure 7 summarizes the maximum roll response of the Lear Jet-23 to the C-5A, CV-990, and DC-9 generating aircraft. These data represent upsets experienced by the Lear Jet-23 where partial or full aileron control was applied to oppose the vortex-induced roll. The bank angles indicated are the maximums that were attained in the results. In general, these data indicate the effect of aircraft size on the strength and dissipation of the vortex by observing the average trend of the data, relative to each of the generating airplanes. It is obvious that the Lear Jet-23 response is considerably reduced between the C-5A and CV-990 tests. In the case of the DC-9, the minimal data are due to the fact that the vortex trail was not as well defined as that of the other airplanes.

The trend of the general aviation airplane data recorded during similar tests is consistent with these results.

Minimum Separation Distance

The data presented thus far have shown the response of the various probe aircraft to the vortex wake of the respective generating airplane. However, the question arises as to how the information may serve to aid in the development of a logical separation distance.

The next series of figures will illustrate a means by which these data and similar testing may be employed to establish a rational out-of-ground-effect baseline reference for aircraft separation. The primary objective of this approach is to determine a ratio of the maximum vortex-induced roll-acceleration response of the probe airplane to the maximum roll-control power of the probe airplane as a function of separation distance. The rationale for separation assumes that when the maximum control power of the probe aircraft is equal to the induced rolling moment from the generating-aircraft wake, then the separation from the generating aircraft is considered to be a safe minimum. Once the baseline is established, then factors can be applied to account for variables which would

be present, such as wind and temperature gradients and ground effect, particularly for terminal-area flight operations.

To illustrate the technique, data derived from several test runs of the DC-9 probing the wake of the C-5A are presented in figure 8. These data were obtained with both airplanes in the landing configuration. The previously described ratio is plotted as a function of separation distance for several test runs and a line was drawn to represent the maximum boundary of the data. The point at which the boundary line intersected the value of 1 is considered to be the point at which the minimum separation would be specified for the conditions tested. In this case the indication is that the minimum separation should be around 12.6 km (6.8 n. mi.). The scatter in the data is attributed to the fact that the DC-9 was not always in the region of maximum vortex-wake intensity.

By expanding this procedure to include a range of probe- and generating-airplane combinations, a relationship of separation distance to pertinent generating-airplane characteristics may be established. Figure 9 summarizes data obtained from tests of the CV-990, DC-9, and Lear Jet-23 probing the wake of the C-5A and CV-990. The solid lines represent boundaries obtained from data behind the C-5A and the dashed lines are data obtained in the wake of the CV-990. Again, as in the previous figure, the point of interception where the ratio is equal to 1 is considered to be the advisable separation distance for the particular combination indicated.

Figure 10 summarizes the spacing-criteria results determined from figure 9 in terms of separation distances as a function of the average gross weight of the generating airplane. It is conceivable that a relationship of wing loading or wing-span ratio could be applied here as a basis of comparison; however, the gross weight was used for convenience. In addition, pilot opinion is included for comparison purposes to establish the validity of the technique. The pilot opinion was based on the ability to maintain the airplane in the vortex wake and within a limited bank-angle range or roll rate. In the case of the general aviation aircraft these limits were approximately $\pm 30^\circ$ and 45 deg/sec, respectively. The limits were reduced to approximately $\pm 15^\circ$ and 30 deg/sec for airplanes in the general transport class. Consideration was also included in the pilot assessment for the normal operation of the particular airplane being tested, and the anticipated average crew and passenger response to a similar disturbance.

In the average-gross-weight range of 272 154 kg (600 000 lb), it may be observed that there is general agreement between the criteria and the pilot opinion. In the case of the CV-990 and the DC-9 it appears that the pilot would tolerate a separation distance of 0.9 to 2.8 km (0.5 to 1.5 n. mi.) less than that dictated by the criteria. However, with regards to the Lear Jet-23 the agreement was very good, and if anything, pilot opinion would indicate a slightly greater spacing requirement than that specified by the criteria. In the average-gross-weight range of 90 720 kg (200 000 lb) the agreement between the

measured data and the pilot opinion is very good and there appears to be a deviation of only 926 to 1390 m (0.5 to 0.75 n. mi.). It is fully appreciated that these data do not constitute a broad statistical base for the final acceptance of a separation standard and that other factors must be considered. However, it is believed that the technique and trends that have been presented are pertinent to the problem and applicable to the development of a rational separation criteria.

CONCLUDING REMARKS

In summary, the exploratory flight investigation of the wing vortex wake generated by a representative cross section of current jet transports operating under terminal-area conditions has indicated the following results:

1. At holding or landing-approach speeds the average vertical downwash path of the vortex can extend 229 m (750 ft) to 305 m (1000 ft) below the flight level of the generating airplane, at a range of 18.5 km (10 n. mi.).
2. Atmospheric conditions can produce sinusoidal oscillations of 30 m (100 ft) to 61 m (200 ft) about the mean downward path of the vortex.
3. The wake strength and dissipation are predominately influenced by the generating-airplane weight and configuration.
4. The strongest wake turbulence was noted when the generating airplane was in the clean configuration.
5. The resulting upsets experienced by the short-haul jet transports, the executive jets, and the general aviation airplanes indicate a need for a more conservative airway-spacing criteria in major airport areas.
6. Finally, a method has been suggested for using the existing test data to assess current airway-spacing procedures or to conduct further investigations.

SUMMARY OF AIRCRAFT USED IN WING VORTEX PROGRAM

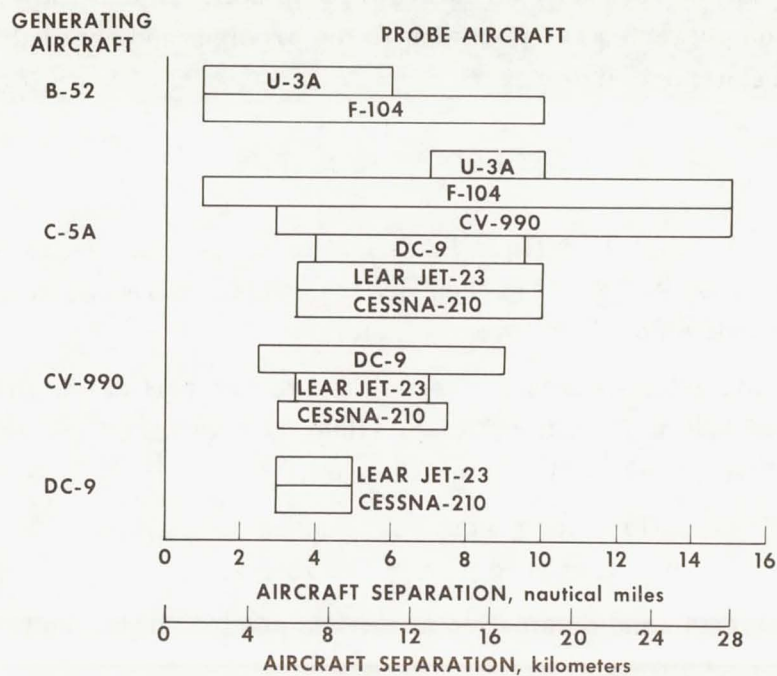


Figure 1

PROCEDURE USED TO PROBE THE GENERATOR AIRCRAFT VORTEX WAKE

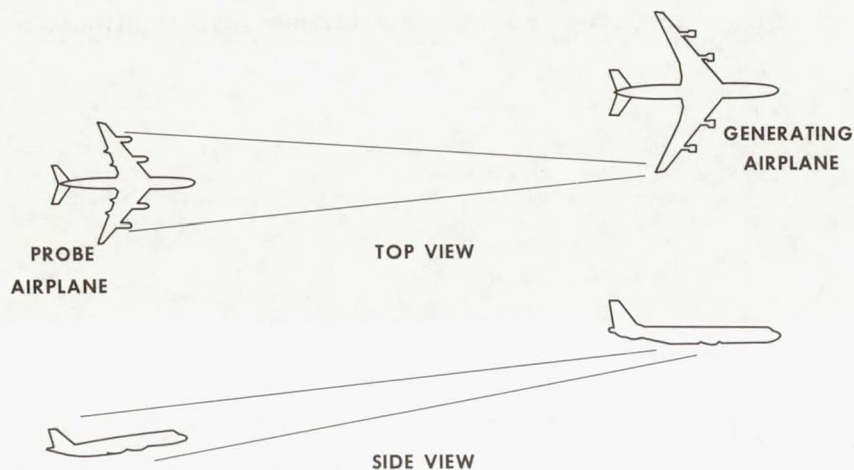


Figure 2

CV-990 FLIGHT PATH IN C-5A VORTEX WAKE

C-5A, $V_i = 170$ KNOTS; CV-990, $V_i = 250$ KNOTS

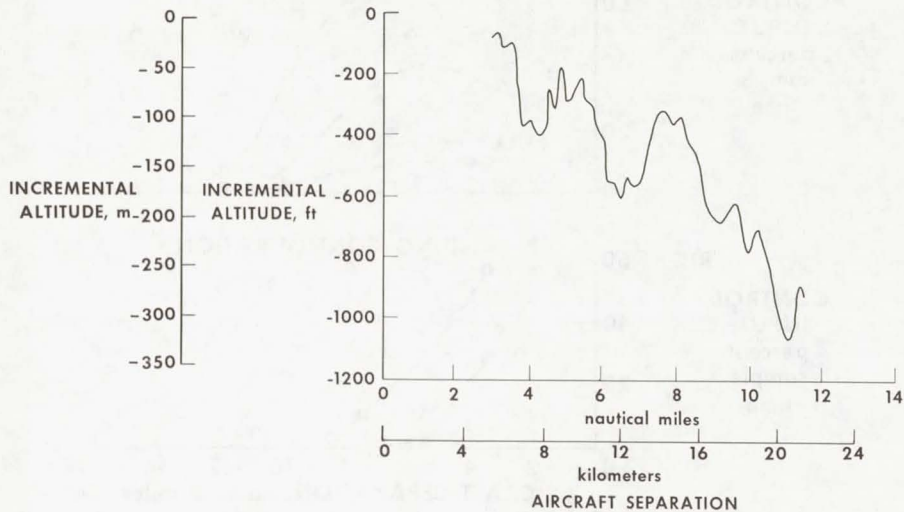


Figure 3

CV-990 ROLL RESPONSE IN C-5A VORTEX WAKE

CLEAN CONFIGURATION, 5.6 KILOMETER (3.0 NAUTICAL MILE) SEPARATION

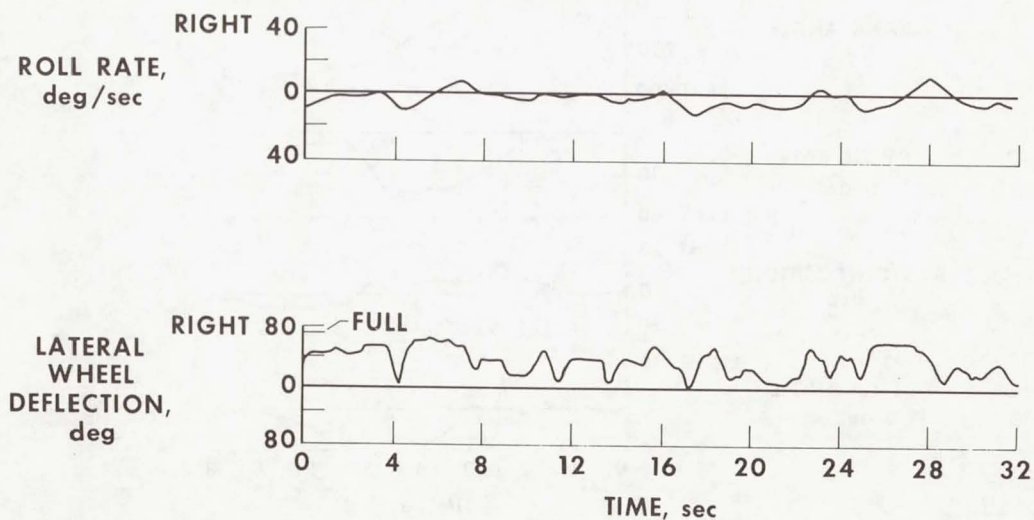


Figure 4

LATERAL CONTROL USED IN C-5A VORTEX WAKE

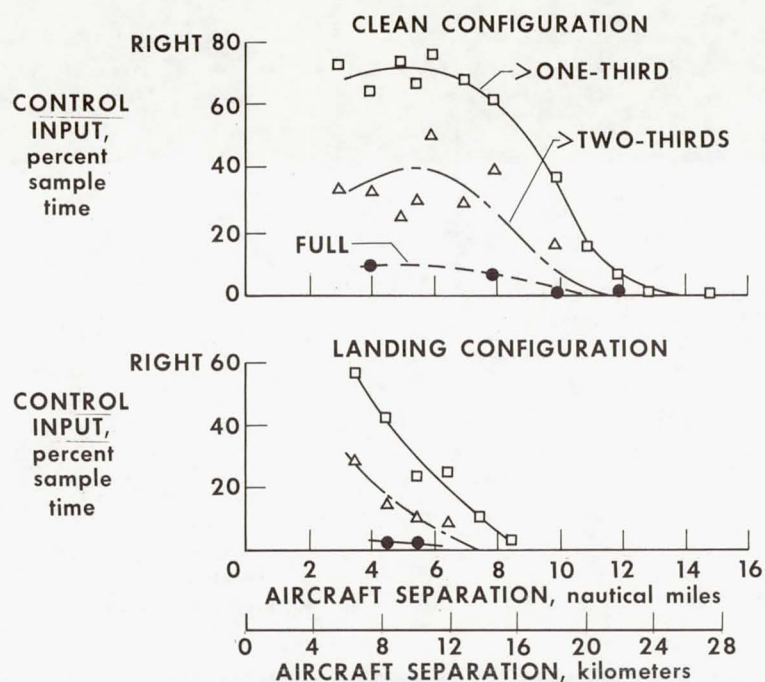


Figure 5

LEAR JET-23 LATERAL RESPONSE IN C-5A VORTEX WAKE LANDING CONFIGURATION, 6.9 KILOMETER (3.7 NAUTICAL MILE) SEPARATION

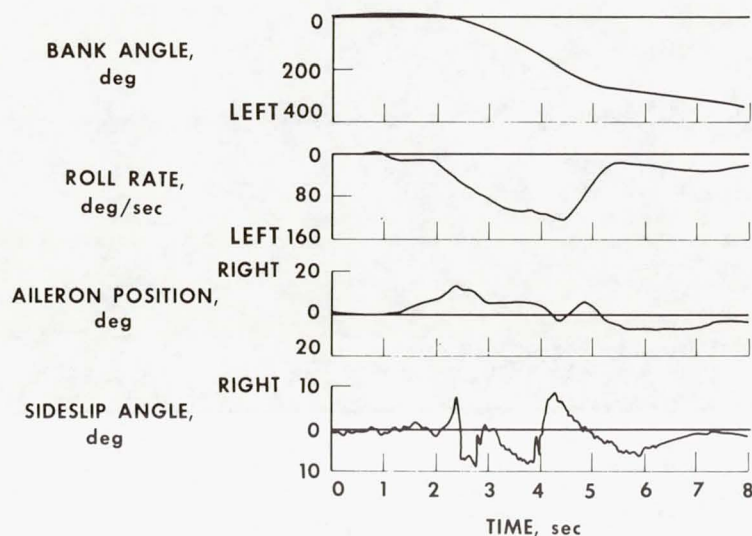


Figure 6

LEAR JET-23 MAXIMUM ROLL RESPONSE

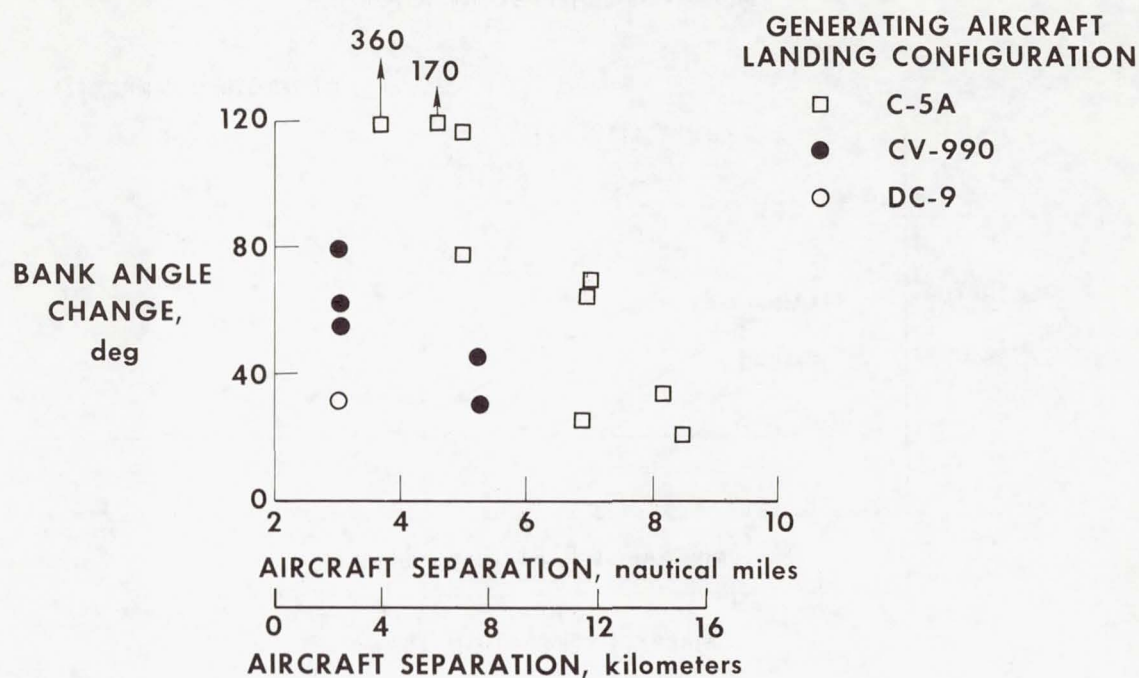


Figure 7

PROPOSED METHOD FOR DETERMINING AIRCRAFT SEPARATION

GENERATING AIRCRAFT, C-5A; PROBE AIRCRAFT, DC-9;
LANDING CONFIGURATION

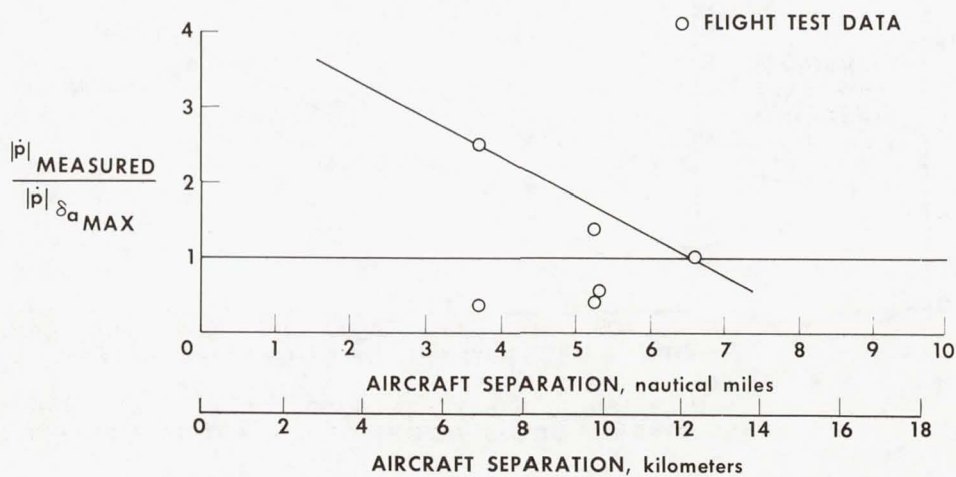


Figure 8

PROPOSED METHOD FOR DETERMINING AIRCRAFT SEPARATION LANDING CONFIGURATION

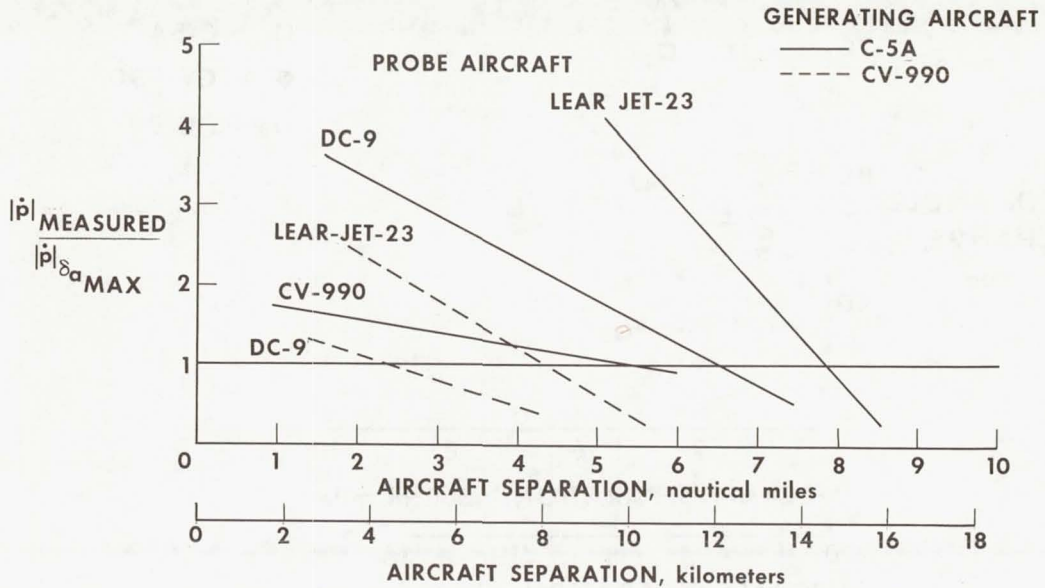


Figure 9

SEPARATION CRITERIA SUMMARY

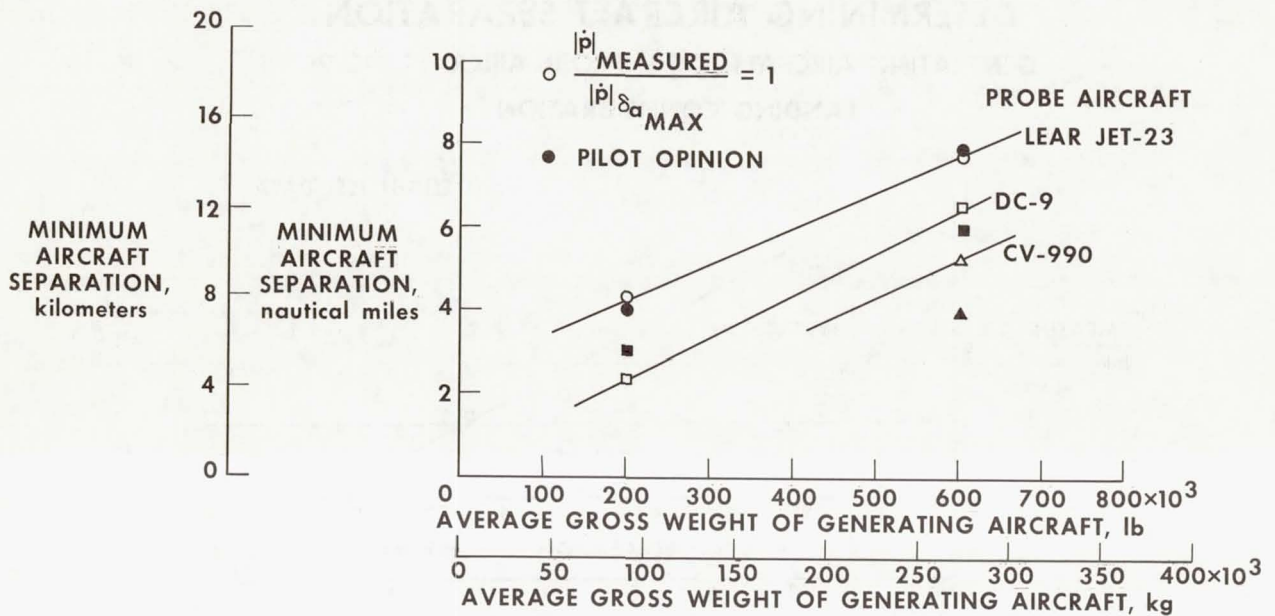


Figure 10

STATUS OF RESEARCH ON RUNWAY ROUGHNESS

By Albert W. Hall, Paul A. Hunter, and Garland J. Morris
Langley Research Center

INTRODUCTION

The operating problems related to runway and taxiway roughness are caused by the airplane response to the roughness input. This airplane response results in structural loads and contributes significantly to the fatigue load spectrum. In some instances, the roughness has caused extremely large airplane pitching and heaving motions, and thereby has created piloting difficulties.

As previously shown in reference 1, the general magnitude of roughness which causes airplane response problems is illustrated in figure 1, which shows a portion of an elevation profile for an extremely smooth runway and for a runway which was considered to be rough when jet transports were first placed in service. Both profiles appear to contain waves of varying length (distance) and amplitude (elevation). For the smooth runway, the elevation deviations are considerably less than 0.03 m (0.1 ft) for all wavelengths. For the rough runway, the wavelengths longer than 30 m (100 ft) show elevation deviations greater than 0.03 m (0.1 ft). The elevation deviations for the shorter wavelengths (less than 6 m (20 ft)) appear to be about the same for both runways. Further details of runway roughness characteristics, airplane response characteristics, and the relationship between airplane ground speed and roughness wavelengths and amplitudes are given in references 1, 2, 3, and 4.

This paper describes research related to runway roughness that is in progress or has been accomplished since the last NASA Conference on Aircraft Operating Problems in 1965. Typical data available from these programs are illustrated and briefly discussed. The programs described are related to two areas of roughness research, one to define roughness by measuring runway and taxiway profiles and the other by measuring airplane response to roughness.

DISCUSSION

Definition of Runway and Taxiway Roughness

Modern computing techniques and equipment have greatly improved the capability of predicting airplane response to runway roughness if the roughness characteristics are known. The roughness characteristics can be defined basically by profiles determined from elevations measured at close intervals along the length of the path to be defined.

These profiles may be used directly or they may be transformed to power-spectral-density curves as the input data for computing airplane response.

In the past, runway profile data have been obtained by various organizations, such as the National Advisory Committee for Aeronautics, the U.S. Air Force, aircraft manufacturers, and the NATO Advisory Group for Aeronautical Research and Development. Reference 5 gives a summation of existing profile data, which represent both military and commercial airports. These profiles generally are single track and relatively short compared with the runway length for present-day large commercial airports.

The NASA is conducting a program which was undertaken specifically to define the ground environment for large commercial aircraft. This program was necessary because it was impossible to determine whether the existing data were representative of present-day large commercial airports, also, there were very few three-track data available and practically no data representative of taxiway profiles. The multitrack profiles are necessary in order that the computed airplane response properly account for the effects of pitch and roll excitation at the landing gear, as illustrated by the sketch in figure 2.

Description of method.- The procedure established to define the environment for large commercial airports was to measure representative runway and taxiway profiles at 10 United States international airports. Three-track profile data are being obtained at each airport for one long runway and for one or more straight sections of taxiway. The profiles are obtained by measuring the elevations at 0.6-m (2-ft) longitudinal intervals along the center track and along tracks 4.6 m (15 ft) on each side of the center track, as shown in figure 3. The elevations relative to an arbitrary 15.24-m (50-ft) datum are measured to the nearest 0.001524 m (0.005 ft) by conventional surveying techniques with rod, level, and tape.

Profile data.- The airports participating in this program are listed in table I. It is expected that the surveying work will have been completed at all 10 airports by the end of 1971. A description and status of the data are given in table II. Table II also shows the length of runway or taxiway paths for which profile data have been obtained at each airport. Data for two government runways are also described in table II. Although these data are not for large commercial airports, they do represent a similar type of runway construction and, therefore, are representative of profiles to be encountered during the operation of large airplanes.

As indicated in table II, the available profile data are presented in references 6, 7, and 8. These data are also being made available to various interested organizations in the form of punched cards for electric accounting machines or as magnetic tapes. The data published in references 6, 7, and 8 have been presented in tabular form without analysis or discussion relative to the degree of roughness for each runway or taxiway. The following analysis is intended to give some definition of roughness levels.

Power spectra of profiles.- The power-spectral-density functions for the elevation profiles of the center track for airports A, B, C, D, and E are given in figure 4 for the runways and figure 5 for the taxiways. Many papers, such as references 2 and 3, have discussed the use of elevation power spectra plots to represent relative amplitudes of roughness corresponding to particular wavelengths for various pavement profiles. The larger value of power spectral density indicates the greater roughness level.

Figure 4 shows two straight lines representing the function

$$\Phi(\Omega) = \frac{C}{\Omega^2}$$

where Φ is the power-spectral-density function, Ω is the reduced frequency, and C is a constant, which is $6.096 \mu\text{m-rad}$ ($20 \times 10^{-6} \text{ ft-rad}$) for the upper line and $2.042 \mu\text{m-rad}$ ($6.7 \times 10^{-6} \text{ ft-rad}$) for the lower line. These values of the power-spectral-density function were suggested several years ago in reference 3 as a form of roughness criteria in which $\Phi(\Omega)$ for existing runways should not exceed the upper line ("needs repair") and $\Phi(\Omega)$ for "new construction" should not exceed the lower line. Although these criteria were never found to be practical for use in construction or repair, they are provided here as a convenient means of relating the roughness levels of these recently measured profiles to previous measurements.

Figure 4 shows that for wavelengths greater than 15 m (50 ft), the runway at airport E has a level of roughness exceeding the "needs repair" criterion and, therefore, is apparently the roughest of these five runways. Figures 4 and 5 show that the roughness levels are similar for both the runways and taxiways at the shorter wavelengths (below about 15 m (50 ft)). However, at the longer wavelengths, the taxiways generally show much higher levels of roughness than the runways.

The larger amplitudes of roughness shown for the longer wavelengths of taxiways have been indicated in the past by the pilot's operational practice of reducing the taxi speed on certain taxiways. This reduced speed results in the airplane responding primarily to the short wavelength content of the taxiway roughness spectra where the amplitude levels are similar to those of the runway spectra. This speed effect accounts for the fact that even though the taxiways are rougher overall than the runways, the airplane response during taxi generally has been found to be less than during the takeoff and landing run.

Figures 4 and 5 show that both the runway and the taxiway at airport B are much smoother than those at the other airports at the longer wavelengths. In addition to the present measurements, this runway at airport B was surveyed by the NASA in 1961 just prior to being placed in service. This profile is the smooth runway shown in figure 1. On the basis of the 1961 measurements, this runway is described in reference 2 as being

extremely smooth and representative of the effectiveness of the existing construction criteria. Figure 6 shows a comparison of the power spectral levels of the present runway surface with those determined previously, when the runway was new. According to the power spectral levels, there has been no noticeable deterioration of the smoothness during some 7 years of use. On the basis of all known profile measurements to date, it appears that the present three-track profile data for the runway at airport B represent the lowest level of roughness that will be encountered during the operation of large commercial airplanes.

Airplane Response to Surface Roughness

Another measure of roughness is to determine the airplane response to roughness. The NASA has obtained airplane response data for ground operations in both statistical form and unique time-history form. The statistical data provide information needed to define loading conditions for ground operations and are particularly useful in the determination of fatigue spectra. The unique data have been obtained with reference to particular runway problems where the measured airplane response has been related to a particular runway input.

Statistical data.- For many years the NASA VGH program has been providing statistical data which have been used to define the conditions of various phases of airplane operation. As part of this continuing program, statistical ground-loads data have been obtained on several current types of transport airplanes operated by United States and foreign airlines. These data consist of the normal acceleration measured at the center of gravity during the taxi, takeoff, and landing phases of ground operation. The data described herein represent seven different "operations" where each operation is taken to mean a combination of airline and airplane type. Each operation is identified alphabetically in table III. The data sample size for each operation is given in table III and ranges from 158 flights for operation F to 827 flights for operation C. A detailed description of these data is given in reference 9.

The frequency distributions of positive and negative accelerations for preflight taxi, takeoff, landing rollout, and postflight taxi conditions are tabulated in reference 9 for the seven operations. The total frequency distributions of positive and of negative accelerations for each operation and the number of flights represented by each frequency distribution are also given in reference 9. For takeoff and landing rollout, the frequency distributions are also given for each of three speed intervals.

The positive and the negative portions of the total distribution for each of the seven operations given in table III of this paper were combined without regard to sign and are shown in figure 7 in terms of the cumulative frequency of occurrence per flight. The results show that center-of-gravity normal accelerations greater than 0.4g occur once

every 3 to 10 flights. For normal acceleration values greater than 0.4g, the data for operation C begin to deviate significantly from the trend followed by most of the other operations. For example, an acceleration as great as 0.5g occurred about once every 12 flights during operation C; whereas an acceleration of this magnitude occurred about once every 100 flights during operation B. This difference is caused almost entirely by differences in the landing rollout category of ground operations, as shown in figure 8.

Figure 8 shows that the normal accelerations during preflight taxi, postflight taxi, and takeoff were similar for both operations. During landing rollout, however, operation C generally shows larger acceleration values more frequently than does operation B. Figure 8 also shows that for each operation a given acceleration occurs more frequently during landing rollout than during taxi or takeoff.

The larger accelerations shown for landing rollout are a reflection of the method of data evaluation by which accelerations subsequent to the initial positive landing impact are evaluated in the landing rollout category. The cumulative frequency of acceleration values for landing rollout is significantly influenced by a few large acceleration peaks which immediately follow the landing impact. Thus, the total accelerations experienced during ground operations, given in figure 7, reflect not only the response to runway and taxiway roughness but also the particular landing impact response of the airplane. Therefore, data representing the accelerations experienced as a result of surface roughness must be selected for the preflight taxi, postflight taxi, and takeoff categories only.

The statistical data, such as shown in figures 7 and 8, show the number of acceleration peaks that can be expected per flight during ground operation for each of several different combinations of airline and airplane types. Thus, for a given airline and airplane type, the data represent the airplane response for the average of the airports served by that airline.

Unique data.- The NASA has been asked to assist some military and civilian airport operators in determining the adequacy of particular runways for given airplane types. These unique programs represent unscheduled research in that the programs have generally been undertaken at the request of an outside organization as a result of some complaints of roughness. This type of problem can be investigated analytically by measuring the surface profile and using it as an input to calculate the airplane response as suggested in reference 10. Alternatively, the problem can be investigated directly by instrumenting an airplane to measure various response quantities while the airplane is being taxied over the surface in question.

The latter method has been used during recent years for the unique programs which have been accomplished jointly between NASA and other organizations. Data obtained from a number of these programs have been summarized in reference 4. Figure 9 illustrates a sample of these data, which were obtained during a joint Air Force-NASA program

to investigate a military runway which was reported to cause problems during takeoff operations with turbojet tanker airplanes.

The data in figure 9 show the variation of the jet-tanker normal-acceleration response and the runway elevation with longitudinal distance along the runway. These data represent the middle portion of a takeoff ground run where the ground speed was increasing from 122 to 138 knots. Figure 9 serves as a good illustration to summarize previous NASA work regarding runway roughness as indicated both by the profile measurements and by the airplane response measurements. For example, the long wavelength bump and depression shown at the beginning of the profile has an elevation deviation about 2 to 3 times larger than that illustrated by the rough runway of figure 1. The airplane response to this particular section of roughness showed cockpit vertical accelerations of about $+0.4g$. Since the region of runway illustrated in figure 9 was the primary source of pilot complaints about this particular runway, these response measurements tend to add further support to the $\pm 0.4g$ cockpit acceleration level previously proposed in reference 1 as a dividing line between satisfactory and unsatisfactory runways.

CONCLUDING REMARKS

This paper has presented a description of NASA research related to runway roughness and a description of recent data. Three-track profile data are being made available to represent the runway and taxiway roughness environment at present-day large commercial airports. Data representing approximately 10 United States international airports will be made available by the end of 1971.

The NASA VGH program is providing statistical data which describe the loading conditions for ground operations of several current transport-type airplanes. The NASA has continued to assist other organizations by participating in joint programs to measure airplane response characteristics related to particular complaints of runway roughness.

REFERENCES

1. Morris, Garland J.; and Hall, Albert W.: Recent Studies of Runway Roughness. Conference on Aircraft Operating Problems, NASA SP-83, 1965, pp. 1-7.
2. Coleman, Thomas L.; and Hall, Albert W.: Implications of Recent Investigations on Runway Roughness Criteria. AGARD Rep. 416, Jan. 1963.
3. Houbolt, John C.: Runway Roughness Studies in the Aeronautical Field. Proc. Amer. Soc. Civil Eng., J. Air Transport Div., vol. 87, no. AT 1, Mar. 1961, pp. 11-31.
4. Morris, Garland J.: Response of Several Turbojet Airplanes to Runway Roughness. NASA TN D-5740, 1970.
5. Wignot, J. E.; Durup, P. C.; Gamon, M. A.; Ginsburg, T. A.; and Ortasse, R.: The Development of Dynamic Taxi Design Procedures. DS-68-11, FAA, June 1968.
6. Hall, Albert W.: Three-Track Runway and Taxiway Profiles Measured at International Airports A and B. NASA TN D-5444, 1969.
7. Hall, Albert W.: Three-Track Runway and Taxiway Profiles Measured at International Airports C and D. NASA TN D-5703, 1970.
8. Morris, Garland J.: Three-Track Runway Elevation Profiles Measured at Two United States Government Installations. NASA TN D-5545, 1969.
9. Hunter, Paul A.: Summary of Center-of-Gravity Accelerations Experienced by Commercial Transport Airplanes in Landing Impact and Ground Operations. NASA TN D-6124, 1971.
10. Hall, Albert W.; and Kopelson, Sheldon: The Location and Simulated Repair of Rough Areas of a Given Runway by an Analytical Method. NASA TN D-1486, 1962.

TABLE I.- AIRPORT PARTICIPATION

1. Anchorage
2. Baltimore
3. Boston
4. Dulles
5. Honolulu
6. Los Angeles
7. New York (Kennedy)
8. Portland
9. San Francisco
10. (To be selected)

TABLE II.- DESCRIPTION AND STATUS OF RECENT PROFILE DATA

Airport	Surface	Length		Status
		meters	feet	
A	Runway	2865	9 400	Data published (ref. 6)
A	Taxiway	1341	4 400	Data published (ref. 6)
A	Taxiway	975	3 200	Data published (ref. 6)
B	Runway	2987	9 800	Data published (ref. 6)
B	Taxiway	2926	9 600	Data published (ref. 6)
C	Runway	3048	10 000	Data published (ref. 7)
C	Taxiway	2743	9 000	Data published (ref. 7)
D	Runway	3048	10 000	Data published (ref. 7)
D	Taxiway	2438	8 000	Data published (ref. 7)
E	Runway	2896	9 500	Report being prepared
E	Taxiway	2438	8 000	Report being prepared
F	Runway	3048	10 000	Report being prepared
F	Taxiway	914	2 998	Report being prepared
F	Taxiway	884	2 900	Report being prepared
F	Taxiway	552	1 810	Report being prepared
G	Runway	3353	11 000	Survey completed; data being reduced
G	Taxiway	1524	5 000	Survey completed; data being reduced
G	Taxiway	914	3 000	Survey completed; data being reduced
H	Runway	3048	10 000	Survey completed; data being reduced
H	Taxiway	1524	5 000	Survey completed; data being reduced
H	Taxiway	914	3 000	Survey completed; data being reduced
1	Runway	3048	10 000	Data published (ref. 8)
2	Runway	2438	8 000	Data published (ref. 8)

TABLE III.- IDENTIFICATION OF OPERATION AND DATA SAMPLE
SIZE FOR VGH GROUND-LOADS DATA

Operation	Airplane type	Type of operation	Number of flights in sample
A	4-engine turbojet	U.S. international	562
B	4-engine turbofan	Foreign international	751
C	4-engine turbojet	U.S. international	827
D	4-engine turbojet	U.S. domestic medium haul	666
E	4-engine turboprop	U.S. domestic short haul	762
F	2-engine turboprop	U.S. domestic feeder line	158
G	2-engine turbofan	U.S. domestic short haul	705

MEASURED PROFILES

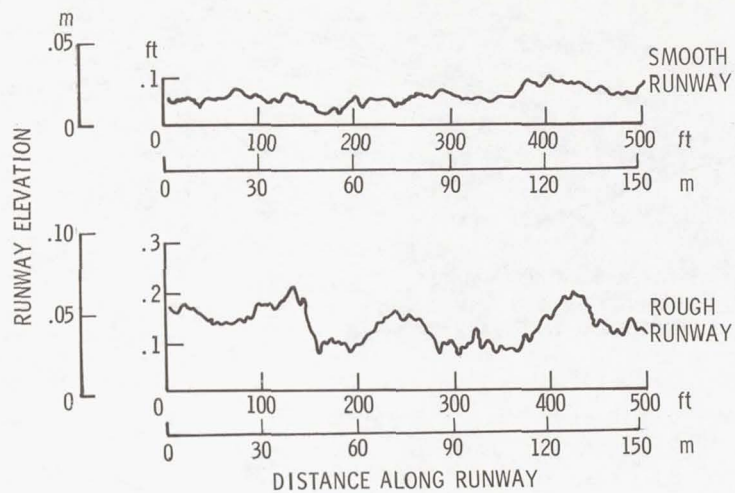


Figure 1

THREE-TRACK PROFILES

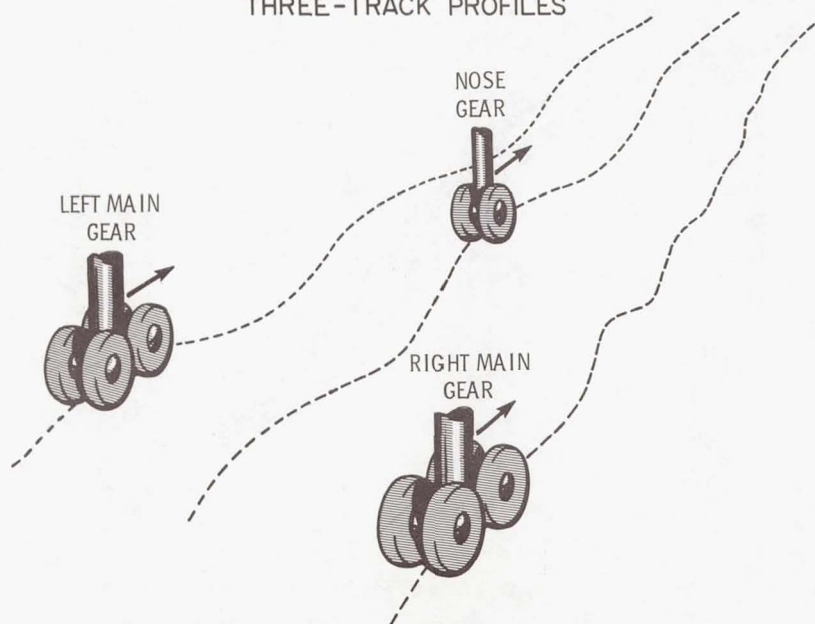


Figure 2

PROFILE MEASUREMENTS AT A TYPICAL AIRPORT

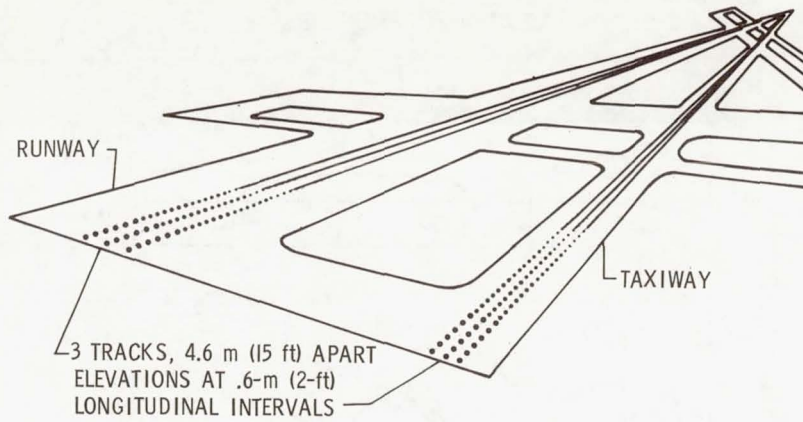


Figure 3

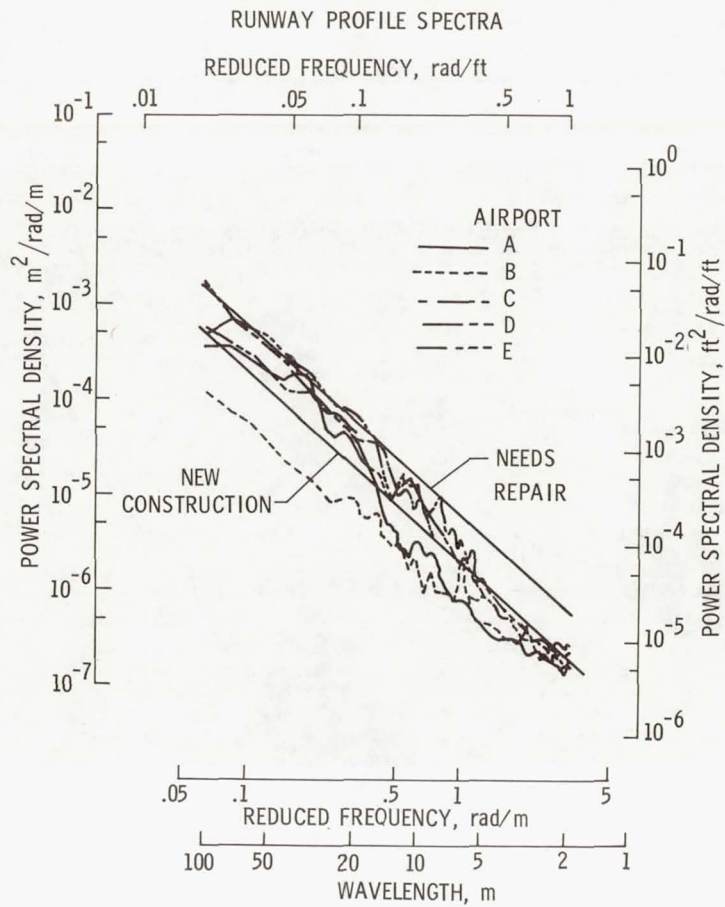


Figure 4

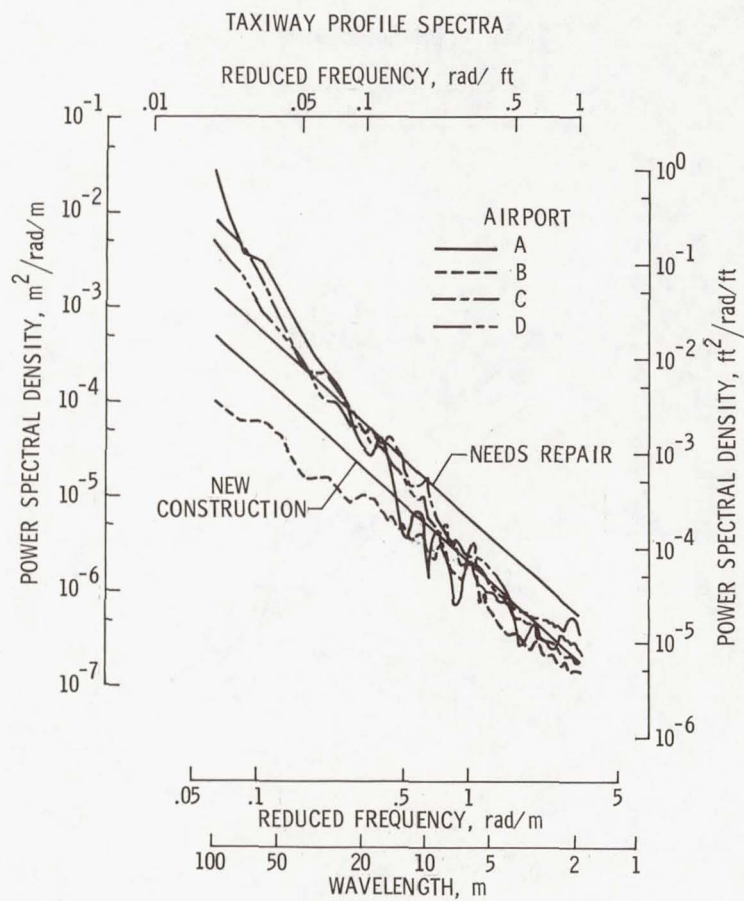


Figure 5

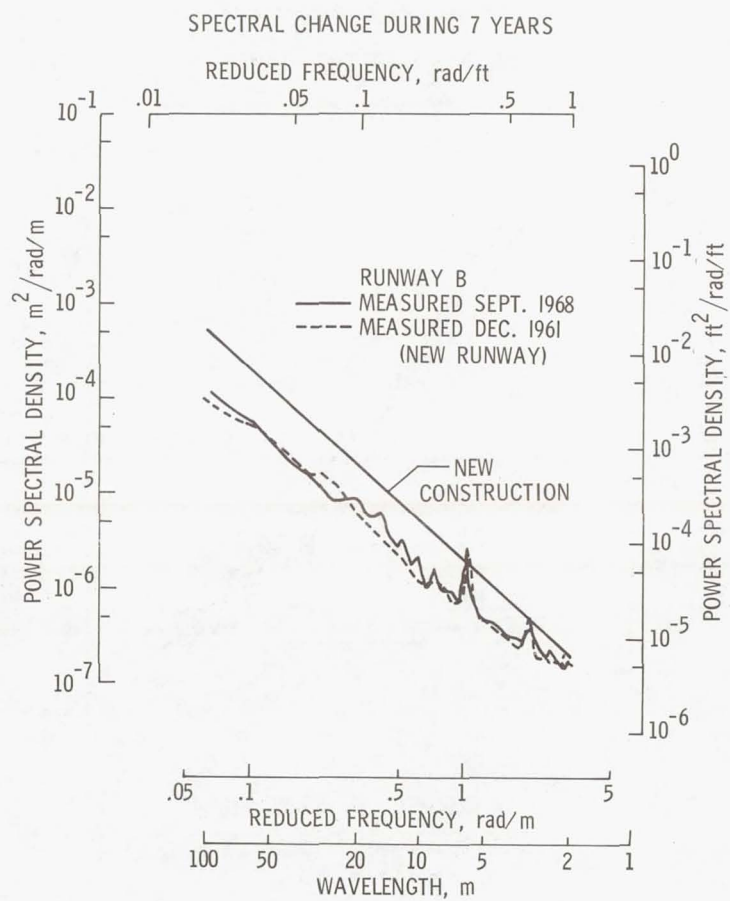


Figure 6

TOTAL NORMAL ACCELERATIONS DURING GROUND OPERATIONS

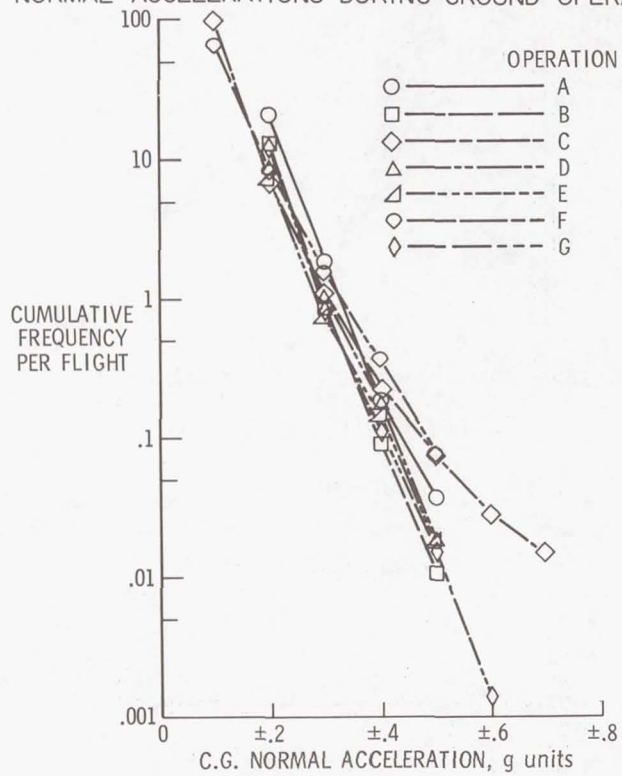


Figure 7

NORMAL ACCELERATION DURING EACH GROUND OPERATION CATEGORY

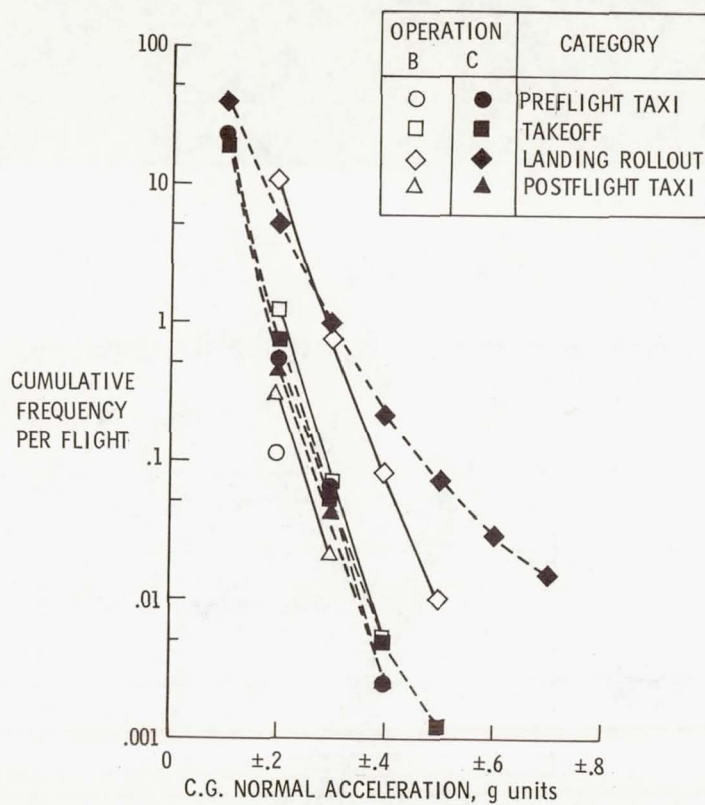


Figure 8

AIRPLANE RESPONSE

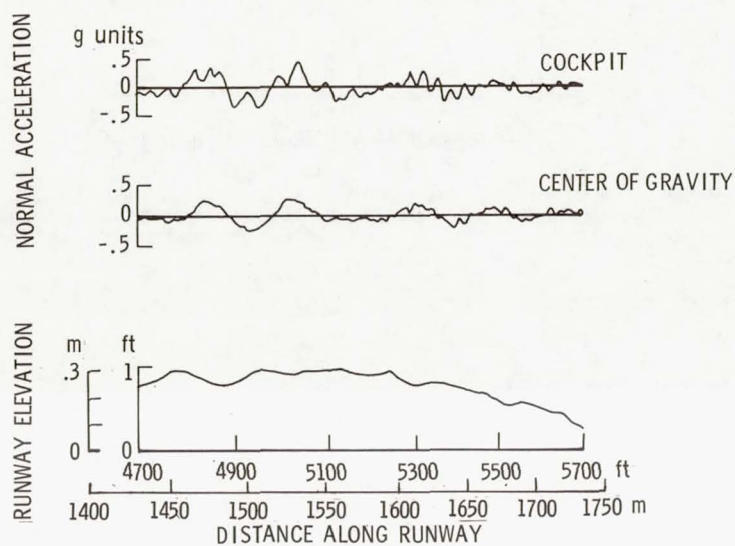


Figure 9

RUNWAY SLIPPERINESS

By Walter B. Horne
Langley Research Center

INTRODUCTION

When airplanes slide off the end or the side of runways during adverse weather conditions, the questions most frequently posed at the time of the accident or incident are "Was the pilot or the airplane at fault?" or "Was the runway slippery?" The answers to these questions are very complex since the stopping and directional control capability of aircraft are the result of the interaction of factors such as the aircraft tire, the aircraft design, the runway surface contaminants, and the runway surface structure itself. The tire inflation pressure, tread rubber compound, and tread design combine to determine the maximum friction coefficient achievable between the tire and a dry pavement. Aircraft factors, such as spoilers, brake torque limitation, antiskid system, and landing-gear geometry, reduce the ability of the pilot or aircraft to utilize all of this friction capability. As a consequence, at the same touchdown speed a four-engine jet transport with effective spoilers, individual antiskid wheel control, and low-pressure tires will stop on a dry runway in one-half the distance required by a jet fighter using high-pressure tires and a paired wheel antiskid braking system. An unknowing runway observer watching these airplanes land would assume that the dry runway was twice as slippery for the fighter than for the transport. Runway contaminants and pavement surface properties combine to further degrade the tire braking or lateral traction potential and, thus, produce slippery conditions which can, in some instances, lead to completely unsafe aircraft stopping and directional control performance.

It is the primary purpose of this paper to discuss the effects of runway contaminants and pavement surface properties on runway slipperiness.

RUNWAY CONTAMINANTS

Water, slush, snow and ice, dust, oil and rubber deposits are some of the main runway contaminants. Research shows that when the runway is covered with thin- or thick-fluid films, phenomena such as viscous hydroplaning, dynamic hydroplaning, and reverted rubber hydroplaning occur. These phenomena result from fluid pressures developed in the tire-ground footprint which vary with ground speed (fig. 1). The viscous properties of the contaminating fluid can create fluid pressures of sufficient magnitude to lift the tire off the pavement at extremely low speeds. This action is viscous hydroplaning. Similarly, density properties of the fluid can also produce a dynamic pressure which increases as the square of the speed and results in dynamic hydroplaning.

PAVEMENT SURFACE PROPERTIES

Several properties of pavement surfaces play most important roles in producing or alleviating runway slipperiness. These important properties of the pavement are its microtexture, macrotexture, and porosity. Microtexture is defined as the small-scale (0.00254 to 0.254 mm (0.0001 to 0.01 inch)) sharp-edge roughness of the surface texture (mortar and aggregate). Macrotexture is defined as the large-scale (0.254 to 25.4 mm (0.01 to 1.0 inch)) roughness of the surface texture (aggregate size, etc.). Porosity is the ability of the pavement surface to allow vertical drainage of fluid film through the pavement (as an ink blotter). In figure 2, several different types of pavement are categorized according to microtexture and macrotexture. Pavement surfaces must have microtexture to puncture and displace the contaminating thin-fluid film. It is absolutely essential that pavement surfaces possess macrotexture so that drainage paths can form between the tire rubber and the pavement surface and remove trapped bulk water from the tire-ground contact zone; otherwise, at higher speeds the pavement becomes slippery from dynamic hydroplaning effects. The smooth pavement is seen to be the slipperiest because it possesses no microtexture or macrotexture. It is most difficult, for example, to get good microtexture and macrotexture on a newly laid concrete surface because of the nature of the plastic concrete. Grooving can provide a good microtexture and macrotexture to this type of surface after it sets. The sharp corners of the grooves provide the microtexture; the groove channels supply the necessary macrotexture. The degree of benefit grooving provides in alleviating viscous and dynamic fluid pressures in the footprint depends upon the width, depth, and spacing of the groove pattern. The British recently added a new dimension to drainage in the tire-ground contact zone by providing the runway with a porous surface overlay (up to 2.54 cm (1 inch) thick). The added vertical fluid drainage that this feature provides when used with a properly laid aggregate (microtexture and macrotexture) gives practically dry performance to aircraft under wet conditions. Both grooving and the porous pavement have the added benefit of reducing wheel splash and, thus, of minimizing spray ingestion.

The braking friction developed by a smooth-tread aircraft tire tested on a smooth concrete surface (no microtexture or macrotexture) and on a plant-mix asphalt (good microtexture and fair macrotexture) under damp and flooded conditions is shown in figure 3. For the damp condition in which insufficient bulk water is present to permit dynamic hydroplaning, the plant-mix asphalt with good microtexture does a much better job in preventing viscous hydroplaning than does the smooth concrete surface with no microtexture. For the flooded condition, the smooth-surface braking friction coefficients are only slightly higher than those for the damp condition at high ground speeds because of fluid drag effects, and the plant-mix asphalt with the macrotexture does not prevent dynamic hydroplaning.

At the present time, approximately 800 major runways are used by this country for military and civil aircraft operations. Approximately 5 percent of these runways were tested for wet runway slipperiness in the recently completed joint USAF-NASA Combat Traction Program (ref. 1). Results from this program are presented in figure 4. Also included in the figure are the results from several British runways. Clean, uncontaminated areas of each runway were artificially wetted by water trucks and tested with both an instrumented Lockheed C-141A jet aircraft and a NASA diagonal-braked vehicle (DBV). Good correlation was obtained in the program between the aircraft and the DBV wet/dry stopping distance ratios. A DBV stopping distance ratio of 1.0 indicates that the wet runway gives dry performance. The present Federal Aviation Administration landing rule uses a factor of 1.92 to determine the wet runway landing field length. Figure 4 shows that DBV wet/dry stopping distance ratios obtained on some of the concrete and asphalt runways studied exceeded this slipperiness value. The figure further shows that runway grooving and the application of the British porous asphalt yielded DBV wet/dry stopping distance ratios which were significantly less than 1.92. Thus, the benefit of these surface treatments to alleviate viscous pressures and the related viscous hydroplaning is readily seen.

On the basis of this and other flooded runway research, runway grooving (fig. 5) and the British porous asphalt runway surface treatment (fig. 6) appear to be the best available techniques to use to alleviate runway slipperiness from fluid or fluid-acting contaminants.

RUBBER DEPOSITS

The advent of jet aircraft with large multiwheel landing gears has significantly increased runway contamination in the form of rubber deposits which resulted from wheel spin-up in the runway touchdown areas. These rubber deposits tend to reduce both the existing microtexture and macrotexture of the runway surface and thus the airplane would be more susceptible to viscous hydroplaning when this section of the runway surface is covered with a fluid film.

The data of figure 7 show that the slipperiness of conventional concrete and asphalt runway surfaces is greatly increased when covered with heavy rubber deposits. In fact, little change in slipperiness is indicated between wet and damp runway conditions. This result indicates that rubber-coated runway surfaces will be slippery whenever slight precipitation or even a heavy dew occurs on a runway. The data in this figure also indicate that runway grooving may be an effective way to combat this contaminant problem since the slipperiness of rubber-coated grooved runways is much less than that for the conventional runway surfaces. It is believed that the porous asphalt runway surface treatment

will not be as effective as runway grooving in combating this problem because the rubber deposits will tend to fill the surface voids which exist in this type of pavement.

Many organizations are presently engaged in research to determine effective methods to remove rubber deposits from runways. A chemical treatment was recently tried at a moderately busy airport. Photographs of the rubber-contaminated runway area before, 4 days after, and approximately 4 months after rubber removal are presented as figure 8. The effectiveness of this treatment is illustrated by the data in figure 9 from DBV wet/dry stopping distance ratio tests. These data indicate that the treatment was successful in reducing the slipperiness of the contaminated-runway surface to the level associated with that of the clean-runway surface. However, 4 months later, rubber deposits had again built up on the runway to such a degree that the contaminated surface was almost as slippery as it was prior to the treatment. Hence, to be effective in reducing runway slipperiness, rubber-removal treatments must be applied frequently (at least several times a year) on heavily trafficked runways.

SLUSH, SNOW, AND ICE CONTAMINATION

Slipperiness created by snow or ice covering the runway can be quite different in character from the slipperiness produced by fluid or fluid-acting contaminants. Under normal braking or cornering conditions for a rolling tire (not locked), the braking or cornering friction produced is nearly constant with speed. The level of friction depends upon the snow or ice temperature; the colder the temperature, the higher the friction. As the snow or ice temperature nears the melting point (0°C), a water film is formed on the snow and ice and drastically reduces the friction level because of viscous hydroplaning. If the aircraft braking system allows locked wheels to occur at low ground speeds, frictional heating in the contact area of the sliding tire continuously creates a water film which cannot be dissipated by the tire. Viscous hydroplaning for this locked wheel condition persists practically down to a full stop and the frictional level is only slightly higher than that of the tire during unbraked rolling. Extremely slippery runway conditions exist for this situation as shown in figure 10. It should be noted that dry-packed snow and ice runway conditions can quickly degenerate to a wet or slushy condition when ambient temperatures rise as in a thaw.

The behavior of a slush cover on the runway is similar to the behavior of the fluid covers previously described except that slush is more viscous acting than water and thus makes the aircraft more susceptible to viscous hydroplaning.

The only really effective remedy for the snow, ice, or slush contamination problem on the runway is an efficient removal program by use of plowing, snow blowers, and other snow or ice moving equipment.

CONCLUDING REMARKS

Research has shown that contaminants, such as water, slush, snow, ice, and rubber deposits, on conventional pavement surfaces can produce intolerable levels of runway slipperiness in terms of safety of aircraft operation. When wet, conventional surfaces vary considerably in slipperiness due to pavement surface microtexture and macrotexture. A more consistent safe level of slipperiness appears achievable with new surface treatment techniques such as runway grooving and porous asphalt overlays. Research in this problem area is continuing with the hope of meeting the following goals:

- (1) Develop a standard military/civil method for measuring runway slipperiness
- (2) Identify and remedy existing slippery runways
- (3) Develop accurate methods to account for aircraft performance on slippery runways
- (4) Perfect grooved and porous pavement surface treatments

REFERENCE

1. Yager, Thomas J.; Phillips, W. Pelham; Horne, Walter B.; and Sparks, Howard C. (With appendix D by R. W. Sugg): A Comparison of Aircraft and Ground Vehicle Stopping Performance on Dry, Wet, Flooded, Slush-, Snow-, and Ice-Covered Runways. NASA TN D-6098, 1970.

DEVELOPMENT OF FLUID PRESSURE IN
TIRE-GROUND FOOTPRINT
SMOOTH TIRE; SMOOTH PAVEMENT SURFACE

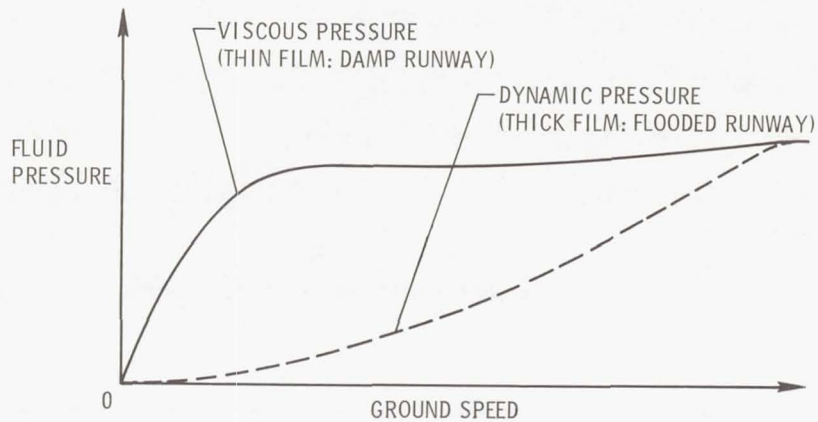


Figure 1

PAVEMENT SURFACE CHARACTERISTICS

PAVEMENT	TEXTURE		ABILITY TO ALLEVIATE PAVEMENT WETNESS	
	MICRO	MACRO	DAMP (VISCOUS PRESSURE)	FLOODED (DYNAMIC PRESSURE)
SMOOTH	NO	NO	POOR	POOR
SANDPAPERY	YES	NO	EXCELLENT	POOR
SMOOTH STONES	NO	YES	POOR	POOR TO GOOD
FRACTURED STONES	YES	YES	EXCELLENT	POOR TO GOOD
GROOVES	NO	YES	GOOD	GOOD TO EXCELLENT
GROOVES	YES	YES	EXCELLENT	GOOD TO EXCELLENT
POROUS	YES	YES	EXCELLENT	EXCELLENT

Figure 2

PAVEMENT SURFACE EFFECTS ON AIRCRAFT TIRE TRACTION

- DRY ASPHALT AND CONCRETE
- - - - PLANT-MIX ASPHALT (GOOD MICROTEXTURE, FAIR MACROTEXTURE) ;
- SMOOTH CONCRETE (NO MICROTEXTURE, NO MACROTEXTURE)

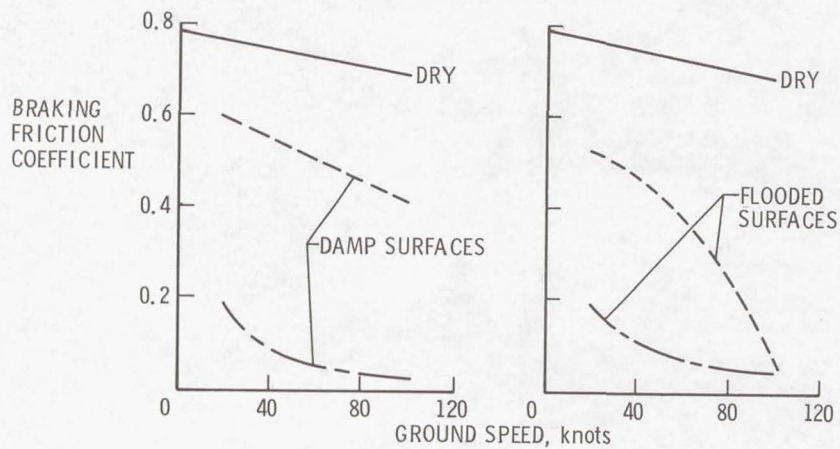


Figure 3

RUNWAY SLIPPERINESS SURFACE: CLEAN (NO RUBBER DEPOSITS); ARTIFICIALLY WET

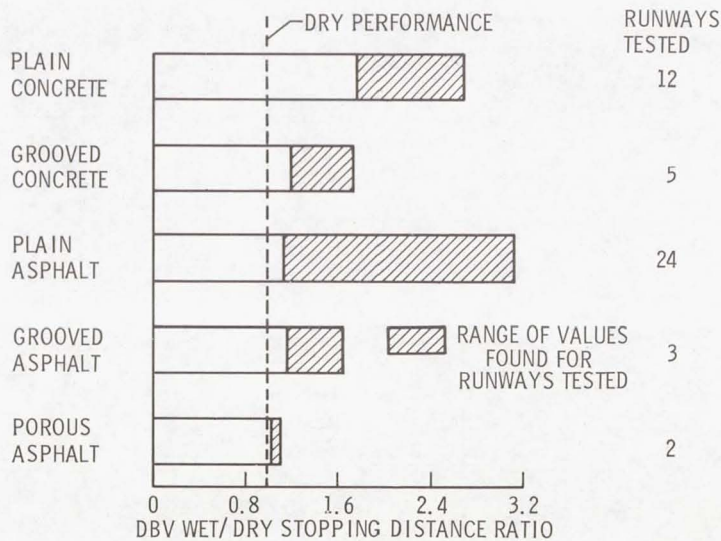


Figure 4



Figure 5

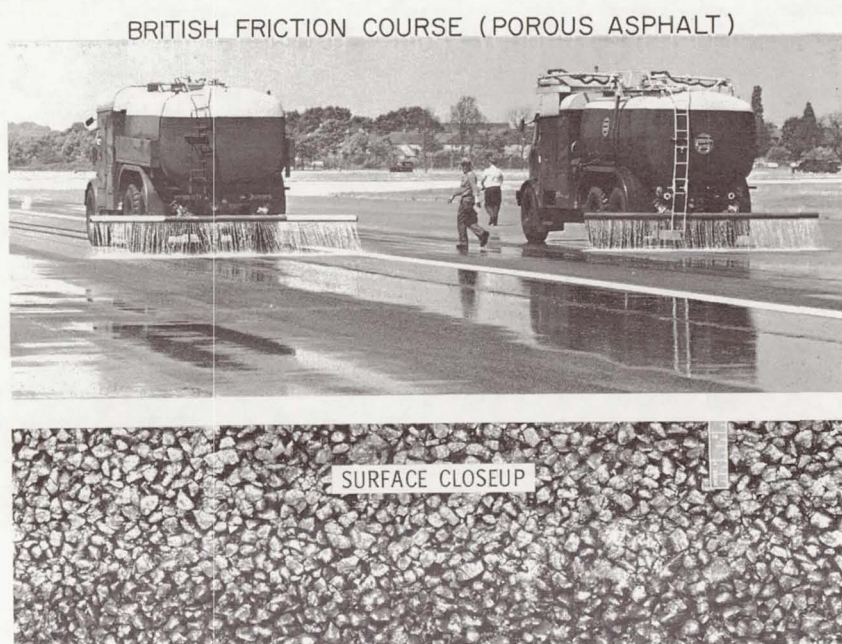


Figure 6

INCREASE IN RUNWAY SLIPPERINESS FROM RUBBER DEPOSITS

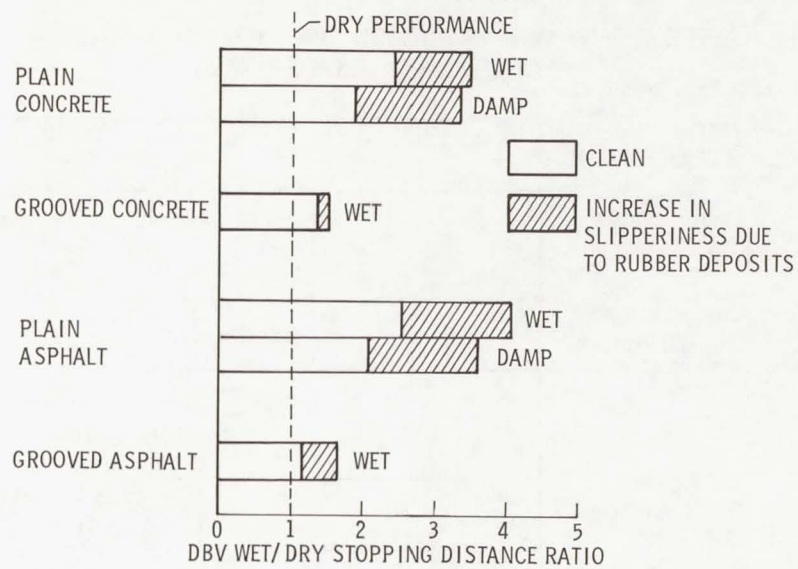


Figure 7

RUBBER DEPOSITS ON CONCRETE RUNWAY BEFORE AND AFTER RUBBER-REMOVAL PROGRAM



Figure 8

EFFECT OF REMOVING RUBBER (BY CHEMICAL TREATMENT) ON RUNWAY SLIPPERINESS

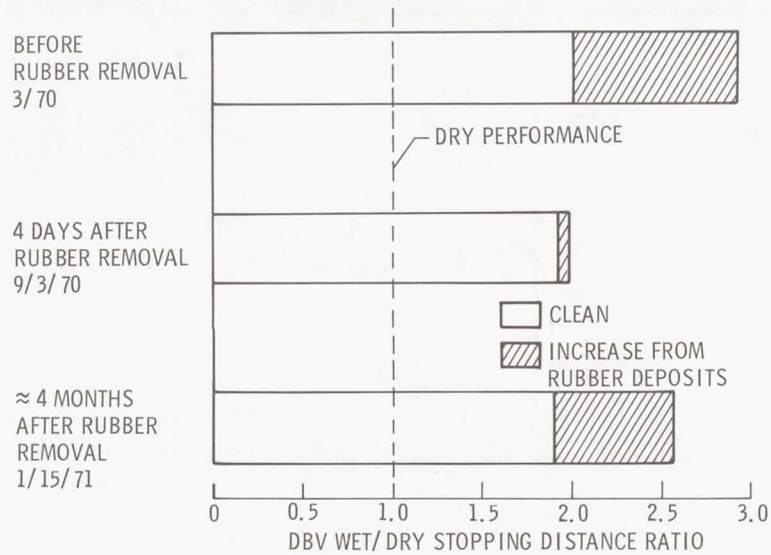


Figure 9

SLIPPERINESS OF SLUSH, SNOW, AND ICE -COVERED RUNWAYS DURING AIRCRAFT LANDING

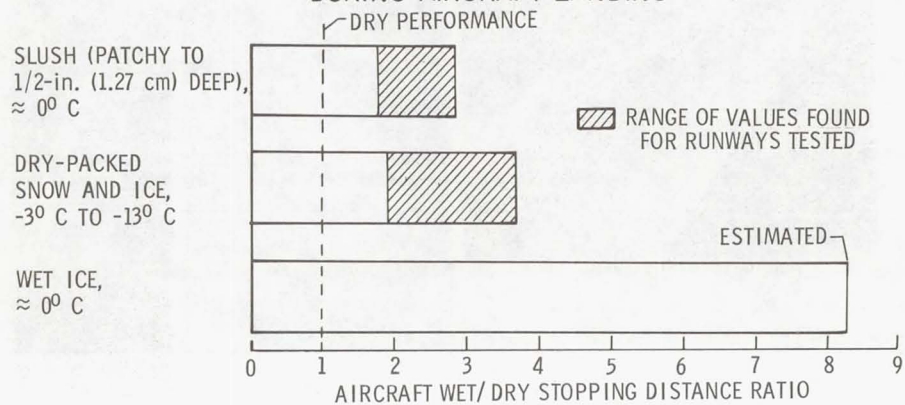


Figure 10

EFFECT OF AIRPLANE OPERATIONS ON TIRE WEAR

By John L. McCarty and Upshur T. Joyner
Langley Research Center

INTRODUCTION

Tire wear is a major economic concern to commercial and military aviation, with tire replacement accounting for approximately half the overall landing-gear maintenance costs of present-day jet airplanes. Tire wear is associated with all phases of the normal ground operations of an airplane but principally in the touchdown, roll-out, and taxi phases. The wear which occurs in the touchdown phase is evidenced by runway rubber deposits; however, this wear is generally considered to be less significant than that due to the braking and cornering required during the roll-out and taxi phases. With the recent advent of runway grooving, tire wear in the form of chevron-cutting damage now poses a potential economic problem for some airplanes in the touchdown phase. The purpose of this paper is to review the results of current tire-wear research in two specific areas: namely, chevron cutting and wear as related to the braking cycle. The contribution to tire wear attributed to cornering will be the subject of future research.

CHEVRON CUTTING

An illustration of chevron-cutting tire damage resulting from the touchdown of an airplane on a grooved surface is given in figure 1. This figure presents a photograph of one of four tires which experienced chevron cutting and a photograph of the corresponding touchdown skid patch on the grooved surface. The term "chevron cutting" is derived from the general shape of the superficial cuts in the damaged area. Visual inspection of airplane tires at airports having grooved runways indicated that only large tires under high inflation pressures experienced this type of damage. Because of the limited number of existing grooved runways, chevron cutting does not appear at the present time to be a detriment to tire service life. However, as more and more runways are grooved, chevron cutting has the potential of becoming a tire wear problem for airplanes using large, high-pressure tires. Factors which were believed to affect chevron cutting include those associated with the touchdown velocity, the runway surface, and the tire. Both the airplane forward speed and sink rate at touchdown would appear to be contributing factors to chevron cutting. In addition to the grooving pattern, the runway material composition (concrete and asphalt, as examples) and surface finish could possibly influence chevron-cutting damage. Tire parameters such as size, tread design, rubber compounding, and inflation pressure were also believed to be potential factors. A research program was

initiated at the Langley landing-loads track in an effort to isolate some of these many potential variables and to study their effects on tire chevron cutting.

Test Apparatus

Tires.- Figure 2 is a photograph of the four test tires used in this investigation and their corresponding footprints under a 66.8-kN (15 000 lb) vertical loading. All tires were of the same size, 49 by 17, which has a history of susceptibility to chevron cutting. Tires I, II, and III were recapped tires; tire I was equipped with a tread having five equally spaced, wide grooves, and tires II and III were recapped by the same manufacturer but with four- and five-groove tread patterns, respectively. Tire IV was a new tire of five unevenly spaced narrow grooves. Tests at the track revealed that chevron cutting occurs at the spot on the tire which initially contacts the surface, and the damage is the result of the scrubbing action of the tire as it skids over the grooves. Chevron cutting appears to cease when the tire commences to rotate as evidenced by comparing the width of the tire damage area of figure 1 with that of the corresponding skid patch. Thus, the larger the tire, the greater the inertia and the corresponding force necessary to induce rotation which helps to explain why the small tires of fighter-type airplanes are not susceptible to chevron cutting.

Grooved surfaces.- The eight grooved test sections employed in this study are described in figure 3 and consist of grooving patterns generally considered for airport use. These patterns are defined by the spacing between the grooves, the groove width, and the groove depth and consist of rectangular grooves, with and without rounded troughs and corners. All grooves were in the transverse direction (i.e., perpendicular to the runway) and were formed by two techniques: combed, wherein the surface was raked or combed while in the plastic state, and sawed, the technique generally employed in grooving runways and roads. The test surface materials consisted of concrete sections having a transverse brush finish, a section of float-finish concrete, and a section of small aggregate asphalt.

Test Results

Preliminary results from tests to evaluate chevron-cutting damage as affected by the groove pattern, the surface finish, and tire differences are presented in the sections which follow.

Effect of groove pattern.- Figure 4 summarizes the results of chevron-cutting damage as a function of horizontal touchdown velocity of one tire (tire I) on transverse brush-finish concrete for the groove patterns described by A to F in figure 3. The damaged volume is defined as the product of the affected area of the tire tread and the maximum cut depth. As an example, a damaged volume of 50 cm³ (3 in³) describes cuts

approximately 0.24 cm (3/32 in.) deep over a 30-cm (12 in.) circumferential distance in the two center ribs of tire I. The figure shows that there was no chevron cutting below approximately 85 knots with this tire and that the extent of the damage increased with increasing velocity; also, chevron cutting is essentially independent of the grooving patterns evaluated since the data can be faired by a single curve.

Effect of surface finish.- The effect of surface finish on chevron cutting is illustrated in figure 5. The figure presents the results of tests, again obtained with tire I, conducted on the float-finish concrete (pattern G), on the transverse brush-finish concrete (pattern C), and on the asphalt surface (pattern H). The data were derived from tests with the tire at its nominal inflation pressure p of 117 N/cm² (170 psi) and overinflated to a pressure of 145 N/cm² (210 psi). The figure shows that the grooved transverse brush-finish concrete is less damaging to the tire than grooved float-finish concrete. The lower damage levels associated with pattern C may be attributed to the edges of the grooves which are less distinct and more rounded than those sawed into the float-finish concrete. This assumption helps to explain the low damage level for asphalt pattern H which was observed to have even more rounded grooves. Thus, it would appear, on the basis of these test results, that tires are least susceptible to chevron cutting on asphalt surfaces, and, for concrete surfaces, a transverse brush finish would provide for better tire wear while possibly improving runway drainage. The figure also points out that the extent of tire damage is essentially independent of the two test inflation pressures. Limited testing at 69 N/cm (100 psi), however, did indicate that the tire was less susceptible to chevron cutting at low inflation pressures.

Effect of tire differences.- Figure 6 shows the difference in the susceptibility of three of the test tires to chevron-cutting damage on a selected groove pattern. The data indicate that tire I was most susceptible to cutting and that tire III showed no evidence of chevron cutting up to 112 knots - the maximum test speed available with the apparatus. Differences in the damage levels may be explained, at least partially, by differences in the tread patterns of these tires which are reflected in the net bearing pressure in the tire-pavement interface. Another contributing factor to these differences in tire damage may be the composition of the rubber compound. The composition of each tire is unknown; however, differences in the failure modes of the tires, as illustrated in figure 7, suggest differences in the rubber compounding. The damage of tire I has a "gouge" appearance, whereas that of tire IV shows distinct cuts in the tire tread.

Future Research

Future chevron-cutting research planned will entail additional testing at the Langley landing-loads track and a limited flight test program. The testing at the track will conclude the evaluation of the effects of various grooving patterns on tire touchdown damage

and the planned flight test program will be a joint FAA-USAF-NASA effort to extend the track results to include realistic touchdown velocities.

TIRE WEAR DURING BRAKING

The second current research effort in the field of tire wear is that related to braking during the landing roll-out and taxi phases of airplane ground operations. An example of the braking response of a smooth-tread automotive tire at a yaw angle ψ of 4° is given in figure 8, where the drag- and side-force friction coefficients are plotted as a function of the wheel slip ratio. Slip ratio is a relationship involving the braked and unbraked wheel angular velocity and equals 0 when the wheel is unbraked or freely rotating and equals 1.0 when in a locked wheel skid. The curve for the drag-force friction coefficient, which is a measure of the braking capability, is typical for tires on a dry surface, peaking at slip ratios between 0.1 and 0.2 and then decreasing to a lower level when the wheel is locked. Correspondingly, the side-force friction coefficient, which is a measure of the cornering or steering capability of the tire, decreases from a maximum at no braking to 0 when the wheel is no longer rotating. Thus, in the interest of safety, it is desirable to maintain low slip ratios which would provide near-maximum cornering capability to keep the aircraft from leaving the side of the runway during cross-wind landing conditions. Tire life at a slip ratio of 1.0 can be measured in terms of meters (feet) along the runway since wear is limited to an isolated area of the tire. At slip ratios less than 1.0, the tire is rotating and the wear is distributed around the tire periphery which thereby increases tire life, until at a slip ratio of 0, tire life is measured in thousands of kilometers (miles). The variation of tire wear with slip ratio between the locked wheel and the freely rotating states is unknown and is the subject of this research program.

Test Approach

Preliminary tests to evaluate tire wear during braking were conducted with a smooth-tread automotive tire under a vertical loading of 4.67 kN (1050 lb). The testing technique involved gearing the tire to a driving wheel of a ground test vehicle to provide operations at a constant preselected slip ratio on test surfaces which included grooved and ungrooved asphalt and concrete runways. Tire wear was determined by weighing the tire prior to and at intervals over test distances which, in some instances, extended to 56 km (35 miles).

Test Results

In figure 9, the tire wear rate in grams per kilometer (pounds per mile) and the corresponding drag friction coefficient are presented as a function of slip ratio for operations on an asphalt runway with a very abrasive overlay. The figure shows an approximate

linear variation of tire wear rate with slip ratio. The slight inflection noted in the curve at the low slip ratios may be attributed to the elastic behavior of the tire which would result in reduced relative slippage in the tire-pavement interface and, thus, lower wear rates. The corresponding friction coefficient, obtained by monitoring the vertical and drag loads on the tire during testing, is shown to vary with slip ratio in a manner similar to that of figure 8 which was obtained during an actual braking cycle. It is significant to note that present-day antiskid brake controls customarily operate about the maximum friction coefficient and use the spin-down of the tire to serve as an input signal to reduce brake pressure. Thus, under antiskid braking, the tire is forced to operate at slip ratios which are somewhat in excess of that associated with peak braking. Based upon the data from these tests, antiskid operations at slip ratios up to 0.3, which are not uncommon, can extend the tire wear rate to approximately 140 g/km (0.5 lb/mile). However, similar friction coefficient levels can be developed at a lower slip ratio where the wear rate is considerably reduced and where increased cornering capability is provided. Thus, it would appear to be not only safer but economically advantageous to have a brake control system capable of limiting the slip ratio to the minimum necessary to produce the required braking force.

Figure 10 presents the results from preliminary tests to evaluate the effects of runway grooving on tire wear. Data obtained at a test speed of 17.4 knots are included in the figure which describe the tire wear rate on grooved and ungrooved asphalt and concrete test surfaces as a function of slip ratio for slip ratios up to that for maximum friction. The data indicate that over this range of slip ratios, tire wear is unaffected by runway grooving. The curves of this figure are not intended to imply that tire wear is more severe on all concrete runways than on all asphalt runways; however, the differences in the curves do suggest that runway surfaces can be rated on the basis of tire wear.

The test apparatus is currently undergoing modification to accommodate an airplane tire (22 x 5.5, 8 ply) and future plans include tire wear studies which involve a variety of runway surfaces and test conditions.

CONCLUDING REMARKS

Tire wear studies are currently underway to explore chevron-cutting damage resulting from airplane touchdown on grooved runways and to examine the wear attributed to airplane braking operations. From the preliminary results of these studies the following observations are made:

Chevron cutting occurs at the spot on the tire which initially contacts the surface and the damage is the result of the scrubbing action of the tire as it skids over the grooves prior to any rotation. Chevron cutting has been observed on only large tires which,

because of their high inertia, require a large force to induce rotation. Furthermore, inflation pressure appears to be a contributing factor since large low-pressure tires appear to be less susceptible to chevron-cutting damage than do similar size high-pressure tires. Studies at the Langley landing-loads track indicate that chevron cutting is primarily a function of the airplane touchdown velocity. These studies further show that, with respect to the runway surface, chevron-cutting damage is essentially independent of the grooving patterns generally considered for airport use but strongly dependent upon the nature of the surface finish. Tests with different tires of the same size also indicate that tire tread pattern and/or rubber composition significantly affect the extent of chevron-cutting damage.

The results from tire wear measurements during braking indicate the economic advantage of an airplane brake control system capable of limiting the wheel slip ratio to the minimum necessary to produce the required braking force. Additional results from limited tests in the low slip-ratio range suggest that tire wear is unaffected by runway grooving but, in view of differences in the wear rate associated with the various surface materials, do suggest that runways can be rated on the basis of tire wear.

TIRE DAMAGE FROM TOUCHDOWN ON GROOVED RUNWAY

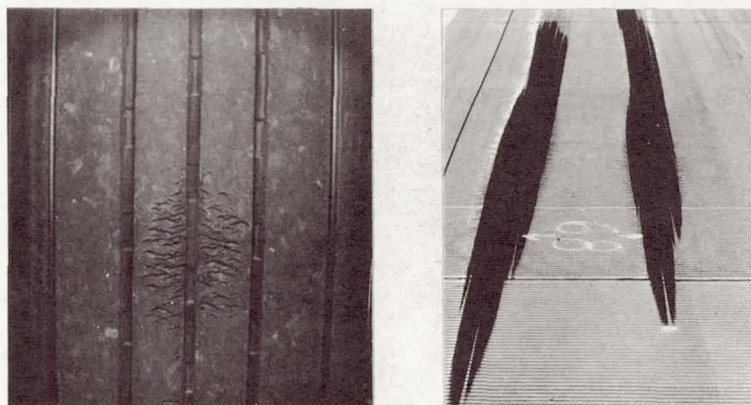


Figure 1

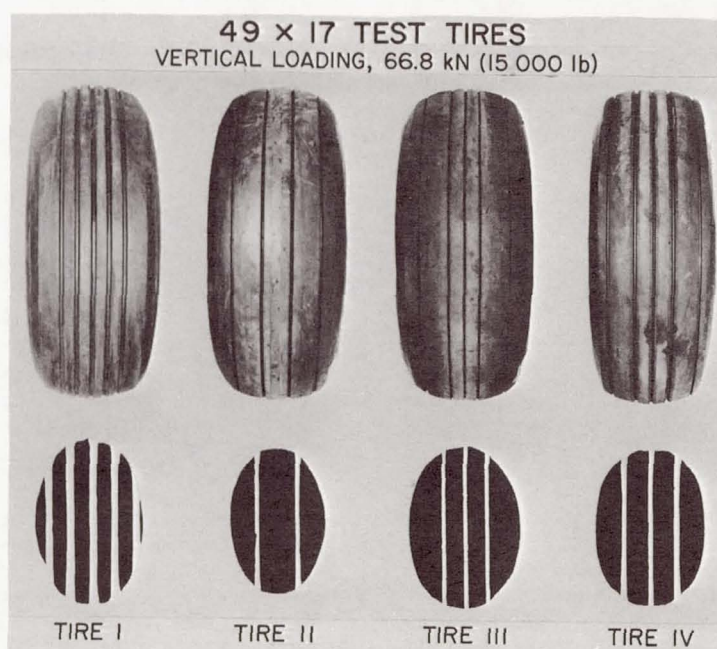


Figure 2

GROOVED TEST SECTIONS

GROOVING PATTERN				GROOVING TECHNIQUE	SURFACE AND FINISH
cm		in.			
1.9 × .3 × .3	A	3/4 × 1/8 × 1/8		COMBED	CONCRETE, BRUSH
3.2 × .6 × .6	B	1-1/4 × 1/4 × 1/4		"	"
"	C	"		SAWED	"
"	D	"		"	"
"	E	"		"	"
3.2 × .5 × .5	F	1-1/4 × 3/16 × 3/16		"	"
2.5 × .6 × .6	G	1 × 1/4 × 1/4		"	CONCRETE, FLOAT ASPHALT, SMALL AGGREGATE
"	H	"		"	

Figure 3

EFFECT OF GROOVE PATTERN ON CHEVRON CUTTING CONCRETE; BRUSH FINISH

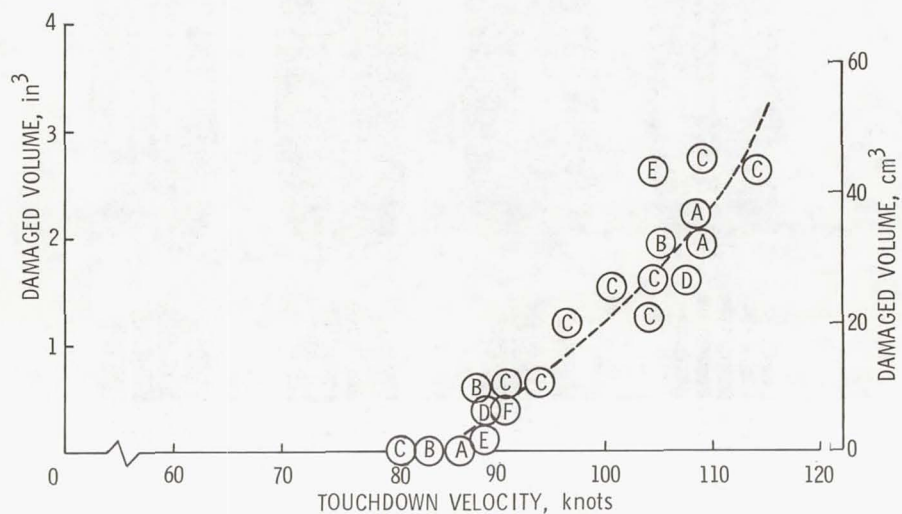


Figure 4

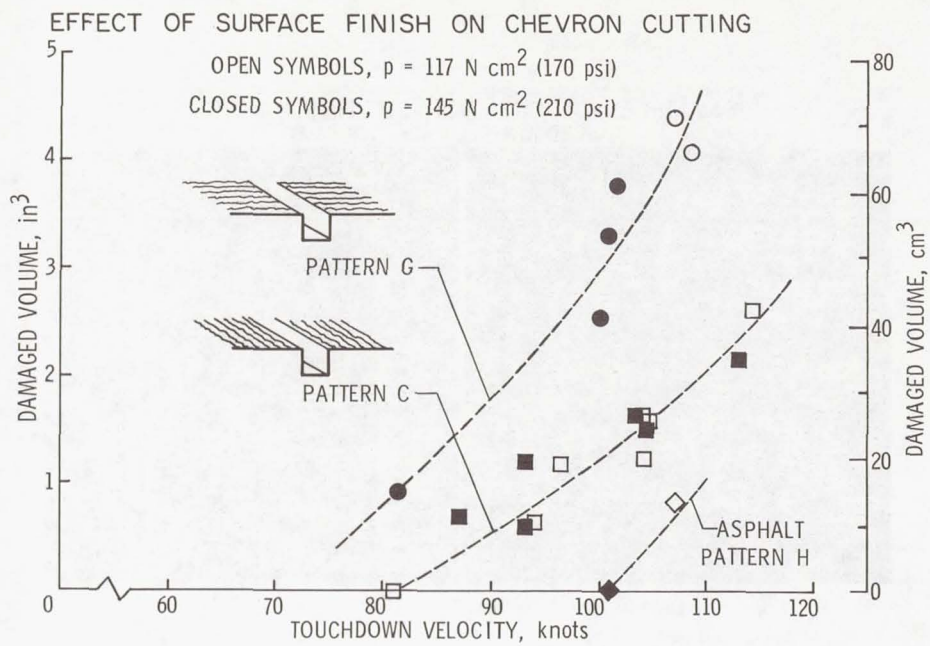


Figure 5

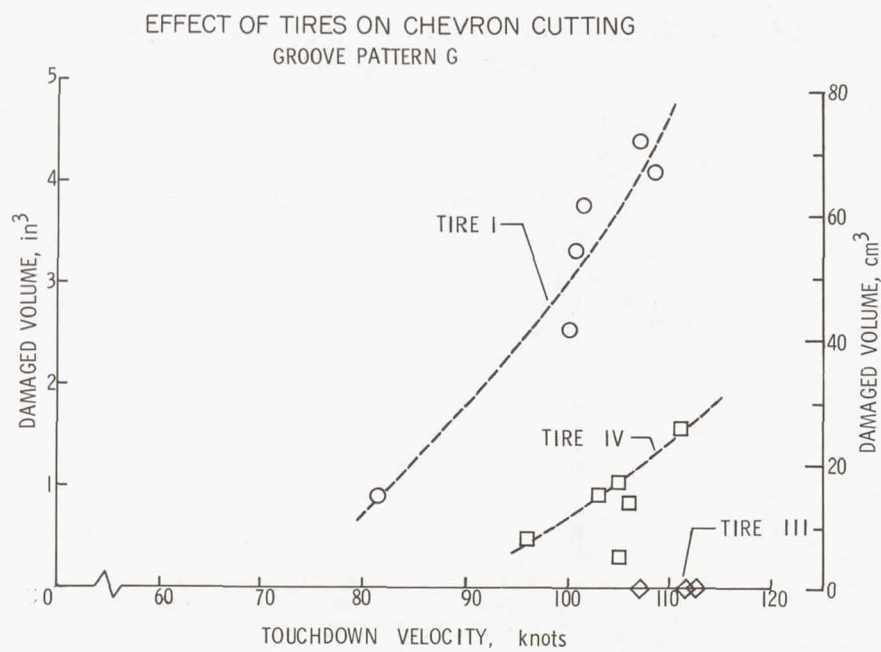


Figure 6

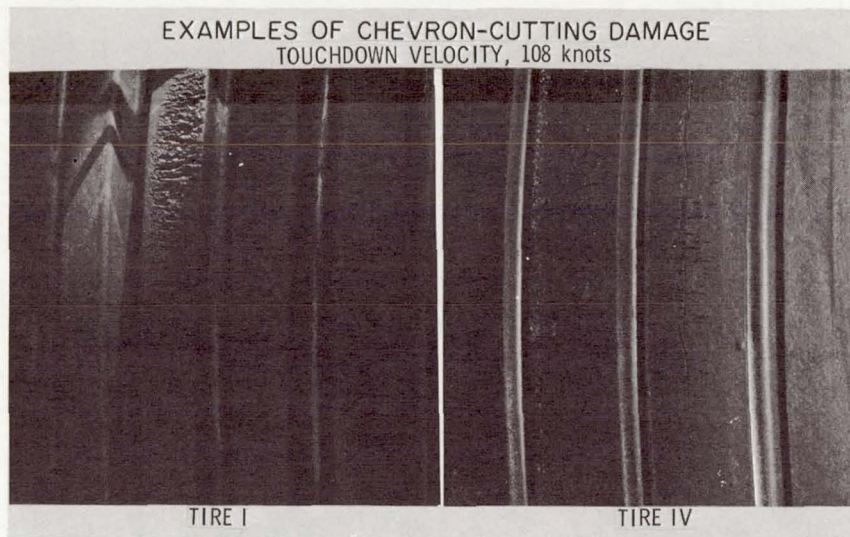


Figure 7

EFFECT OF SLIP RATIO ON FRICTION COEFFICIENTS
SMOOTH-TREAD TIRE; $\psi = 4^\circ$

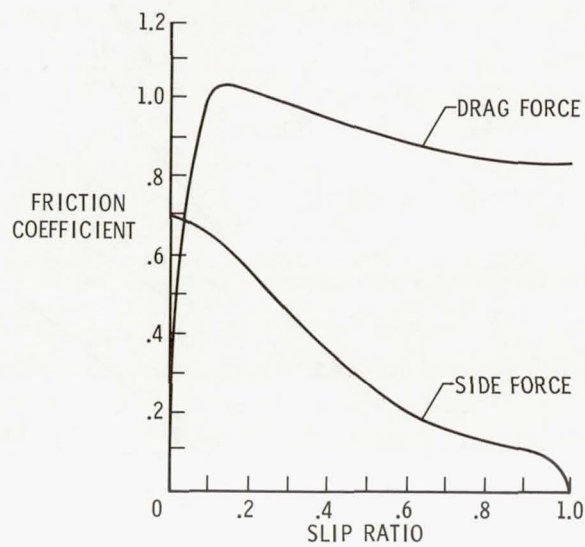


Figure 8

EFFECT OF SLIP RATIO ON TIRE WEAR AND FRICTION COEFFICIENT
ASPHALT SURFACE; SMOOTH-TREAD TIRE

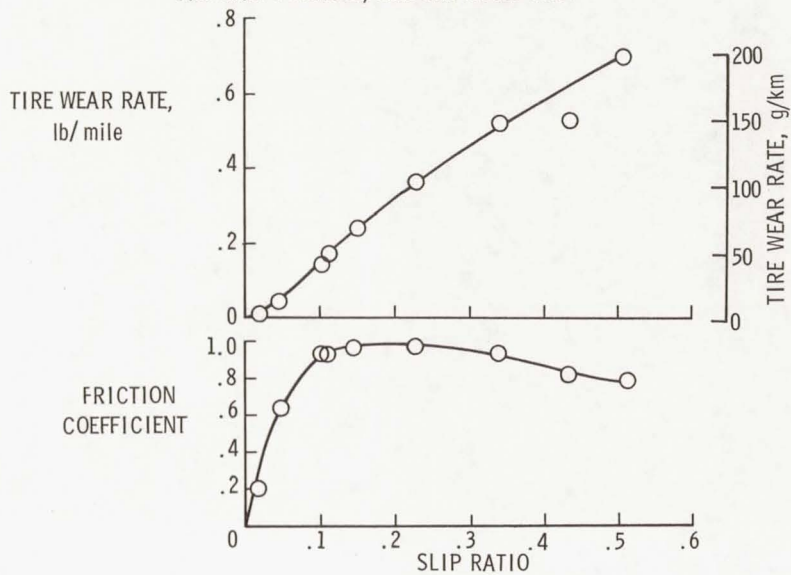


Figure 9

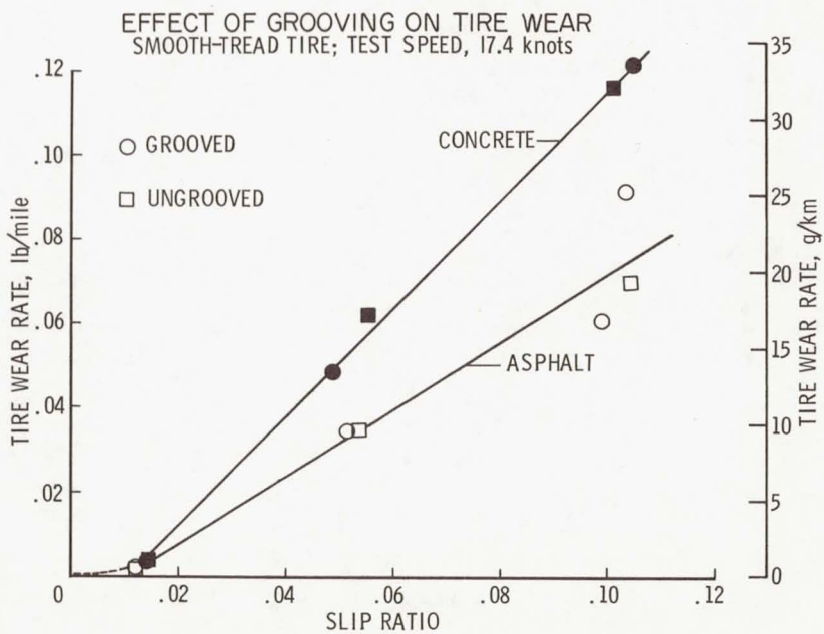


Figure 10

Page intentionally left blank

APPLICATION OF ADVANCED AERODYNAMICS TO FUTURE TRANSPORT AIRCRAFT

By Albert L. Braslow and Theodore G. Ayers
Langley Research Center

INTRODUCTION

The performance of long-range subsonic transport aircraft is limited by the formation of shock waves that form over the wings as the forward speed approaches the speed of sound. Significant improvements in performance have been made over the years through the use of improved engines, wing sweep, and modified wing sections. Recent advances in the design of wing sections offer a new possibility of further significant improvements in performance. These sections are referred to as supercritical airfoils, and their development and integration into airplane configurations are the result of seven years of intensive research primarily by Dr. Richard Whitcomb of the Langley Research Center.

The purpose of this paper is to review briefly the status of this emerging technology of supercritical aerodynamics and the program underway to promote its application to improved transport aircraft.

SYMBOLS

b	span
g	acceleration due to gravity
C_L	lift coefficient
C_m	pitching-moment coefficient
C_p	pressure coefficient
M	Mach number
t/c	thickness-chord ratio
W/S	ratio of weight to wing area

y span location
 α angle of attack

SUPERCritical AIRFOIL

The fundamental difference between a conventional wing section and a supercritical wing section should be considered first. Figure 1 is a comparison of the flow fields and the pressure distributions. As an airplane approaches the speed of sound, the flow over the curved upper surface accelerates to local velocities in excess of sonic on both airfoils. This is indicated by the pressure coefficients above the sonic value and by the shaded areas of the flow fields. For each airfoil, the supersonic flow is terminated by a shock wave, indicated by the rapid increase in pressure. The shock on the conventional airfoil is usually strong enough to separate the flow from the surface and thereby causes a large drag increase, severe airfoil buffeting, and stability and control problems. The supercritical airfoil has a reduced upper-surface curvature with reduced velocities ahead of the shock wave. The associated shock is weaker, and the flow on a properly designed section is able to continue to the trailing edge without separating. The drag is appreciably lower, buffeting is eliminated, and control effectiveness is maintained. To compensate for the reduced lift on the upper surface of the supercritical airfoil resulting from the reduced curvature, the airfoil has increased camber near the trailing edge.

APPLICATIONS TO TRANSPORT AIRCRAFT

The characteristics of the supercritical airfoil suggest two possible applications to transport aircraft (fig. 2). For aircraft designed for moderate subsonic speeds, for example, about Mach 0.70 to 0.85, the concept may permit reductions in structural weight through the use of thicker wing sections or reduced sweep, or both, without penalizing the aerodynamic performance. These weight reductions might permit an increased payload or increased fuel capacity for longer range, or they might be traded to compensate for possible weight penalties associated with techniques for reducing engine noise and pollution emissions. The other application of supercritical technology to transport aircraft may be to permit efficient cruise very near the speed of sound by delaying the transonic drag rise. An increase in speed has passenger appeal because of the enroute time saved, although, of course, improvements are also required for the ground phase of air travel. Increased speed should also decrease the direct operating cost (DOC) because range is a direct function of Mach number and also because it may be possible to increase aircraft utilization. Whether or not a reduced DOC can be attained is currently being studied.

Progress is being made in the areas of theory, wind-tunnel experiments, and exploratory flight research on both possible applications. This paper concentrates on the experimental aerodynamic results that have a significant influence on transport operating considerations.

Increased Structural Efficiency

The possible application to thickened wings of increased structural efficiency is first considered because some early flight-test results are available. The test vehicle for the supercritical wing is a modified T-2C trainer (fig. 3), and the program is being conducted by North American Rockwell Corporation at Columbus, Ohio, as a joint effort with the U.S. Navy and NASA. The left airplane is the basic airplane with a 12-percent-thick conventional wing, and the right airplane has a 17-percent-thick supercritical wing designed by Mr. William E. Palmer of North American Rockwell Corp. The modified wing was obtained by bonding balsa to the original wing structure and overlaying it with fiber glass. This airplane, of course, is not a transport, and the wing-fuselage arrangement has not been optimized. It does, however, provide a reasonable test bed for flight evaluation of the aerodynamic characteristics of the wing. Some very encouraging results are being obtained.

In figure 4 the increment in wing-section drag-rise Mach number from the value obtained with the conventional 12-percent-thick wing is plotted against wing thickness-chord ratio at the design lift coefficient of 0.5. The use of supercritical sections permitted the increase in thickness to 17 percent with no decrement in drag-rise Mach number. Wind-tunnel tests indicate that a similar increase in thickness for a conventional wing would decrease the drag-rise Mach number by about 0.08.

In figure 5 buffet boundaries are plotted in the form of altitude against Mach number. The solid lines are for the supercritical wing, and the dashed lines are for the conventional wing. The results for the conventional wing are based on flight data, whereas the results for the supercritical wing include wind-tunnel data (lines) and flight data (circles). For each wing, 1g and 1.5g boundaries are presented. Good agreement between the wind-tunnel and flight results for the supercritical wing is apparent. The maneuvering g margin (the altitude increment between the design cruise altitude and the buffet boundary at a constant Mach number) is improved for the thicker supercritical wing. The low-speed cruise margin (the Mach number increment between the design cruise Mach number and the low-speed buffet boundary at a constant altitude) is also improved. The overspeed buffet margin (the Mach number increment between the design cruise Mach number and the high-speed buffet boundary at a constant altitude) is slightly reduced for the thick supercritical wing as compared with the much thinner conventional wing. The same increase in thickness of a conventional wing, however, would cause a much larger reduction in the high-speed boundary, as indicated by the reduction in drag-rise Mach number.

Another interesting result of the flight tests was obtained at low speeds. In figure 6 lift coefficient is plotted against angle of attack for the conventional wing with flaps up and down and for the supercritical wing with flaps up. Maximum lift for the supercritical wing with flaps up was higher than for the conventional wing with flaps down. This result can be attributed to the much larger leading-edge radius of the supercritical wing. The T-2C flight program is continuing to measure lateral-directional stability and control characteristics and to evaluate the flying qualities at both high and low speeds. In addition, detailed boundary-layer measurements are to be made in order to assist in the understanding of boundary-layer characteristics in the presence of local shocks and in extreme pressure gradients.

A final point to be made regarding the early flight results concerns the possible sensitivity of the supercritical wing to local variations in contour. The wing being flown in the T-2C program is far from ideal. Although special care was taken to maintain a fair leading-edge region, many local waves exist rearward of this region. It is very encouraging that the favorable drag, buffet, and lift characteristics were obtained in the presence of these surface waves.

Cruise Near a Mach Number of 1

What is involved in using supercritical technology to push cruise Mach number to or near Mach 1? Of major importance in attaining a Mach number of 1 is the need for very careful integration of the wing, fuselage, tail assembly, and propulsion system. Figure 7 is a photograph of a configuration that Dr. Whitcomb is developing for cruise at a Mach number of 1. It is a three-engine configuration with two engines aft mounted on the fuselage and with one engine mounted in the vertical tail of a T-tail assembly. The forebody shape, the area ruling of the fuselage in the region of the wing, the extension of the wing chord at the root, the contouring of the fuselage in the vicinity of the engines, the extension of the engine pylons, and the supercritical airfoils used for the tail surfaces are all critical features in obtaining the combination of a good overall area distribution with local contours that avoid adverse interactions between the shock and boundary layer. Other investigations are in progress on configurations with two and four wing-mounted engines.

Wind-tunnel drag results for this three-engine configuration are presented in figure 8. Drag coefficient at the design cruise lift coefficient is plotted against Mach number for the supercritical configuration and for early and current jet transports. The current-generation jets attained an increase in drag-rise Mach number primarily through the use of increased sweep and new airfoil shapes. It appears that through use of the supercritical airfoil, additional increase in sweep, and very careful area ruling, a further increase in drag-rise Mach number of about 15 percent can be attained.

An indication of the buffet characteristics of a Mach 1 transport wing was obtained in wind-tunnel tests of an F-8 airplane model incorporating the same transport-type wing used in the three-engine sonic-transport configuration. These results are presented in figure 9 (solid lines) and are compared with buffet boundaries of a conventional-wing transport (dashed lines). The same wing loading was assumed for both airplanes to provide a realistic comparison. For the sonic-transport wing, the maneuvering g margin and the low-speed cruise margin appear to be about equal to the margins for the conventional transport. No data are available yet to define the overspeed buffet boundary for the sonic-transport wing, but there is no reason to anticipate that it is any worse than for the conventional transport at the lower design Mach number.

As indicated in the figure, the increased speed of a sonic transport may permit flight at a higher altitude than the current transports because of the ability to attain at least the same buffet-free lift coefficient at the higher speed. The actual cruise altitude, of course, will also depend on other factors, such as the cruise wing loading and the availability of suitable engines for the conditions of high altitude and high Mach number. Should this higher cruise altitude be possible, another advantage of sonic transports is that they would not add to the congestion in the existing cruise corridors.

The longitudinal stability problem associated with sweptback wings is of some concern with respect to a sonic transport. The increased sweepback of this airplane would be expected to aggravate the pitch-up due to flow separation at the wing tips as angle of attack is increased. Figure 10 presents plots of pitching-moment coefficient against angle of attack for the F-8 model with the transport-type supercritical wing. At a Mach number of 0.99, the pitch-up (dashed curve) occurs at an angle of attack of about 6° , which is above the cruise value of about 3° . Previous experience indicates that two conditions that exist in flight, but not in the wind tunnel, will alleviate the severity of the pitch-up. One is the increased Reynolds number, and the other, an unloading of the wing tips due to wing deflection. Both conditions should delay tip separation to higher angles of attack. In any event, an attempt has been made to provide a positive means of controlling the pitch-up. It consisted of a vortex generator located on the wing lower surface near the leading edge at 60 percent of the semispan. The vortex formed runs along the upper surface and effectively blocks the outward flow of the boundary layer, attenuating the separation at the tip and the associated pitch-up, as shown by the solid line. The buffet boundaries presented in figure 9 were obtained without the vortex generator. Addition of the generator should, of course, improve the buffet margins as well as the pitch-up characteristics.

Why were models of an F-8 airplane tested with a supercritical wing? The reason is that the NASA Flight Research Center is now conducting a flight-test program of a Mach 1 transport-type supercritical wing installed on an F-8 airplane (fig. 11). Like the

T-2C airplane, the F-8 is not representative of a complete transport configuration but it provides a good test bed for the wing. For this flight-test program, the complete F-8 wing was replaced with the supercritical wing.

The primary objectives of the flight-test program are

1. To demonstrate the high force-break Mach number indicated in the wind tunnel because there is still some question about the reliability of wind-tunnel results at a Mach number of 1
2. To evaluate the maneuver and speed margins, also for the same reason
3. To determine off-design performance nearer full-scale transport conditions than can be obtained in the wind tunnel (for example, the effectiveness of the vortex generator in controlling pitch-up)
4. To identify problems associated with actual high-lift and lateral-control devices
5. To determine the sensitivity of the wing to contour variations associated with manufacturing processes and deformations of the wing under flight loads

Since the first phase of the program has only recently begun, no quantitative data are available. The emphasis of the early flights is on checking aircraft systems and on broadly defining the flight envelope. Flights have been made up to a Mach number of 0.95 so far, and all systems are operating satisfactorily. The wing presently on the airplane is a rather stiff "boiler plate" wing, and therefore, complete evaluation of the effects of wing deformations cannot be accomplished. In addition, high-lift devices of the type used on transport aircraft are not included. Consideration, therefore, is being given to a "follow-on" program with a wing representing transport flexibility characteristics and with representative high-lift devices.

CONCLUDING REMARKS

Although the emphasis of this paper has been on aerodynamic considerations, it is important to know that advances are being pursued in all areas of technology that offer a possibility of improving the characteristics of a next-generation long-range transport. In addition to the work in aerodynamics, investigations are proceeding in the areas of propulsion, structures, structural materials, flight dynamics, avionics, environmental factors, and aircraft systems. Tradeoffs among these various technology areas are being studied to define potential aircraft with reduced adverse effects on our environment and with improved efficiency, productivity, and safety.

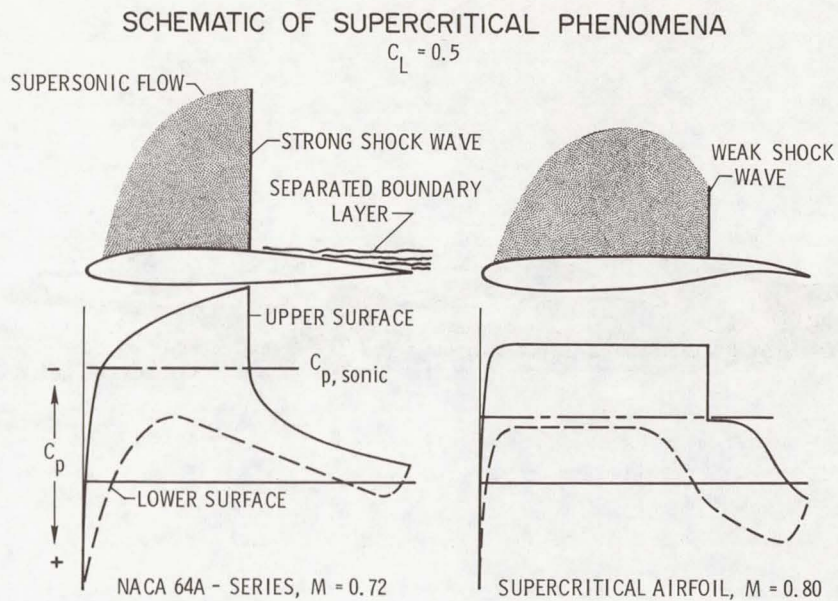


Figure 1

POSSIBLE APPLICATIONS OF SUPERCRITICAL TECHNOLOGY TO TRANSPORT AIRCRAFT

- MAY PERMIT REDUCTIONS IN STRUCTURAL WEIGHT THROUGH USE OF THICKER WING SECTIONS OR REDUCED WING SWEEP
- MAY PERMIT EFFICIENT CRUISE VERY CLOSE TO THE SPEED OF SOUND BY DELAYING TRANSONIC DRAG RISE

Figure 2

T-2C AIRPLANES

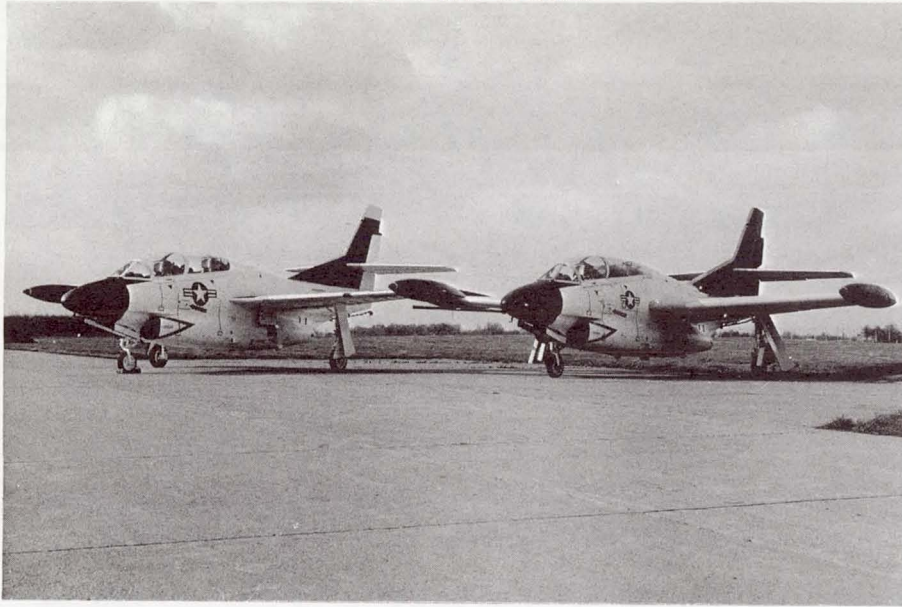


Figure 3

INCREMENTAL DRAG-RISE MACH NUMBER — T-2C WING SECTIONS $C_L = 0.5$

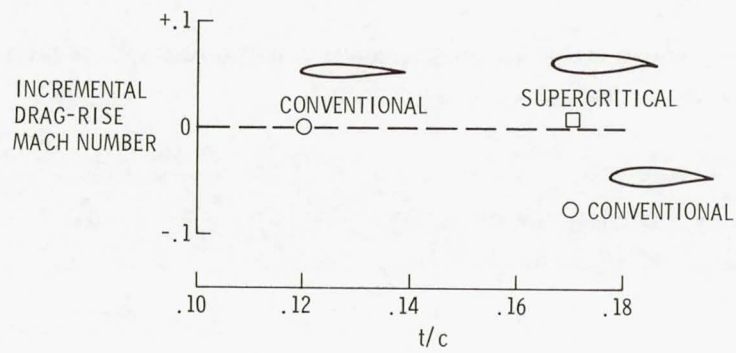


Figure 4

BUFFET BOUNDARIES-T-2C

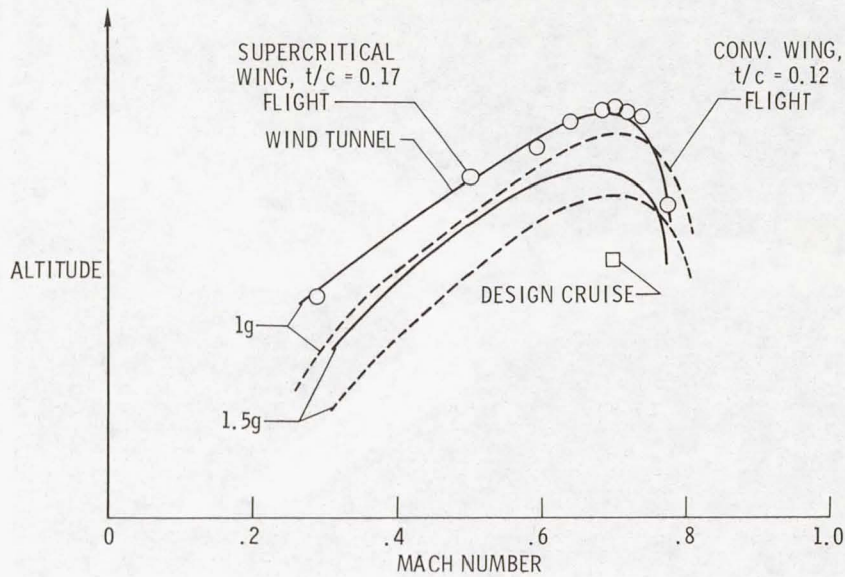


Figure 5

LIFT CHARACTERISTICS-T-2C AIRPLANE LOW SPEED; IDLE POWER

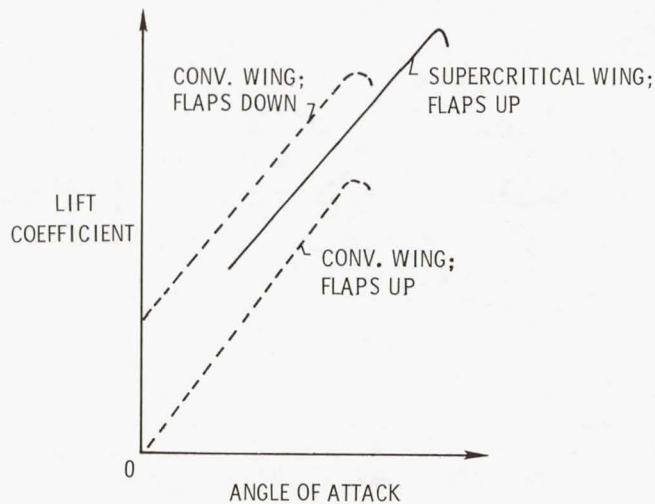


Figure 6

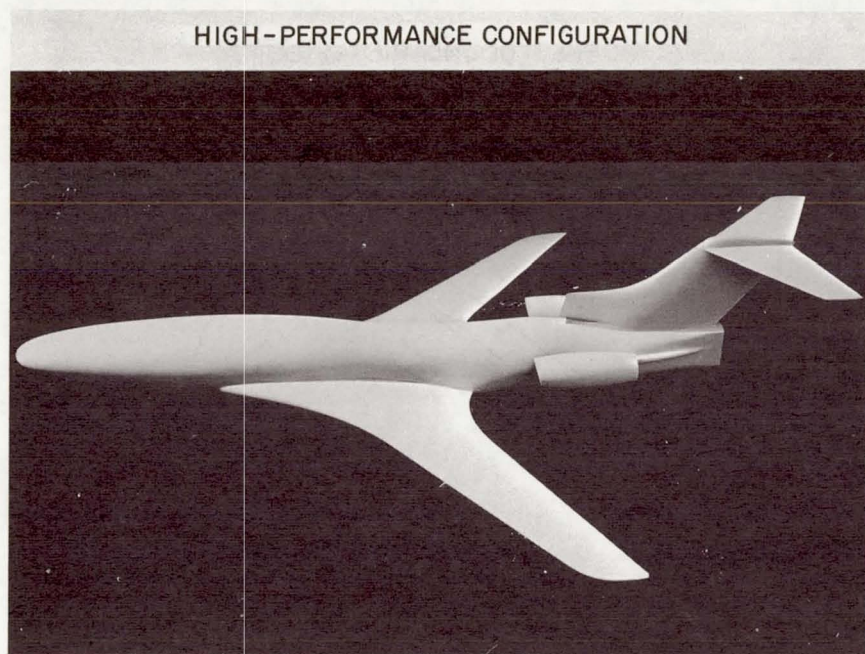


Figure 7

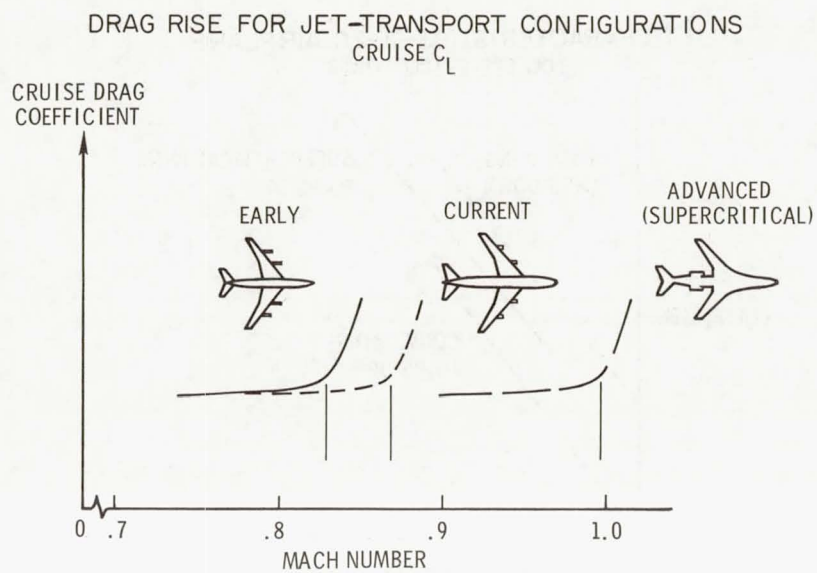


Figure 8

BUFFET BOUNDARIES - CONVENTIONAL AND SUPERCRITICAL WINGS

$$W/S = 4.07 \text{ kN/m}^2 \text{ (85 lb/ft}^2\text{)}$$

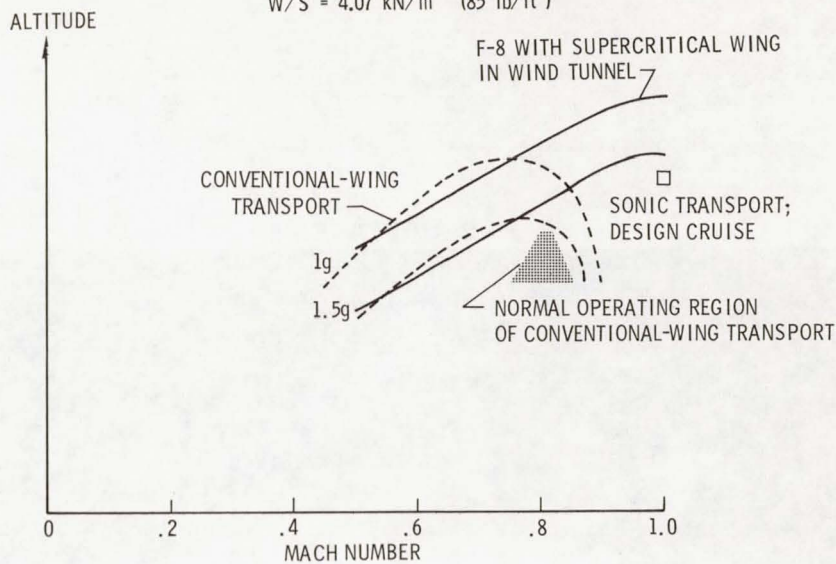


Figure 9

VORTEX GENERATOR EFFECTS F-8 WITH SUPERCritical WING; $M = 0.99$

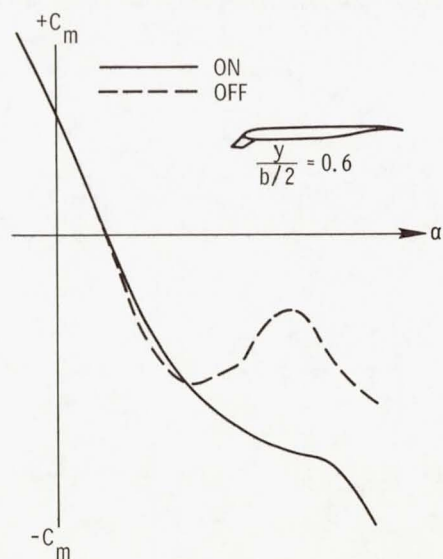


Figure 10

F-8 AIRPLANE



Figure 11

FLIGHT EVALUATION OF A DISPLAY FOR STEEP APPROACH

By R. Earl Dunham, Jr., Jack J. Hatfield,
Henry C. Elkins, and Richard H. Sawyer
Langley Research Center

INTRODUCTION

Since the last conference on operating problems (ref. 1) NASA has conducted and reported on studies of steep instrument approaches with 11 airplanes:

<u>Commercial transports</u>	<u>Business</u>
C-47	Learjet
DC-8	<u>Military</u>
880	T-33
990	F-8C
707-320	<u>Research</u>
720	367-80
727	

All the airplanes except the C-47 were turbine-powered, and all except the Boeing 367-80 research airplane were tested with conventional instrument displays and control systems. The results of these studies are documented in references 2 to 7.

In these tests, the two-segment glide slope illustrated in figure 1 was one of the steep-approach concepts investigated. Note that altitude is plotted to a scale about 10 times that for distance from glide-slope intercept. The two-segment glide slope concept consists of a steepened slope for the initial portion, a transition phase, and the conventional glide slope. Significant noise reduction is obtained on the ground under the steepened portion, both because of the increase in altitude compared with a conventional approach and because of the lower power required. Also investigated were single-segment steep glide slopes consisting of the steep slope down to about 150 meters (500 feet), at which altitude the landing flare was initiated. From a number of operational considerations, the two-segment glide slope was preferred in general over the single-segment glide slope.

For the airplanes tested, 6° was considered to be the maximum slope on which speed and flight path could be consistently controlled. With the airplanes having conventional displays and control systems, the pilots preferred the transitions from the steep to the conventional slope to be completed by an altitude of about 245 meters (800 feet) in order to have time to stabilize on the conventional glide slope before breakout at 60 meters (200 feet).

During these tests with the conventionally equipped jet transports, several problems connected with the operations on the steep approaches were noted. The guidance provided by the unmodified flight director or the cross-pointer indicators was inadequate for the transition from the steep to the conventional slope. There was also inadequate situation information for judgment on when to make throttle and attitude changes for this maneuver. The result was a tendency toward deviation below the glide slope during and after the transition. Correction of the deviation was a demanding task that greatly increased the pilot's workload and also increased the noise. Lack of capability for precise flight-path control in these airplanes and, in some cases, poor engine response at the low thrust level used on the steepened slope added to the difficulties.

TEST OBJECTIVES AND DISPLAY CONCEPT

This paper is concerned with the results of a preliminary investigation of a display concept designed to alleviate the problems of inadequate guidance and display information for making steep approaches. The $6^{\circ}/3^{\circ}$ two-segment glide slope was used for the task. The display concept evaluated is shown in figure 2. Vertical-situation information is presented to the pilot on an outside profile view of the position of the airplane relative to the glide slope. The airplane position, shown by the circle, moves from right to left across the graph as the approach progresses. An attached line indicates the airplane velocity direction by rotation about the circle. This display concept is similar to one investigated by the Air Force Flight Dynamics Laboratory (ref. 8) in simulator and flight tests for application to helicopter instrument approaches. To provide increased sensitivity for glide-path control near the ground, the display was divided into the three segments shown in figure 3: intercept, transition, and final. These segments were stacked vertically, creating the display format shown in figure 4; the intercept segment is at the top, the transition segment in the middle, and the final segment at the bottom. The segments overlap and two airplane symbols are provided so that the airplane position is not lost in the change from one segment to the next. The edges of the shaded area define the limits of conventional ILS guidance; that is, a deviation from the glide path to the edge of the shaded area is equivalent to full-scale needle deflection on a conventional glide-path deviation indicator.

The vertical-situation information provided by this display includes, in addition to the deviation from glide slope, the distances to intercept, transition, and breakout. Also, the pilot obtains qualitative information on altitude with respect to breakout. The velocity vector provides predictive information useful in making the flight-path changes at intercept and transition and in general flight-path management.

Lateral guidance is provided by the localizer deviation indicator at the bottom of the display. This information is in a form similar to that of a conventional localizer

deviation indicator – the circle moves horizontally to show deviation from course. The triangles depict the localizer boundary limits. For some tests, a velocity vector attached to the circle was used to provide horizontal-velocity information.

DISPLAY GENERATION METHOD

The display format was created by a unique method developed at the Langley Research Center. The method consists of synthesizing the display on the ground and transmitting it to the airplane by television. (See ref. 9.) The display is presented in the cockpit on a high-brightness monitor. This method is illustrated in figure 5. Airplane position and rates during the landing approach are obtained from a tracking radar and telemetered data from the airplane. These data are used to derive, by means of a computer, glide-slope and localizer deviation and velocity information. These signals are used either to drive conventional electromechanical flight instruments or to drive symbols on oscilloscopes. Television cameras are used to view the displays. The synthesized displays are created by video mixing the television images of the dynamic oscilloscope symbols and static background graphs. The picture of either the conventional flight instrument or the synthesized display is transmitted to the airplane and displayed on a TV monitor. In the synthesized vertical-situation display shown in figure 4, the circles and attached line symbols are images on oscilloscopes, and the rest of the display is a background image. The display generation method is an excellent, flexible research tool which provides the capability for study of a variety of display concepts.

FLIGHT-TEST PROGRAM

The vertical-situation display was developed and evaluated in a flight-test program with an Aero Commander airplane. The display installed in the airplane is shown in figure 6. Note that the format being studied at the time of the photograph did not include an intercept path. The apparent curvature of the upper segment is caused by the curvature of the face of the cathode-ray tube. Because of installation difficulties, the vertical-situation display could not be integrated into the panel to provide the best scan pattern arrangement. For comparative tests, the vertical-situation image was replaced by a televised image of a conventional cross-pointer deviation indicator.

Instrument flight was simulated by obscuring the evaluation pilot's outside view. The task was to intercept and follow a $6^{\circ}/3^{\circ}$ two-segment glide slope. An approach air-speed of 120 to 125 knots was used to simulate as closely as possible the approach speeds of jet transports. At the breakout altitude of 60 meters (200 feet), the safety pilot took over and initiated a go-around. The display development and initial evaluation phases of

the test program were conducted with four NASA research pilots. The final evaluation was conducted by five Air Line Pilots Association pilots.

RESULTS AND DISCUSSION

Operational Capability

Results from a typical approach with the Aero Commander airplane, with guidance provided by a picture of a conventional cross-pointer indicator televised to the airplane, are given in figure 7. Shown is the glide-slope tracking performance, the deviation of calibrated airspeed from nominal approach speed, and the throttle motions. The tracking results show that the pilot was able to follow the steepened path reasonably well; however, he was unable to anticipate the transition, as is evident by the deviation below the glide slope during transition and the delay in increasing power until into the transition. Recovery from this situation led to a loss of airspeed and several power changes. The total effect was extra noise during flight along the final glide-slope segment and a high workload for the pilot just before breakout.

Results from a typical approach with the same airplane, but with guidance provided by the vertical-situation display, are given in figure 8. The tracking results show that the pilot was able to follow the steepened slope very well. With this display, however, the pilot does not feel constrained to fly the glide slope tightly. During transition, when a deviation above the glide slope occurred, the pilot was not concerned as he could see that there was plenty of time to correct before breakout. By making a gradual correction of the flight path, the transition and approach to breakout were accomplished with only small variations in airspeed and only the one required power change.

A comparison of tracking performance for a number of approaches with the cross-pointer indicator and with the vertical-situation display is shown in figure 9. Note that the vertical scales for the two sets of data have been offset. Although the overall deviations from the glide slope are not significantly different for the two sets of data, the tracking performance with the cross-pointer deviation indicator is more oscillatory than that with the vertical-situation display. This oscillatory performance is apparently associated with the pilot's attempt to fly the glide slope tightly because of the lack of situation information and the poor deviation-rate information provided by this indicator. The smoothness of the tracking with the vertical-situation display, on the other hand, reflects the pilot's more relaxed attitude toward correcting deviations because of the improved situation information and deviation-rate information provided. Comparison of the tracking at altitudes approaching breakout at 60 meters (200 feet) shows much better overall control of the flight path with the vertical-situation display. It is evident that because the vertical-situation display furnishes better information with regard to where

the airplane is relative to the glide slope, where the airplane is headed, and the distance to transition and breakout, for example, the pilot is relieved of the tight flight-path control required with conventional instruments.

Pilots' Comments

In their evaluation of the vertical-situation display, the pilots indicated that the information could be readily interpreted – no reversal of sensing or control in pitch occurred, as can be the case with cross-pointer and flight-director instruments. Path control was easy – their ability and confidence in this task was enhanced. The transition was simplified; the pilot was able to choose his own rate. The sensitivity of the display, however, was considered too low for the tasks of determining arrival at the minimum ceiling, level-off at this height, or go-around. In addition, the pilots commented that the arrangement of the vertical-situation display with respect to the other instruments resulted in an undesirable instrument scan pattern which, for these tests, increased the task of lateral-directional control.

In general, the pilots recommended that the vertical-situation display be evaluated in a jet transport in order to include in the task the factors associated with size and with flight and engine characteristics.

CONCLUDING REMARKS

In conclusion, the vertical-situation display concept investigated appears promising as a source of vertical guidance and situation information for steep approaches. The results indicated better flight-path control, airspeed control, and power management than with a conventional cross-pointer indicator. The improved guidance and situation information provided by the vertical-situation display allowed considerably more freedom in flight-path management and made the task less demanding.

From a broader viewpoint, the vertical-situation display concept would appear to have potential for general application to the instrument approach task – on conventional as well as steep glide slopes, and for all classes of aircraft.

REFERENCES

1. Conference on Aircraft Operating Problems. NASA SP-83, 1965.
2. Hall, Albert W.; and McGinley, Donald J., Jr.: Flight Investigation of Steep Instrument Approach Capabilities of a C-47 Airplane Under Manual Control. NASA TN D-2559, 1965.
3. Hall, Albert W.; and McGinley, Donald J., Jr.: Flight Investigation of Steep Instrument Approach Capabilities of a T-33 Airplane Under Manual Control. NASA TN D-2775, 1965.
4. Zalovcik, John A.; and Schaefer, William T., Jr.: NASA Research on Noise-Abatement Approach Profiles for Multiengine Jet Transport Aircraft. NASA TN D-4044, 1967.
5. Zalovcik, John A.: Effect of Thrust and Altitude in Steep Approaches on Ground Track Noise. NASA TN D-4221, 1967.
6. Sawyer, Richard H.; and Schaefer, William T., Jr.: Operational Limitations in Flying Noise-Abatement Approaches. NASA TN D-5497, 1969.
7. Quigley, Hervey C.; Snyder, C. Thomas; Fry, Emmett B.; Power, Leo J.; Innis, Robert C.; and Copeland, W. Latham: Flight and Simulation Investigation of Methods for Implementing Noise-Abatement Landing Approaches. NASA TN D-5781, 1970.
8. Bondurant, Robert A., III; and Kearns, John H., III: V/STOL Vertical Situation Display. [Preprint] 690694, Soc. Automot. Eng., Oct. 1969.
9. Elkins, Henry C.; and Hatfield, Jack J.: Televised Graphic Displays for Steep Approach-to-Landing Research. The 1970 IDEA Symposium, Soc. Inform. Display, May 1970, pp. 86-87.

TWO-SEGMENT GLIDE SLOPE

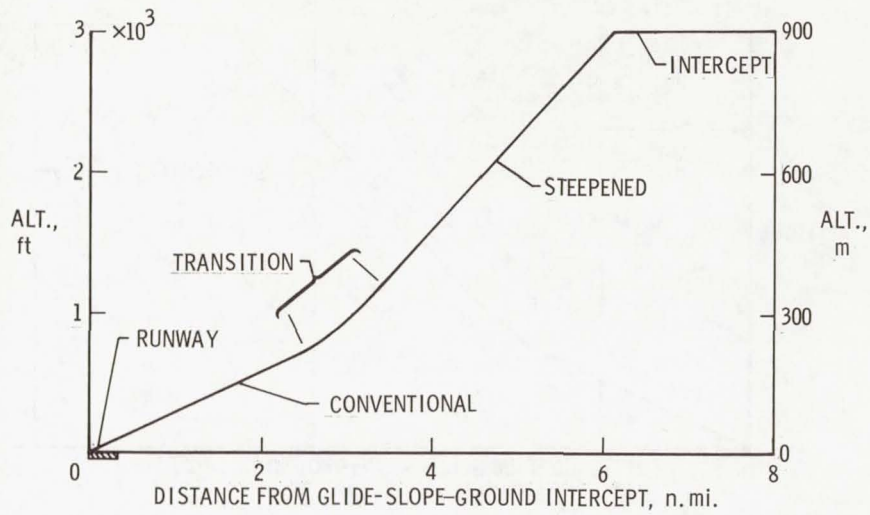


Figure 1

VERTICAL-SITUATION DISPLAY CONCEPT

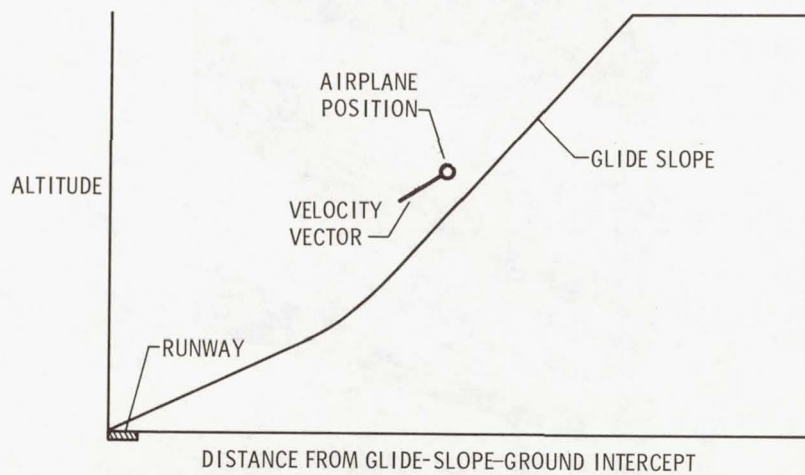


Figure 2

GLIDE-SLOPE SEGMENTS USED IN DISPLAY FORMAT

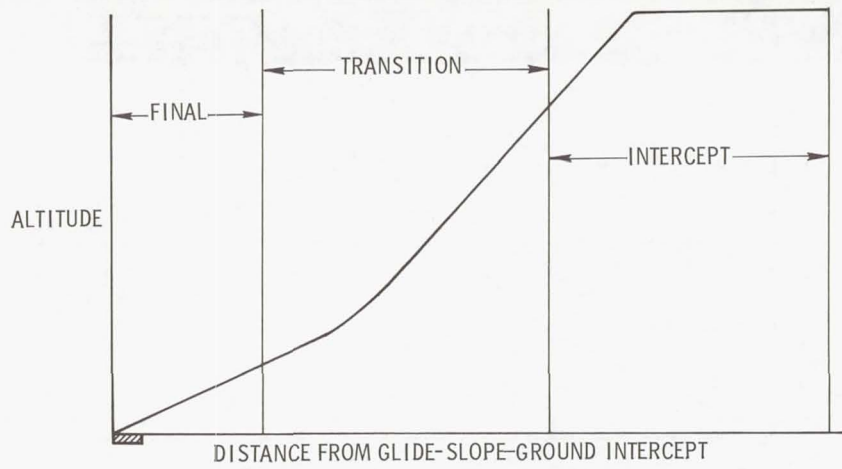


Figure 3

VERTICAL - SITUATION DISPLAY

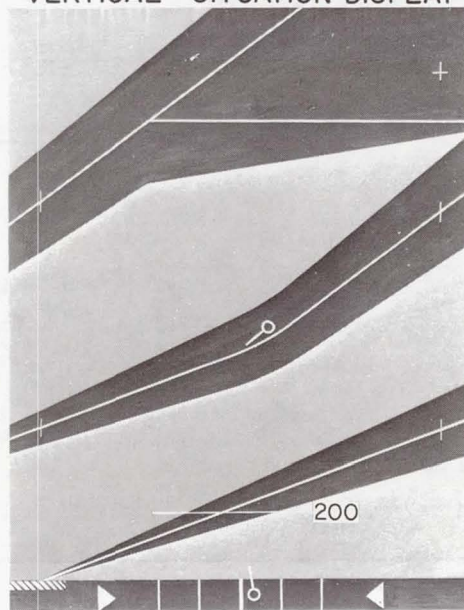


Figure 4

DISPLAY GENERATION METHOD

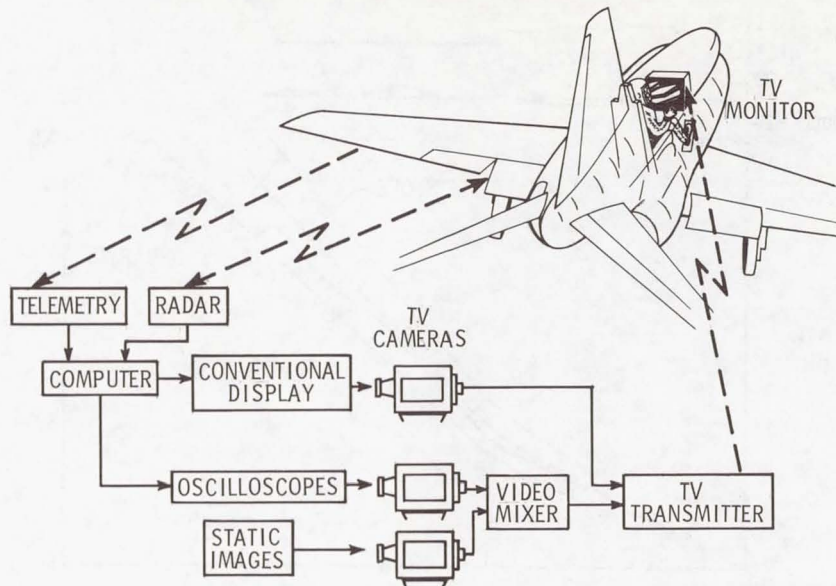


Figure 5

AERO COMMANDER INSTRUMENT PANEL

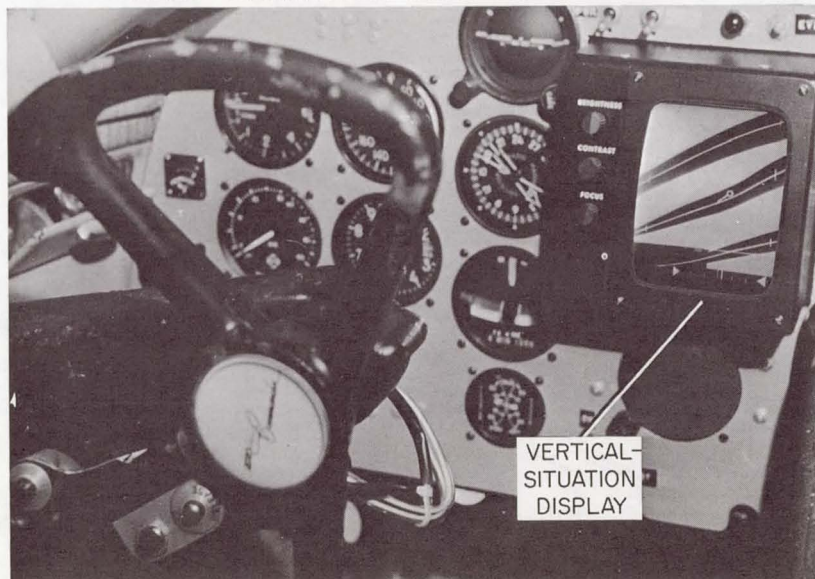


Figure 6

APPROACH WITH CONVENTIONAL CROSS-POINTER DISPLAY

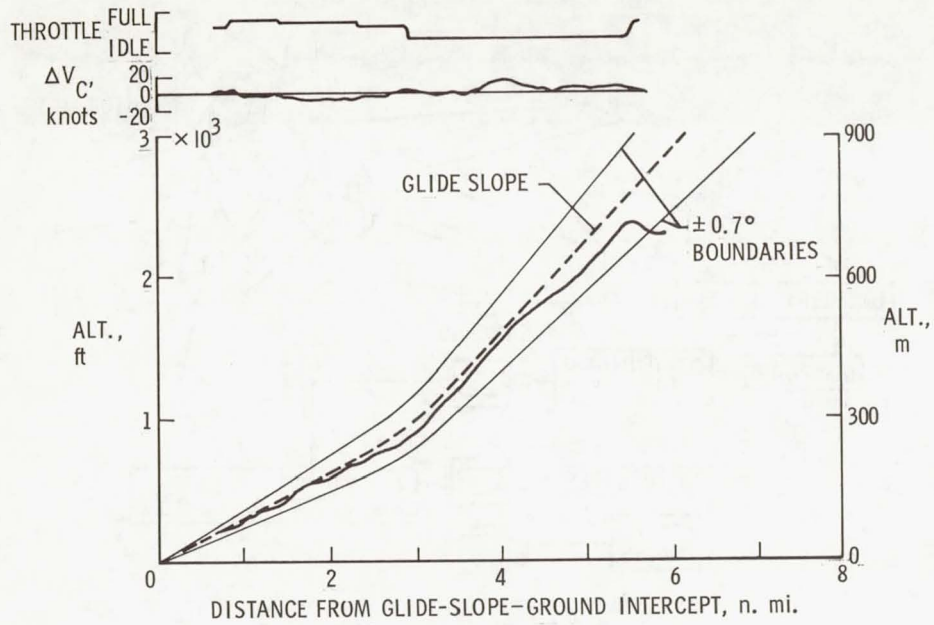


Figure 7

APPROACH WITH VERTICAL-SITUATION DISPLAY

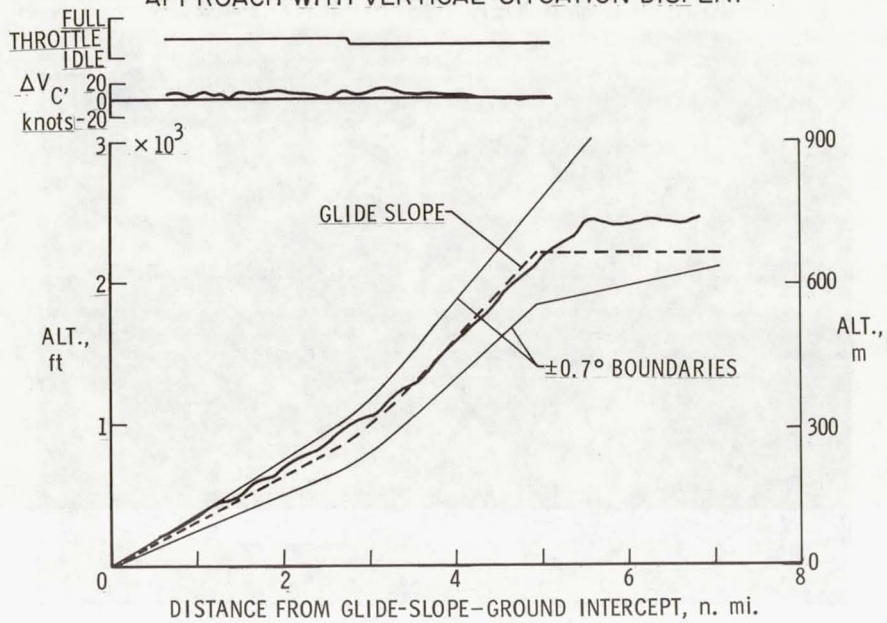


Figure 8

GLIDE-PATH TRACKING PERFORMANCE COMPARISON AERO COMMANDER AIRPLANE

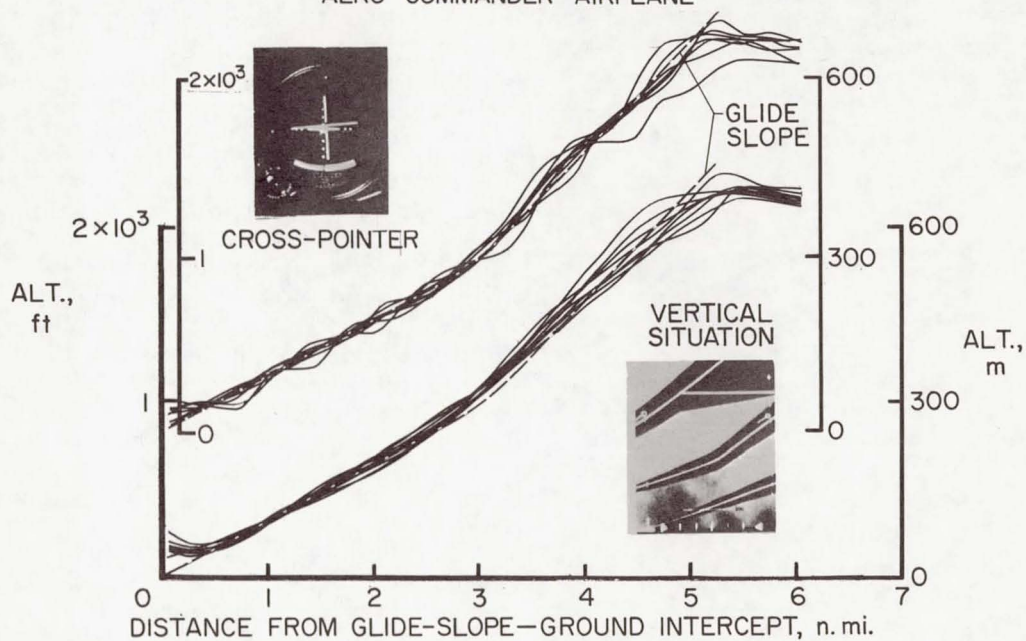


Figure 9

Page intentionally left blank

HANDLING QUALITIES OF LIGHT AIRCRAFT WITH ADVANCED CONTROL SYSTEMS AND DISPLAYS

By Paul C. Loschke, Marvin R. Barber, Calvin R. Jarvis,
and Einar K. Enevoldson
Flight Research Center

SUMMARY

Flight tests to determine the benefits of advanced control systems and displays on the handling qualities of general aviation aircraft, primarily during ILS (Instrument landing system) approaches in turbulence, have shown that very significant benefits can be achieved. The use of a flight-director display and an attitude-command control system in combination was shown to transform a typical light aircraft into a flying machine that borders on being perfect from a handling-qualities standpoint during ILS approaches in turbulent air. The singular use of either the flight-director display or the attitude-command control system provided significant benefits. A rate-command control system was found to provide significantly less benefit than an attitude-command control system.

The command control systems tested tended to improve the poststall response of the basic aircraft, but degraded its stall-warning characteristics. The control systems improved the response of the aircraft to sudden engine failures.

INTRODUCTION

Several years ago the Flight Research Center conducted a handling-qualities survey of a representative cross section of light general aviation aircraft. (See ref. 1.) This study indicated that personal-owner aircraft have generally satisfactory handling qualities for visual flight and for instrument flight in smooth air, but that atmospheric turbulence severely degrades these handling qualities. The degradation was most noticeable during ILS approaches because of the marked increase in pilot workload. A broad spectrum of stability and control deficiencies contribute to the high workload. Excessive control-system friction, low levels of longitudinal and spiral stability, high adverse yaw, objectionable Dutch roll characteristics, excessive trim changes with changes in gear, flaps, and power, and control-system float combine to make precise instrument tracking tasks, in the presence of turbulence, difficult even for experienced instrument pilots. In addition, poor and inconsistent instrument displays tend to compound the problem.

There appeared to be two disciplinary approaches toward achieving a quantum improvement in aircraft behavior or in alleviation of the problems found. One involves

extreme attention to aerodynamic design variables; the other involved the use of advanced control-system concepts. Improved displays would be necessary for either approach.

Therefore, the Flight Research Center has conducted an exploratory program to determine the effectiveness of advanced control systems and displays for the alleviation of light-aircraft handling-qualities problems.

The purpose of this paper is to relate the experience obtained with the advanced systems during approximately 72 flights, representing 120 hours of operation. Particular emphasis is given to the ILS approach in turbulence.

TEST AIRCRAFT, CONTROL SYSTEMS, AND DISPLAYS

Aircraft

The systems were tested in the aircraft shown in figure 1. It is a modified, six-place, low-wing, twin-engine aircraft that is representative of the type of general-aviation personal-owner aircraft that are involved in current instrument flight operations.

Control Systems

The systems tested were a rate-command control system and an attitude-command control system. Figure 2 presents a simplified schematic of the mechanization of the test systems. The basic installation of the pitch, roll, and yaw axes is the same but for simplicity, only the pitch axis is shown.

In a conventional general-aviation aircraft, when the pilot moves the control wheel, he is commanding a control-surface position which is directly proportional to his control-wheel displacement. The surface movement is achieved by a solid tie, either control cables or push rods, between the wheel and the surface. In the rate- or attitude-command modes, control-wheel movement generates an electronic signal which is fed through the computer to an actuator which transforms the signal to a control-surface movement. The aircraft response that results from the surface movement is then sensed by the gyros and summed in the computer with the pilot's control input to null the difference between the command signal and the aircraft attitude or rate. In other words, for a given pilot input, only one attitude or rate, depending on the mode, will allow the system to null and therefore allow the aircraft to stabilize.

The results of the systems operation on the response of the aircraft is presented in figure 3, which compares time histories of pitch angle, pitch rate, and angle-of-attack response of the aircraft to a control step command, for the basic control system, the rate-command control system, and the attitude-command control system. The step input to the basic control system is shown to yield an essentially constant angle-of-attack response

with a varying pitch angle and rate. With this type of response, the aircraft tends to maintain an elevated g until the speed reduction causes the g to dissipate and the aircraft to stabilize at a new $1g$ trim speed. The step input to the rate command control system is shown to yield a constant pitch-rate response with a varying angle of attack and attitude. With this type of response, the aircraft tends to maintain a constant pitch rate as long as the command is present and would therefore experience an increase in α (and g) until the aircraft either stalled or the command is removed. The step input to the attitude-command system is shown to yield a constant pitch-angle response with a varying pitch rate and angle of attack. With this type of response, normal acceleration of the aircraft increases only until the pitch angle stabilizes; from that point on, the aircraft is trimmed in $1g$ flight, either climbing or diving, depending on the command. The speed varies until the aircraft stabilizes on a new trim speed. Therefore, except for throttle manipulations, the attitude-command system essentially provides flight-path control.

Neither rate nor attitude command were required in the yaw axis of the aircraft. Therefore, the tests were conducted with a yaw damper during the rate-command evaluations and with a yaw-heading-hold mode during the attitude-command evaluations. A heading-hold-unlock switch operated as a function of bank angle to release the heading-hold system for turning flight. An aileron-rudder interconnect was utilized to eliminate adverse yaw during both the rate- and attitude-command evaluations.

It should be noted that the prime objective of the investigation was to determine the maximum benefits that these systems could achieve. Therefore, high-quality systems were provided with no concern for the economics of the test equipment.

Displays

The flight-director display is shown in figure 4 and can be compared with the basic display which is shown in figure 5. The greatest difference between the basic and flight-director displays is the steering information provided by the command bars of the flight director. A null indication on the command bars tells the pilot that he is either on the ILS beam or that he has a proper intercept roll angle. Therefore, the ILS approach can be flown with reference only to the command bars and airspeed indicator.

Another difference between the two displays is the flight-director's course-deviation bar, which displays the aircraft's position and intercept angle with respect to the localizer.

To utilize the command features of the flight director display on an ILS approach, the pilot needs only to select the runway course on the Horizontal Situation Indicator, and select the approach mode on the Flight-Director Indicator. During the approach, basic position information is provided by a runway symbol for localizer and a pointer for glide slope.

INSTRUMENTATION

A pulse-cone-modulated (PCM) digital data-acquisition system was used during the flight-test program. Data were recorded onboard the airplane and by telemetry at a ground station. The recorded parameters are as follows:

- Airspeed and altitude
- Angle of attack and sideslip
- Three-component linear accelerations (center of gravity)
- Angular velocities (pitch, roll, and yaw)
- Angular displacements (pitch, roll, and yaw)
- Control forces (longitudinal, lateral, and directional)
- Control-surface positions (longitudinal, lateral, and directional)
- Glide-slope and localizer deviations
- Turbulence intensity

In addition, a cockpit camera was used to photograph the cockpit display.

A turbulence-intensity-measurement system was utilized during the program. It was obvious, at the outset, that the command-augmentation control systems would in some manner mask the apparent turbulence level from the pilot. Therefore, it was considered desirable to obtain a quantitative measure of the turbulence environment in which the aircraft was operating. This measurement was made with the system described in figure 6. A pitot probe and differential-pressure transducer measured the longitudinal-pressure fluctuations in front of the aircraft. A bandpass filter was then utilized to attenuate the deviations below 6 Hz and above 20 Hz. This attenuation is necessary so that the signal can be electronically integrated in an analog computer without including unwanted high-frequency noise or low-frequency content due to the airplane response to turbulence and pilot inputs. The computer also compensates for variations in aircraft velocity. The integrated signal from the computer was recorded on the data system. This signal is directly proportional to the hatched area under the turbulence power spectrum presented on the left half of figure 6. The power spectrum shown represents the standard format for quantitative turbulence measurements. This format is the result of exhaustive turbulence research which has empirically shown that the log-log plot of the gust-velocity power spectrum is linear with a constant and repeatable slope throughout the wavelength range of 3.05 to 305 meters (10 to 10^3 feet); therefore, changes in turbulence intensity do not change the slope of the spectrum, only its magnitude. The slope invariance is illustrated by the levels, taken from reference 2, of the light-moderate and moderate plus turbulence spectra shown in the figure. Therefore, the hatched area varies directly with the level of turbulence intensity. This area is also directly proportional to the mean-square value of the gust velocity, which is identically equal to the magnitude of the area under the whole power spectral curve.

RESULTS AND DISCUSSION

Effect of Command Control Systems and Displays on ILS Approach Handling Qualities

Experience has shown that the ILS approach task is probably the best real-life situation for the evaluation of the overall handling qualities of an aircraft. During these approaches the pilot must exercise all the controls, provide power changes, maintain radio communications, and make the utmost utilizations of his instrument displays in order to navigate the airplane from 6 to 11 kilometers (4 to 7 miles) down a relatively small beam fixed in space. This task then enables a pilot to evaluate aircraft stability, control harmony, display location and efficiency, and overall man-machine integration. Most of the evaluations were made by two NASA test pilots. However, other pilots were called in throughout the program to round out the background of the evaluators.

Basic aircraft.— Figure 7 shows Cooper-Harper pilot ratings for the ILS approaches flown in the basic aircraft and illustrates the effect that atmospheric turbulence has on the pilot's ability to perform the task. The ordinate shown in the figure is a condensation of the Cooper-Harper rating scale and depicts the major adjectives utilized on the scale. The abscissa is the measured RMS value of turbulence intensity. The adjectives on the abscissa were determined by previous tests of the turbulence-measurement system in the test aircraft, the U.S. Weather Bureau's turbulence reporting criteria (table I) being used as a baseline. (See ref. 3.)

As shown, the ratings start in relatively smooth air at 4, which is something less than satisfactory, and degrade to an 8 when the turbulence reaches a moderate level. The latter rating indicates that the handling characteristics are unacceptable and require substantial pilot skill to maintain control. The biggest problems with the basic aircraft are the continual Dutch roll oscillations, and the trim changes — both longitudinal and directional — with power. Because of the combination of the poor display and the lightly damped Dutch roll oscillations, one can never be sure, within 10^0 , of either the heading he is flying or the heading he should fly.

When this situation is compounded by power changes, which are often required to correct for up and down drafts, and which result in directional and longitudinal trim changes, the pilot is well on his way to becoming saturated. In addition, the basic pitch-axis stability of the airplane is such that the airplane tends to pitch into each gust; thereby, the trim changes caused by the gusts are amplified.

Rate-command controls.— Figure 8 compares the pilot ratings for the approaches with the rate-command system with the basic aircraft pilot ratings. The figure shows that atmospheric turbulence did not have as much effect on the pilots' impressions when they

were flying the rate-command system as it did when they were flying the basic aircraft. However, the ratings for the task still fell in the unsatisfactory region. These ratings tend to indicate that the rate-command system, although not easing the pilots' control task in smooth air, did do a good job of damping the turbulence response of the aircraft. This indication was verified by the pilots' comments and by the quantitative power spectral measurements of the turbulence response of the aircraft. The pilots commented that the rate-command system did a good job of eliminating the trim changes with changes in gear, flaps, and power, and was appreciated in this respect. However, the system was difficult to trim and the aircraft tended to drift incessantly about the pitch and roll axes. The drift rates were similar in magnitude to the spiral divergence of the basic airplane and required an ever-present eye and hand to keep them from causing deviations from the ILS beam. Therefore, the only significant improvements provided by the rate-command system were the increased damping or decreased turbulence response, and the elimination of the trim changes.

Attitude-command controls.- Figure 9 presents the pilot ratings for the approaches flown with the attitude-command system, and illustrates the improvement that was achieved with this system over the basic aircraft and rate-command systems. As shown, the attitude-command ratings do not vary with turbulence intensity out to very high levels and have now been lowered into the satisfactory region of the rating scale.

The attitude-command system did a good job of damping the response of the aircraft to turbulence; and since it was providing attitude stabilization, it required very little of the pilot's attention for the control task. When flying the ILS, the pilot could take his mind from the control task to read an approach plate, or for other purposes, and be assured that when he returned to the task, the aircraft would be in the same attitude. This feature is most beneficial in a task as demanding as the ILS approach. The attitude-command system eliminated the trim changes with changes in gear, flaps, and power; it provided essentially infinite pitch and roll stability, and therefore reduced the aircraft's tendency to pitch into gusts; it eliminated the objectionable Dutch roll characteristics; and the aileron-rudder interconnect eliminated the adverse yaw. Overall, it provided a very significant improvement over the handling qualities of the basic airplane.

Flight director.- Figure 10 presents the pilot ratings for the ILS approaches flown with and without the flight director in the basic aircraft control mode. The figure shows that the flight director significantly improves the pilots' impressions of the task. However, their impressions or ratings are still degraded by turbulence. The improved scan pattern provided by the flight-director display had a significant effect on the improvement of the pilot ratings.

The scan pattern, during ILS approaches, of the basic display (fig. 5) is such that the pilot must continually monitor instruments that are situated throughout half of the

panel; and to monitor the engine performance instruments, the pilot must look completely to the other side of the cockpit. Head movement for instrument monitoring over large areas causes a significant amount of time loss in order to refocus the eyes. The distance from the ILS displays to the directional gyro is particularly inefficient. In addition, the attitude indicator is very difficult to interpret rapidly because of its lack of sensitivity, the coarseness of its symbols, its small size, and its cluttered appearance. These deficiencies make it impossible to interpret the instrument peripherally.

In contrast, the locations of the instruments in the flight-director display, which are shown in figure 4, are such that the primary scan pattern is in a significantly reduced area; however, engine monitoring still requires large head movements. Also, the size and clarity of the flight-director's attitude and compass displays are such that they are much easier to interpret rapidly and read peripherally. The location of the two displays, one being on top of the other, also makes it easier for peripheral interpretation. In addition, the flight-director's compass display is slaved to the magnetic heading; thereby the pilot is relieved of the manual compass-setting task, which is difficult and inaccurate in turbulence.

The command features of the flight director reduce the pilot's mental tasks while performing the ILS approaches. The mental process required to calculate a heading that would maintain the localizer in the presence of a crosswind, in addition to the integration required to determine heading leads on roll-out, are eliminated by the flight-director's steering commands. However, the pilots commented that most of the benefit from the flight-director display was obtained by the improved scan pattern and not the command features.

Figure 11 presents the pilot ratings for the ILS approaches flown with and without the flight director in the attitude-command control mode. The combination of systems (i.e., attitude command and flight director) lowers the average pilot rating from approximately 2.5 for attitude command alone to 1.3, which is almost a perfect rating. It is significant to note that at the lower turbulence levels, several perfect ratings are given. Obviously, the improvement provided by the flight director stems from the improved scan pattern and the relieved mental processes.

It is interesting to note by comparing figures 10 and 11 that the benefits provided by the singular use of the attitude-command control or the flight director, in smooth air, are approximately equal. However, turbulence degrades the basic-control mode and flight-director ratings at approximately the same rate that the basic-control-mode ratings are degraded. These facts indicate that the slope of the pilot-rating curve is a function of the control task, and that the intercept is primarily determined by the display.

Other Effects of Command Control Systems

Gust alleviation.- Figure 12 presents a time history of various aircraft response parameters and illustrates one of the most dramatic effects of the command augmentation control systems, that is, the alleviation of the aircraft's turbulence response. The time histories were obtained alternately with the attitude control system on and then off. The data were taken on consecutive runs; therefore, the turbulence samples are approximately equal. The data show that the attitude-command control system attenuates the aircraft turbulence response. Normal-acceleration deviations are significantly reduced at the short-period frequencies. The reduced lateral-directional motions are primarily the result of increased Dutch roll damping and spiral stability. It should be noted that in the control-system-off run, the pilot had to interject aileron control inputs to keep the aircraft nominally upright.

The importance of the attenuated turbulence response is highlighted in figure 13 which presents the pilots' impressions of the turbulence levels and compares them with the measured RMS turbulence intensities for the three different control-system modes. The pilots' impressions were quantified by the use of a turbulence rating scale which is shown on the ordinate. The prequantified adjectives were based on the U.S. Weather Bureau's turbulence rating criteria (table I), which is presented in terms of aircraft control and passenger response and therefore reflect riding qualities. The figure shows that both command-control systems had a tendency to mask the magnitude of the turbulence from the pilot. The attitude-command system had by far the most significant effect.

Stalls.- Prior to the discussion of the effects of the control system during stalls, it is necessary to point out anomalies in the basic aircraft stall characteristics. With medium power settings, the aircraft develops a roll-off just prior to the stall. This roll-off becomes very sharp if full power is used throughout the stall. When stalled with power settings low enough to remain free of the roll-off, the airplane tends to establish a longitudinal trim at an angle of attack higher than that required for stall if the pilot abruptly commands a large nose-up stabilator input at the first indication of a nose-down pitching tendency. The airplane has relatively good stall warning in the form of airframe buffet, and a large amount of nose-up stabilator is required to "pull" the airplane into a stall.

Both the rate- and attitude-command control systems did a good job of preventing the roll-off inherent in the basic airplane. Even with high power settings, the systems were able to keep the wings level. However, both systems provided the appropriate nose-up elevator commands to place the airplane in the poststall trim condition. This characteristic is deemed to be undesirable because in an aircraft without good airframe buffet or stall warning, it somewhat insidiously leads the pilot to believe he has control of the

aircraft when, in actuality, he must lose a large amount of altitude (approximately 61 meters (200 ft)) in order to recover the aircraft to a level flight path.

Both control systems increased the likelihood of an inadvertent stall. As previously mentioned, a large amount of nose-up stabilator is required to "pull" the basic airplane into a stall. With the rate-command system, a very small control command will provide a nose-up pitch rate that will be sustained until full-up stabilator is reached. During the tests, a highly experienced test pilot inadvertently stalled the aircraft. With the attitude-command system, the pilot can be easily misled by pulling off the power when the control system is commanding a nose-up attitude. In the basic aircraft, the trim changes with power tend to lower the nose when the power is reduced, and thereby, help the pilot to maintain his speed. With the attitude-command system, this effect is not present and it seems obvious that an inadvertent stall situation is present. However, no inadvertent stalls were encountered during the attitude-command evaluations.

These facts point out that improved stall warning or stall elimination, possibly in the form of angle-of-attack limiting, should be designed into command control systems.

Sudden engine failure.- Both the rate- and attitude-command systems improved the responses of the aircraft to sudden engine failures. Each system essentially maintained a wings-level attitude, and the aircraft therefore entered a gentle turn into the "dead" engine.

CONCLUDING REMARKS

The material presented has shown that through improved displays and advanced control systems, it is possible to transform a typical light aircraft into a flying machine that borders on being perfect from a handling-qualities standpoint. Obviously, this type of improvement could provide a quantum improvement in the safety and utility of general aviation aircraft. The only "rub" is that presently it would also cause a quantum increase in the cost of the aircraft, if it were mechanized similar to the research systems. By showing the magnitude of the improvement possible, this paper should stimulate the pursuit of an economical attainment of these systems.

This paper is pointed primarily toward general aviation. It should be noted, however, that the results presented pertain across the aviation board. STOL aircraft, due to their extremely low speeds, have encountered many of the handling-qualities problems that have been noted on light aircraft. Therefore, the extension of these systems to that application appears to be a natural area of endeavor. Also the improved riding qualities should certainly be of interest to all airline operations. This fact is probably most typified by one of the pilot's comments regarding the attitude-command control system.

He said, "this system would be most appreciated by people who are basically afraid of flying because the airplane bounces around so much that they get the impression it is going to roll over and tip them out."

REFERENCES

1. Barber, Marvin R.; Jones, Charles K.; Sisk, Thomas R.; and Haise, Fred W.: An Evaluation of the Handling Qualities of Seven General-Aviation Aircraft. NASA TN D-3726, 1966.
2. Anon.: Airplane Strength and Rigidity Reliability Requirements, Repeated Loads, and Fatigue. Mil. Specif. MIL-A-8866(ASG), May 18, 1960.
3. Anon.: IFR Supplement - United States. DOD FLIP (Enroute), ACIC, U.S. Air Force, Apr. 1, 1971.

TABLE I.- TURBULENCE-REPORTING CRITERIA TABLE

(From ref. 3)

Intensity	Aircraft reaction	Reaction inside aircraft
Light	<p>Turbulence that momentarily causes slight changes in aircraft attitude, altitude or heading. Report as <u>Light Turbulence</u>;</p> <p>or</p> <p>Turbulence (light bumpiness) that causes slight aircraft fluctuations at rapid intervals without appreciable change in altitude, roll or yaw. Report as <u>Light Chop</u>.</p>	Occupants may feel a slight strain against seat belts or shoulder straps. Unsecured objects remain at rest, food service may be conducted, and little or no difficulty is encountered in walking.
Moderate	<p>Turbulence that is similar to Light Turbulence but of greater intensity. Changes in aircraft attitude, altitude or heading occur but the aircraft remains in positive control at all times. Report as <u>Moderate Turbulence</u>;</p> <p>or</p> <p>Turbulence that is similar to Light Chop but of greater intensity. It causes rapid bumps or jolts without appreciable change in aircraft altitude, roll, or yaw. Report as <u>Moderate Chop</u>.</p>	Occupants feel definite strains against seat belts or shoulder straps. Unsecured objects are dislodged. Food service and walking are difficult.
Severe	Turbulence that causes large changes in aircraft altitude, attitude, or heading. It may cause large variations in indicated airspeed. Aircraft may be momentarily out of control. Report as <u>Severe Turbulence</u> .	Occupants are forced violently and repeatedly against seat belts or shoulder straps. Unsecured objects are tossed about. Food service and walking are impossible.
Extreme	Turbulence in which the aircraft is violently tossed about and is practically impossible to control. It may cause structural damage. Report as <u>Extreme Turbulence</u> .	

THREE-VIEW DRAWING OF TEST AIRCRAFT

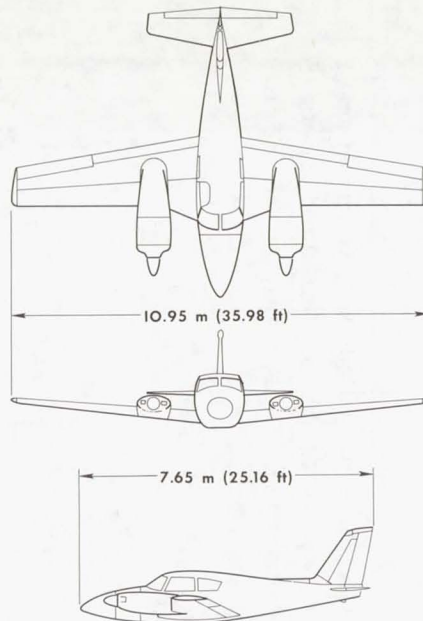


Figure 1

CONTROL SYSTEM SCHEMATIC LONGITUDINAL AXIS

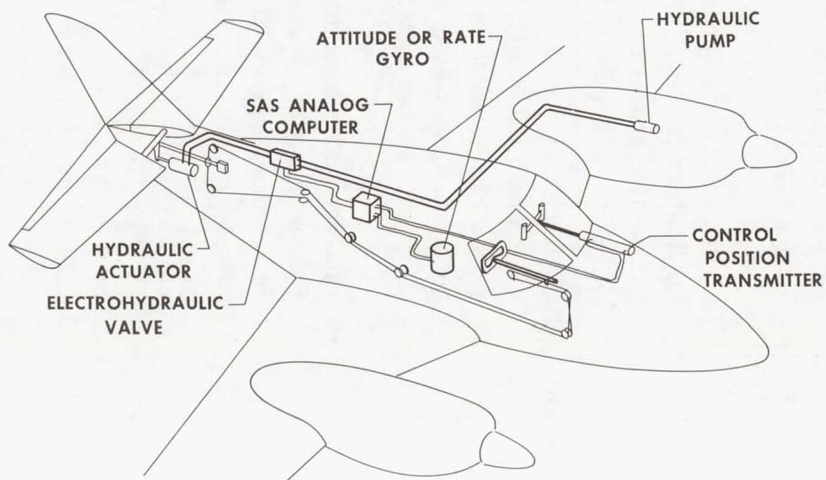


Figure 2

AIRCRAFT PITCH RESPONSE TO CONTROL STEP INPUT

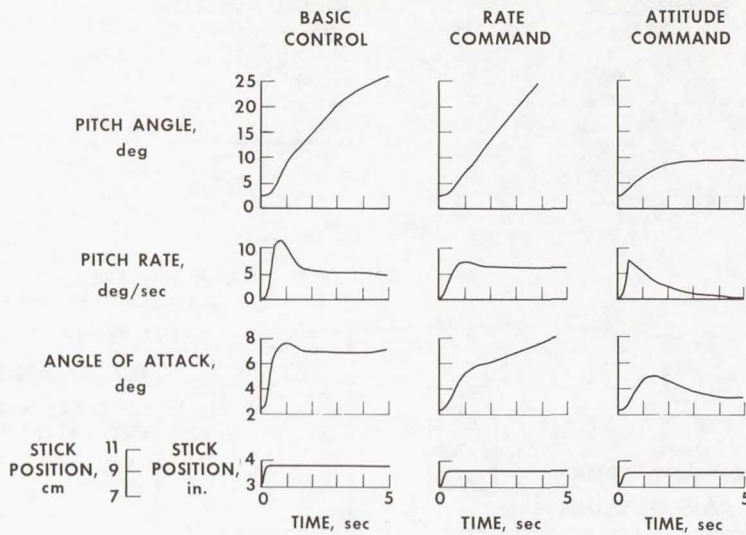


Figure 3

FLIGHT-DIRECTOR DISPLAY

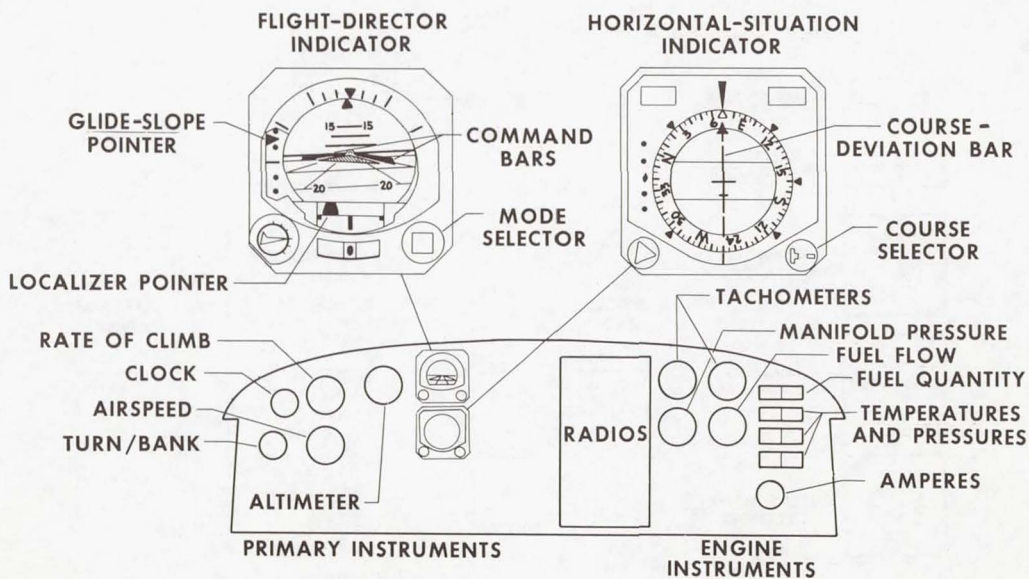


Figure 4

BASIC AIRCRAFT DISPLAY

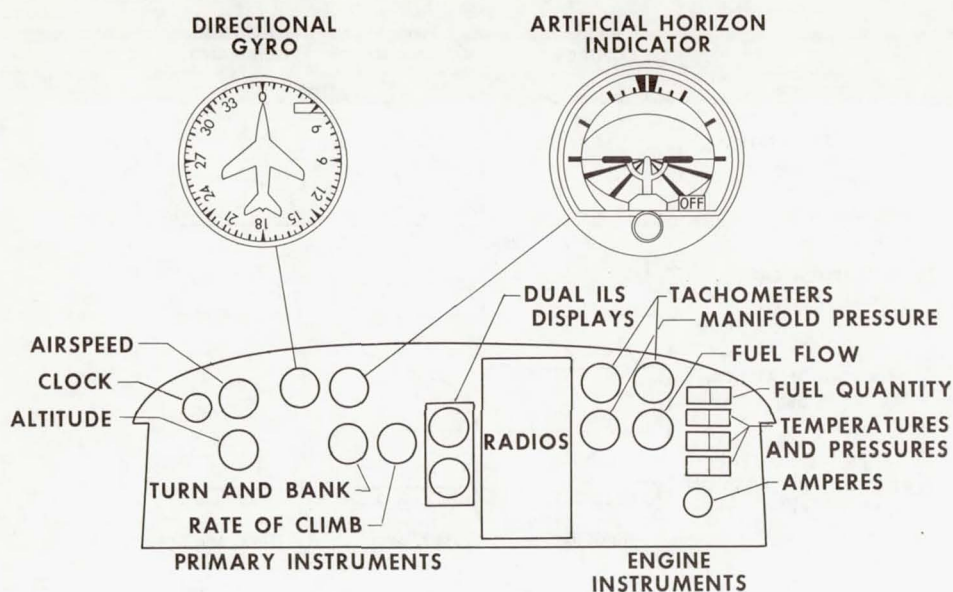


Figure 5

TURBULENCE-INTENSITY-MEASUREMENT SYSTEM

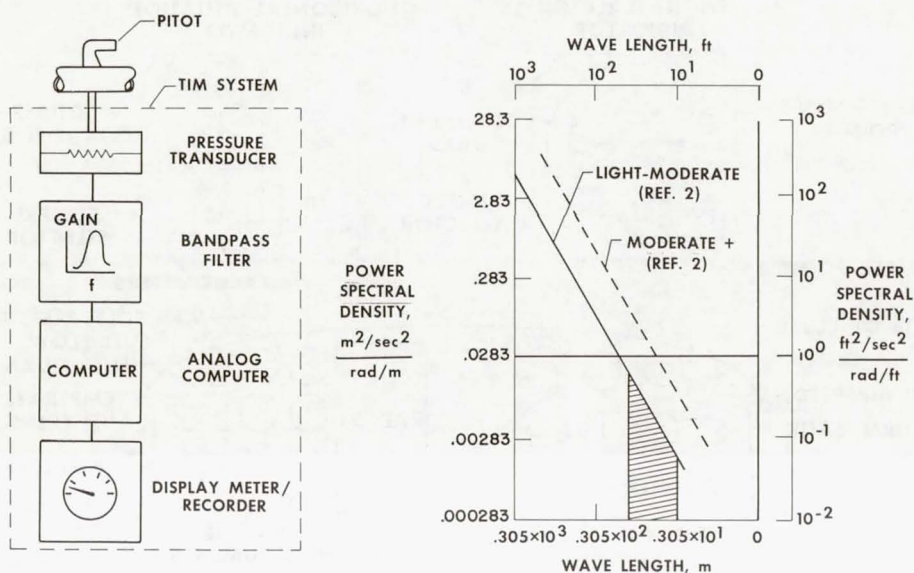


Figure 6

PILOT RATINGS OF ILS APPROACH TASK BASIC CONTROL

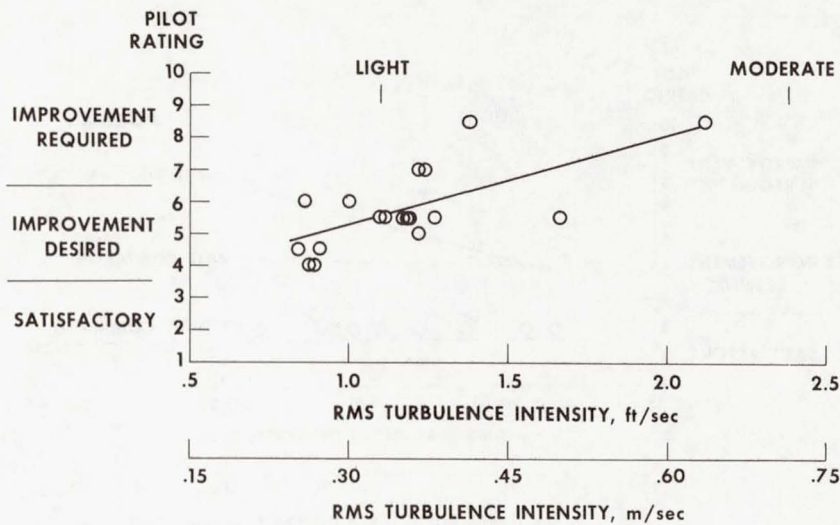


Figure 7

PILOT RATINGS OF ILS APPROACH TASK BASIC AND RATE-COMMAND CONTROL

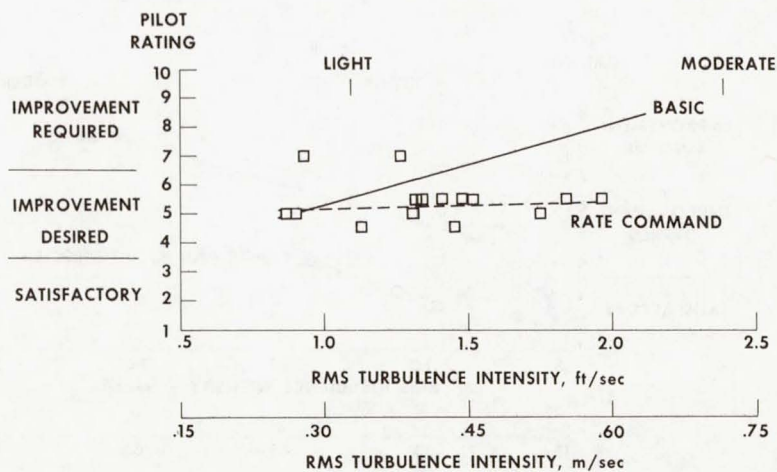


Figure 8

PILOT RATINGS OF ILS APPROACH TASK BASIC, RATE-COMMAND, AND ATTITUDE-COMMAND CONTROL

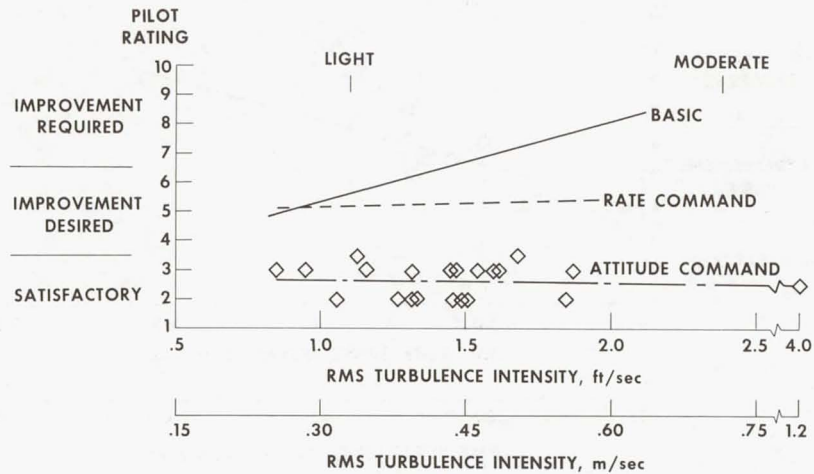


Figure 9

PILOT RATINGS OF ILS APPROACH TASK BASIC CONTROL WITH AND WITHOUT FLIGHT DIRECTOR

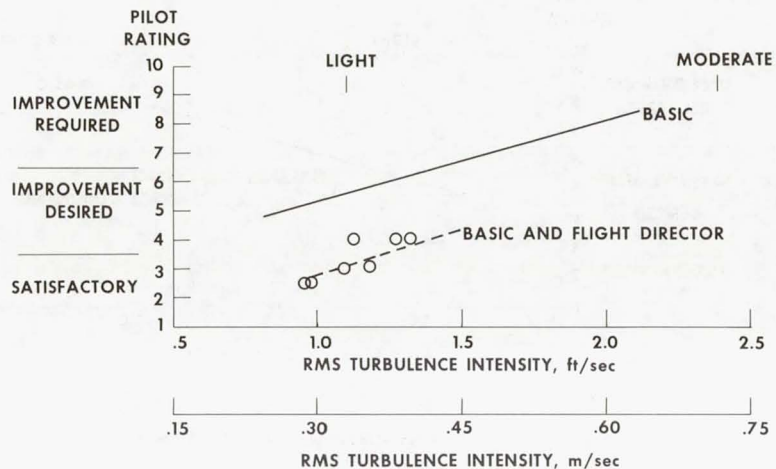


Figure 10

PILOT RATINGS OF ILS APPROACH TASK

ATTITUDE-COMMAND CONTROL WITH AND WITHOUT FLIGHT DIRECTOR

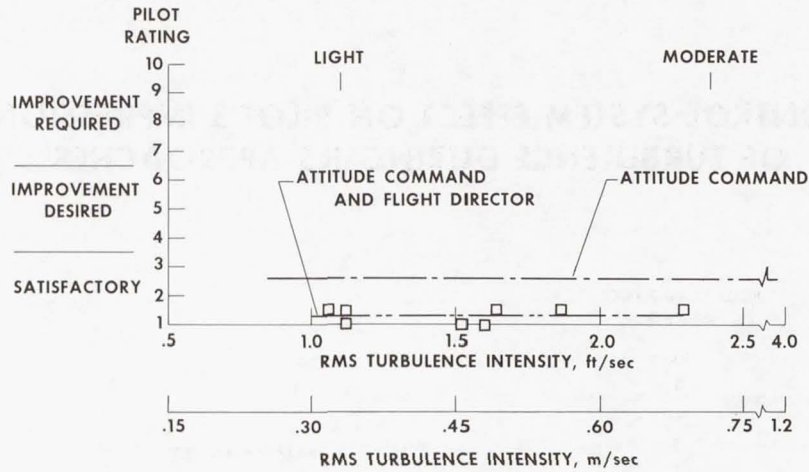


Figure 11

TEST AIRCRAFT RESPONSE TO MODERATE TURBULENCE

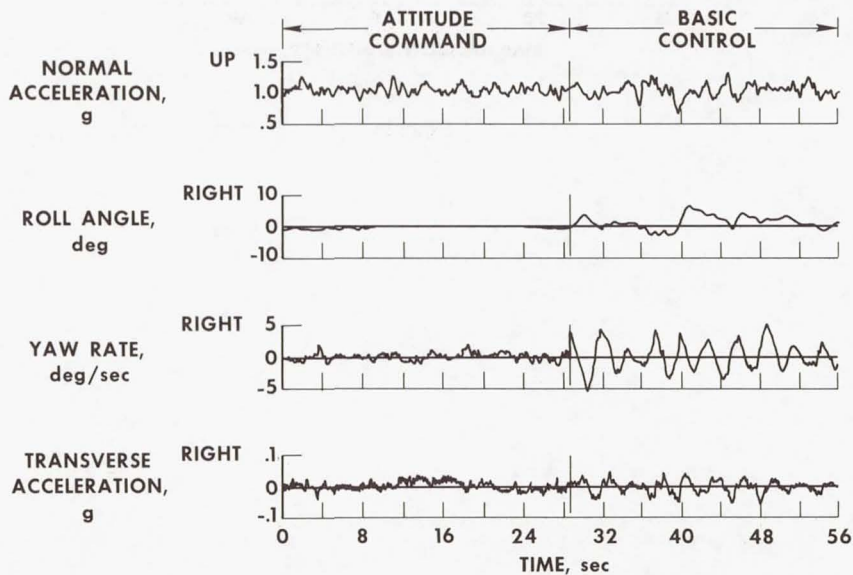


Figure 12

CONTROL-SYSTEM EFFECT ON PILOT'S IMPRESSION OF TURBULENCE DURING ILS APPROACHES

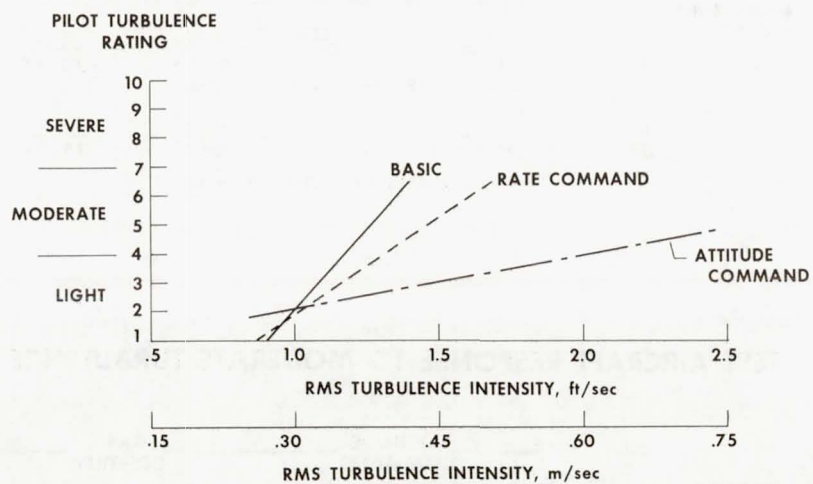


Figure 13

THE INFLUENCE OF MOTION ON THE EFFECTIVENESS OF FLIGHT SIMULATORS IN TRAINING MANEUVERS

By Richard S. Bray, Fred J. Drinkwater III,
and Emmett B. Fry
Ames Research Center

SUMMARY

The use of a new research flight simulator has demonstrated the value of lateral motion cues in the simulation of maneuvers required in the training of air-transport pilots. The availability of very extensive lateral motion has provided the opportunity to form a tentative definition of the minimum lateral motion required to produce the desired simulation fidelity. The less extensive vertical motion capabilities of the simulator provided useful cues but did not markedly reduce the long-standing problem of accurately simulating the flare and touchdown portion of the landing maneuver. The overall effectiveness of the simulator in takeoff and landing maneuvers involving lateral-directional control problems suggests that the scope of simulator training tasks can be expanded beyond those currently performed in flight and simulators.

INTRODUCTION

The past decade has seen the commitment of very large sums of money to the development of flight simulators for the training of civil air-transport pilots. These expenditures will continue in the expectation that the use of this equipment will eliminate most phases of in-flight pilot training. Yet in many critical maneuvers the modern training simulator fails to satisfactorily re-create the piloting task. It fails in maneuvers which are valuable to pilot training, and which, in many cases, inherently involve high risk to the airplane and its occupants.

The use of simulators in research and development in NASA and industry has had a parallel growth. However, research objectives have justified the development of simulators that include special capabilities. The most recent of these, at the NASA Ames Research Center, emphasizes the reproduction of cockpit side motion. The effectiveness of this flight simulator has implications in regard to the design and use of training simulators. This paper will discuss observations obtained during the past year's operation of this machine, particularly with regard to its effective reproduction of critical training maneuvers, and will discuss the expansion of simulator training that these capabilities suggest.

SYMBOLS

g	acceleration due to gravity
K	constant
s	Laplace operator
V_1	takeoff decision speed, knots
V_{MCG}	minimum control speed (ground), knots
V_{MCA}	minimum control speed (airborne), knots
Y_{SIM}	lateral position of simulator cockpit
\ddot{Y}	second derivative of Y
ζ	damping ratio
ϕ	bank angle, deg
ω	frequency, rad/sec

THE FLIGHT SIMULATOR FOR ADVANCED AIRCRAFT

The Flight Simulator for Advanced Aircraft (FSAA) is illustrated in figure 1 and is described in detail in reference 1. It incorporates a transport-type three-man cockpit equipped with collimated television monitor displays of the simulated scene of the terrain and runway. The most unusual feature of the machine is its extensive lateral motion, a total of 24 meters (80 feet). The machine also has travels of 2.4 meters (8 feet) vertically and 1.8 meters (6 feet) longitudinally and extensive excursion capabilities in the three angular motions. All drives are electric. The linear drives can produce accelerations of 4 m/s^2 (13 ft/sec^2). Associated with this mechanical facility are a large-capacity digital computer and extensive data acquisition equipment. An important aspect of any motion simulator is the logic by which it is constrained. The design of the constraint logic which most effectively uses these motion capabilities will be discussed later in this paper.

OPERATIONS

The FSAA has been operating for nearly 18 months, principally in a series of programs utilizing simulations of large transport aircraft in studies of takeoff and landing. Among the airplanes simulated were the Concorde and the Boeing SST. These were sophisticated simulations, including detailed duplication of control forces and landing gear and engine dynamics. The first bending modes of the fuselage were simulated to add to the fidelity of the cockpit environment.

The observations regarding the effectiveness of these FSAA simulations are derived primarily from the experiences of five NASA pilots and more than ten engineering test pilots from other organizations in research not directly related to the development of simulator technology. During the development of the simulator, brief exploratory motion experiments were performed, and the results are offered in recognition of their preliminary nature.

DISCUSSION

The main body of the discussion is organized in the following manner. The unique capability of the FSAA to simulate lateral maneuvering is discussed in the context of critical training maneuvers. Then the lesser effectiveness of the simulator in the basic flare and landing task is described. The observed aircraft motions and the results of motion-cue experiments are used in a tentative definition of lateral motion requirements suitable for training simulators. The discussion concludes with research pilots' assessments of the expanded uses of a training simulator having the effectiveness of the FSAA.

Lateral-Directional Maneuvers

Training maneuvers.- In view of the economic pressures to minimize in-flight training time, the limitations of current training simulators can be inferred from the partial list of training maneuvers, shown in table I, that must still be conducted in the airplane. This list discloses that all the maneuvers involve critical directional control tasks, and, except for simulated engine failure during takeoff, all maneuvers are associated with the landing. A lack of fidelity in these lateral-directional maneuvers has been recognized in the research simulators that have no lateral motion, but the FSAA provides new capabilities. The research programs previously mentioned dealt in great detail with takeoff and landing maneuvers. Hundreds of these maneuvers were performed, and many included engine failures, cross winds, and heavy turbulence. The critical tasks listed in table I were performed repeatedly. In addition, several other critical maneuvers not usually seen in training, such as takeoff rotation abuses and refused takeoffs, were performed repeatedly.

Pilot assessment of lateral motion cues.- For most of the tests, the lateral and roll motions of the FSAA were programed to provide an exact reproduction, not a "washed out" representation, of cockpit lateral acceleration. The procedure for this is described in figures 2 and 3. The acceleration computed for each motion mode is modified by a second-order high-pass filter. The effect of this filtering, or washout, is seen in the roll motions shown in figure 2. Simultaneously, lateral accelerations proportional to the cockpit roll angle are applied to the simulator carriage to eliminate the "false" side forces that would otherwise be sensed by the pilot as the cockpit tilts. To reproduce the computed side forces, the motion logic of figure 3 is applied. Though the acceleration applied to the lateral drive mode is "washed out," the correct value is maintained in the cockpit by programing the appropriate tilt into the simulator roll drive. Thus, a true reproduction of pilot-sensed side force is realized, at the expense of some "false" roll inputs.

Each pilot, upon his first exposure to these simulated motions of flight, has spontaneously expressed strong approval of the realism of the cockpit environment. The strength of these positive impressions was surprising, for the values of side accelerations accompanying normal maneuvering are very modest. Values as low as 0.3 to 0.6 m/s^2 (1 to 2 ft/sec^2) are obviously sensed by the pilots and inspire the appropriate use of directional control. Coordination of turn entries with normal rudder techniques is instinctive. This strong positive reaction to correct lateral acceleration cues appears to be the direct corollary to the adverse reaction a pilot exhibits in the limited-motion simulator when cockpit roll motions are allowed to produce "false" representations of side acceleration.

In the maneuver first on the list of training maneuvers, critical engine failure on takeoff, the directional control task is not exaggerated as it is in the absence of motion. This allows realistic performance of the critical primary task of establishing climbout with limited airplane performance. Similar effectiveness was noted in the landing maneuvers involving asymmetric thrust.

Cross-wind landing.- Special attention is given to one maneuver on the list in table I - the cross-wind landing - because of its training significance, and because it involves a deliberate sideslip maneuver prior to touchdown and a demanding directional control task in the following seconds, where the aerodynamic and ground reaction moments are complex and rapidly varying. In no other maneuver was the simulation of side force more obviously necessary to a realistic level of performance. Figure 4 illustrates two simulated landings of a large delta-wing airplane in a 30-knot direct cross wind - one with cockpit motion, one without motion. The aircraft approach speed was 160 knots, producing an initial crab angle on the approach of about 10° . In both cases shown here, a partially successful heading correction maneuver had been accomplished

at touchdown. Sideslip angles of about 6° had been attained. Due to the remaining drift angles of 4° , significant side-force transients were generated at touchdown. With cockpit motion, an accurate reproduction of the side force shown, the airplane drifted upwind slightly after touchdown until the heading could be completely corrected, and the rollout continued under normal control. The pilot was utilizing about half of his directional control. Without motion, the computed side accelerations shown were not sensed, and the pilot had only his visual information from the runway scene. After touchdown, control was lost in a directional oscillation. The pilot overcontrolled in his attempt to counter the effect of the cross wind. Not as obvious, but equally significant, is the evidence of oscillatory behavior in lateral control before touchdown as the deliberate sideslip was initiated.

Simulation of Flare and Touchdown

The preceding discussion has described what appears to be a significant success – the essential duplication, with a ground-based simulator, of some critical control tasks. However, the motion capabilities of the FSAA still have not eliminated one universal inadequacy of simulators. Since the development of the visual simulation attachment, numerous documentations have been made of pilots' inability to reproduce flight performance in the longitudinal control of flight path near touchdown. (See refs. 2 and 3.) In figure 5 it is demonstrated that the FSAA, which has ± 1.2 meters (± 4 feet) of vertical motion, still has limitations in this maneuver. Shown here are landing performances, in terms of rate of descent at touchdown, from a simulation of a large delta-wing airplane compared with those obtained on the early flights of the airplane. The conditioning of these data is not seriously dissimilar. The simulator data represent the initial experience of three pilots. These landings were performed after they had several hours of experience with the simulation in other flight regimes. The flight data also include the early experience of a small group of pilots. The mean of the simulator values is near 1.8 m/s (6 ft/sec), or nearly twice that measured with the airplane, and there were several touchdowns at obviously destructive levels of vertical velocity. Some of these may in fact be a result of the pilot "giving up" in his frustration at not being able to produce his expected performance. This example of initial performance in a landing simulation is in accord with past experience. The blame for this simulation deficiency in the past has been widely attributed to the remaining obvious limitations of visual simulation, the limited field of view, the absence of retinal disparity, and the reduced resolution inherent in television displays; yet no one has produced conclusive evidence in this matter. The visual simulation used with the FSAA shares these limitations, but appears to be as effective as any of the television systems currently in operation. Of course, the other factor missing from all landing simulations is the full vertical acceleration spectrum of flight. Tests in which pilots have landed real aircraft by reference to television images of the

runway support the argument that the lack of vertical motion is a significant reason for poor performance in the simulator. The vertical motion capabilities of the FSAA have neither proved nor disproved this contention. With ± 1.2 meters (± 4 feet) of travel, only a small portion of the acceleration spectrum can be represented accurately.

Subjectively, the motion was appreciated, and its objective effects may be reflected in the data shown in figure 6. Shown here are simulated performances of three pilots who had the opportunity to continue working with the simulation. These data are from their final tests, a programmed series of landings including turbulence, cross winds, and shears – even several simulated night landings. The performance shown is much better than the initial performance, and even better than that measured in the early flights of the airplane. This level of performance is slow in developing – perhaps as many as 50 or 60 landings are required for the pilot to accommodate to the modified visual and motion cues of the simulation – but a subjective acceptance of the task as a useful reproduction of the flight maneuver appears to occur much earlier. Without the support of definitive data, it is observed that this accommodation progresses more rapidly with the limited vertical motion cues provided by the FSAA than it does in fixed-cockpit simulators.

Minimum Motion Requirements

It was mentioned earlier that the experience with the FSAA would be used to define minimum motion capabilities that would produce the required fidelity in the training maneuvers. In regard to vertical motion, it appears that considerably more than ± 1.2 meters (± 4 feet) might be required to provide high-fidelity simulation of the longitudinal flight task. There is insufficient information from which to extrapolate a vertical motion requirement. However, for lateral motion requirements extrapolation is not necessary. Experiments have indicated the extent to which the roll and side-force cues of flight can be distorted and remain effective. This information can be applied to the real envelope of roll and side accelerations generated in the training maneuvers to provide a tentative definition of simulator motion requirements. These considerations are summarized in table II. The stated low values of bank angle and cockpit side acceleration reflect the fact that the critical phases of the training maneuvers are near or on the ground and bank angles are constrained. Several independent tests including those of reference 4 have defined the acceptability of the acceleration attenuations shown in the lower portion of table II. Preliminary tests have indicated the acceptability of a motion-constraining washout logic utilizing a high-pass filter with break frequencies less than 0.5 rad/sec, which provide essentially in-phase motion at frequencies above 1.0 rad/sec.

Described in figure 7 is the relationship between acceleration, washout filter frequency, and motion requirements. It can be seen from the filter description that at low

frequencies or steady state, the excursions are inversely proportional to the square of the washout filter frequency ω . Shown are the travel requirements for two values of steady-state lateral acceleration as they vary with washout filter frequency. An acceleration of 0.73 m/s^2 (2.4 ft/sec^2) meets the requirements shown in table II if the attenuation factors are applied. It can be seen that for this value of lateral acceleration, a washout filter frequency of 0.5 rad/sec defines a minimum lateral travel of ± 3 meters (± 10 feet). The value of 0.5 rad/sec is not a sharply defined criterion, but values below 0.5 rad/sec appear to insure pilot acceptance in the maneuvers that have been discussed. In the experiments, the washout frequency was varied from 0.25 to 1.4 rad/sec , and the subjective observations are summarized in the figure. Between 0.5 and 0.8 rad/sec , the cues are decreasingly real but still beneficial. Above that frequency, some disturbing disorientations were noted by the pilots.

Training Effectiveness

This paper concludes with some expansion of the pilots' observations regarding the training effectiveness of a simulator with the basic capabilities of the FSAA. In their view, the demonstrated limitations in the reproduction of the flare task are not grounds for fear of negative training. The pilots feel that the FSAA characteristics are adequate for the listed training tasks; and they are even more impressed by the obvious training opportunities these capabilities afford in maneuvers and flight environments not now included in training – not in flight or simulation. In table III are offered a few examples of such maneuvers. It is obvious why these are not demonstrated in flight – they are either too hazardous, or are environment dependent, but it is equally obvious that flight safety is enhanced with the pilot's full awareness of what these maneuvers involve. Paper no. 21 discusses the FSAA simulation of the rejected takeoff, and its critical control tasks. The simulator is very effective in demonstrating the delays in initial deceleration that can be induced by the directional control disturbance of engine failure. Slippery runways have not been seriously simulated with the FSAA, but the capability exists to provide effective training in what appears to be a troublesome operational area. Simulated flight at speeds below minimum control speed (V_{MCA}) is suggested as representing a list of maneuvers in which the simulated aircraft is flown to the limits of control for the general enlightenment of the trainee. With respect to flight in severe turbulence, the FSAA motion system offers no unique capability relative to the newest training simulators. The FSAA programs have included turbulence and flexural mode representations, and the pilots are impressed with the training potential in the re-creation of the alarming vibrational environment that can be induced in the cockpit of a large aircraft.

CONCLUDING REMARKS

This paper has discussed seriously only one of the elements in successful simulation. Effective visual simulation and an accurate description of the aircraft are necessary. But at least in the lateral mode of maneuvering, motion cues are seen as the key to effective simulation. Further careful experimentation and analysis are required to increase the definition of these lateral motion requirements in the tasks which have been addressed, and to expand definitions to a broader range of tasks. The definition of both motion and visual cue requirements for the desired reproduction of the flare and touch-down maneuver is much more obscure and will be the subject of further study.

REFERENCES

1. Zuccaro, Joseph J.: The Flight Simulator for Advanced Aircraft - A New Aeronautical Research Tool. AIAA Paper No. 70-359, Mar. 1970.
2. Armstrong, B. D.: Difficulties With the Simulation of Aircraft Landings. Tech. Rep. 68116, Brit. R.A.E., May 1968.
3. Brown, A. D.: An Examination of Simulator Landing Problems. AIAA Paper No. 70-344, Mar. 1970.
4. Bergeron, Hugh P.: The Effects of Motion Cues on Compensatory Tracking Tasks. AIAA Paper No. 70-352, Mar. 1970.

TABLE I

TRAINING MANEUVERS INVOLVING DIRECTIONAL
CONTROL PROBLEMS

- CROSS-WIND LANDING
- LANDING WITH ENGINE FAILED
- LANDING FROM ILS APPROACH WITH ENGINE FAILED
- MISSED APPROACH WITH ENGINE FAILED
- LANDING WITH TWO OF FOUR ENGINES FAILED
- CRITICAL ENGINE CUT AT V_1 , TAKEOFF

TABLE II

FACTORS DEFINING LATERAL MOTION REQUIREMENTS
FOR TRAINING MANEUVERS

MANEUVER ACCELERATIONS:

- RARELY EXCEEDED SUSTAINED ANGLE OF BANK,
10 degrees [$g \cdot \sin \phi \sim 2 \text{ m/s}^2$ (6 ft/sec²)]
- RARELY EXCEEDED SUSTAINED SIDE ACCELERATION,
 1.2 m/s^2 (4 ft/sec²)

ACCEPTABLE MOTION DISTORTION:

- 0.4 TRUE ROLL ACCELERATION
- 0.6 TRUE SIDE ACCELERATION
- WASHOUT FREQUENCY LESS THAN
0.5 radians per sec

TABLE III

ADDITIONAL SIMULATED TRAINING MANEUVERS

- REJECTED TAKEOFF, CRITICAL ENGINE CUT BEFORE V_1 OR BEFORE V_{MCG}
- LANDINGS ON SLIPPERY RUNWAYS IN CROSS WINDS
- DEMONSTRATION OF AIRPLANE CHARACTERISTICS BELOW V_{MCA} , ONE AND TWO ENGINES OUT
- DEMONSTRATION OF COCKPIT ENVIRONMENT IN SEVERE TURBULENCE

FLIGHT SIMULATOR FOR ADVANCED AIRCRAFT

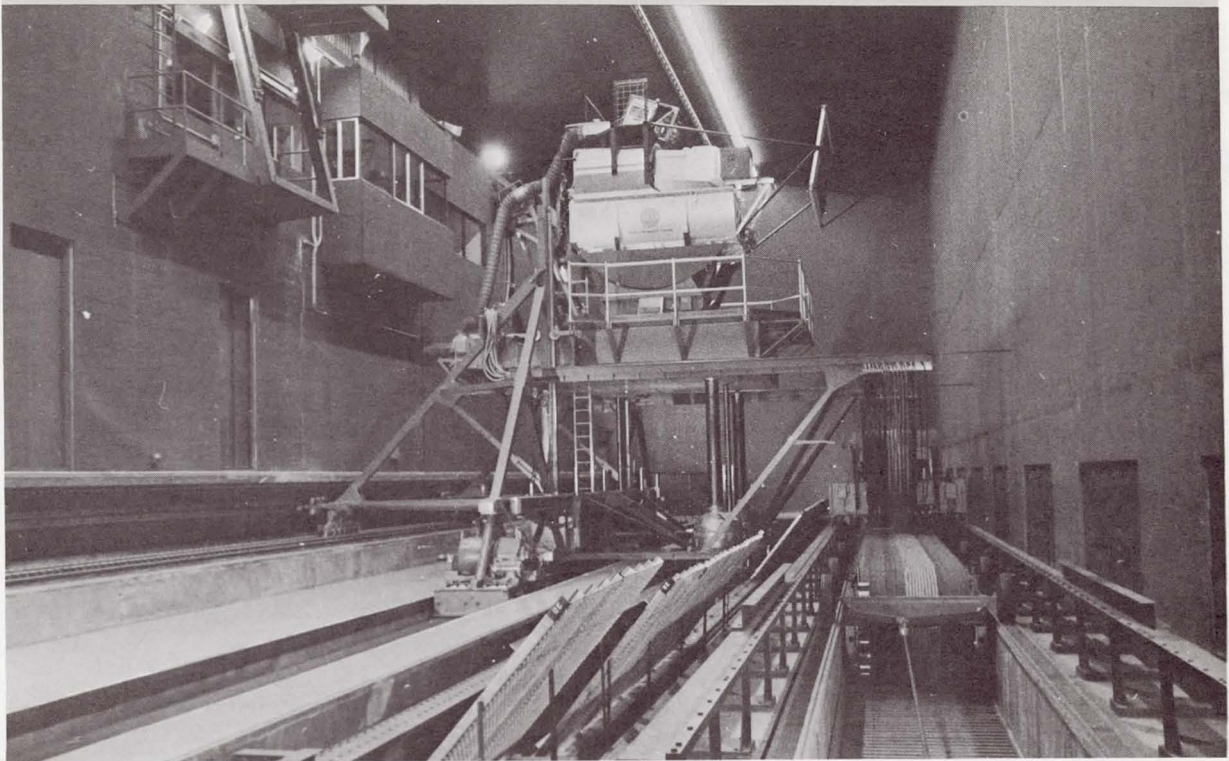


Figure 1

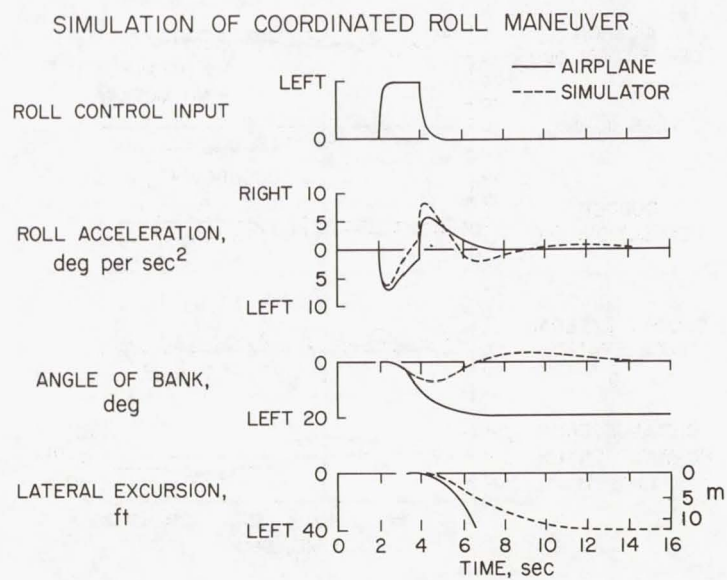


Figure 2

SIMULATOR MOTIONS REQUIRED TO RE-CREATE SIDE ACCELERATIONS

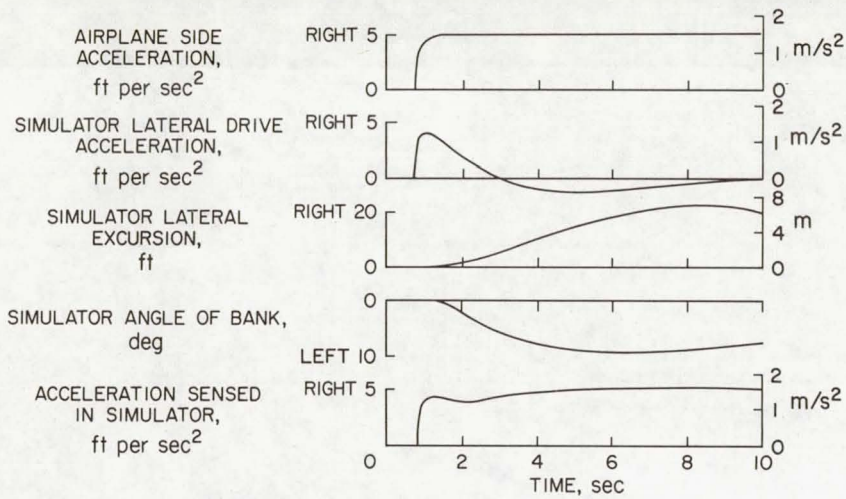


Figure 3

SIMULATED LANDINGS IN CROSS WIND

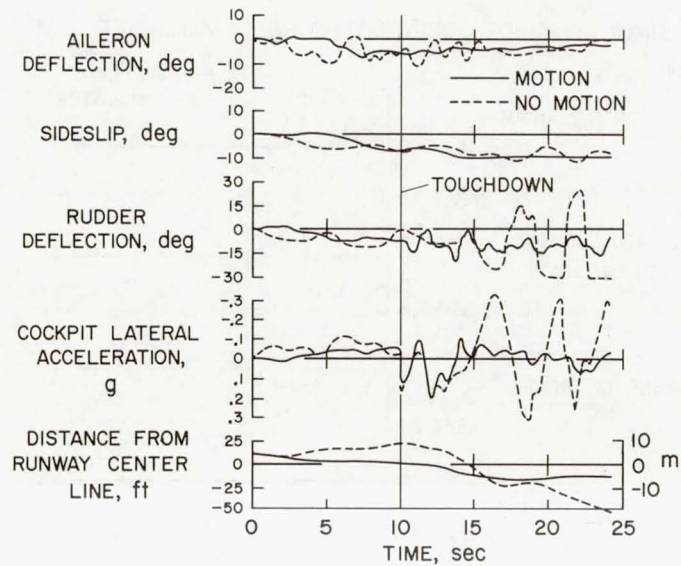


Figure 4

COMPARISON OF IN-FLIGHT AND SIMULATED TOUCHDOWNS EARLY EXPERIENCES

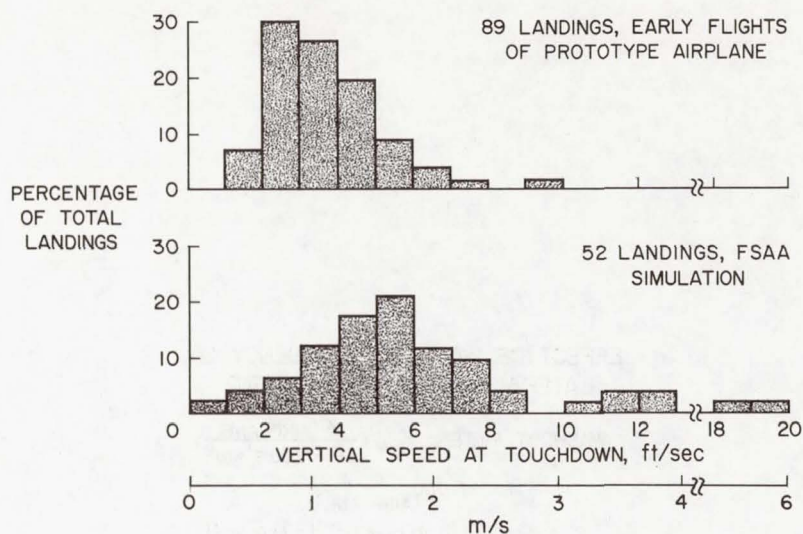


Figure 5

PERFORMANCE IN SIMULATED LANDINGS EFFECT OF LEARNING

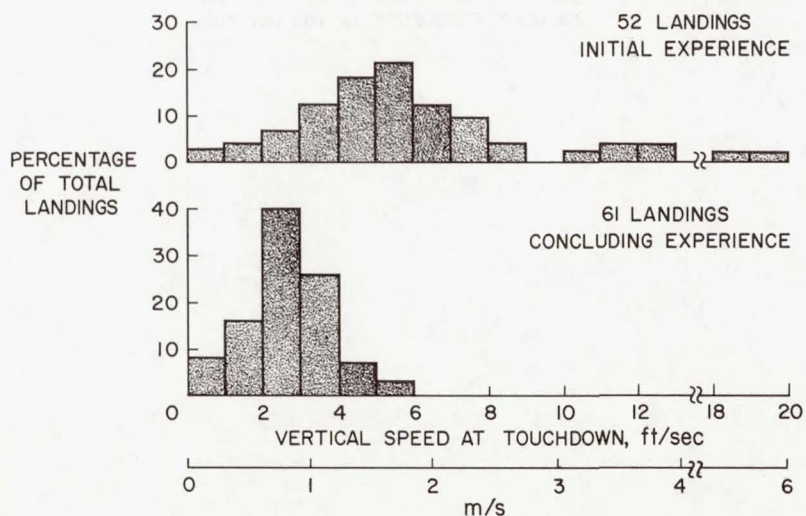


Figure 6

EFFECT OF WASHOUT FREQUENCY ON LATERAL MOTION REQUIREMENT

$$\text{WASHOUT FILTER: } Y_{\text{SIM}} = \frac{K \ddot{Y}_{\text{AIRPLANE}}}{s^2 + 2\zeta\omega s + \omega^2}$$

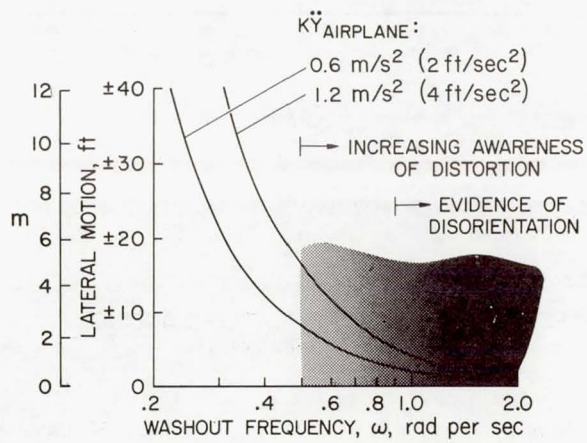


Figure 7

SAFETY CONSIDERATIONS FOR POWERED-LIFT STOL AIRCRAFT

By Curt A. Holzhauser and Robert C. Innis
Ames Research Center

INTRODUCTION

Data obtained with the variety of STOL aircraft shown in figure 1 have recently been reviewed to develop airworthiness criteria for this class of aircraft. Descriptions and characteristics of these aircraft are contained in reference 1. On the basis of this review, selected safety margins and restrictions that must be considered for commercial operation of powered-lift STOL transports will be discussed.

Several questions immediately arise: First, what is a powered-lift STOL aircraft, and second, why must the airworthiness considerations be different than for conventional aircraft? A powered-lift STOL aircraft is an aircraft that obtains a significant portion of its low-speed lift and control from the propulsion system. Several methods of developing powered lift in an approach are illustrated in figure 2. The top sketch shows a propulsion element which is deflected through a large angle by the flap system. In the left sketch the entire wing and propulsion system is tilted. In the right sketch the propulsion system is deflected independently of the wing lifting system. Although these represent vastly different methods, they have one thing in common – the propulsive force is turned through a large angle so that it can contribute significantly to the low-speed lift. This is further illustrated in the vector diagram for steady descent at the flight-path angle $-\gamma$. To be in balance, the resultant force must equal the aircraft weight. The lift and drag form the total aerodynamic force, and to close the force triangle in this example, the propulsion force must be nearly normal to the flight path (that is, it must be turned 90°) and it must have a magnitude about the same as the aerodynamic force, nearly $1/2$ of the resultant force. The effect of this contribution on low-speed performance is illustrated in figure 3, where the steady-state flight path is plotted as a function of airspeed for a STOL and a CTOL aircraft in the landing configuration. The upper curves are defined by the maximum installed thrust and the lower curves by the minimum thrust. The envelope for a conventional aircraft is bounded on the left by the stall, and the stall speed is relatively unaffected by the thrust level. For a STOL aircraft it may be difficult to define the stall other than as a minimum steady speed, which is very much affected by the thrust. In order to exploit the large beneficial effects of powered lift during takeoff and landing, the speeds must be related to the thrust that can be safely used, rather than to a power-off stall speed. The method of control must be modified, and additional emphasis must be placed on effects of propulsion system failures. For these reasons powered-lift STOL transports require different detailed low-speed airworthiness considerations than their conventional counterparts.

Before airworthiness criteria could be developed, it was first necessary to determine the operational requirements for commercial STOL transports. The safety, high-speed performance, and ride qualities of conventional aircraft must be retained. To this must be added the ability to descend quickly and safely into a congested area using minimum airspace and runway length. The current interest is in a commercial field length of 450 to 600 meters (1500 to 2000 feet) with approach and takeoff flight paths of at least 6° . These requirements translate roughly into approach and takeoff speeds of 60 to 80 knots and thrust-weight ratios of 0.4 to 0.6. Since the aircraft must operate routinely in IFR conditions and in a gusty, turbulent environment with wind shears, good handling must be provided. Lastly, the aircraft must have low noise levels to be compatible with close-in operational requirements.

After these broad requirements were established, the published and unpublished data obtained with various research vehicles were readdressed by NASA to develop criteria for safe low-speed operation and good handling of commercial powered-lift transports. The flight tests with STOL aircraft have shown the need to concentrate on the approach and landing regime because more new airworthiness considerations must be dealt with to safely utilize thrust in this mode than during the takeoff. The resulting criteria and substantiating data were presented in reference 1. Tentative standards were assembled by the FAA in reference 2. In the following discussion a landing envelope for a STOL aircraft is reviewed so that selected margins and restrictions can be imposed in order to illustrate the considerations for safe STOL operation.

NOTATION

CTOL	conventional takeoff and landing
STOL	short takeoff and landing
V	true airspeed, knots
V_a	approach airspeed, knots
V_{min}	minimum airspeed in steady-state flight at reference power condition, knots
V_{stall}	stall airspeed, knots
α	angle of attack, deg

γ flight-path angle (above horizon, positive), deg

Δg incremental normal acceleration

DISCUSSION

Low-Speed Envelope

Since thrust has such a large effect on the lift and control of a powered-lift STOL aircraft, it is necessary to look at the aircraft capability in terms of parameters that interrelate lift, drag, and thrust with operating constraints. This can be done with the envelope of figure 4, which shows the variation of steady-state flight path with airspeed for different thrust levels and angles of attack in the landing configurations. By adding restrictions to this envelope, a safe operating area can be defined for a commercial STOL transport. This is illustrated in figure 5. The first restriction is to accommodate an engine failure. The example chosen is a four-engine transport, and the maximum climb gradient is lowered to the curve for a three-engine thrust level. The transport has the propulsion system interconnected, and since an engine failure does not produce asymmetry, there is no minimum control speed restriction. (This will be discussed in more detail later.) The lower restriction is defined by a maximum descent rate of 5 m/sec (1000 ft/min), which the pilots were reluctant to exceed below 60 meters (200 feet) of altitude. The left boundary is defined by a speed margin needed for maneuvering and avoiding stall. This margin will be discussed next in more detail because the method of compliance is so different than for conventional aircraft.

Speed Margin

In general, the speed margin in an approach must be sufficient to provide the pilot with the following capabilities:

1. Normal acceleration for maneuvering to acquire the ILS, to track the glide slope, to flare and land, or to reject the approach
2. Speed margin for protection from wind shears or inadvertent speed excursions
3. Angle-of-attack margin for protection from vertical gusts

For a CTOL aircraft these margins are simply interrelated by the ratio of approach speed to stall speed because thrust contributes very little to the normal force of the aircraft. This is not the case for a powered-lift STOL aircraft, and the problem is more complex. The reason for this is shown in figure 6 where the incremental normal acceleration theoretically available is plotted against the ratio of approach speed to minimum or stall speed. For conventional aircraft the normal acceleration is produced by angle-of-attack changes and is dependent only on the ratio of approach speed to stall speed;

the lowest approach speed normally used is 1.3 times the stall speed in order to permit development of adequate normal acceleration and yet retain a sufficient speed and angle-of-attack margin to avoid stalling the aircraft while maneuvering. It can be seen in figure 6 that with a powered-lift STOL aircraft, normal acceleration can be developed either by angle-of-attack changes or by thrust changes; this is possible because the thrust has been rotated to be normal to the fuselage axis rather than parallel. The normal acceleration produced by angle-of-attack changes is only about $1/2$ of that for the CTOL aircraft. This results because the thrust contribution to the normal force reduces the aerodynamic lift contribution which is the only portion that changes with angle of attack. The fact that less normal acceleration is attainable by angle-of-attack changes for STOL aircraft does not mean that it will require a larger speed margin because the deficiency is compensated by the normal acceleration produced by modulating thrust. Not only is the thrust used for longitudinal flight-path control, but also in turning flight, to produce the normal acceleration without increasing airspeed or decreasing the stall margin. By being able to develop normal acceleration without angle-of-attack changes, one can examine the maneuver margins separately from speed margins.

Flight experience with STOL aircraft has shown that a normal acceleration capability of 0.1g to 0.2g is sufficient for maneuvering to acquire and track the ILS in the approach and also to land from moderate approach angles. For the example shown in figure 6, the pilot could obtain this acceleration at low approach speed margins either by modulating thrust or by pitching the aircraft. When good thrust response existed in the approach (time constants of 1 second or less), the pilot preferred to modulate thrust for tracking the ILS because the stall margin was not reduced, and the pitch attitude was nearly constant. Generally, STOL landings were initiated by pitching the aircraft rather than by applying power. For approach angles above 8° , 0.2g to 0.3g was needed to flare the aircraft rapidly to avoid initial contact by the nose gear and to avoid excessive air distances. Because of the low normal-acceleration requirements and the ability to modulate thrust, it is reasonable to expect that, from the standpoint of maneuvering, powered-lift STOL aircraft may be able to safely approach at lower speed margins than conventional aircraft, which need an extra speed margin to avoid stall.

In addition to considering the maneuvering requirement, a safe approach speed must include a margin of speed or angle of attack that allows the pilot to maintain control when wind shears, gusts, and turbulence are encountered, and to permit inadvertent speed or angle-of-attack deviations. The airspeed margins selected by the pilots of five powered-lift STOL aircraft are summarized in figure 7 for a range of descent angles. It is seen that a 15-percent margin (1.15 times the minimum airspeed defined by the approach power) was selected for flight-path angles less than 8° . At descent angles above 8° the margin had to be increased to provide additional normal acceleration to flare the aircraft safely. In figure 5, which shows the operational envelope, the left-hand

cross-hatched area corresponds to the margin of figure 7. This margin provided adequate normal acceleration and at least a 10-knot speed margin or a 10° angle-of-attack margin from the stall or minimum speed defined by the approach power. The pilots felt that these were the lowest acceptable values. It was calculated that this margin when combined with the use of power for lift and control permitted any of the following: (1) a vertical gust of 10 knots without buffeting, and larger magnitudes without exceeding lift and control limits, (2) an instantaneous 7.5-knot horizontal airspeed reduction with only a small altitude loss, (3) a steady 30° banked turn without reducing the stall margin, and (4) 0.2g by increasing angle of attack only. Since minimum speed is dependent on the thrust used at the particular approach angle, there is no single approach reference speed that can be used for all approach angles. However, the 15-percent line is roughly parallel to the constant angle-of-attack line, and angle of attack, not airspeed, is the parameter which has been used as a reference on most STOL aircraft NASA pilots have flown.

Although the different STOL aircraft have been flown over a fairly wide range of atmospheric and operating conditions, it is possible that more severe environmental conditions might be encountered in commercial operation, and then larger margins could be required. If a larger margin is needed, problems can be introduced because of excessive nose-down attitudes. For example, with a 30-percent margin ($1.3V_{\min}$), the pitch attitude would be -15° for an 8° approach angle. Since this attitude is incompatible with the ground attitude, it must be slowly increased before touchdown. The result is a longer flare, with floating, which causes a large landing performance penalty.

Considerations of Propulsion System Failure

Safe operation of a commercial transport must be assured with the most critical power-plant system inoperative (ref. 2). This means that STOL takeoff and landing can be routinely continued with a single propulsion system failure without extensive pilot compensation. Since a large portion of thrust is used during the approach, in contrast to conventional aircraft, greater attention must be placed on engine failures in this mode in order to safely operate in IFR conditions as a STOL. Because a large portion of lift is generated by the thrust with powered-lift systems, both static and dynamic aspects of engine failures must be examined. The example in figure 5 was a four-engine aircraft with an interconnected propulsion system. A gas generator failure merely lowers the upper boundary without introducing a minimum control speed restriction because there is no lateral-directional asymmetry. Longitudinally, there will be an altitude loss; the magnitude is dependent on the lift loss and vertical damping of the aircraft, pilot recognition time, and engine response time. For the example shown, the altitude loss due to an engine failure was small, less than 6 meters (20 feet), because the pilot could rapidly compensate the loss in lift with increased power. It is also necessary that the pilot have the option of discontinuing the approach at any time before he initiates the landing flare.

This means that a climb gradient must exist in the landing configuration with an inoperative engine. Although this capability exists in the example, it may not be sufficient to clear obstacles surrounding the STOL port (ref. 3).

If the powered-lift STOL design does not incorporate propulsion interconnect features, an engine failure can produce large lateral and directional asymmetries, which can not only impose a minimum control speed limit, but may require extensive pilot compensation to keep the aircraft upright at the approach speed, to compensate for the altitude loss, and to safely continue the landing. It is recognized that automatic stabilization systems can minimize the dynamic effects of an engine failure; however, our studies indicate that good handling must remain after an engine failure so that an IFR STOL approach can be safely continued. This means that there will be a premium on minimizing asymmetry.

As a greater portion of power is used to develop lift, a larger loss in lift and altitude will be incurred by an engine failure. The loss in lift is an inherent characteristic of powered-lift concepts, and criteria are not available to determine an acceptable altitude loss. It also will become more difficult to provide good climb capability by only applying power. A method of safely alleviating the climb limitation that was used with one of the STOL aircraft is shown in figure 8. Superimposed on the normal approach envelope is one obtained by a small reduction in flap deflection, designated as an approach climb configuration. Since the flap and propulsion element are deflected nearly 90° , changes in deflection produce primarily drag changes with little lift changes. When this configuration change can be easily made without adverse lift and pitching moment, a larger portion of the power can be utilized in the approach without compromising the climb performance with an engine inoperative.

After all the various margins and restrictions are placed on the operational envelope, it might appear that only a small area of safe operation remains. Such an interpretation would not be correct. The open area merely defines the initial operating area so that the pilot can still safely enter the shaded areas during transients of maneuvering or atmospheric disturbance.

CONCLUDING REMARKS

Powered lift offers a large potential for satisfying the requirements of commercial STOL transports. By using the propulsion system to control normal force, an approach speed as low as 1.15 times the minimum speed at approach power can be considered. To exploit powered lift, it will be necessary that the airworthiness considerations account for the propulsion system contribution to lift and control. Changes are needed to credit the benefits of powered lift and also to assess the consequences of propulsion system

failures during the approach mode. Due to the large contribution of propulsion system to normal force, greater attention must be placed on avoiding lateral asymmetry with an engine failure in the approach so that the handling qualities are not deteriorated to the point where excessive pilot compensation is required.

REFERENCES

1. Innis, Robert C.; Holzhauser, Curt A.; and Quigley, Hervey C.: Airworthiness Considerations for STOL Aircraft. NASA TN D-5594, 1970.
2. Anon.: Tentative Airworthiness Standards for Powered Lift Transport Category Aircraft. Flight Stand. Serv., FAA, Aug. 1970.
3. Anon.: Planning and Design Criteria for Metropolitan STOL Ports. AC No. 150/5300-8, Airports Serv., FAA, Nov. 5, 1970.

STOL AIRCRAFT TESTED BY NASA

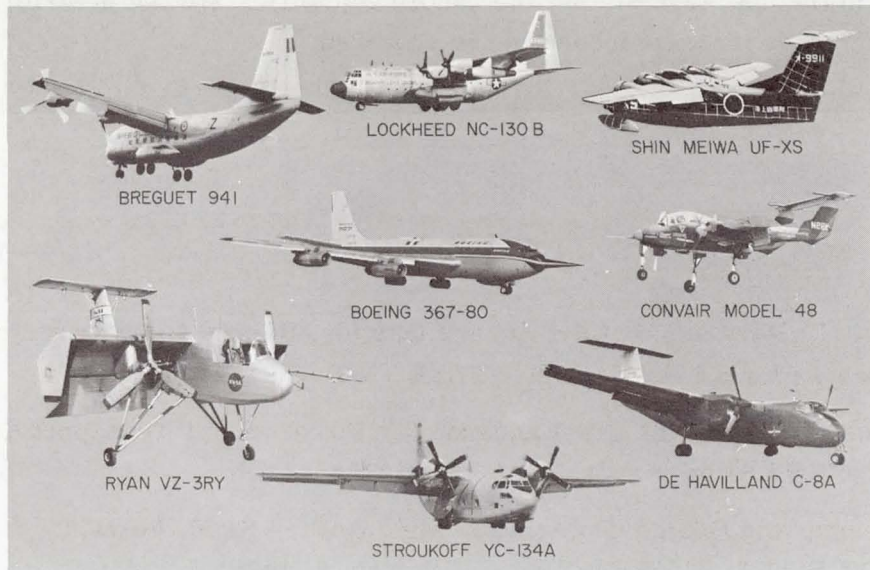
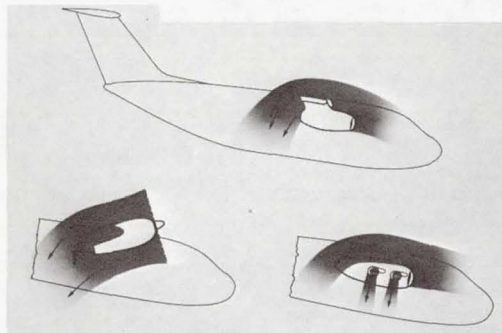


Figure 1

POWERED LIFT IN APPROACH

(a) METHODS



(b) VECTOR DIAGRAM

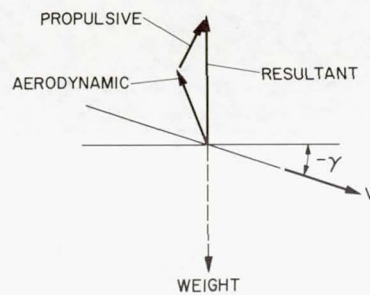


Figure 2

LOW-SPEED ENVELOPE

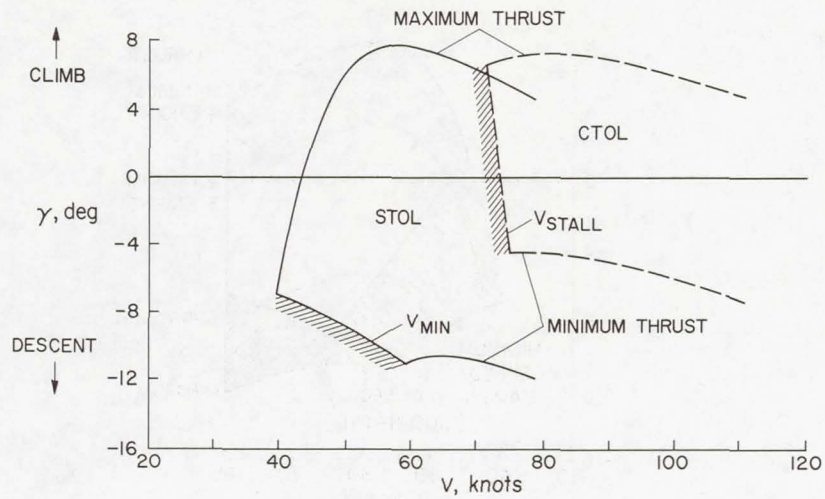


Figure 3

STOL ENVELOPE

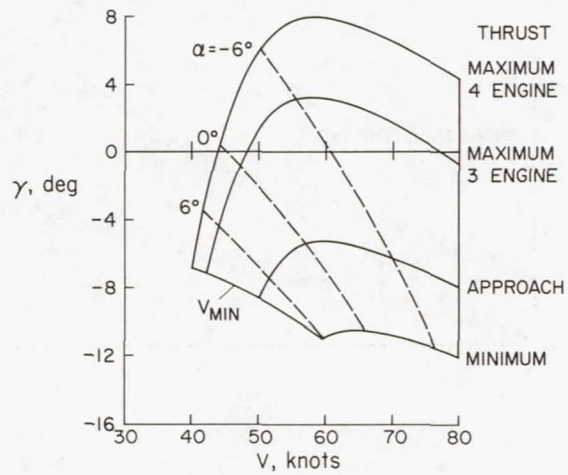


Figure 4

STOL ENVELOPE WITH RESTRICTIONS

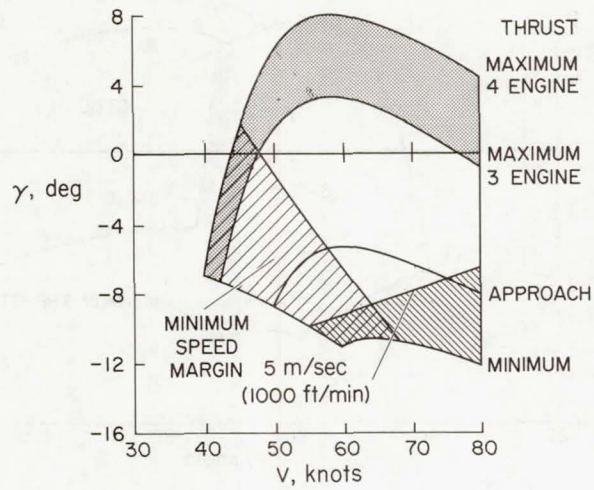


Figure 5

NORMAL ACCELERATION CAPABILITY

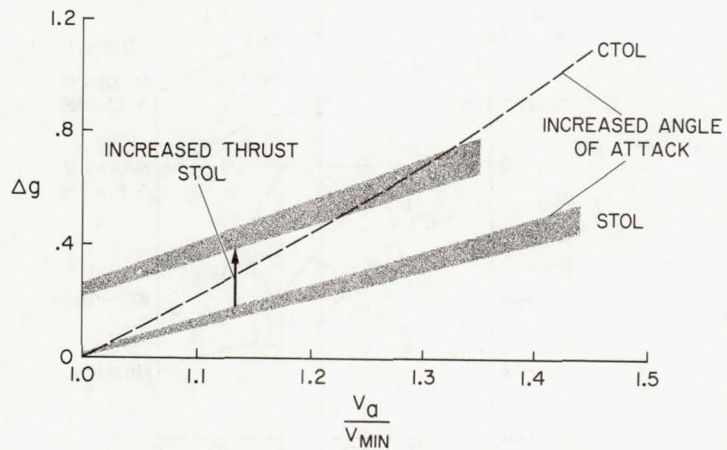


Figure 6

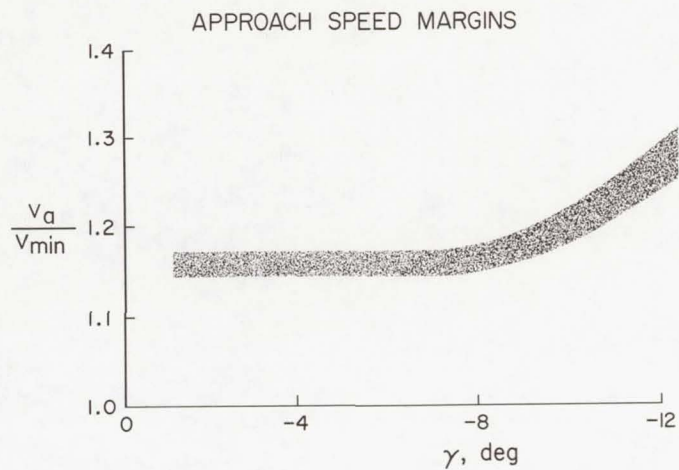


Figure 7

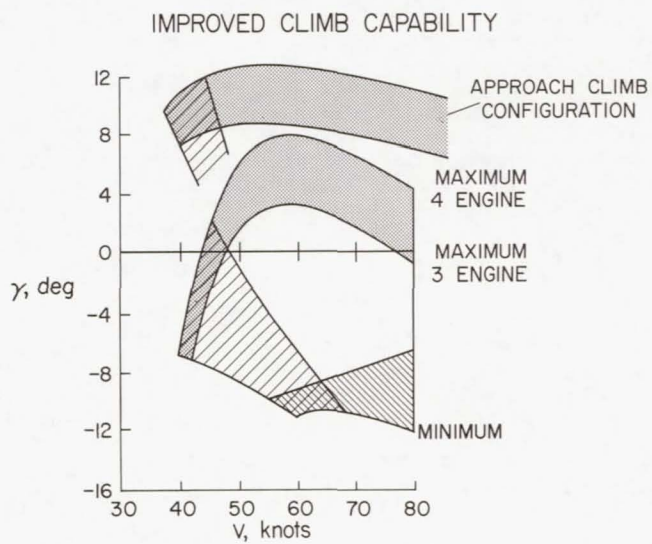


Figure 8

Page intentionally left blank

OPERATIONAL ASPECTS OF V/STOL INSTRUMENT APPROACHES

By Lee H. Person, Jr., and Samuel A. Morello
Langley Research Center

and

Curt A. Holzhauser and Ronald M. Gerdes
Ames Research Center

INTRODUCTION

Commercial V/STOL aircraft have the potential of offering added passenger convenience by operating into nearby or small airfields. This potential cannot be realized without routine instrument operations where time, fuel, and airspace requirements in the terminal area are minimized. Considerable NASA research has been expended on terminal area studies using various V/STOL configurations. The primary objective of these studies was to develop an operational technique for managing powered lift during simulated precision approaches from cruise to landing. The purpose of this paper is to integrate the results of these studies into a realistic appraisal of V/STOL instrument approach techniques.

The configurations evaluated are discussed first, including the powered-lift concepts they represent and the powered-lift controls available to the pilot. Then, the mechanics of a generalized powered-lift concept relative to an approach glide path are investigated. Finally, the operational aspects of powered lift are discussed with regard to (1) stabilization requirements, (2) conversion maneuver, (3) glide-path control, and (4) velocity control or deceleration schedule on the approach.

CONFIGURATIONS EVALUATED

Figure 1 shows the configurations evaluated. These four aircraft, the Kestrel (a vectored jet), the XV-5B (a fan in wing), the XC-142A (a tiltwing), and the Do-31 (a mixed-propulsion jet), represent fundamentally different V/STOL concepts. A brief description of the powered-lift system in each aircraft and the controls available to the pilot for managing the systems is presented herein. Complete aircraft descriptions are given in references 1 to 5.

Kestrel

The Kestrel (fig. 2) is the simplest of the powered-lift concepts. Jet thrust from a single Pegasus 5 turbofan engine is vectorable from horizontally aft for wingborne flight

through slightly forward of vertically downward for powered lift by rotating the pairs of exhaust nozzles located midway on either side of the fuselage. Nozzle angle is controlled by a selector lever, inboard of the throttle, which is the only additional cockpit control required for V/STOL flight. Reaction controls located at aircraft extremities are mechanically connected to the conventional aerodynamic control surfaces and provide control moments during powered-lift flight. The aircraft has no stability augmentation but is equipped with a well tailored flight control system.

XV-5B

Figure 3 illustrates the fan-in-wing concept of the XV-5B. During low-speed flight, turbojet exhaust is diverted to tip turbines driving two lift fans (mounted in the wings) and a smaller nose fan which provides some powered lift and also is used for pitch control. Louvers, mounted under each wing fan, control the thrust vector angle and magnitude. The pilot has a lift stick (similar to a helicopter collective) which controls the opening and closing of the louvers for thrust modulation and a beeper switch, mounted on the lift stick, which controls the vector angle from 7° forward through 45° aft of vertically downward. Roll control and yaw control are provided by differential thrust modulation and angle modulation of the louvers, respectively. The XV-5B has limited-authority rate damping augmentation.

XC-142A

The powered-lift system of the XC-142A is illustrated in figure 4. The XC-142A is a tiltwing—deflected-slipstream transport powered by four free turbine gas generators driving cross-shafted propellers ahead of the wing and a small tail propeller which is used only for pitch control. In addition to the conventional aircraft controls, the pilot has a collective lever to modulate thrust magnitude through propeller blade angle at a constant speed and a beeper switch on the collective lever to control wing angle. Roll control is provided by differential main propeller pitch, and yaw control is provided by slipstream deflection with the aileron/flap system. Both rate damping and low-gain attitude stabilization are provided by the stability augmentation system.

Do-31

The concept represented by the Do-31 is illustrated in figure 5. The Do-31 is a mixed-propulsion jet transport powered by two Pegasus 5 lift-cruise main engines and eight RB-162 lift jets. The Pegasus engines, mounted under the wing, are vectorable from the cruise position through 30° forward of vertically downward. The pure lift jets, housed in the wing tip pods, are inclined 15° and provide a forward thrusting component.

In addition to the conventional flight controls, there is a main engine nozzle control lever for vector angle control and a single throttle for lift engine thrust modulation. Reaction controls at the extreme rear of the aircraft provide pitching moments. Rolling and yawing moments are provided by differential thrust and vector angle modulation of the lift engines. This aircraft has a full-authority attitude command flight control system for the pitch and roll axes with rate command for yaw control during powered-lift operations.

MECHANICS OF POWERED LIFT

The fundamental differences between these four V/STOL concepts or configurations seem to disappear during a powered-lift approach. Figures 6 and 7 help to explain the mechanics of a generalized powered-lift concept and its relationship to an approach glide path. The aircraft is supported by both the powered-lift vector and aerodynamic forces. The magnitude of the powered lift or thrust vector essentially compensates for wing lift lost as the approach velocity is reduced. The vector angle determines deceleration rate and final approach velocity.

Pitch attitude is a function of the glide-path angle γ and the lift the pilot hopes to generate on the aircraft through angle of attack. The approach angle in figure 6 is obviously exaggerated but, since steep approaches are in vogue, let's discuss some effects of glide-path steepening relative to the aircraft, the pilot, and the passenger. As the approach angle increases,

(1) Approach velocity must decrease to limit the rate of descent at a visual breakout altitude of 61 meters (200 feet) to about 152 to 213 meters/minute (500 to 700 feet/minute) (ref. 6).

(2) Pitch attitude is compromised between possible aerodynamic problems at high angles of attack and vectoring capability for velocity control at low angles of attack. If steep approaches are flown with a fuselage attitude which is approximately level, less forward vectoring capability is required for velocity control but the aircraft is exposed to high angles of attack and the possibility of a pitch-up or an aerodynamic stall on the wing, fan, or engine inlet. If nose-down approaches are flown, the aerodynamic problems are reduced but more forward vectoring capability is required for velocity control.

(3) Pilots as well as passengers may balk at steep nose-down approach attitudes. The pilot is faced with difficult landing transition following the visual breakout and the passenger is left hanging in his lap belt. A 12° nose-down attitude subjects pilots and passengers to an equivalent longitudinal deceleration of 0.2g and any deceleration along the flight path is additive.

STABILIZATION REQUIREMENTS

One of the pilot's primary concerns during instrument flight is maintaining or controlling the aircraft attitude. The acceleration (or g) cues, which normally warn the pilot of an attitude or rate divergence, are missing at the lower powered-lift approach velocities (ref. 7). Without stability augmentation, the pilot's total workload during precision instrument approaches will probably exceed his capabilities.

The need for attitude stabilization was appreciated early in the Kestrel program because of angle-of-attack and directional instabilities encountered in low-speed powered-lift operations. Figure 8 illustrates the effects of an angle-of-attack instability and documents a nose-down pitch divergence during an 85-knot powered-lift flight. This figure presents a time history of pitch rate, pitch attitude, and tailplane position during the divergence and recovery. In the first 5 seconds there were no pilot inputs to the pitch controls, as indicated by the constant tailplane angle. In this same time period, the pitch rate increased to 12° per second and there was an abrupt nose-down attitude divergence of 20° . What this means to the pilot is that any minor distraction from his basic attitude control scan during instrument flight could lead to a dangerous attitude near the ground or a complete loss of control. Stability problems in the XV-5B were somewhat reduced by the limited-authority rate stabilization system which slowed the rate of attitude divergence. Since both the Kestrel and XV-5B are single-pilot configurations, neither aircraft could be flown safely with the pilot hooded. Simulated instrument approaches in these aircraft were performed in a peek-a-boo fashion, where the pilot concentrated on the instrument task but had the benefit of peripheral visual cues for attitude stabilization and reduced localizer workload.

The more sophisticated flight control systems, stability augmentation, and the comforting proximity of a safety pilot allowed hooded flights in both the XC-142A and Do-31. Simulated instrument approaches in these aircraft pointed out additional benefits of attitude stabilization in the powered-lift mode.

Although the remainder of the discussion in this paper is directed toward powered-lift management in the vertical approach path, that doesn't mean that there are no problems associated with the lateral-directional axis. Indeed, relatively high turn rates and heading errors always accompany small inadvertent roll angles in low-speed flight. In addition, weak directional stability may allow dangerously high sideslip angles to develop. Test results from the XC-142A and Do-31 programs indicate that in addition to roll attitude stabilization, turn coordination for localizer maneuvering must be included in the control augmentation system.

CONVERSION MANEUVER

Figures 9 and 10 illustrate two operationally feasible conversion techniques. A basic question has been, When and where should this conversion be performed? Must it be performed in level flight to simplify the pilot's task or could it be accomplished on the glide path? In either case, for economic operations the objective is to minimize the time and fuel required on the approach.

The conversion in level flight (fig. 9) seems to have two inherent problems. The optimum point to initiate the conversion for glide-path acquisition at the desired approach speed is difficult for the pilot to predict, but must be precisely defined to minimize the time required at high power. In addition, if glide-path tracking time is to be minimized, a low final approach velocity would require an unrealistically low intercept altitude, both from the standpoint of safety and the ground noise footprint associated with the high thrust requirements away from the airfield.

On the other hand, there are apparent advantages to a conversion on the glide path (fig. 10). Acquisition and initial tracking of the glide path can be performed in wing-borne flight with a low thrust requirement and at a somewhat higher than usual intercept altitude. The conversion to final approach velocity can be delayed to a predetermined altitude (based on the deceleration and tracking time required to satisfy the pilot), and the conversion point is well defined by this altitude on the glide path. This technique reduced the Kestrel approach time at high power by about 25 percent which, in turn, reduced approach fuel requirements and the ground noise footprint.

Glide-path conversions were successfully performed in these tests. The pilots believe that glide-path conversion is operationally feasible, and with adequate attitude stabilization the workload is acceptable. Considering pilot workload, the number of sequenced steps involved, controls to be operated, and parameters to be controlled during the conversion was too large with some of these configurations (ref. 8). Conversion procedures must be simplified or automated for commercial use of advanced configurations.

GLIDE-PATH CONTROL

Having acquired the glide path and performed the conversion, the pilot is primarily interested in glide-path control. The powered-lift vector suggests two basic techniques of glide-path control: vector angle modulation and vector magnitude or thrust modulation. Both techniques were investigated. Vector angle modulation was ineffective; the pilot workload was high and the tracking results were poor. Thrust modulation was preferred by all pilots. With this technique, the vector angle is dictated by the final approach velocity, pitch attitude is stabilized, and thrust is modulated for direct lift control of the

glide path. Although there are small variations in angle of attack during the correction, airspeed or deceleration schedule is essentially unaffected.

TRACKING PERFORMANCE

Figures 11 to 14 illustrate powered-lift glide-path tracking performance from ILS approaches using raw glide-path error signals for guidance. Curvilinear approaches are desirable where airspace is at a premium (ref. 6). The test aircraft lacked the complex guidance systems required for curvilinear approaches; however, the powered-lift management techniques developed on the straight-in approaches should still apply. Typical selected data from Kestrel, XV-5B, and Do-31 approaches are used to illustrate procedures and several approaches from the XC-142A, to emphasize stabilization benefits.

Kestrel

Tracking performance using direct lift control in the Kestrel is illustrated in figure 11, which presents throttle position, nozzle angle, tailplane angle, pitch attitude, airspeed, and glide-path errors during a 7° 85-knot approach.

Acquisition and initial tracking were performed in wingborne flight at 165 knots. The conversion to powered lift was initiated at 488 meters (1600 feet) by vectoring thrust to predetermined values, and pitch attitude was established at 1° nose-down (more or less) for a nominal approach angle of attack of 6° . As the final approach velocity is determined by vector angle, airspeed control is no longer a primary concern of the pilot. Direct lift control produced good tracking results with frequent small thrust corrections.

XV-5B

Figure 12 illustrates similar performance parameters for a 10° decelerating approach in the XV-5B. The fuselage attitude (10° nose-down) paralleled the glide path and unloaded the wing. The conversion to 85 knots was performed in level flight. As the glide path was acquired, the aircraft was nosed over to parallel the approach path and the vector angle was adjusted to maintain airspeed. Direct lift control was used for glide-path corrections. Two additional vector steps were performed at predetermined attitudes to decelerate the final approach to a hover over the touchdown point. The improvement in pitch attitude control over the Kestrel is attributed to stability augmentation.

XC-142A

Having looked at peek-a-boo approaches in the unaugmented Kestrel and in the XV-5B with limited-rate stabilization, let's investigate the effects of a little attitude

stabilization and a collective or power command indicator in the XC-142A. Figure 13 presents glide-path tracking performance during several hooded approaches in the XC-142A. The point to grasp is the significant improvement in tracking performance provided by the addition of low-gain attitude stabilization to the basic stability augmentation system. The stabilization allowed pilots more time to concentrate on powered-lift management and the tracking task. Most of these approaches traversed the steep back-side portion of the XC-142A power-required curve, which explains why the pilot occasionally falls out of the sky when he's busy with attitude control instead of power management. Realizing the benefits of this low-gain attitude stability augmentation system, pilots expressed the desire for a higher gain system.

Do-31

The Do-31 has complete attitude stabilization and a full-authority attitude command control system. Figure 14 presents tracking performance data from a 7⁰ decelerating hooded approach in the Do-31. The 610-meter (2000 foot) intercept altitude was predicated on a wingborne acquisition, lift engine start, conversion to powered-lift flight, and a one-step deceleration on the glide path.

Pitch attitude control on this approach was essentially hands off, provided by an attitude preselect feature in the control system. The pilot has an attitude override capability, but as can be seen in the stick position trace there are no significant pilot inputs.

At intercept, a simultaneous pitch-attitude and vector-angle adjustment is required for initial glide-path tracking at 140 knots. Once on the glide path, lift engines are started and remain at idle thrust until the conversion.

At the conversion point, several things happen very quickly as follows:

- (1) Approach attitude is selected by pressing a trim-release button on the control stick.
- (2) Main engine vector angle is adjusted for the desired deceleration schedule.
- (3) Lift and main engine thrusts are increased to nominal hover settings.

Lift engines are modulated for direct lift control on the glide path and for hover-height control. Direct-lift-control tracking is, again, excellent.

CONCLUDING REMARKS

Flight studies of aircraft representing four V/STOL concepts (vectored jet, fan in wing, tiltwing, and mixed-propulsion jet) indicated that for any powered-lift V/STOL aircraft to be flown safely on instruments, attitude stabilization is required. Whether the

most desirable control system is an attitude command (as in the Do-31) or rate command attitude hold (the authors' personal preference) is debatable; but, whatever the system is, the pilot wants the aircraft to stay where it is when he turns loose of the control stick.

The primary objective of the studies – to develop an operational powered-lift approach technique – appears to have been realized with the attitude stabilized in the powered-lift mode. This approach technique includes a wingborne acquisition of the glide path, conversion to powered-lift flight on the glide path, thrust modulation for direct lift control of the glide path, and deceleration during the approach. This technique minimizes the time, fuel, and airspace requirements in the terminal area.

REFERENCES

1. McKinzie, Gordon A.; Ludwig, John H.; Bradfield, Edward N., Jr.; and Casey, William R.: P-1127 (XV-6A) VSTOL Handling Qualities Evaluation. FTC-TR-68-10, U.S. Air Force, Aug. 1968.
2. Harnish, R. L.; and Everett, W. L.: XV-5A Pilot Operating Manual. Rep. No. 64B150, Ryan Aeronaut. Co., Dec. 17, 1964.
3. Anon.: XV-5A Lift Fan Flight Research Aircraft. Phase I Flight Test Results – Vol. I. Rep. No. 166 (Contract DA 44-177-TC-715), Gen. Elec. Co., Mar. 1966.
4. Down, Harry W., Jr.; Satterwhite, James J.; and Jones, Gay E.: XC-142A Limited Category II Stability and Control Tests. FTC-TR-68-9, U.S. Air Force, Sept. 1968.
5. Wood, Drury W., Jr.: The DO-31 VSTOL Jet Transport. 1967 Report to the Aerospace Profession, Tech. Rev., vol. 8, no. 4, Soc. Exp. Test Pilots, 1967, pp. 125-146.
6. Schade, R. O.: VTOL Aircraft Terminal Area Operations Research. [Preprint] 680663, Soc. Automot. Eng., Oct. 1968.
7. Reeder, John P.: The Changing World of the Pilot in the Next Decade – V/STOL Aircraft Operations. Paper presented at Human Factors Society National Symposium (San Francisco, Calif.), Oct. 1970.
8. Kelley, Henry L.; and Champine, Robert A.: Flight Investigation of a Tilt-Wing VTOL Aircraft in the Terminal Area Under Simulated Instrument Conditions. AIAA Paper No. 71-7, Jan. 1971.

CONFIGURATIONS EVALUATED

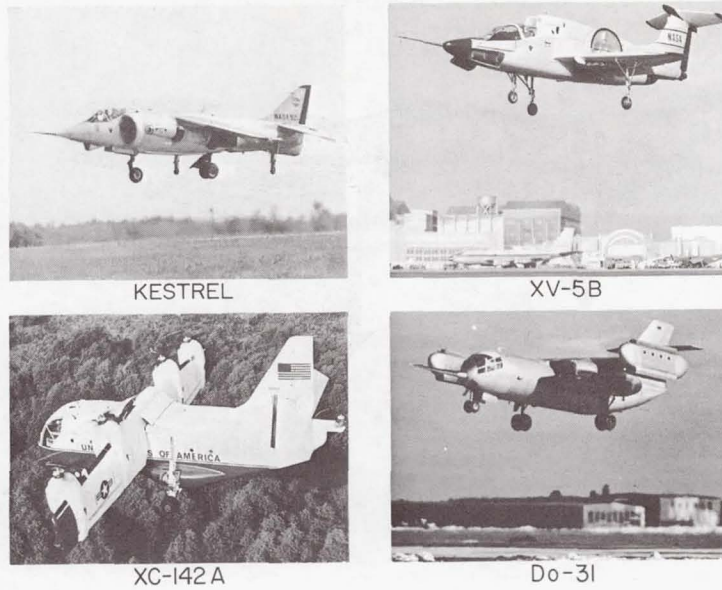


Figure 1

KESTREL VECTORED JET THRUST

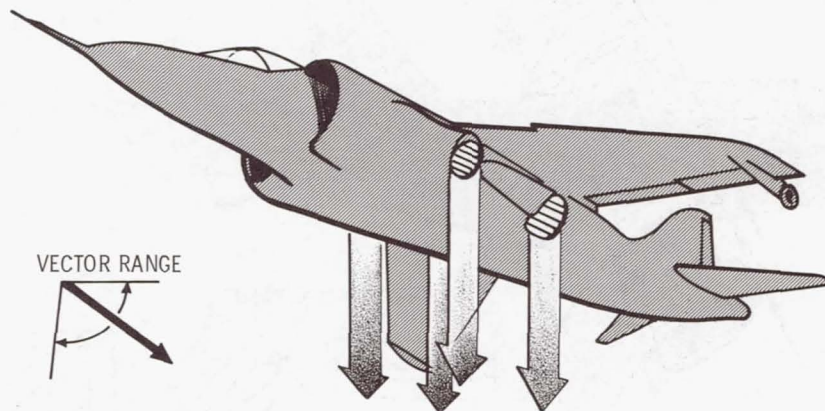


Figure 2

XV-5B
LIFT FAN

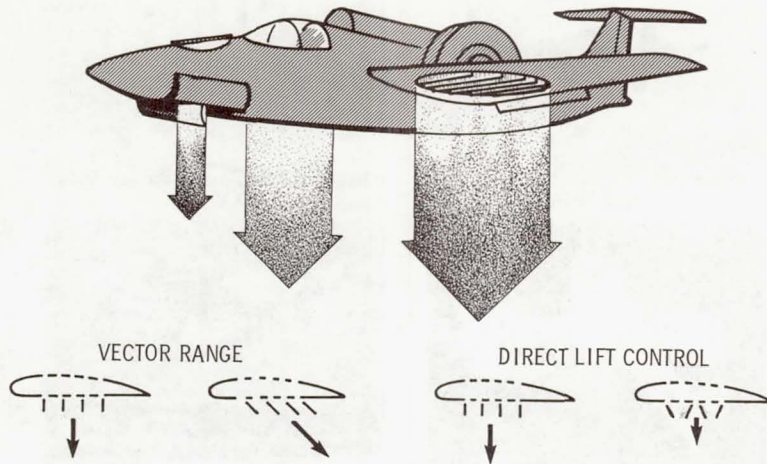


Figure 3

XC-142 A
TILTWING

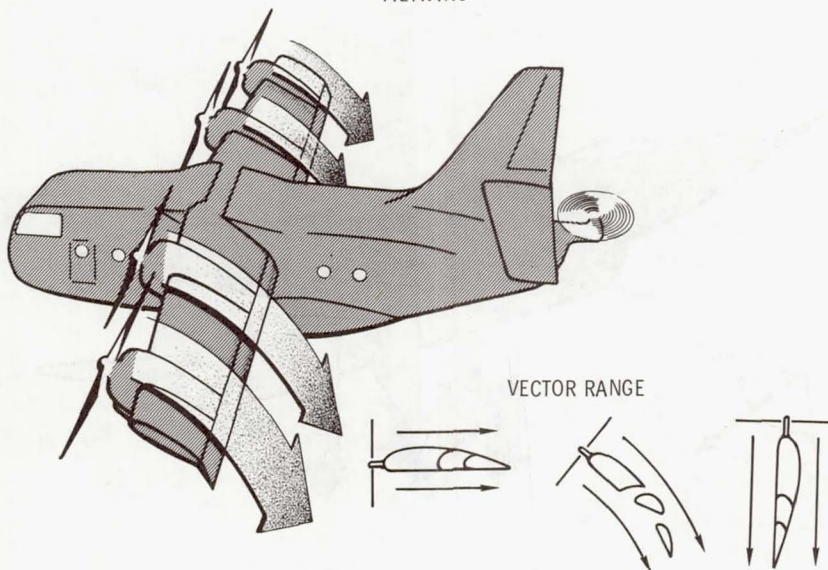


Figure 4

Do-31
MIXED-PROPULSION JET

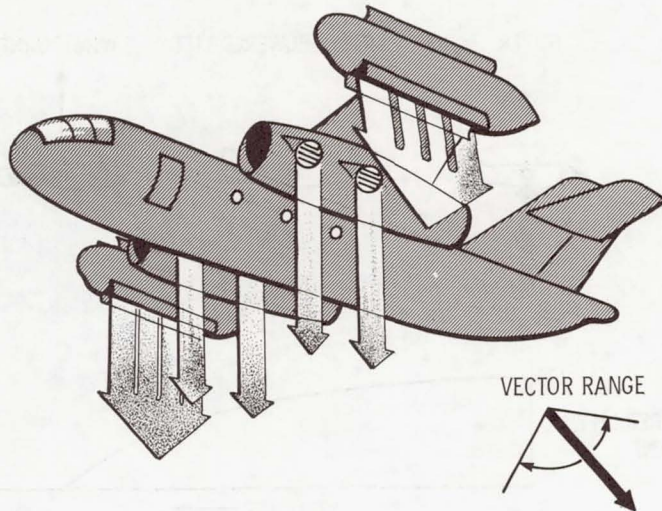


Figure 5

MECHANICS OF POWERED LIFT

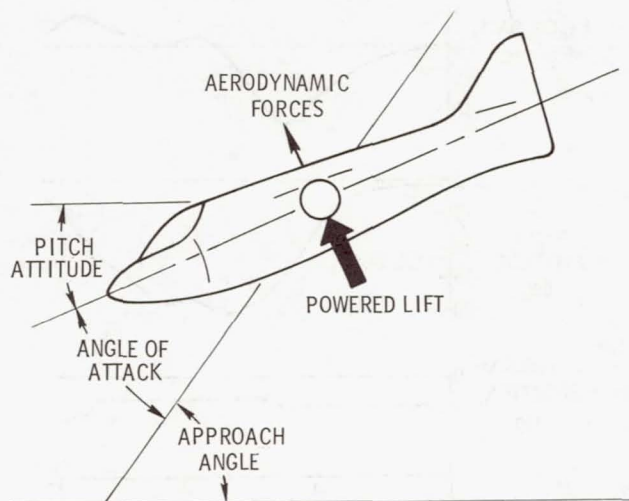


Figure 6

POWERED-LIFT REQUIREMENTS

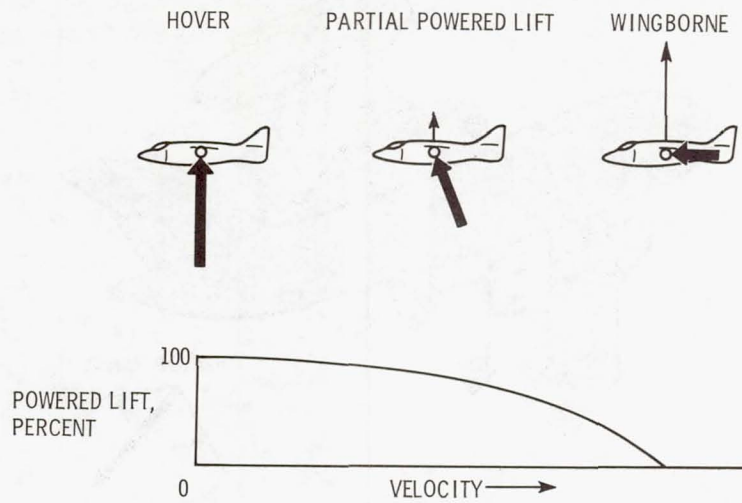


Figure 7

KESTREL LONGITUDINAL PITCH DIVERGENCE

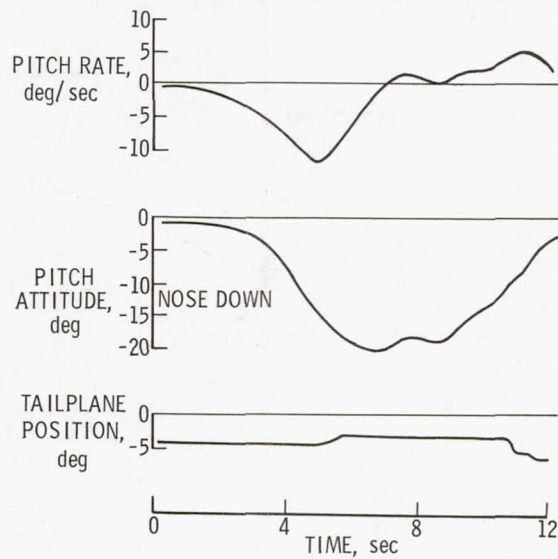


Figure 8

CONVERSION TO POWERED-LIFT FLIGHT
CONVERSION IN LEVEL FLIGHT

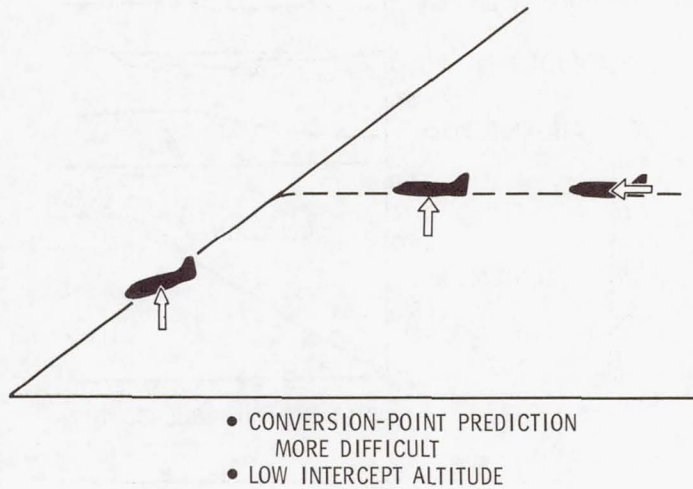


Figure 9

CONVERSION TO POWERED-LIFT FLIGHT
CONVERSION ON GLIDE PATH

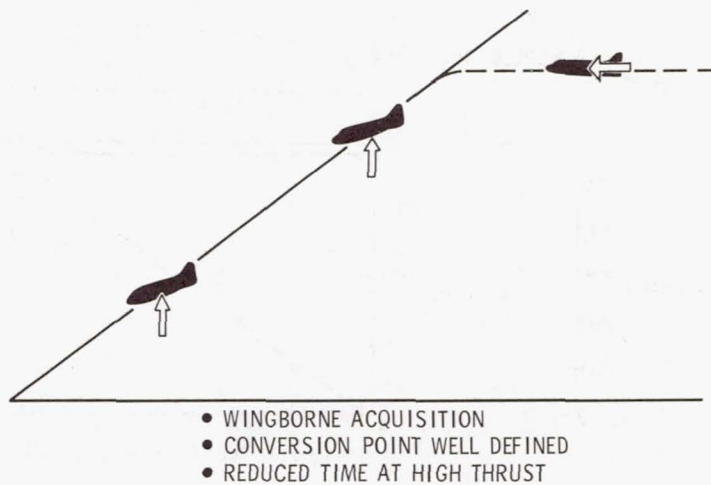


Figure 10

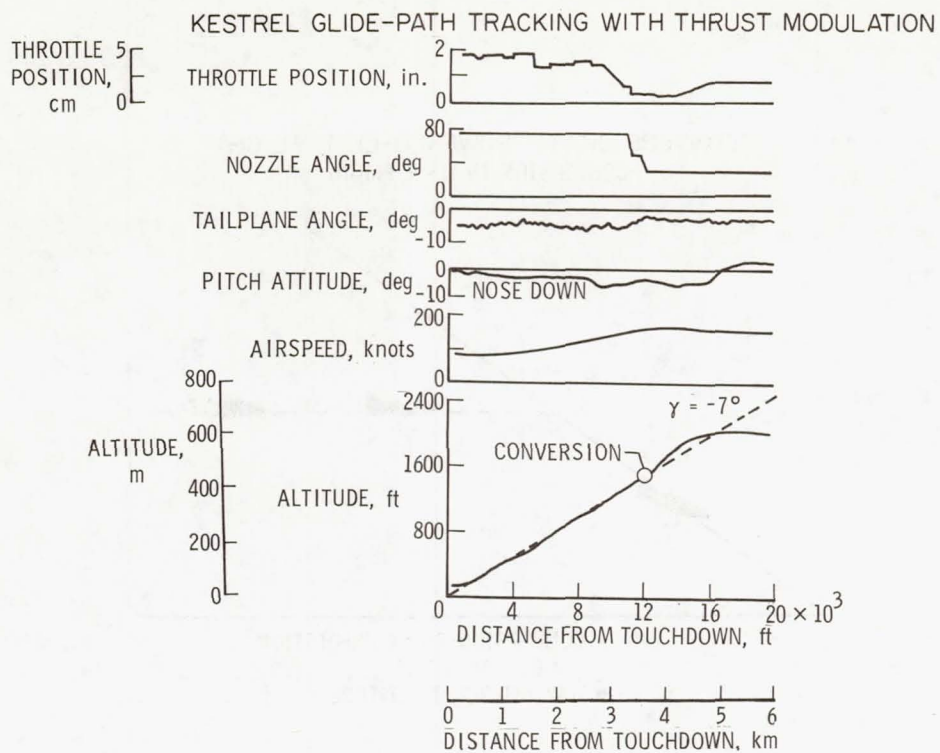


Figure 11

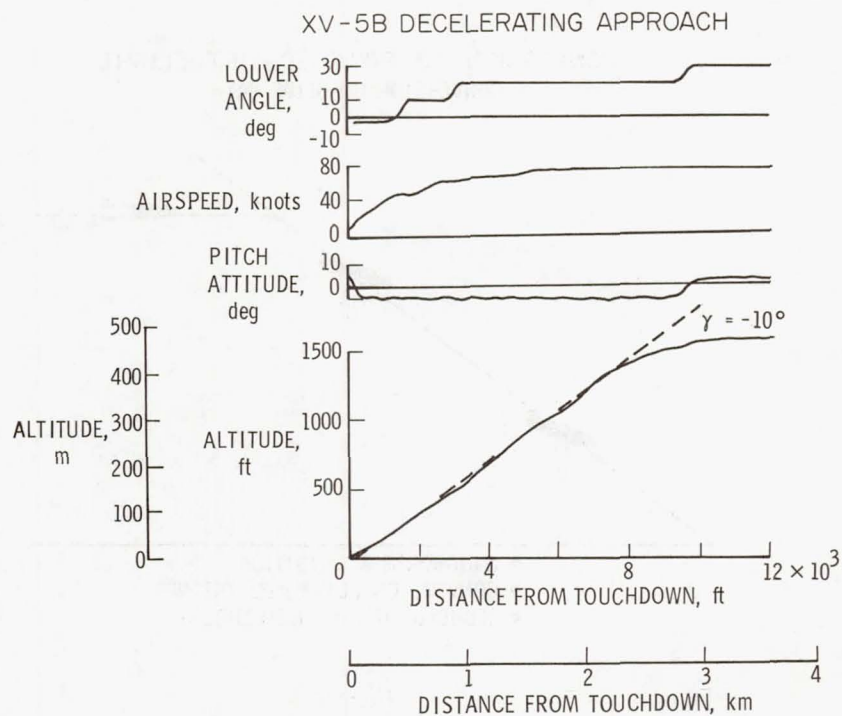


Figure 12

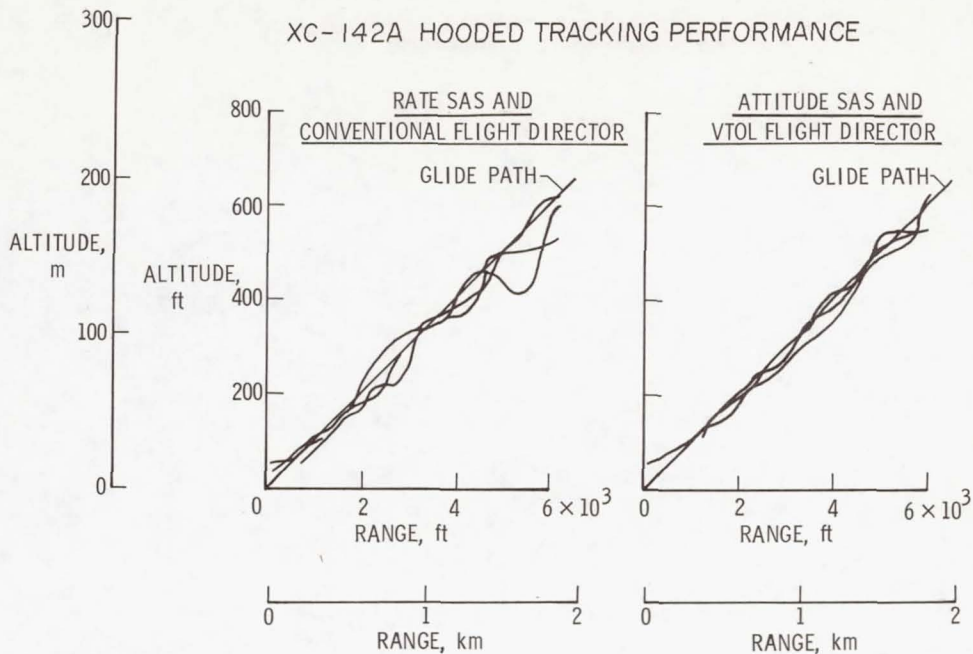


Figure 13

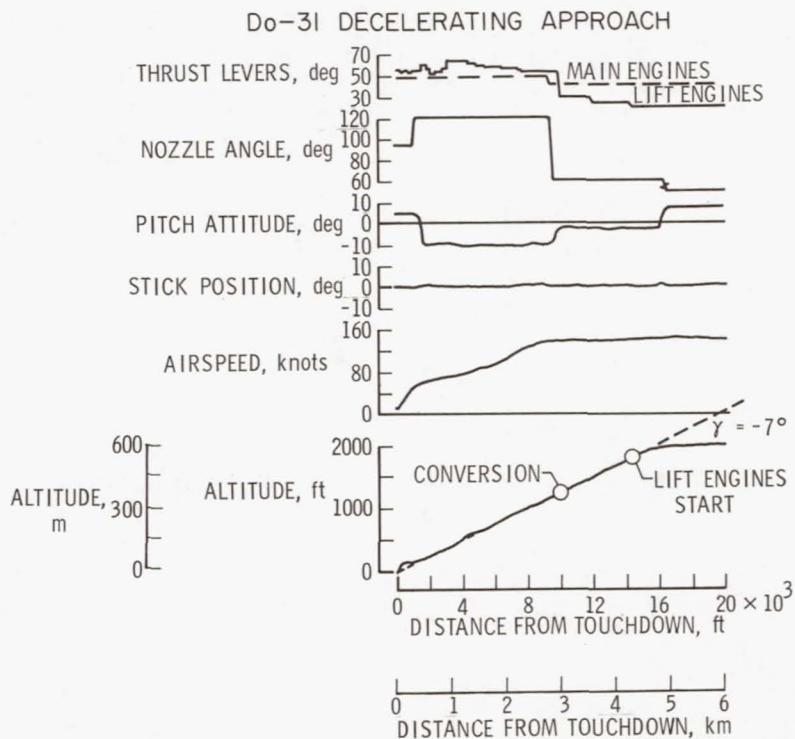


Figure 14

Page intentionally left blank

ANALYSIS OF SOME HELICOPTER OPERATING PROBLEMS

By Charles E. K. Morris, Jr., John F. Ward,
Julian L. Jenkins, Jr., and William J. Snyder
Langley Research Center

INTRODUCTION

Helicopters differ from fixed-wing aircraft not only in their appearance but also in their unique capabilities. Along with their unique capabilities, however, they have some unique operating problems. This paper presents some insight into these problems gained at the Langley Research Center through analysis and experimental studies of some current helicopter operating conditions. Four separate topics are covered.

LOW-SPEED DIRECTIONAL-CONTROL LIMITATION

The first topic is a directional-control limitation that affects some helicopters with tail rotors as they seek to maintain a heading while hovering near the ground in a low-speed tailwind (ref. 1). When the limitation is encountered, the pilot cannot maintain his heading, and the power surges experienced have damaged the tail-rotor gear boxes.

The flow field determined by wind-tunnel tests to be associated with the directional-control limitation is shown in figure 1. To see how this flow pattern is formed, begin with the side view of a helicopter hovering near the ground. The helicopter main rotor pulls air through the rotor disk and forces this air downward and outward. A low-speed wind rolls the upstream portion of the main-rotor flow up on itself. This swirling boundary of the main-rotor flow is called a ground vortex. The upper, oblique view shows how the ground vortex lies near the ground and curls around the helicopter. As windspeed is increased past a critical value, the ground vortex is both diminished and carried under the rotor, and then vanishes.

The relationship between this flow field and the directional-control limitation was determined by an investigation in the Langley full-scale wind tunnel. The investigation obtained data on the aerodynamics of a helicopter hovering near the ground in a low-speed wind from the rear. One of the special features of the model used (fig. 2) was that the tail-rotor assembly was mounted on a separate balance from the rest of the model. This arrangement permitted independent measurements to be made of tail-rotor performance.

Some of the data obtained with this model in a pure tailwind are presented in figure 3. The tail-rotor blade-pitch requirements for directional trim in a tailwind are presented as the ratio of blade pitch required at a given tailwind velocity to the blade

pitch required at zero velocity. Thus, at zero velocity the blade-pitch ratio is 1. Peak values of blade pitch are required when, between 10 and 15 knots, the ground vortex envelops the tail rotor. The data curve for tail-rotor power required is almost identical and has peak values at the same tailwind velocity. In the critical windspeed range, small fluctuations in windspeed can cause large fluctuations in pitch and power as the pilot seeks to control heading. The relative magnitude of tail-rotor power that might be reached under these dynamic conditions is even greater than the curve indicates, since the curve applies only to requirements for trim in a steady tailwind. When these requirements exceed the physical limitation on blade pitch, the pilot cannot maintain heading control. The tunnel data show fairly conclusively that the control limitation is produced by the effects of immersing the tail rotor in the ground vortex.

Several solutions have been tried with varying degrees of success. To limit the damage due to tail-rotor power surges, the amount of available blade pitch has been reduced in some vehicles. However, this change only serves to assure that the modified vehicle will have inadequate control when these flow conditions are encountered. In other instances, good results were obtained by relocating the tail rotors on the opposite side of the tail fin and changing the direction of rotation. Recent flight tests have shown that the problem can be alleviated in some cases by making the tail-rotor direction of rotation opposite to the ground-vortex direction of rotation (ref. 2). Now that the mechanism of the problem is better understood, possibly other, more general, design solutions can be applied.

ROTOR OSCILLATORY LOADS IN MANEUVERS

Rotor oscillatory loads in maneuvers are significant, since they produce one of the boundaries on the operating envelope of almost every helicopter. Figure 4 presents a typical helicopter operating envelope in terms of load factor and airspeed. At low speeds, a power limit restricts the steady load factor that the helicopter can achieve. At high speeds, the vibration boundary limits the load factor; this boundary is due to structural vibration produced by high levels of rotor oscillatory loads. The vibration boundary was explored during a flight investigation with an extensively instrumented, four-blade, articulated rotor system. The results of this investigation indicate that the rotor oscillatory loads are increased by interactions between the rotor blades and the tip vortices that they trail (ref. 3).

The flight investigation data can be more easily interpreted by first considering figure 5, which shows the top view of a four-blade rotor and the schematic representation of the trailed-vortex pattern at 90 knots. Note that as the reference blade section follows the dashed line, it crosses the paths of three tip vortices. In level flight, the trailed-vortex pattern normally lies below the rotor; this is not the case during some maneuvers.

The difference between data for level flight and a pullup maneuver can be seen in figure 6. These aerodynamic pitching-moment data were obtained by integrating pressure measurements taken at the 95-percent blade radius. The calculated azimuthal locations of the trailed-vortex crossings indicated in figure 6 correspond to the trailed-vortex crossings indicated in figure 5. The three strong fluctuations in the data for a 1.5g maneuver indicate vortex strikes. During the maneuver, the flight path became sufficiently curved for the rear of the rotor to cut through a portion of the rotor wake. This produced strong interactions between the blade and vortex not seen in data for 1g, level flight. The pitching-moment fluctuations are seen by each blade as torsional excitation at the frequency of the vortex strikes.

Correlation between blade torsional excitation and its response is indicated in figure 7. Both torsional response and frequency of the vortex strikes are shown as functions of airspeed; the torsional natural frequency of the rotating blade is constant with airspeed. As indicated in figure 7, the vortex-strike frequency decreases with increasing airspeed until, at some airspeed, the vortex-strike frequency is at the blade torsional natural frequency. When this occurs, the torsional excitation is acting on the blade at its resonant frequency. As can be anticipated, the torsional-response data, presented in figure 7, show a pronounced increase as the airspeed for this resonance is approached. The increasing torsional response of all the blades is felt by the maneuvering helicopter as rotor oscillatory loads. These loads in turn contribute significantly to the vibration boundary that limits helicopter maneuver capability.

The results presented in figure 7 suggest two methods for alleviating the problem. One method is to reduce the blade torsional natural frequency in order to increase the airspeed at which resonance occurs. Caution should be used when the torsional stiffness of the rotor system is reduced in order to avoid encountering blade flutter. The other method is to increase the vortex-strike frequency by increasing the number of rotor blades; this method also raises the airspeed at which the blade strikes are in resonance with the blade torsional natural frequency. A third method is to change the relative spacing of the rotor blades in order to minimize interactions between the blades and the tip vortices.

MANEUVER LIFT SHARING OF COMPOUND HELICOPTERS

The third topic is maneuver lift sharing between the wing and the rotor of compound helicopters and means of properly managing this lift sharing. A compound helicopter, shown in the sketch in figure 8, has a larger operating envelope than does a pure helicopter. In steady, level flight the sharing of lift by the rotor and the wing is comparatively simple to control. However, for a compound helicopter to achieve the greater

operational envelope of which it is basically capable, lift sharing must also be controlled in maneuvers.

The basic problem that arises in maneuvering flight is high rotor-lift sensitivity. Rotor-lift sensitivity may be defined as the change in rotor lift per unit load factor. Thus, when an aircraft with this problem performs a maneuver, the rotor-lift increase tends to be greater than the wing-lift increase. High rotor-lift sensitivity produces two adverse effects — first, the wing is used inefficiently, and second, the rotor encounters the same problems of high loads and vibration levels that are encountered on a pure helicopter.

Two methods can be used to improve maneuver lift sharing. One is fuselage attitude control by means of aerodynamic control surfaces. In this case, the rotor does not have to generate the control moment necessary to maneuver the aircraft: an airplane-type control surface, such as an elevator, pitches the fuselage and wing to the desired angle of attack. Another method is rotor-control feedback in the form of blade cyclic or collective pitch. Feedback for rotor-lift control is somewhat analogous to a conventional fixed-wing stability augmentation system except that commanded control inputs would be modified to effect a change in rotor lift. Langley Research Center personnel have conducted U.S. Army sponsored flight investigations with several compound helicopters each of which demonstrates one method of rotor-lift control. Published results for flight tests with a compound helicopter with rotor-control feedback are given in reference 4. Experimental trends from these flight tests are presented in figures 9 and 10.

The data in figure 9 illustrate the effect of fuselage control with an elevator on rotor-lift sensitivity in maneuvering flight at 140 knots. Rotor-lift sensitivity is expressed as the ratio of the incremental increase in rotor lift to the incremental lift required for the maneuver. Thus, a value of 1 indicates that the maneuver is accomplished solely by the addition of rotor lift. This ratio of rotor-lift change to total-lift change is plotted against the percentage of elevator control. The design of the flight-test vehicle allowed the control mode to be varied from pure rotor control to pure elevator control. At zero percent elevator control (pure rotor control) the rotor provides almost all the additional lift for a maneuver. With increasing percentage of elevator control, the elevator can better control fuselage attitude and the wing contributes an increasing proportion of the lift required for a maneuver. This, of course, results in decreasing rotor-lift sensitivity.

Flight-test results for rotor-lift sensitivity with rotor-control feedback are presented in figure 10. In this case, cyclic-control feedback occurs through a mechanical-control gyro which limits the aircraft rate for a given control input by the pilot. The same expression is used for rotor-lift sensitivity as in figure 9, but it is plotted against airspeed. The trend of the flight-test results indicates a desirable decrease in sensitivity

with airspeed. This means that rotor-lift requirements diminish at higher speeds, where the rotor has less lift capability. Although this curve does not in itself indicate the effect of rotor-control feedback, the theoretical curve which accounts for the cyclic-control requirement does predict the correct trend, and this theory indicates that feedback can be used effectively to reduce the rotor-lift sensitivity.

In summary, compound helicopters can have a significantly larger operating envelope if the lift sharing between the wing and rotor is properly controlled. Data and analytical tools are now becoming available to guide design considerations for maneuver lift-sharing control for compound helicopters.

FUSELAGE VIBRATION AND PASSIVE ISOLATION

The last topic to be covered is fuselage vibration and the use of passive isolation to control it. The adverse effects of fuselage vibration, listed in figure 11, are poor ride qualities (paper no. 25) and reduced structural integrity of the vehicle. Also, several methods of reducing vibration are listed in figure 11. First, direct reduction in rotor oscillatory loads decreases the vibratory energy at its source. Another approach is the absorption of vibration energy by helicopter components or additional masses designed for this purpose. A third approach is the isolation of portions of the fuselage from the rotor oscillatory loads.

The simplest technique, passive cabin isolation, was used in a flight investigation at Langley as a first step in studying fuselage vibration reduction methods. Figure 12 is a schematic illustration of the passive isolation system and sensor locations on the vehicle. A large, soft isolation spring separated the cabin from the fuselage. This spring was designed to isolate the cabin from only vertical vibrations produced by the three-blade main rotor. Accelerometers were placed in the cabin and on the cabin support structure to record the vibration levels in each location.

The isolation system installed in the test vehicle had some of the undesirable characteristics that can occur with passive cabin isolation designs. First, since the mechanical-control linkages had to cross the vibration barrier, any differential motion between the cabin and the rest of the airframe resulted in mechanical-control coupling. Second, the large, soft spring amplified low-frequency motions. Third, the static deflection of the spring due to the cabin weight used up much of the spring deflection capability. As a result, cabin bottoming in a high g maneuver was a distinct possibility. These problems notwithstanding, the passive system did provide a significant improvement in cabin vibration levels.

Flight-test data from the accelerometers are presented in figure 13, which permits a comparison to be made of isolated and nonisolated systems at 120 knots airspeed. A

spectral analysis was performed on the vibration records from the accelerometers. The results are presented as the significant spectral components of vibration power, a measure of the vibration energy a structure must absorb. These components are given for the first three harmonics of main-rotor blade passage frequency. Both bar graphs are plotted to the same scale of vibration power. Data for the nonisolated system show that the cabin must absorb more vibration power at all frequencies. The data for the isolated system indicate that the perceived vibration power for the cabin was significantly lower than for the nonisolated system. However, cabin vibration power is negligible when compared with that which the cabin support must absorb. This illustrates a potential disadvantage of isolation systems: a decrease in the vibration level in one part of the vehicle can be accompanied by an increase in the levels elsewhere.

A review of the general results and potential problems of passive cabin isolation is given as figure 14. Passive isolation produced the desired attenuation in high-frequency vibrations in the cabin. However, it also produced amplification of high-frequency vibrations in the cabin support, amplification of low-frequency motions in the cabin, mechanical-control coupling, and instances of cabin bottoming. In general, passive isolation appears to be one of the less desirable means of reducing fuselage vibration. Work is now underway in preparation for flight testing of an active cabin isolation system which will be installed in place of the passive system.

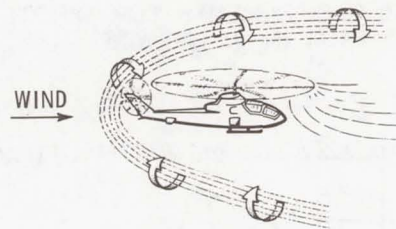
CONCLUDING REMARKS

The helicopter operating problems discussed in this paper have been shown to be amenable to analysis and experimental evaluation. Work continues in each of the areas discussed in an effort to develop practical solutions for the problems identified.

REFERENCES

1. Huston, Robert J.; and Morris, Charles E. K., Jr.: A Wind-Tunnel Investigation of Helicopter Directional Control in Rearward Flight in Ground Effect. NASA TN D-6118, 1971.
2. Batra, N. N.: Results of a Tail Rotor Direction-of-Rotation Test. J. Amer. Helicopter Soc., vol. 16, no. 2, Apr. 1971, pp. 43-44.
3. Ward, John F.: Helicopter Rotor Periodic Differential Pressures and Structural Response Measured in Transient and Steady-State Maneuvers. J. Amer. Helicopter Soc., vol. 16, no. 1, Jan. 1971, pp. 16-25.
4. Jenkins, Julian L., Jr.; and Deal, Perry L.: Investigation of Level-Flight and Maneuvering Characteristics of a Hingeless-Rotor Compound Helicopter. NASA TN D-5602, 1969.

HELICOPTER AND GROUND VORTEX



OBLIQUE VIEW



SIDE VIEW

Figure 1

DIRECTIONAL-CONTROL INVESTIGATION HELICOPTER MODEL



Figure 2

TAIL-ROTOR REQUIREMENTS FOR DIRECTIONAL TRIM IN A TAILWIND

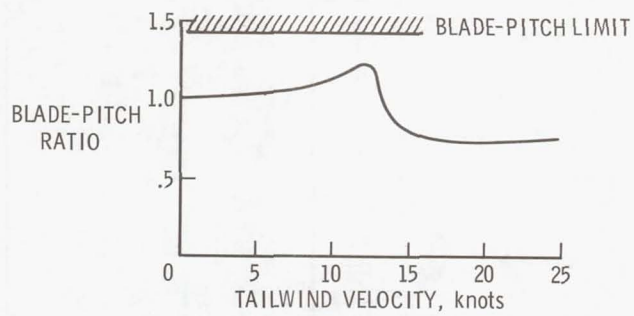


Figure 3

HELICOPTER OPERATING ENVELOPE

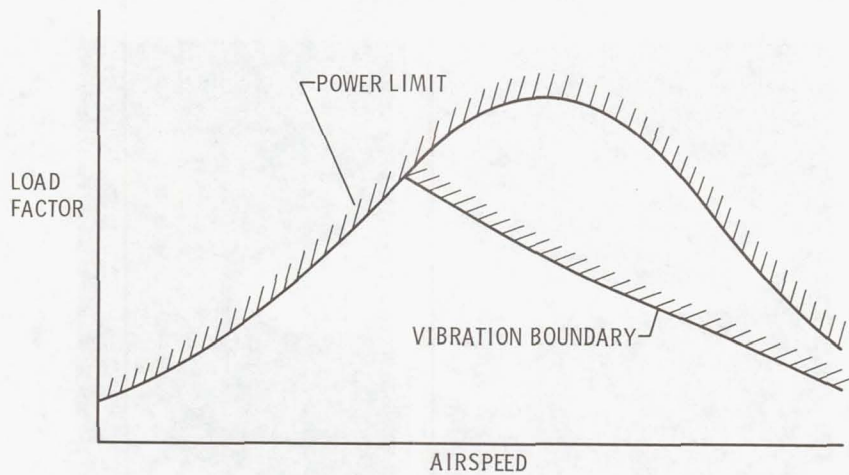


Figure 4

TRAILED-VORTEX PATTERN AT 90 knots

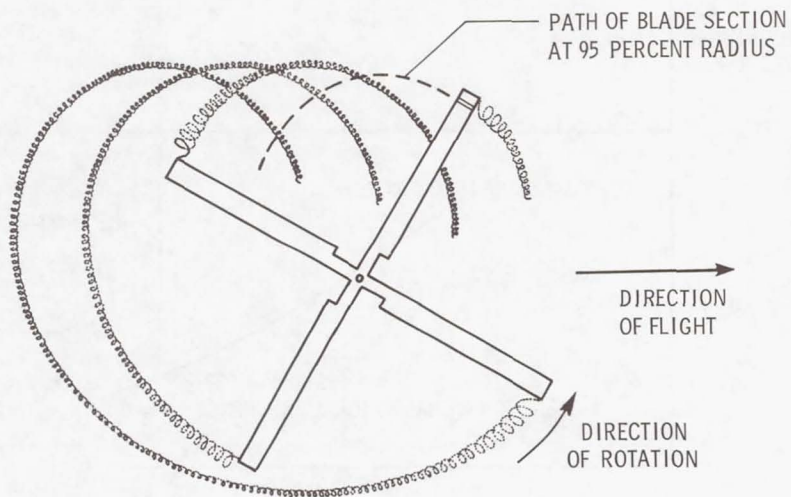


Figure 5

AERODYNAMIC PITCHING MOMENT AT 95 PERCENT BLADE RADIUS ONE ROTOR REVOLUTION AT 90 knots

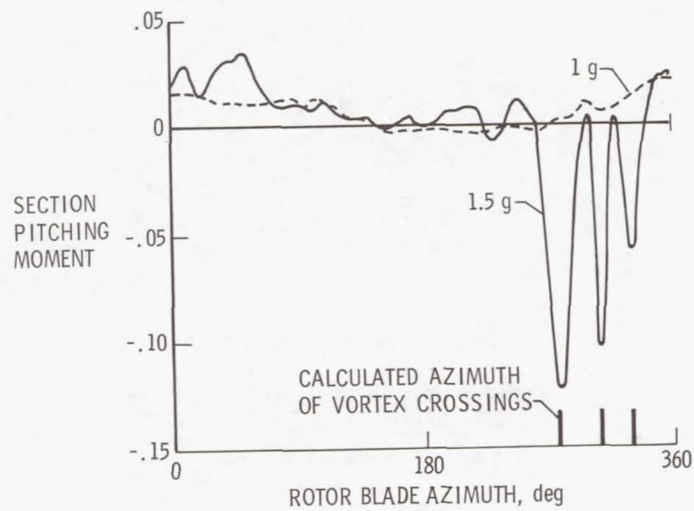


Figure 6

BLADE TORSIONAL EXCITATION AND RESPONSE

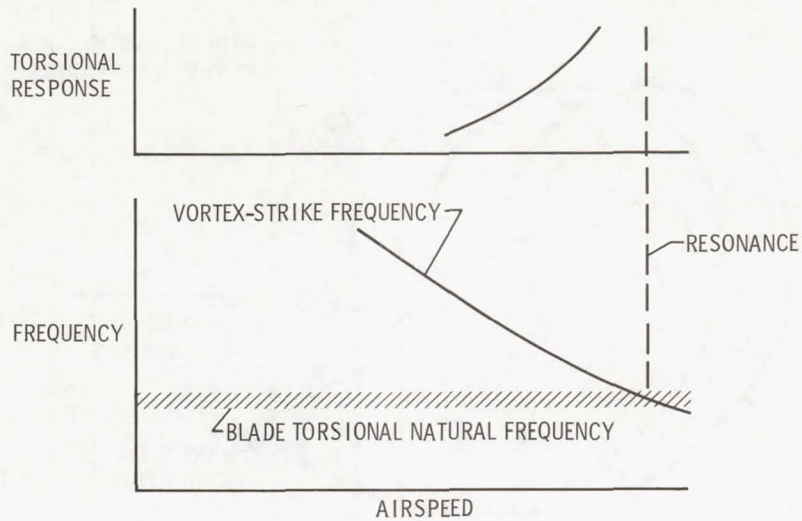
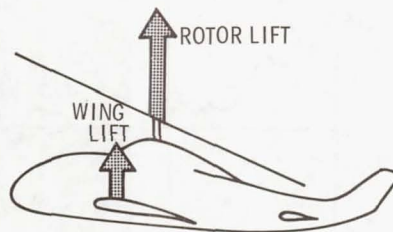


Figure 7

MANEUVER LIFT SHARING OF COMPOUND HELICOPTERS



PROBLEM:

- HIGH ROTOR-LIFT SENSITIVITY

METHODS TO IMPROVE MANEUVER LIFT SHARING:

- FUSELAGE CONTROL
- ROTOR-CONTROL FEEDBACK

Figure 8

EFFECT OF FUSELAGE CONTROL ON ROTOR-LIFT SENSITIVITY
AIRSPEED: 140 knots

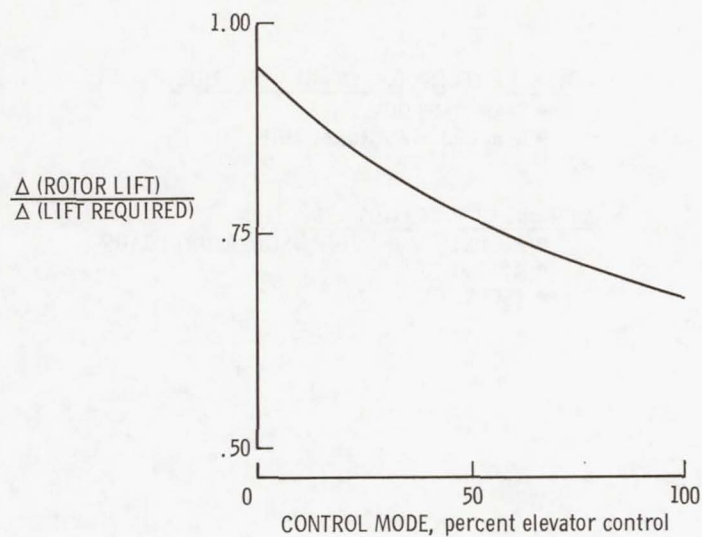


Figure 9

ROTOR-LIFT SENSITIVITY WITH ROTOR-CONTROL FEEDBACK

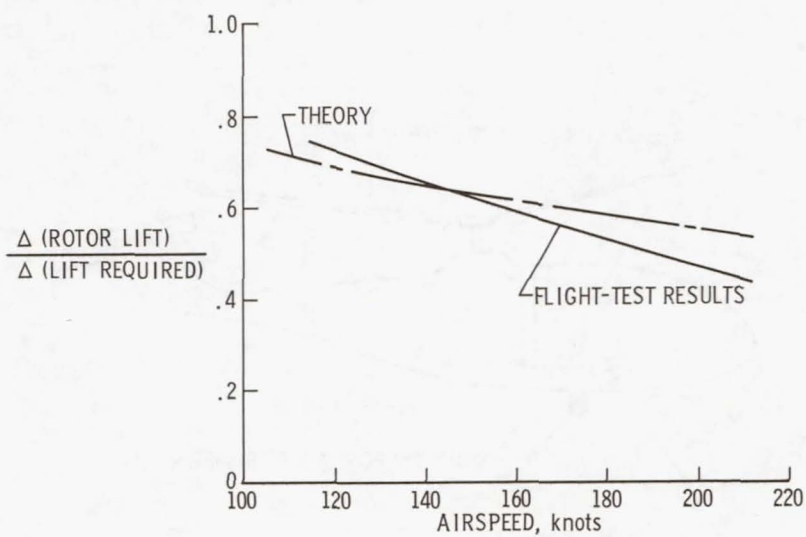


Figure 10

FUSELAGE VIBRATION

ADVERSE EFFECTS OF FUSELAGE VIBRATION:

- POOR RIDE QUALITIES
- REDUCED STRUCTURAL INTEGRITY

METHODS OF VIBRATION REDUCTION:

- REDUCTION OF ROTOR OSCILLATORY LOADS
- ABSORPTION
- ISOLATION

Figure 11

PASSIVE ISOLATION SYSTEM AND SENSOR LOCATIONS

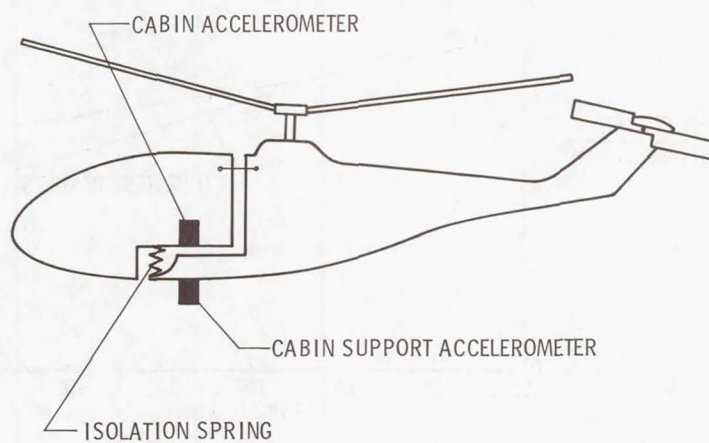


Figure 12

EFFECT OF ISOLATION SYSTEM

AIRSPEED: 120 knots

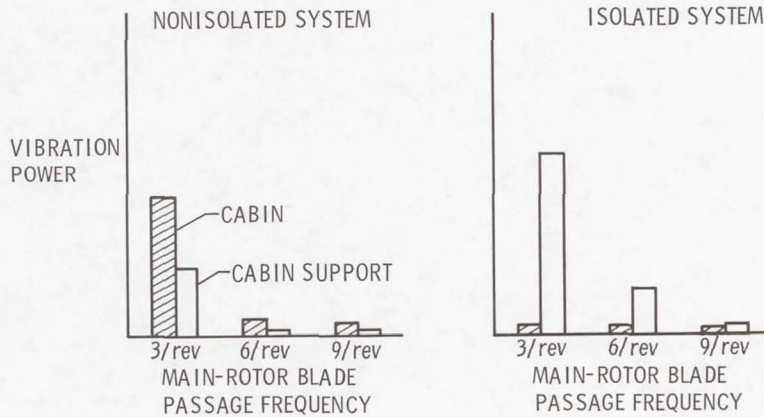


Figure 13

PASSIVE CABIN ISOLATION

GENERAL RESULTS:

- ATTENUATION OF HIGH-FREQUENCY VIBRATIONS IN CABIN

POTENTIAL PROBLEMS:

- AMPLIFICATION OF HIGH-FREQUENCY VIBRATIONS IN CABIN SUPPORT
- AMPLIFICATION OF LOW-FREQUENCY MOTIONS IN CABIN
- MECHANICAL-CONTROL COUPLING
- CABIN BOTTOMING

Figure 14

Page intentionally left blank

SOME ASPECTS OF THE AERODYNAMICS OF STOL PORTS

By Hermon M. Parker and Jeffry N. Blanton

University of Virginia

and

Kalman J. Grunwald

Langley Research Center

INTRODUCTION

There have been a number of proposals to provide STOL service to metropolitan areas by operating from the tops of buildings. A concept of an elevated STOL port is shown in figure 1. Of course, many problems, both technical and psychological in nature, are involved in operating from elevated STOL ports. At the present stage of investigation, it is not certain that all the problems have even been recognized.

In this paper, some aspects of elevated-STOL-port aerodynamics are considered. Two problems of concern are (1) crosswinds and (2) building-induced flow fields. It is obvious that there may be occasions, perhaps many occasions, when large crosswinds will produce severe operational problems. The steady crosswind velocity profile in the landing region may itself be a problem. The phrase "building-induced flow fields" suggests that flow separation, vortex shedding, or other unsteady flow phenomena may contribute significantly to the hazards of landing a STOL craft. In some instances, it is likely that surrounding buildings or other structures would influence the airflow over a STOL port, but the present discussion of building-induced flow fields is confined to the flow induced by the STOL-port building itself.

Two possible approaches to the solution of the crosswind and building-induced-flow-field problems are (1) aircraft design and operation and (2) modifications to the elevated-STOL-port building. For the work reported herein, the second approach was used. The investigation has been and is a joint effort of the NASA Langley Research Center and the University of Virginia. It was begun a little over a year ago at the encouragement of the Federal Aviation Administration. The first phase of the study was conducted at Langley. Some quantitative measurements of dynamic pressure were made, but most of the observations were qualitative flow visualizations - smoke and tuft. The second phase was conducted at the University of Virginia and involved the effect of fence structure and geometry on changes in crosswind velocity profiles.

SYMBOLS

b	building width
h_r	height above elevated rooftop runway
s	distance between fences
V_a	airspeed
V_{cw}	crosswind speed
V_g	ground speed
$V_{cw,l}/V_{cw,max}$	ratio of local crosswind speed to maximum crosswind speed

DISCUSSION

First Phase of Study

Figure 2 is a photograph of one of the configurations tested at Langley, and figure 3 shows cross sections of six of the configurations tested. The first configuration in figure 3 is the solid rectangular parallelepiped building itself. Next is a series of four configurations, each having an elevated rooftop (or raised deck). The first in this series is the basic raised deck. The second has side ramps, which were tried because they had been suggested as a method of lateral containment of landing STOL craft. A curved (actually circular) side overhang was also tried (see third configuration in the series). Finally, porous side fences were added to the raised deck with curved overhang in an attempt to modify the crosswind velocity profiles; each side fence was constructed of three pieces of stainless screen wire of different heights placed fairly close together. Figure 2 is a photograph of this fourth elevated-rooftop configuration with its curved overhang (rounded edges) and porous side fences; viewed from this camera angle, the deck does not appear to be raised, but it is. The last configuration in figure 3 differs from the preceding one in that the space under the raised deck is closed in order to determine whether the raised deck is necessary.

The building models are 1.2 meters by 2.4 meters by either 41 or 51 cm high depending on the configuration (that is, 4 feet by 8 feet by either 16 or 20 inches). If one

thinks of the full-scale building as being 152 meters (500 feet) wide, then the 15-cm (6-inch) height of the model fences corresponds to an actual fence height of 19 meters (62.5 feet), and the full-scale building would be 51 or 63 meters high (167 or 208 feet high). A building model can be placed at any angle to the tunnel flow; in figure 2 the tunnel flow is parallel to the model runway.

A motion-picture film supplement showing smoke flow over the various building models has been prepared and is available on loan.* Six frames from this film are presented as figures 4 to 9. Figures 4 to 7 show the flow over the four configurations in the elevated-rooftop series. Figure 8 shows the flow over the solid rectangular parallel-piped building alone, and figure 9 is of the solid building with rounded edges but no fences. In each case, the flow is from left to right and the tunnel flow is at 90° to the runway.

Figure 4 shows the flow over the model with the basic raised deck (the first in the elevated-rooftop series in fig. 3). The flow is not good. It is separated at the leading edge, and reattachment does not occur. Over the entire rooftop, the flow is highly turbulent and unsteady.

Flow over the second configuration in the elevated-rooftop series is shown in figure 5. The addition of side ramps to the basic raised deck is seen to be detrimental. The separation angle is larger. In the center region, the flow is even more turbulent and unsteady. The unsteady flow region extends very high above the model. This configuration has the worst flow of any configuration tested.

Figure 6 shows the flow over the third configuration in the elevated-rooftop series. The effect of adding rounded edges to the raised deck is dramatic. Some turbulence can be seen, but the flow pattern is very much better than for the first two elevated-rooftop configurations.

Success having been achieved by the addition of rounded edges, fences were added next to determine whether the flow would remain smooth and whether the crosswind profile would change. The flow over the resulting configuration (fourth in the elevated-rooftop series in fig. 3) is shown in figure 7. One must not confuse the spreading of the smoke due to turbulence and unsteadiness with the spreading due to low velocities. The lazy action of the smoke in this figure indicates low velocities. The drift of the smoke toward the viewer indicates that the model is perhaps a degree or two off of the 90° tunnel-flow angle. Close to the deck, the velocities are certainly very low.

*This film supplement (16 mm, 3 min, color, silent) may be obtained on loan by requesting film serial number L-1101 from NASA Langley Research Center, Att.: Photographic Branch, Mail Stop 171, Hampton, Virginia 23365.

Figure 8 shows that the flow over the solid parallelepiped building alone is not good – that is, it is separated and turbulent. In fact, it seems to be slightly worse than the flow over the basic-raised-deck configuration (fig. 4).

Again, the effect of adding rounded edges is dramatic. Figure 9 shows that over the solid building with rounded edges, the flow is attached and fairly smooth and steady everywhere; it seems to be as smooth as the flow over the raised-deck configuration with rounded edges (fig. 6). At this stage of the study, it was concluded that the raised deck is not necessary to obtain good attached flow but that the rounded edges are the important factor. Although not illustrated, it should be noted that the addition of fences to the solid building with rounded edges was successful. The flow remained smooth and the crosswind velocities near the building rooftop were greatly reduced. Most of the subsequent work has been without raised decks on the models.

This first phase of the effort gave encouragement to the expectation that smooth, attached flow over an elevated STOL port could be achieved and that the crosswind profile could be modified in some desirable fashion.

Second Phase of Study

The next phase of the study was a somewhat more detailed investigation at the University of Virginia. Some selected results concerning the influence of fence structure and geometry on changes in crosswind velocity profile are presented.

Figure 10 shows schematically the type of effect one expects fences on either side of a STOL-port runway to have on the crosswind velocity profile. The left-hand sketch shows the tunnel flow with the tunnel boundary layer. In the right-hand sketch, the dashed line indicates the profile on the STOL-port model at the center line with no fences. With fences, the profile is modified as shown by the solid curve. The curves in this figure are, of course, just illustrative.

The effects of a crosswind velocity on an aircraft attitude and airspeed can be seen in figure 11, which is a schematic diagram of a STOL craft, designed to land at an airspeed of 60 knots, landing at a STOL port between fences in a 30-knot crosswind. The right-hand side of the figure indicates the situation initially in the full 30-knot crosswind; the airspeed is 67 knots, the ground speed is 60 knots, and the crab angle is 27° . The left-hand side indicates the situation at a place where the fences have reduced the crosswind speed to 15 knots, with the assumption of perfect decrabbing and a constant ground speed of 60 knots. The airspeed is now 62 knots and the crab angle is 14° . The effect of crosswind angles of other than 90° could be examined in a similar fashion.

It seems obvious that if a pilot had to land such a STOL craft at an elevated STOL port in a 30-knot crosswind, he would be concerned about such factors as the following:

At what height does the crosswind component begin to change? How rapidly does it change? At what height above the runway does the crosswind become negligible?

It should be noted that the results to be presented herein are not given as a "solution" to the crosswind problem. With a given, unfenced STOL-port building and a given flow over it, there will be a certain crosswind velocity profile provided by nature. If this profile is acceptable to all concerned, there is no problem. If it is not acceptable, then some mechanism of making the crosswind velocity profile acceptable becomes of interest. The question to which the present work is addressed is simply this: What are the possibilities of crosswind profile modification by putting fences on either side of the STOL-port building?

Figure 12 shows the test setup for a building model that is 76 cm (30 inches) wide and 15 cm (6 inches) high. The rounded edges of the model are circular and of 7-cm (2.75-inch) radius. If the 76-cm (30-inch) model width corresponds to a 152-meter (500-foot) full-scale building width, then the 15-cm (6-inch) model height corresponds to a 30.5-meter (100-foot) building height. Also, the 7-cm (2.75-inch) model overhang radius corresponds to a 14-meter (46-foot) building overhang radius, and the 7.6-cm (3-inch) model fence height corresponds to a 15-meter (50-foot) full-scale fence height. The fences were constructed of one, two, or three wire screens. The wire screen was approximately 30-percent solid.

Figure 13 shows the measured profiles at the model center line for three different fence configurations. The ordinate is height above the model runway h_r measured in units of model width b . The dashed line indicates the top of the fences. The model is 76 cm (30 inches) wide and all the fence configurations are 7.6 cm (3 inches) high. The abscissa is the ratio of local crosswind velocity to the maximum crosswind velocity. It is obvious that increasing the number of screens causes the center-line velocities near the deck to decrease and causes the height to which the fence effect extends to become larger. It is apparent that fence structure has a large influence on center-line crosswind velocity profiles.

Again, it is not suggested that any of these profiles is a "solution" to the crosswind problem. Rather, these profiles indicate that profiles can be modified. Moreover, it is suggested that if the STOL pilots would specify the profile they would like, then it just might be possible to produce such a profile.

Figure 14 shows the results of a separate experiment conducted at Langley, where the third author (Kalman J. Grunwald) tried to "hand tailor" a pair of three-screen fences to produce a linear profile. In view of the fact that the mesh spacing is a fairly large fraction of the fence height, the results are good. These results indicate that center-line profiles are adjustable over a considerable range and suggest that one might learn how to predict profiles for given fence structures and geometries.

It is also interesting to examine crosswind velocity profiles at other positions between the fences (besides the center line). The investigation at the University of Virginia included an experiment to determine the effects of measurement position. Figure 15 shows the profiles at three different positions between a pair of two-screen fences. The ordinate and abscissa are the same as in figures 13 and 14. The following two trends are noted: (1) the crosswind velocity decreases as the measurement position is moved downstream and (2) the height to which the fence effects extend increases as the measurement position is moved downstream. An additional experiment showed that the center-line profile was essentially the same with and without the downstream fence. Thus, one tentatively concludes that the profiles in the runway area are fixed by the upstream fence and are independent of the downstream fence. Some additional evidence on this point is provided in figure 16. A single two-screen fence was placed approximately at the center-line position, and profiles were measured 5 cm (2 inches) upstream and 5 cm (2 inches) downstream of the fence (that is, $0.07b$ upstream and downstream of the fence). The other curve (through the square symbols) is the no-fence profile at the fence position. The data clearly show that a fence alters the downstream flow velocity very much more than it does the upstream velocity. These results provide some insight into the mechanism by which fences alter the adjacent upstream and downstream flow fields.

CONCLUDING REMARKS

The results for the small-scale models used in the present investigation show that smooth, attached flow over elevated STOL ports can be achieved by proper building design. The results also indicate that crosswind velocity profiles in the landing region can be tailored by proper fence design (fence location and porosity). Of course, it is realized that the present data were obtained at a very small scale and that large-scale data are needed for verification.

CONCEPT OF AN ELEVATED STOL PORT



Figure 1

BUILDING MODEL IN TUNNEL

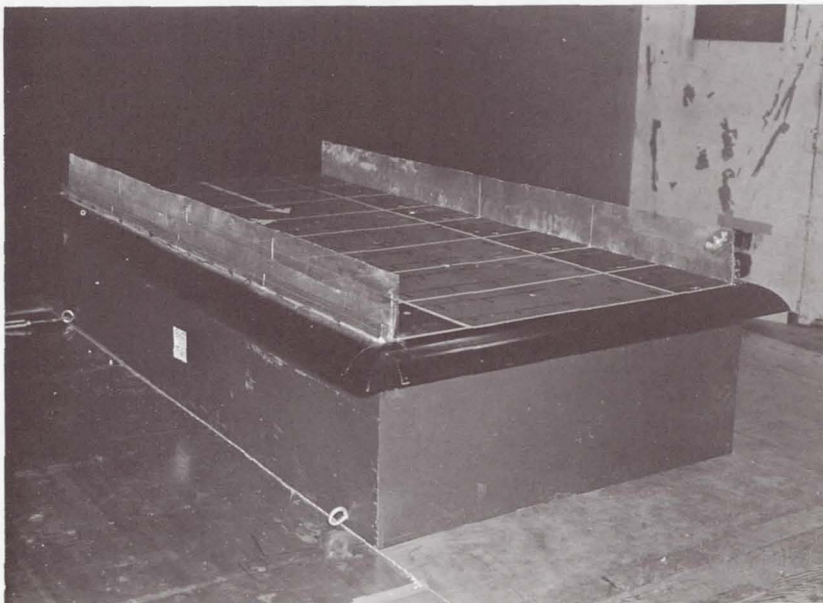


Figure 2

CROSS SECTIONS OF ROOFTOP CONFIGURATIONS TESTED

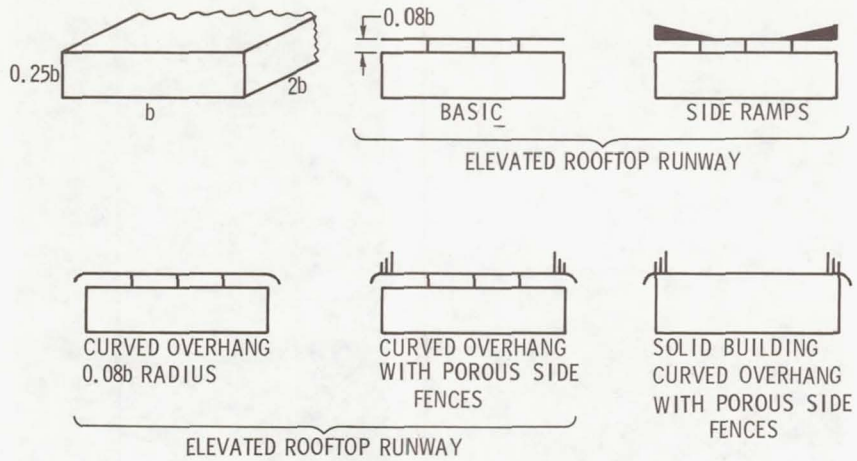


Figure 3



Figure 4

SMOKE FLOW
SIDE RAMPS ADDED

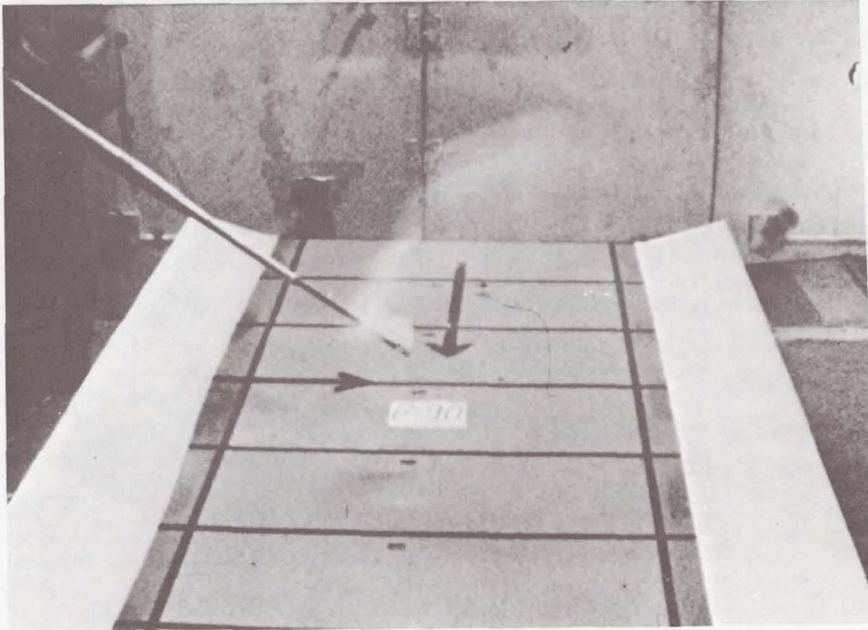


Figure 5

SMOKE FLOW
CURVED OVERHANG ADDED

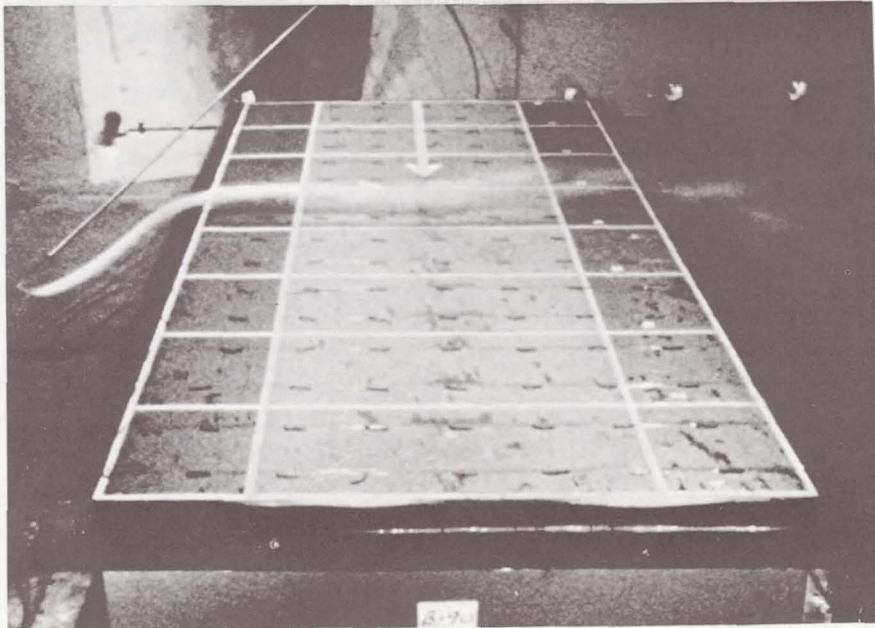


Figure 6

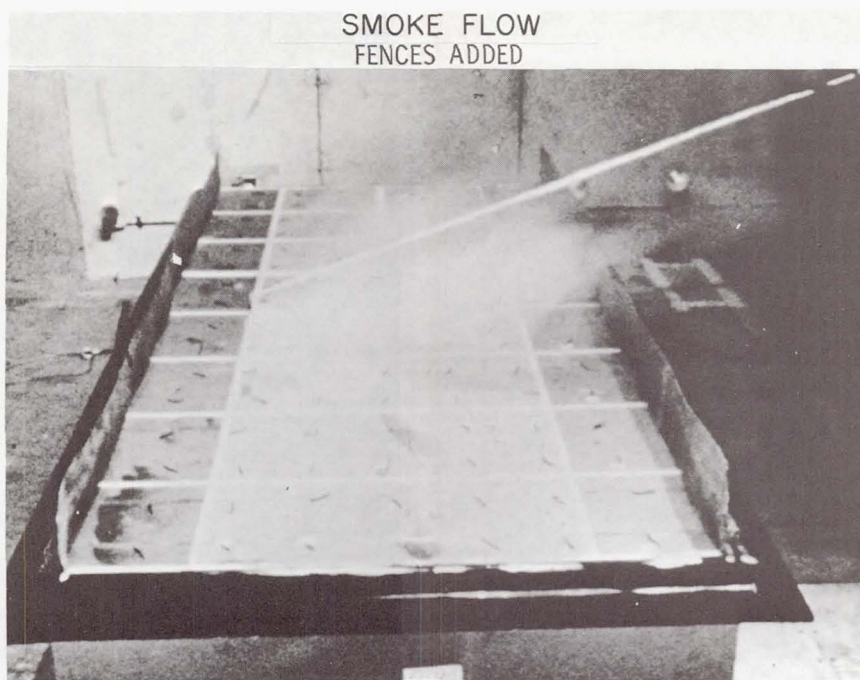


Figure 7

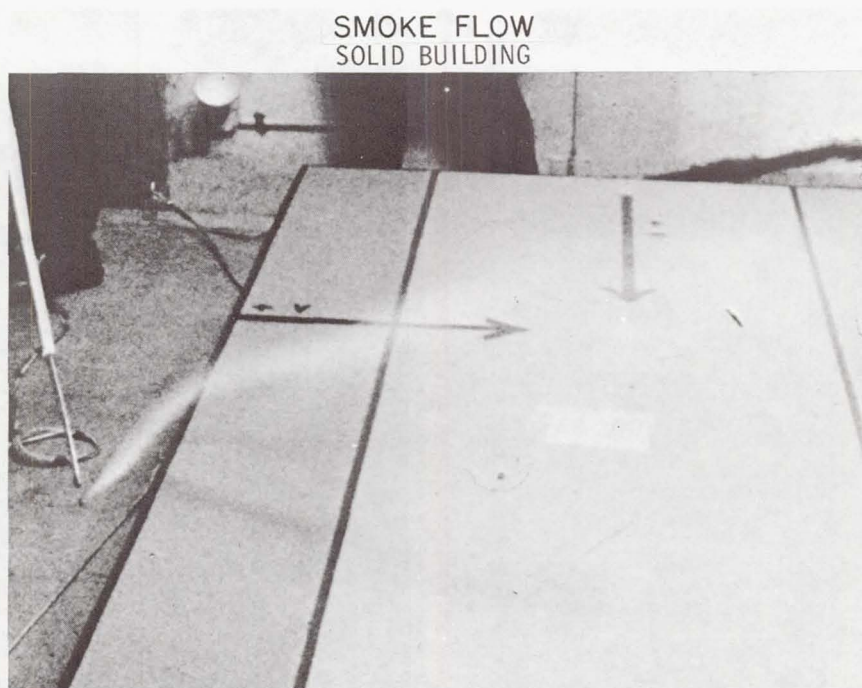


Figure 8

SMOKE FLOW
CURVED OVERHANG ADDED TO SOLID BUILDING

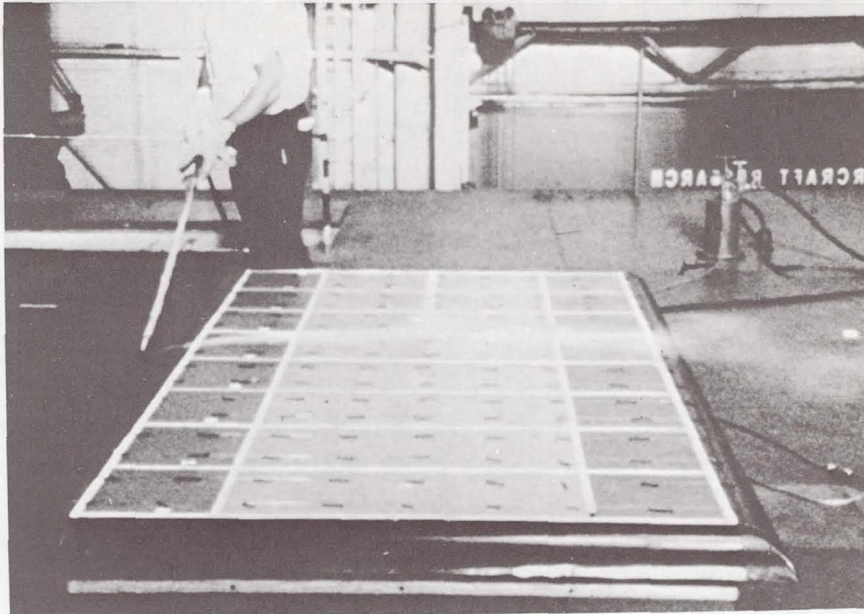


Figure 9

CROSSWIND VELOCITY PROFILE
AS A RESULT OF FENCE INSTALLATION

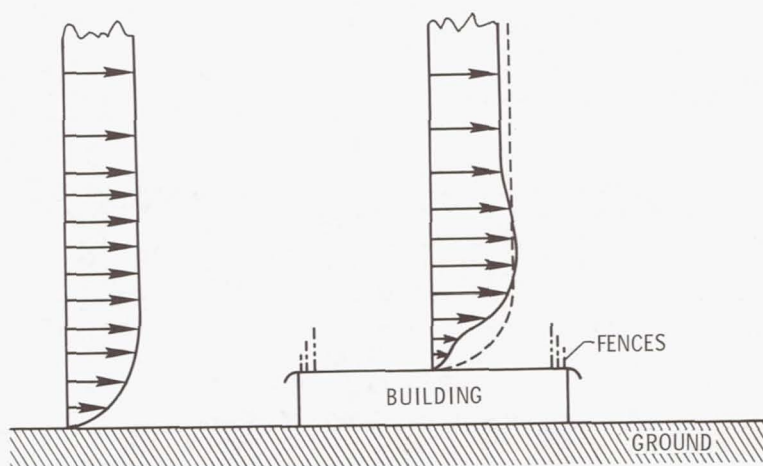


Figure 10

CROSSWIND LANDING FACTORS 30-knot CROSSWIND

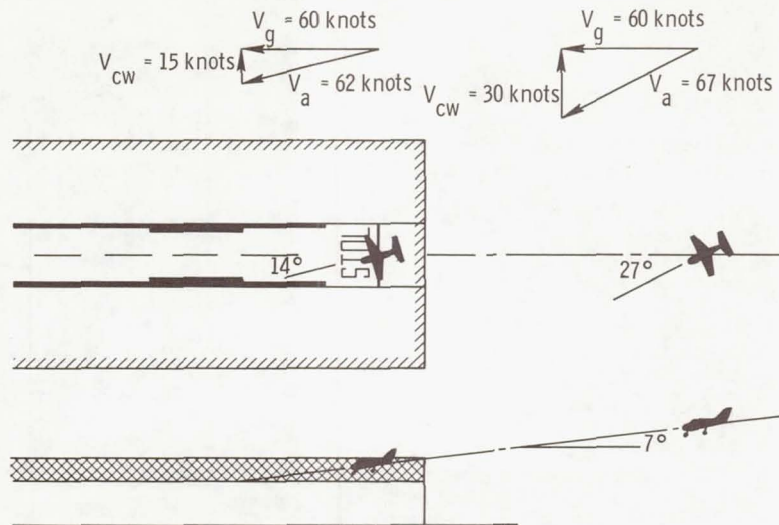


Figure 11

TEST SETUP

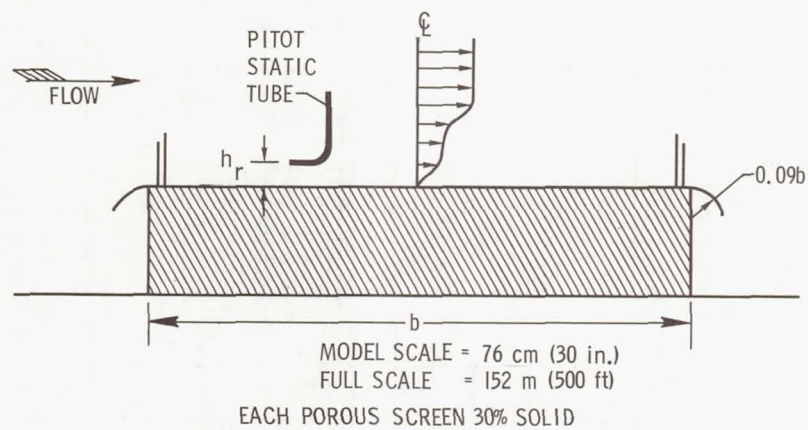


Figure 12

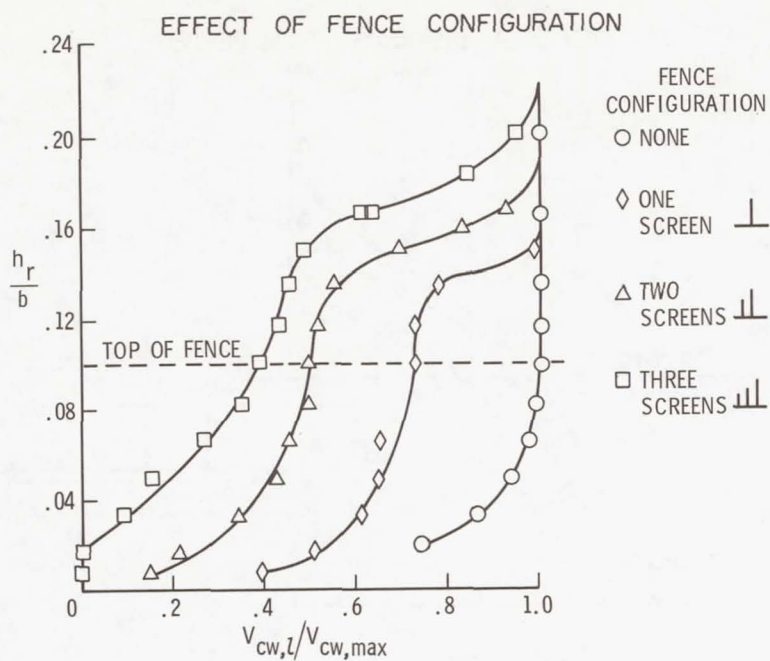


Figure 13

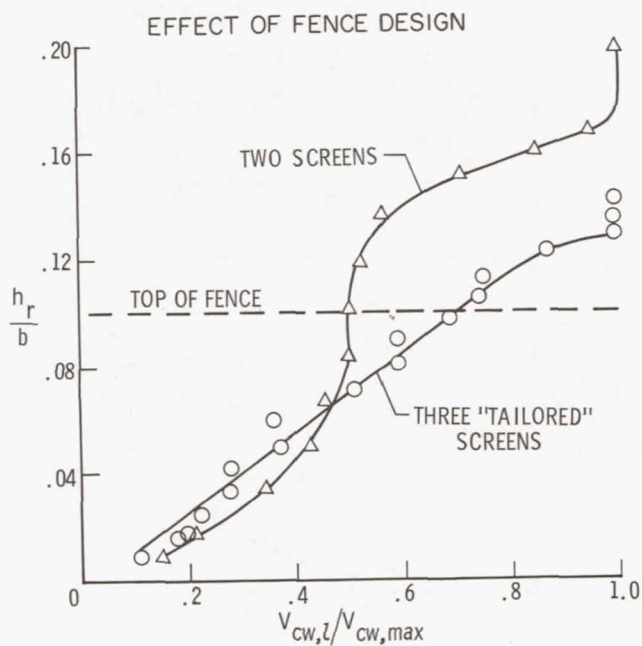


Figure 14

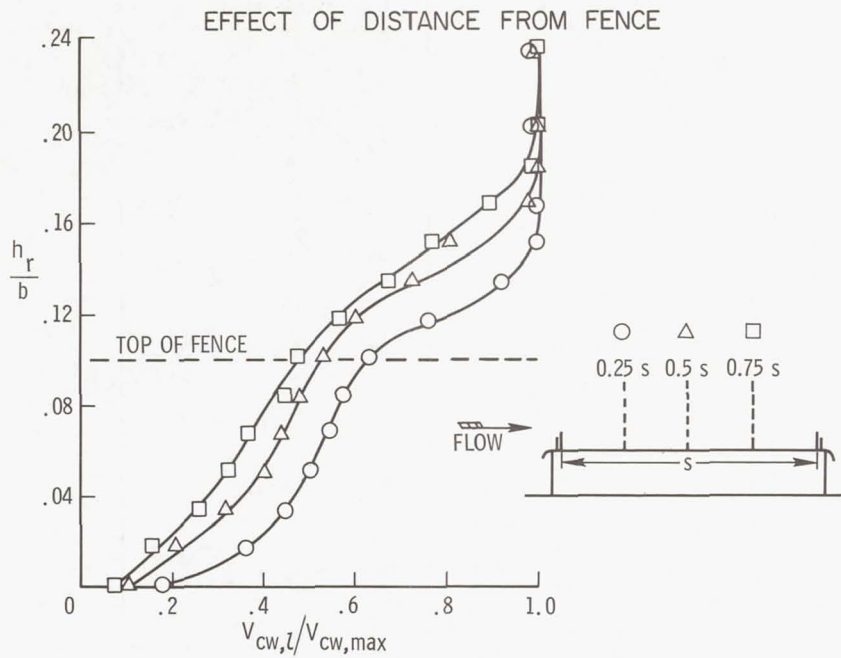


Figure 15

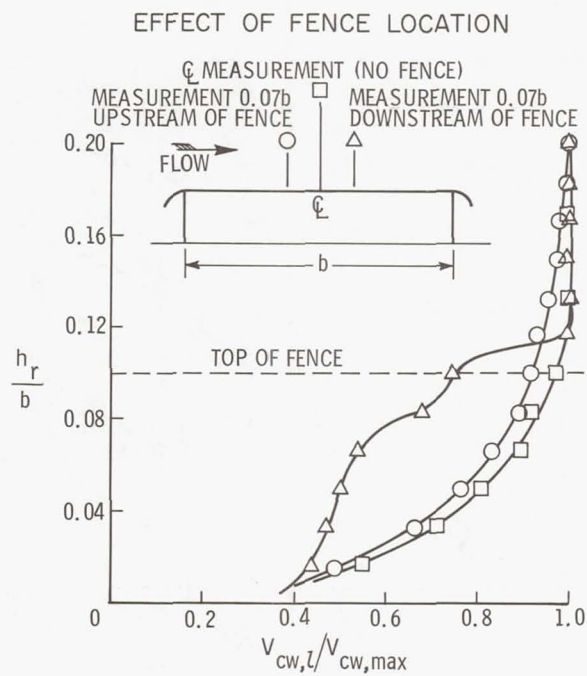


Figure 16

SIMULATION STUDIES FOR DEVELOPMENT OF CERTIFICATION CRITERIA APPLICABLE TO SST TAKE-OFF

By C. Thomas Snyder, Richard S. Bray, and Fred J. Drinkwater III
Ames Research Center

and
Raymond D. Forrest
Federal Aviation Administration

INTRODUCTION

A cooperative research program by the National Aeronautics and Space Administration (NASA) and Federal Aviation Administration (FAA) is being conducted at Ames Research Center using the Flight Simulator for Advanced Aircraft, a facility described in a previous paper by Bray, Drinkwater, and Fry. The general objective of this program is to provide information leading to improved airworthiness standards for large transport airplanes; and the emphasis to date has been on the development of supersonic-transport (SST) standards applicable to the take-off and landing flight regimes.

Two factors have made these studies necessary, safety and economics. SST design objectives aimed at providing efficient supersonic flight have resulted in performance and handling characteristics differing significantly from those of current subsonic jet transports. Recognition of these differences on both sides of the Atlantic led to the formulation of two sets of modified airworthiness standards for SST's joint British-French requirements (ref. 1) and U.S. requirements (ref. 2). Both groups of authorities recognized the need to evaluate the proposed standards and to unify the two sets into a common one. In addition, operating economics are critically dependent on the selected criteria; a realistic compromise must be defined between requirements that are overconservative and those that might prove unsafe. Overly stringent requirements have twice the impact on the ultimate payload for supersonic-transport airplanes as for subsonic airplanes since their ratio of payload to gross weight is only about one-half that of the subsonic airplanes.

This paper presents results from the trial application of some of these proposed criteria pertinent to the climb-limited take-off and some measurements obtained during surprise refused take-offs.

PROGRAM DESCRIPTION

A variety of airplane configurations have been utilized in the test program; figure 1 shows these configurations scaled to reflect relative sizes. The three generalized airplane configurations shown in the upper portion of the figure were compared in early tests. More recent testing has focused on SST configurations which closely approximate actual SST designs and which are shown in the lower portion of the figure. Nearly 2000 take-offs and 800 landings have been made in this program.

Two NASA and three FAA research test pilots have participated throughout the program. In addition, pilot-engineer teams from the British Air Registration Board and the French Flight Test Center participated in two joint exercises of about two weeks each. The British and French airworthiness pilots had flown the Concorde supersonic transport before the simulator exercises.

DISCUSSION

Take-Off Speed Requirements

Some of the SST take-off characteristics differ from those of today's subsonic transports. High thrust-weight ratios are reflected in high take-off acceleration and outstanding all-engines-operating performance. High take-off speeds result in a greater sensitivity of take-off distance to piloting variations such as time leads and lags. Large ground effect on lift makes it easier to lift-off at speeds too low to accomplish a satisfactory climbout at marginal thrust-weight ratios. High-induced drag means that speed diverges more rapidly when maneuvering and climb performance is sensitive to speed variations. The lack of a definable stall removes a long-standing reference point from which speeds were previously defined. These items created uncertainties as to the applicability of current airworthiness standards to supersonic transports.

The emphasis of the take-off studies has been devoted to definition of requirements related to V_2 , the minimum climbout speed with one engine inoperative and V_R , the take-off rotation speed. Considerable time has been spent on various proposed take-off abuse tests to define appropriate ones and discard unnecessary ones.

The current U.S. requirements on V_2 applicable to four-engine subsonic transports (ref. 3) state that V_2 must not be less than $1.2V_{\text{stall}}$ and must provide at least 3-percent climb gradient with one engine inoperative and gear retracted. Requirements proposed for SST airplanes (ref. 1) state that V_2 be not less than 1.15 times the zero-rate-of-climb speed V_{ZRC} . This proposal was considered as a rational replacement for the factored stall-speed requirement. In addition, the climb-gradient requirement was defined as a function of induced drag:

$$\gamma \geq 1.8 + 13 \frac{D_i}{W}$$

where

γ	one-engine-inoperative, gear-retracted climb gradient in percent
D_i	induced drag
W	gross weight

By using this equation, a larger minimum gradient is required at V_2 for high-induced-drag airplanes (about 4.5 percent for typical SST configurations).

An airplane with climb performance equal to the minimum demanded by airworthiness regulations is defined as "climb limited." While it is unlikely that SST airplanes will be climb limited under normal conditions, some designs can become climb limited under heavy-weight, high-airport-altitude, and/or hot-day conditions. It is in this condition that the induced-drag effects are most significant; therefore, the following discussion will deal with climb-limited airplanes.

Figure 2 illustrates the need for modified V_2 requirements by showing climb gradient in percent as a function of change in climb speed. As a floor, a 2-percent gradient can be considered necessary to clear obstacles and terrain along the take-off path. Some margin of climb above this amount is needed to account for the variations that occur in operation, and definition of this margin was a key objective. The SST's climb performance sensitivity to speed variations can be seen by the steeper slope. A speed abuse of only 6 knots from a V_2 speed based on current requirements (ref. 3) completely wipes out the margin over the 2-percent obstacle-clearance gradient. For the subsonic transport, a speed abuse of about 13 knots can be tolerated.

Not only is the SST's performance more sensitive to speed variations, but some of the characteristics mentioned previously can make these airplanes more susceptible to speed errors. In extreme contrast with the all-engines-operating condition, with an engine out, a critical piloting task exists to avoid lift-off at speeds below V_2 and to avoid a speed loss during the flareup. Rotation 1 second early can cause lift off 5 knots early; the large spread between V_R and V_2 makes rotation-rate critical, and excessive "g" during flareup causes rapid bleedoffs.

Reference speeds satisfying British-French proposed requirements (ref. 1) for SST's are also shown in this figure, with V_2 equal to $1.15V_{ZRC}$ and providing slightly more than the required 4.5-percent gradient. The proposed and current speeds were compared in the early tests. These tests demonstrated that the current requirements

(ref. 3) did not provide adequate margin for the piloting variations which occur and indicated that the proposed requirements provided a comfortable margin.

As previously indicated, these V_2 requirements exert a profound impact on the operating economics. Estimates of allowable payload corresponding to these two sets of requirements produce striking figures. For example, for an SST operating from a limited-length runway in a climb-limited condition, the payload difference represented is over 35 percent.

Thus, the question arises, can a reduction in the V_2 requirements be considered from those originally proposed? Considerable attention was devoted to this objective during the second joint exercise which included the British and French airworthiness authorities. Four intermediate conditions were evaluated, corresponding to climb-gradient levels of 4.7, 4.3, 3.8, and 3.5 percent. Corresponding speed margins from the zero-rate-of-climb speed ranged from 15 percent down to 11 percent. An additional condition was evaluated in which the drag polar was modified to provide a reduced-speed margin from V_{ZRC} (about 10 percent) while retaining a 4.3-percent gradient condition.

The sequence of take-offs evaluated by each pilot for each test condition included a series of reference take-offs, a series of abused take-offs, and a series of operational take-offs. During these take-offs, the copilot in the right seat called out decision and rotation speeds V_1 and V_R as these speeds were reached and retracted the gear on command. First a series of reference performance take-offs were made, both with all engines operating and with one engine inoperative, to train the pilot to the target speeds, to check the suitability of the selected V_R for the specified V_2 speed, and to establish a preliminary "scheduled" field distance. A series of abused take-offs followed; the effects of the abuses on take-off distance and climbaway capability were assessed to determine whether the given gradient was satisfactory or not. For further assurance, a series of operational take-offs were then conducted which included random surprise engine failures occurring in various stages of the take-off, out-of-trim conditions, wind shear, turbulence, crosswind, and combinations of these.

As indicated previously, a large number of abused take-off tests were evaluated in the course of this program. Figure 3 indicates the various types of proposed abuse tests which were initially evaluated. In several cases, tests with the same intent were specified using different procedures. At the conclusion of the study, by agreement of the joint airworthiness authorities, a combined list of some 12 abuses was reduced to the four demonstrations indicated by arrows, thus the number of costly flight tests was decreased and an agreed-upon common set of abuses was provided. In addition, these tests were made more rational, and interpretation of procedure was clarified.

Take-off abuses were previously assessed on the basis of distance to 10.7-m (35-ft) height. Figure 4(a) illustrates the need for assessing abuse effects on both

take-off distance and climbaway capability. It shows the airspeed, pitch attitude, and altitude records from an early rotation abuse test with one engine inoperative. Speeds were scheduled on the basis of current criteria and rotation was initiated 5 percent early or at 0.95 of the scheduled V_R . The nearly constant airspeed trace indicates that all of the performance capability was being used to produce climb. Although the field-distance criterion was satisfied, climbout performance was not sufficient to clear the 2-percent obstacle gradient. Figure 4(b) shows the results of the same 5-percent early rotation test at the same thrust-weight ratio as shown in figure 4(a), but with speeds scheduled on the basis of proposed criteria. In this case, the 2-percent obstacle gradient was cleared with some margin remaining. The oscillatory trend especially apparent in the attitude and airspeed records of figure 4(a) are indicative of the sensitive longitudinal piloting chore involved in addition to the lateral control task created by the failed engine. In an attempt to find the appropriate target pitch attitude, the pilot was adjusting attitude within ± 1 degree while referring to airspeed rate and within a speed band of ± 2 knots.

At the conclusion of the tests, it was agreed by the joint authorities that a relaxation of the proposed requirements on V_2 discussed previously was in order. This conclusion was based on several considerations, including findings from the Ames work, Concorde flight experience to date, and from the FAA's flight-test program using an F-102.

It had been shown that V_{ZRC} could be easily demonstrated and provided a useful substitute performance reference speed in absence of a stall speed. As shown in figure 5, it was agreed to reduce the V_{ZRC} margin to 12.5 percent and, in addition, that a gradient level of about 4.0 to 4.1 percent appeared acceptable. These changes typically represented about 40-percent reduction in the difference between the proposed and current requirements. In addition, the form of the gradient requirement was modified. Application of the formula gradient is complicated by the need to separate out the induced drag of the airplane, a difficult flight-test problem. As an alternate means of accomplishing the same objective in an easily demonstrable form, it was proposed that the airplane satisfy the 2-percent net-gradient requirement in a banked turn. Simulator results and a paper study over a range of airplane configurations indicated that a bank angle of 18° was an appropriate value.

Figure 6 illustrates the degradation in climb performance with varying bank angle, showing the effects of the high induced drag of low-aspect-ratio SST aircraft in comparison with subsonic transports. A bank angle of 18° produces a loss in gradient of about 1 percent for the subsonic transports, equal to the margin between the 3-percent gross gradient required and the 2-percent net obstacle-clearance gradient. For SST airplanes, this 18° bank angle corresponds to about 2.1-percent gradient loss, which, when added to the 2 percent, produces the 4.1 percent found to be appropriate. Thus, applicant airplanes must demonstrate a 2-percent engine-out climb in an 18° banked turn.

The various modifications to the requirements agreed upon are still subject to some internal processing within each airworthiness group, but these changes have been drafted, as reflected by reference 2.

With regard to pilot training for transition to SST's, it is strongly recommended that pilots be exposed to an engine-out take-off in the climb-limited condition and shown the effect of a speed abuse on performance. This could very satisfactorily be accomplished in simulator training.

Refused Take-Off Findings

This discussion presents some findings on pilot action times in surprise refuse take-offs (RTO's), take-offs in which an engine failure is recognized before reaching the take-off-decision speed and the take-off is aborted. The need for such information was expressed in a recent AIAA paper (ref. 4), yet it is impractical to obtain such information using real airplanes. The capabilities of the Flight Simulator for Advanced Aircraft together with a framework of a large number of take-offs presented a unique opportunity to obtain these data. The realism of the simulator cockpit, visual scene, and 1:1 lateral motion available during the take-off allowed real world cues to alert the pilot to the failure of an engine; consequently his responses would be very like an operational situation.

The certification of an airplane (ref. 3) includes measurements of the accelerate-stop distance to determine the take-off decision speed V_1 and to provide one of the factors used to establish the take-off field length. Reference 4 presents a review of the criteria used to obtain this distance and indicates several areas where additional test data would help to resolve differences between the interpretation of the regulations as applied to flight-test measurements and observed operational procedures, especially with regard to brake application.

Reference 3 defines the accelerate-stop distance as the sum of the distances necessary to

1. Accelerate the airplane from a standing start to V_1 and
2. Come to a full stop from the point at which V_1 is reached, assuming that the critical engine fails at V_1

As indicated in figure 7, the greatest flexibility in the interpretation of this regulation is in the determination of the transition distance traveled from the point of engine failure to the attainment of the full-deceleration configuration. Because this diagram shows velocity as a function of time, the area under the curve defines the distance. The distance traveled during the transition is, of course, primarily dependent on the transition time and the speed at engine failure and depends to a smaller degree on the speed gained

after engine failure. In addition, however, the control sequence plays a large role in the speed gain after engine failure, and this kinetic-energy gain has a significant effect on the distance to stop after achieving the full-deceleration configuration.

During the simulator testing, the timing and sequencing of the pilot's actions following engine failure were recorded for a total of 20 surprise RTO's involving four pilots and three airplanes. The pilots had been briefed to expect engine failures before V_1 , however a ratio of one RTO for each 25 take-offs maintained a significant surprise factor. The only technique briefed was to have the pilot keep his hands on the throttles until V_1 was called by the copilot, an approved operational procedure. In all cases, nose-wheel steering through the rudder pedal was provided on dry runway conditions. Most of the failures occurred about 15 knots before V_1 . Pilots considered the cues accompanying engine failure to be realistic and their reactions normal.

The timing of the pilot's control actions is shown in figure 8. The control sequence used was basically the same for all three airplanes and four pilots. In all cases, the throttles were retarded first and, in all but four cases, brakes were applied before spoilers. Average times from engine failure were 1.6 seconds, 3.9 seconds, and 5.5 seconds for throttle chop, brake application, and spoiler actuation, respectively.

The consistency of the pilot's control sequence, as seen in these tests, indicated a well-developed behavior pattern formed through training and from experience in normal stops which reinforce this sequence. In addition, the pilots' primary initial concern was with maintaining directional control. The decision to stop was followed by retardation of throttles and application of rudder to correct the track down the runway. Simultaneous rudder input for yaw control and brake application did not occur. Once the throttles were retarded the pilot's hands were free to apply spoilers. The fact that the pilots delayed braking until yaw control was applied introduced a significant delay in attaining the full-deceleration configuration.

The control sequence generally applied during the certification process and the sequence observed in these tests are compared in figure 9. The flight-test values shown here are from the certification program on a current series subsonic jet transport. The certification procedure provides for a pilot reaction time after engine failure to the point of brake application, followed by the allotted times for retardation of throttles and application of spoilers and/or other approved deceleration controls. In addition to the measured times, 1 second is added for each additional control action after brake application. The significant difference between the results of this procedure and that measured in the simulator tests is the brake-application time. During certification tests to measure transition time intervals, the pilot is aware that an accelerate-stop test is in progress and applies brakes immediately upon recognition of the failure. The simulator

results indicate that in the event of an unanticipated failure, the brakes will not be applied immediately. These differences would result in significant increases in stopping distance for subsonic airplanes, and the effect could be amplified for SST airplanes with higher decision speeds.

CONCLUSIONS

1. Engine-failure take-off testing of high-induced-drag SST designs confirmed the need for more stringent take-off-speed requirements for such airplanes. However, these tests demonstrated that proposed requirements, intended to provide the additional protection, were overconservative and economically penalizing. New minimum requirements were defined and agreed upon during joint testing by British, French, and U.S. airworthiness authorities.

2. The large number of proposed take-off abuse tests was reduced to a common set of four demonstrations agreed upon by the joint airworthiness authorities; thus, the number of costly flight tests was decreased.

3. During surprise refused take-offs, the sequence of application of deceleration devices (throttles, brakes, spoilers) was found to differ from that commonly assumed in the certification process of determining the accelerate-stop distance and has the effect of increasing the stopping distance. The effects of this difference could be amplified for SST airplanes.

REFERENCES

1. Anon.: TSS Standards. Pt. 2 - Performance; Pt. 3 - Flying Qualities. Air Registration Board (England) or Secrétariat Général à l'Aviation Civile (France), July 28, 1969.
2. Anon.: Tentative Airworthiness Standards for Supersonic Transports. Flight Standards Service, FAA, Nov. 1, 1965; Revision 7, Jan. 1, 1971.
3. Anon.: Airworthiness Standards: Transport Category Airplanes. Federal Aviation Regulations, vol. III, pt. 25, FAA, Sept. 18, 1970.
4. Foxworth, T. G.; and Marthinsen, H. F.: Another Look at Accelerate-Stop Criteria. AIAA Paper No. 69-772, July 1969.

AIRPLANES SIMULATED

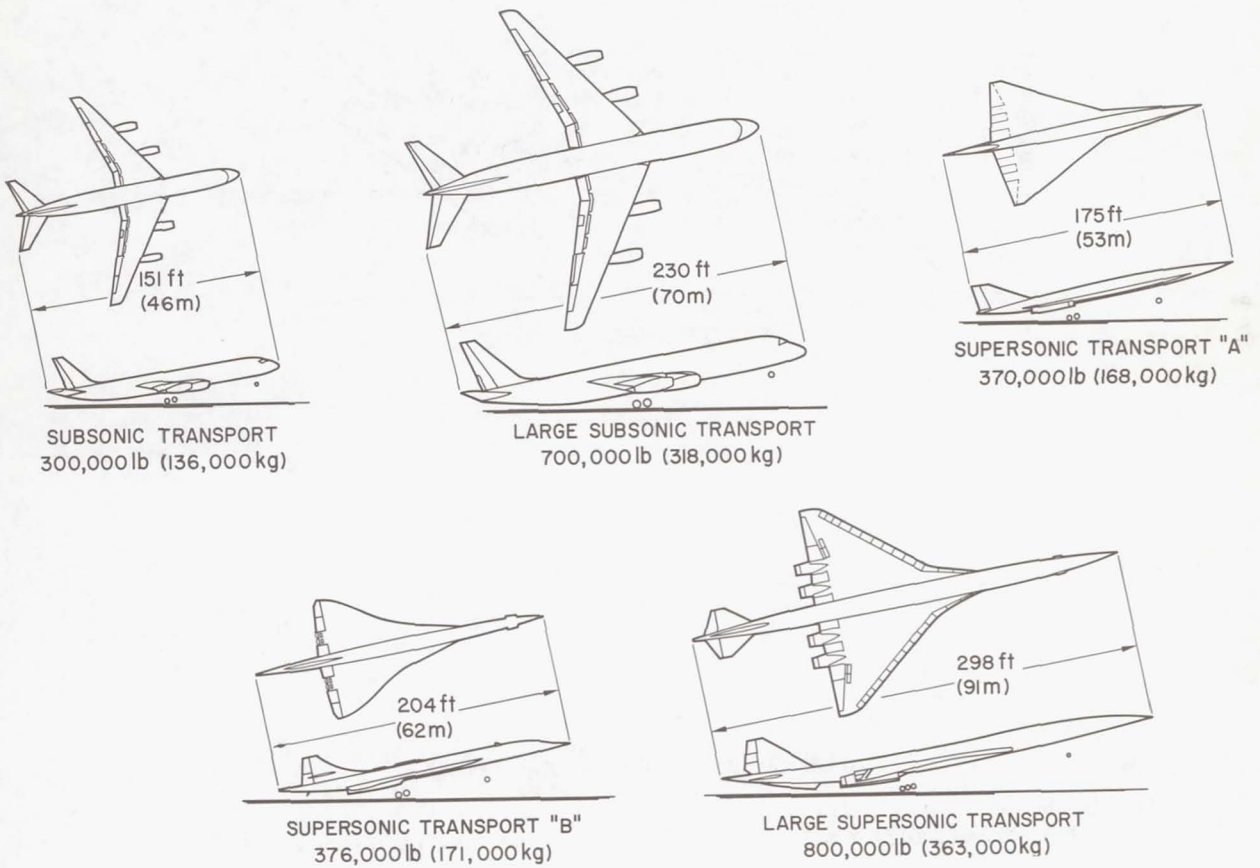


Figure 1

ONE-ENGINE-INOPERATIVE TAKE-OFF PERFORMANCE

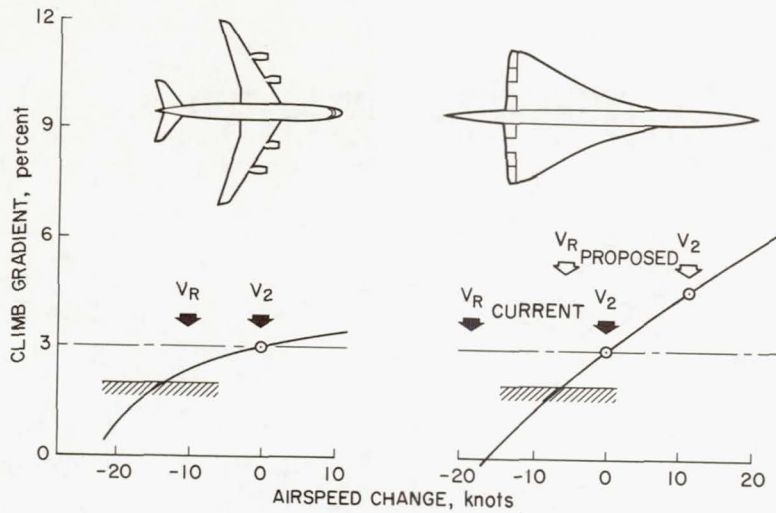


Figure 2

PROPOSED TAKE-OFF ABUSE TESTS

ALL ENGINES OPERATING

- EARLY ROTATION
- LATE ROTATION ←
- SLOW ROTATION
- UNDERROTATION
- OVERROTATION
- EARLY OVERROTATION ←
- EARLY RAPID ROTATION
- MINIMUM UNSTICK

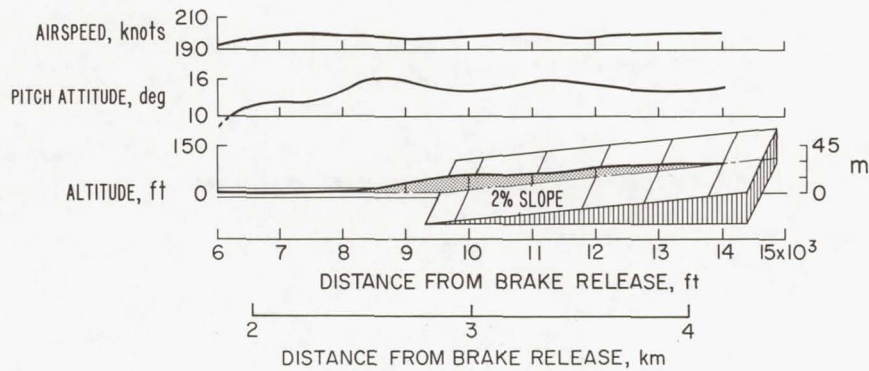
ONE ENGINE INOPERATIVE

- EARLY ROTATION ←
- RAPID ROTATION ←
- OVERROTATION
- MINIMUM UNSTICK

Figure 3

5% EARLY ROTATION ABUSED TAKE-OFF
ONE-ENGINE-INOPERATIVE SST

(a) SPEEDS FROM CURRENT CRITERIA



(b) SPEEDS FROM PROPOSED CRITERIA

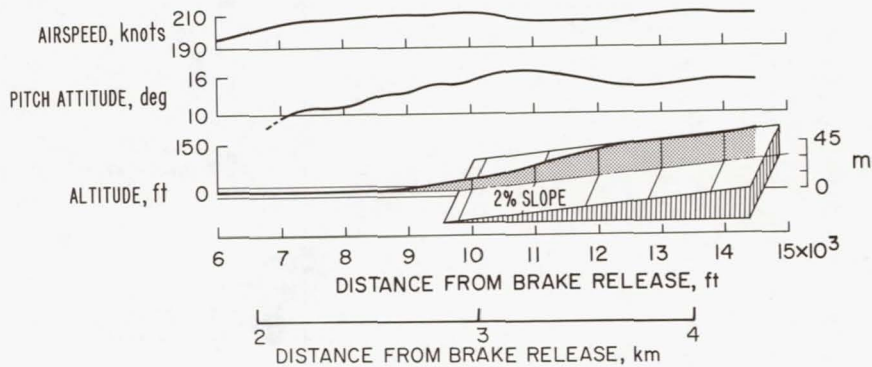


Figure 4

RESULTING V_2 REQUIREMENTS
AGREED UPON BY BRITISH, FRENCH AND U.S. AUTHORITIES

- NOT LESS THAN $1.125 V_{\text{ZERO CLIMB}}$
- 2% ENGINE-OUT CLIMB GRADIENT IN AN 18-DEG BANKED TURN

Figure 5

EFFECT OF A BANKED TURN ON CLIMB PERFORMANCE

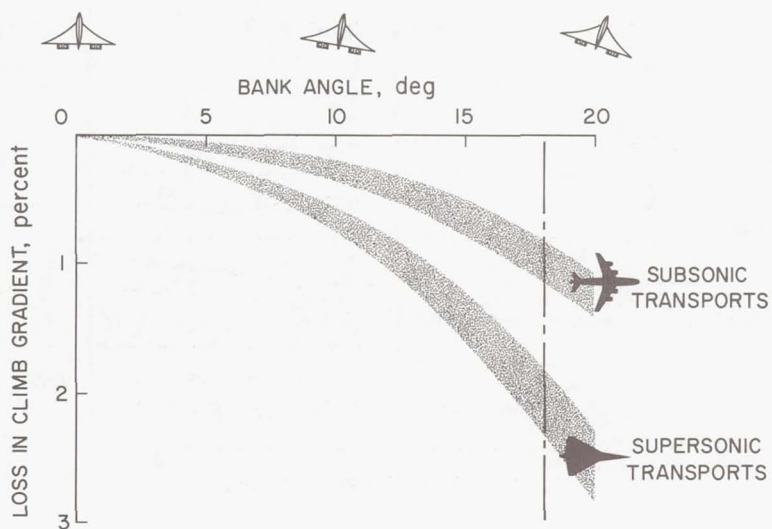


Figure 6

ACCELERATE-STOP DIAGRAM

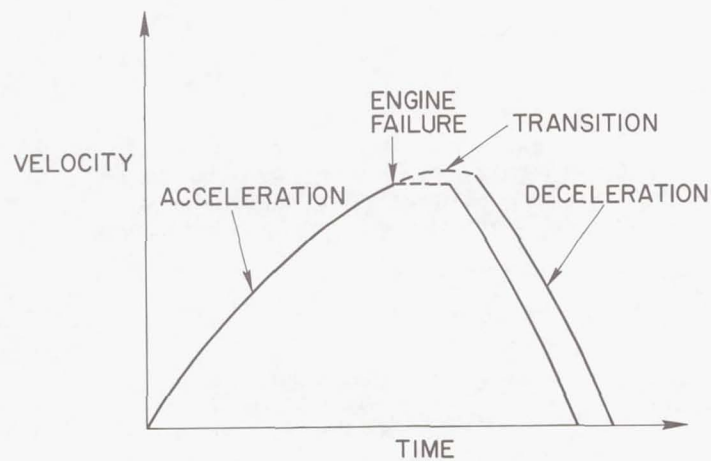


Figure 7

TIMING OF PILOT ACTIONS DURING SIMULATED REFUSED TAKE-OFFS

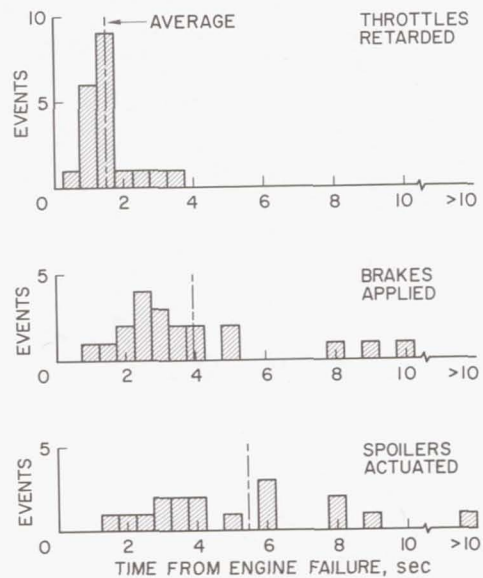


Figure 8

ACCELERATE-STOP PILOT ACTION TIMES
 EXAMPLE FROM AN ACTUAL CERTIFICATION
 PROGRAM COMPARED WITH SIMULATOR FINDINGS

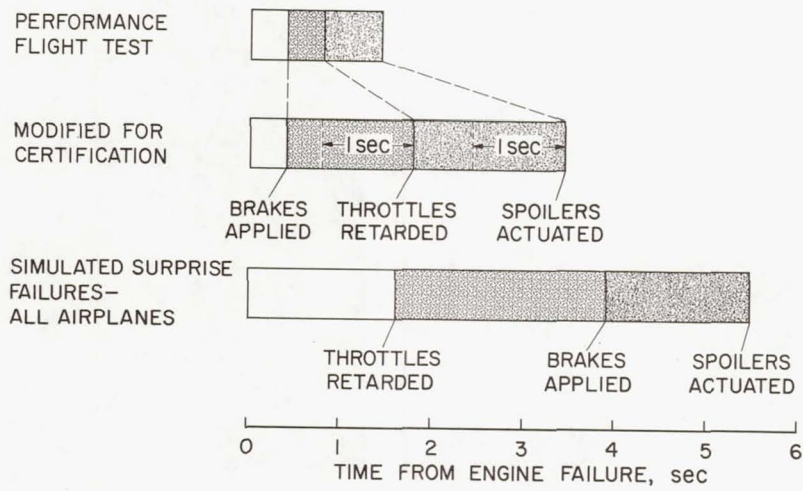


Figure 9

DEVELOPMENT OF TURBULENCE AND WIND SHEAR MODELS FOR SIMULATOR APPLICATION

By Richard L. Kurkowski,
Ames Research Center

George H. Fichtl,
George C. Marshall Space Flight Center

and Joseph Gera
Langley Research Center

INTRODUCTION

Atmospheric turbulence and wind shears contribute to piloting problems and may limit safe operation of aircraft. Investigations of handling and control problems in rough air and wind shear can be accomplished very effectively on pilot simulators but this requires good models of the atmospheric disturbances.

The purpose of this paper is to present information on some continuing studies aimed at producing realistic models of turbulence and wind shears for handling qualities studies. These studies include an evaluation of analytical models of turbulence which have non-Gaussian gust distributions, a statistical analysis of wind shear, and a brief evaluation of the effects of wind shear on aircraft operations.

SYMBOLS

$a(t), b(t)$	random functions of time
G	transfer function
k	Von Karman parameter
n	Gaussian white noise signal with zero mean value
S	Laplace transform variable
t	time
u_*	friction velocity

\bar{u}	mean wind speed
\bar{u}_r	mean wind at reference level z_r
w	vertical gust velocity
z	altitude
z_0	roughness length
z_r	reference altitude
\bar{z}	height to midpoint of altitude layer Δz

Abbreviations:

IFR	Instrument Flight Rules
ILS	instrument landing system
rms	root mean square
STOL	short take-off and landing

NON-GAUSSIAN MODEL STUDY

Gaussian Turbulence Model

The classical method presently used for turbulence simulation is the filtered white noise technique illustrated in figure 1. Time histories are generated by linearly filtering Gaussian white noise and amplifying the resultant signal so that the normalized spectrum and rms intensity match those of real turbulence. Dryden or Von Karman equation forms are normally used to model the power spectrum.

One of the dominant objections to the Gaussian simulation is that it does not reproduce the patchy nature of real turbulence, that is, the variations of intensity encountered while flying through continuous turbulence. This difference is illustrated in figure 2. The difference in patchiness is best illustrated by comparing the derivative of the velocity. Two sample time histories of the vertical-velocity derivative are shown. One is from measured flight records, the other is from a filtered white noise source and is labeled "Gaussian." Note that the intensity for the Gaussian model is nearly constant

whereas the measured turbulence exhibits the typical patchy or burst characteristic. One obvious question arises, Why try to model turbulence when there are measured time histories of the real thing? The answer is that for some studies, recorded turbulence may be the preferable method. There can be little argument concerning the realism of such a technique. However, it is difficult to adjust the measured time histories to allow for conditions other than those for which it was recorded. No allowances can be made for changes of altitude or different atmospheric conditions. Experimental data for these varying conditions are sparse. Also, extended run times cannot be accommodated without repetition. Therefore, this method does not appear to be very flexible and a more general, realistic model is needed.

Non-Gaussian Turbulence Model

The patchy nature of turbulence suggests that a realistic turbulence simulation can be produced by multiplying two independent random variables, one to represent the turbulence within a patch and the other to represent the variations of intensity with time. Such a scheme has been suggested by Bullen (ref. 1) and mechanized by Reeves. Early analytical work by Reeves was supported by the Air Force Flight Dynamics Laboratory (ref. 2), and current evaluation of this approach is continuing under an Ames research grant. Figure 3 shows the block diagram of a turbulence simulation employing the idea of signal multiplication. Only the vertical gust component is shown for clarity. Two independent Gaussian white noise generators drive linear filters, which produce Gaussian random variables *a* and *b*. These variables are then multiplied to produce a vertical gust time history. The longitudinal and lateral gusts would be produced in a similar manner.

Simulator Study

Both the Gaussian and non-Gaussian turbulence simulations have been produced, and the resulting time histories have been compared with real turbulence. The real turbulence used for comparison was obtained from the U.S. Air Force LO-LOCAT program (ref. 3). The $5\frac{1}{2}$ -minute LO-LOCAT record selected was for flight conditions over flat country, at an altitude of 76.2 meters (250 ft), in near neutrally stable air. The rms intensity level for the vertical gust velocity was 1 m/sec (3.3 ft/sec) with peak values of about ± 4.6 m/sec (15 ft/sec). The data were measured at an airspeed of 91.5 m/sec (300 ft/sec). The recorder data were played back at a slower speed to obtain turbulence at a simulated airspeed of 36.6 m/sec (120 ft/sec). This was the speed selected for the evaluation tests.

Figure 4 shows the vertical-velocity derivatives for these three sources. The measured and Gaussian records, shown previously, are now compared with the non-Gaussian record. Note that the non-Gaussian model exhibits a patchy characteristic similar to

measured turbulence. The non-Gaussian model is flexible, and an even closer match can be obtained by using different filters or by adding Gaussian and non-Gaussian systems.

Simulator

This section and the section on "Results" are a progress report on attempts to evaluate these non-Gaussian turbulence models by using piloted simulators. A preliminary set of tests has been conducted but it produced rather inconclusive results. However, the test procedures and results are presented for information and the probable causes for the inconclusive results are discussed.

Evaluation tests with one degree of motion were conducted on the Ames height control simulator during the summer of 1970. This simulator is shown in figure 5. It consists of a single-man cab which rides on a vertical track on the side of the Ames 40- by 80-foot tunnel. This simulator was chosen because the large vertical travel of 30.5 meters (100 ft) permitted good duplication of the low-frequency disturbances. The match of computed acceleration and measured cab acceleration was considered to be very good.

Four Ames test pilots participated in the series of tests. The pilot's task was to fly constant altitude under IFR conditions in a simulated STOL transport, while being subjected to vertical motion associated with turbulence. Precision tracking of the ILS approach type was used. Although motion cues were limited to vertical accelerations only, the visual cues for IFR were complete. Both longitudinal and lateral disturbance responses were displayed to the pilot. The aircraft selected for the tests is shown in figure 6. The Twin Otter was chosen because of its relatively high response to gusts and because of the current interest in the STOL class of aircraft. Flight time in this aircraft was obtained so that the pilots could validate the simulator with flight experience for the same aircraft.

Three turbulence conditions were compared in the simulator tests: (a) measured time histories of three-component velocity data for actual turbulence, (b) Dryden turbulence models of the three-component data with Gaussian gust distributions, and (c) Dryden turbulence models with non-Gaussian gust distributions. The power spectra of the Dryden models were matched to the power spectrum of the measured turbulence. From preliminary runs, the pilots determined that the measured disturbance level was too high for a landing approach type of task. They said that the approach would be aborted in a real world situation and an alternate field would be used. Therefore, the level of power in the turbulence records was cut in half for the subsequent data runs.

Results

Each pilot "flew" each of the three disturbance conditions two times. The conditions were presented in a mixed order. At the end of each simulator flight, the pilot was

asked to evaluate his task performance, his workload, the intensity level of turbulence, and the realism of the simulated turbulence. Figure 7 shows each pilot's mean ratings of realism from "very poor" to "very good" for each of the three disturbances, that is, the measured turbulence, the non-Gaussian model, and the Gaussian model. The variation in the ratings of the measured turbulence reflects the type of turbulent flight experience of the individual pilots. The pilots who were accustomed to lighter wing loading aircraft downrated the measured turbulence because the aircraft response was not as abrupt as they were used to.

The relative rating trend that was anticipated is exhibited by the data for Pilot A. He rated the non-Gaussian model at about the same level as the measured turbulence and downrated the Gaussian model. Unfortunately this relative rating trend was not true for the rest of the pilots. Pilot B rated the non-Gaussian model higher than the Gaussian but downrated the measured turbulence. Pilot C rated both models the same and downrated the measured turbulence. Pilot D rated all disturbances about the same, with a trend opposite to that expected. All pilots rated the measured turbulence lower than the non-Gaussian model. Pilot C mentioned a low-frequency "roller coaster" effect associated with the measured turbulence. The reason for this seems to be that the measured turbulence had a stronger correlation between the longitudinal and vertical gust components than the Gaussian or non-Gaussian models and produced larger resultant vertical motions. This was also evident in pilot estimates of workload, with the measured turbulence being slightly harder than the models. The pilots were asked to rate patchiness. The patchiness for all disturbances was rated "about right." All the pilots were bothered by the lack of lateral motions which are normally associated with turbulence.

This has been a status report on a continuing program. The data from preliminary tests show no clear-cut preference for the non-Gaussian model even though a better match of the patchy characteristics of real turbulence is evident in the time histories. The limitations of the preliminary tests will be corrected, and further tests are planned to investigate these models on the Ames six-degree-of-freedom simulator, in order to assess the lateral motion along with the vertical motion. A more careful match will be made between the models and the measured turbulence statistical properties, including correlation of longitudinal and vertical gusts. In addition, the aircraft turbulence response model will be refined to include time delays for the gust to reach the tail surfaces and spatial distribution of gusts across the wing span.

STATISTICAL WIND SHEAR MODEL

The rest of this paper is concerned with the wind shear in the atmospheric boundary layer. Wind shear is composed of two parts, the mean shear and fluctuations about the mean shear. The mean shear is related to the mean wind profile whereas the

fluctuations are produced by the action of atmospheric turbulence. In previous aircraft operations studies, such as reported in reference 4, only the wind shear associated with the mean wind profile has been considered. This part of the paper will show that the fluctuating wind shear should also be studied for a total picture of wind shear effects. The shear for the mean wind profile is discussed first, and then an analytical example of statistical data of wind shear associated with fluctuating wind profiles is shown.

Mean Wind Shear

The generalized mean shear model, which is presented later, is based on the standard logarithmic relationship shown in figure 8. In this figure, a theoretical velocity profile is compared with measured mean velocity data from the White Sands Missile Range 32-meter tower (ref. 5) for near neutrally stable air. The data show good agreement with the predicted profile. The theoretical velocity profile for neutral stability is a function of friction velocity u_* , the Von Karman parameter k , and a roughness length z_0 . The value of k is generally accepted to be 0.4. Friction velocity u_* is determined from the velocity conditions at some reference level, in this case 4.3 m/sec at 4 meters. The roughness length z_0 is a function of the terrain. A value of 0.1 was assumed for the tall natural growth conditions at this particular tower location.

Terminology used in the generalized mean shear curve is illustrated by a simplified sketch shown as figure 9. Wind shear is the change in velocity Δu with a change in altitude Δz . Note that this is the inverse of the slope of the curve as shown in the figure. The height to the midpoint of the altitude layer Δz is shown as \bar{z} . The greatest wind shear occurs at low altitude or small values of \bar{z} . The actual values of the shear for any mean wind profile can now be determined by using the nondimensional curve shown in figure 10. Here the change in the mean wind shear $\Delta \bar{u}$, normalized by the surface friction velocity u_* is plotted as a function of $\Delta z/\bar{z}$. The equation is shown. This curve shows in a generalized sense that the change in mean wind increases with increasing layer thickness Δz , decreasing mean altitude \bar{z} , or decreasing friction velocity u_* .

The question now arises as to how to classify wind shear strengths. One such classification has been suggested by the World Meteorological Organization in 1967. Their recommended classification of wind shear is shown in table I. The categories were listed as light, moderate, strong, and severe, and the associated wind shear magnitude is shown in units of m/sec for a 30-meter layer. This classification was not officially accepted because it is not universal. For example, moderate shear for a high minimum speed aircraft could correspond to strong shear for a relatively low minimum speed airplane. Nevertheless, the classification of shear in table I gives estimates of the shear magnitudes that are important to aircraft operations.

Fluctuating Shear

As stated earlier, in order to assess total wind shear effects, fluctuations of the wind about the mean value should be considered. The question now arises, What is the risk of encountering the shear magnitudes as given in table I for specific wind and surface conditions? To answer this question, assume that the nondimensional shear fluctuations have a Gaussian distribution. This assumption permits the calculation of the wind shear associated with a given probability or risk level. Calculations were made for a neutral stability atmosphere condition. Typical values for the ratio of turbulence standard deviation to friction velocity were used. These values were based on experimental data obtained by Prasad and Panofsky of Pennsylvania State University (ref. 6, pp. 65-92). A vertical layer Δz of 30 meters (100 ft) with a midpoint height \bar{z} of 50 meters (164 ft) and a roughness length $z_0 = 1$ meter (3.3 ft) were used in the calculations. This value is representative of city surface conditions. A reference mean velocity u_r at a reference height z_r of 10 meters (33 ft) was assumed to be known.

Figure 11 shows some typical data on wind shear plotted against probability for three levels of reference mean velocity: 2, 4, and 10 m/sec (4, 8, and 20 knots). The wind shear category levels are shown on the right. The 50-percent probability level corresponds to the mean wind profile, and it was found that levels of shear that could be classified as moderate were not obtained until u_r was about 22 m/sec (44 knots). However, when turbulence or shear fluctuation was included in the analysis the shear magnitude was found to increase as probability increased or, conversely, as risk decreased. The figure shows that for a given mean wind speed at some reference level, the dispersion about the mean is relatively large. In this example case the 95-percent probability shear is approximately equal to the mean wind at the reference level (i.e., 2 (m/sec)/30 m for $u_r = 2$ m/sec, etc.).

WIND SHEAR APPLICATION

The mean and fluctuating wind shear having been explored, the effects of wind shear on aircraft operation and safety will now be examined. As an aircraft ascends or descends through the boundary layer it will normally encounter wind shear. If the wind shear is sufficiently large and an aircraft is operating near minimum speed conditions, it is possible for the aircraft to develop large sink rates near the ground. For example, a 15-percent speed margin has been suggested for STOL aircraft. For a 30.7-m/sec (60 knot) stall-speed configuration, this would mean a speed margin of 4.6 m/sec (9 knots). From figure 11, it can be seen that for a very nominal mean wind of 4 m/sec (8 knots), a 4.6 m/sec per 30-meter (100 ft) shear occurs with a 95-percent probability. In other words, there is a 5-percent risk that the aircraft speed will go below minimum, if no airspeed control action is taken. Of course, this is a dynamic situation and the

conditions may not linger long enough to be a problem. These dynamic effects of a fluctuating wind shear on a STOL aircraft should be studied.

An effect which is related to speed control is the effect of wind shear on aircraft flight path. Figure 12 shows an example case of a STOL aircraft during landing approach, with a nominal 6° glide path. Height is plotted against ground track. An approach speed of 36 m/sec (70 knots) was assumed. The flight path for trimmed condition with controls and throttle fixed is shown for a steady 7.6-m/sec (15 knot) head-wind condition and for a linear mean wind profile decreasing from a head wind of 7.6 m/sec at 90 meters (300 ft) down to a value of 0 at ground level. The same constant throttle setting was assumed for both conditions. With wind shear, the aircraft follows a curved path and would undershoot the runway without corrective action. With the assumed shear condition, the undershoot would be about 150 meters (500 ft).

A third effect that wind shear can produce is a change in dynamic stability of the aircraft motion. A study at Langley Research Center has shown that for high levels of steady wind shear, the phugoid mode can become unstable. This should not be a problem, however, since the phugoid period is generally long enough for easy control by the pilot. Of more significance, the study showed that there was a negligible effect of steady wind shear on the short-period mode.

CONCLUDING REMARKS

It can be seen that work on turbulence and wind shear models is not finished. Further studies of the non-Gaussian turbulence models are scheduled on the Ames six-degree-of-freedom simulator. A more refined turbulence response aircraft model will be used. The wind shear models presented were for a neutral stability condition. The analysis should be extended to the unstable and stable boundary layers. Additional statistical data from tower measurements and instrumented aircraft are needed. Of course, application of these turbulence and wind shear models for handling quality studies and autopilot design must be a continuing process.

REFERENCES

1. Bullen, N. I.: Aircraft Loads in Continuous Turbulence. AGARD Rep. 116, Apr.-May 1957.
2. Reeves, Paul M.: A Non-Gaussian Turbulence Simulation. AFFDL-TR-69-67, U.S. Air Force, Nov. 1969.
3. Gault, J. D.; and Gunter, D. E., Jr.: Atmospheric Turbulence Considerations for Future Aircraft Designed To Operate at Low Altitudes. J. Aircraft, vol. 5, no. 6, Nov.-Dec. 1968, pp. 574-577.
4. Snyder, C. Thomas: Analog Study of the Longitudinal Response of a Swept-Wind Transport Airplane to Wind Shear and Sustained Gusts During Landing Approach. NASA TN D-4477, 1968.
5. Campbell, Gaylon S.; Hansen, Frank V.; and Dise, Raymond A.: Turbulence Data Derived From Measurements on the 32-Meter Tower Facility: White Sands Missile Range, New Mexico. Tech. Rep. ECOM-5314, U.S. Army, July 1970. (Available from DDC as AD 711 852.)
6. Panofsky, H. A.; Busch, N.; Prasad, B.; Hanna, S.; Peterson, E.; and Mares, E.: Properties of Wind and Temperature at Round Hill, South Dartmouth, Mass. Tech. Rep. ECOM-0035-F, U.S. Army, Aug. 1967. (Available from DDC as AD 659 430.)

TABLE I

WIND SHEAR CLASSIFICATION

<u>CATEGORY</u>	<u>MAGNITUDE</u> (m/sec) / 30 m
LIGHT	0 — 2.5
MODERATE	2.5 — 4.5
STRONG	4.5 — 6.0
SEVERE	>6

GAUSSIAN TURBULENCE SIMULATION

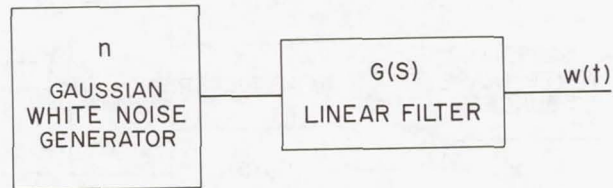


Figure 1

DERIVATIVE OF VERTICAL VELOCITY 40 sec SAMPLES



Figure 2

NON-GAUSSIAN TURBULENCE SIMULATION

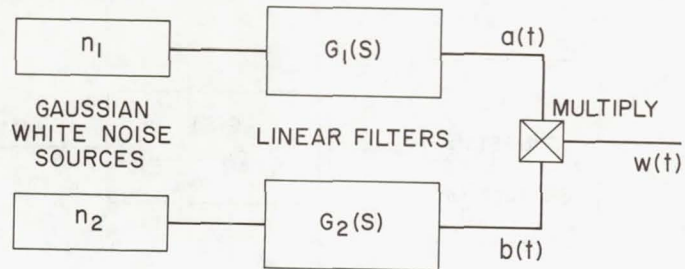


Figure 3

DERIVATIVE OF VERTICAL VELOCITY 40 sec SAMPLES

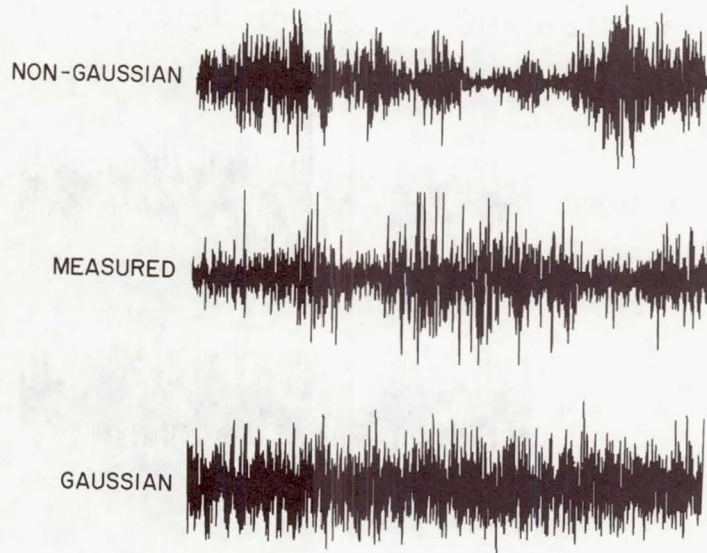


Figure 4

SIMULATOR



Figure 5

STOL AIRCRAFT



Figure 6

TURBULENCE REALISM RATING SIMULATOR STUDY RESULTS

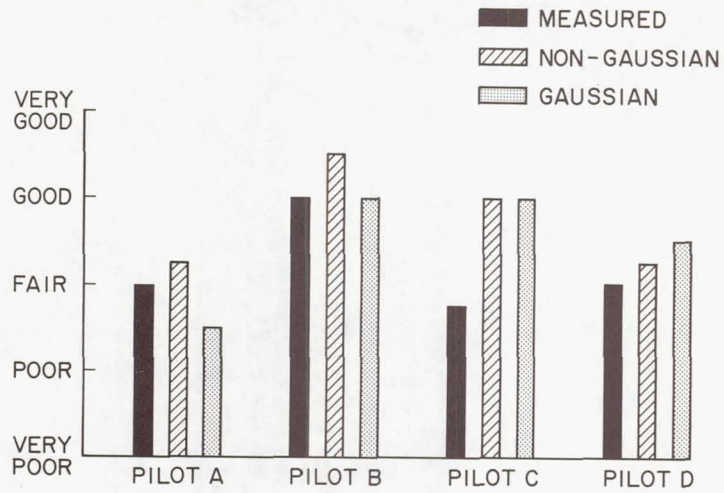


Figure 7

TYPICAL WIND PROFILE MEASURED vs THEORY

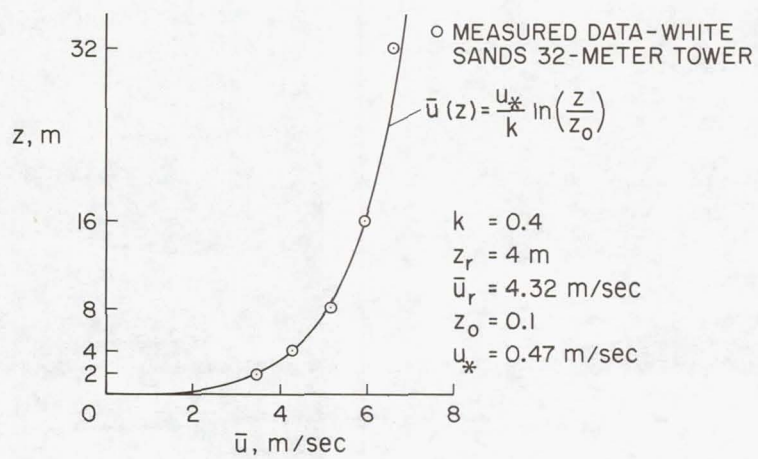


Figure 8

WIND PROFILE

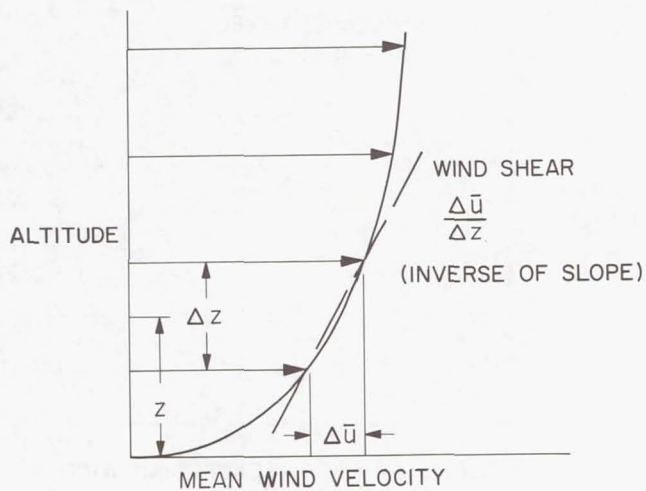


Figure 9

GENERAL CURVE FOR WIND SHEAR MEAN WIND

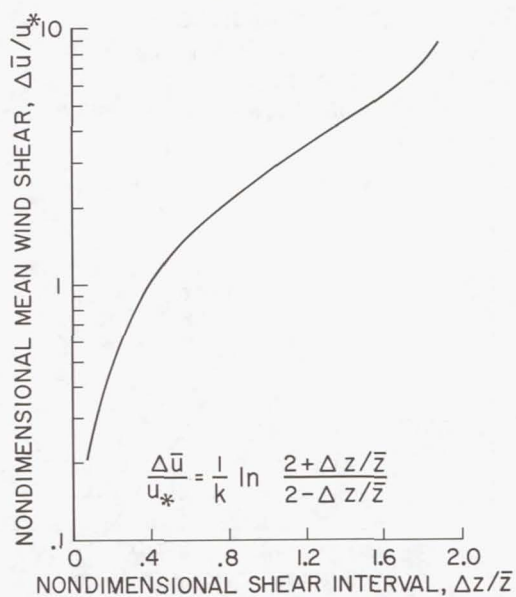


Figure 10

FLUCTUATING SHEAR

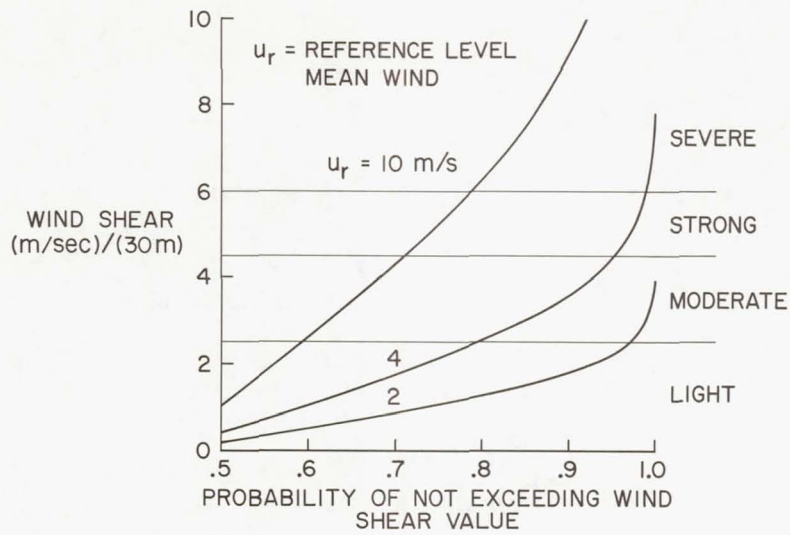


Figure 11

APPROACH PROFILES OF A STOL AIRCRAFT

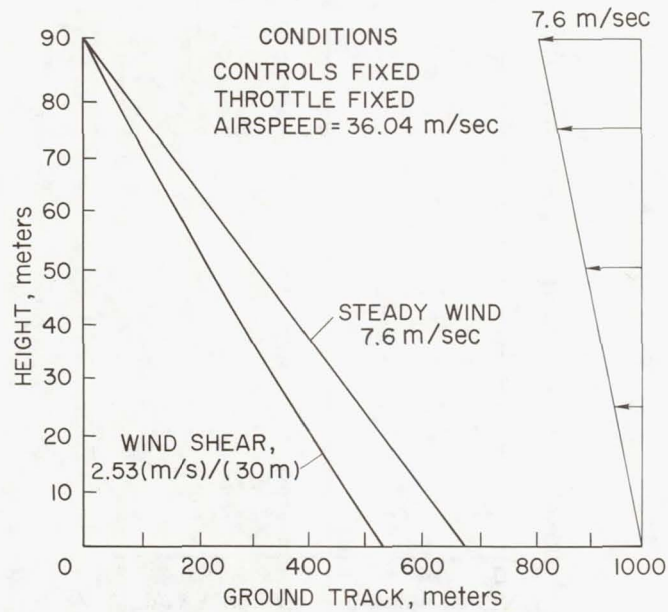


Figure 12

RADIATION SAFETY IN HIGH-ALTITUDE AIRPLANE TRAFFIC

By Trutz Foelsche
Langley Research Center

SUMMARY

A brief survey of results up to 1970 of an experimental and theoretical study of biologically important radiation components and dose equivalents due to galactic and solar cosmic rays in the high atmosphere, especially at supersonic transport (SST) altitudes, is presented.

The dose equivalent rate for the flight personnel flying 500 hours per year at cruise altitudes of 18.2 to 19.8 km (60 000 to 65 000 ft) in high magnetic latitudes turned out to be about 0.75 to 1.0 rem/yr averaged over the solar cycle. This rate is about 15 to 20 percent of the maximum permissible dose (MPD) rate for radiation workers (5 rem/yr), as established by the International Commission on Radiological Protection (ICRP) for peacetime operations.

Most passengers do not encounter major solar events and would be exposed only to the low-level galactic cosmic rays. Such exposure would amount to a few mrem per high-latitude trip and is therefore negligible. If the airplane happened to pass through the impact zone of a rare giant solar event such as that of February 23, 1956, its passengers would be exposed to 0.45 rem, which is 90 percent of the permissible limit (0.5 rem/yr) for individuals of the general population, provided a total of 5 rem up to age 30 is not exceeded. This exposure of 0.45 rem is based on the assumption that the airplane descends to subsonic altitudes at the beginning of the event and continues its flight at the lower altitude. At cruise altitude the maximum permissible limit would be exceeded. The suggested evasion measure of descending to lower altitudes is therefore sufficient to avoid overexposure of passengers in such rare cases.

Proposed systems of in-flight radiation warning and monitoring are briefly discussed.

INTRODUCTION

High-altitude commercial airplanes, as they are envisioned for the future, will cruise at altitudes of 18.2 to 19.8 km (60 000 to 65 000 ft). At these altitudes only about 6 percent of the mass of the atmosphere is left above the airplane, which affords little protection against space radiations such as galactic and energetic solar cosmic rays. Therefore, there has been continuing concern about the radiation safety in airplanes such as the SST. In fact, the nuclear reactions of the cosmic rays within this upper 6 percent

of the atmosphere produce many secondaries, including the particularly biologically effective neutrons, whose net biological effect may exceed that of the primaries.

This paper is a review of what is now known, to the author, of this problem — mainly as it concerns the radiation exposure of the crew and passengers at SST and lower altitudes — and what evasion measures might have to be taken during times of high-energy, high-intensity solar particle events.

DATA SOURCES

Our understanding is based to a large extent on Langley Research Center experiments with high-altitude balloons and airplanes measuring cosmic rays and their variations with solar activity, from 1965 to the present, over a large part of the solar cycle (refs. 1 and 2).

Figure 1 is a brief review of these data sources. Through the 4 years from 1965 through 1968, 20 balloon launches, five each year, were conducted by Langley from Fort Churchill, on Hudson Bay, Canada. From 1968 to the present about 300 U-2 and RB-57F flights from London, England; Maine, U.S.A.; and mostly from Eielson AFB, Alaska have been made, the latter in cooperation with the Air Force and Federal Aviation Administration. Spot checks in lower latitudes were conducted with balloons from Hyderabad, India, and from Palestine, Texas. Furthermore, five latitude scans with RB-57F airplanes from Eielson AFB, Alaska, to Albuquerque, New Mexico, and down to the equator were made. A complete latitude scan at 10.7 km (35 000 ft) was conducted by participating in the 65-hour globe-circling flight over both poles with a Boeing 707 airplane in 1966.

Most flights were made in high magnetic latitudes. The reason is that one is mostly interested in maximum doses and these occur at latitudes greater than about 50° , which contain the North Atlantic and Canadian routes and possibly routes from Moscow to the U.S.A. Below a magnetic latitude of 50° the doses fall off rather rapidly because the magnetic field of the earth deflects the cosmic ray particles at the lower latitudes. The dose rates decrease by about a factor of 6 toward the equator, according to the above measurements. Thus, precautionary measures would not be necessary on the Pacific and Southeast Asian routes.

Because of their possible importance and the large uncertainty of fluxes and energy spectra, the neutrons were measured separately in the Langley program with a special neutron spectrometer developed and maintained by R. Mendell at New York University. The detection of neutrons with this instrument is based on discrimination of pulse shapes in a liquid scintillator surrounded by a plastic scintillator, the latter for exclusion of charged particles (refs. 3 and 4).

In addition to neutrons, cascades of protons, mesons, electrons, and photon electrons penetrate to SST altitudes. To determine the doses produced by these more lightly ionizing particles, a tissue-equivalent ion chamber was designed and built by Avco Corp. This chamber, which was supplemented with a recorder and was maintained by Richard R. Adams, Langley Research Center, was used in the flight experiments. The neutron spectra and tissue absorbed dose were measured with these instruments. They were first suspended in free air and then inside spherical phantoms of tissue-equivalent material representing the human body to derive the dose equivalents in extremities (small tissue sample represented by the sensors) and in the depth of the body.

Heavy-primary hits, or penetrations, and fragments heavier than protons produced in nuclear interactions with air are neglected in the calculation of dose rates for the SST. According to measurements of Yagoda (ref. 5) and also unpublished measurements in the course of the Langley program, the fluxes of heavy primaries and of energetic heavy fragment are practically zero at altitudes of 18.2 to 19.8 km (60 000 to 65 000 ft), or 60g/cm^2 of air shielding. The same results with respect to heavy nuclei have been obtained in theoretical estimates of Schaefer (ref. 6).

Additional relevant data were obtained from ground experiments and extensive theoretical analyses made at Oak Ridge National Laboratory (ORNL) in an 8-year study under NASA and AEC sponsorship (refs. 7 to 12 and references therein). Studies at Langley Research Center have extended the ORNL methods to higher energies (John W. Wilson at Langley) and have applied the developing dose calculation methods to accumulated spectral data on solar events, especially those of the highly active solar cycle 19, from 1954-1964 (refs. 13 to 17).

"RADIATION SAFETY"

Biological doses which are internationally accepted as "radiation safe," or, more exactly, as maximum permissible doses (MPD's) for peacetime operations, have been established by the ICRP. Maximum permissible doses applicable to crew and passengers are briefly summarized in figure 2. The doses are given in rem, which stands for roentgen equivalent man, instead of in rad. The rad measures only the energy absorbed per gram. For a given amount of absorbed energy, heavily ionizing nuclei and neutrons do much more biological damage than X-rays, electrons, or other lightly ionizing particles for which rem and rad are the same. The rem is the dose corrected for this increased biological effectiveness. For example, for fast neutrons as they occur at high altitudes, the dose equivalent, or rem, is about 10 times the absorbed dose.

It may be noted in figure 2 that the average MPD for radiation workers is 10 times higher (5 rem/yr) than the MPD for individuals of the general population in a single year (0.5 rem/yr). The reason is that radiation workers are a small group of adults. The general population encompasses children, including infants — even the fetuses in pregnant

women — who are much more sensitive to radiation. In fact the guidelines for the general population are even more restrictive. "Total of 5 rem up to age 30" means that on the average, only 0.167 rem/yr is permissible up to age 30. Thus, not for every year is 0.5 rem allowed.

For high-altitude flight, the crew or flight personnel are equated to radiation workers because they are adults, and the passengers are equated to the general population. Thus, the following two numbers may be noted:

<u>For the crew</u>	5 rem/yr on the average over long periods, say 10 to 30 years, are safe or permissible
<u>For passengers</u>	a maximum of 0.5 rem/yr in single years, or one time in a single year, is considered permissible, provided a total of 5 rem up to age 30 is not exceeded

MAXIMUM EXPOSURE OF SST OCCUPANTS AND COMPARISON WITH MPD's

To obtain the maximum exposures of SST occupants and compare these with the MPD's, some of the results on galactic and solar cosmic ray dose rates at SST and subsonic altitudes and at high latitudes will now be presented.

Galactic Cosmic Ray Dose Rates

Galactic cosmic rays are of low intensity; however, they are always present. Their intensity varies by a factor of about 2 in the high-energy range and by a factor of about 4 in the low-energy range during the 11-year sunspot cycle.

In figure 3, the circles show the measured dose rates as a function of altitude. The scale is on the right-hand side, and is given in rads — not corrected for biological effectiveness. This dose rate is nearly constant above SST altitude for the year 1967. The squares show the fast-neutron flux measured separately. The scale is on the left-hand side. Note that the neutron flux has a maximum just at SST altitudes.

Figure 4 shows the biological dose rates or dose equivalent rates in mrem/hr derived from measurements made with the ion chamber and neutron spectrometer. Consider first the lines labeled 1965. The dashed curve shows the contribution mainly of the lightly ionizing particles; the dotted line shows the contribution of the neutrons (rem minus rad); and the x-symbols show the contribution of the stars (rem minus rad) produced by protons, which are the sites of nuclear reactions resulting in extensive local damage to cells. (The calculated values for stars from protons and neutrons are in fair agreement with the measurements made by P. J. N. Davison, University of Bristol, England, within tissue equivalent emulsions.) The light solid line, which is the total dose equivalent rate

as a function of altitude, indicates a maximum at SST altitude, as did the curve for neutron flux in figure 3. Note that the curve is labeled 1965. That was near the sunspot minimum of the solar cycle, when the galactic cosmic ray flux is at a maximum. The average over the 11-year solar cycle would be less, about as shown by the heavy line. The curve shows approximately 1.2 mrem/hr at SST altitude.

From the dose equivalent rates in figure 4, the following results are obtained:

(1) If the crew fly about 500 hr/yr at high altitudes, their average dose rate due to galactic cosmic rays would be about

$$500 \times 1.2 \frac{\text{mrem}}{\text{hr}} = 0.6 \frac{\text{rem}}{\text{yr}}$$

or only about 12 percent of their maximum permissible dose rate of 5 rem/yr.

(2) The large majority of passengers, who would cross the North Atlantic, for example, only a few times a year and not encounter solar events, would be exposed in 2 hours at cruise altitude to only about 3 mrem, which is negligible in comparison with their permissible limit of 500 mrem/yr, or 0.5 rem/yr.

(3) The circles labeled "Theory" on the total dose curve for 1965 (fig. 4) were calculated by starting from the known cosmic ray spectrum in space and using a computer program developed at the Langley Research Center to determine the dose at various depths in the atmosphere. The fairly good agreement with the measurements suggests that such a computer code may be useful to monitor the dose rate in the SST with fair accuracy from the primary spectra measured, for example, in synchronous satellites far out in space, without having instruments onboard the SST. (This point will be discussed again later.)

Solar Cosmic Ray Dose Rates

Solar cosmic rays or solar particle events, accompanying some — but not all — flare outbursts on the sun, are transient particle showers (duration 8 to 24 hours); however, in some cases their intensity may be 1000 times higher than that of galactic cosmic rays.

In figure 5 the two curves on the left correspond to a high-energy event of very low intensity that occurred on March 30-31, 1969. The increments of intensity (ordinates) are plotted against time in hours (abscissa).

The neutron monitor on the ground showed only a 5-percent increase over its background (the background is due to the steady flux of galactic cosmic rays). The airplane measurements at SST altitude, however, yielded about a 90-percent increase in biological dose rate, or nearly 20 times more than the neutron increment on the ground. (The factor 20 is not very conspicuous on the log scale on the ordinate; however, the log scale is

needed to present in the same figure the much higher increment observed in 1956 for a very intense, high-energy event.)

The event on the right is this famous giant event of February 23, 1956, which is the largest event observed in at least 30 years. Instead of 5 percent, an increase of 3600 percent on the ground, or 36 times galactic cosmic ray background, was observed. No measurements at altitude could be made in 1956 during the main phase of the event; however, if the same factor of about 20 that was found for the smaller flare is used, an increase of 720 times that of March 1969 is obtained. This represents a dose rate of 1000 mrem/hr or 1 rem/hr at the beginning of the event.

Since the dose that would be accumulated during, say, 2 hours at cruise altitude is apparently above the permissible limit for passengers, it is very important to confirm this high dose rate in any possible way. This was done (refs. 16 and 17) by using the fluxes and spectra above the atmosphere in space which were estimated by Meyer, Parker, and Simpson (ref. 18) from ground measurements over a wide latitude range at that time (see also refs. 19 and 20).

Figure 6 shows the result of these dose calculations for different altitudes. The maximum dose equivalent rate for February 1956 at SST altitude is found to be between 0.5 rem/hr and 3 rem/hr, which is in fair agreement with figure 5. The large difference between the upper and lower limit is due mainly to the uncertainty in the lower energy part of the prompt spectrum ($E < 1$ GeV), which could not be measured in 1956.

Similar dose calculations have been made for the most significant of the 60 solar events of the particularly active solar cycle 19 starting with the energy spectra in space derived from balloon, rocket, satellite, riometer, and scattering-network data. The second largest event was that of November 12-13, 1960, which is seen at two different times in figure 6. The dose equivalent rates are only of the order of 30 to 50 mrem/hr at SST altitude.

On the basis of these measurements and calculations for solar events, conclusions may be drawn first on the average exposure of the crew from solar cosmic rays assuming, conservatively, that the crew were exposed in altitude to the maximum phase of each major event of solar cycle 19. The results are given in figure 7. One sees that the contribution of all major events, except that of February 1956, is very low. If the February 1956 event is included, an upper limit of 0.3 rem/yr is obtained as the average contribution per year from solar events of one cycle. Of course, in none of the single years was the maximum permissible dose rate of 5 rem/yr for the crew reached, even if the airplane had remained at cruise altitude during the events. When the previously given galactic cosmic ray average dose rate of 0.6 rem/yr is added, the total is 0.9 rem/yr from solar plus galactic cosmic rays. This is the average over the solar cycle and is only 15 to 20 percent of the maximum permissible exposure for radiation workers. To be

correct, it should be added that this exposure on high-latitude routes is slightly higher than the exposure of 90 percent of the radiation workers in the nuclear industry, who are actually exposed to only about 10 percent of the MPD for radiation workers.

The most important result so far is that to the best of our present knowledge, the permissible exposure of passengers is exceeded if the SST flies at its cruise altitude during such giant events as that of February 1956. This would be contrary to the internationally accepted radiation protection guidelines.

Fortunately, because of atmospheric attenuation, timely descent to subsonic altitude during such events would reduce the conservatively high estimated accumulated dose to below 0.5 rem, or below the MPD for passengers. In figure 6 it is seen that the maximum dose rate at 9 km (30 000 ft) would be 0.45 rem/hr. This is the dose rate at the peak of the event – of about 10 minutes duration. This dose rate fell off very fast in the first hours (as in all high-intensity, high-energy events observed so far). The accumulated dose for the first 3 hours, about the maximum time that the SST would remain at subsonic altitudes, would not be more than 0.45 rem. Thus, such an evasion measure is sufficient to keep the dose within safe limits in such rare cases.

Furthermore, it appears that in all the other of the approximately 60 solar events, such evasion would not have been necessary in order to comply with the requirement to stay below the maximum exposure limit of 0.5 rem, because the maximum dose rate even for the November 12, 1960, event was only of the order 30 to 50 mrem/hr at SST altitude. Since it is desirable to hold any exposure as low as possible, the airplanes may descend to lower altitudes in such cases also, that is, if a level of 50 mrem/hr or even less is reached. Even when evasion in such cases is included, solar cosmic radiation will only in rare cases interfere with the normal operation of the airplanes, since only three more events comparable in size and energy with the November 12 event were observed in the highly active cycle 19.

It may be emphasized that an in-flight radiation warning and monitoring system is required to minimize evasion measures or interference with the normal operation of the SST planes. Other precautionary measures such as delaying flights or rerouting the airplanes to lower latitudes in case active regions on the sun are about to erupt would interfere considerably more with the economical operation of high-altitude aircraft, since as yet, even experienced forecast centers cannot predict if and when such regions will erupt and if high-energy particles with high intensity will be produced. Only very rare intense high- or medium-energy events require evasion measures. Giant events comparable with that of February 23, 1956, have occurred only one to two times per 11-year cycle in the past three decades.

A design requirement for evasion by descent to subsonic altitude is that the airplanes have sufficient subsonic capability to reach the next airport at subsonic altitude

from every point of their route. This capability was specified for the American SST and is probably specified for the French-English and the Russian versions of the SST for safety reasons.

MONITORING SYSTEMS

Proposed in-flight monitoring systems required for the necessary evasion measure of descent to subsonic altitude will now be discussed briefly. Two such systems are under consideration:

1. Equipping the airplanes with qualified monitoring instruments which indicate the biological dose rate within acceptable error limits, especially the neutron dose equivalent rate.

2. Using synchronous-orbit satellites for measuring the solar particle spectra far out in space, calculating the corresponding complex radiation in the SST's in real time in the satellite or ground computer, and transmitting this information to the SST pilots by relay stations. NASA and the Environmental Science Services Administration (ESSA) are engaged in a feasibility study for the satellite system. The SMS-GOES synchronous satellites are presently in the design stage (for other purposes). It is considered important that any such radiation monitoring system indicate the in-flight accumulated dose equivalent with sufficient accuracy, and within known error limits, to serve as proof that the actual exposure is below the permissible limit, in order to protect the airlines from legal liabilities.

SUMMARY ON RADIATION RESULTS AND CONCLUSIONS

The results obtained on radiation exposure and safety measures may be summarized as follows:

1. The maximum exposure of the crew due to galactic and solar cosmic rays, as listed in the upper half of figure 8, is found to be 0.75 to 1.0 rem/yr, or 15 to 20 percent of the maximum permissible dose rate for radiation workers. This exposure would of course also be the same for passengers, such as perhaps airline executives, who fly as often as the crew on high-latitude routes. It is presumed that these persons are adults; therefore, they would incur no significant radiation risk either.

2. The large majority of passengers do not encounter major solar events and would be exposed only to the low-level galactic cosmic rays. Such exposure would amount to a few mrem per high-latitude trip and is therefore negligible. If the airplane should encounter the radiation from a rare giant solar event such as that of February 1956, the most intense high-energy event in three decades, its passengers would be exposed to a

maximum of 0.45 rem, or 90 percent of their permissible limit per year (fig. 8). The maximum value of 0.45 rem is the exposure if the airplane descends to subsonic altitude at the beginning of the event and continues its flight at the lower altitude.

From these results and the infrequency of major solar events, the following conclusions are reached:

1. If the suggested precautionary measure of timely descent or other evasion measures can be taken in case of giant solar events, cosmic radiation appears to pose no hazard to the health and safety of passengers and the crew in commercial SST flight — assuming, of course, the validity of the present internationally accepted exposure limits, especially for pregnant persons, for which case there still exists some uncertainty.
2. If a radiation monitoring system is provided to indicate to the pilots in time when to descend to subsonic altitudes, and if the pilots can reach the next airport at subsonic altitude, cosmic radiation will only in very rare cases interfere with the normal operation of high-altitude aircraft.

There are as yet mainly two unsolved problems. The first is to establish with more certainty the validity of the maximum permissible doses for pregnant passengers. The second concerns the synchronous-satellite monitoring system which appears more economical than to provide and maintain, on say 300 SST's, rather sophisticated instruments which are actually needed only one to four times in 10 years. Except to equip synchronous-orbiting satellites with a particle spectrometer which is capable of measuring the energy spectra up to 5 to 10 GeV/nucleon and to establish communication lines, the problem is to determine the error limits of the Langley computer code for protons and to develop a similar code for the heavy primaries, which produce a large part of the biologically effective secondaries at SST altitudes. These problems require controlled experiments on a high-energy proton and heavy-nuclei accelerator.

REFERENCES

1. Foelsche, Trutz: Radiation Measurements and Doses at SST Altitudes. NASA paper presented at National Symposium on Natural and Manmade Radiation in Space (Las Vegas, Nevada), Mar. 1971.
2. Foelsche, T.; Mendell, Rosalind; Adams, Richard R.; and Wilson, John W.: Measured and Calculated Radiation Levels Produced by Galactic and Solar Cosmic Rays in SST Altitudes and Precaution Measures To Minimize Implications at Commercial SST-Operations. NASA paper prepared for French-Anglo United States Supersonic Transport Meeting (Paris, France), Mar. 3, 1969.
3. Mendell, R. B.; and Korff, S. A.: Fast-Neutron Detector With Discrimination Against Background Radiation. *Rev. Sci. Instrum.*, vol. 34, no. 12, Dec. 1963, pp. 1356-1359.
4. Mendell, R. B.; and Korff, S. A.: Fast-Neutron Flux in the Atmosphere. *J. Geophys. Res.*, vol. 68, no. 19, Oct. 1963, pp. 5487-5495.
5. Yagoda, Herman: Cosmic-Ray Monitoring of the Manned Stratolab Balloon Flights. AFCRL-TN-60-640, U.S. Air Force, Sept. 1960.
6. Schaefer, Hermann J.: Public Health Aspects of Galactic Radiation Exposure in Supersonic Transport. NAMI-1033, U.S. Navy, Mar. 1968. (Also available as NASA CR-94760.)
7. Bertini, Hugo W.: Preliminary Data From Intranuclear-Cascade Calculations of 0.75-, 1-, and 2-GeV Protons on Oxygen, Aluminum, and Lead, and 1-GeV Neutrons on the Same Elements. ORNL-TM-1996, U.S. At. Energy Comm., Dec. 1967.
8. Kinney, W. E.: The Nucleon Transport Code, NTC. ORNL-3610, U.S. At. Energy Comm., Aug. 1964.
9. Kinney, W. E.; and Zerby, C. D.: Calculated Tissue Current-to-Dose Conversion Factors for Nucleons of Energy Below 400 MeV. Second Symposium on Protection Against Radiation Hazards in Space, NASA SP-71, 1965, pp. 161-172.
10. Turner, J. E.; Zerby, C. D.; Woodyard, R. L.; Wright, H. A.; Kinney, W. E.; Snyder, W. S.; and Neufeld, J.: Calculation of Radiation Dose From Protons to 400 MeV. *Health Phys.*, vol. 10, no. 1, Nov. 1964, pp. 783-808.
11. Irving, D. C.; Alsmiller, R. G., Jr.; Kinney, W. E.; and Moran, H. S.: The Secondary-Particle Contribution to the Dose From Monoenergetic Proton Beams and the Validity of Current-to-Dose Conversion Factors. Second Symposium on Protection Against Radiations in Space, NASA SP-71, 1965, pp. 173-176.

12. Armstrong, T. W.; Alsmiller, R. G.; and Barish, J.: Calculation of the Radiation Hazard at Supersonic Aircraft Altitudes Produced by an Energetic Solar Flare. Nucl. Sci. Eng., vol. 37, no. 3, Sept. 1969, pp. 337-342.
13. Foelsche, T.: Radiation Exposure in Supersonic Transports. Symposium on Supersonic Air Transport, Conf. 14/WP-SYMP/49, Int. Air Transp. Assoc., Apr. 1961; also comments.
14. Foelsche, Trutz: Radiation Exposure in Supersonic Transports. NASA TN D-1383, 1962.
15. Foelsche, T.; and Graul, E. H.: Radiation Exposure in Supersonic Transports. Atompraxis, vol. 8, no. 10, 1962, pp. 365-380.
16. Foelsche, Trutz: The Ionizing Radiations in Supersonic Transport Flights. Second Symposium on Protection Against Radiations in Space, NASA SP-71, 1965, pp. 287-299.
17. Wilson, John W.; Lambiotte, Jules J., Jr.; Foelsche, Trutz; and Filippas, Tassos A.: Dose Response Functions in the Atmosphere Due to Incident High-Energy Protons With Application to Solar Proton Events. NASA TN D-6010, 1970.
18. Meyer, P.; Parker, E. N.; and Simpson, J. A.: Solar Cosmic Rays of February, 1956 and Their Propagation Through Interplanetary Space. Phys. Rev., vol. 104, no. 3, Second ser., Nov. 1, 1956, pp. 768-783.
19. Van Allen, J. A.; and Winckler, J. R.: Spectrum of Low-Rigidity Cosmic Rays During the Solar Flare of February 23, 1956. Phys. Rev., vol. 106, no. 5, June 1, 1957, pp. 1072-1073.
20. Winckler, John R.: Cosmic-Ray Increase at High Altitude on February 23, 1956. Phys. Rev., vol. 104, no. 1, Second ser., Oct. 1, 1956, p. 220.

HIGH ALTITUDE RADIATION MEASUREMENTS 1965 - 1971

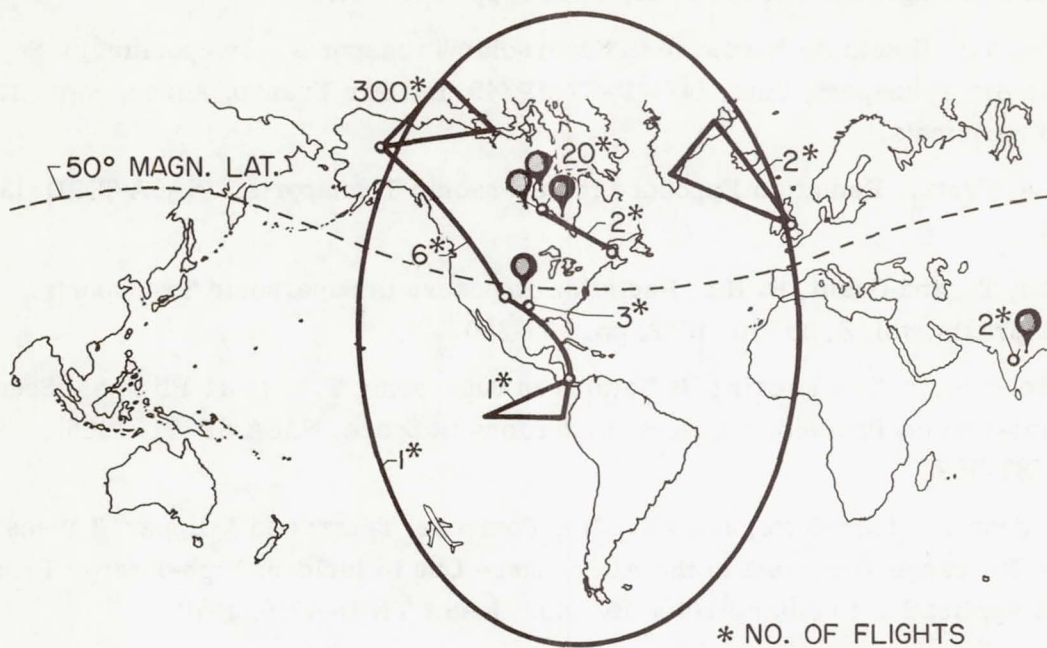


Figure 1

MAXIMUM PERMISSIBLE DOSES (MPD'S)

RADIATION WORKERS: WHOLE BODY	$\frac{5 \text{ rem}}{\text{yr}} = \frac{0.6 \text{ mrem}}{\text{hr}}$
POPULATION: INDIVIDUAL	$\frac{0.5 \text{ rem}}{\text{yr}}$ (TOTAL OF 5 rem UP TO AGE 30)

Figure 2

GALACTIC COSMIC RAYS
FORT CHURCHILL BALLOON TO 43 km (140 000 ft), JULY 15, 1967

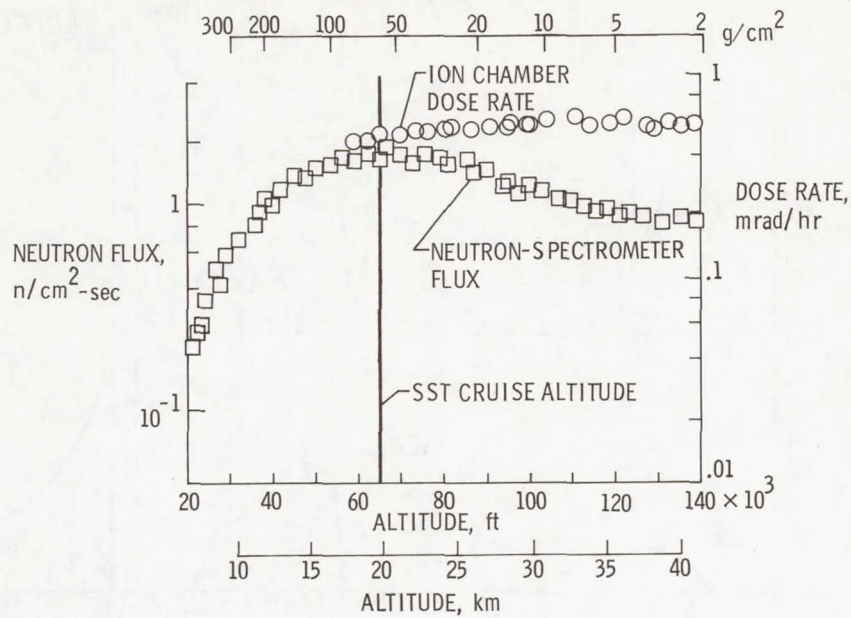


Figure 3

BODY DEPTH DOSES FROM GALACTIC COSMIC RAYS

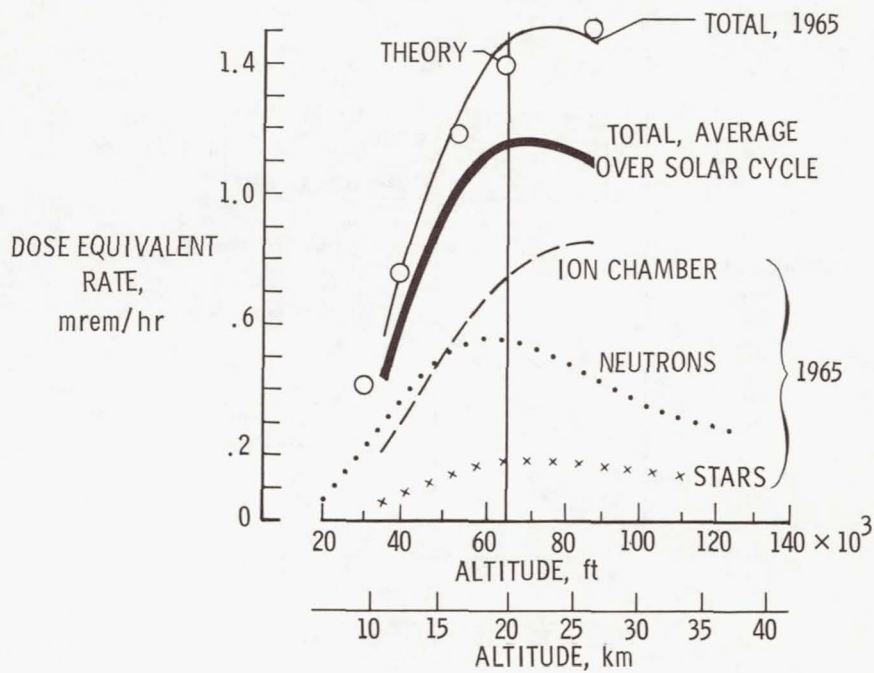


Figure 4

ENERGETIC SOLAR EVENTS MEASURED ON THE GROUND AND AT SST ALTITUDES

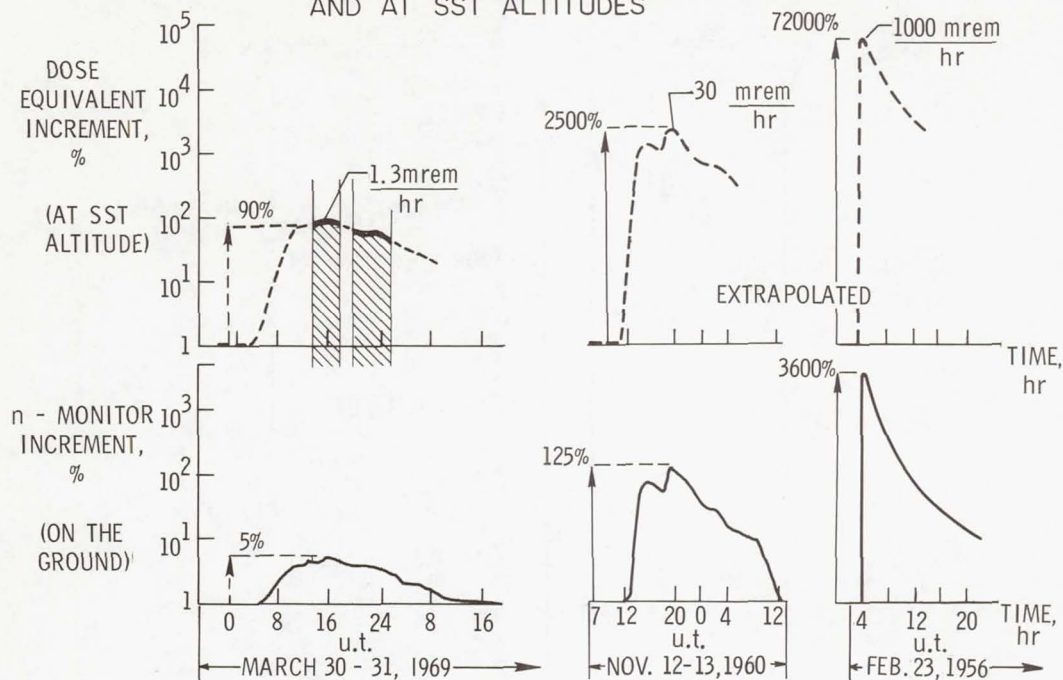


Figure 5

CALCULATED SOLAR FLARE DOSES

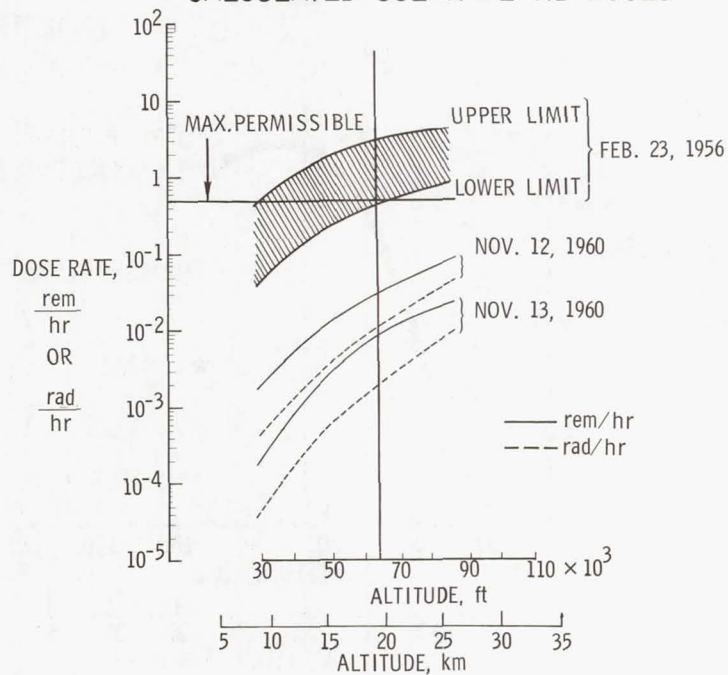


Figure 6

GALACTIC AND SOLAR COSMIC RAY CREW DOSE RATES AVERAGED OVER 10-YEAR DUTY

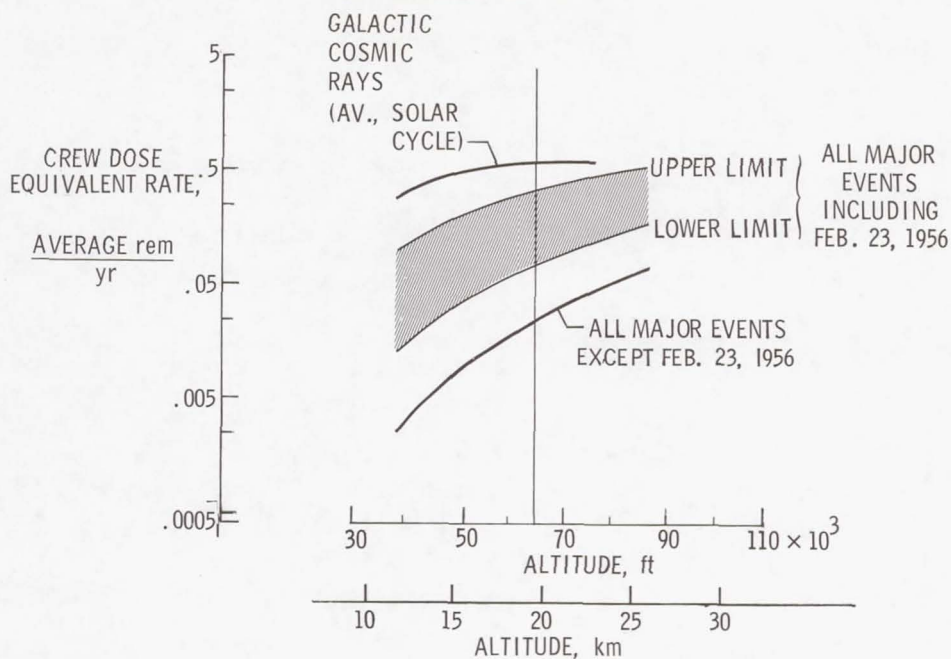


Figure 7

DOSE EQUIVALENTS FOR SST OCCUPANTS

	EXPOSURE	PERCENT OF MPD'S
CREW: ($>55^\circ$ MAGNETIC LATITUDE, AVERAGE OVER SOLAR CYCLE)	0.75 TO 1 rem/yr	15 TO 20% OF MPD FOR RADIATION WORKERS
PASSENGERS: LARGE MAJORITY	NEGLIGIBLE	
INDIVIDUALS (WITH EVASIONS, FEB. 1956)	< 0.45 rem/yr	$< 90\%$ OF MPD FOR POPULATION, ONE TIME IN 10 yr

Figure 8

Page intentionally left blank

PRELIMINARY STUDY OF AIRPLANE-AUTOPILOT RESPONSE TO ATMOSPHERIC TURBULENCE

By Waldo I. Oehman
Langley Research Center

SUMMARY

A preliminary study was made to determine how the response of a particular airplane to atmospheric turbulence would be affected by automatic controls operating in altitude-hold and attitude-hold modes. The calculations show that excursions of the response variables from their equilibrium values may be reduced by these relatively simple controls. The calculations also show that excursions in the augmented airplane altitude and normal acceleration, caused by response to atmospheric turbulence, may lead to buffeting and passenger discomfort. In order to obtain the most desirable response, the control systems should be more complex than those considered.

INTRODUCTION

The problem of airplane flight in turbulent air has been studied from early years of flight history. The primary purpose of these studies generally has been the determination of gust loads and the development of structural design criteria. Obviously, the safety of the airplane and passengers has been the motivation. However, the effect of turbulence on the motion of the airplane, although structural load limits may not be exceeded, could result in excursions of the motion quantities to conditions that would endanger the flight. Also, these excursions, if not dangerous, may cause discomfort for the passengers.

Several analytical and experimental studies have been made in the past to determine the effectiveness of control systems designed specifically for gust load alleviation and passenger comfort. The purpose of the present study was to examine a different aspect of the same problem. It was an analytical study to determine whether or not an automatic pilot, designed for attitude and/or altitude hold, could be made to provide some reduction in airplane response to atmospheric turbulence.

Responses of a medium jet transport airplane have been calculated at an assumed cruise altitude and at several cruise Mach numbers. The basic airplane and the airplane with three automatic control systems were studied. Motion quantities calculated are root-mean-square values of airspeed, angle of attack, attitude angle, altitude, and normal acceleration. The turbulence has been assumed to be severe.

SYMBOLS

The symbols used in this paper are as follows:

a_n	normal acceleration, meters/second ² (feet/second ²)
\bar{c}	wing mean aerodynamic chord, meters (feet)
C_D	drag coefficient, $\frac{2 \text{ Drag}}{\rho S V^2}$
C_L	lift coefficient, $\frac{2 \text{ Lift}}{\rho S V^2}$
C_m	pitching-moment coefficient, $\frac{2 \text{ Pitching moment}}{\rho S \bar{c} V^2}$
C_T	thrust coefficient, $\frac{2 \text{ Thrust}}{\rho S V^2}$
g	gravitational constant, meters/second ² (feet/second ²)
h	altitude, meters (feet)
Δh	altitude perturbation, meters (feet)
\dot{h}	altitude rate, meters/second (feet/second)
k_Y	radius of gyration, meters (feet)
K_1, K_2, K_t	automatic control gains
L	scale of turbulence, meters (feet)
m	mass, kilograms (slugs)
M	Mach number
q	pitch rate, degrees/second

S	wing area, meters ² (feet ²)
t	time, seconds
t'	parameter, $\frac{tV}{\bar{c}}$
U	vertical velocity of local air mass (gust velocity), meters/second (feet/second)
V	airspeed, meters/second (feet/second)
ΔV	airspeed perturbation, meters/second (feet/second)
W	weight, kilograms (pounds mass)
α	angle of attack, degrees
$\Delta\alpha$	angle-of-attack perturbation, degrees
δ_e	elevator deflection angle, degrees
$\delta_{e,c}$	command elevator deflection angle, degrees
δ_t	throttle deflection
ζ	damping ratio
θ	attitude angle, degrees
$\Delta\theta$	attitude-angle perturbation, degrees
θ_c	command attitude angle, degrees
λ	Laplace variable
μ	parameter, $\frac{m}{\rho S \bar{c}}$
ρ	air density, kilograms/meter ³ (slugs/foot ³)

$\Delta\rho$ air-density perturbation, kilograms/meter³ (slugs/foot³)

σ_U rms vertical gust velocity, meters/second (feet/second)

σ_V rms airspeed, meters/second (feet/second) or knots

σ_α rms angle of attack, degrees

σ_θ rms attitude angle, degrees

σ_h rms altitude, meters (feet)

σ_n rms load factor

$\Phi(\omega')$ spectral density function, (meters/second)² ((feet/second)²)

ω circular frequency, degrees/second

ω' reduced frequency, $\frac{\omega \bar{c}}{V}$

$$C_{D_\alpha} = \frac{\partial C_D}{\partial \alpha}, \text{ per degree}$$

$$C_{m_\alpha} = \frac{\partial C_m}{\partial \alpha}, \text{ per degree}$$

$$C_{L_\alpha} = \frac{\partial C_L}{\partial \alpha}, \text{ per degree}$$

$$C_{m_{\alpha'}} = \frac{\partial C_m}{\partial \alpha'}, \text{ per degree}$$

$$C_{L_{\alpha'}} = \frac{\partial C_L}{\partial \alpha'}, \text{ per degree}$$

$$C_{m_{\theta'}} = \frac{\partial C_m}{\partial \theta'}, \text{ per degree}$$

$$C_{L_{\theta'}} = \frac{\partial C_L}{\partial \theta'}, \text{ per degree}$$

$$C_{m_{\delta_e}} = \frac{\partial C_m}{\partial \delta_e}, \text{ per degree}$$

$$C_{L_{\delta_e}} = \frac{\partial C_L}{\partial \delta_e}, \text{ per degree}$$

$$C_{T_\rho} = \frac{\partial C_T}{\partial \frac{\Delta\rho}{\rho}}$$

$$\alpha' = \frac{d\alpha}{dt'}$$

$$\beta = -\frac{\partial \frac{\Delta \rho}{\rho}}{\partial h}$$

$$\theta' = \frac{d\theta}{dt'}$$

METHOD OF ANALYSIS

For the purpose of this preliminary study, the longitudinal motion of the airplane about an equilibrium flight condition may be described by the Laplace transform of linear differential equations. These equations, which include the short-period oscillatory mode and the phugoid, are as follows:

$$\begin{aligned} \left(2\mu\lambda - \frac{\partial C_T}{\partial \frac{\Delta V}{V}} \cos \alpha + \frac{\partial C_D}{\partial \frac{\Delta V}{V}} \right) \frac{\Delta V}{V} + (C_{D\alpha} - C_L) \Delta \alpha + \left(\frac{2W}{\rho S V^2} \right) \Delta \theta + \left[\beta \bar{c} (C_T + C_{T\rho}) \cos \alpha \right] \frac{\Delta h}{\bar{c}} \\ = \left[\frac{C_T}{h} (\lambda) \right] \Delta h + C_{D\alpha} \frac{U}{V} \end{aligned}$$

$$\begin{aligned} \left(\frac{\partial C_T}{\partial \frac{\Delta V}{V}} \sin \alpha + 4 \frac{W}{\rho S V^2} \right) \frac{\Delta V}{V} + \left[C_{L\alpha} + C_T \cos \alpha + (C_{L\alpha'} + 2\mu) \lambda \right] \Delta \alpha + (C_{L\theta'} - 2\mu) \lambda \Delta \theta \\ - \left[\beta \bar{c} (C_T + C_{T\rho}) \sin \alpha \right] \frac{\Delta h}{\bar{c}} = -C_{L\delta_e} \left[\frac{\delta_e}{\theta} (\lambda) \right] \Delta \theta + (C_{L\alpha} + C_{L\alpha'} \lambda) \frac{U}{V} \end{aligned}$$

$$\begin{aligned} - \left(\frac{\partial C_m}{\partial \frac{\Delta V}{V}} \right) \frac{\Delta V}{V} - (C_{m\alpha} + C_{m\alpha'} \lambda) \Delta \alpha + \left(2\mu \frac{k_Y^2}{\bar{c}^2} \lambda^2 - C_{m\theta'} \lambda \right) \Delta \theta \\ = C_{m\delta_e} \left[\frac{\delta_e}{\theta} (\lambda) \right] \Delta \theta + (C_{m\alpha} + C_{m\alpha'} \lambda) \frac{U}{V} \end{aligned}$$

$$\Delta \alpha - \Delta \theta + \lambda \frac{\Delta h}{\bar{c}} = \frac{U}{V}$$

The bracketed terms on the right-hand side of the equations are the transfer functions of the control systems. Note that the turbulence input implies that the instantaneous vertical velocity of the local air mass, divided by the airplane airspeed, is approximately a change in angle of attack in degrees. Hereafter, the instantaneous vertical velocity of the local air mass U is called gust velocity.

Control motions will be limited to those produced by automatic control systems. Specifically, the automatic controls are as shown schematically in figure 1. The upper loop is an "altitude-hold" control system which combines altitude and altitude rate and, with the gain K_t , produces a throttle movement. The purpose of this autothrottle is to maintain altitude. Therefore, whenever altitude and altitude rate increase, the throttle is moved to cause a decrease in thrust and, consequently, a decrease in altitude. Thus, the airplane tends to stay at its original altitude. Similarly, the lower loop is an attitude-hold control system and combines attitude angle and pitch rate with respective gains K_1 and K_2 to produce elevator deflections that tend to hold the airplane at its equilibrium attitude angle. Transfer functions for these control systems, in Laplace transform notation, are given as follows:

Altitude-hold control system

$$\frac{C_T}{h}(\lambda) = \frac{\delta_e}{h}(\lambda) \frac{C_T}{\delta_e}(\lambda) = \left[-K_t \left(0.0001 + 0.004 \frac{V}{c} \lambda \right) \right] \underbrace{\left[\frac{17.6}{\left(\frac{V}{c} \lambda + 0.25 \right) \left(\frac{V}{c} \lambda + 0.2273 \right)} \right]}_{\text{Time lag}}$$

Attitude-hold control system

$$\frac{\delta_e}{\theta}(\lambda) = \underbrace{\left[K_1 + \frac{K_2}{4} \frac{18.5 \frac{V}{c} \lambda}{\left(\frac{V}{c} \lambda + 1 \right) \left(\frac{V}{c} \lambda + 18.5 \right)} \right]}_{\text{Band-pass filter}} \underbrace{\left[\frac{144}{\left(\frac{V}{c} \lambda + 12 \right)^2} \right]}_{\text{Servo}}$$

where $\theta_c = 0$. The gains K_t , K_1 , and K_2 are assumed to be adjustable. The adjustments are discussed in a subsequent section.

The random air velocities in turbulence produce forces and moments to disturb the airplane motion from equilibrium. Consequently, random process theory has been used to calculate the statistics of the airplane response variables. The theory provides the relationship between the spectral density of the response variables and the spectral density of the gust velocities. The relationships of interest herein are

$$\Phi_O(\omega') = |H(\omega')|^2 \Phi_I(\omega')$$

$$\sigma_O^2 = \int_0^\infty \Phi_O(\omega') d\omega' = \int_0^\infty |H(\omega')|^2 \Phi_I(\omega') d\omega'$$

where $|H(\omega')|^2$ is the absolute value, squared, of the frequency response function of the linear system and the functions $\Phi_O(\omega')$ and $\Phi_I(\omega')$ denote output and input spectral densities, respectively. The root-mean-square value of an output quantity is denoted by σ_O . For the results presented, the Von Kármán spectral density function for vertical gust velocities has been used.

The calculations have been made on a digital computer for the following airplane data:

Weight	79 379 kg	(175 000 lbm)
Wing area	236.9 m ²	(2550 ft ²)
Wing span	40.7 m	(133.5 ft)
Mean aerodynamic chord	5.86 m	(19.22 ft)
Aspect ratio	7	

and the assumed flight conditions. The spectral density for the turbulence is shown in figure 2. The airplane described is a medium jet transport assumed to be cruising at an altitude of 10 668 m (35 000 ft) and at Mach numbers from 0.6 to 0.85. The turbulence is characterized by a "scale of turbulence" of 762 m (2500 ft), and the value of the mean-square vertical gust velocity σ_U^2 may be chosen to represent the turbulence intensity. For example, a root-mean-square gust velocity σ_U of about 10 m/sec (32.8 ft/sec) is characteristic of severe turbulence. In turbulent air, gust velocities as large as 3 times the root-mean-square value are likely to be encountered. The responses presented in a subsequent section are for severe turbulence.

RESULTS AND DISCUSSION

Stability

In applying random process theory to a linear system, it is necessary that the system be stable. The airplane — without the automatic controls engaged — has an unstable phugoid for all the Mach numbers except $M = 0.85$. With only the attitude-hold mode of the autopilot engaged, the phugoid is stabilized by adjusting the gain K_1 with $K_2 = 0$.

Hereafter, the basic airplane includes this automatic stabilization (that is, $K_1 = 0.236$, $K_2 = 0$, and $K_t = 0$). Thus, the basic airplane is stable, and the damping ratio ζ of the short period is about 0.18 for all the Mach numbers. This value of the short-period damping ratio is rather low, and to provide a more desirable value, the gain K_2 was adjusted so that the short-period damping ratio was at least 0.7 for all Mach numbers of interest. The altitude-hold control system gain K_t was adjusted so that the throttle motion would not be excessive for small changes in altitude and altitude rate. The gains chosen as described are given in the following table:

Mach number	K_1	K_2	ζ	K_t
0.6	0.236	20.8	0.7	0.027
.7	.236	3.2	.7	.027
.8	.236	6.4	.8	.027
.85	.236	6.4	.85	.027

With these gains, the root-mean-square values of the motion quantities were calculated.

Response to Turbulence

The variations with Mach number of the calculated response variables are shown in figure 3. The curves shown are the response of the basic airplane to a root-mean-square gust velocity σ_U of 0.3048 m/sec (1 ft/sec). Note that a large decrease of airspeed occurs near a Mach number of 0.85 and that normal acceleration is the only variable that increases with Mach number.

A comparison of the response to severe turbulence of the basic airplane and the airplane with the various automatic controls in operation is shown in figure 4 for a Mach number of 0.6. The trends shown are expected to be valid for other Mach numbers.

The results in figure 4 show that the attitude-hold automatic control was effective in producing a sizable reduction in the rms attitude angle as well as small reductions in the other variables. Also, the altitude-hold control was effective in producing a sizable reduction in the rms altitude. Reductions in both altitude and attitude angle were obtained with the two control systems operating simultaneously.

Perhaps the significance of the results obtained can be further emphasized by consideration of the operating envelope shown in figure 5. The envelope is a buffet boundary for a normal acceleration of 1.5g. On the lines for constant Mach number, the large ovals, centered at the appropriate flight condition, indicate the rms altitude ($\sigma_h = 240$ m (786 ft) to $\sigma_h = 372$ m (1220 ft)) and rms airspeed ($\sigma_V = 2.59$ m/sec (8.5 ft/sec) to $\sigma_V = 2.1$ m/sec (6.9 ft/sec)) excursions of the basic airplane while in severe turbulence.

The small ovals indicate the excursions when the altitude-hold control system is engaged. The airplane normal acceleration is about 1.5g which corresponds to an rms load factor σ_n of 0.5. In severe turbulence, the airplane will, on the average, remain below the buffet boundary. However, as mentioned previously, the gust velocity will likely be 3 times the rms value which means that the response variables will be 3 times their rms values. Thus, altitude excursions of about 900 meters (2953 feet) and normal acceleration excursions of 1.5g (that is, airplane normal acceleration is 2.5g) will cause the airplane to be above the buffet boundary. Even in less severe turbulence (that is, turbulence characterized by an rms gust velocity about 70 percent of the rms gust velocity for severe turbulence), the airplane would be likely to cross the buffet boundary. Further, if the turbulence is mild enough (say, 50 percent of severe), then the airplane might not cross the buffet boundary, but the motions, occurring at low frequencies, could be uncomfortable for passengers.

CONCLUDING REMARKS

A preliminary study was made to determine how the response of a particular airplane to atmospheric turbulence would be affected by automatic controls operating in altitude-hold and attitude-hold modes. The calculations show that excursions of the response variables from their equilibrium values may be reduced by these relatively simple controls. The calculations also show that excursions in the augmented airplane altitude and normal acceleration, caused by response to atmospheric turbulence, may lead to buffeting and passenger discomfort. In order to obtain the most desirable response, the control systems should be more complex than those considered.

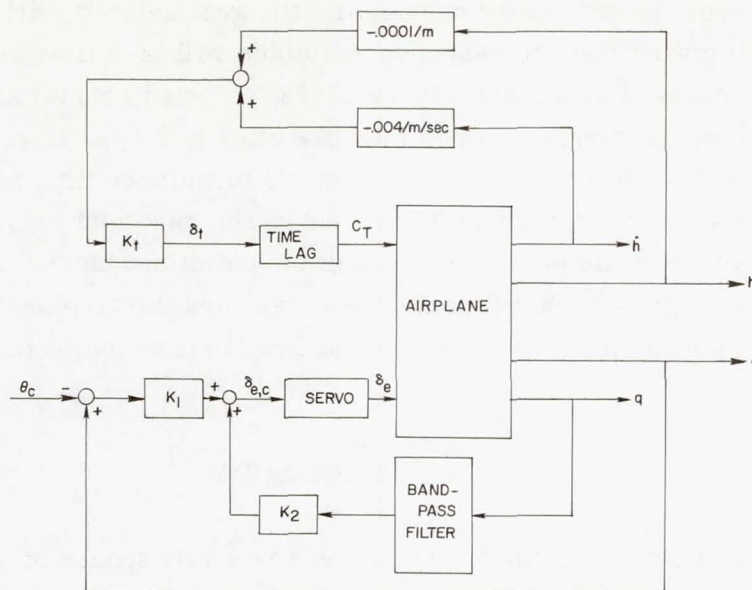


Figure 1.- Automatic control representations.

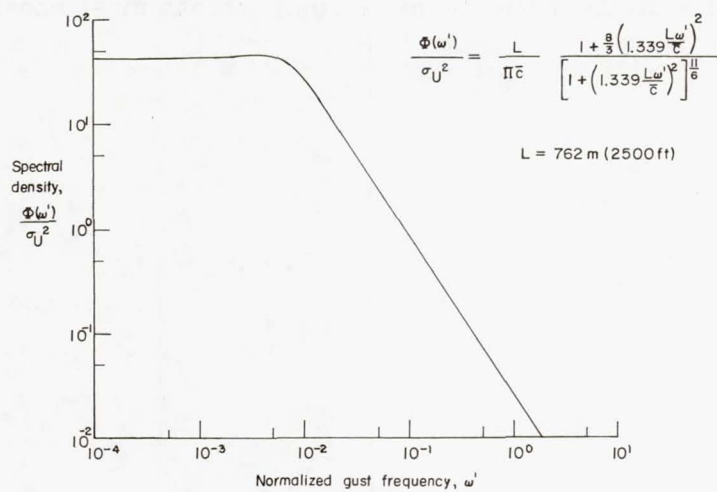


Figure 2.- Von Kármán spectral density function for vertical gusts.

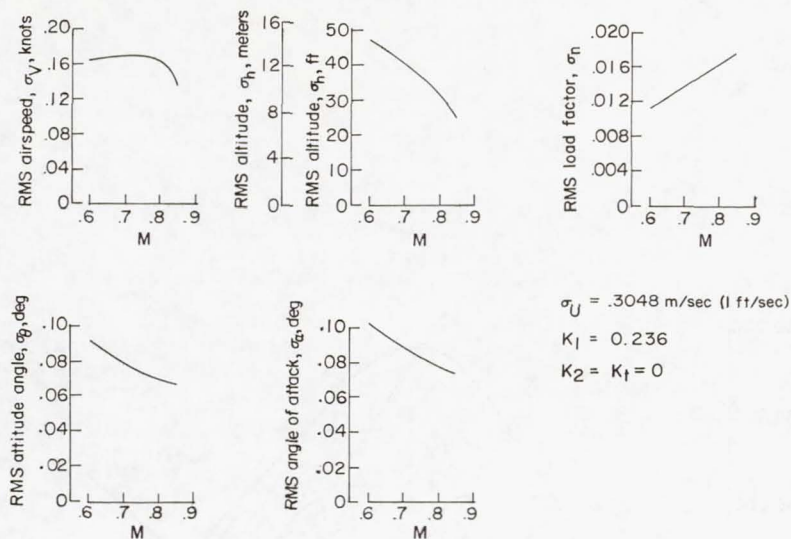


Figure 3.- Basic airplane response. Altitude = 10 668 m (35 000 ft);
W/S = 335 kg/m² (69 lbm/ft²).

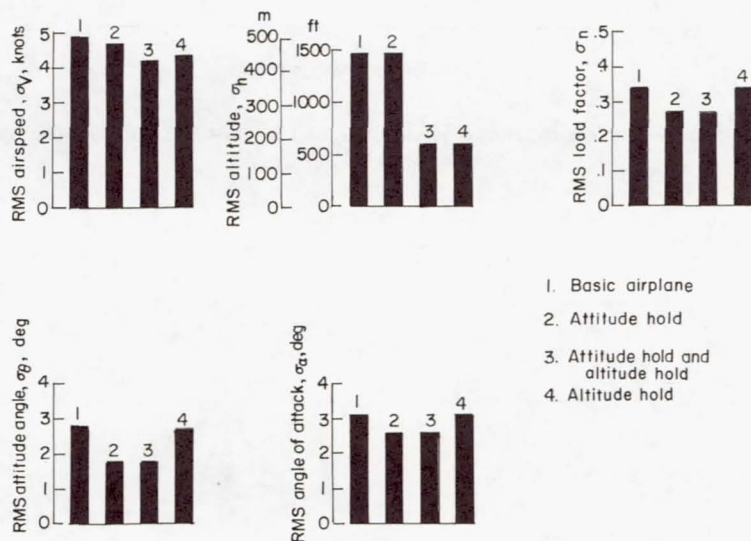


Figure 4.- Effectiveness of automatic controls. M = 0.6; Altitude = 10 668 m (35 000 ft);
 $\sigma_U = 9.1 \text{ m/sec (30 ft/sec)}$.

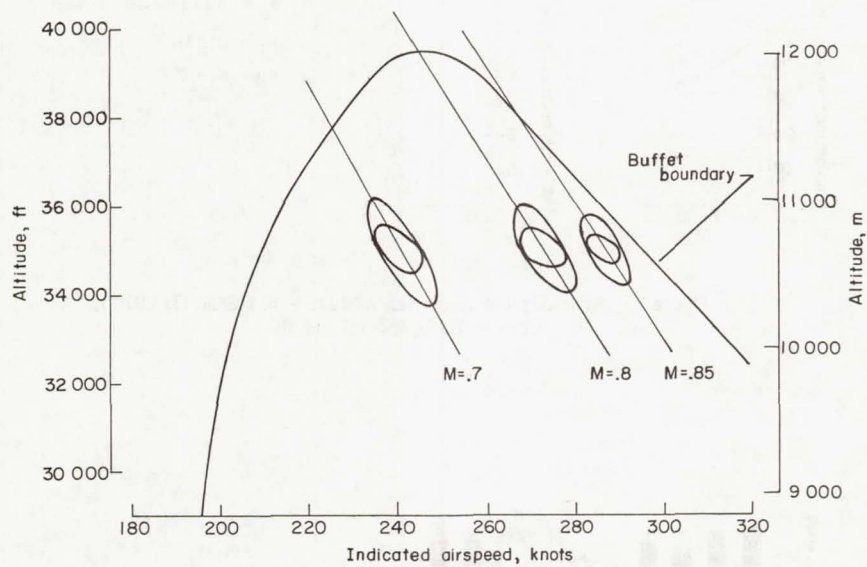


Figure 5.- Airplane operating envelope for $a_n = 1.5g$. $W = 79\,379\text{ kg}$ (175 000 lbm); $W/S = 335\text{ kg/m}^2$ (69 lbm/ft²).

PRELIMINARY STUDY OF EFFECT OF VIBRATION ON AIRCRAFT RIDE QUALITY

By Sherman A. Clevenson, William J. Snyder,
and John J. Catherines
Langley Research Center

INTRODUCTION

During a recent STOL demonstration study, some complaints were voiced about its ride quality and passenger acceptability. Extended periods of low-altitude flight with this type of aircraft have revealed that ride-quality considerations are of major importance for such a system. However, meaningful criteria relating to the comfort of people while they are subjected to low-level random vibrations, typically encountered in this type of aircraft, are not very well defined.

Factors affecting ride quality are shown in figure 1. The figure shows input, transfer function, and output. Basically, the input is either of aerodynamic or mechanical origin. Part of the transfer function is mechanical in the form of a conventional, short, or vertical take-off and landing aircraft (CTOL, STOL, or VTOL). The human provides his own individual transfer function to the various inputs and registers his own responses. In this paper the primary consideration is the low-frequency vibration input through the system.

Part of the difficulty in developing ride criteria and/or acceptable vibration levels stems from problems in measuring and recording the relatively low-level vibration environment associated with passenger vehicles in the low-frequency (0 to 30 Hz) regime. The portable, self-contained measuring/recording system used for this low-frequency range is described in this paper. In addition, examples of real-time data, peak accelerations, and statistical vibration results are given. The results of controlling the environmental input to a helicopter pilot are also shown.

DISCUSSION

The portable instrumentation system used to measure the low-frequency, low-amplitude vibration is shown in figure 2. The system consists of three mutually perpendicular accelerometers and their electronics in one box and a stereo tape recorder. The system, including its batteries, weighs about 13 kilograms. The accelerometer outputs through FM electronics are multiplexed to one channel of the stereo tape recorder, leaving the second channel available for voice annotation. An encoder is also used to facilitate rapid data reduction.

Data reduction is accomplished by use of a high-speed digital computer. Various programs are used which result in power-spectral-density and percent-exceedance plots. An exceedance plot is one that shows the percentage of the time that the selected magnitude of acceleration is exceeded.

Examples are given of measured and reduced data for the CTOL, VTOL, and STOL aircraft shown in figure 3. The particular aircraft for which data were obtained are a Boeing 727 passenger aircraft, a CTOL; an OH-4A light observation helicopter, a VTOL; and the Breguet demonstration aircraft, a STOL. Figure 4 shows real-time acceleration measurements from the STOL traveling at 210 knots during a banking maneuver. Acceleration is plotted against time for the three directions – vertical, longitudinal, and lateral. The 1g that is always present in the vertical direction has been electronically subtracted. A 15-Hz filter is used to remove the higher frequencies that show up due to panel resonances. Although vibrations occur at higher frequencies in all three directions (note the hash on the traces) the predominant vibrations occur in the vertical direction, at low frequencies, and particularly during maneuvers.

From data such as these real-time records, peak accelerations for various times of flight are obtained. Examples of peak acceleration in the vertical direction for the three aircraft in figure 3 are shown in figure 5. The maximum peak g levels for the helicopter at take-off and for the STOL during level-flight cruise are around 0.24g. Both levels are considerably higher than the vibration of the conventional aircraft (CTOL) – which is around 0.06g. It should be noted that only representative examples are shown and that there are large differences between aircraft. The data for this figure and for the forthcoming data figures are based on a small number of flights (6 or less for each aircraft) covering about 6 hours of flight time during good weather with the aircraft flying in its normal environment. The STOL and the helicopter cruise at around a 610-meter (2000-foot) altitude or less, and the Boeing 727 cruises at 7600 meters (25 000 feet) or higher. The magnitudes of these peak accelerations in the lateral direction are shown in figure 6. It can be seen that the peak levels in general are lower and that again the conventional aircraft has lower levels than the STOL or the helicopter. Although the lateral levels are lower than the vertical levels, it should be noted that these levels did cause some discomfort on the STOL. But these maximum peak levels are not the whole story. One question is, How often do these peaks occur?

In figures 7 and 8 exceedance values corresponding to the peak accelerations in the vertical and lateral directions, respectively, are shown for the three aircraft. Acceleration in g units is plotted as a function of occurrence in percent of time. Note the acceleration values in figure 7; for example, the value 0.1g is exceeded less than 1 percent of the time by the conventional aircraft, 5 percent by the STOL, and 20 percent of the time by the helicopter. Similar results of exceedance measurements in the lateral direction are

shown in figure 8. Again the vibration measurements in the lateral direction are considerably lower than in the vertical direction.

The exceedance values are an important statistical parameter. Another important statistical parameter indicates the frequencies at which the vibrational energies are concentrated. An example of this parameter is shown in figure 9 where the power spectral density in g^2/Hz is shown as a function of frequency for the same aircraft for accelerations in the vertical direction. Note that all three aircraft have concentrations of energy in the low-frequency range, less than 1 Hz. Also, the helicopter has a large vibration energy concentration at its rotor 2P frequency, about 12 Hz. The 2P represents two cycles of force per rotor revolution for the rotor system, and the rotor speed is 360 revolutions per minute. Figure 10 shows energy concentrations in the lateral direction. The main difference between vertical and lateral vibration is that the energy levels are lower in the lateral direction for all the aircraft (note change in scale) and, in addition, the STOL has a large energy concentration at around 8 Hz in the lateral direction.

As shown in figure 1, the transfer function of the aircraft affects the human response. A study is being made in which the transfer function of the aircraft is modified. The vehicle used for this study is shown in figure 11. The entire cabin of this XH-51 helicopter is mounted on springs to passively isolate the cabin from the rest of the aircraft. Thus, the transfer function of the vehicle is greatly modified. This helicopter was more fully described in paper no. 19 by Charles E. K. Morris, John F. Ward, Julian L. Jenkins, Jr., and William J. Snyder.

An example of percent-exceedance values for this helicopter is shown in figure 12. Again, vibration level in g units is plotted as a function of occurrences in percent of time. It can be seen that, based on the occurrence of peak magnitudes, the vibration levels in the isolated cabin are about one-half the vibration levels in the nonisolated cabin.

The power spectral density for this helicopter is shown in figure 13, where the power spectra in g^2/Hz are plotted against frequency. The dashed curve represents the vibration levels in the nonisolated cabin, and the solid curve represents the vibration levels in the isolated cabin. This figure shows the large reduction in vibration levels due to the 3P vibrations at 18 Hz. However, due to the low natural frequency of the passive vibration isolation system (3 Hz) and due to the control coupling mentioned in paper no. 19, low-frequency pitching motions of the helicopter at $1\frac{1}{2}$ Hz are amplified by the isolated cabin.

In figure 14 peak acceleration ranges in g units are shown as a function of airspeed. The upper shaded area represents the vibration levels in the nonisolated cabin, and the lower shaded area represents the vibration levels in the isolated cabin. The figure also shows that lower vibration levels are obtained by isolating the cabin. It should be noted that these vibration levels are primarily due to the 3-cycle-per-revolution forces from

the 3-blade rotor system. During these flight measurements, ratings were obtained from the pilot and copilot, who used a rating scale to indicate the degree of ride quality from "Imperceptible" to "Most uncomfortable." In the lower speed range, up to about 95 knots, excellent agreement between ratings and vibration levels was obtained. However, at the higher airspeeds, the pilots rated both the isolated and nonisolated cabins as "Most uncomfortable" in contrast to the measured vibrations. The pilots were able to identify the frequencies causing their discomfort. In the nonisolated cabin, the offending frequency was at 3P or about 18 Hz, whereas in the isolated cabin, the offending frequency was between $1\frac{1}{2}$ and 2 Hz, the frequency of the pitching motions of the helicopter which are amplified by the isolated cabin. Note the energy at this low frequency (fig. 13). Thus, in controlling the environment due to 3P vibration, a new problem resulting from the passive isolation system and control coupling has been introduced. Additional studies are being conducted to use an active isolation system, that is, one using hydraulic actuators with feedback rather than passive springs. Such a system should improve the ride-quality characteristics at all speeds.

CONCLUDING REMARKS

Some of the factors affecting ride quality have been indicated. The low-frequency measuring/recording system has been discussed and examples of real-time data, power spectral densities, and percentage exceedance levels for a STOL, helicopter, and a conventional aircraft have been shown. Some effects of helicopter cabin isolation have also been discussed.

RIDE-QUALITY FACTORS

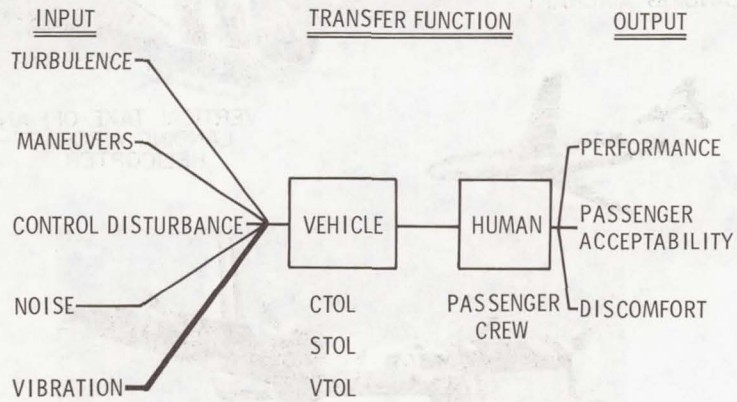


Figure 1

PORTABLE VIBRATION MEASURING/RECORDING SYSTEM

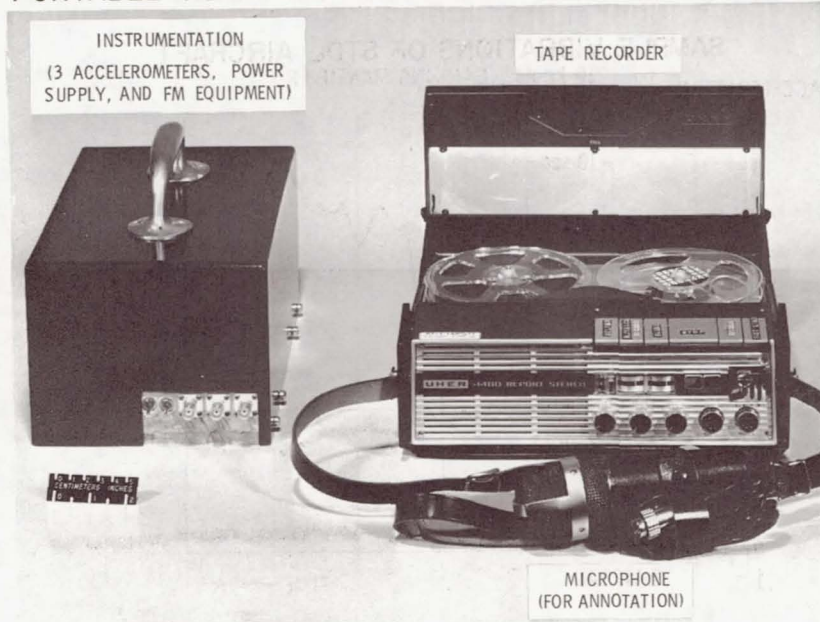


Figure 2

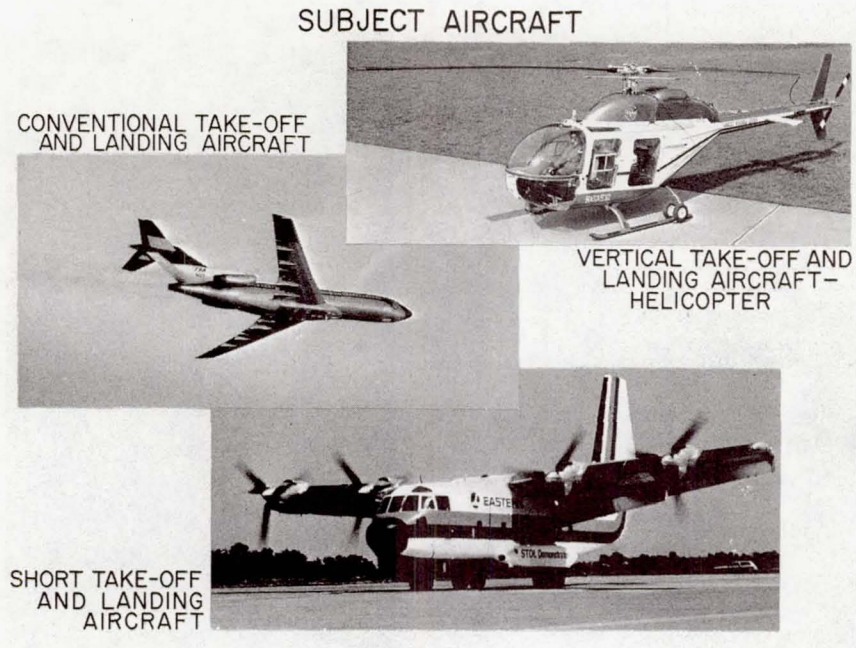


Figure 3

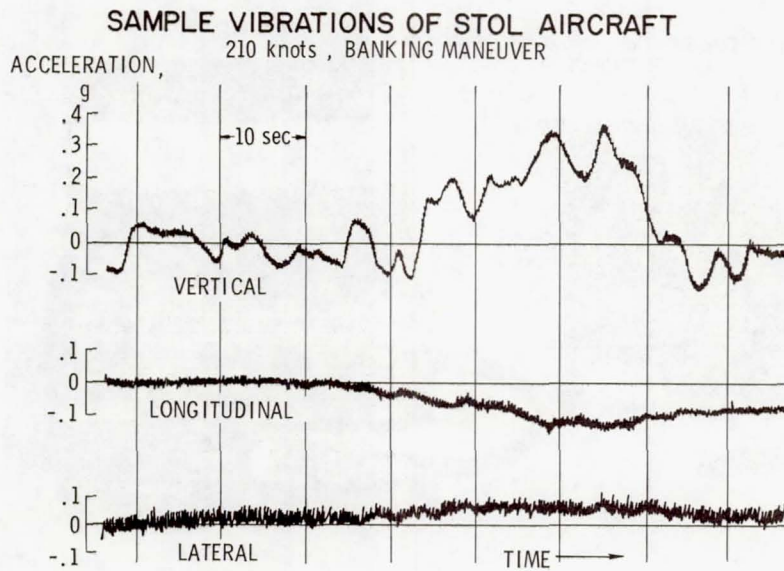


Figure 4

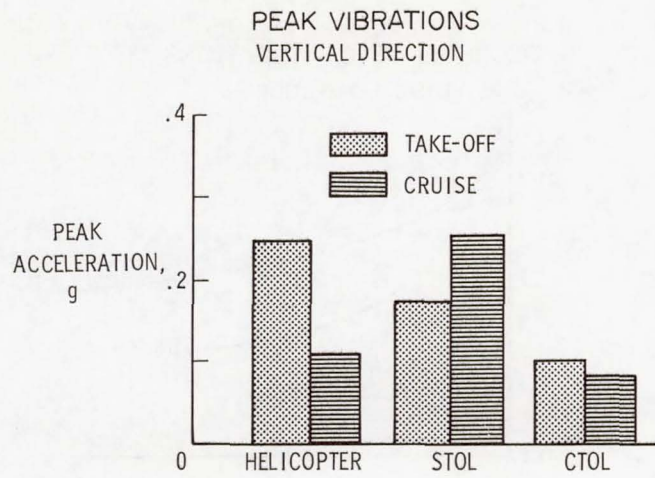


Figure 5

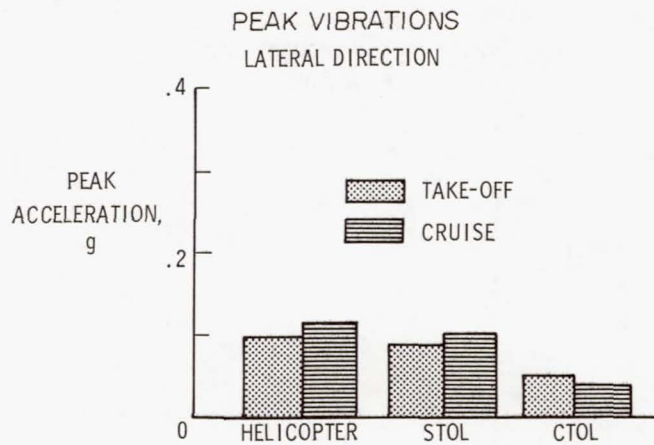


Figure 6

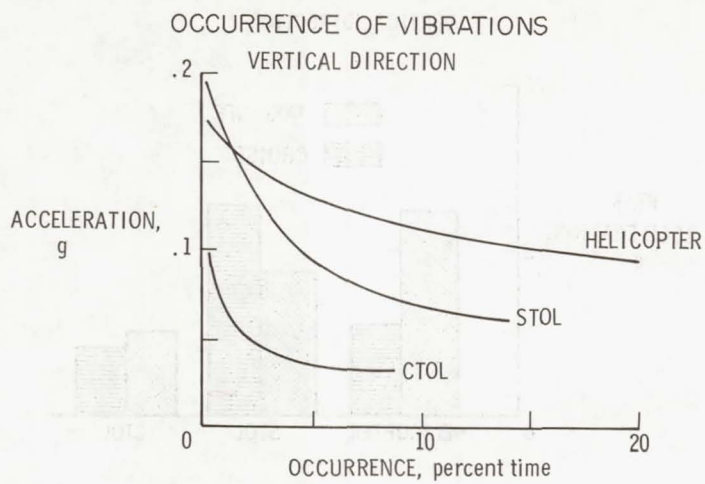


Figure 7

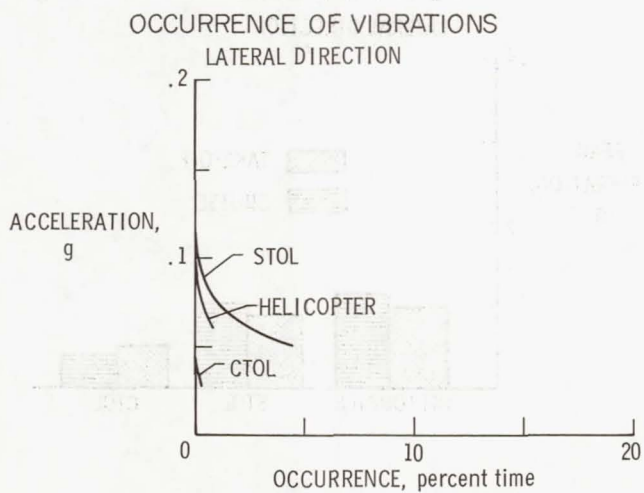


Figure 8

TYPICAL VIBRATION ENERGY CHARACTERISTICS VERTICAL DIRECTION

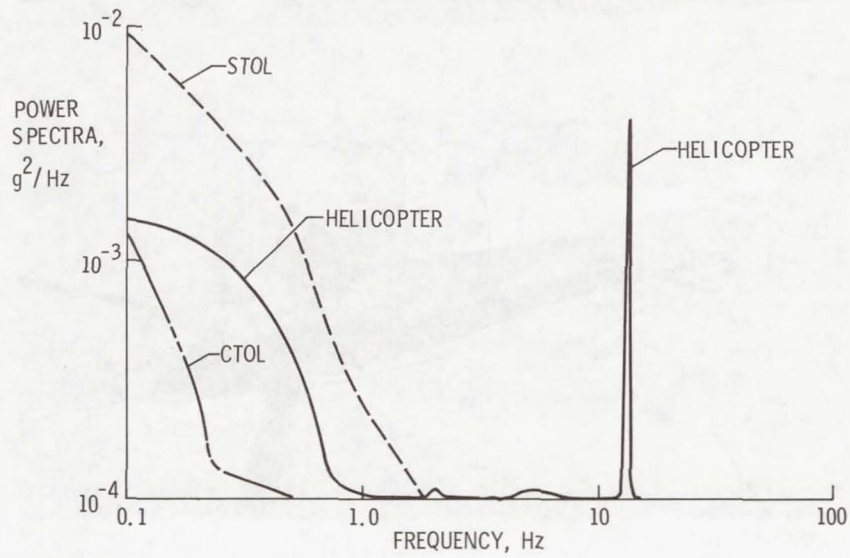


Figure 9

TYPICAL VIBRATION ENERGY CHARACTERISTICS LATERAL DIRECTION

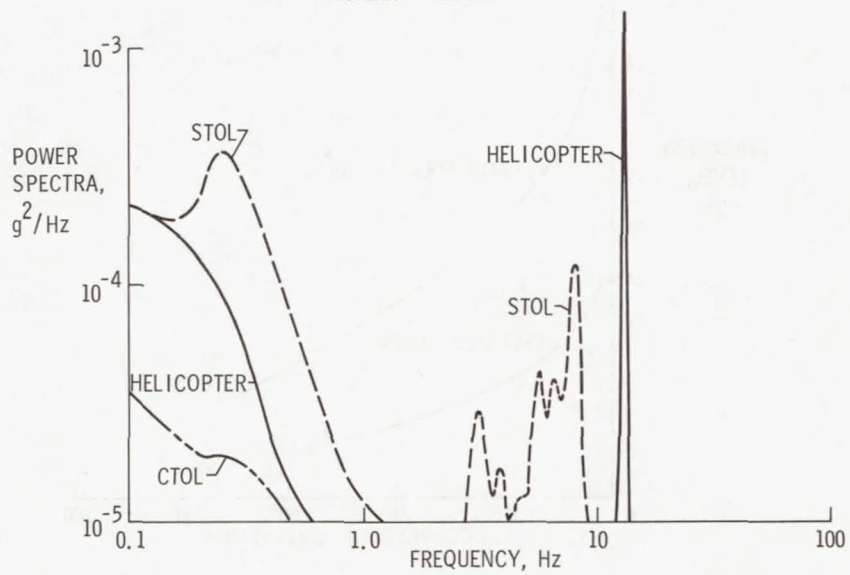


Figure 10

XH-51 HELICOPTER



Figure 11

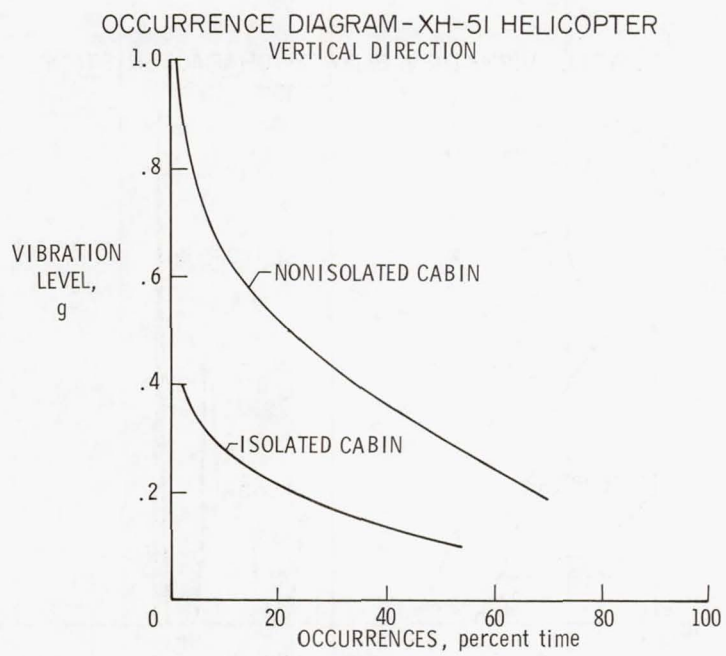


Figure 12

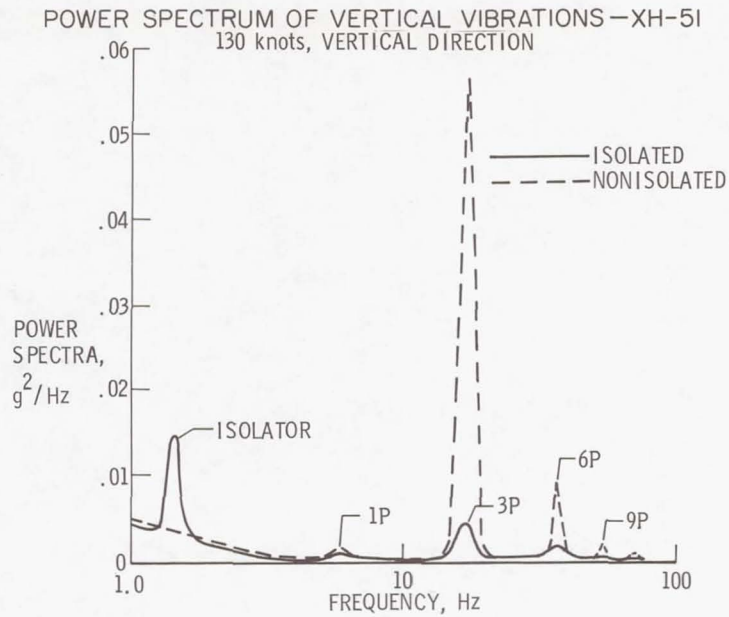


Figure 13

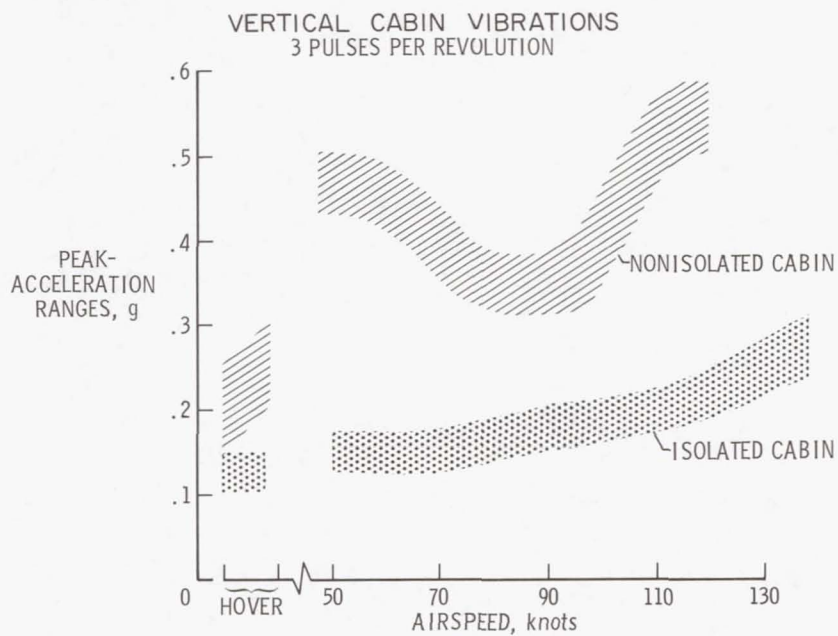


Figure 14

Page intentionally left blank

PROGRESS REPORT ON THE NASA V-G/VGH GENERAL AVIATION PROGRAM

By Joseph W. Jewel, Jr.
Langley Research Center

SUMMARY

An analysis is presented of 79 000 hours of data obtained from NASA V-G and VGH flight recorders installed on 134 general aviation aircraft engaged in eight types of operations. Information is presented on typical mission characteristics, on airspeed practices, on gust accelerations and derived gust velocities encountered, on maneuver-acceleration experience, and on the initial positive landing-impact accelerations. Comparisons are also made of the actual gust and maneuver loads experienced with the design gust and maneuver loads.

INTRODUCTION

A progress report on the results of an analysis of 79 000 hours of data obtained from NASA V-G and VGH flight recorders installed on 134 general aviation aircraft is presented herein. The data analyzed were obtained under the NASA General Aviation Program established in the early 1960's to provide a source of information on the flight and ground loads and on the operating practices of light aircraft as they are being flown in their normal usage. Previous reports covering lesser samples of data obtained from the general aviation program are listed in references 1 to 3.

SYMBOLS

a_n	normal acceleration measured from the 1.0g-level flight position of the accelerometer trace, g units ($1g = 9.8 \text{ m/sec}^2$)
a_{nLLF}	normal acceleration corresponding to the gust- or maneuver-limit load factor measured from 1.0, g units
f	frequency of occurrence
K_g	gust factor, $\frac{0.88\mu_g}{5.3 + \mu_g}$
m	slope of lift curve per radian

n_g	gust-limit load factor measured from 1.0
n_m	maneuver-limit load factor measured from 1.0
S	wing area, m^2 (ft^2)
U_{de}	derived gust velocity, $\frac{2Wa_n}{K_g\rho_0V_e mS}$, m/sec (ft/sec)
V_C	design cruising speed, knots
V_D	design diving speed, knots
V_e	equivalent airspeed, m/sec (ft/sec)
V_{NE}	never-exceed speed, knots
W	airplane weight, newtons (lb)
μ_g	airplane mass ratio
ρ_0	air density at sea level, kg/m^3 (slugs/ ft^3)

INSTRUMENTATION

The NASA VGH and V-G recorders used to obtain the data are shown in figures 1 and 2, respectively. The VGH recorder provides a time-history record of the indicated airspeed, pressure altitude, and normal acceleration at the center of gravity of the instrumented airplanes. The V-G recorder gives envelope-type information of the maximum in-flight accelerations and their corresponding airspeeds. The V-G and VGH recorders are completely described in references 4 and 5, respectively. A sample VGH record is shown in figure 3, and a sample V-G record in figure 4.

PROGRAM DESCRIPTION

In order to obtain a representative segment of general-aviation-aircraft usage, eight types of operations were sampled. These operations are twin-engine executive, single-engine executive, personal, instructional, commercial survey, aerobatic, aerial application, and commuter. Three types of aircraft were normally selected as being typical aircraft in a given type of operation. Four aircraft of each of these given types were instrumented, one with a VGH recorder and three with V-G recorders, for a total of

12 instrumented aircraft in a given operation. Typical missions flown in each of the operations are as follows:

Twin- and single-engine executive:

Charter flights – cargo and personnel.

Business flights – company and individual.

Instrument check flight – training for instrument card.

Instructional flights – check-out for larger aircraft.

Personal:

Flying club owned – aircraft flown by club with 3 to 21 members; used for pleasure, instruction, or business flights.

Individually owned – used for pleasure and business.

Company owned – airplane rented to individual for business or pleasure flying; also aircraft used as check-out for heavier airplane.

Instructional:

Training flights – all instrumented airplanes owned by flying schools; used as basic trainers for private license; also used by student after solo for cross-country flight.

Commercial survey:

Pipeline-patrol flights – patrols flown from 76 to 91 meters (250 to 300 feet) above terrain to check for leaks or breaks in the pipeline.

Forest-patrol flights – patrols flown 457 meters (1500 feet) above terrain for fire detection. When fire is spotted, descents are made to 61 to 91 meters (200 to 300 feet) to check condition of terrain around the fire.

Pathfinder flights – flies to fire perimeter and marks drop area. Descents are made to 15 to 46 meters (50 to 150 feet) above terrain to insure turbulence is not too severe for chemical bomber during dropping run. Chemical bomber drops are observed, and effects on fire are noted.

Fish-spotting flights – patrols flown 457 to 610 meters (1500 to 2000 feet) above water. Occasional descents are made to 91 to 152 meters (300 to 500 feet).

Aerobatic:

Noncompetitive flights – aircraft flown by amateurs. Occasional aerobatics are performed, usually as individual maneuvers.

Competitive flights – aircraft flown in airshows, in national and international aerobatic competition, and in practice sessions. Obligatory maneuvers, one immediately after another, are performed in a restricted cube of air.

Aerial application:

Crop dusting and/or spraying flights – aircraft flown at heights ranging from 0.9 to 5.5 meters (3 to 18 feet) above crops. Spreading runs are characterized by sharp pushover at start and hard pull-up at end of spreading runs.

Commuter:

Operational flights – normally scheduled passenger carrying operations.

Crew flights – crew training, or flights on which structural or mechanical tests are made on the aircraft.

Figure 5 indicates the geographical location of the instrumented aircraft. Open symbols denote the location of aircraft instrumented with V-G recorders, and closed symbols indicate those instrumented with VGH recorders. Care was taken in selecting aircraft for a particular operation to insure that the home bases were located throughout the continental United States. This selection eliminated biasing the data since it came from various geographical areas; the data, therefore, should be representative.

Some of the pertinent physical characteristics of the instrumented aircraft, which are identified by number, are given in table I. In addition, the table shows the number of aircraft of a given type instrumented with V-G and with VGH recorders, the flight hours recorded by a particular type of aircraft, the design and placard speeds, and the limit maneuver and gust incremental local factors. All aircraft in the program were owned by individuals or companies who were personally contacted, briefed on the program, and asked to participate on a voluntary basis. Generally, on any one installation, an attempt was made to collect the data over at least the four seasons and for a period of 1000 hours.

The status of the program, through calendar year 1970, is shown in figure 6. The number of aircraft involved in the program, the number of hours flown by these aircraft, and the average hours collected per aircraft per year are noted in figures 6(a) to 6(c), respectively. The buildup in instrumented aircraft and in the hours collected from 1963 to 1968 is apparent. From 1968 on, the program is relatively stable. As a matter of interest, the data reported on amount to about 0.05 percent of the total hours flown by general aviation aircraft in the period the data sample was taken.

RESULTS AND DISCUSSION

Typical mission characteristics of the instrumented airplanes are shown in figure 7. The average operating pressure altitude, indicated airspeed, and flight duration are shown in figures 7(a) to 7(c), respectively. The type of operation and the airplane type (noted by numbers) are shown along the abscissa. The highest average operating altitudes and airspeeds were recorded by turbojet-powered aircraft, types 1 and 2 in twin-engine executive operations. Turboprop-powered aircraft, type 3 in twin-engine executive operations and types 26 and 28 in commuter operations were generally flown at higher average operating speeds than the piston-powered airplanes. Airplane type 3 was flown at higher average altitudes than airplane types 26 and 28; however, this should be expected since the average flight duration for type 3 was 1 hour, which is four times the average flight duration for type 26 and twice that for type 28. The inference here is

that there is no need to climb to the higher altitudes for relatively short flights. The piston-powered aircraft were usually flown below 3 km (10 000 feet). Eleven of the 19 piston-powered aircraft had average operating altitudes below 1.5 km (5000 feet). Flight durations for the various aircraft were generally 1 hour or less. Aircraft in survey-type operations had average flight duration ranging from over 4 hours for the commercial fish spotter to slightly over 1 hour for the pathfinder aircraft. Forest-patrol and pipeline-patrol aircraft had flight durations of about $2\frac{1}{2}$ hours. Crop dusting flights averaged about one-quarter hour in duration, and commuter flights ranged from one-quarter to one-half hour.

Overall In-Flight Loads

Figures 8(a) to 8(h) show composite velocity-acceleration signatures obtained from V-G recorders installed on various aircraft flown in the eight types of operations listed in the "Program Description" section. The composites were formed by superimposing individual V-G signatures from aircraft of a given type, one over the other. Load factor is noted along the ordinate and indicated airspeed in knots along the abscissa. The shaded area in the center of the figures is the V-G signature. The design cruising speed and design diving speeds are labeled above each composite by V_C and V_D , respectively. The solid line around the V-G signature denotes the design flight envelope based on the aircraft's maximum gross weight, and the dashed outline denotes the design flight envelope based on the minimum flying weight. Notations to the right of each of the V-G signatures list a number, corresponding to the numbers in table I, to identify the airplane type from which the V-G signature was obtained; the number of aircraft of that type from which the signature was collected; the number of V-G records used to form the composite; and the number of flight hours represented by the composite.

Figure 8 shows that although the V-G signatures were normally contained within the design flight envelopes, the commuter operation was the only one in which the design flight envelope was not equaled or exceeded by at least one plane in the operation. Most of the operations show exceedances of the envelope in the low-speed regime. These exceedances are believed to result from landing impacts and are not considered significant. The most severe loads were experienced by aircraft in competitive aerobatics. Airspeed indications on records from these aircraft are probably in error since the pitot-static tube is exposed to extreme angles of attack and sideslip during rolling and pitching maneuvers of the airplane; however, acceleration indications are believed to be valid. It should be mentioned that airplane types 21 and 21A had structural modifications that increased the design flight envelope to values larger than those noted in the figure. The values shown are for the original structure and were obtained from the manufacturer. The true value of the design flight envelope is not known. Other severe exceedances of the design flight envelope were recorded by aircraft type 9D in commercial survey

operations and aircraft types 13 and 15 in instructional operations. Airplane type 9D was flown in pipeline patrol in the Rocky Mountain regions of Wyoming and Colorado. It was exposed to continuously severe turbulence and sustained one negative gust load of $-3.6g$. Airplane type 13 was flown by a student pilot in such a manner that the design flight envelope at the design dive speed was exceeded in both the positive and negative directions. Airplane type 15 was destroyed in a crash. The high acceleration values above $4.0g$'s and the dashed portion of the V-G signature from 140 to 180 knots are believed to have occurred when the airplane struck the ground.

To summarize, aircraft in personal, instructional, commercial survey, and aerial application operations experienced overall in-flight loads that were closer to the design flight loads than aircraft involved in executive or commuter operations. The most severe in-flight loads were recorded during competitive aerobatics.

Airspeed Practices

While the V-G records in figure 8 do not provide detailed information on airspeed operating practices, they do denote maximum speeds and indicate airspeed trends of the instrumented airplane.

All aircraft, except two type 23 aircraft in aerial application, were flown at speeds above the design cruising speed, V_C . Seven of the aircraft were flown above the design dive speed, V_D . The V_D exceedance by airplane type 5B in twin-engine executive operations occurred during a demonstration flight when the airplane was being sold and should therefore not be considered as typical of airspeed practices by executive aircraft. The one V_D exceedance in personal operations was recorded by aircraft type 11. Compared with other types of aircraft in the operation, this particular aircraft was very clean aerodynamically. Its ability to obtain speeds near V_D is indicated by the thickness of the V-G signature in the region between V_C and V_D . Aircraft in instructional operations appear to be more susceptible to V_D exceedances than aircraft in any of the other operations. Three aircraft types, 13, 16A, and 16C, of the six types instrumented were flown at speeds above V_D . Discussions with the fixed-base operators whose aircraft were flown above V_D indicated the exceedances were recorded when the aircraft was flown solo by student pilots. Since few exceedances were recorded by aircraft in other operations, which were generally flown by more experienced pilots, it is suspected that the inexperienced pilots either through poor judgment or an adventurous nature placed the aircraft in such an attitude that recovery without high speed was impossible. The last two aircraft in the data sample flown above V_D were types 21A and 22 in aerobatic operations. Both exceedances occurred during national or international aerobatic competitive meets. As mentioned previously, the "negative" airspeeds recorded by airplane types 21, 21A, and 22 were the result of tumbling of the aircraft and are not considered true indications of the airspeed.

Gust-Acceleration Data

The distribution of positive and negative gust accelerations for aircraft instrumented with NASA VGH recorders is listed in table II. The acceleration values were measured from the 1.0g-level flight position of the acceleration trace on the VGH record when turbulence was encountered in level flight or from the maneuver position of the acceleration trace when turbulence was encountered while the aircraft was being maneuvered. Values of these accelerations are shown in 0.1g-class intervals. The hours, number of flights, and nautical flight miles flown in each sample are noted at the bottom of the table.

It is interesting to note that calculations show roughly 97 percent of the positive and negative gust accelerations recorded were less than 0.8g. The most severe gust accelerations, from a repeated-loads standpoint, were recorded by aircraft flown on pipeline patrol in commercial survey operations. The largest gust acceleration was recorded over the foothills of the Rocky Mountains by an aircraft flown in instructional operations.

Gust-Acceleration Fractions

Gust-acceleration fractions were obtained by dividing the incremental (measured from 1.0g-level flight) gust acceleration by the incremental (measured from 1.0) gust-limit load factor at the design cruising speed. This ratio relates the gust acceleration to the aircraft's design limit load. A ratio of 1.0 therefore indicates that the design gust-limit load has been reached. The ratio is also useful for comparing the gust-acceleration experience of a number of different aircraft since the data are normalized.

Figure 9 shows the cumulative frequency of occurrence per nautical flight mile that gust-acceleration fractions were equaled or exceeded by aircraft involved in seven types of operations. VGH data from aerobatic operations were not evaluated because of the limited data sample. The key for each operation identifies the type aircraft and notes the size of the data sample in flight hours. Dashed lines representing the upper and lower boundaries of gust-acceleration fractions experienced by short-haul jet transports are included in each figure for comparative purposes.

The largest spread between the gust-acceleration-fraction experience for aircraft in a single operation occurred in twin-engine executive operations. Variations of the frequency of occurrence of a given gust-acceleration fraction were as high as four orders of magnitude between airplane types 1 and 4 in figure 9. It is also interesting to see the relationship between operating altitudes, noted in figure 7(a) for the individual aircraft, and the frequency of occurrence of gust-acceleration fraction. As the average operating altitude increases, the frequency with which gust-acceleration fractions are encountered decreases. This trend is particularly notable in comparing the piston aircraft which

normally fly at relatively low altitude with the jet aircraft which are flown at the higher altitudes.

The gust-limit load factor was reached by two aircraft in the program, type 4 in twin-engine executive operations and type 16 in instructional operations. Both aircraft were being flown over mountainous terrain when the exceedance occurred.

The highest rate of experiencing gust accelerations was recorded by aircraft in pipeline patrol. These aircraft were flown near (46 to 91 meters (150 to 300 feet)) the surface and were subjected to both mechanical and thermal convections. The extent of the turbulence can be appreciated when it is noted that the aircraft were immersed in it 97 percent of their flight time.

A comparison of the gust-acceleration-fraction experience of the general aviation aircraft with that for the short-haul jet transports indicates that, with few exceptions, the general aviation aircraft were subjected to gust accelerations nearer to the design gust-limit load factor than the jet-transport aircraft. Operations in a more turbulent environment and at a lower operating weight are contributing factors to these results.

Derived Gust Velocities

Table III lists the positive and negative derived gust velocities in intervals of 1.22 m/sec (4 ft/sec) for aircraft instrumented with VGH recorders in the seven types of operations. Roughly 98 percent of the derived gust velocities encountered by the instrumented aircraft were less than 6.1 m/sec (20 ft/sec). The largest number of gusts was experienced by aircraft in pipeline-patrol flights. The most severe, a 17- to 18.3-m/sec (56- to 60-ft/sec) gust was encountered by airplane type 16A in instructional operations. The least number of gusts was recorded by aircraft in crop dusting operations.

Figure 10 shows the derived-gust-velocity experience per nautical flight mile for aircraft in seven types of operations. The dashed lines in the figures represent the boundaries of the derived-gust-velocity experience for three short-haul jet-transport aircraft. The type aircraft and the hours involved in the sample are noted in the key in each figure.

Four of the operations, twin-engine executive, single-engine executive, aerial application, and commuter, experienced gust velocities that were generally similar to the gust-velocity distribution for the short-haul jet-transport aircraft. The remaining three operations had one or more aircraft that encountered gust velocities by an order of magnitude more often than those encountered by the short-haul jet-transport aircraft. Derived gust velocities equal to or less than 3.6 to 4.9 m/sec (12 to 16 ft/sec) were generally experienced more often by the general aviation aircraft than by the jet transports.

Two operations, twin-engine executive and instructional, had aircraft which experienced derived gust velocities of 14.6 and 17 m/sec (48 and 56 ft/sec), respectively.

Maneuver-Acceleration Data

Table IV lists the positive and negative maneuver accelerations in 0.1g-class intervals for aircraft in seven operations. For these distributions, the accelerations were measured from the 1.0g-level flight position of the accelerometer trace. The hours, number of flights, and nautical flight miles shown in each sample are noted at the bottom of the table.

One of the operations, aerial application, recorded more positive and negative maneuver accelerations than all of the other general aviation operations combined. The largest maneuver accelerations were recorded by aircraft flown in pipeline patrol, in instructional operations, and in aerial application. Positive accelerations generally outnumbered negative accelerations by a factor of 3 or 4, and large negative maneuver accelerations were rare.

Maneuver-Acceleration Fractions

Figure 11 shows the cumulative frequency of occurrence per nautical flight mile of maneuver-acceleration fractions for aircraft in seven types of operations. Aircraft and the data-sample size are identified in the key. Dashed lines in each figure represent the boundaries of maneuver-acceleration distributions for short-haul jet-transport aircraft.

The majority of the general aviation aircraft recorded maneuver accelerations that, for a given frequency of occurrence, were closer to the design maneuver-limit load factor than the maneuver-load experience for short-haul jet transports. Two aircraft, airplane type 1 in twin-engine executive operations and airplane type 15 in instructional operations, recorded maneuver accelerations that equaled or exceeded the design maneuver-limit load. About 900 hours of the 1300-hour data sample for airplane type 1 were recorded when the aircraft was used as a sales demonstrator. For this reason, it is felt that the maneuver loads indicated for airplane type 1 are more typical of demonstration flights than of twin-engine executive operations. The maneuver-acceleration experience of airplane type 15 up to an acceleration fraction of 0.4 was comparable with that for the other aircraft involved in instructional operations. For acceleration fractions larger than 0.4, frequency of occurrence increased above that for the other aircraft. The training syllabus used by the operator of airplane type 15 apparently included more rigorous maneuvers than the syllabus used by other operators in instructional operations.

From a repeated loads standpoint, aircraft in crop dusting operations experienced given maneuver-acceleration fractions more often, from 10 to 1000 times, than the next

most severe operation, pipeline patrol. Airplane type 19, flown as a pathfinder in fire-fighting operations, also was subjected to frequent and relatively large maneuver loads.

Differences between the frequency of occurrence of maneuver loads recorded by aircraft flown in commuter operations and those flown in short-haul commercial transport operation were insignificant in both operational flights and in check flights.

Landing-Impact Accelerations

The probability of equaling or exceeding a given initial positive acceleration on landing touchdown by aircraft in seven types of operations is shown in figure 12. Probability is given along the ordinate and acceleration along the abscissa. The type of propulsive system, the type of operation, and the number of landings used in the data sample are given in the key. The dashed outline represents the boundaries of the landing-impact accelerations recorded by four types of short-haul jet transports. (See ref. 6.)

A comparison of the frequency of occurrence of the landing-impact acceleration recorded by the general aviation aircraft with those recorded by the jet transports indicates that, generally, only aircraft in two operations, instructional and crop dusting, experienced given impact accelerations more frequently than the jet-transport aircraft that formed the upper boundary line. It should be noted that if this particular aircraft had not been considered in establishing the limits for the short-haul jet transports, the upper limit for the transports would have been just slightly above the curve for the prop twin-engine executive aircraft.

The largest landing-impact acceleration was recorded by aircraft flown in instructional operations. These aircraft also experienced next to the highest frequency of occurrence of a given landing impact. The highest frequency of occurrence of a given landing-impact acceleration was recorded by aircraft involved in crop dusting operations. This result stemmed from operations off rough ground near the field being dusted. Such procedures were necessary to reduce the time lost between the loading zone and the spraying operation. The probability of experiencing a specific landing-impact acceleration by aircraft flown in personal operations fell midway between that for commercial survey operations on the low side and instructional operations on the high side.

CONCLUDING REMARKS

The preceding analysis of 79 000 hours of data, collected from NASA V-G and VGH flight recorders installed on 134 general aviation aircraft involved in eight types of operations suggests the following concluding remarks:

Aircraft flown in personal, instructional, commercial survey, and aerial application operations experienced in-flight loads that were nearer to the design flight loads than

aircraft flown in executive or commuter operations. The most severe in-flight loads were recorded in competitive aerobatics.

All aircraft, except two in crop dusting operations, were flown at speeds above the design cruising speed. Seven aircraft were flown above the design dive speed. Aircraft in instructional operations appeared to be more susceptible to V_D exceedance than aircraft in all operations except competitive aerobatics.

Approximately 97 percent of the gust accelerations recorded by the VGH instrumented aircraft were less than 0.8g. General aviation aircraft experienced gust accelerations that were closer to the design gust-limit load factor than short-haul jet-transport aircraft. The most severe gust loading, from a repeated-loads standpoint, was recorded by aircraft flown in pipeline-patrol operations.

Three general aviation operations, personal, instructional, and commercial survey, had at least one aircraft that encountered given gust velocities by an order of magnitude more often than the short-haul jet transports.

Aircraft flown in aerial application recorded more positive and negative maneuver accelerations than all of the other general aviation operations combined. Positive maneuver accelerations generally outnumbered negative maneuver accelerations by a factor of 3 or 4, and large negative maneuver accelerations were rare.

Aircraft in instructional operations experienced the largest landing-impact accelerations. The highest frequency of occurrence of a given landing-impact acceleration was recorded by aircraft in crop dusting operations.

REFERENCES

1. Jewel, Joseph W., Jr.; and Walker, Walter G.: Operational Experiences of General Aviation Aircraft. Conference on Aircraft Operating Problems, NASA SP-83, 1965, pp. 257-263.
2. Donely, Philip; Jewel, Joseph W., Jr.; and Hunter, Paul A.: An Assessment of Repeated Loads on General Aviation and Transport Aircraft. Paper presented at 5th I.C.A.F. Symposium "Aircraft Fatigue - Design, Operational and Economic Aspects" (Melbourne, Australia), May 1967.
3. Jewel, Joseph W., Jr.: Initial Report on Operational Experiences of General Aviation Aircraft. [Preprint] 680203, April 1968.
4. Richardson, Norman R.: NACA VGH Recorder. NACA TN 2265, 1951.
5. Taback, Israel: The NACA 0.1-Damped V-G Recorder. NACA TN 2194, 1950.
6. Hunter, Paul A.: Summary of Center-of-Gravity Accelerations Experienced by Commercial Transport Airplanes in Landing Impact and Ground Operations. NASA TN D-6124, 1971.

TABLE I.- CHARACTERISTICS OF INSTRUMENTED AIRCRAFT

	Twin-engine executive type							
	1	2	3	4	5A	5B	5C	6
V-G installations	0	0	0	8	4	4	1	1
V-G hours	0	0	0	6753	3035	3369	145	320
VGH installations	4	1	2	1	1	0	0	0
VGH hours	1309	597	358	500	1145	0	0	0
Maximum gross weight:								
kN	117.7	55.6	40.0	21.4	21.5	22.7	22.2	30.2
lb	26 455	12 500	9000	4800	4830	5100	4990	6800
Wing span:								
m	16.3	11.5	14.0	11.3	11.0	11.2	11.2	12.1
ft	53.5	37.6	45.9	37.0	36.0	36.9	36.9	39.8
Wing area:								
m ²	41.0	21.5	26.0	19.2	16.3	16.3	16.3	18.6
ft ²	441	231.8	279.7	207	175	175	175	200
Type propulsion	Turbojet	Turbojet	Turboprop	Piston	Piston	Piston	Piston	Piston
V _C at sea level, knots . . .	388	350	208	172	182	182	182	200
V _{NE} at sea level, knots . .	^a 437	^a 358	234	216	215	223	219	236
V _D at sea level, knots . . .	485	400	260	240	239	248	243	262
Δn _m at V _C	1.50	3.40	2.70	2.80	2.80	2.80	2.80	2.60
-Δn _m at V _C	2.00	2.76	2.68	2.52	2.52	2.52	2.52	2.44
Δn _g at V _C	3.40	2.44	2.10	2.10	1.97	1.84	1.91	1.93

^aMaximum operating speed.

	Single-engine executive type												
	7A	7B	8A	8B	8C	8D	8E	8F	8G	9A	9B	9C	9D
V-G installations	2	1	0	2	1	2	1	0	1	1	2	0	2
V-G hours	1032	68	0	897	23	1392	142	0	997	785	1170	0	1302
VGH installations	2	0	1	0	0	0	1	1	1	1	0	1	0
VGH hours	196	0	149	0	0	0	229	16	75	423	0	94	0
Maximum gross weight:													
kN	12.9	12.9	11.8	12.3	12.3	13.1	13.9	14.7	15.1	11.3	11.8	11.8	12.5
lb	2900	2900	2650	2775	2775	2950	3125	3300	3400	2550	2800	2650	2800
Wing span:													
m	11.0	11.0	10.0	10.0	10.0	10.0	10.2	10.2	10.2	11.0	11.0	11.0	11.0
ft	36.0	36.0	32.8	32.8	32.8	32.8	33.5	33.5	33.5	36.0	36.0	36.0	36.2
Wing area:													
m ²	16.5	16.5	16.5	16.5	16.5	16.5	16.8	16.8	16.8	16.2	16.2	16.2	16.2
ft ²	178	178	177.6	177.6	177.6	177.6	181	181	181	174	174	174	174
Type propulsion	Piston	Piston	Piston	Piston	Piston	Piston	Piston	Piston	Piston	Piston	Piston	Piston	Piston
V _C at sea level, knots	156	156	139	152	152	174	161	165	165	139	139	139	139
V _{NE} at sea level, knots	197	197	175	175	182	195	195	195	195	160	167	162	167
V _D at sea level, knots	219	219	217	217	201	217	217	217	217	177	186	180	186
Δn _m at V _C	2.80	2.80	3.40	3.40	3.40	3.40	3.40	3.40	3.40	2.80	2.80	2.80	2.80
-Δn _m at V _C	2.52	2.52	2.76	2.76	2.76	2.76	2.76	2.76	2.76	2.52	2.52	2.52	2.52
Δn _g at V _C	2.65	2.45	2.40	2.58	2.88	2.75	2.43	2.35	2.37	2.50	2.33	2.33	2.50

TABLE I.- CHARACTERISTICS OF INSTRUMENTED AIRCRAFT - Continued

	Personal type					Instructional type						
	10A	10B	11	12A	12B	13	14	15	16A	16B	16C	17
V-G installations	1	3	5	1	6	4	6	2	1	1	3	0
V-G hours	533	997	1114	99	2540	862	3407	557	1294	1173	2206	0
VGH installations	1	0	1	0	4	2	1	1	1	0	0	1
VGH hours	123	0	220	0	369	909	546	311	833	0	0	160
Maximum gross weight:												
kN	9.8	10.2	11.5	9.8	10.7	6.7	7.3	8.7	6.7	7.1	7.1	10.0
lb	2200	2300	2575	2200	2400	1500	1650	1950	1500	1600	1700	2250
Wing span:												
m	11.0	11.0	10.7	9.1	9.1	10.7	9.1	9.1	10.2	10.2	10.0	10.7
ft	36.0	36.2	35.0	30.0	30.0	35.2	30.0	30.0	33.4	33.6	32.7	35.0
Wing area:												
m ²	16.2	16.2	15.5	14.9	14.9	15.8	13.7	14.9	14.9	14.9	14.6	16.8
ft ²	174	174	167	160	160	170	147	160	160	160	157	181
Type propulsion	Piston	Piston	Piston	Piston	Piston	Piston	Piston	Piston	Piston	Piston	Piston	Piston
V _C at sea level, knots	122	126	130	122	122	87	96	122	104	104	104	117
V _{NE} at sea level, knots	148	158	164	148	148	117	129	149	137	141	141	147
V _D at sea level, knots	165	175	182	165	165	130	143	164	152	156	156	164
Δn _m at V _C	2.80	2.80	2.80	2.80	2.80	3.52	3.40	2.80	3.40	3.40	3.40	2.60
-Δn _m at V _C	2.52	2.52	2.52	2.52	2.52	2.20	2.76	2.52	2.76	2.76	2.76	2.52
Δn _g at V _C	2.40	2.77	2.42	2.30	2.30	2.38	2.00	2.30	2.59	2.46	2.40	2.46

	Commercial survey type						
	9A	9B	9D	16A	16C	18	19
V-G installations	6	0	1	6	1	0	0
V-G hours	1005	0	2541	18 658	1381	0	0
VGH installations	0	1	0	1	0	1	1
VGH hours	0	763	0	1301	0	888	45
Maximum gross weight:							
kN	11.3	12.5	12.5	6.7	7.1	6.7	13.1
lb	2550	2800	2800	1500	1600	1500	2950
Wing span:							
m	11.0	11.0	11.0	10.2	10.0	10.7	10.0
ft	36.0	36.0	36.2	33.33	32.7	35.2	32.8
Wing area:							
m ²	16.2	16.2	16.2	14.9	14.6	16.6	16.5
ft ²	174	174	174	160	157	178.5	177.6
Type propulsion	Piston	Piston	Piston	Piston	Piston	Piston	Piston
V _C at sea level, knots	139	139	139	104	104	96	152
V _{NE} at sea level, knots	160	167	167	137	141	129	219
V _D at sea level, knots	177	186	186	152	156	143	243
Δn _m at V _C	2.80	2.80	2.80	3.40	3.40	3.40	5.00
-Δn _m at V _C	2.52	2.52	2.52	2.76	2.76	2.76	4.00
Δn _g at V _C	2.50	2.33	2.50	2.59	2.40	2.59	2.26

TABLE I.- CHARACTERISTICS OF INSTRUMENTED AIRCRAFT - Concluded

	Aerobatic type				Aerial application type			Commuter type		
	20	21	21A	22	23	24	25	26	27	28
V-G installations	1	2	1	1	2	3	2	2	2	1
V-G hours	50	163	166	27	690	593	354	1923	2068	367
VGH installations	1	0	0	0	1	1	0	1	0	1
VGH hours	12	0	0	0	309	178	0	714	0	226
Maximum gross weight:										
kN	7.3	8.9	8.9	5.1	26.7	12.9	20.0	51.6	37.8	46.3
lb	1650	2000	2000	1150	6000	2900	4500	11 600	8500	10 400
Wing span:										
m	9.8	9.5	9.5	Upper, 5.3 Lower, 5.2	13.5	11.0	Upper, 10.9 Lower, 10.4	19.8	15.3	14.0
ft	32.0	31.3	31.3	Upper, 17.3 Lower, 16.8	44.3	36.2	Upper, 35.7 Lower, 34.0	65	50.3	45.9
Wing area:										
m ²	15.7	16.0	16.0	Upper, 4.6 Lower, 4.5	30.3	17.0	Upper, 15.6 Lower, 14.9	39.0	27.3	26.0
ft ²	169	172	172	Upper, 50.0 Lower, 48.4	326.6	183.0	Upper, 168.0 Lower, 160.0	420	293.9	279.7
Type propulsion	Piston	Piston	Piston	Piston	Piston	Piston	Piston	Turboprop	Piston	Turboprop
V _C at sea level, knots . . .	114	109	109	126	117	108	87	164	178	226
V _{NE} at sea level, knots . . .	226	174	174	176	148	135	128	202	234	226
V _D at sea level, knots . . .	251	200	200	195	164	151	142	225	260	282
Δn _m at V _C	5.00	5.00	5.00	5.00	2.80	2.80	3.20	2.21	2.70	2.29
-Δn _m at V _C	6.00	4.00	4.00	4.00	2.90	2.52	2.00	2.50	2.60	2.31
Δn _g at V _C	3.10	-----	-----	3.07	1.78	1.83	1.85	2.35	1.95	1.95

TABLE II.- GUST-ACCELERATION DISTRIBUTION

Incremental normal acceleration, a_n , g units	Frequency of occurrence for -														
	Twin-engine executive type					Single-engine executive type							Personal type		
	1	2	3	4	5A	7A	8A	8E	8F	8G	9A	9C	10A	11	12B
3.3															
3.2															
3.1															
3.0															
2.9															
2.8															
2.7															
2.6															
2.5															
2.4															
2.3															
2.2															
2.1				1											
2.0															
1.9															
1.8										1					
1.7		1													
1.6					2										
1.5										1	1				
1.4				1	1				4			2	1		
1.3				1	1						1				
1.2			2	4	3				5		4	1			
1.1				4	1	4		1	5	2	6		2		
1.0	3	1	2	9	2	3	2	5	16		7	3	2		2
0.9		7	4	24	15	4	3	15	25	1	33	12	1	4	3
0.8	6	13	7	60	43	20	3	34	60	4	83	14	5	14	5
0.7	12	34	13	125	117	50	18	113	147	6	242	34	10	32	12
0.6	26	50	45	330	344	153	64	333	344	11	523	98	67	95	35
0.5	68	219	154	750	981	603	187	1 070	743	57	1 586	277	184	273	183
0.4	290	696	781	1 819	2 843	1 487	637	2 139	1 281	252	4 166	556	635	805	839
0.3	1 461														
0.2	5 647														
Positive total	7 513	1 021	1 008	3 128	4 353	2 324	914	3 710	2 632	333	6 652	997	907	1 223	1 079
-0.2	4 637														
-0.3	1 401														
-0.4	270	659	561	1 968	2 328	1 274	425	1 345	935	127	3 507	397	531	550	683
-0.5	68	222	165	748	802	444	105	452	681	29	1 149	194	226	153	198
-0.6	23	50	36	290	261	131	32	112	299	6	405	77	54	53	51
-0.7	5	15	12	116	86	43	12	28	130	2	146	24	21	20	13
-0.8	1	5	13	43	21	13	3	12	57		65	8	3	5	5
-0.9	1	3	3	17	14	3	2	5	18		22	1	1		1
-1.0		1	2	17	5	1			6		7		1	2	
-1.1				6	4				6		5			1	1
-1.2			1	4							3			1	
-1.3				4	1				1		2		1		1
-1.4					1						3				
-1.5															
-1.6				1							1				
-1.7															
-1.8															
-1.9															
-2.0															
-2.1															
Negative total	6 406	955	793	3 214	3 523	1 909	579	1 954	2 133	164	5 315	701	838	785	953
Pos. and neg. total	13 919	1 976	1 801	6 342	7 876	4 233	1 493	5 664	4 771	497	11 967	1 698	1 745	2 008	2 032
Hours	1 309	597	358	490	1 145	196	149	229	75	16	423	94	123	220	369
Number of flights	1 209	721	340	530	1 504	193	161	154	119	33	503	96	144	217	630
Nautical flight miles	458 590	217 170	68 437	75 579	189 050	21 186	18 328	34 395	11 523	2268	55 067	11 588	11 315	28 413	33 668

TABLE II. - GUST-ACCELERATION DISTRIBUTION - Concluded

Incremental normal acceleration, a_n , g units	Frequency of occurrence for -												
	Instructional type					Commercial survey type				Aerial application type		Commuter type	
	13	14	15	16A	17	9B	16A	18	19	23	24	26	28
3.3				1									
3.2													
3.1													
3.0													
2.9													
2.8													
2.7													
2.6													
2.5													
2.4													
2.3													
2.2													
2.1				2									
2.0													
1.9													
1.8							1						
1.7						1	1						
1.6						3							
1.5				1		1							
1.4	1					1	2					1	
1.3				2		7	5		2				
1.2	1					5	6					1	
1.1			2	4		11	30					3	1
1.0	1	1				17	71	1	1			1	1
0.9	9	1	3	14		58	322	1	4			3	2
0.8	9	4	9	28	2	89	1 278	1	11			7	12
0.7	32	16	27	68	8	265	5 256	2	19		1	52	21
0.6	74	67	93	210	16	857	17 271	16	55	1	4	86	73
0.5	380	282	270	823	82	2 696	42 413	41	123	4	29	211	259
0.4	1 718	1 564	783	2 777	256	8 769	61 502	131	238	23	152	940	649
0.3													
0.2													
Positive total	2 225	1 935	1 187	3 930	364	12 780	128 158	193	453	28	186	1 305	1 018
-0.2													
-0.3													
-0.4	1 322	1 251	645	2 087	276	9 013	49 332	78	283	12	132	893	542
-0.5	280	254	248	771	71	3 703	37 826	21	114	7	19	208	250
-0.6	70	41	69	209	18	1 251	18 409	10	35		4	89	72
-0.7	22	8	17	88	6	441	8 565	3	11		1	25	30
-0.8	8	2	14	22		169	3 555	1	12			13	12
-0.9	2	2	5	9		71	1 317	3	2	1		6	6
-1.0				4		43	509		2			2	4
-1.1				5	1	13	189					1	
-1.2						7	74	1				1	1
-1.3	1			1		2	37		1				
-1.4				2		1	17		1				
-1.5				3			5						
-1.6				1		1	4						
-1.7							2		1				
-1.8				1			1						
-1.9				1									
-2.0													
-2.1							4						
Negative total	1 705	1 558	998	3 204	372	14 715	119 846	117	462	20	156	1 238	917
Pos. and neg. total	3 930	3 493	2 185	7 134	736	27 495	248 004	310	915	48	342	2 543	1 935
Hours	909	546	311	833	160	763	1 301	888	45	309	178	714	226
Number of flights	2 688	826	523	1 088	388	324	501	211	41	1 417	835	2 466	418
Nautical flight miles	68 298	41 371	25 743	67 918	13 914	84 924	114 993	54 312	5589	25 977	14 220	95 681	41 983

TABLE III. - DERIVED-GUST-VELOCITY DISTRIBUTION

Derived gust velocity, U _{de}		Frequency of occurrence for -														
		Twin-engine executive type					Single-engine executive type							Personal type		
m/sec	ft/sec	1	2	3	4	5A	7A	8A	8E	8F	8G	9A	9C	10A	11	12B
17.07 to 18.29	56 to 60															
15.85 to 17.07	52 to 56															
14.63 to 15.85	48 to 52				1											
13.41 to 14.63	44 to 48													1		
12.19 to 13.41	40 to 44		1													
10.97 to 12.19	36 to 40	1	1			2										1
9.75 to 10.97	32 to 36	1				1				3				2		
8.53 to 9.75	28 to 32	2		2	2	3					1	2	1	2		1
7.32 to 8.53	24 to 28	8	6	2	5	11				2	1	3	1	2		2
6.10 to 7.32	20 to 24	70	37	9	22	26	1	1	1	7		4	5	3		15
4.88 to 6.10	16 to 20	259	106	30	96	180	7	8	15	35	4	36	17	9	4	13
3.66 to 4.88	12 to 16	1 060	375	268	473	923	62	91	185	200	18	321	78	73	59	222
2.44 to 3.66	8 to 12	3 231	466	673	2 138	3 103	861	567	1 911	1 406	134	2 754	535	580	616	809
1.22 to 2.44	4 to 8	2 881	29	24	391	104	1 393	247	1 598	979	175	3 532	360	235	544	16
Positive total		7 513	1 021	1 008	3 128	4 353	2 324	914	3 710	2 632	333	6 652	997	907	1 223	1 079
-1.22 to -2.44	-4 to -8	2 468	19	11	499	108	1 133	130	991	697	96	2 672	207	169	337	44
-2.44 to -3.66	-8 to -12	2 650	463	475	2 129	2 555	722	378	876	1 234	65	2 363	422	571	374	657
-3.66 to -4.88	-12 to -16	956	357	253	477	694	52	60	79	183	2	238	66	76	68	223
-4.88 to -6.10	-16 to -20	250	89	38	81	131	2	10	8	16	1	29	5	10	4	22
-6.10 to -7.32	-20 to -24	58	21	13	20	29		1		3		9	1	6	2	4
-7.32 to -8.53	-24 to -28	13	4	2	4	3						3		3		1
-8.53 to -9.75	-28 to -32	10	2	1		3						1		2		2
-9.75 to -10.97	-32 to -36				2									1		
-10.97 to -12.19	-36 to -40				1											
-12.19 to -13.41	-40 to -44	1			1											
-13.41 to -14.63	-44 to -48															
-14.63 to -15.85	-48 to -52															
-15.85 to -17.07	-52 to -56															
-17.07 to -18.29	-56 to -60															
Negative total		6 406	955	793	3 214	3 523	1 909	579	1 954	2 133	164	5 315	701	838	785	953
Pos. and neg. total		13 919	1 976	1 801	6 342	7 876	4 233	1 493	5 664	4 771	497	11 967	1 698	1 745	2 008	2 032
Hours		1 309	597	358	490	1 145	196	149	229	75	16	423	94	123	220	369
Number of flights		1 209	721	340	530	1 504	193	161	154	119	33	503	96	144	217	630
Nautical flight miles . . .		458 590	217 170	68 437	75 579	189 050	21 186	18 328	34 395	11 523	2268	55 067	11 588	11 315	28 413	33 668

TABLE III. - DERIVED-GUST-VELOCITY DISTRIBUTION - Concluded

Derived gust velocity, U_{de}		Frequency of occurrence for -												
		Instructional type					Commercial survey type				Aerial application type		Commuter type	
m/sec	ft/sec	13	14	15	16A	17	9B	16A	18	19	23	24	26	28
17.07 to 18.29	56 to 60				1									
15.85 to 17.07	52 to 56													
14.63 to 15.85	48 to 52			1										
13.41 to 14.63	44 to 48													
12.19 to 13.41	40 to 44			1	1		1							
10.97 to 12.19	36 to 40				2			1					1	
9.75 to 10.97	32 to 36			2	1		3	2						
8.53 to 9.75	28 to 32	1		3	5		6	2					3	4
7.32 to 8.53	24 to 28	4	1	2	8	2	5	15		1			2	1
6.10 to 7.32	20 to 24	9	4	12	18		35	110	1	1		1	15	15
4.88 to 6.10	16 to 20	26	29	77	67	7	171	897	2	12	2	7	68	51
3.66 to 4.88	12 to 16	144	310	399	374	68	1 303	11 754	40	48	6	127	315	346
2.44 to 3.66	8 to 12	1 436	1 580	681	2 820	257	9 793	83 976	475	281	16	51	901	601
1.22 to 2.44	4 to 8	605	11	9	633	30	1 463	31 401	396	110	4			
Positive total		2 225	1 935	1 187	3 930	364	12 780	128 158	914	453	28	186	1 305	1 018
-1.22 to -2.44	-4 to -8	407	3	5	472	42	1 625	25 198	301	95				
-2.44 to -3.66	-8 to -12	1 157	1 243	618	2 265	266	11 080	76 868	420	297		63	885	518
-3.66 to -4.88	-12 to -16	109	276	315	332	55	1 711	15 436	19	52	7	82	268	321
-4.88 to -6.10	-16 to -20	15	21	46	53	7	234	1 983	3	11	9	9	60	57
-6.10 to -7.32	-20 to -24	9	11	11	29	2	53	293	1	3	3	2	17	16
-7.32 to -8.53	-24 to -28	2	3	3	18		7	52	1	2			7	4
-8.53 to -9.75	-28 to -32	5	1		17		5	9		1			1	2
-9.75 to -10.97	-32 to -36	1			9			7						
-10.97 to -12.19	-36 to -40				5					1				
-12.19 to -13.41	-40 to -44													
-13.41 to -14.63	-44 to -48				3									
-14.63 to -15.85	-48 to -52													
-15.85 to -17.07	-52 to -56													
-17.07 to -18.29	-56 to -60				1									
Negative total		1 705	1 558	998	3 204	372	14 715	119 846	745	462	19	156	1 238	917
Pos. and neg. total		3 930	3 493	2 185	7 134	736	27 495	248 004	1 659	915	48	342	2 543	1 935
Hours		909	546	311	833	160	763	1 301	888	45	309	178	714	226
Number of flights		2 688	826	523	1 088	388	324	501	211	41	1 417	835	2 466	418
Nautical flight miles . . .		68 298	41 371	25 743	67 918	13 914	84 924	114 993	54 312	5589	25 977	14 220	95 681	41 983

TABLE IV. - MANEUVER-ACCELERATION DISTRIBUTION

Incremental normal acceleration, a_n , g units	Frequency of occurrence for -														
	Twin-engine executive type					Single-engine executive type							Personal type		
	1	2	3	4	5A	7A	8A	8E	8F	8G	9A	9C	10A	11	12B
3.5 to 3.6															
3.4															
3.3															
3.2															
3.1															
3.0															
2.9															
2.8															
2.7															
2.6															
2.5															
2.4															
2.3															
2.2		1												1	
2.1															
2.0			1												1
1.9		1													
1.8															1
1.7								2		1					
1.6		2	1												1
1.5	1			1											
1.4	2	1								1	4	1			4
1.3	6	2			2				1		4	2			4
1.2	6	4			2		1				3	1			4
1.1	8	3	1	3	9		2	1	1	2	4	1	1		9
1.0	7	3		2	19		2		2		12	1	5		17
0.9	13	11	1	1	18		7		4	3	18		5	2	33
0.8	23	26	8	5	39		2		1	2	31		4		51
0.7	51	46	8	5	55	2	2	6	7	6	44	2	12	1	67
0.6	78	100	8	24	93	1	10	8	9	6	72		16	5	120
0.5	143	205	39	51	164	1	23	11	15	19	136	6	33	12	220
0.4	267	719	62	189	452	12	42	63	42	15	232	17	65	44	407
0.3	769														
0.2	2 456														
Positive total	3 830	1 124	129	281	853	16	91	91	82	55	560	31	141	65	939
-0.2	1 443														
-0.3	266														
-0.4	72	363	19	53	134	3	24	10	23		43	8	42	4	140
-0.5	17	78	6	9	35		8	1	3	2	12	1	12	1	81
-0.6	6	31	3	7	13		1	5	1	2	10		8		43
-0.7	2	7			6				1		12		9		27
-0.8	1	7		1	7			1					1		14
-0.9							1				2			1	3
-1.0								1			1				1
-1.1															3
-1.2															1
-1.3															1
-1.4															
-1.5															
-1.6															
-1.7															
-1.8															
-1.9															
-2.0															
-2.1															
Negative total	1 807	486	28	70	195	3	34	18	28	4	80	9	72	6	314
Pos. and neg. total	5 637	1 610	157	351	1 048	19	125	109	110	59	640	40	213	71	1 253
Hours	1 309	597	358	500	1 145	196	149	229	75	16	423	94	123	220	369
Number of flights	1 209	721	340	555	1 504	193	161	154	119	33	503	96	144	217	630
Nautical flight miles	458 590	217 170	68 437	76 811	189 050	21 186	18 328	34 395	11 523	2268	55 067	11 588	11 315	28 413	33 668

TABLE IV. - MANEUVER-ACCELERATION DISTRIBUTION - Concluded

Incremental normal acceleration, a _n , g units	Frequency of occurrence for -															
	Instructional type					Commercial survey type				Aerial application type		Commuter type				
	13	14	15	16A	17	9B	16A	18	19	23	24	26	26 (Check flight)	28	28 (Check flight)	
3.5 to 3.6									1							
3.4									2							
3.3																
3.2				1												
3.1				2												
3.0																
2.9				1					3							
2.8				1					5							
2.7				1												
2.6				2					4							
2.5									4	1						
2.4				1					1	3						
2.3						1			2	7						
2.2				2					3	14						
2.1	1	2	3						4	26						
2.0			1	2	2				7	46						
1.9		2	2	3	1		1	1	6	110						
1.8		2	2	2	7		1	10	11	183						
1.7		1	4	5				15	6	297	5					
1.6		4	8	5	17	1		18	10	512	4		2			
1.5		10	5	6	6			28	10	823	6					
1.4		11	3	4	34	1		67	10	1 216	3		1			
1.3		19	12	6	7	2	5	187	12	1 622	16		1			
1.2		29	10	14	62	4	2	468	1	23	2 225	26		1		
1.1		43	27	14	22	4	7	1 019		26	3 002	67				
1.0		72	41	36	111	13	9	1 854	1	24	3 828	136		2		
0.9		88	47	47	39	25	18	2 755	2	40	4 714	253	4			
0.8		131	66	90	229	29	24	3 559	7	48	5 606	486	3	1		
0.7		191	126	130	101	63	36	3 880	14	61	6 068	830	9	3	1	
0.6		338	208	223	533	89	49	4 054	22	93	6 043	1 445	18	4	1	
0.5		562	378	339	292	170	82	3 957	41	175	5 928	2 468	43	3	2	
0.4		1 090	746	573	2 102	419	245	3 356	123	177	5 119	3 697	229	10	9	1
0.3																
0.2																
Positive total	2 594	1 688	1 513	3 565	821	479	25 228	211	768	47 393	9 442	306	28	13	1	
-0.2																
-0.3																
-0.4		892	333	129	966	230	51	35	10	37	3 143	751	101	2	0	
-0.5		466	142	77	91	63	18	12	2	22	2 529	238	20	1		
-0.6		197	45	27	310	24	7	1	3	7	2 292	88	4	1		
-0.7		42	16	10	9	12	1		2	2	2 212	24	7	1		
-0.8		10	1	5	49	5	2	1			1 963	7	1	1		
-0.9		1	4	4	5	1	2	1		1	1 159		1			
-1.0		2		3	14	1	2	2		1	550					
-1.1		2					3	1			182					
-1.2		1					1				31					
-1.3			1				1									
-1.4										1						
-1.5																
-1.6																
-1.7										1						
-1.8																
-1.9										1						
-2.0																
-2.1							1									
Negative total	1 613	542	255	1 444	336	89	53	17	70	14 064	1 108	134	6	2	0	
Pos. and neg. total	4 207	2 230	1 768	5 009	1 157	568	25 281	228	838	61 457	10 550	440	34	15	1	
Hours	909	546	311	833	160	763	1 301	888	45	309	178	709	5	223	3	
Number of flights	2 688	826	523	1 088	388	324	501	211	41	1 417	835	2 457	9	413	5	
Nautical flight miles	68 298	41 371	25 743	67 918	13 914	84 924	114 993	54 312	5589	25 977	14 220	95 014	667	41 522	461	

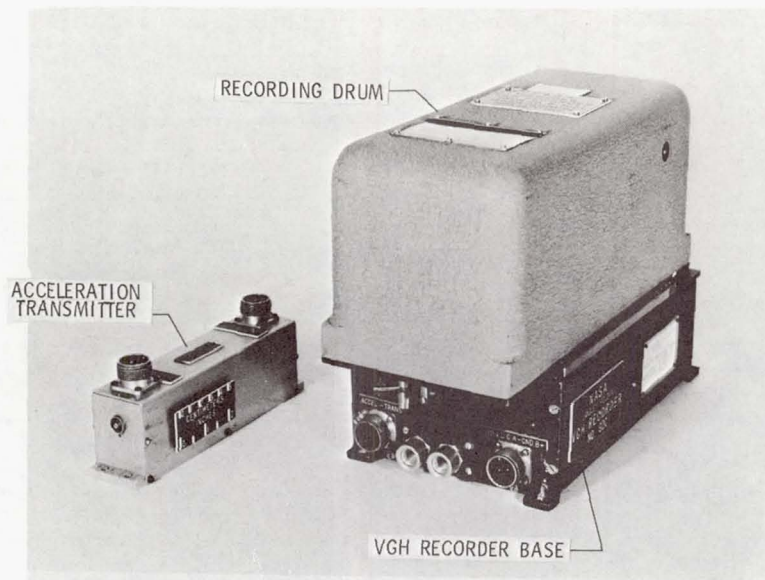


Figure 1.- NASA VGH recorder.

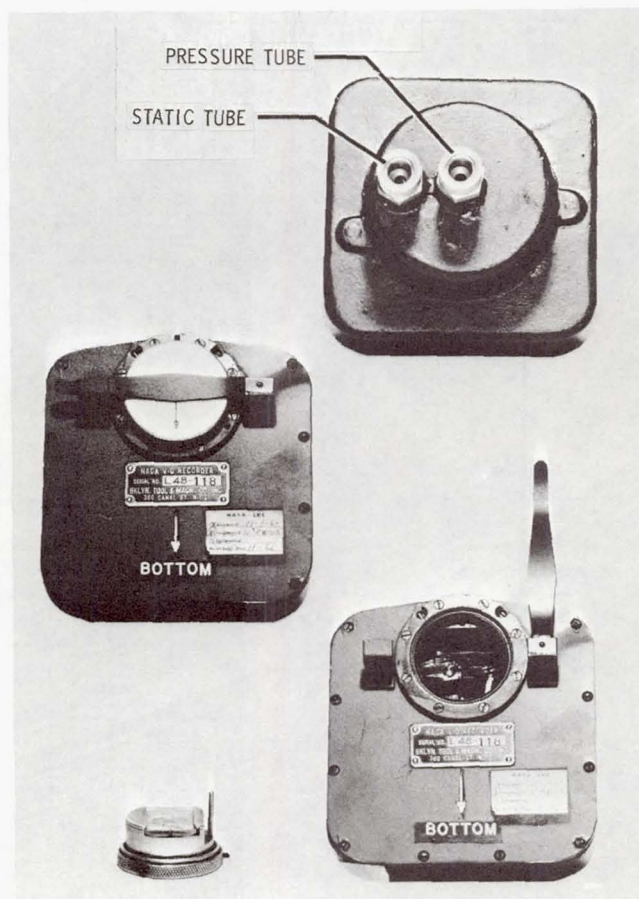


Figure 2.- V-G recorder.

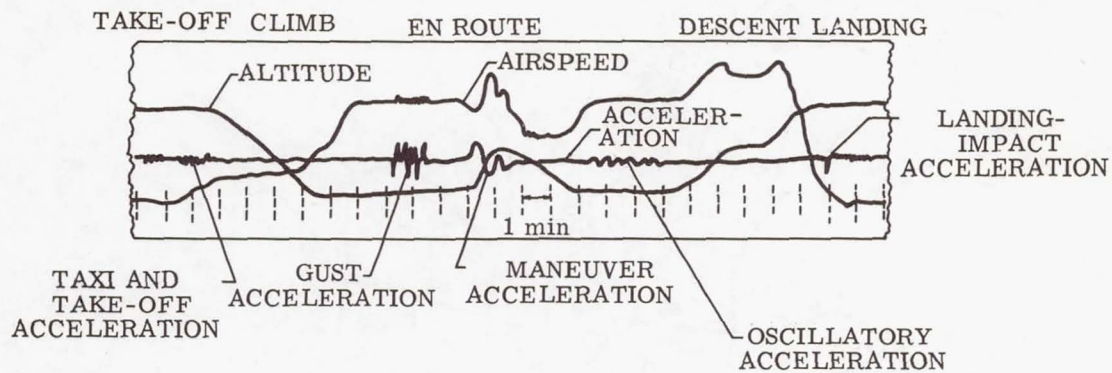


Figure 3.- Illustrative VGH record.

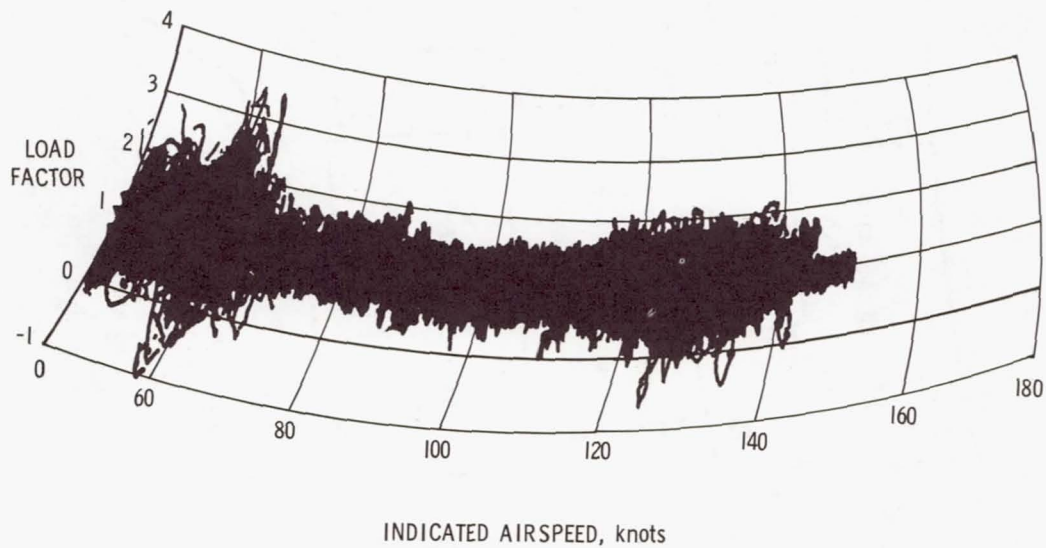


Figure 4.- Example of V-G record.

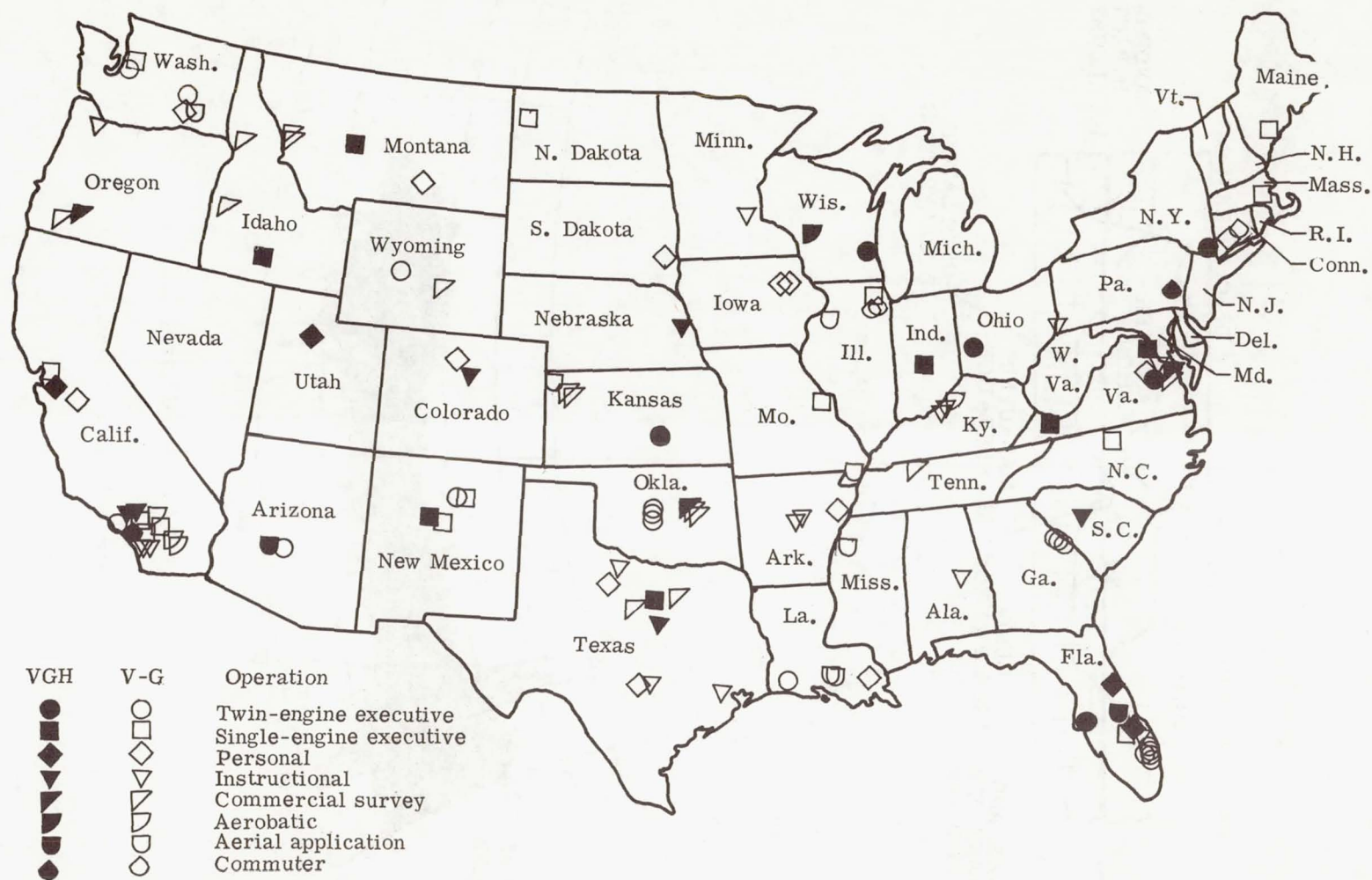
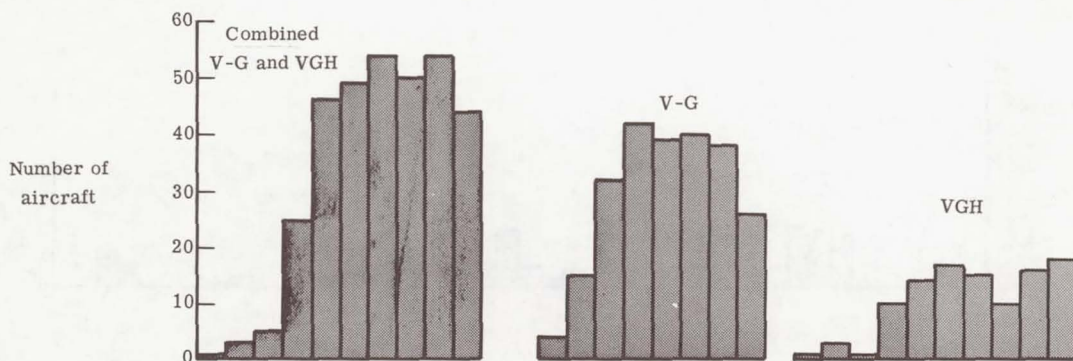
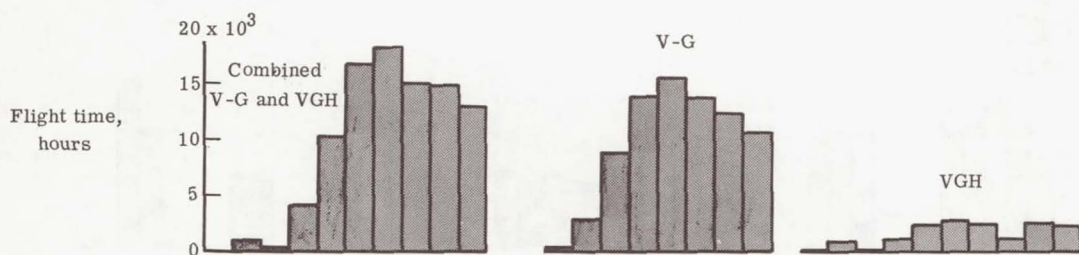


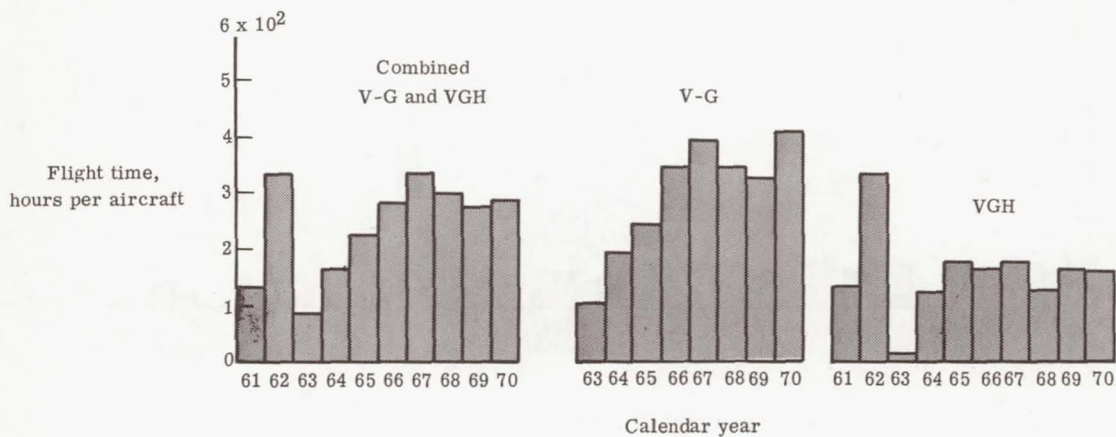
Figure 5.- Map indicating location of home bases of instrumented aircraft.



(a) Aircraft involved.

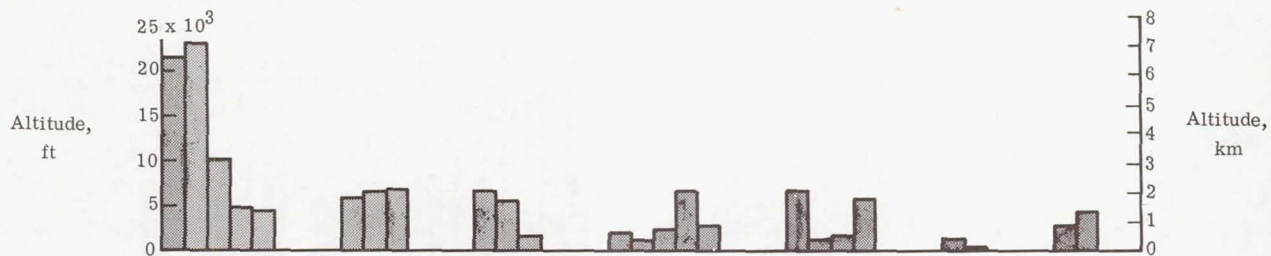


(b) Hours recorded.

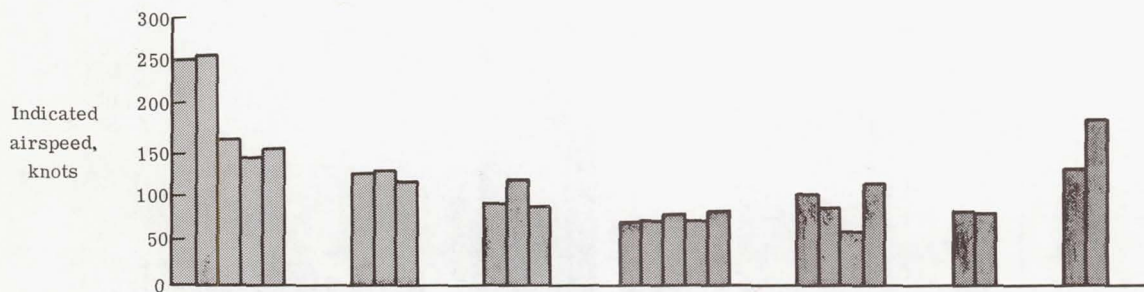


(c) Hours per aircraft per year.

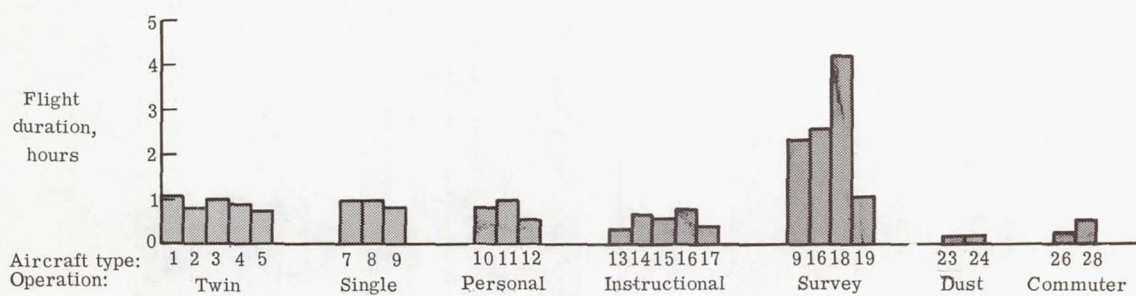
Figure 6.- Histogram of general aviation program.



(a) Average pressure altitude.

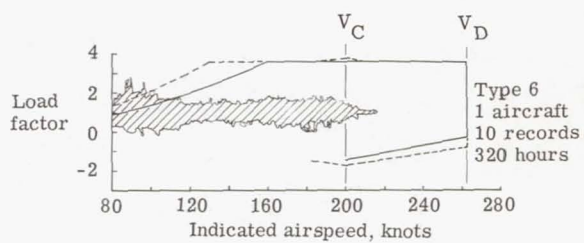
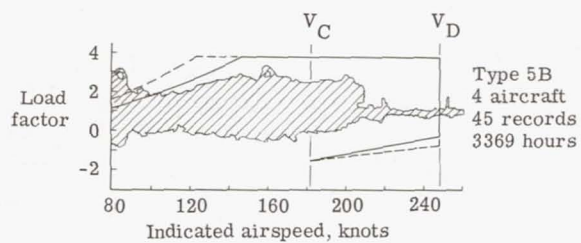
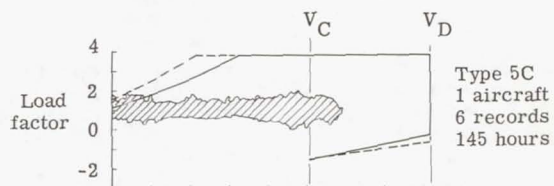
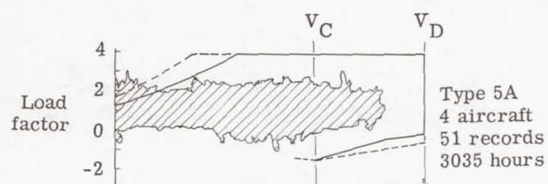
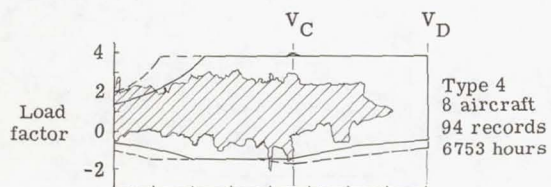


(b) Average indicated airspeed.



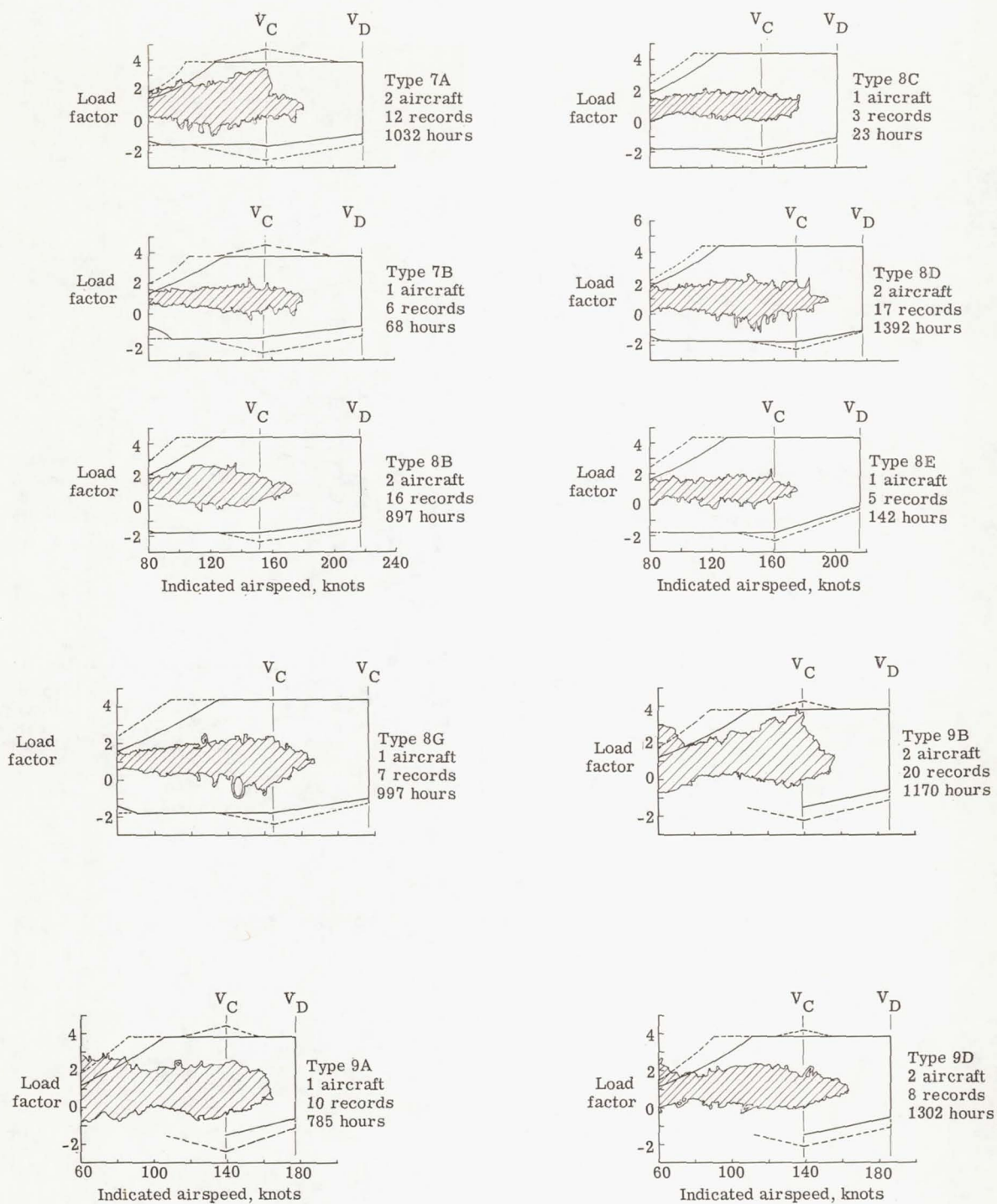
(c) Average flight duration.

Figure 7.- Typical mission characteristics of VGH instrumented aircraft.



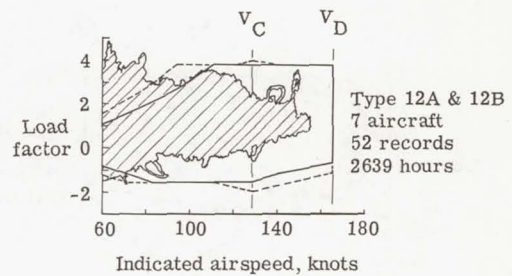
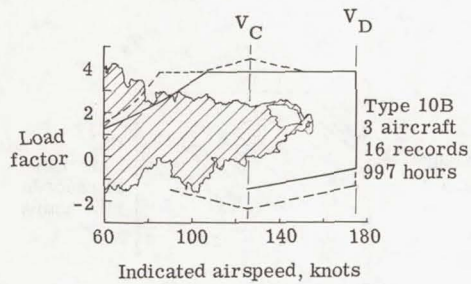
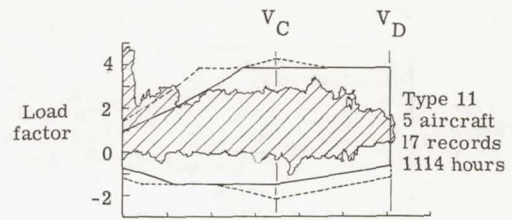
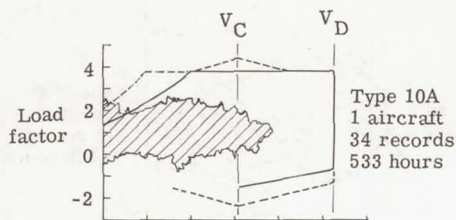
(a) Twin-engine executive.

Figure 8.- Composite V-G records from aircraft in eight types of operations.

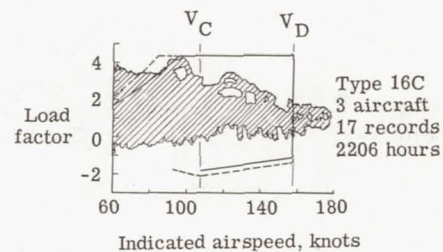
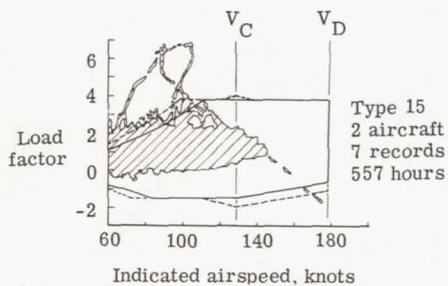
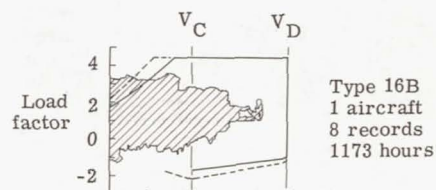
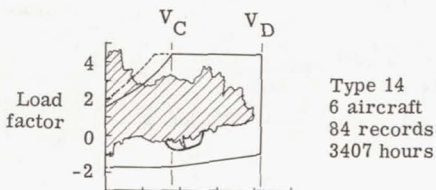
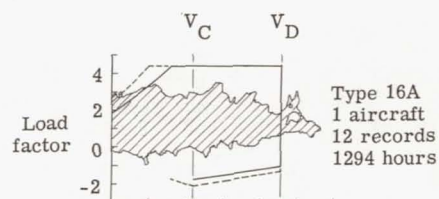
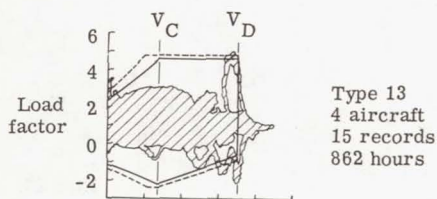


(b) Single-engine executive.

Figure 8.- Continued.

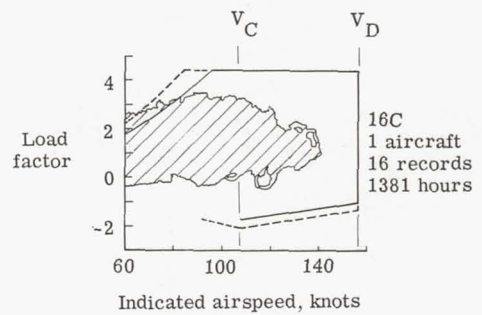
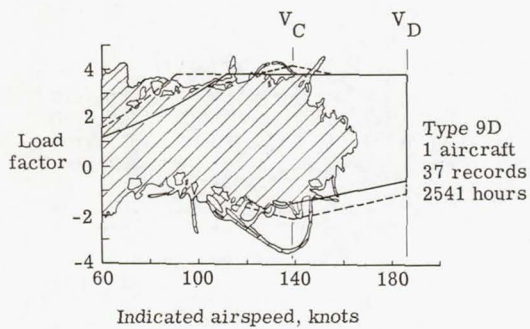
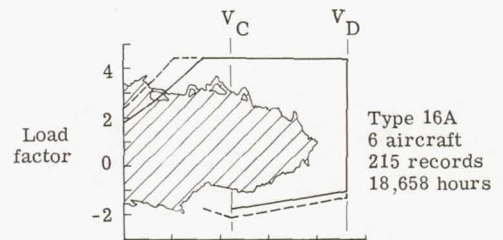
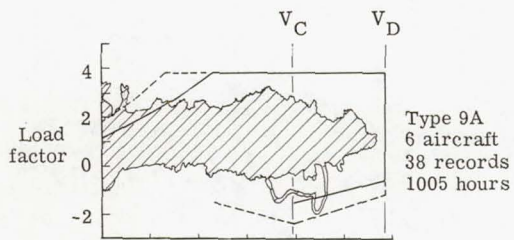


(c) Personal.

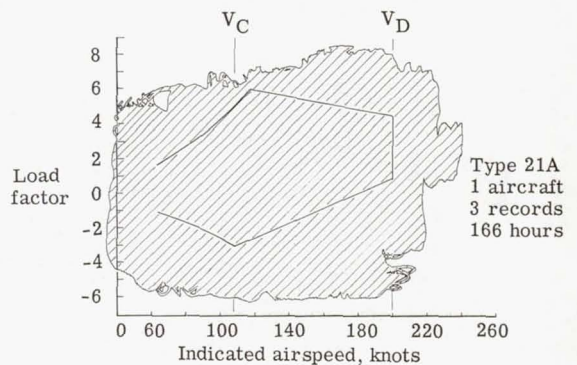
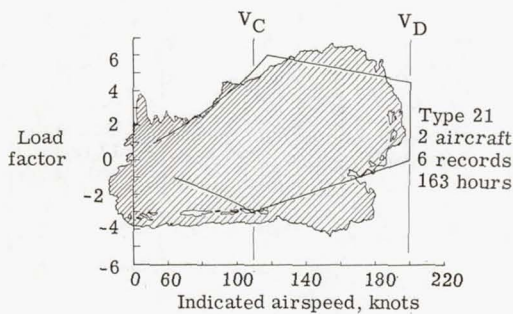
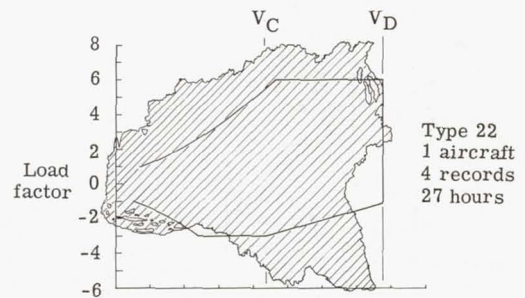
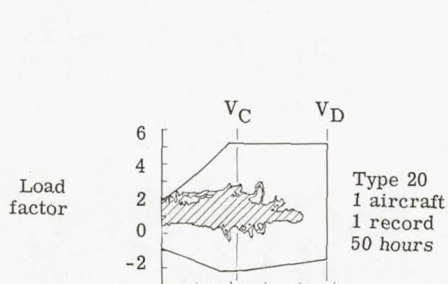


(d) Instructional.

Figure 8.- Continued.

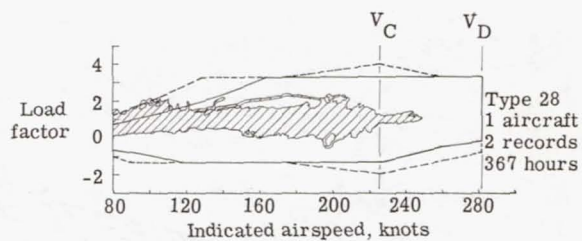
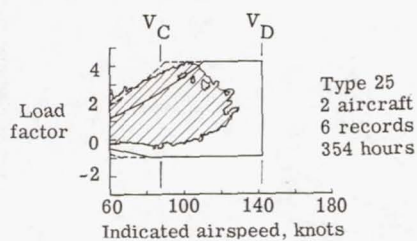
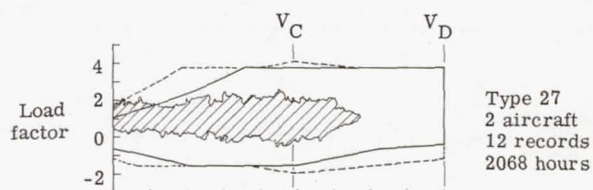
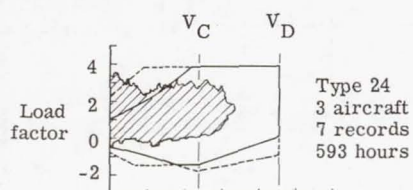
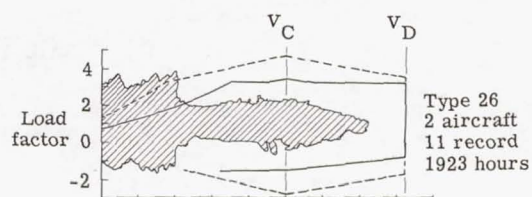
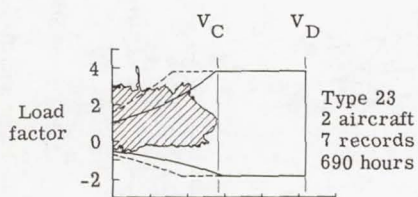


(e) Commercial survey.



(f) Aerobatic.

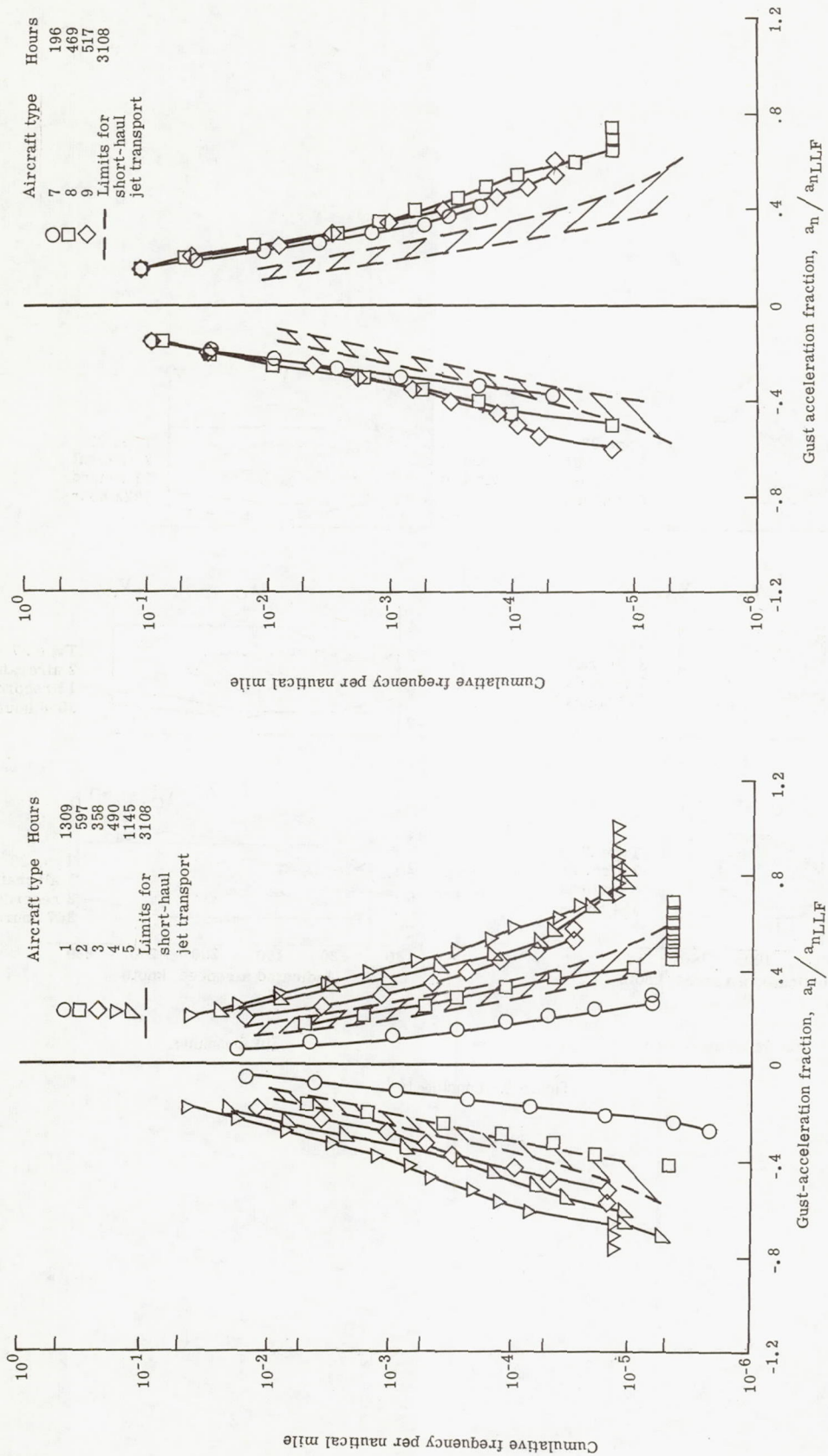
Figure 8.- Continued.



(g) Aerial application.

(h) Commuter.

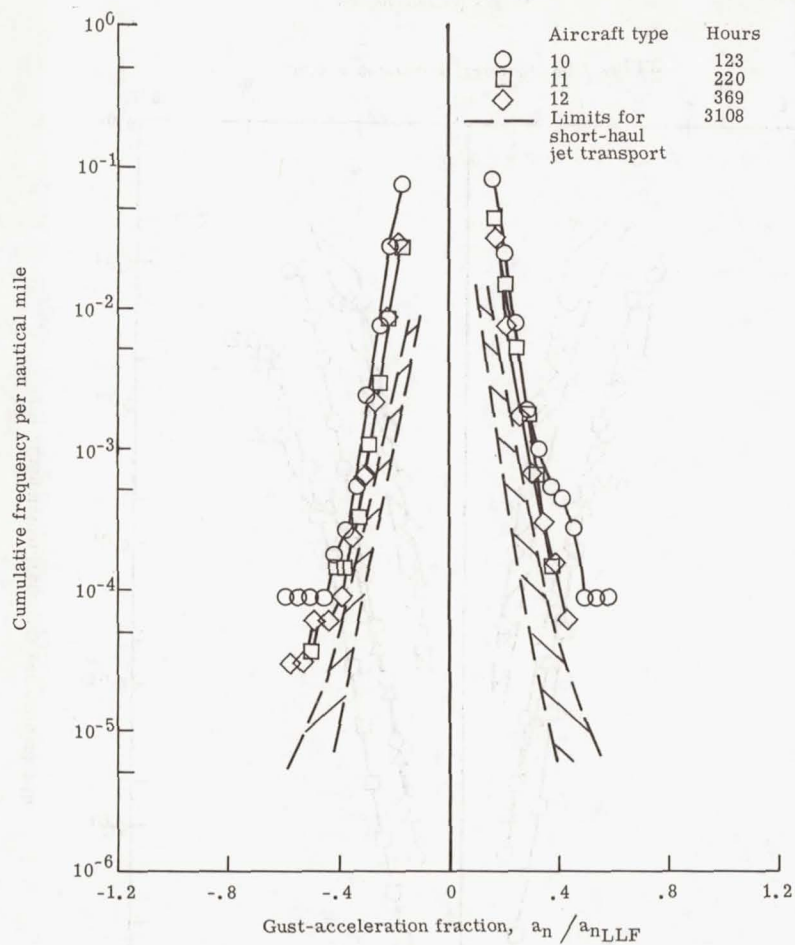
Figure 8.- Concluded.



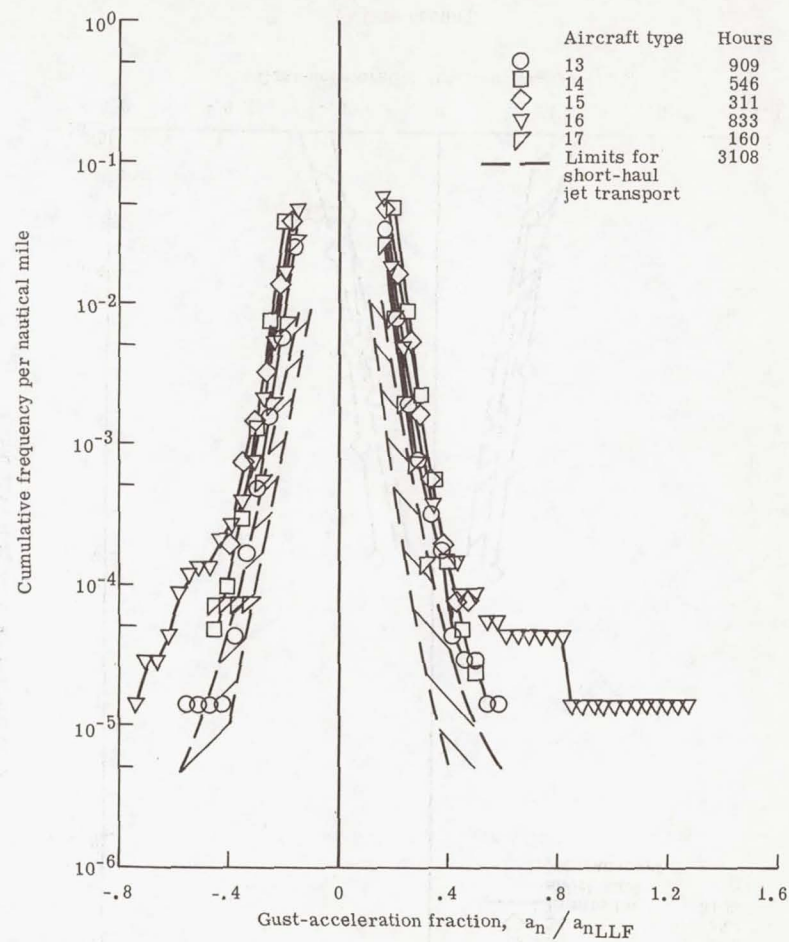
(a) Twin-engine executive.

(b) Single-engine executive.

Figure 9.- Gust-acceleration-fraction experience per nautical flight mile for aircraft in seven types of operations.

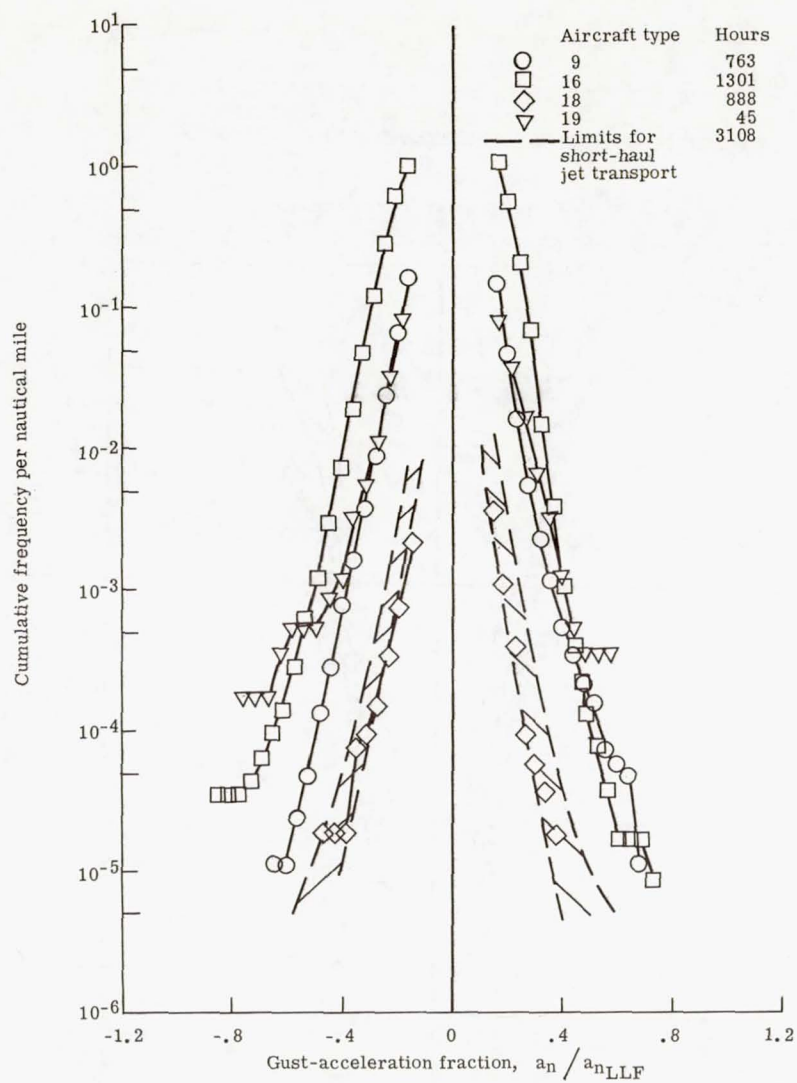


(c) Personal.

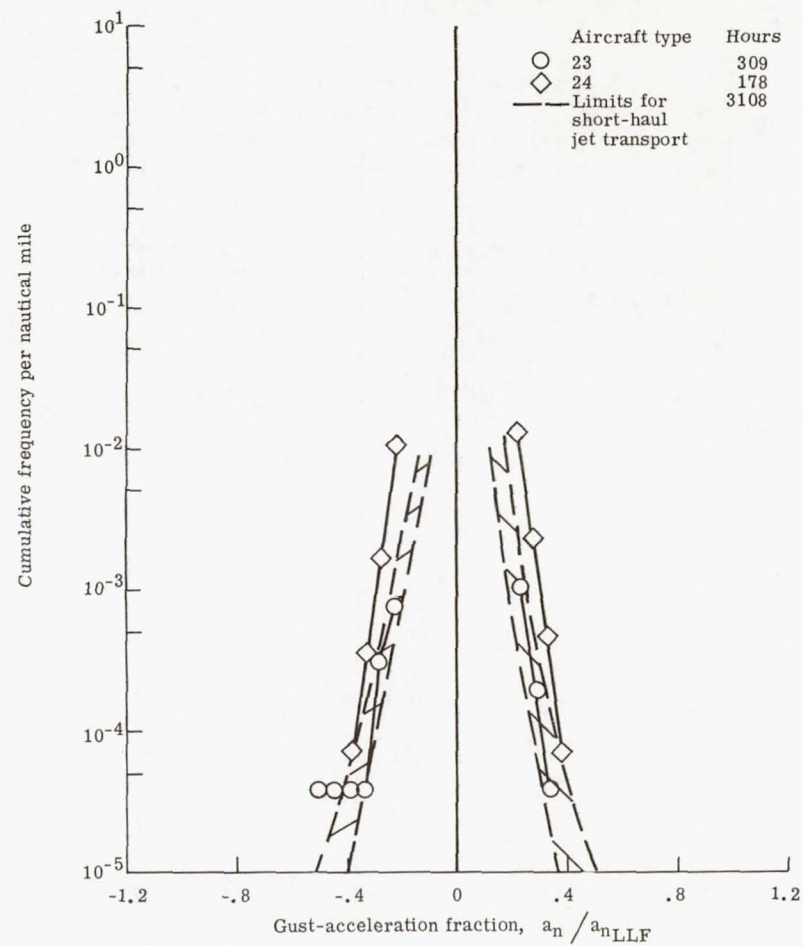


(d) Instructional.

Figure 9.- Continued.

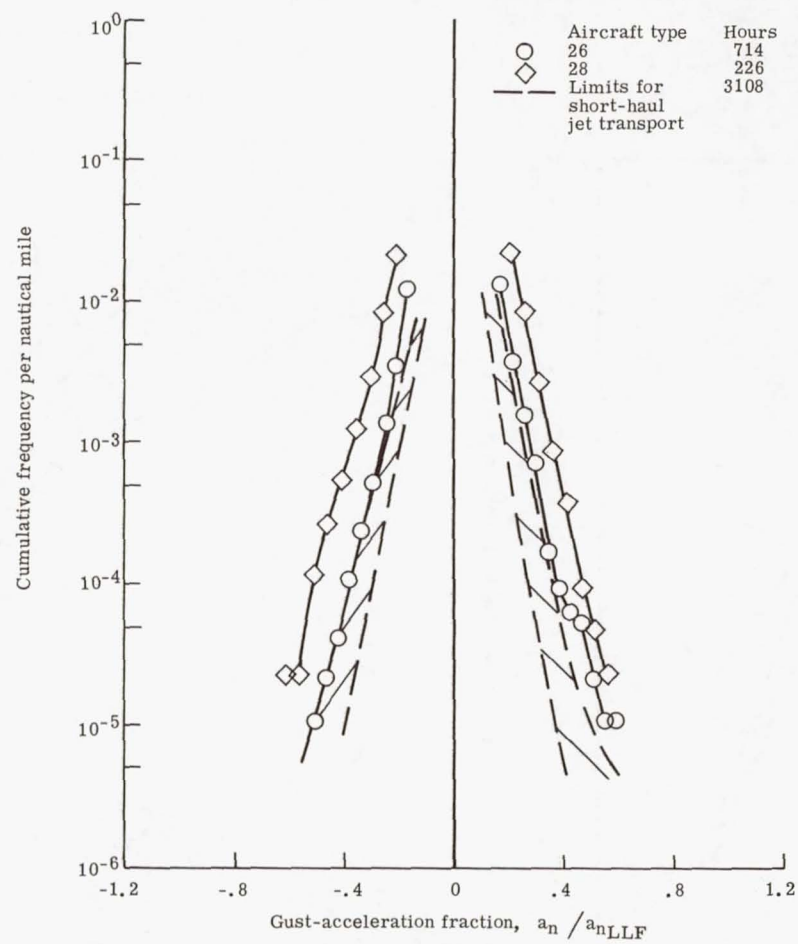


(e) Commercial survey.



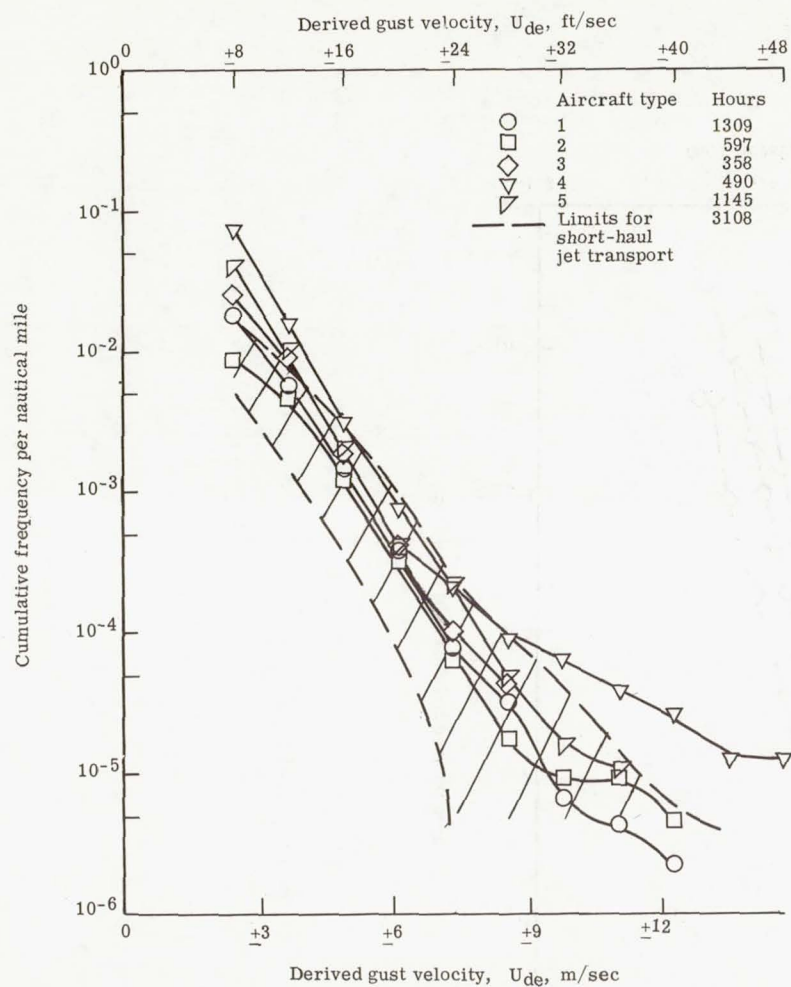
(f) Crop dusting.

Figure 9.- Continued.

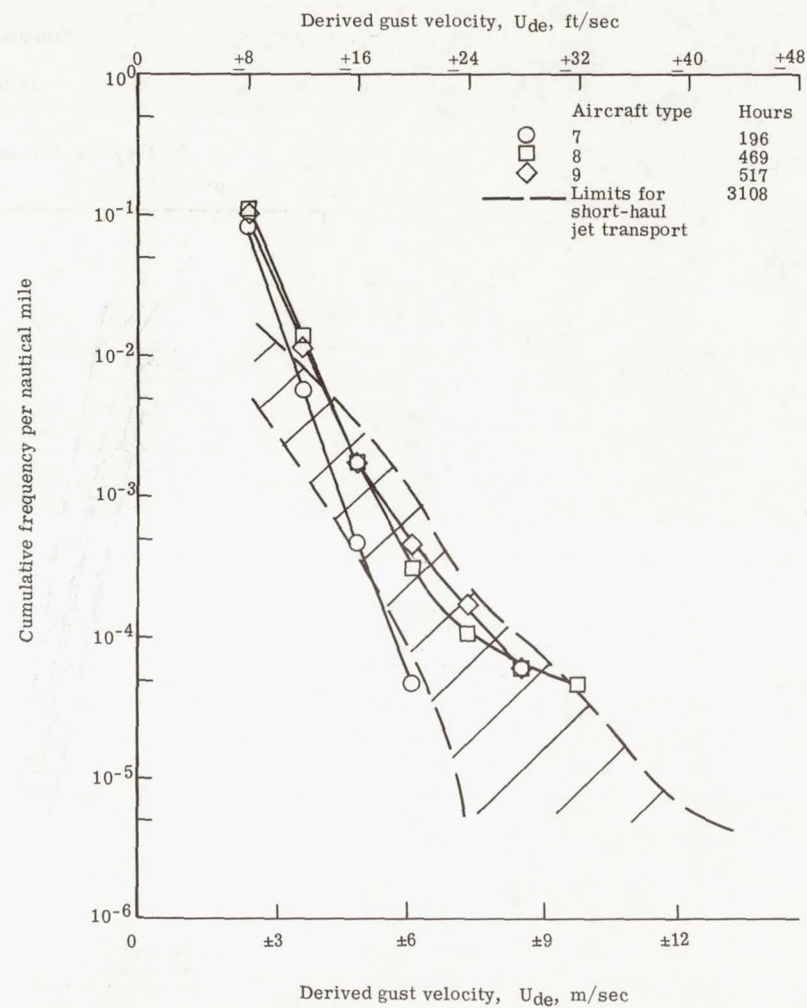


(g) Commuter.

Figure 9.- Concluded.

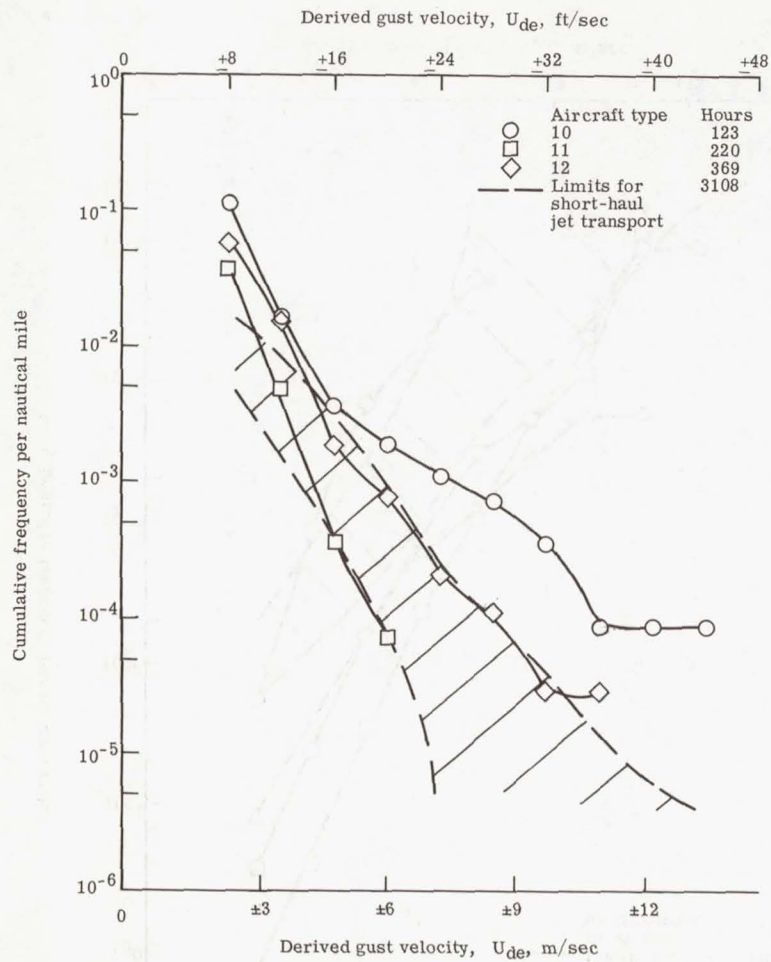


(a) Twin-engine executive.

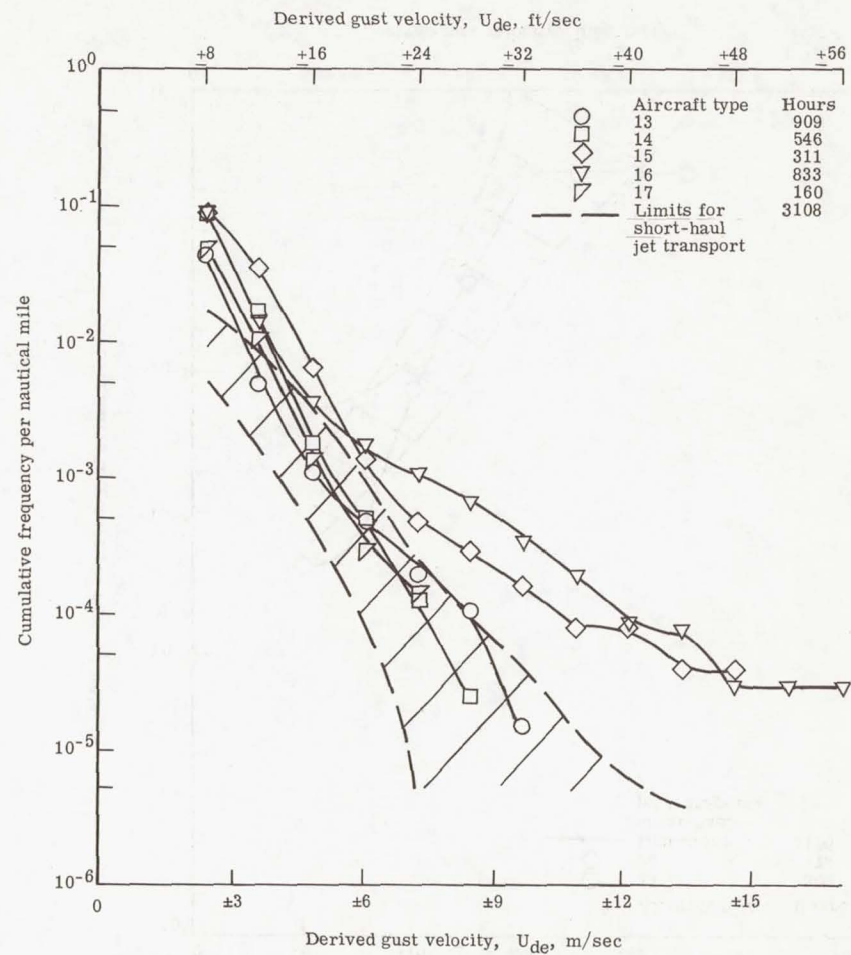


(b) Single-engine executive.

Figure 10.- Derived-gust-velocity experience per nautical flight mile for aircraft in seven types of operations.

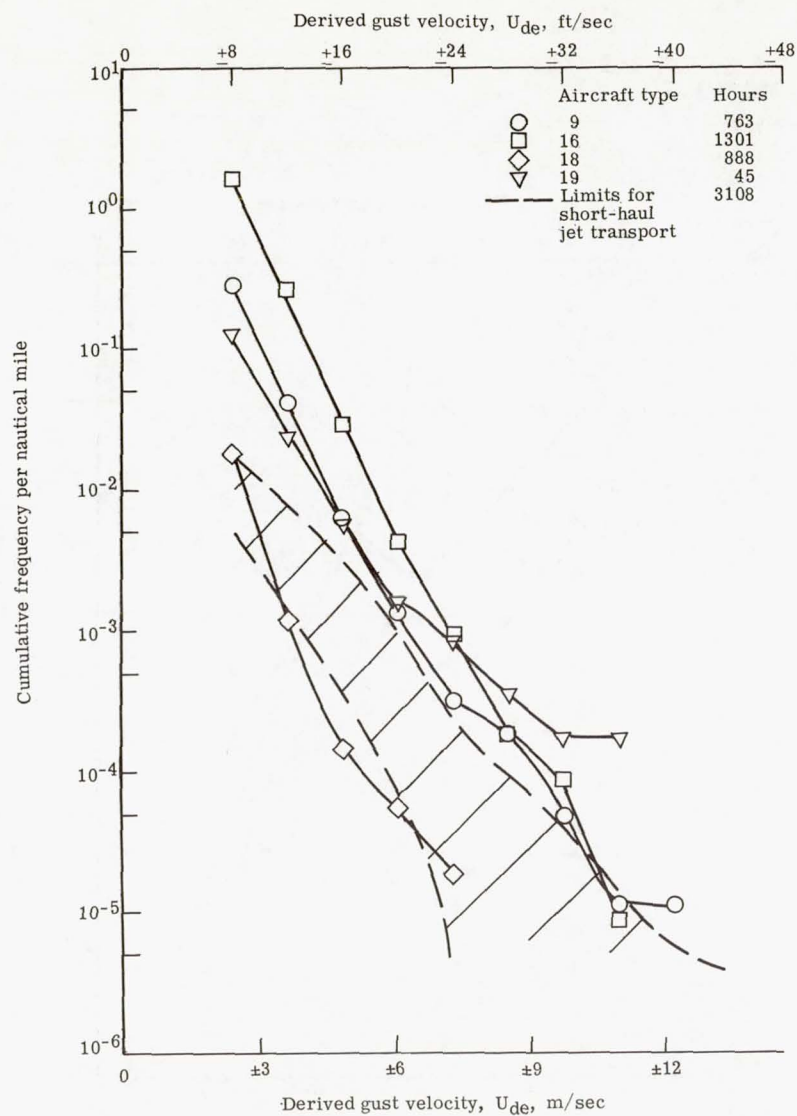


(c) Personal.

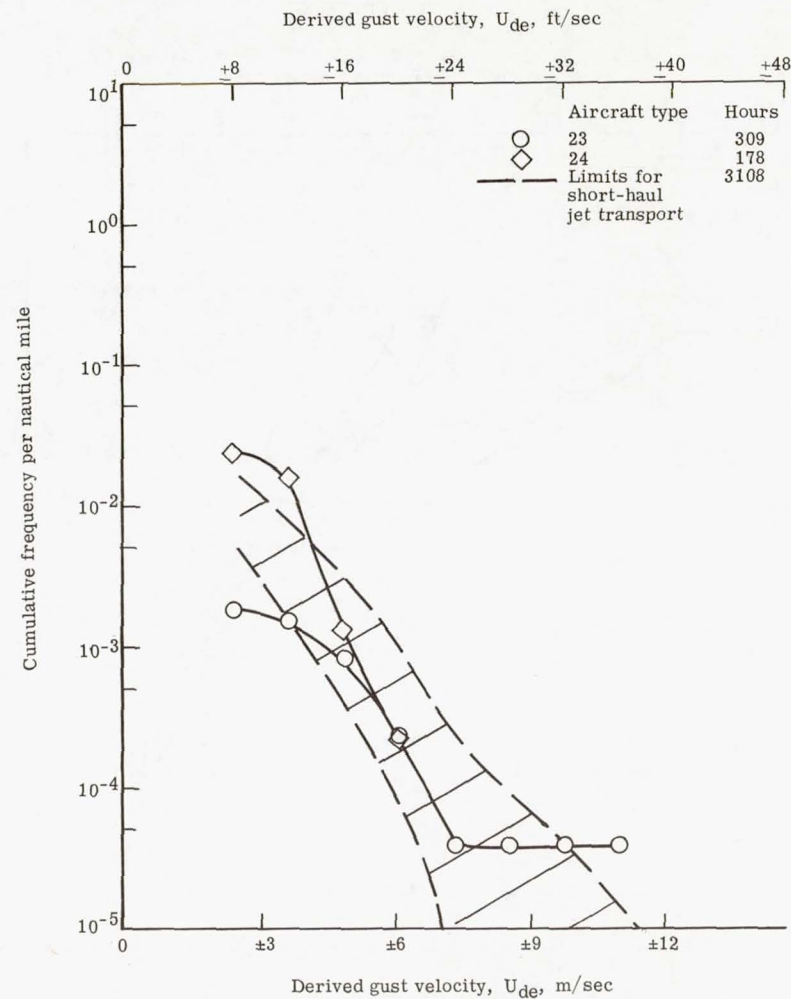


(d) Instructional.

Figure 10.- Continued.

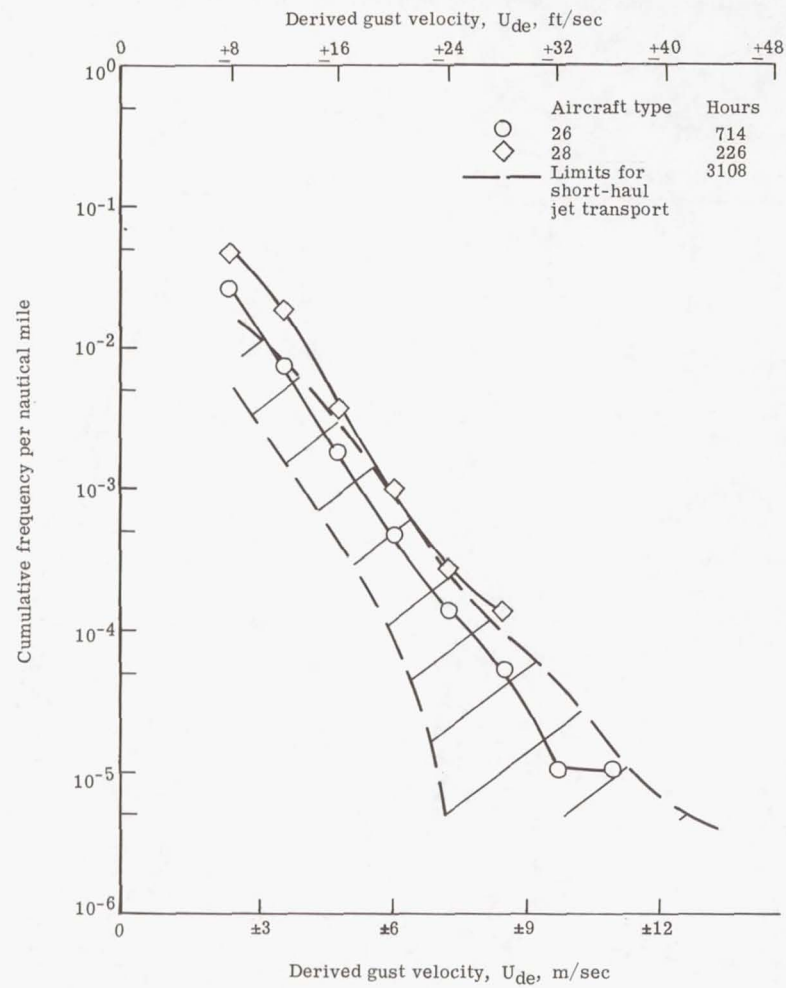


(e) Commercial survey.



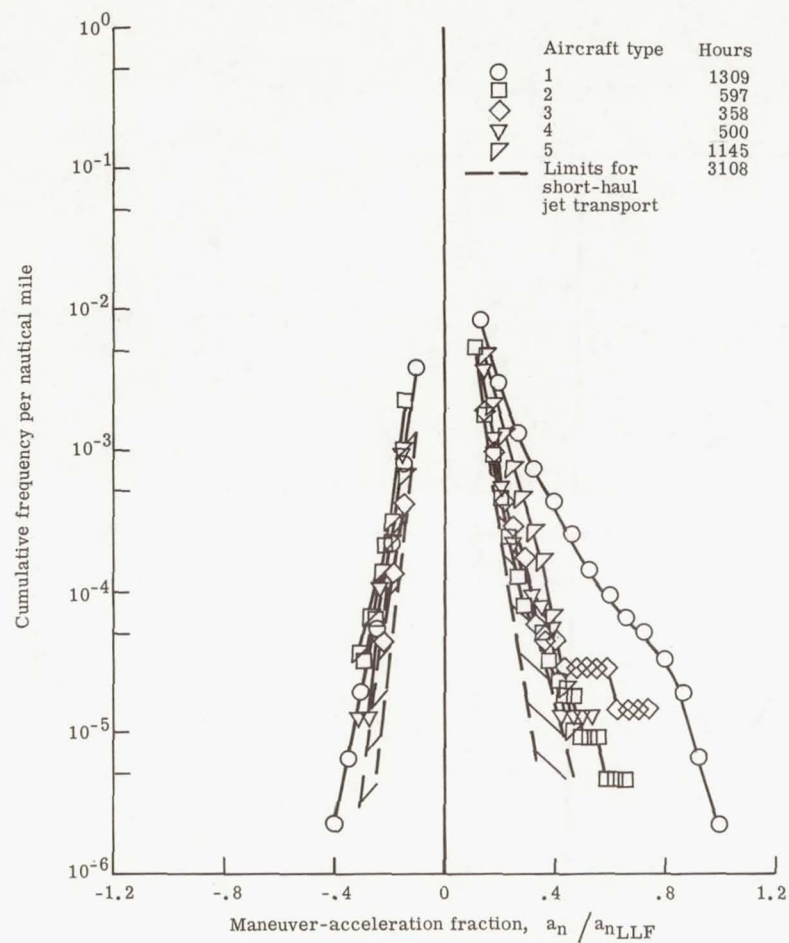
(f) Aerial application.

Figure 10.- Continued.

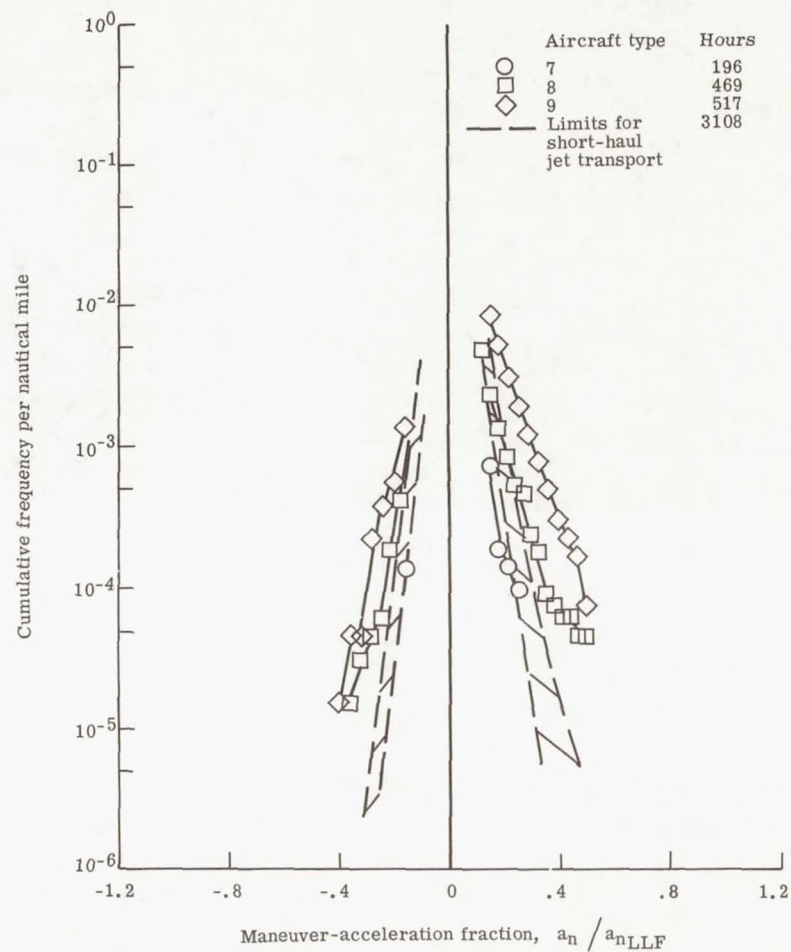


(g) Commuter.

Figure 10.- Concluded.

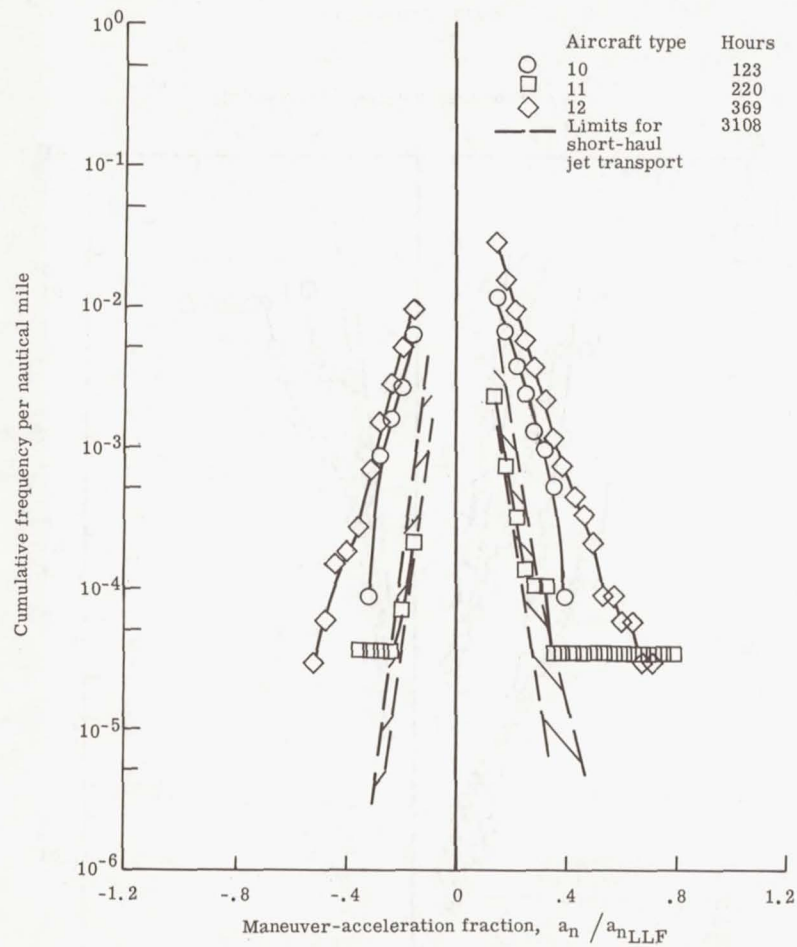


(a) Twin-engine executive.

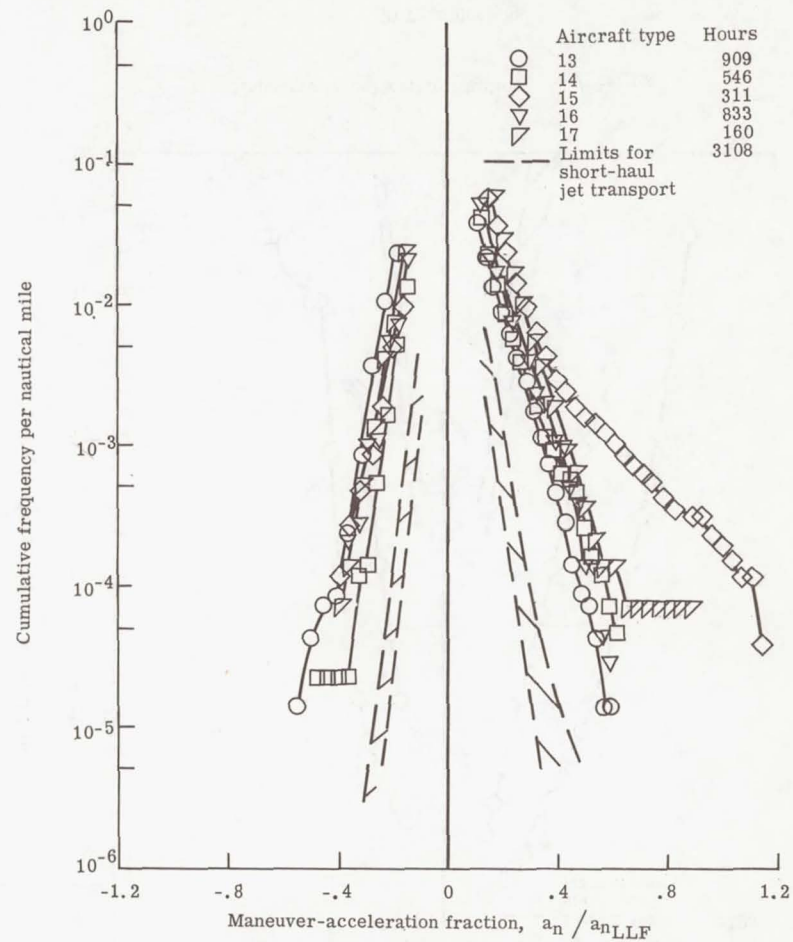


(b) Single-engine executive.

Figure 11.- Maneuver-acceleration-fraction experience per nautical flight mile for aircraft in seven types of operations.

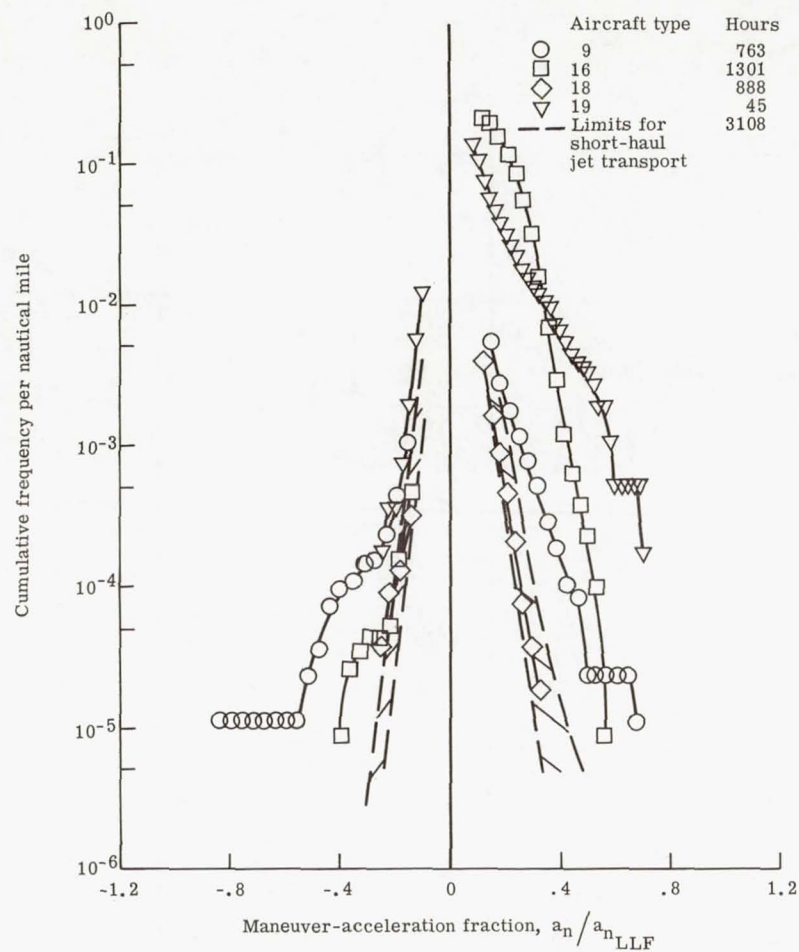


(c) Personal.

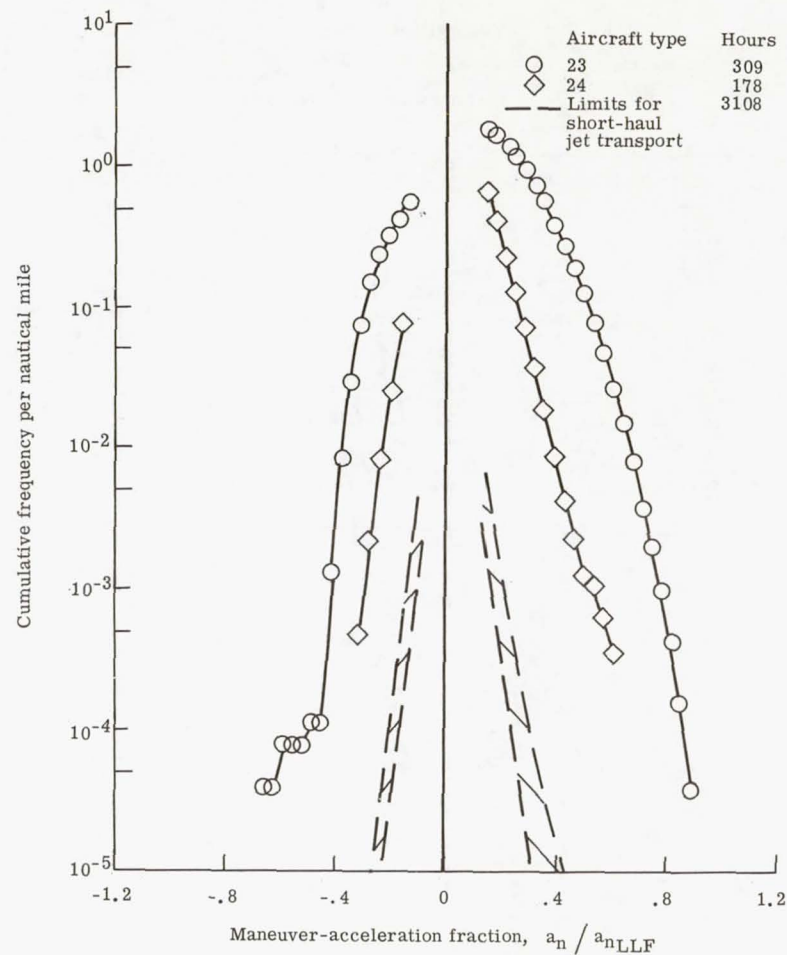


(d) Instructional.

Figure 11.- Continued.

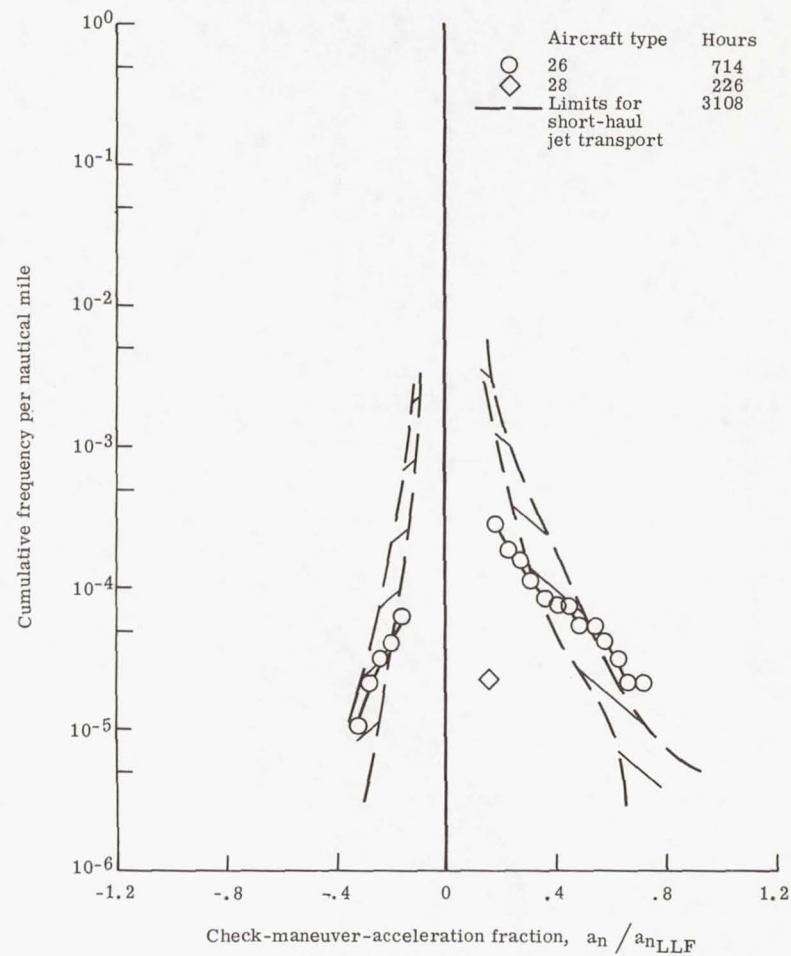
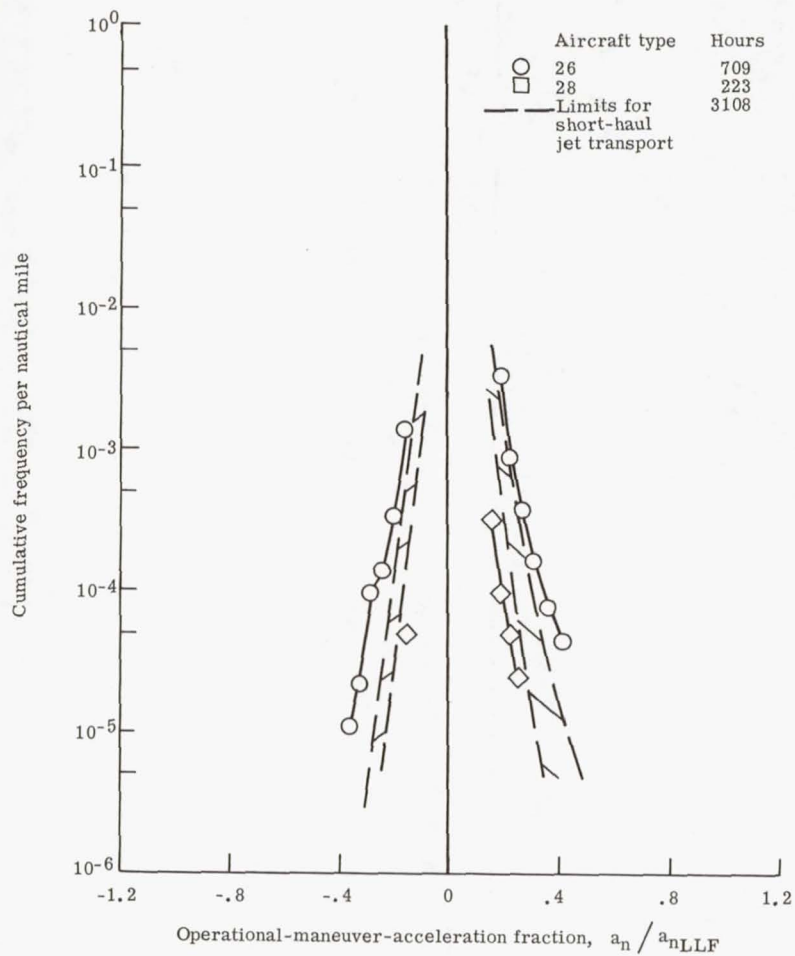


(e) Commercial survey.



(f) Crop dusting.

Figure 11.- Continued.



(g) Commuter.

Figure 11.- Concluded.

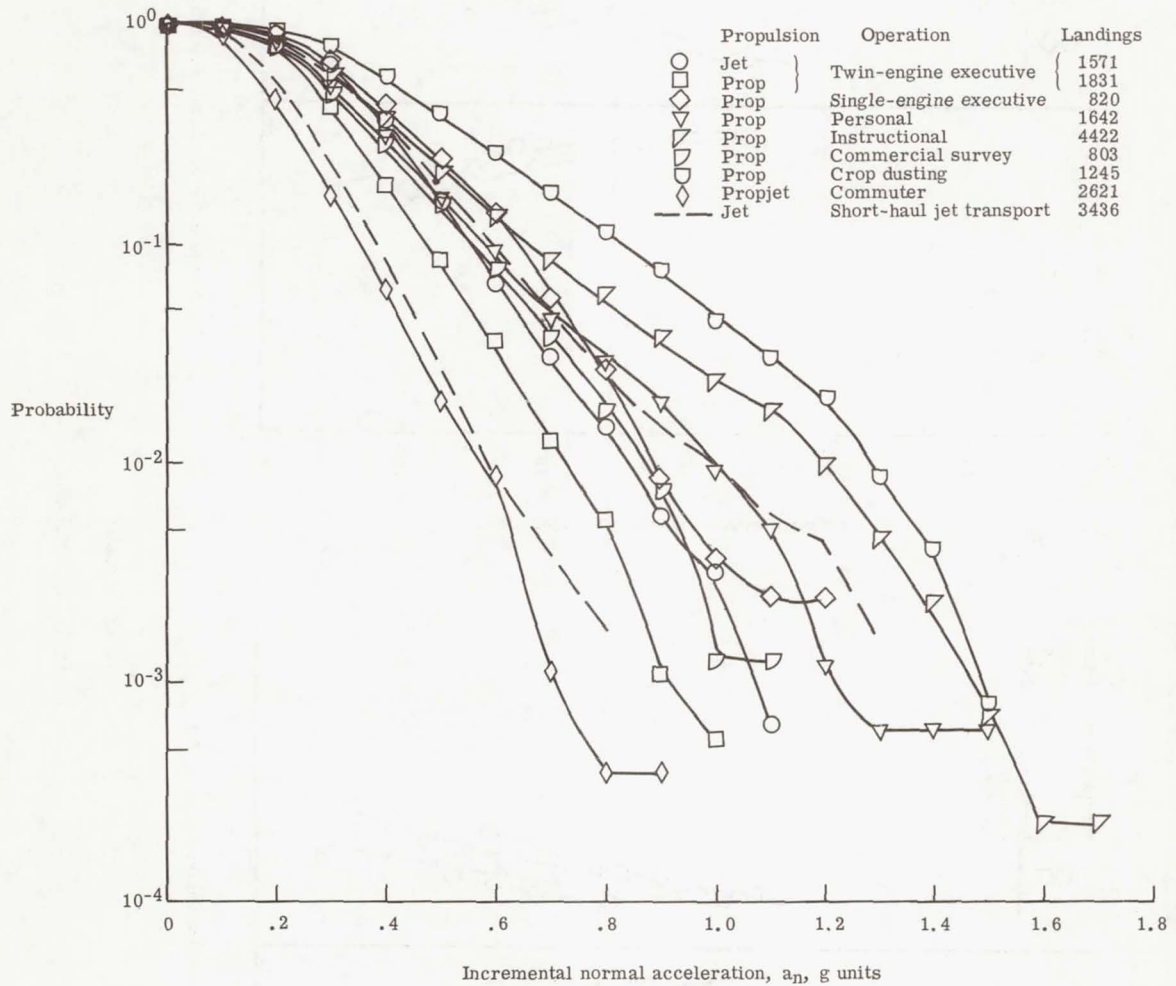


Figure 12.- Probability of equaling or exceeding various impact accelerations for aircraft in seven types of operations.

SOME FACTORS THAT AFFECT THE INSPECTION OF AIRCRAFT FOR FATIGUE DAMAGE

By C. C. Poe, Jr., and Herbert A. Leybold
Langley Research Center

SUMMARY

On the basis of fatigue crack growth and residual strength, a relationship between inspection interval and length of the smallest crack that must be detected to prevent failure within the inspection interval was determined. The effect on inspection of material, structural configuration, and aircraft load spectra was investigated. The results show that the efficient use of high-strength materials requires frequent inspection for very small cracks, that the use of stiffeners can result in a tolerance for long cracks and less frequent inspections, and that aircraft with fighter-type usage must be inspected much more frequently than aircraft with transport-type usage.

INTRODUCTION

The state of the art in the design of aircraft structure has not yet reached the point where fatigue failures can be totally eliminated through design. Moreover, fatigue failures are sometimes caused by errors in design and defects introduced in the manufacture or operation of the aircraft. Errors in design can usually be discovered and corrected by fatigue testing the structure. However, the defects introduced in manufacture and operation are very difficult to detect. The designer cannot use large factors of safety to prevent failures in these cases because of the resulting weight penalties. Thus, it is probably more feasible to control rather than to eliminate fatigue failures. Past experience has shown that a good control for fatigue failures is a fail-safe design along with a good inspection procedure. Inspections are normally made on the basis of calendar time or cumulative flight-hours. The interval between inspections is usually chosen according to manufacturers' recommendations, Federal Aviation Administration directives, and past inspection experiences.

In the present paper, an inspection philosophy is developed in terms of fatigue crack growth and residual strength. Based on this philosophy, the effect on inspection of the following important factors will be discussed:

1. Material behavior
2. Structural configuration
3. Aircraft load spectra

Other factors such as special nondestructive inspection methods, corrosion, fretting, and temperature effects can affect inspection, but they will not be discussed here.

SYMBOLS

F_{tu}	ultimate tensile stress
l	crack length
\bar{l}	length of crack that will grow to failure in two inspection intervals
NDI	nondestructive inspection

BASIS OF INSPECTION

Figure 1 shows how the strength of a component is reduced by a crack. The residual strength divided by density is plotted against crack length for a through-the-thickness crack in a very wide plate. Curves are shown for 2024-T3 and 7075-T6 aluminum alloys, Ti-6Al-4V duplex-annealed titanium alloy, and D6ac steel. The strength of each material is shown to the right of each curve. The choice of materials for aircraft structure is influenced strongly by structural weight, which is inversely proportional to the ratio of strength to density. The curves show that the high-strength alloys are very efficient when cracks are not present. However, their strength diminishes rapidly with increasing crack length, and for long cracks the lower strength materials are more efficient. Also for a given strength, the crack length at failure will be smaller for the higher strength materials.

Figure 2 shows how inspection interval can be related to crack length by considering the behavior of fatigue crack growth and residual strength. The curve of flight time against crack length is representative of actual crack-growth behavior for a through-the-thickness crack. The curve shows that the length of the crack increases with time, and when the residual strength is reduced below some high load in the spectrum, failure occurs. To prevent such a failure through inspection, a suitable procedure must find at least those fatigue cracks that are long enough to grow to failure before the next inspection. In order to allow for a crack to be overlooked once and thus provide some margin of safety, a crack-growth period equivalent to two inspection intervals was chosen for this study. For convenience, the length of the crack that will grow to failure in this period will be referred to as \bar{l} . By equating \bar{l} to the smallest crack length that can be readily detected, the crack-growth curve can be used to determine the largest allowable inspection interval. The curves for crack growth in the remaining figures were calculated for

the various configurations and load spectra by using fracture-mechanics methods along with data from simple tests.

MATERIAL

Figure 3 shows the effect of material behavior on inspection. Inspection interval in flights is plotted against the crack length \bar{l} for very wide sheets of the same materials shown in figure 1. The curves were calculated for a load spectrum of a transport airplane (see fig. 22 of ref. 1) with a limit load factor of 2.5 and a limit load stress equal to one-half the ultimate tensile stress. The number of flights was chosen as the basis for inspection for the transport aircraft. Analysis of loads and fatigue data for transport aircraft (see refs. 1 and 2) shows that the number of flights provides a better correlation of the data than cumulative flight-hours, flight miles, or calendar time. The curves show that the higher strength materials must be inspected more frequently than the lower strength materials, especially the D6ac steel which is typical of high-strength steels. Also, a lower limit for nondestructive inspection (NDI) is shown in this figure as a crack length of 3.8 mm (0.15 in.). The Air Force is using this crack size as a lower limit for nondestructive inspection in the design of the advanced bomber. Tests with dye penetrants and ultrasonic and X-ray inspection methods show that it is very difficult to find cracks that are smaller than this size. Because the length of the crack at failure is very small for the D6ac steel, most of the curve is to the left of this NDI limit. Therefore, high-strength materials like this will require very sensitive inspection methods.

The size of a critical crack in a D6ac specimen is shown in figure 4. This specimen contains a hole 9.5 mm (0.38 in.) in diameter. The dark textured surface is the static fracture surface. The size of the fatigue crack that caused the failure is shown by the light area at the corner of the hole. The longest dimension of this crack is 2 mm (0.08 in.), which is about one-half the NDI limit of 3.8 mm (0.15 in.). The load at fracture was only 40 percent of the ultimate tensile strength without a crack. Because of the high stresses at the edge of the hole, the size of the crack at failure in this specimen is smaller than the size of the through-the-thickness crack at failure in figure 3.

CONFIGURATION

Figure 5 shows the effect of stiffeners on inspection. Inspection interval in flights is plotted against the crack length \bar{l} for very wide sheets with and without riveted stringers. The stringers are assumed to be 76 mm (3 in.) apart and represent one-half the total area of the panel, and the rivets are 25 mm (1 in.) apart. The crack was assumed to be only in the sheet. The curves were calculated for a 7075-T6 aluminum alloy, the transport spectrum used in figure 3, and a limit load stress equal to one-half

the ultimate tensile stress. The curves show that the plain sheet must be inspected much more frequently than the stiffened sheet. A larger scale for crack length has been used in this figure to point out the tolerance of the stiffened sheet for large cracks. The curve for the stiffened sheet shows that reasonably long inspection intervals can be used with much larger values of \bar{l} . Thus, it is not necessary to detect very small cracks, and much less sophisticated inspection methods can be used. Also, the reliability of a given method will be higher for longer cracks. It should be pointed out that integral stringers are not beneficial as are bolted or riveted stringers because a fatigue crack will propagate through the integral stringers as well as the sheet. (See ref. 3.) Integrally stiffened panels behave, instead, like a simple sheet without stringers and with the same total area.

Figure 6 shows wreckage from a Fairchild F-27B airplane that crashed in Alaska in December 1968. The photograph at the top shows a portion of an access door from the lower wing surface. The fracture of the wing passed through this door. The lower photographs are enlargements of the fractured surface at the edge of the door and show that fatigue cracks 50 to 80 mm (2 to 3 in.) in length were present at the time of the crash. These cracks initiated at the holes and are present in all layers of material. The National Transportation Safety Board (see ref. 4) concluded that "the probable cause of this accident was an in-flight structural failure caused by an encounter with severe-to-extreme turbulence The failure occurred in an area of the right wing (WS 197) which had been weakened to an indeterminate degree by pre-existing fatigue cracks." The access door in figure 6 is the area referred to as Wing Station (WS) 197.

Figure 7 shows a radiograph that was made of the access door two inspections prior to the crash. The white objects around the periphery of the access door are the bolt and nut plates that hold the door in place. The enlargement at the left shows one of the bolt holes that contained cracks and was in the plane of the fracture. Careful examination reveals that those cracks were present two inspections prior to the crash. Portions of the cracks are obscured in this film by the nut plates and density changes from other sources. Nevertheless, the visible portion of the cracks was greater than 3.8 mm (0.15 in.). It should be emphasized that the cracks in this film are very difficult to see. There are more than 70 bolt holes and five layers of material around this one access door. The complexity of aircraft structure, such as this, makes it very difficult to detect small fatigue cracks. The photographs in figures 6 and 7 were furnished to NASA by the National Transportation Safety Board.

LOAD SPECTRA

Figure 8 shows the effect of load spectra on inspection. Values of inspection interval in hours are plotted against the crack length \bar{l} for a fighter spectrum (table II of ref. 5) with a limit load factor of 7.33 and the transport spectrum in figure 3. The load

spectrum for the fighter airplane is given in terms of flight-hours. In order to have a common time basis for the fighter and transport spectra, the transport spectrum was converted to flight-hours by assuming the duration of a flight to be 2 hours. The curves were calculated for 7075-T6 aluminum alloy with a limit load stress equal to one-half the ultimate tensile stress. The area between the curves is labeled "general aviation" in order to point out that the load spectra of this class of aircraft are quite broad. The usage of these aircraft may vary from executive and pleasure flying to crop-dusting and surveying. The curves show that the fighter spectrum is much more severe than the transport spectrum. The frequency of inspection for the fighter spectrum is more than 10 times that for the transport. Because inspections are so sensitive to the load spectra, aircraft of the same type may need to be inspected differently because of differences in individual usage. For this reason, it is essential that the operator know the severity of the loading that each aircraft is experiencing. The ideal situation would be to have a simple and inexpensive load-monitoring device on each aircraft.

Toward this end, the Langley Research Center is developing the strain counter shown in figure 9. This device will electronically record the number of times the strain at some point in the structure exceeds four preset levels. The total number of times that these levels are exceeded is shown on the counters, which may be located conveniently and read easily. Only strain-gage and power-supply connections must be made to the counter. An ordinary resistance strain gage can be used as the strain transducer and can be located at any place of interest. The entire package weighs only 1.4 kg (3 lbm), occupies a space of only 150 by 200 by 38 mm (6 by 8 by 1.5 in.), and costs under a thousand dollars. The system can be further miniaturized, and the unit cost will decrease with production in large quantities. The primary application of the strain counter is expected to be in military and general aviation aircraft where individual usage varies widely within a fleet of the same aircraft. The counter is presently being installed on several Air Force aircraft for evaluation.

CONCLUSIONS

An investigation was conducted to determine the relationship between inspection interval and the length of the smallest crack that must be detected to prevent failure within the inspection interval. The effect on inspection of material, structural configuration, and aircraft load spectra was determined. From this investigation the following conclusions are made:

1. Considerations of fatigue-crack growth provide a rational basis for inspection.
2. The efficient use of high-strength materials requires frequent and sensitive inspections.

3. The reliability of nondestructive inspection methods to detect small cracks in complex structures must be improved.
4. The use of stiffeners can result in longer inspection intervals and increased tolerance for long cracks.
5. Different usage of individual aircraft requires different inspection schedules.
6. Relatively simple and inexpensive electronic counters can monitor actual strain experience in individual aircraft.

REFERENCES

1. Coleman, Thomas L.: Trends in Repeated Loads on Transport Airplanes. NASA TN D-4586, 1968.
2. Hardrath, Herbert F.: Some Factors Affecting Fatigue of Aircraft Structures. Conference on Aircraft Operating Problems, NASA SP-83, 1965, pp. 37-44.
3. Poe, C. C., Jr.: Fatigue Crack Propagation in Stiffened Panels. Damage Tolerance in Aircraft Structures, Spec. Tech. Publ. No. 486, Amer. Soc. Testing Mater., 1971, pp. 79-97.
4. Anon.: Aircraft Accident Report - Wien Consolidated Airlines, Inc., Fairchild F-27B, N4905, Pedro Bay, Alaska, December 2, 1968. Rep. No. NTSB-AAR-70-16, Nat. Transp. Safety Board, July 22, 1970.
5. Anon.: Airplane Strength and Rigidity - Reliability Requirements, Repeated Loads, and Fatigue. Mil. Specif. MIL-A-8866(ASG), May 18, 1960.

STRENGTH REDUCTION DUE TO CRACK

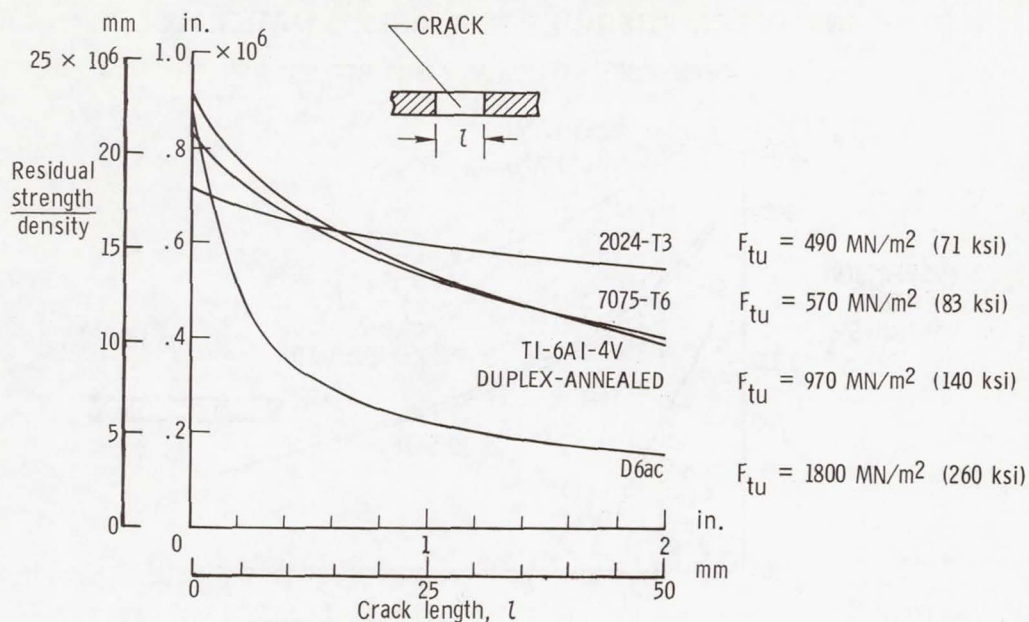


Figure 1

INSPECTION INTERVALS BASED ON CRACK GROWTH

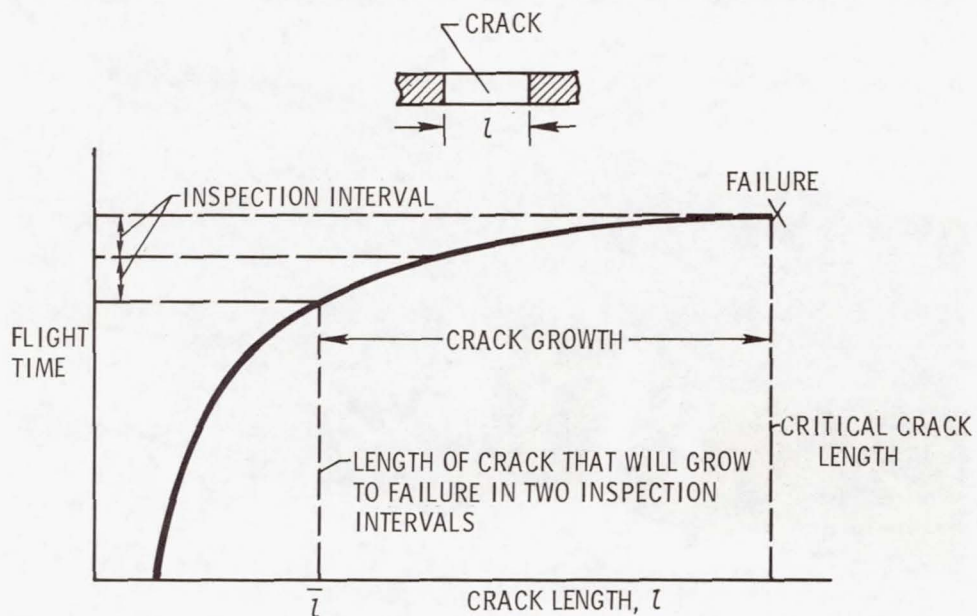


Figure 2

INSPECTION INTERVALS FOR VARIOUS MATERIALS

TRANSPORT SPECTRUM; LIMIT STRESS, $\frac{1}{2} F_{tu}$

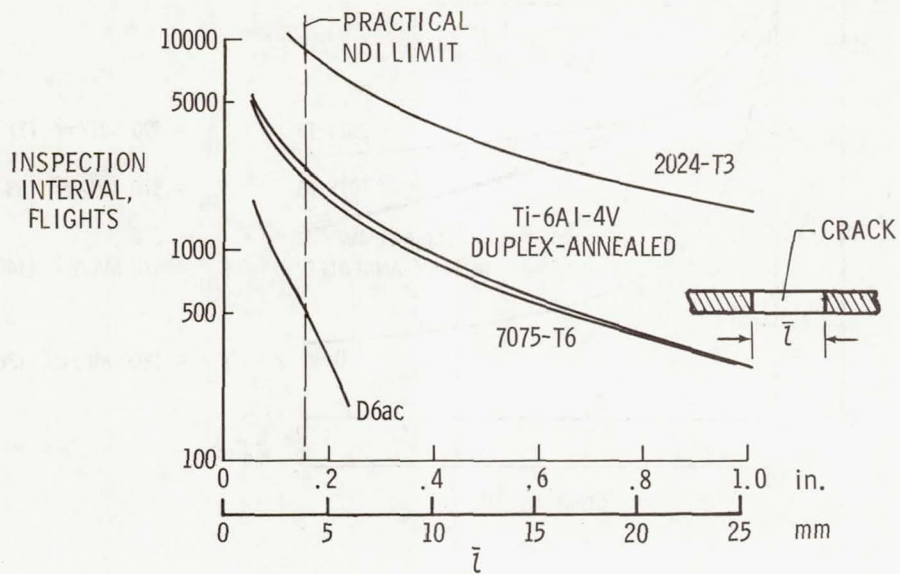


Figure 3

FRACTURED SURFACE OF D6ac SPECIMEN

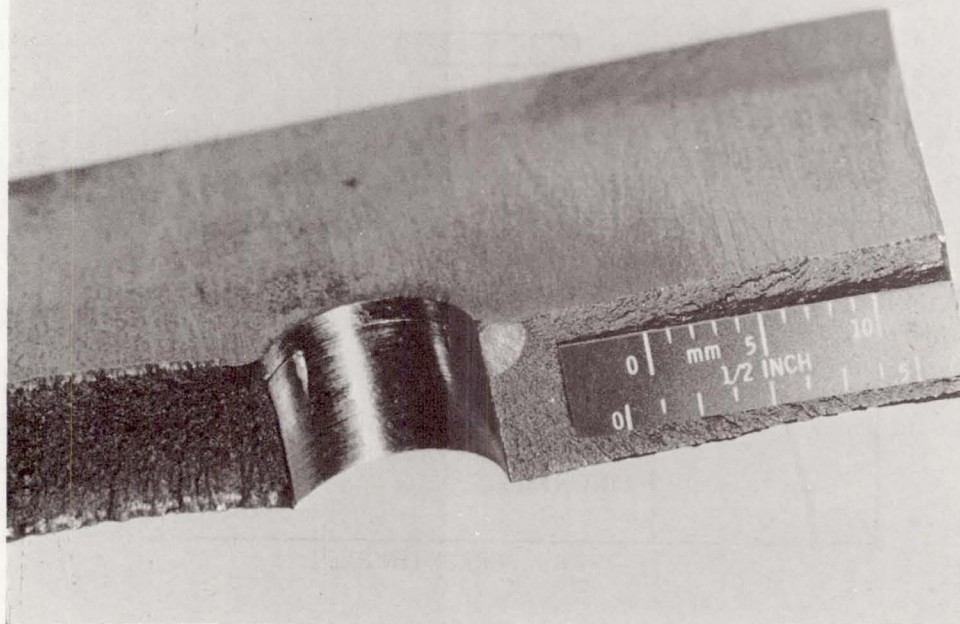


Figure 4

INSPECTION INTERVALS FOR VARIOUS CONFIGURATIONS 7075-T6; TRANSPORT SPECTRUM; LIMIT STRESS, $\frac{1}{2} F_{tu}$

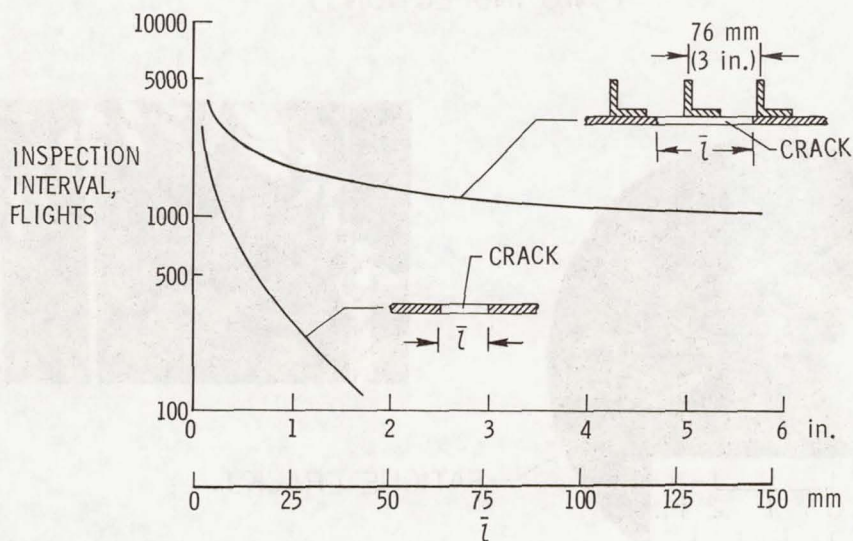


Figure 5

WRECKAGE FROM CRASH OF F-27B AIRCRAFT

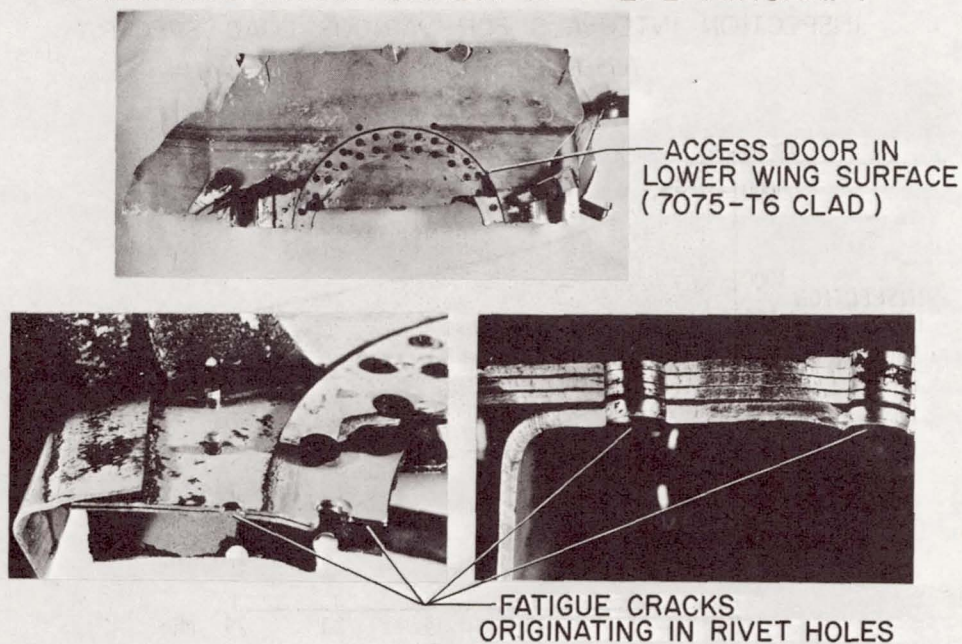


Figure 6

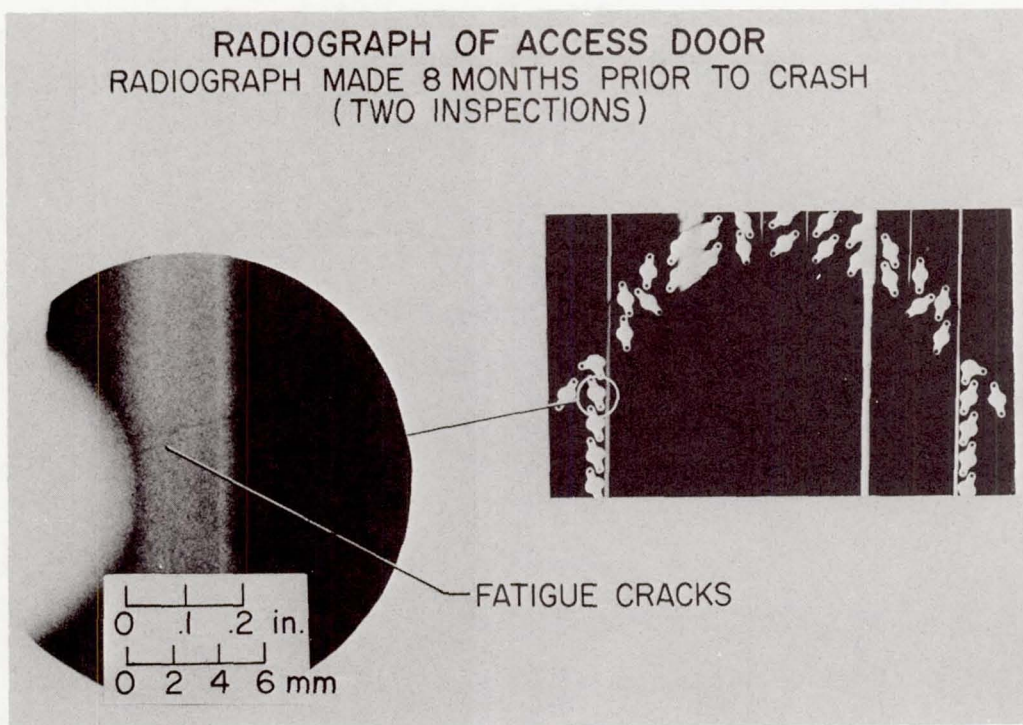


Figure 7

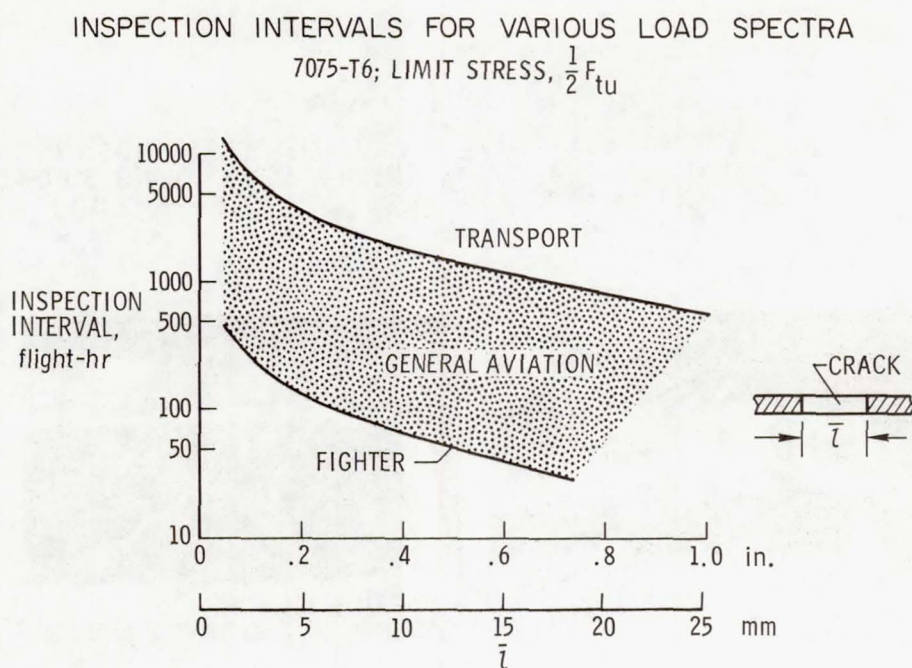


Figure 8

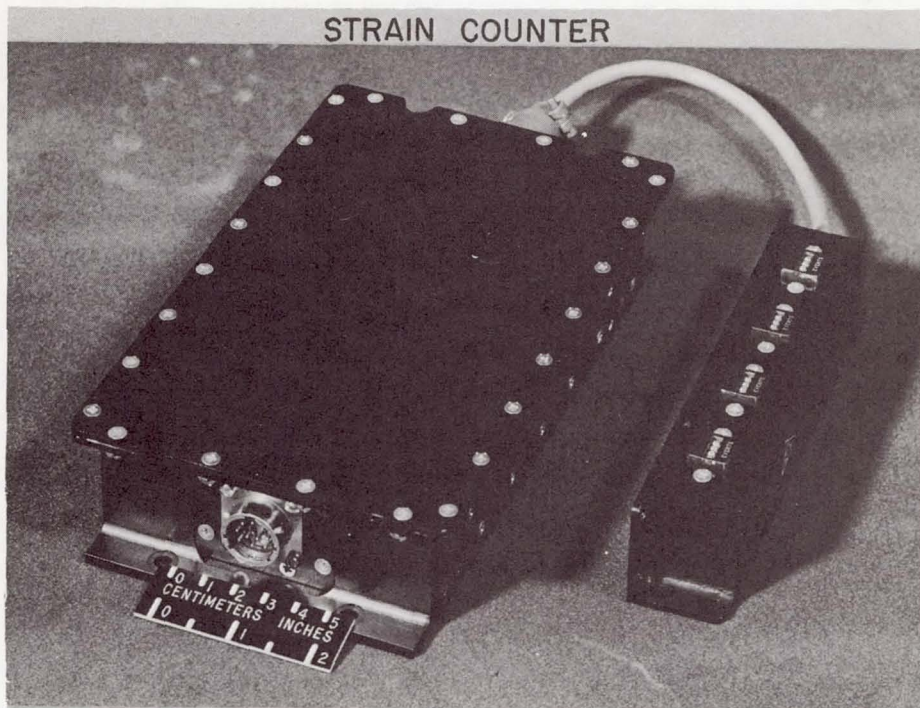


Figure 9

Page intentionally left blank

PROGRESS IN REDUCING EXHAUST POLLUTANTS FROM JET AIRCRAFT

By Helmut F. Butze and Jack Grobman
Lewis Research Center

INTRODUCTION

The problem of pollution emissions from all sorts of fossil fuel-burning sources has received a great amount of attention in the past few years. The aircraft industry has not escaped its share of the blame for environmental pollution. Although, at the present time, pollutant emissions from aircraft constitute less than 1 percent of the total on a nationwide basis (table VI of ref. 1), the projected increase in aircraft usage over the next decade and the anticipated reduction in automotive emissions could alter this picture appreciably. Studies indicate that the major contribution by jet aircraft to the pollution of the atmosphere occurs in the vicinity of commercial airports (ref. 1) where ambient pollution concentrations often equal or exceed those in the nearby industrial communities.

Exhaust emissions at the airport are mainly a function of the mode of operation of the aircraft (ref. 2), as shown in figure 1. The term emission index, grams of pollutant per kilogram of fuel burned (pounds of pollutant per 1000 pounds of fuel), is used instead of the volumetric concentration term, parts per million, in order to normalize emissions on the basis of fuel flow. During idling and taxiing, exhaust emissions consist primarily of carbon monoxide and unburned hydrocarbons; whereas, during take-off and landing, large amounts of smoke and oxides of nitrogen are formed. During cruise, the only significant pollutants are oxides of nitrogen.

Carbon monoxide is toxic, and prolonged exposure to ambient concentrations greater than 500 parts per million could affect the nervous system and ultimately lead to death. Unburned hydrocarbons combine with oxides of nitrogen in the presence of sunlight to form photochemical smog which is injurious to plants and human life and can cause severe visibility problems. Smoke, which consists largely of carbon particles, is not considered particularly harmful, but is objectionable from an aesthetic standpoint. In addition to these readily identifiable pollutants, the odor of exhaust gas is objectionable to many people.

In order to give a better understanding of the combustion process, particularly with respect to pollutant formation, a picture of a typical modern turbojet combustor is shown in figure 2. A diffuser is employed to reduce the velocity of the compressor-exit air and to build up static pressure. Often a snout or flow divider is used to assist in producing the desired airflow split. Fuel is injected through a pressure-atomizing nozzle and combustion is initiated and stabilized in the primary zone. The reaction in this zone is very intense and here most of the pollutants are formed. The remaining air is injected into

the combustor secondary zone through holes and slots and mixes with the hot gases to complete the combustion reaction and achieve the desired exit temperature profile. Air admission into the combustor is gradual; as a result, fuel-air ratios in the various zones of the combustor vary greatly.

SMOKE

Because smoke plumes from jet aircraft are readily visible and thus often become the targets of protests by angry citizens, the problem of smoke formation has received a great deal of attention in the past few years. Smoke consists of about 96 percent carbon and is the result of rich fuel-air mixtures in the primary zone of the combustor. Thus, the obvious approach toward reducing smoke formation would be to bring more air into contact with the fuel in the initial stages of the combustion process. This can be done by making the mixture in the primary zone leaner or by improving the mixing of fuel and air in the primary zone. As usual, there are disadvantages accompanying the use of these expedients and some of the necessary trade-offs are discussed later.

Smoke concentration in the exhaust gas is determined by a stained-filter technique whereby a metered volume of exhaust gas is passed through a paper filter and the carbon particles are deposited on the paper filter. The darkness of the stain, as determined by an optical densitometer and expressed as a smoke number, is a measure of the amount of smoke in the sample. As the smoke concentration increases, the smoke number increases.

At the present time, no reliable method exists for correlating smoke numbers as determined on the test stand with visibility of the smoke plume. Smoke-plume visibility depends on many factors, some of which are the size and numbers of the exhaust stacks, background and viewing angle, and wind conditions. However, as the result of a project sponsored by the Federal Aviation Administration, a tentative correlation between smoke number and plume visibility (fig. 3) suggests that for a nozzle diameter of 1 meter (3.3 feet) exhaust gases with smoke numbers above 25 are readily visible.

Considerable progress in smoke reduction has been made in the last few years, as shown in figure 4 and reference 3. The data shown for the P&W J57 engine are typical of those obtained from early combustors which were purposely designed with fuel-rich primary zones to improve the altitude relight characteristics of the engine. Lately, Pratt and Whitney Aircraft has succeeded in reducing the smoke level of the JT8D combustor to values below the visibility threshold by making the primary-zone mixture leaner. Similarly, more recent engines like the P&W JT9D and GE CF6 have been designed with fuel-lean primary zones to reduce smoke formation. The JT8D engine is the power plant of the Boeing 727, Boeing 737, and McDonnell Douglas DC-9 airplanes, and the JT9D and CF6 engines power the Boeing 747 and McDonnell Douglas DC-10

airplanes, respectively. Increased primary-zone airflow and increased mixing intensity are primarily responsible for the low smoke levels exhibited by the double-annulus and swirl-can combustors tested at the Lewis Research Center. These are full-scale short-length experimental combustors designed to perform at supersonic flight conditions. The experimental sector combustor, designed to study combustion at high pressures, also produces smoke numbers well below the visibility threshold. However, these experimental combustors exhibit poor altitude relight characteristics, and additional work would be required to improve their relight capabilities.

Although the problem of visible smoke seems to be well under control with modern engines, higher pressure ratio engines and higher flight speeds may reemphasize the problem. As shown by the curves for the J57 and the Lewis sector combustor (fig. 4), smoke formation increases greatly with an increase in combustor-inlet pressure. Research is being conducted at Lewis with experimental combustors operating at pressures as high as 25 atmospheres to study, among others, flame radiation and smoke problems. The data indicate that even in a well-designed combustor large amounts of smoke are formed in the primary zone, but that most of this smoke is burned in its passage through the flame zones. (See fig. 5.) Values for primary-zone smoke concentrations were computed from infrared spectral radiation measurements, whereas exhaust smoke concentrations were determined from actual measurements using the stained-filter technique.

Hydrocarbons and Carbon Monoxide

With regard to emissions of gaseous pollutants at the airport, the principal problem seems to be the emission of carbon monoxide and unburned hydrocarbons during the idling and taxiing modes. Combustion efficiency decreases rapidly with a decrease in fuel-air ratio, as shown in figure 6. During idling, typical overall fuel-air ratios are of the order of 0.007 to 0.008, and combustion efficiencies are quite low. Low combustor-inlet temperatures and pressures, lean primary-zone fuel-air ratios, and poor fuel atomization caused by low fuel flows are primarily responsible for the low combustion efficiencies at idle conditions. Some possible ways to improve idle efficiencies are as follows:

- (1) Improving fuel atomization with air-assist fuel nozzles
- (2) Increasing local primary-zone fuel-air ratios by
 - a. Using only alternate fuel nozzles
 - b. Using compressor bleed
 - c. Diverting some of the air away from the primary zone through mechanical controls or diffuser-wall bleed

Recent combustor tests at Lewis with air-assist fuel nozzles have shown significant increases in combustion efficiency as indicated in figure 6. These tests were conducted

with conventional dual-flow nozzles in which the secondary-flow passages were supplied with air from an auxiliary compressor to improve fuel atomization. Airflows less than 0.5 percent of the total combustor airflow and differential discharge pressures as low as 4 atmospheres were required for the air assist. Furthermore, with this mode of operation, normal dual-flow operation could be employed at all conditions other than idle.

Figures 7 and 8 show that the increases in combustion efficiency brought about by the air-assist fuel nozzles were accompanied by large reductions in hydrocarbon and carbon monoxide emissions. At a fuel-air ratio of 0.008, hydrocarbon emissions were reduced from 26 to 3 grams per kilogram of fuel (pounds per thousand pounds of fuel), whereas carbon monoxide emissions were reduced only slightly. However, at fuel-air ratios lower than 0.008 the reductions were more pronounced.

Attempts to increase local fuel-air ratios by operating only alternate fuel nozzles or by reducing airflow through the primary-zone swirlers did not increase combustion efficiencies for this particular combustor. However, there are indications that this mode of operation can bring about increases in combustion efficiency and hence decreases in pollutant emissions with other combustor designs. Tests are being planned to study the use of alternate fuel nozzles and of nozzle modifications under an existing research contract in which a double-annulus ram-induction combustor sector is being developed.

As stated previously, increases in local primary-zone fuel-air ratios could be effected by diverting a portion of the combustion air away from the primary zone through diffuser-wall bleed. A sketch of a typical combustor employing this principle is shown in figure 9. The combustor would be designed with a skewed inlet profile to give a fuel-rich primary zone at idle. Diffuser-wall bleed would then be employed at cruise and take-off to flatten the inlet profile and make the primary-zone mixture leaner. The bleed air could be used for turbine cooling or other uses. Diffuser tests conducted at Lewis have shown that the combustor-inlet airflow profile can be controlled through diffuser-wall bleed, and arrangements are being made to incorporate this principle into an experimental full-scale annular combustor being tested at Lewis. In addition to decreasing pollutant emissions at idle, this mode of operation could provide the fuel-rich primary zones required for good altitude relight capability. Since very little smoke is formed at idle, enrichening the primary-zone mixture should present no problem with smoke formation.

Oxides of Nitrogen

Emission of oxides of nitrogen is of importance only at take-off and cruise conditions. Formation of nitric oxide is the result of high-temperature combustion and reaches a maximum near stoichiometric fuel-air ratios. Fortunately, however, the reaction proceeds very slowly; hence, if the residence time of the reactants in the primary zone could

be shortened, substantial reductions in nitric oxide formation should occur. Work is being conducted at Lewis with an experimental combustor designed for operation at or near stoichiometric fuel-air ratios. This combustor is about 30 percent shorter than conventional combustors and, hence, for equal airflows, the residence time of the gases is considerably shorter. A comparison with a typical commercial combustor is presented in figure 10. The Lewis combustor is shorter in overall length and is made up of 120 discrete combustor elements featuring partial premixing of fuel and air. Although no fixed boundaries can be assigned to the primary zone in any combustor, it is reasonable to assume that the shorter overall length and the partial premixing of fuel and air does result in shorter residence times for the Lewis combustor.

Nitric oxide emission index data for the Lewis experimental combustor are shown in figure 11. For comparison purposes, the emission index for a single-can J57 installation is shown for a combustor-exit temperature of 1144°K (1600°F) which corresponds to that at take-off for the J57 engine. It can be seen that nitric oxide emissions for the short-length Lewis combustor are significantly lower at take-off (about 10 percent) than those for the J57 combustor. Even at maximum values, emissions from the Lewis combustor were about 30 percent lower than those from the J57 combustor. The decrease in nitric oxide emission index observed at the high combustor-exit temperatures can be attributed to the fact that nitric oxide contributions increased only slightly on a volumetric basis (parts per million), while fuel flows increased in direct proportion to the increases in combustor-exit temperatures.

Another source of pollutant emissions is the afterburner. Although it is generally acknowledged that jet-engine afterburners are potentially heavy polluters, very little research effort has been expended on this problem. Hydrocarbon and carbon monoxide emissions for an experimental afterburner tested at Lewis are shown in figures 12 and 13. Emission indices are based on the total fuel flow, including that of the main combustor. The solid symbols denote pollutant emissions obtained with the afterburner not in operation; the straight lines thus represent pollutant concentrations that would be obtained at a given fuel-air ratio if the afterburner contributed no pollutant emissions at all. Since all the data points are above these lines, it is obvious that the afterburner produced appreciable quantities of unburned hydrocarbons and carbon monoxide.

Emission indices for oxides of nitrogen are shown in figure 14. Again the solid line represents the contribution of the main combustor by itself. It can be seen that, within the limits of accuracy of the data, the afterburner did not produce significant amounts of nitric oxide. The generally low levels of nitric oxide production shown in the figure are probably the result of off-design operation of the preheater used to simulate operation of the main combustor.

SUMMARY

It has been shown that the major contribution of jet aircraft to atmospheric pollution occurs in the vicinity of commercial airports. During idling and taxiing, substantial amounts of unburned hydrocarbons and carbon monoxide are formed; whereas, during landing and take-off, emissions of smoke and oxides of nitrogen occur. Results obtained so far indicate that improvements can be made. Reductions in smoke levels from commercial engines have already been accomplished through the use of leaner mixtures in primary zones. In tests conducted at Lewis, substantial reductions in hydrocarbons and carbon monoxide emissions during idling have been realized with air-assist fuel nozzles. At simulated take-off conditions, emissions of oxides of nitrogen from the short-length Lewis combustor amounted to only about 10 percent of those from the longer commercial combustors.

These results strongly point out that in order to reduce pollutant emissions at all aircraft operating conditions, a number of compromises or trade-offs are necessary. For efficient combustion during idling and for good altitude relight capability, fuel-rich primary zones are required. Fuel-rich primary zones, however, lead to excessive smoke formation and possibly high concentrations of nitric oxide. Reductions in oxides of nitrogen can be brought about by reducing the residence time in the combustor primary zone. This expedient, however, could lead to increased carbon monoxide formation and to poor combustor-exit temperature profiles. A reasonable compromise could probably be effected by designing the combustor with a fuel-lean primary zone to reduce smoke formation and as short as possible from the standpoint of combustor-exit temperature distribution. To maintain high combustion efficiency and minimize emissions at idle, it would then be necessary to improve fuel atomization by using some sort of air-assist fuel nozzle. On the other hand, if the primary zone was designed purposely for rich fuel-air mixtures during idling, then some sort of mechanical control or diffuser-wall bleed could be employed to reduce emissions at take-off and cruise.

REFERENCES

1. Anon.: Nature and Control of Aircraft Engine Exhaust Emissions. Report of the Secretary of Health, Education, and Welfare to the U.S. Congress, Dec. 1968.
2. Bristol, C. W., Jr.: Gas Turbine Engine Emission Characteristics and Future Outlook. Conference on Aircraft and the Environment - Pt. 1, Soc. Automot. Eng., Inc., c.1971, pp. 84-92.
3. Grobman, Jack; Jones, Robert E.; Marek, Cecil J.; and Niedzwiecki, Richard W.: Combustion. Aircraft Propulsion, NASA SP-259, 1971, pp. 97-134.

EFFECT OF FUEL-AIR RATIO ON EXHAUST EMISSIONS OF A TYPICAL JET ENGINE

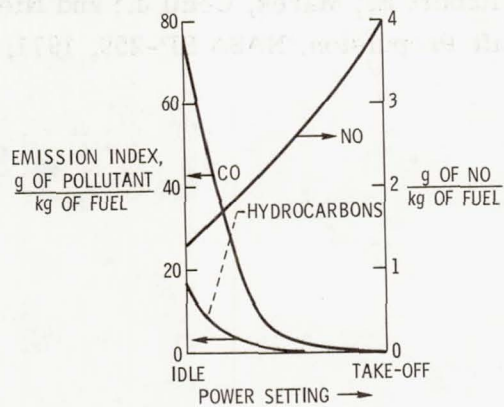


Figure 1

CONVENTIONAL ANNULAR COMBUSTOR

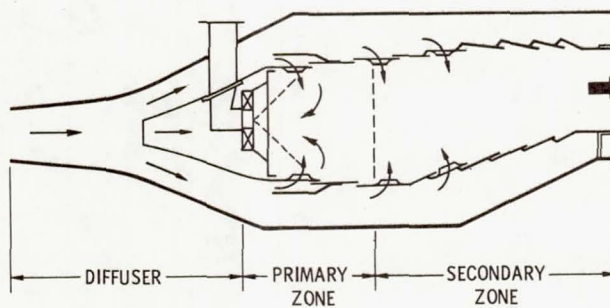


Figure 2

SMOKE-PLUME VISIBILITY VS SMOKE NUMBER

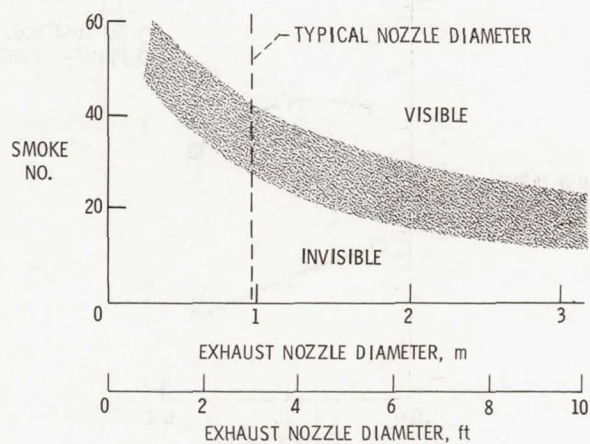


Figure 3

EFFECT OF PRESSURE ON SMOKE

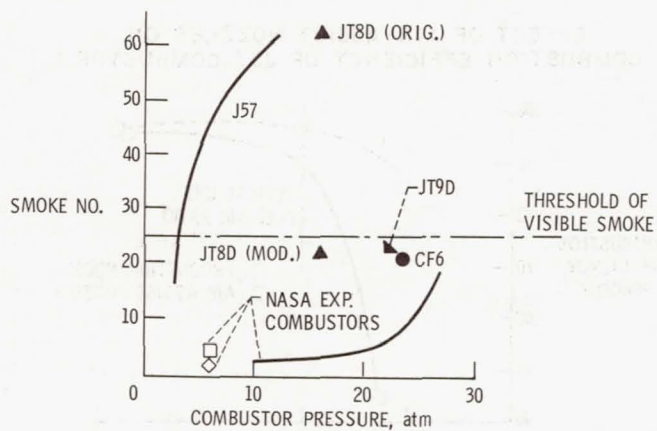


Figure 4

EFFECT OF FUEL-AIR RATIO ON SMOKE FORMATION

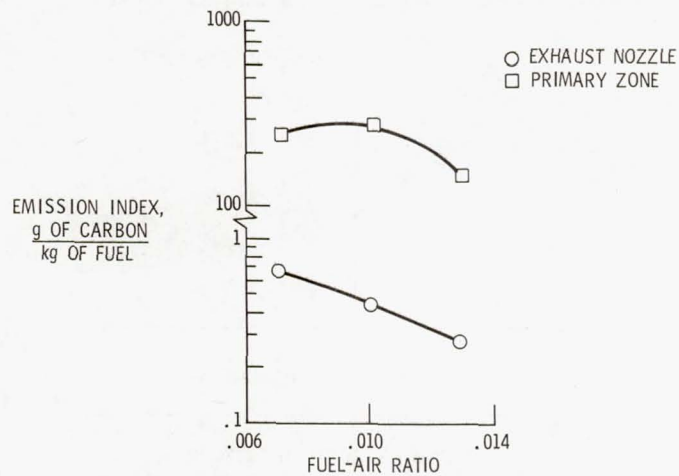


Figure 5

EFFECT OF AIR-ASSIST NOZZLES ON COMBUSTION EFFICIENCY OF J57 COMBUSTOR

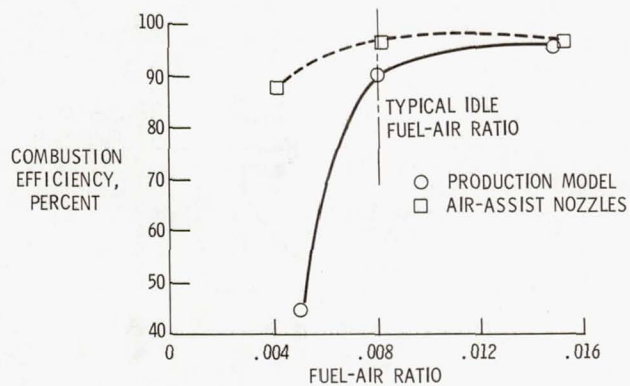


Figure 6

EFFECT OF AIR-ASSIST NOZZLES ON HYDROCARBON EMISSIONS OF J57 COMBUSTOR

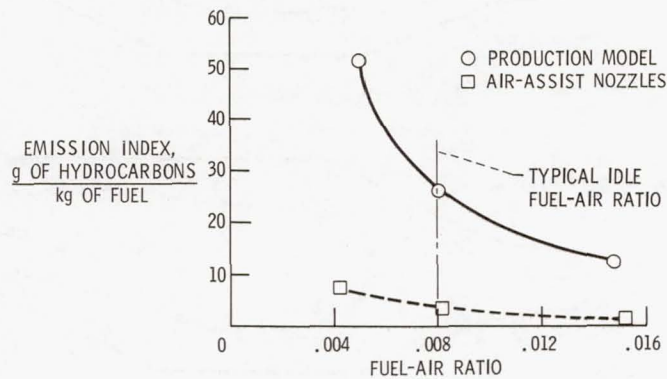


Figure 7

EFFECT OF AIR-ASSIST NOZZLES ON CARBON MONOXIDE EMISSIONS OF J57 COMBUSTOR

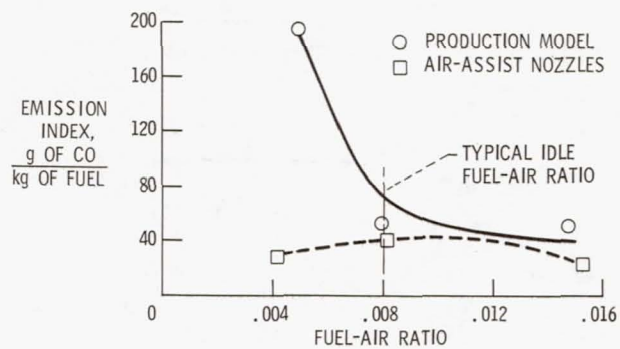


Figure 8

USE OF DIFFUSER-WALL BLEED TO CONTROL COMBUSTOR AIRFLOW DISTRIBUTION

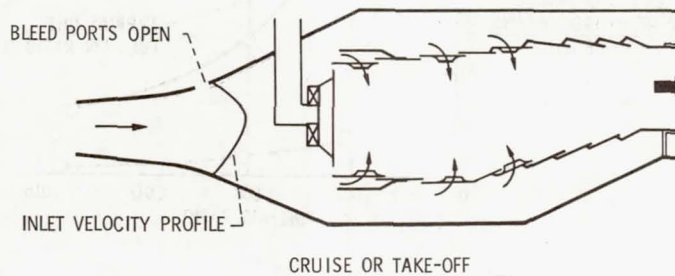
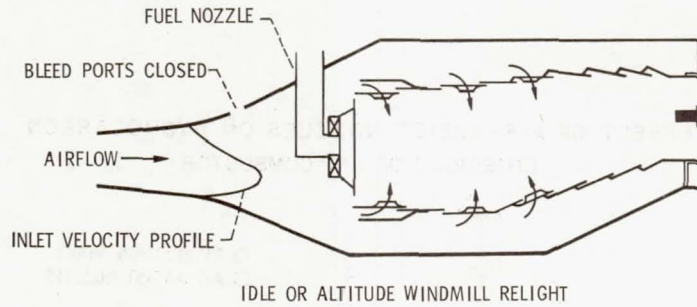


Figure 9

COMPARISON OF CONVENTIONAL AND LEWIS HIGH-TEMPERATURE COMBUSTORS

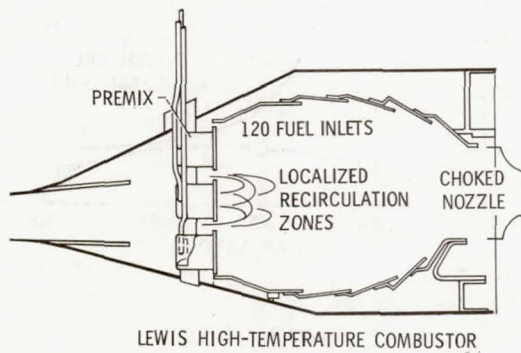
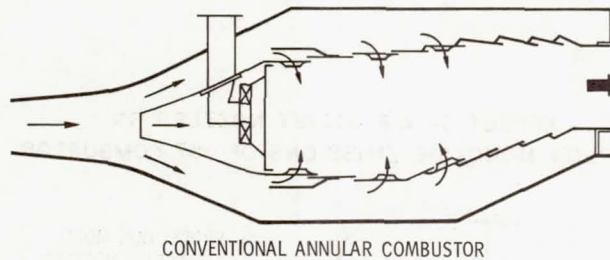


Figure 10

EFFECT OF COMBUSTOR-EXIT TEMPERATURE ON NITRIC OXIDE FORMATION

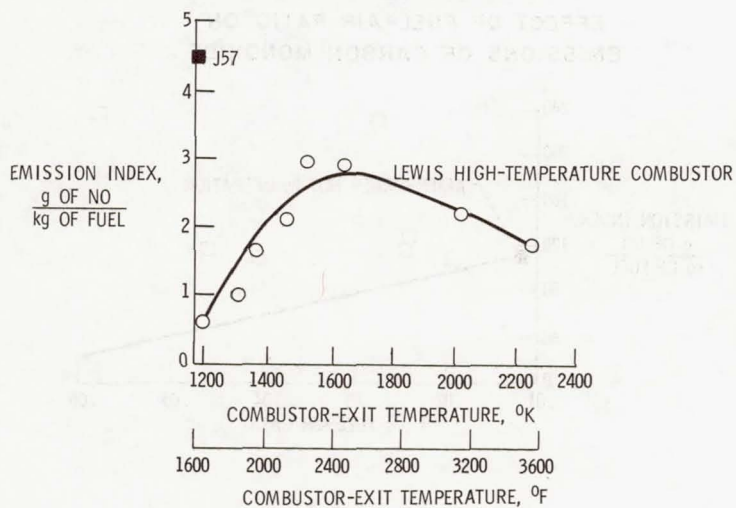


Figure 11

EFFECT OF FUEL-AIR RATIO ON EMISSIONS OF HYDROCARBONS

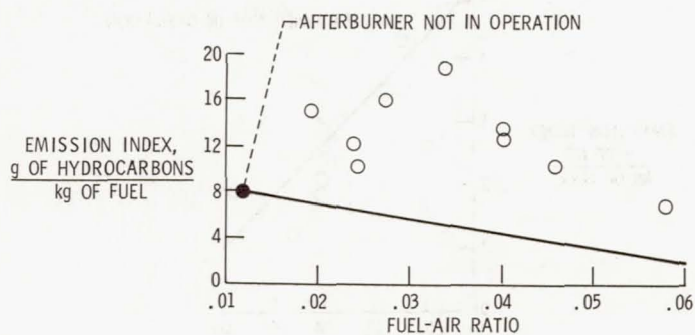


Figure 12

EFFECT OF FUEL-AIR RATIO ON EMISSIONS OF CARBON MONOXIDE

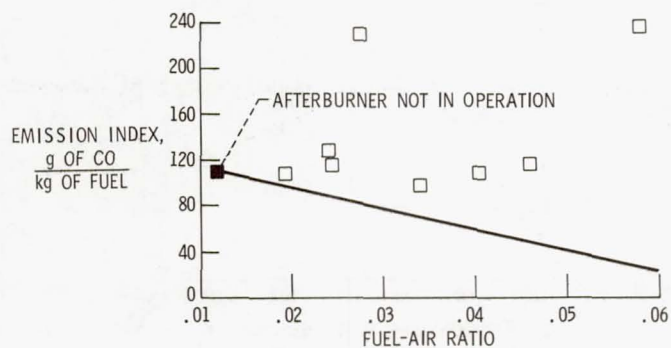


Figure 13

EFFECT OF FUEL-AIR RATIO ON EMISSIONS OF NITRIC OXIDE

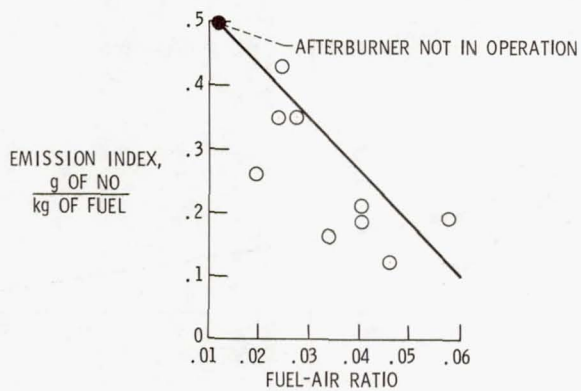


Figure 14

TRENDS IN NOISE CONTROL FOR AIRCRAFT GAS-TURBINE POWER PLANTS

By David Chestnutt and Harvey H. Hubbard
Langley Research Center

and

Charles E. Feiler
Lewis Research Center

INTRODUCTION

Gas-turbine power plants are used in many conventional, vertical, and short take-off and landing vehicles and general-aviation vehicles. Control of noise from such power plants is necessary for the purpose of reducing annoyance during take-off and landing operations near airports. The purpose of this paper is to identify and categorize the sources of noise and to describe current research and development activities relating to noise reduction. In order to meet the varied propulsion requirements of aircraft, gas-turbine engines have developed along the lines indicated in the sketches of figure 1.

The turbojet engine in the upper left is characterized by its high velocity jet exhaust. The resulting noise spectrum contains strong broadband noise components due to jet mixing and some relatively less intense discrete-frequency components or tones which are generated by the rotating components of the engines. These tones are represented by the vertical lines. The turbofan engine has lower exhaust velocities and generally larger rotating machinery components. The resulting noise spectrum contains relatively strong discrete-frequency components in the high frequency range. The next sketch represents one of several possible configurations of an integrated propulsion-lift system. In addition to noise from the engine itself, there may be a significant contribution of noise from the interaction effects of the jet flows and the flow turning devices. The resulting noise spectrum will contain significant broadband and discrete-frequency components. A distinguishing feature of the noise spectrum is that substantial low-frequency components are anticipated. The turboshaft engine has relatively low-level broadband noise components and relatively intense discrete-frequency components which are associated with the driven rotor or propeller. The noise spectrum is characterized by relatively strong low-frequency components.

Each of these types of power plants has several noise-generating components and some of them are common to more than one type of power plant. The significant noise sources are jet exhausts, fans, high-lift devices, and propellers and unducted rotors. In

research work it is convenient to study them separately in order to identify the noise-generating mechanisms, to evaluate the effects of various operating conditions, and to devise noise-control concepts. Therefore, in this paper they are discussed separately.

JET EXHAUST NOISE

The manner in which jet exhaust noise varies with jet velocity is illustrated in figure 2. The shaded area encompasses many jet nozzle and engine measurements for a wide range of exhaust velocities, as illustrated in detail in references 1 and 2. These data have been normalized with respect to the same thrust. A reduction in exhaust velocity is a very powerful factor in reducing the jet exhaust noise; this factor was a basis for the development of the bypass engine. An increasing bypass ratio, as suggested by the sketches at the top of the figure, is associated with lower average jet velocities. Turbojet engines generally operate at exhaust velocities from near 900 m/sec (3000 ft/sec) (with afterburner) down to about 460 m/sec (1500 ft/sec). Current turbofan engines with bypass ratios up to 8 have average jet velocities of about 240 m/sec (800 ft/sec). The jet noise at this lower velocity includes significant contributions from both fan exhaust and the jet core exhaust. Future engines may operate with bypass ratios of about 25 and jet velocities on the order of 90 m/sec (300 ft/sec). For these engines, the fan exhaust jet noise may dominate. However, the rate of noise reduction with velocity decreases markedly in the lower velocity range. Special tests have suggested that the noise in this low velocity region is substantially higher than can be ascribed to the jet mixing alone, which is indicated by the dashed line. The noise level differences between the dashed line and the shaded area are believed to be related to noise-generating mechanisms inside the engine and thus represent the potential for internal noise suppression. Effective noise-suppression devices are anticipated to be required for high-bypass-ratio power plants. On the other hand, in the very high velocity range, representative of turbojet operating conditions, noise suppression devices which have been shown to be most effective are those which affect the jet mixing and are external to the engine.

FAN NOISE

Discrete-Frequency Noise Sources and Treatment Areas

Shown in figure 3 are cutaway views of a proposed advanced engine which incorporates noise-reduction concepts (ref. 2). The top view is a general layout of the engine which serves to identify the major discrete-frequency noise sources, which are the fan, compressor, and turbine sections of the engine. One of the design features to minimize noise is generous clearances between the rotating and stationary stages and the use of a single-stage fan. In addition, the engine is designed in such a way as to make acoustic

treatment most effective. Provision is made for an extended inlet cowl, inlet splitter rings, and low-aspect-ratio fan discharge ducts. The dark areas of the bottom sketch indicate possible regions for the application of acoustic treatment.

Effects of Fan Pressure Ratio

One of the main noise-generating components of such advanced engines will be the large single-stage fan for which data are presented in figure 4. (See refs. 2 and 3.) In this figure, relative perceived noise levels (PNL) are plotted as a function of fan pressure ratio. The top hatched area has been estimated based on large-scale advanced-technology-research fan models tested at the Lewis Research Center. Also shown are measured data from turbofan engines, a lift fan, and a prop-fan. All data have been normalized with respect to the same thrust level and distance. These data generally follow the trend of the predictions. It is significant to note that the fan noise levels decrease as a function of fan pressure ratio. This decrease is brought about in part by the application of lower blade-loading and lower tip-speed factors in the design at the lower pressure ratios. Lower fan jet velocities are associated with the lower fan pressure ratios. The bottom hatched region indicates the estimated fan noise levels after acoustic treatment of the type just described has been applied (refs. 2, 4, and 5). At the higher fan pressure ratios, the addition of treatment results in noise reductions on the order of 15 PNdB. Treatment is also effective at the lower fan pressure ratios; however, the anticipated noise reductions are relatively less due to geometric and weight constraints.

Effects of Inlet Flow Choking

If noise reductions beyond those shown are needed, the use of a choked inlet is indicated for the forward radiated fan noise. Various schemes for flow choking have been studied. (See ref. 6.) However, the concept of using variable-geometry vanes seems to offer the most promise. Figure 5 shows some vane arrangements that may be useful for choking the inlet flow when large noise reductions are required. The arrangements at the top of the figure represent inlet guide vanes in the unchoked-flow mode, whereas those at the bottom represent the choked-flow mode. Shown at the lower left is a mode in which every other guide vane is rotated to produce choked-flow zones at the leading and trailing edges. The choked-flow zones are shown as irregular lines. The arrangement in the center accomplishes the required area reduction by having every other vane translated to create the choked-flow zones as shown. The arrangement on the right operates in a similar manner except that uncambered airfoil shapes are involved.

These devices have been tested as scale models at the Langley Research Center and have shown excellent acoustic properties as indicated in figure 6. Relative noise level is plotted as a function of estimated center-line throat Mach number M_t . PR denotes pressure-recovery values. It should be noted that there are some localized choked-flow

regions in the flow, even at the lower center-line Mach numbers. These choked-flow regions expand as center-line Mach number increases until complete choking occurs at Mach 1. Noise reductions vary from a few decibels for the partial choking conditions to in excess of 40 dB for complete choking. On the basis of maximum noise reduction obtainable, the uncambered airfoil arrangement is superior. On the other hand, the cambered devices give greater noise reductions at intermediate center-line Mach numbers. Also of concern is the aerodynamic performance. All these vane devices introduce some aerodynamic losses. However, the uncambered vanes produce the highest pressure recoveries in the fully choked condition. In the unchoked-flow configuration all these devices have pressure recoveries in excess of 96 percent and, hence, it is obvious that variable-geometry mechanisms are required.

NOISE FROM HIGH-LIFT DEVICES

In consideration of the noise from high-lift devices, all factors so far discussed are significant and the additional factor of the flow turning device itself must also be considered. Some of the concepts that have been proposed for short take-off and landing (STOL) vehicles are indicated schematically in figure 7. (See ref. 7.) In the externally blown jet flap arrangement the engine exhaust is directed toward a flap system which turns the flow downward. In the internally blown jet flap arrangement, the secondary flow from the fan is ducted through an orifice near sonic velocity at the wing trailing edge and over a turning flap. A similar system is used for the augmentor wing except that an augmentor flap system is involved. The turning of the flow involves impingement of the fan exhaust in various ways on the flap surfaces. Studies are underway to evaluate the best way to turn the flow from a noise standpoint and some of the initial results from representative models are shown in figure 8. (See ref. 8.)

Relative noise levels are plotted as a function of nozzle pressure ratio. The solid curve is for the externally blown flap model, the dashed curve for the augmentor wing model, and the lower curve for the internally blown flap model. The internally blown flap model has the best noise characteristics. The augmentor wing has relatively higher noise levels although other tests have shown that its noise characteristics can be improved by means of flap acoustic treatment. The externally blown flap arrangement may require flap acoustic treatment or very low fan pressure ratios or both.

PROPELLER AND UNDUCTED ROTOR NOISE

Noise levels are shown in figure 9 as a function of rotor tip speed for constant thrust. (See refs. 9 and 10.) These data apply directly to helicopter rotors but are qualitatively applicable to other similar devices as well. The most obvious result is that

noise is a function of tip speed. There is also an orderly trend with regard to the spectral content of the noise. Both broadband and discrete-frequency components reduce in amplitude as tip speed is reduced, but the discrete-frequency noise reduces at a faster rate. The net result is a predominately discrete-frequency noise spectrum at high speeds and a broadband noise spectrum at low speeds. In addition to the obvious beneficial tip-speed effects, other significant noise-reduction factors are categorized according to the sources of the noise as follows:

Steady loads

Thinner blades

More blades

Periodic loads

More uniform inflow

Minimize blade-tip—vortex interaction

Minimize cyclic loading

Nonperiodic loads

Smoother airfoils

Minimize turbulent inflow

Minimize separated flow

These sources are noted at the various tip-speed ranges in figure 9.

For instance, in the very high tip-speed range (near sonic speeds), steady blade loads are the dominant noise source, and noise may be reduced by the addition of more blades and the use of thinner blade sections. In the intermediate speed range, where the periodic loads dominate, it is important for noise reduction to minimize all cyclic loading effects, particularly those associated with blade vortex interaction and nonuniform inflow. At the very low tip speeds, the nonperiodic loads associated with viscosity of the air are the important sources of noise. Measures which result in smoother airfoil surfaces, low turbulence inflows, and unseparated flows are significant for reduced noise.

CONCLUDING REMARKS

Attempts have been made to identify the main sources of noise in various types of gas-turbine power plants and to indicate the state of the art in noise reduction. Useful trends in design and operation have been summarized for such noise sources as jet exhausts, fans, high-lift devices, and unducted rotors. A significant result is that lower noise levels generally are associated with lower velocities and lower pressure ratios.

REFERENCES

1. Bushell, K. W.: A Survey of Low Velocity and Coaxial Jet Noise With Application to Jet Prediction. Symposium on Aerodynamic Noise, Loughborough Univ. of Technol. (England), Sept. 1970.
2. Kramer, James J.; Chestnutt, David; Krejsa, Eugene A.; Lucas, James G.; and Rice, Edward J.: Noise Reduction. Aircraft Propulsion, NASA SP-259, 1971, pp. 169-209.
3. Metzger, F. B.; and Ganger, T. G.: Results of Initial Prop-Fan Model Acoustic Testing. Vol. I - Discussion. HSER 5787, Vol. I, United Aircraft Corp., Dec. 4, 1970. (Available as NASA CR-111842.)
4. Anon.: Progress of NASA Research Relating to Noise Alleviation of Large Subsonic Jet Aircraft. NASA SP-189, 1968.
5. Anon.: Proceedings of the Aircraft Noise Symposium - Acoustical Duct Treatments for Aircraft. J. Acoust. Soc. Amer., vol. 48, no. 3, pt. 3, Sept. 1970, pp. 779-842.
6. Chestnutt, David: Noise Reduction by Means of Inlet-Guide-Vane Choking in an Axial-Flow Compressor. NASA TN D-4682, 1968.
7. Loftin, Laurence K., Jr.; and McKinney, Marion O., Jr.: NASA Aerodynamic Research Applicable to Business Aircraft. [Preprint] 710378, Soc. Automot. Eng., Mar. 1971.
8. Maglieri, Domenic J.; and Hubbard, Harvey H.: Preliminary Measurements of the Noise Characteristics of Some Jet-Augmented-Flap Configurations. NASA MEMO 12-4-58L, 1959.
9. Wright, S. E.: Sound Radiation From a Lifting Rotor Generated by Asymmetric Disk Loading. J. Sound Vib., vol. 9, no. 2, Mar. 1969, pp. 223-240.
10. Schlegel, Ronald; King, Robert; and Mull, Harold: Helicopter Rotor Noise Generation and Propagation. USAAVLABS Tech. Rep. 66-4, U.S. Army, Oct. 1966.

GAS-TURBINE-ENGINE NOISE CHARACTERISTICS

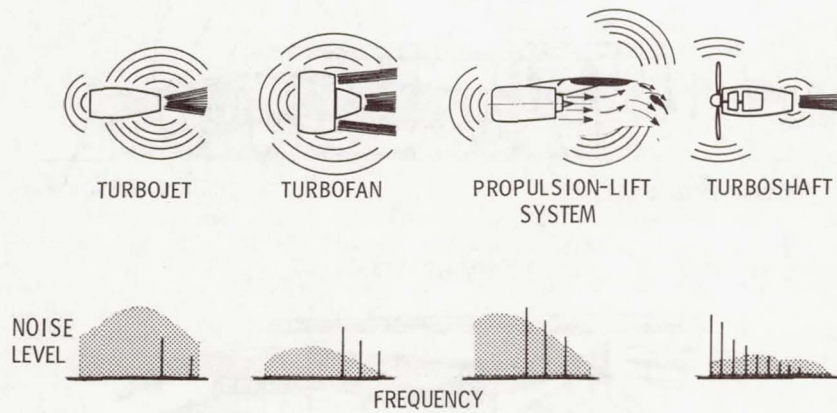


Figure 1

EFFECTS OF JET EXHAUST VELOCITY

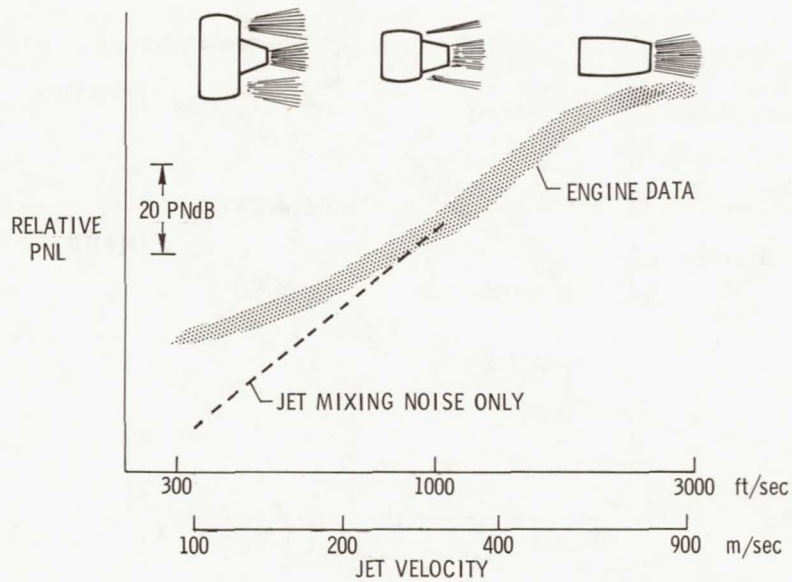


Figure 2

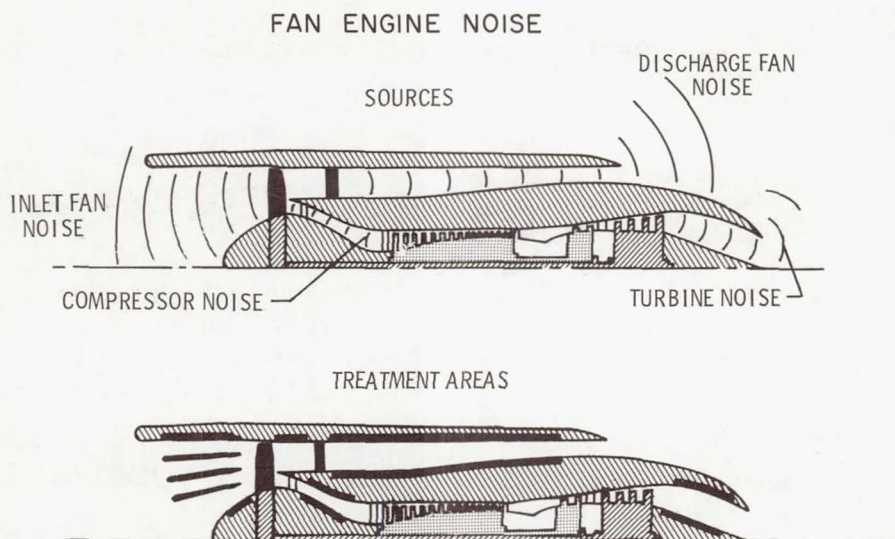


Figure 3

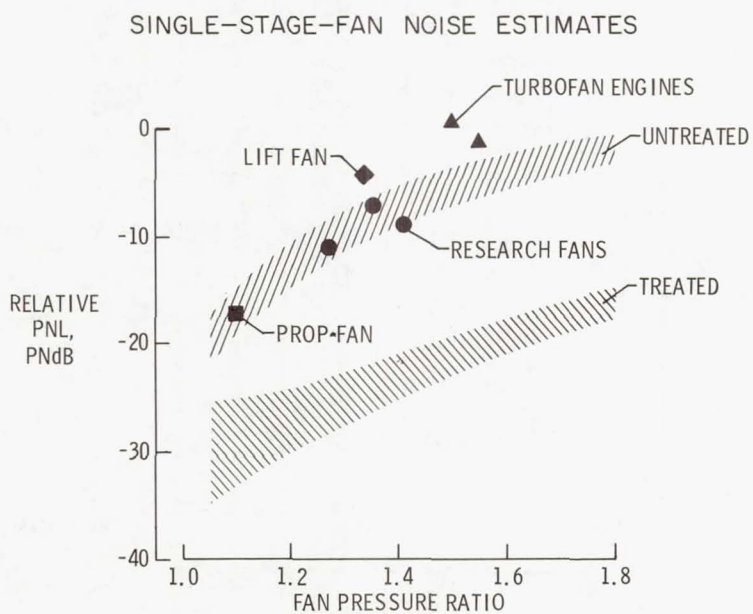


Figure 4

INLET-FLOW-CHOKING MECHANISMS

UNCHOKED-FLOW MODE



CHOKED-FLOW MODE

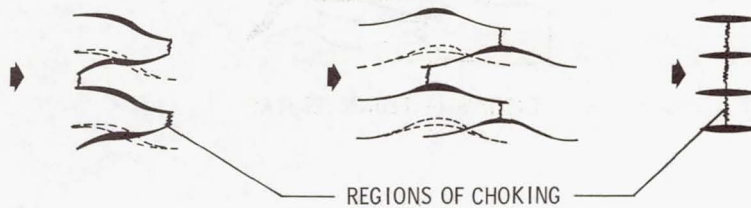


Figure 5

PERFORMANCE OF CHOKED-FLOW MECHANISMS

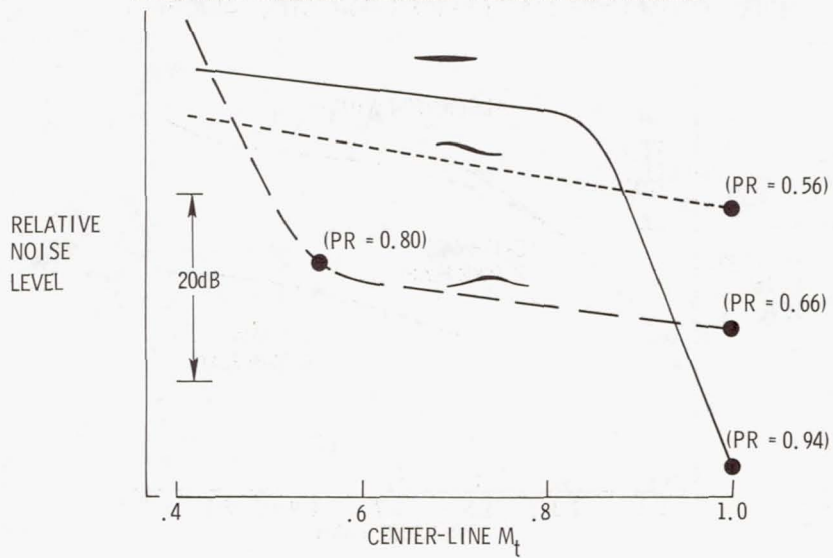


Figure 6

JET FLAP CONCEPTS

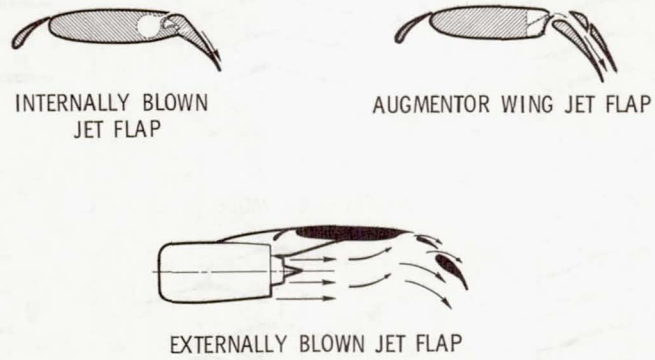


Figure 7

NOISE FROM HIGH-LIFT DEVICES FOR STOL AIRCRAFT

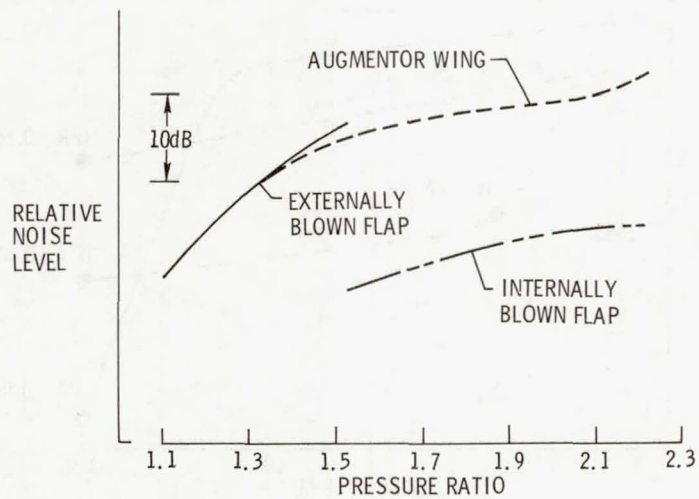


Figure 8

UNDUCTED-ROTOR NOISE ESTIMATES
CONSTANT THRUST

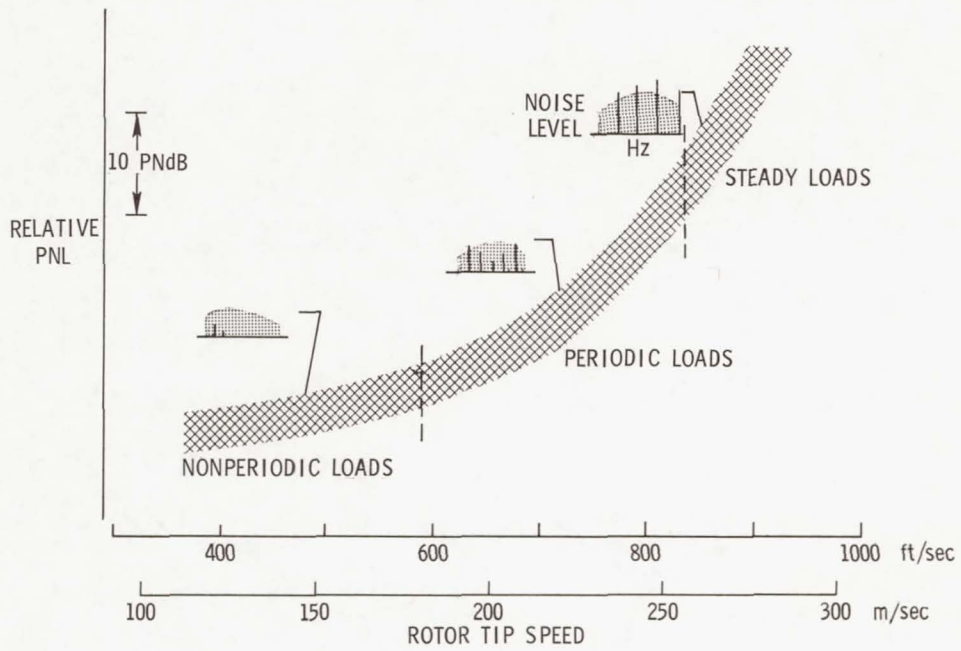


Figure 9

Page intentionally left blank

EVALUATION OF MEASURES OF AIRCRAFT NOISE

By Philip M. Edge, Jr., Randall M. Chambers,
and Harvey H. Hubbard
Langley Research Center

INTRODUCTION

One of the aspects of the aircraft noise problem that has involved a substantial amount of research work in recent years is the development of measurement units to represent properly human responses to aircraft noise. The purpose of this paper is to present a status report on this work.

The needs for such measurement units are as follows. Accurate units are desired for use in the systematic design of quieter aircraft to meet noise specifications and in various aspects of aircraft noise certification. Units which are simple in concept and easy to use are needed in connection with the prediction of community annoyance and complaint patterns, land use planning near airports, and airport traffic monitoring and control. It is, of course, desirable to have one measurement unit that would be adequate to fill all these needs.

In figure 1 are indicated the nature of the airport noise problem in communities near airports and the significant factors in noise-induced responses. Noise is a problem because of the low-altitude operations of aircraft in landing approach and in take-off and climbout operations. Of particular significance are the psychophysiological characteristics of people which are significant in their responses to noise, as well as the physical characteristics of the aircraft noise stimuli. Also of importance in most cases are such factors as the nature of the airport traffic, including the use of preferential runways, the mix of aircraft types, and flight scheduling; and community environment considerations, including background noise levels, economic factors, and types of community activities.

HUMAN RESPONSES TO NOISE

It is known that a person may respond to noise in various ways as indicated in figure 2. Such responses as subjective annoyance, speech interference, sleep interference, degradation of task performance, and hearing loss are identified, and the significant ranges of noise level for each response are indicated. (See ref. 1.) One of the obvious results from such response studies is the wide variation among people in the way each responds to noise. This accounts at least in part for the wide range of significant levels. All these responses may be important in real life. Each has been studied separately in laboratory situations and, as a result, subjective annoyance responses are judged to be of

particular importance in airport community situations. The measurement units discussed in the remainder of the paper are those which relate to subjective annoyance and which include considerations of the physical characteristics of the noise and the psycho-physiological characteristics of people.

SUBJECTIVE TESTING PROCEDURES

In the development of subjective annoyance units, studies to date have been limited to a few test situations where the environment could be controlled. One example situation is shown in the photograph in figure 3, which was taken in a laboratory of Bolt Beranek and Newman, Inc. (See refs. 2, 3, and 4.) This is a small anechoic room having wall treatment such that echoes are eliminated. A loudspeaker system is provided for playback of aircraft noise signals, and the people are arranged in a manner suitable for obtaining comparative subjective judgments of the noises. The advantage of such an experimental setup is that many of the factors in the tests are under very close control. The disadvantage, however, is that the environment for the subjects is lacking in realism.

Another type of study is illustrated by the photographs in figures 4 and 5. Figure 4 shows one of the test sites of the Moses Lake flyover experiments involving Boeing 707 airplanes. (See ref. 5.) A standard Boeing 707 airplane was compared with a similar airplane modified to reduce its approach noise levels by means of nacelle acoustic treatments. Subjects were grouped both outdoors under awnings and inside of house trailers for purposes of making subjective judgments.

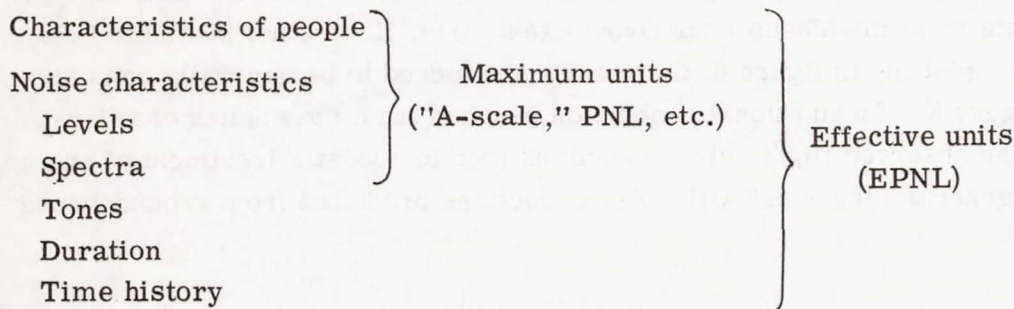
Figure 5 shows the test setup for similar studies at the NASA Wallops Station. (See ref. 6.) For these studies about a dozen different aircraft, including helicopters, were used, and juries of subjects were located both outside and inside resident-type structures for subjective reaction studies. Although it is realized that such studies as those illustrated in figures 4 and 5 do not completely represent real-life situations, they are more realistic than those of figure 3.

TYPES OF MEASUREMENT UNITS

Two general types of annoyance measurement units for flyover noise exposure are illustrated in figure 6. The noise exposure consists of a transient signal which varies in noise level as a function of time in a manner suggested by the curves in the figure. The two types of units are characterized as maximum units and effective units. The maximum units are determined with the aid of a filter with appropriate weighting features plus a direct-reading meter. The function of the filter is to provide an appropriate frequency weighting to represent the annoyance value of the noise. The significant meter reading is the maximum value. With regard to the effective units the significant values are

determined by a more sophisticated data analysis which is performed by a computer and takes into account the significant features of the entire time-history exposure.

These noise evaluation units can be further categorized as follows:



The maximum units include such units as "A-scale" and PNL (perceived noise levels), which along with about 10 other similar units can be properly filtered by a frequency-weighting network. These units are designed to account for the psychophysiological responses of people to noise and to account for such features of the noise as levels and spectral content.

The effective units, on the other hand, are designed in such a way as to account for such additional features of the noise as its tone content, the duration of exposure, and other aspects of its time history. An example of such effective units is the EPNL (effective perceived noise level). In studies to date about 2 or 3 dozen different effective units have been evaluated and these, in general, are related to the basic concept of effective perceived noise level.

EVALUATION OF MEASUREMENT UNITS

In order to evaluate the two types of measurement units, the results of a number of recent studies are summarized in figures 7 and 8. (See refs. 3 and 5 to 10.) Data from a number of different studies, as indicated by the letters A to E, are included in figure 7 for both maximum units and effective units. Each of the symbols represents the results of a separate evaluation test of a particular measurement unit. For each of these tests hundreds, or sometimes thousands, of judgments were made and the results were identified with a standard-deviation value. If perfect agreement had been obtained between the judgment data and the predictions based on physical measurements of the noise signal, the data points would be on the zero line. Obviously, perfect agreement was not obtained for any of the units studied. The units for which large standard deviations were obtained are of little interest because of their obvious inaccuracies. The units for which the smallest standard deviations were obtained are the ones of greatest interest. It can be seen, in general, that the best effective units are more accurate than the best maximum units.

Similar data from flyover studies are shown in figure 8. (See ref. 11.) The data are presented in the same format except that results are included for both indoor and outdoor observer situations. These data, which were obtained in the Wallops Station flyover studies, are in general agreement with those of figure 7, and the accuracies are comparable. Although data from the Moses Lake flyover tests (ref. 12) are not available in a form convenient for plotting in figure 8, the results are judged to be generally consistent with the data in figure 8. An additional conclusion reached from the studies of reference 12 was that the observed flight noise reductions (due to acoustic treatment of engine nacelles) were in general agreement with noise reductions predicted from ground-based measurements.

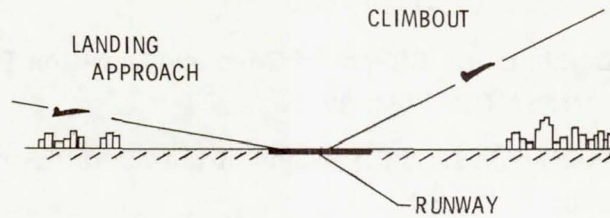
CONCLUDING REMARKS

Recent studies to evaluate noise measurement units have been summarized and the general status of units categorized as maximum and effective has been discussed. It is indicated that maximum units are simple in concept, simple to use, and require a minimum of electronic equipment for measurement and analyses. They are thus judged to be adequate for most planning and monitoring functions regarding noise around airports. The effective units, on the other hand, are noted to be more sophisticated in concept and more cumbersome to use. The electronic equipment involved is more sophisticated, bulkier, costlier, and requires expert operators. Effective units have important use in the development and design of quieter aircraft and in the noise certification of aircraft.

REFERENCES

1. Kryter, Karl D.: The Effects of Noise on Man. Academic Press, Inc., 1970.
2. Pearsons, Karl S.; Horonjeff, Richard D.; and Bishop, Dwight E.: The Noisiness of Tones Plus Noise. NASA CR-1117, 1968.
3. Pearsons, Karl S.: Combination Effects of Tone and Duration Parameters on Perceived Noisiness. NASA CR-1283, 1969.
4. Fidell, Sanford; and Pearsons, Karl S.: Study of the Audibility of Impulsive Sounds. NASA CR-1598, 1970.
5. Little, J. W.; and Mabry, J. E.: Empirical Comparisons of Calculation Procedures for Estimating Annoyance of Jet Aircraft Flyovers. J. Sound Vib., vol. 10, no. 1, July 1969, pp. 71-80.
6. Kryter, K. D.; Johnson, P. J.; and Young, J. R.: Judgment Tests of Flyover Noise From Various Aircraft. NASA CR-1635, 1970.
7. Hinterkeuser, Ernest G.; and Sternfeld, Harry, Jr.: Subjective Response to Synthesized Flight Noise Signatures of Several Types of V/STOL Aircraft. NASA CR-1118, 1968.
8. Hecker, Michael H. L.; and Kryter, Karl D.: Comparisons Between Subjective Ratings of Aircraft Noise and Various Objective Measures. Tech. Rep. NO-68-33, FAA, Apr. 1968.
9. Ollerhead, J. B.: Subjective Evaluation of General Aviation Aircraft Noise. Tech. Rep. NO-68-35, FAA, Apr. 1968.
10. Young, J. R.: Attenuation of Aircraft Noise by Wood-Sided and Brick-Veneered Frame Houses. NASA CR-1637, 1970.
11. Kryter, K. D.: Possible Modifications to the Calculation of Perceived Noisiness. NASA CR-1636, 1970.
12. Boeing Co.: Study and Development of Turbofan Nacelle Modifications To Minimize Fan-Compressor Noise Radiation. Vol. VII - Subjective Evaluation Tests. NASA CR-1717, 1971.

FACTORS IN AIRPORT COMMUNITY NOISE



- CHARACTERISTICS OF PEOPLE
- AIRCRAFT NOISE CHARACTERISTICS
- AIRPORT TRAFFIC
- COMMUNITY ENVIRONMENT

Figure 1

RESPONSES OF PEOPLE TO AIRCRAFT NOISE

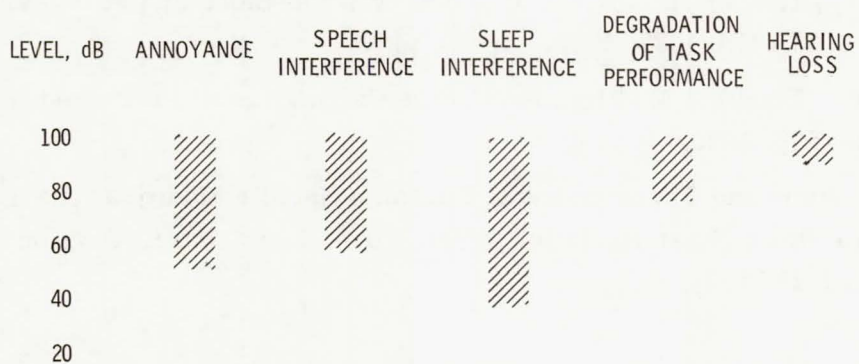


Figure 2

LABORATORY TEST SETUP



Figure 3

MOSES LAKE FLYOVER TEST SETUP



Figure 4

WALLOPS FLYOVER TEST SETUP



Figure 5

TYPES OF MEASURES FOR AIRCRAFT FLYOVER NOISE

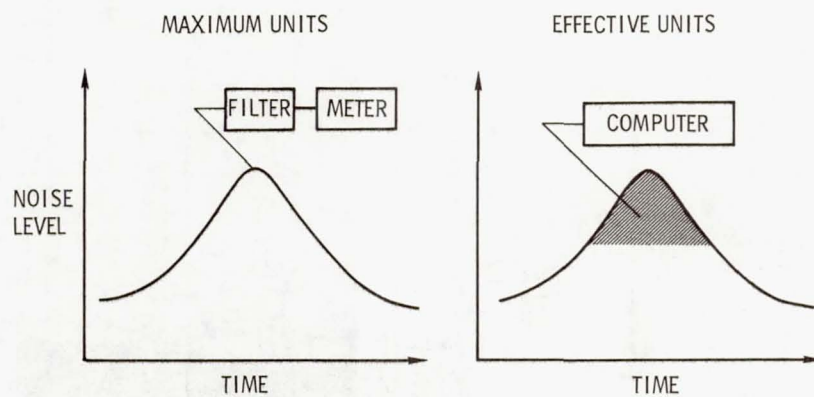


Figure 6

RESULTS OF LABORATORY STUDIES

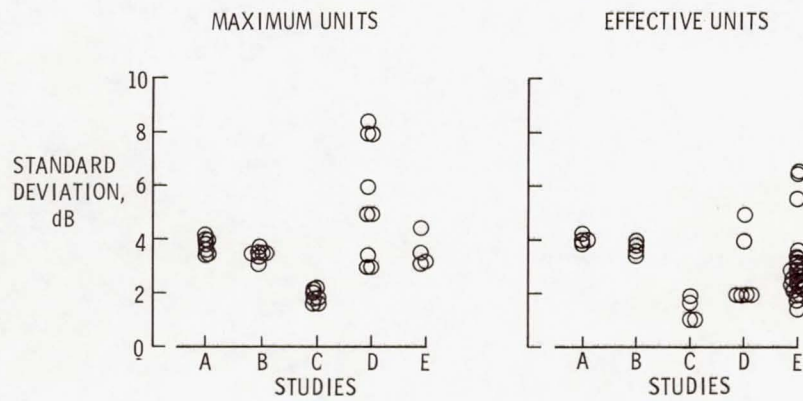


Figure 7

RESULTS OF WALLOPS FLYOVER STUDIES

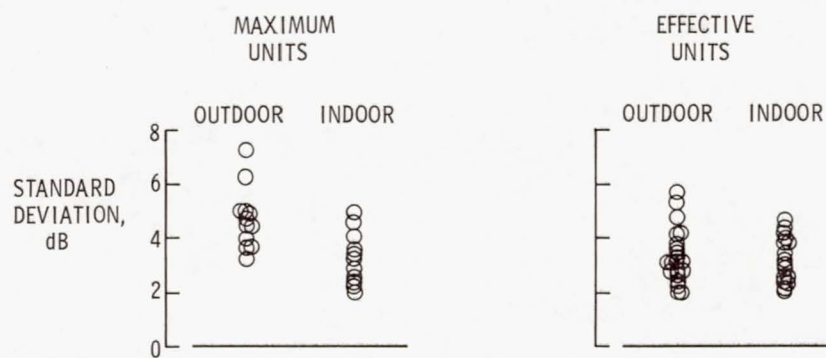


Figure 8

Page intentionally left blank

STATUS OF STUDIES ON SONIC BOOM

By Domenic J. Maglieri and Harry L. Carlson
Langley Research Center

and

Norman J. McLeod
Flight Research Center

INTRODUCTION

At the last conference on Aircraft Operating Problems, information regarding sonic-boom phenomena associated with supersonic flight was presented in references 1 and 2. Figure 1 (used in ref. 2) seems appropriate to serve as an introduction to the present material. Shown schematically in the figure is an airplane flight track extending from subsonic to supersonic speeds. Beneath the flight track are shown sketches of the shock-wave impingement patterns and the associated distributions of N-wave pressures, both along the track and perpendicular to it. In references 1 and 2, information was presented regarding the state of knowledge of the sonic-boom phenomena dealing with the ontrack and lateral ground exposures during steady flight for quiescent atmosphere conditions, the effects of atmospheric dynamics on bringing about sonic-boom-signature variations, and the pressure buildups resulting from accelerated flight.

The purpose of this paper is to present results from recent experiments which update the existing information relative to supersonic operations and broaden the flight regimes under study to include operations at hypersonic speeds and low supersonic speeds as illustrated in figure 2. The significant factors which affect the sonic boom include airplane design, which involves weight, size, and volume and lift distributions; airplane operations, which involve altitude, Mach number, and flight path; and the atmosphere, which involves pressure, temperature, and wind gradients and turbulence. Discussions of the effects of each of these factors as they relate to the three operating regimes shown in figure 2, are presented.

SYMBOLS

a	sound speed gradient
d	width of sonic-boom pattern on ground (or total lateral extent of boom)
I_{pos}	positive impulse of sonic-boom ground pressure signature

M	Mach number
Δp	sonic-boom overpressure
T	period of N-wave signature
V	airplane velocity
τ	rise time of N-wave

Subscripts:

calc calculated

meas measured

g ground

SONIC-BOOM EXPOSURES FOR STEADY FLIGHT AND A STEADY ATMOSPHERE

Ontrack Measurements

Presented in figure 3 are the sonic-boom overpressures (associated with the N-wave shape signature shown in the sketches) as a function of airplane altitude for a number of airplanes including a fighter, a bomber, a supersonic transport, and a hypersonic transport. The experimental points obtained from overflights of the Lockheed F-104, Convair B-58, and XB-70 airplanes (ref. 3) represent averages of a large number of measurements. The shaded areas represent the predicted and estimated nominal values based on current theory, a standard atmosphere with no wind being assumed. The results given in figure 3 indicate that the overpressure decreases with increasing altitude and with decreasing airplane size. Good agreement exists between theory and experiment for a wide range of airplanes and operating conditions. The estimated levels for the hypersonic airplane are thought to be reasonable even though the theory is being extended beyond the current state of the art (ref. 4) where experimental verification is not available.

Lateral-Spread Measurements

The data in figure 4 relate to lateral-spread measurements from the XB-70 airplane at two altitudes and two Mach numbers. (See ref. 3.) The sonic-boom overpressures are

shown as a function of lateral distance to either side of the airplane ground track. The data symbols represent the average of measurements from a large number of microphones for 4 flights and 13 flights of the XB-70 at 11.3 km (37 000 ft) and 18.4 km (60 000 ft), respectively. Also shown in the figure are the calculated curves and lateral "cutoff" distances with current theory being used and a standard atmosphere with no wind being assumed. Again good agreement is noted to exist between theory and experiment. In addition, both theory and experiment show that the boom overpressures are highest on the ground track and decrease with increasing lateral distance, until the shock waves are refracted at the lateral cutoff. (See ref. 5.)

Comparisons of the calculated and measured lateral extent of the sonic-boom patterns as a function of airplane altitude and Mach number for steady flight in a standard atmosphere are given in figure 5. The data points represent averages of a number of measurements involving various airplanes. The widths of the sonic-boom patterns on the ground increase with increasing altitude and Mach number. For example, at an altitude of 6.1 km (20 000 ft) and $M = 1.5$ the total width of the pattern is 20 n. mi. At 18.4 km (60 000 ft) and $M = 2.0$ the pattern width is about 60 n. mi. However, as is illustrated by the two sketches at the top of the figure, supersonic flights at low altitude result in narrow width patterns having higher overpressures, whereas at higher altitudes the pattern widths are much broader but with lower ground overpressures. Good agreement is noted to exist between measured and calculated values. The hypersonic airplanes will operate at altitudes and Mach numbers beyond the current experience. However, there is no reason to believe that theory would not provide reasonable estimates of the pattern width for this flight regime.

SONIC-BOOM MINIMIZATION

The discussions thus far have related to the nominal ontrack and lateral sonic-boom pressure distributions and it has been shown that sonic-boom effects are minimized through increased distance between the airplane and the ground. Minimizing the sonic booms through airplane design modifications have also been investigated (refs. 5 and 6). The basic approaches that have been considered are illustrated in the sketches of figure 6. Sonic-boom minimization can be achieved through a reduction in the overpressure or an increase in the signature rise time, each of these parameters being significant with regard to human and structural response (ref. 7). As illustrated in the left-hand sketches of figure 6, reduced overpressures can be obtained by reducing the size of the airplane (that is, low airplane weights) or by proper shaping of the airplane geometry to provide a modified signature (a flat top signature). These two approaches have been given much consideration in the past and reduction in bow-wave overpressures of the order of about 30 percent seems obtainable.

More recent minimization techniques involving increasing rise times have been investigated (ref. 8). If the rise time of the signature could be increased to the point where a sine wave would result instead of an N-wave, the sine-wave pressure signature would not be audible to an outdoor observer although building responses would still result. In order to obtain finite rise times of the order of 10 to 15 milliseconds, the airplane length would have to be increased by at least a factor of 3 (to about 310 m (1000 ft)) over the greatest length now being considered. This in itself is a very impractical approach. Another means would be to alter the airstream so that the same effects associated with the increased length are obtained. This could be accomplished by the addition of heat or other forms of energy. Recent studies (refs. 5 and 8) regarding the airstream alteration or "phantom body" concept suggest that large amounts of heat or energy are required (at least the equivalent of the output from four more propulsion engines) to obtain finite rise-time signatures.

EFFECTS OF THE ATMOSPHERE

The effect of the atmosphere on sonic-boom propagation is to cause variations in the measured signatures as illustrated by the data of figure 7. (See ref. 9.) The variations in the bow-wave overpressures as measured along the instrumented linear array of 2438 m (8000 ft) are shown for an airplane in steady level flight. The line represents the nominal overpressure calculated for a standard atmosphere with no wind. Overpressure variation along the ground track is cyclic in nature. The high overpressures are usually associated with peaked signatures, whereas the lower pressures are associated with rounded signatures. These signature distortions are attributed to the lower layers of the atmosphere. The phenomena are thus statistical in nature and they occur either as a function of time or distance.

A summary of the variations of the ontrack overpressures for steady level flight resulting from the atmosphere is given in figure 8. This statistical analysis comprises most of the planned sonic-boom experiments that have been conducted in this country. Data are included for a wide range of airplanes, a Mach number range from 1.2 to 3.0, and an altitude range from 3.04 km (10 000 ft) to above 21.4 km (70 000 ft). A total of 12 406 data samples have resulted from 1625 supersonic flights. Although the number of data samples would be considered small from a statistical standpoint, they are large from an experimental standpoint.

Plotted in figure 8 is a relative cumulative frequency distribution and histogram for ontrack measurements showing the probability of equaling or exceeding the ratio of the measured overpressure to the calculated or nominal overpressure for steady flight in a standard atmosphere. For this type of presentation, all the data would fall in a straight line if the logarithm of the data fitted a normal distribution. Rounded signatures of the

wave form shown in the figure are usually associated with overpressure ratios less than 1. Nominal or N-wave signatures are observed on the average, and peaked signatures of higher overpressures are observed usually at ratios greater than 1. The data of figure 8 indicate that variation in the sonic-boom signatures as a result of the effects of the atmosphere can be expected during routine operations.

EFFECTS OF AIRPLANE MANEUVERS

Sonic-boom enhancement can result from various airplane maneuvers (ref. 3). In figure 9 are illustrated three types of maneuvers which could result in pressure buildups at ground level (a longitudinal acceleration, a 90° turn, and a pushover maneuver). In each maneuver, pressure buildups occur in the localized regions suggested by the shaded areas shown in the sketches of figure 9. It should be pointed out that although the airplane and shock waves are moving, the area on the ground in which pressure buildups occur are fixed and do not move with the airplane. The pressure buildups in these focus areas are a function of the type of maneuver and acceleration involved. Operationally, pressure buildups will always result for the longitudinal maneuver when the airplane accelerates from subsonic to supersonic speeds. The effects can be minimized by reducing acceleration rates. The pressure buildup areas associated with turns and pushover maneuvers can be minimized or avoided by reducing acceleration or by simply avoiding the maneuver.

The overpressure buildups, or focus factors, in these maneuvers are shown as a function of airplane acceleration in figure 10. The information contained in this figure is a result of flight experiments conducted in this country (refs. 3 and 10) and in France (refs. 11 and 12). The data points shown represent the highest levels measured thus far for longitudinal accelerations and turning maneuvers. The hatched boundary, therefore, would represent the current upper bound. At the lower values of acceleration, which are usually associated with longitudinal accelerations, the overpressure in the focus is of the order of from about 2 to 5 times the nominal overpressure for steady level flight at the same altitude and Mach number. For a turn maneuver involving a 2g acceleration, a focus factor of up to 9 has been measured.

LOW SUPERSONIC OPERATIONS

The discussions thus far have been concerned with airplane operations in which the shock waves extend to the ground and are reflected from the ground as illustrated in the upper right-hand sketch of figure 11. Now consider low supersonic operations where the shock waves extend down toward but do not intersect the ground, as suggested by the sketch in the upper left of the figure. The range of Mach numbers and altitudes over

which cutoff Mach number operations can be performed is shown in figure 11, with steady level flight in a standard atmosphere with no wind being assumed. (See ref. 13.) Flights at Mach numbers to the left of the hatched curve will result in no booms reaching the ground, whereas flights at Mach numbers to the right of the curve will result in booms reaching the ground. In figure 11, the highest speed at which the airplane could operate in a standard atmosphere without producing booms at the ground is about $M = 1.15$. In the real atmosphere, variations in sound speed gradient do exist because of temperature and winds. For example, headwinds at altitude and higher temperatures at the surface would increase M_{cutoff} ; conversely, tailwinds at altitude and colder temperatures at the surface would decrease M_{cutoff} . The practical range of M_{cutoff} for a fairly wide range of atmosphere (ref. 14) is shown to vary from about 1.0 to about 1.3.

A description of the cutoff phenomenon may be obtained by examining the ray-shock diagram shown in figure 12. The top sketch relates to the operating conditions in which the airplane velocity over the ground V_g is greater than the sound speed at the ground a_g . The airplane is shown moving in a direction from right to left and, for simplicity, only the bow wave is shown. The shock wave extends to the ground and is reflected upward. As the disturbances that form this shock wave are emitted from the airplane, they travel toward the ground along ray paths indicated by the solid lines. These rays intersect the ground and are reflected upward, as illustrated by the dashed lines. Any number of such rays can be drawn from the airplane at different times along the flight path. Two consecutive rays are essentially parallel and tend to converge only slightly as they approach the ground.

The bottom sketch of figure 12 relates to the conditions when the airplane speed over the ground V_g is less than the sound speed at the ground a_g . These conditions would be associated with an airplane flying below the cutoff Mach number. The rays have a greater curvature than those for the higher airplane speed and are totally refracted at an altitude above the ground. The rays, which have been drawn for various positions of the airplane along the flight track, become tangent to each other at the cutoff altitude. The areas between adjacent rays, as indicated by the shaded region, decrease until they theoretically approach 0 where the rays become tangent. The pressures are expected to markedly increase in the regions where the area between the rays is decreasing. Thus, a caustic, or line focus, is formed where the rays become tangent at the cutoff altitude.

Recent experiments have been made to define the pressure field associated with the shock-wave extremities for flights at low supersonic Mach numbers (ref. 5). The results shown in figure 13 are indicative of the sonic-boom phenomenon associated with flights at cutoff Mach number. The experiments utilized a 457-m-high (1500 ft) tower with microphones placed at 30-m (100 ft) intervals along the tower and also along the ground. The airplane was flown so that the shock patterns terminated within the tower heights. The

solid lines represent shock waves, and the dashed lines represent the refracted waves. Also shown in the figure are the measured sonic-boom signatures that were observed as the shock-wave system moved across the microphones on the tower. In this particular experiment, the shock extremity was positioned so that pressure disturbances in the supersonic, sonic, and acoustic regions were measured. At the top of the tower, a normal N-wave sonic-boom signature was measured that included the incident bow and tail shocks and their refractions. At midtower, which was the approximate location of the shock extremity, a U-shape (caustic) signature was measured for which the amplitudes were larger than those associated with the N-wave signatures observed in the supersonic flow region. Near the base of the tower, below the shock extremity, the signatures are rounded or sinusoidal in shape and suggest acoustic disturbances.

The bow overpressure from signatures such as those shown in figure 13 for the flight operations near cutoff Mach number are presented in figure 14. The measurements, which represent the average values obtained from the ground and tower microphones, are from steady level flights of the F-104 airplane at 10.26 km (33 700 ft). The solid curve represents the overpressure variations suggested by theory and the data points represent the measurements. Because M_{cutoff} varied somewhat (from about $M = 1.09$ to 1.12) from flight to flight and over the 3-day test period because of variations in atmospheric conditions, the measured data have been normalized so that the overpressures associated with the caustic or U-shape signatures are located at a cutoff Mach number of $M = 1.1$.

At Mach numbers below $M = 1.1$ very low overpressure levels were measured, and these were associated with the acoustic type of signature shown at the top left of figure 14. At Mach numbers greater than $M = 1.1$, normal N-wave types of signatures were observed from which the pressure increased gradually with increasing Mach number as predicted by theory. Near $M = 1.1$, U-shape waveforms were generally observed. The predicted overpressure values would approach infinity because of the presence of the caustic line. The measured caustic signatures generally indicate overpressure enhancement compared with those associated with the higher Mach numbers. The highest enhancement factor suggested by the data of figure 14 is 3. The experiments also suggested that very stable conditions of the atmosphere, especially the lower layers, are required to produce the U-shaped signatures of high overpressures.

SUMMARY OF RESULTS

The information contained in the present paper is summarized in figure 15, in which are shown the variations with Mach number of the nominal overpressures for cruising flight in the low supersonic, supersonic, and hypersonic operating regimes. The hatched area represents the amount of boom minimization that may be attainable through airplane design.

Above a Mach number of about 2, increasing Mach number results in decreasing overpressure. The decrease in overpressure results primarily from the increased altitudes required for flight efficiency and range as the speed increases. In attaining cruising Mach numbers, however, both the supersonic and hypersonic vehicles would pass through the low altitude Mach number region, where higher overpressures would be experienced. As the cruise Mach number is increased, sonic-boom minimization through airplane design is shown to be less effective.

Perturbations on the nominal values can be expected as a result of routine operations in the atmosphere. In addition, pressure enhancement resulting from maneuvering flight would also increase the nominal overpressure values. Certain of the overpressure buildups resulting from maneuvering flight are unavoidable; however, others are avoidable or can be minimal. Studies, thus far, suggest that the atmospheric and maneuver pressure enhancements are not additive. In conducting low supersonic operations intended to prevent shock waves from extending to the ground, great care must be exercised to match airplane operations to local weather conditions to avoid the sudden onset of large amplitude transonic booms.

REFERENCES

1. Carlson, Harry W.; McLean, F. Edward; and Middleton, Wilbur D.: Prediction of Airplane Sonic-Boom Pressure Fields. Conference on Aircraft Operating Problems, NASA SP-83, 1965, pp. 235-244.
2. Maglieri, Domenic J.; and Hilton, David A.: Significance of the Atmosphere and Aircraft Operations on Sonic-Boom Exposures. Conference on Aircraft Operating Problems, NASA SP-83, 1965, pp. 245-256.
3. Seebass, A. R., ed.: Sonic Boom Research. NASA SP-147, 1967.
4. Miller, David S.; Morris, Odell A.; and Carlson, Harry W.: Wind-Tunnel Investigation of Sonic-Boom Characteristics of Two Simple Wing Models at Mach Numbers From 2.3 to 4.63. NASA TN D-6201, 1971.
5. Schwartz, Ira R., ed.: Third Conference on Sonic Boom Research. NASA SP-255, 1971.
6. Schwartz, Ira R., ed.: Second Conference on Sonic Boom Research. NASA SP-180, 1968.
7. Stanford Res. Inst.: Sonic Boom Experiments at Edwards Air Force Base. NSBEO-1-67 (Contract AF 49(638)-1758), NTIS, U.S. Dep. Com., July 28, 1967. (Available from DDC as AD 655 310.)
8. Miller, David S.; and Carlson, Harry W.: A Study of the Application of Heat or Force Fields to the Sonic-Boom-Minimization Problem. NASA TN D-5582, 1969.
9. Garrick, I. E.; and Maglieri, D. J.: A Summary of Results on Sonic-Boom Pressure-Signature Variations Associated With Atmospheric Conditions. NASA TN D-4588, 1968.
10. Maglieri, Domenic J.; Hilton, David A.; and McLeod, Norman J.: Experiments on the Effects of Atmospheric Refraction and Airplane Accelerations on Sonic-Boom Ground-Pressure Patterns. NASA TN D-3520, 1966.
11. Vallee, [J.]: Mesure de l'Intensité des Bangs Soniques Engendrés par un Avion Volant en Palier Accéléré Supersonique. Rapp. d'Étude No. 272, Centre d'Essais en Vol, Annexe d'Istres, Oct. 1967.
12. Vallee, J.: Étude Expérimentale des Focalisations de Bangs Soniques Engendrées par le Vol Supersonique en Accélération Rectiligne ou en Virage d'un Avion Mirage IV à l'Altitude de 11 000 m. Rapp. d'Étude No. 277, Centre d'Essais en Vol, Annexe d'Istres, May 1969.

13. Randall, D. G.: Methods for Estimating Distributions and Intensities of Sonic Bangs.
R. & M. No. 3113, Brit. A.R.C., 1959.
14. Kane, Edward J.; and Palmer, Thomas Y.: Meteorological Aspects of the Sonic Boom.
SRDS Rep. No. RD64-160 (AD 610 463), FAA, Sept. 1964.

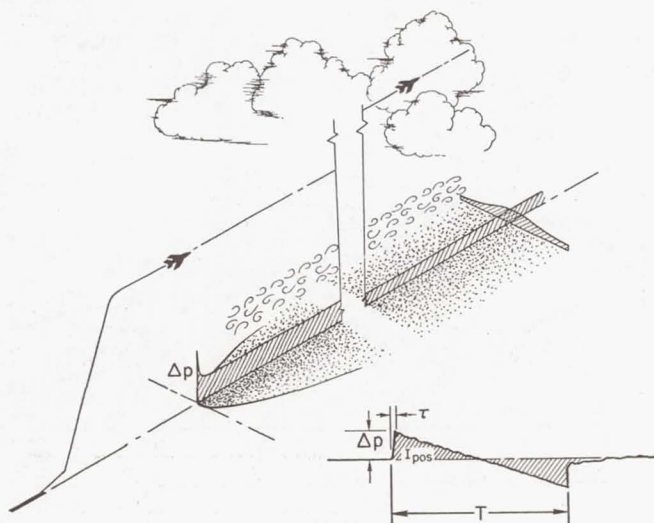


Figure 1.- Sonic-boom ground-pressure patterns.

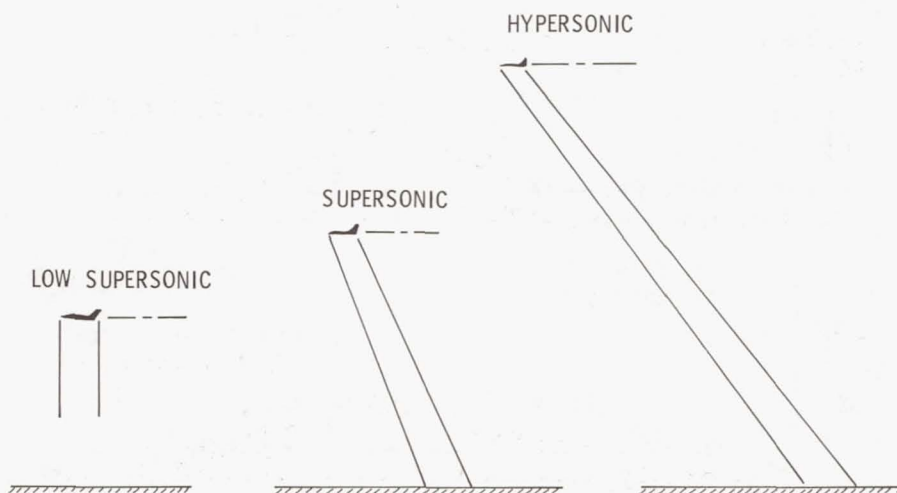


Figure 2.- Schematic of shock waves associated with three operating regimes.

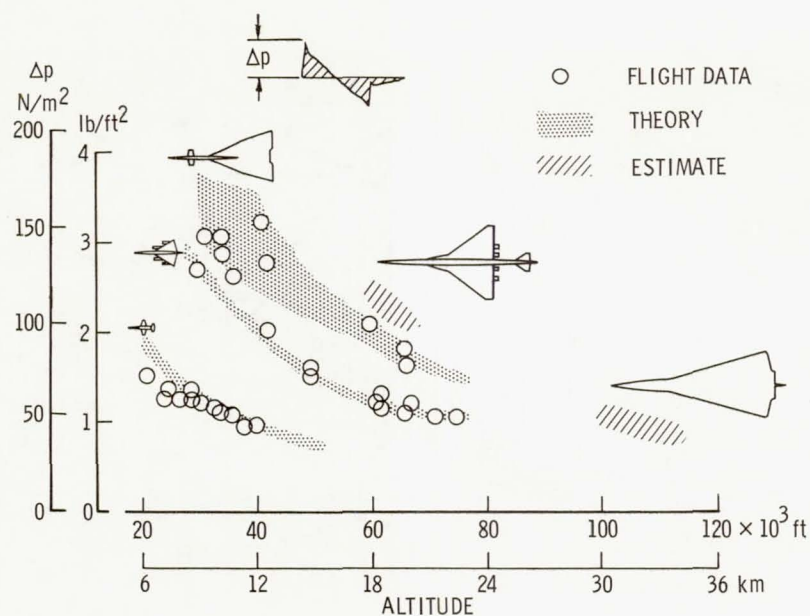


Figure 3.- Sonic-boom overpressure characteristics of various supersonic airplanes as a function of altitude.

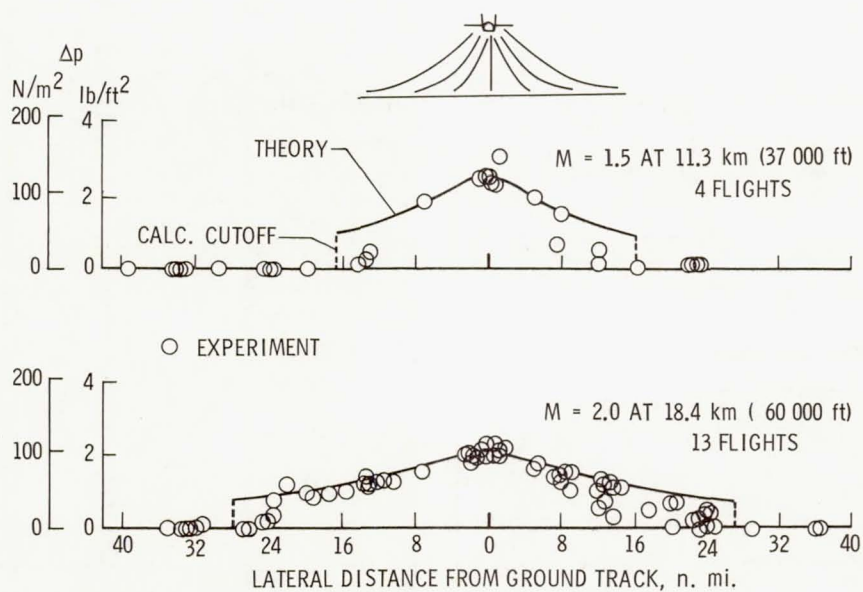
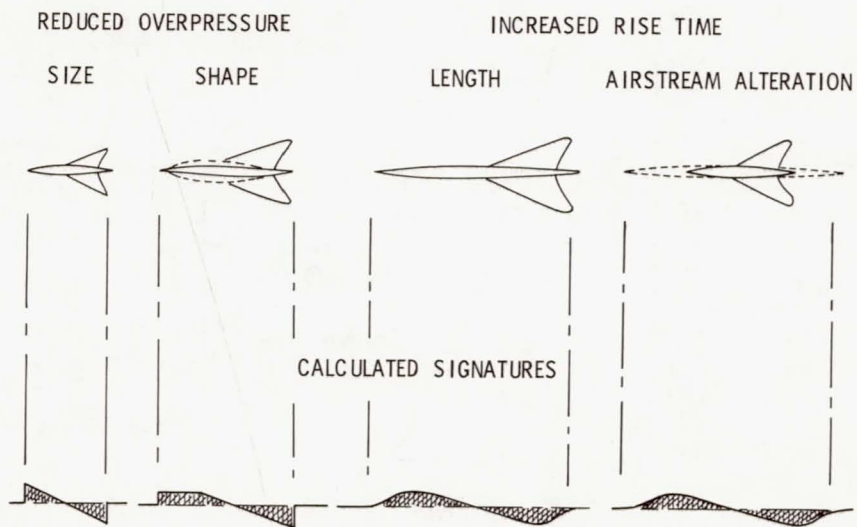
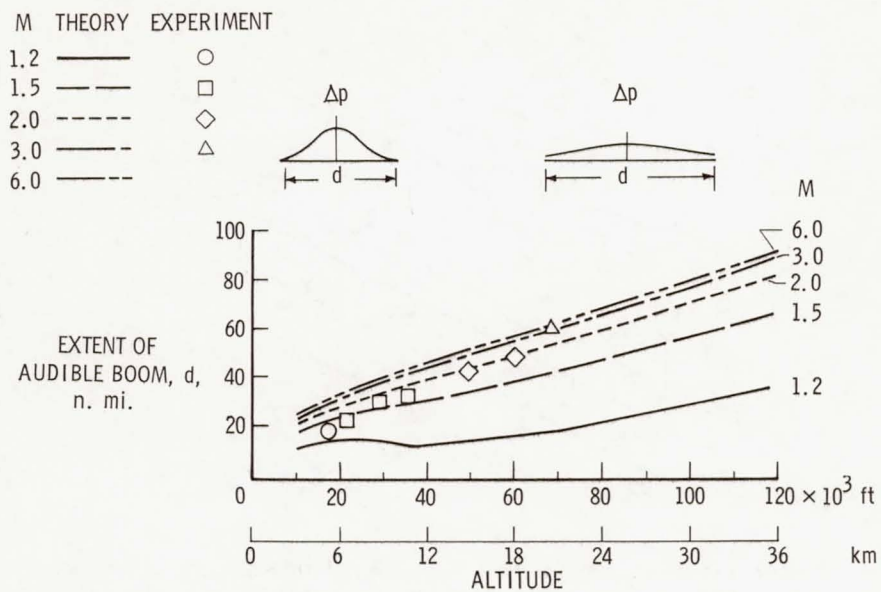


Figure 4.- Sonic-boom overpressures for the XB-70 airplane as a function of lateral distances for two different flight conditions.



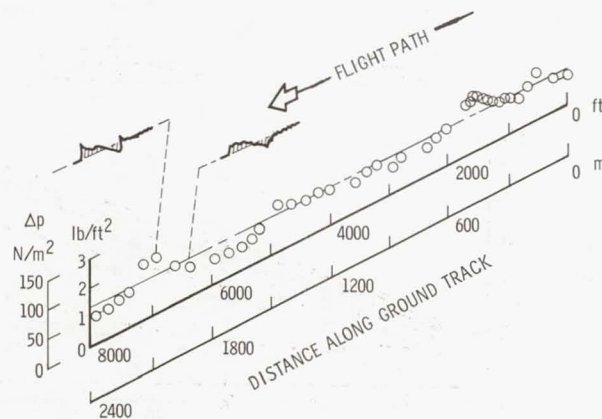


Figure 7.- Sonic-boom overpressures as a function of distance along the ground track for a fighter airplane in steady flight at a Mach number of 1.3 and an altitude of 9.3 km (30 500 ft) along with sample signatures.

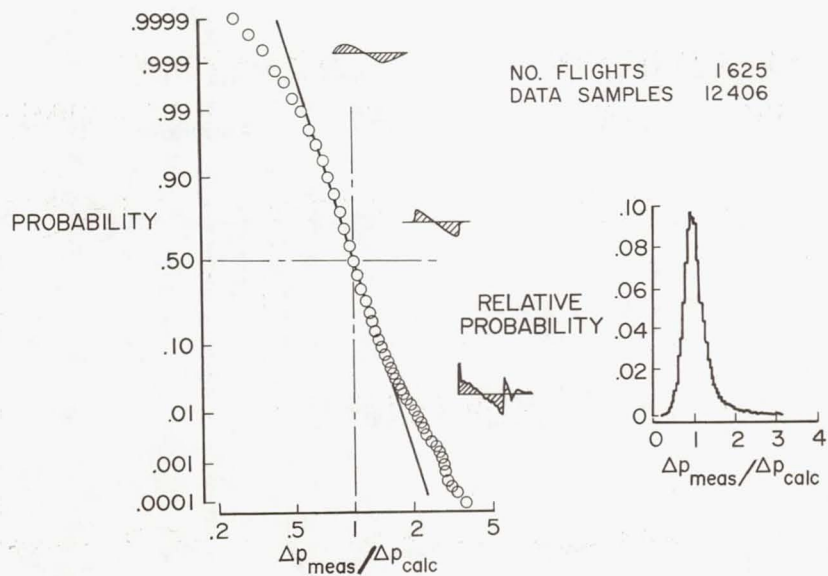


Figure 8.- Probability of exceeding given values of measured to calculated sonic-boom ground overpressures along the airplane flight track.

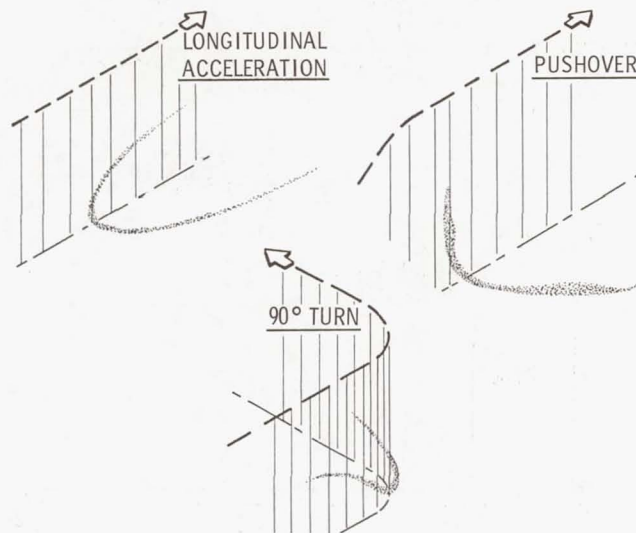


Figure 9.- Areas on the ground exposed to focused sonic booms resulting from three different airplane maneuvers.

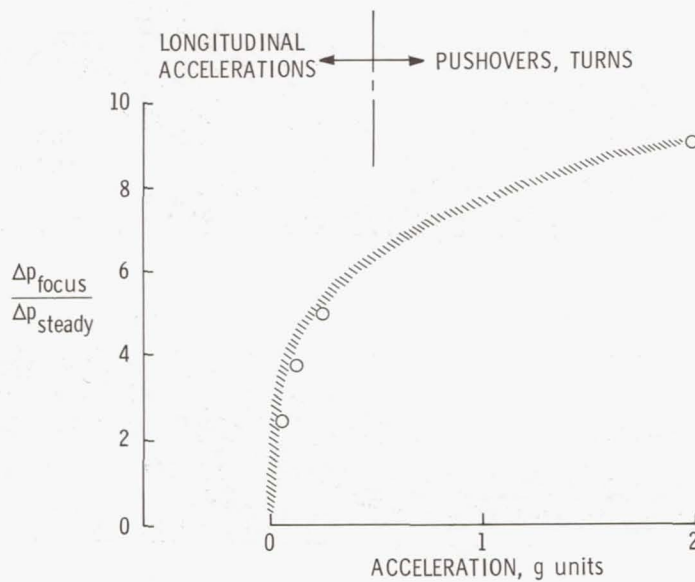


Figure 10.- Effect of airplane acceleration on sonic-boom overpressure builds in maneuvering flight.

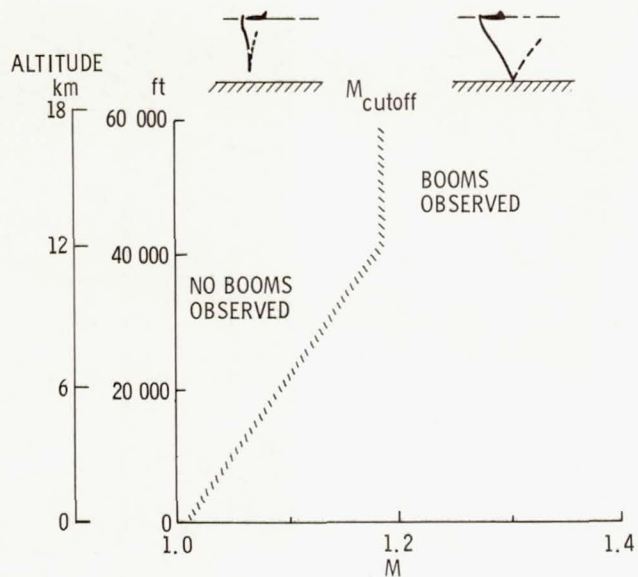


Figure 11.- Combinations of airplane Mach number and altitude for complete sonic-boom cutoff for steady level flight in a standard atmosphere with no wind.

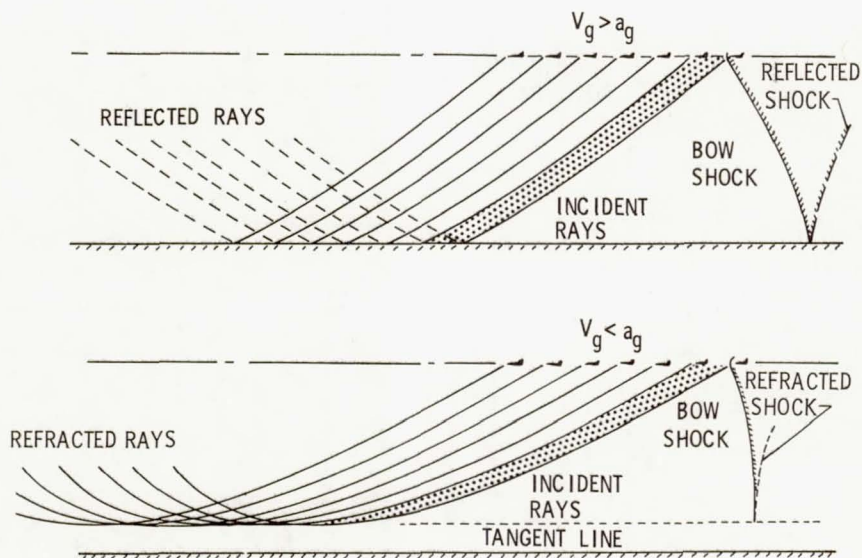


Figure 12.- Ray-shock diagram for airplane operating at Mach numbers above and below the sonic-boom cutoff Mach number.

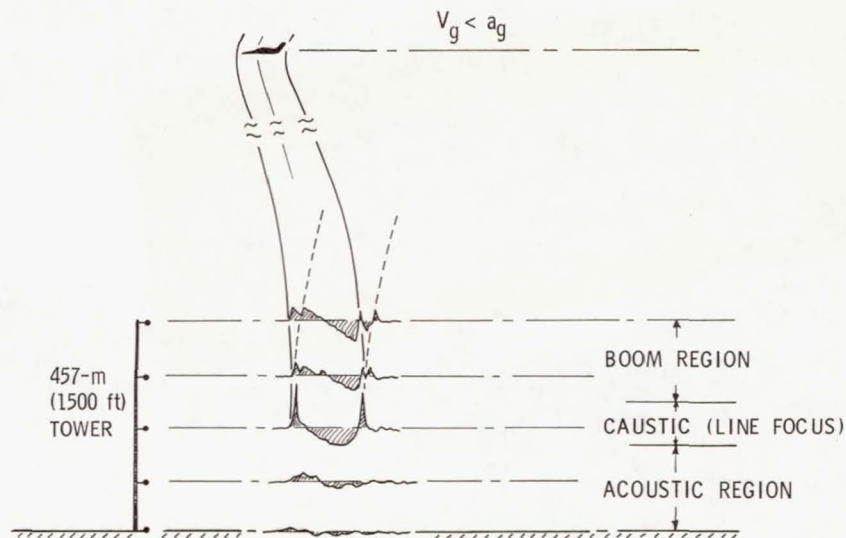


Figure 13.- Measured sonic-boom signatures at various heights above the ground for an F-104 in steady level flight at cutoff Mach number. Altitude, 10.26 km (33 700 ft); $M = 1.095$.

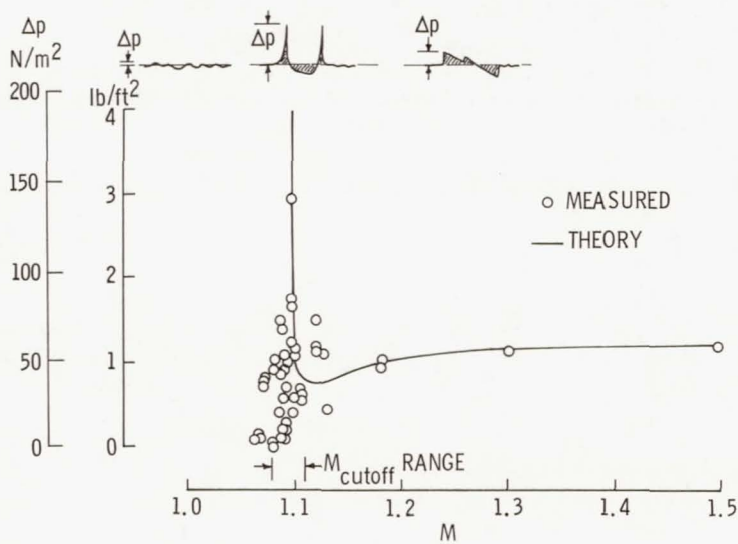


Figure 14.- Variation of sonic-boom overpressure with airplane Mach number for an F-104 in steady level flight at 10.26 km (33 700 ft).

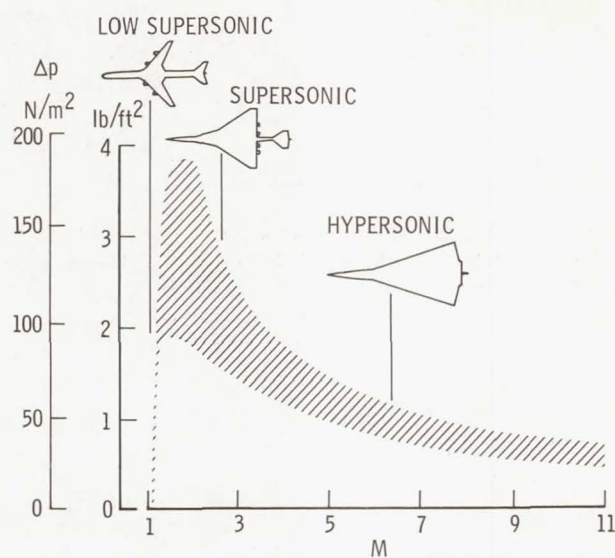


Figure 15.- Variation of sonic-boom overpressure along ground track with airplane cruise flight speed.

NATIONAL AERONAUTICS AND SPACE ADMINISTRATION

WASHINGTON, D. C. 20546

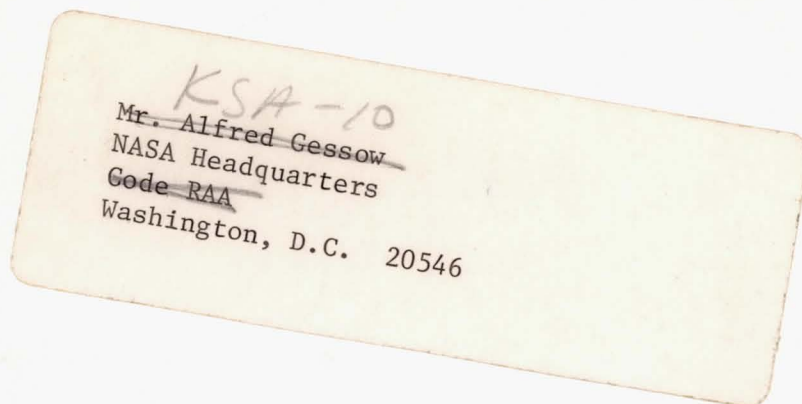
OFFICIAL BUSINESS

PENALTY FOR PRIVATE USE \$300

FIRST CLASS MAIL



POSTAGE AND FEES PAID
NATIONAL AERONAUTICS AND
SPACE ADMINISTRATION



POSTMASTER: If Undeliverable (Section 158
Postal Manual) Do Not Return

"The aeronautical and space activities of the United States shall be conducted so as to contribute . . . to the expansion of human knowledge of phenomena in the atmosphere and space. The Administration shall provide for the widest practicable and appropriate dissemination of information concerning its activities and the results thereof."

— NATIONAL AERONAUTICS AND SPACE ACT OF 1958

NASA SCIENTIFIC AND TECHNICAL PUBLICATIONS

TECHNICAL REPORTS: Scientific and technical information considered important, complete, and a lasting contribution to existing knowledge.

TECHNICAL NOTES: Information less broad in scope but nevertheless of importance as a contribution to existing knowledge.

TECHNICAL MEMORANDUMS: Information receiving limited distribution because of preliminary data, security classification, or other reasons.

CONTRACTOR REPORTS: Scientific and technical information generated under a NASA contract or grant and considered an important contribution to existing knowledge.

TECHNICAL TRANSLATIONS: Information published in a foreign language considered to merit NASA distribution in English.

SPECIAL PUBLICATIONS: Information derived from or of value to NASA activities. Publications include conference proceedings, monographs, data compilations, handbooks, sourcebooks, and special bibliographies.

TECHNOLOGY UTILIZATION PUBLICATIONS: Information on technology used by NASA that may be of particular interest in commercial and other non-aerospace applications. Publications include Tech Briefs, Technology Utilization Reports and Technology Surveys.

Details on the availability of these publications may be obtained from:

SCIENTIFIC AND TECHNICAL INFORMATION OFFICE

NATIONAL AERONAUTICS AND SPACE ADMINISTRATION

Washington, D.C. 20546